

Magnetic Resonance Imaging of Catalysts and Catalytic Processes

L. F. GLADDEN, M. D. MANTLE and A. J. SEDERMAN

Department of Chemical Engineering, University of Cambridge, Pembroke Street, Cambridge CB2 3RA, UK

Magnetic resonance (MR), in the form of solid-state nuclear magnetic resonance (NMR) spectroscopy, is well established as a research tool for investigations of the structures of solid catalysts and molecular species adsorbed on them. However, during the past decade there has been increasing interest in using magnetic resonance imaging (MRI) techniques to study, in particular, flow fields inside reactors. These studies have recently been extended to measurements of chemical conversion within model reactor systems. The real power of MR techniques is that by bringing together spectroscopy, diffusion, micro-imaging, and flow imaging, they provide a non-invasive, chemically specific measurement technique which can characterize a system over length scales ranging from the angstrom- to the centimeter scale. In this review, recent developments in MRI pulse sequences are summarized and applications to investigations of both hydrodynamics and catalytic conversion within catalysts and catalytic reactors are presented.

Materials: 2M2B; 2-methyl-2-butene; HZSM-5; zeolite with MFI framework (IUPAC nomenclature); NaCaA; zeolite with LTA framework (IUPAC nomenclature); NaX; zeolites with FAU framework (IUPAC nomenclature); Pd/Al₂O₃; alumina supported palladium catalyst; TAME; tert-amyl methyl ether or 2-methoxy-2-methylbutane; TAOH; tert-amyl alcohol or 2-methyl-butan-2-ol

Abbreviations: BET; Brunauer Emmett Teller; adsorption isotherm model; BLIPPED EPI; MR pulse sequence; CFD; computational fluid dynamics; CSI; chemical shift imaging; MR pulse sequence; DANTE; delays alternating with nutations for tailored excitation; MR pulse sequence; DANTE TOF; delays alternating with nutations for tailored excitation time of flight; MR pulse sequence; DEPT; distortionless enhancement by polarization transfer; MR pulse sequence; EPI; echo planar imaging; MR pulse sequence; FID; free induction decay; FLASH; fast low-angle shot; MR pulse sequence; FSE; fast spin echo; MR pulse sequence; GERVAIS; gradient echo rapid velocity and acceleration imaging sequence; MR pulse sequence derived from EPI; GRASE; gradient and spin echo; MR pulse sequence; MBEST-EPI; modulus blipped echo planar single-pulse technique; MR pulse sequence derived from EPI; MR; magnetic resonance; MRI; magnetic resonance imaging; NMR; nuclear magnetic resonance; Pe; dimensionless group characterizing flow; PEPI, π -EPI; MR pulse sequence derived from EPI; PFG; pulsed field gradient; MR pulse sequence; PGSE; pulsed gradient spin echo; MR pulse sequence; RARE; rapid acquisition with relaxation enhancement; MR pulse sequence; Re; Reynolds number; dimensionless group characterizing flow; REPI; radial EPI; MR pulse sequence derived from EPI; SEMI-RARE; single excitation multiple image rapid acquisition with relaxation enhancement; MR pulse sequence derived from RARE; SNAPSHOT; MR pulse sequence; SPRITE; single point ramped imaging with T_1 enhancement; MR pulse sequence; TMS; tetramethylsilane; TOF; time of flight; TSE; turbo spin echo; MR pulse sequence

Nomenclature: *Greek*, Δ ; observation time in transport measurement pulse sequence (s), Φ ; net phase offset (rad), γ ; gyromagnetic ratio ($\text{rad s}^{-1}\text{T}^{-1}$), δ ; time for which pulsed magnetic field gradient is applied (s), ϕ ; phase offset (rad), χ ; liquid holdup, χ_{dynamic} ; dynamic liquid holdup, χ_s ; surface wetting, θ ; pulse angle (rad), ρ ; spin density (m^{-3}), τ ; delay time (s), ω ; angular frequency (rad s^{-1}), ω_0 ; resonance or Larmor frequency (rad s^{-1}); *Roman*, B ; magnetic field (T), B_0 ; external magnetic field (T), G ; magnetic field gradient for imaging (T m^{-1}), M ; magnetization (A m^{-1}), M_0 ; equilibrium magnetization (A m^{-1}), P_s ; displacement propagator, S ; acquired signal intensity, T_1 ; spin–lattice relaxation time (s), T_2 ; spin–spin relaxation time (s), T_2^* ; time constant of the free induction decay in the presence of B_0 inhomogeneities (s), X ; conversion, a ; acceleration (m s^{-2}), e ; component of the stress tensor (s^{-1}), g ; magnetic field gradient employed in transport measurements (T m^{-1}), \mathbf{k} ; reciprocal space vector employed in imaging (m^{-1}), \mathbf{q} ; reciprocal space vector employed in transport measurements (m^{-1}), \mathbf{r} ; position vector (m), t ; time (s), t_d ; delay time in the spin–echo pulse sequence (s), v ; velocity (m s^{-1}), x , y , z ; Cartesian laboratory-frame coordinates, x' , y' , z' ; Cartesian rotating-frame coordinates

I. Introduction

Until the early 1990s, application of magnetic resonance (MR) to studies of *in situ* catalysis was almost exclusively the domain of the chemist employing increasingly sophisticated solid-state MR pulse sequences to investigate the mechanisms of catalytic processes. Such work has been reviewed extensively by many workers, including Packer (1), Dybowski *et al.* (2), Roe *et al.* (3), Baba and Ono (4), Fraissard (5), Haw (6), Ivanova (7), Parker (8), van der Klink (9), Hunger and Weitkamp (10), and Han *et al.* (11). These reports of *in situ* catalysis address the molecular-scale events occurring during the catalytic process and give valuable information regarding structure–function relationships in catalytic materials. To a lesser extent, spatially unresolved measurements of molecular diffusion have been made within catalysts by use of pulsed field gradient (PFG) techniques (e.g., Kärger and Freude (12)). The present review is an evaluation of the role of MR in investigations of *in situ* catalysis from a quite different perspective—that of imaging.

Traditionally the technique of the medical physicist, magnetic resonance imaging (MRI) has long been used to investigate the internal structure of the human body and the transport processes occurring within it; for example, MRI has been used to characterize drug transport within damaged tissue and blood flow within the circulatory system. It is therefore a natural extension of medical MRI to implement these techniques to study flow phenomena and chemical transformations within catalysts and catalytic reactors.

Figure 1 is a schematic illustration of the length scales probed by various MR techniques and the areas of catalysis that can therefore be addressed. Across these length scales, the ability of MR to quantify both structure and dynamics, non-invasively and with chemical specificity within optically opaque systems, offers great opportunities for increasing our understanding of catalysts and catalytic reactors. Existing MRI investigations tend to fall into two broad categories:

Microimaging studies of single catalyst pellets. In these investigations, spatial resolutions of $\sim 30\text{--}50\ \mu\text{m}$ are typically achieved, and steady- and unsteady-state

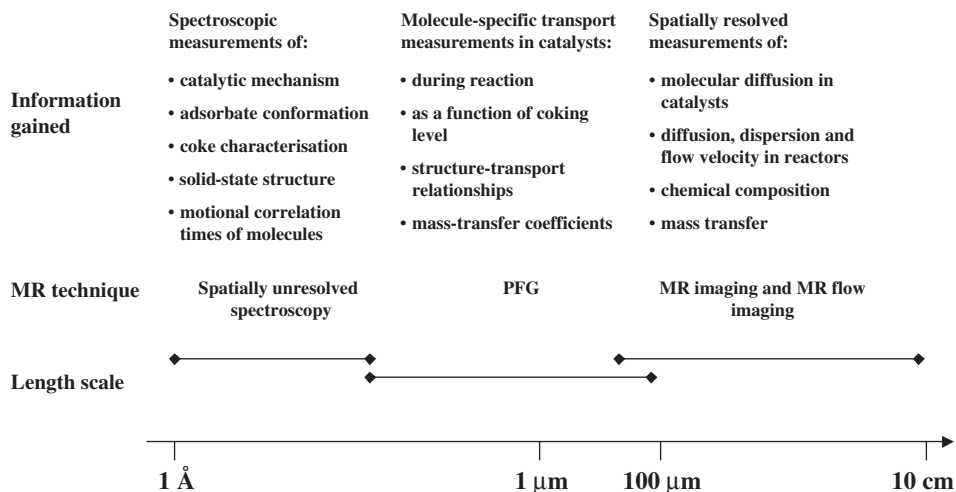


FIG. 1. The MR Toolkit: MR techniques yield information about chemical and physical processes over length scales of Å to cm. Imaging pulse sequences may be integrated with spectroscopy and molecular diffusion measurements providing maps of chemical composition and molecular transport phenomena at spatial resolutions of 30–500 μm.

liquid distributions within the individual pellets have been imaged. A variety of applications has been reported. For example, the characterization of processing–structure–function relationships in catalyst manufacture and, in particular, the effect of catalyst manufacturing processes on the micro- and meso-scale pore structure of the resulting catalyst pellet and hence the molecular transport processes occurring within the catalyst. The same methods also lend themselves to investigation of liquid transport processes during catalyst preparation, such as liquid and ion transport occurring during a catalyst preparation by ion exchange. With respect to the catalytic reaction process itself, liquid re-distribution as a result of temperature gradients caused by chemical reaction has been demonstrated. Coke deposition can also be followed.

Microimaging and flow imaging of reactors. MRI has found considerable success in imaging the internal phase distributions and liquid flow fields inside reactors, at spatial resolutions of 100–500 μm. The dimensions of systems studied are constrained to the dimensions of the bore of the superconducting magnet used. In vertical bore systems, standard magnet hardware allows reactor diameters of 2.5–6 cm to be investigated, with a similar field-of-view along the direction of the axis of the magnet. In the case of horizontal bore systems, medical imaging magnet technology provides magnet bores of ~30 cm in diameter, which provide a field-of-view of ~20 cm in vertical and horizontal directions. Although these constraints do not allow us to study the large fixed-bed catalytic processes used in plants in, say, the petroleum refining sector, we are able to investigate scaled-down reactors of dimensions typical of those used in industrial research and

development. Furthermore, with increasing interest in the design of micro-reactor technologies, many new reactor designs do actually fit inside the magnet at full scale.

The motivation to extend these measurements and, in particular, to integrate MR spectroscopy, transport measurements, and imaging techniques is strong. In principle, we should be able to study the behavior of a single catalyst pellet within a reactor while it is operating within the fixed bed and observe directly the effects of catalyst form (i.e., pellet size and shape) and reactant–solid contacting patterns within the reactor on overall catalyst activity, selectivity, and lifetime. MR offers the opportunity to bridge the length scales from the angstrom- to the centimeter scale by incorporating MR spectroscopy into imaging strategies, thereby spatially resolving spectral acquisition. Currently, such imaging experiments are in their infancy and yield spatial resolutions of the order of 50–600 μm , sufficient to show, for example, the spatial variation of conversion within a fixed-bed reactor. To use MR routinely in *in situ* studies of catalysis, new MR techniques will have to be developed and implemented to retain the inherent, quantitative nature of the MR measurement in catalyst and reactor systems, which are characterized by strong variations in magnetic susceptibility and fast nuclear spin relaxation time processes. In this regard, catalyst and reactor systems are very different from the human body in terms of the sample response to the radio frequency excitation and pulsed magnetic field gradients used in an MR experiment; consequently, medical MRI strategies do not translate directly into catalysis research. It is also worth reiterating the known limitations of MR techniques regarding systems that can be investigated. From a practical point of view, large ferromagnetic objects cannot be handled within and close to a superconducting magnet. However, units comprising aluminum and brass can be used within the magnet. With respect to the sample itself, the ability to characterize a given system is very material-specific. Ferromagnetic and paramagnetic particles act to distort the local magnetic fields and influence relaxation times within the sample, thereby making all investigations based upon quantitative analysis extremely challenging. However, each system should be considered on a case-by-case basis. For example, the strong influence of paramagnetic ions on signal intensity can be successfully exploited to follow the evolution of redox reactions with time.

The aim of this review is to introduce the language of MRI to the catalysis community and to describe the early achievements in this field. The structure of this article is as follows:

- (a) Section II introduces the principles of MRI methods and describes the MRI pulse sequences currently used in *in situ* studies of chemical reactors.
- (b) Sections III and IV review work done in imaging fluid distribution and transport at the length scale of catalyst pellet (Section III) and reactor (Section IV).
- (c) Section V brings together the work done in spatially resolving spectroscopic measurements within model reactor environments; these experiments allow us to follow reactions *in situ*.
- (d) Section VI provides a brief forward look on the future role of MRI in catalysis research.

II. Introduction to MRI Techniques

There are two main families of MRI methods used in catalysis: microimaging and flow imaging. Microimaging usually refers to the imaging of the internal structure of a sample, perhaps with spatial mapping of chemical composition, distribution of gas and liquid, and even transport properties such as molecular diffusivity; the images typically have a spatial resolution of $\sim 30\ \mu\text{m}$. Flow imaging is usually performed at a slightly poorer spatial resolution of $\sim 100\ \mu\text{m}$, and it gives images of the flow field within the system of interest. In Section II.A, the two essential concepts required to understand an MRI experiment are described, namely, (i) the action of an applied magnetic field gradient to introduce spatial resolution into a standard spectroscopy experiment, and (ii) the nature and importance of nuclear spin relaxation processes in image acquisition. The section concludes with a description of the \mathbf{k} -space raster representation of an imaging experiment, an understanding of which is essential if the more advanced pulse sequences in MRI are to be understood. Section II.B addresses transport measurements—diffusion, dispersion, and flow. The three main data acquisition strategies are outlined. Section II.C describes how any type of image may be made selective to specific chemical species or phases within the sample. To achieve this selectivity in the image acquisition, contrast mechanisms are introduced into the data acquisition. This is achieved by exploiting differences in resonance frequency, relaxation times or molecular mobility between different phases or species within the system. Section II.D draws the reader's attention to the fact that temperature can, in principle, be mapped within the system. Section II.E develops the ideas of the \mathbf{k} -space raster further and shows how it can be used to understand "fast" MRI pulse sequences that are now being used to study unsteady-state processes in catalysis and catalytic reactors. For a detailed introduction to the principles of MR techniques the interested reader should refer to excellent texts by Callaghan (13) and Kimmich (14).

A. PRINCIPLES OF MR MEASUREMENTS

A.1. *Obtaining an Image*

The principles of MR are likely to be well known to the reader (see also the chapter by Hunger and Wang in this volume, p. 149). When a nucleus of non-zero nuclear spin quantum number is placed in an external magnetic field (typically a superconducting magnetic field of 2–10 T), its nuclear spin energy levels become non-degenerate. As a result, at the equilibrium state of the spin system, there exists a net magnetization vector aligned parallel to the direction of the external magnetic field, assumed to be along the z -direction. By exposing the system to electromagnetic energy of appropriate frequency (radio-frequency (r.f.)), a resonant absorption occurs between these nuclear spin energy levels. The specific frequency at which this resonance occurs is called the resonance (or Larmor) frequency and is proportional to the strength of the external magnetic field, B_0 , used in the experiment. The precise energy-level splitting is specific to a given isotope of an element, and the

resonance frequency (ω_0) is given by

$$\omega_0 = \gamma B_0, \quad (1)$$

where γ is the gyromagnetic ratio, which is an isotope-specific property. The precise energy-level splitting is slightly modified by the electronic environment of the nucleus under study; thus ω_0 is also modified and becomes specific to individual molecules containing the element of interest. Thus, we can take a spectrum of a mixture of chemical species and identify the presence of particular molecular species in that mixture (i.e., a conventional NMR or MR spectroscopy experiment). In principle (Section II.A.2), the measurement is quantitative. A standard way of representing the basic MR measurement is shown in Fig. 2. Initially, the net magnetization vector, \mathbf{M} , is aligned along the direction of the magnetic field. The action of the excitation pulse, in this case a pulse of r.f. applied at right angles (along x') to the direction of the superconducting field, is therefore to rotate \mathbf{M} about the x' -axis. In this example, the r.f. excitation is applied for sufficient time that \mathbf{M} is rotated to lie along the y' -axis in the x' - y' plane. If this condition is met, the r.f. pulse is referred to as a $\pi/2$ (or 90°) pulse; that is, it has rotated \mathbf{M} through $\pi/2$ rad. These processes are actually occurring in the “rotating frame” of reference (hence the primed symbol) which, in the laboratory frame, precesses about the z -axis (i.e., about \mathbf{B}_0) at the Larmor frequency. This convention is adopted to simplify the representation of the action of the r.f. pulses. In this rotating frame representation,

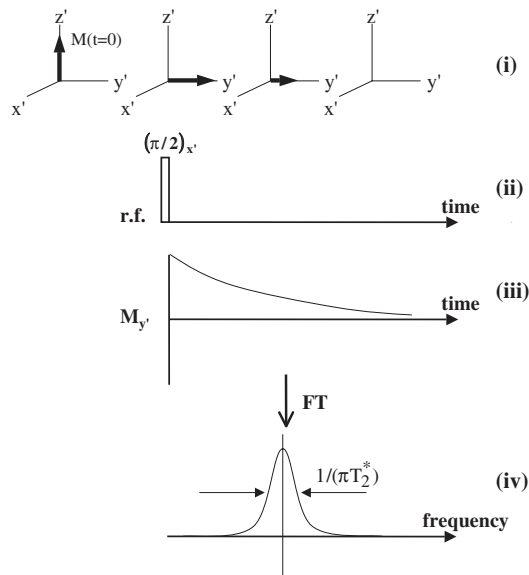


FIG. 2. The behavior of the magnetization vector (i) is shown in response to the application of a single $\pi/2$ r.f. pulse along x' , (ii). The decay of the magnetization vector in the x' - y' plane yields the received time-domain signal, called the FID, shown in (iii). The result of a Fourier transformation of the FID is the spectrum shown in (iv). For a liquid-like sample, the full-width at half-maximum-height of the spectral signal is $1/\pi T_2^*$ (Section II.A.2).

the MR time domain signal, following r.f. excitation, is measured by acquiring the signal (i.e., the magnitude of the magnetization vector) aligned along y' as a function of time; this signal will decay with time due to the recovery of the magnetization along z' and, at shorter timescales, due to the loss of phase coherence of the spin isochromats comprising the net magnetization vector along the y' -axis. (These decay processes are termed the spin–lattice and spin–spin relaxation processes and are discussed further in Section II.A.2) The decay of the magnetization along the y' -axis is recorded as a decaying voltage in a receiver coil. Fourier transformation of this time-domain signal (usually referred to as the free induction decay, FID) yields the frequency domain spectral response in which the area under the spectral peak, following appropriate calibration, gives a quantitative measure of the number of nuclear spins associated with that spectral frequency (i.e., a quantitative measure of the number of molecules of a given molecular species that are present). Thus, MR is an intrinsically chemical-specific, quantitative measurement. This is the essential attribute that makes it such a powerful tool in science and engineering research.

To obtain spatial resolution, the basic spatially unresolved experiment is still performed, but by applying a spatially varying magnetic field, in addition to the large static field B_0 , the resonance frequency of species within the sample becomes a function of position and strength of the applied gradient. Thus, for a magnetic field gradient applied along the z -direction, G_z :

$$\omega_z = \gamma(B_0 + G_z z). \quad (2)$$

Clearly, this is the basis of an imaging experiment; the measurement can be calibrated such that the relationship between resonance frequency and spatial position is known. Figure 3 illustrates the basic principles of an imaging experiment for a simple example of water contained in two test tubes. Without application of the linear gradient in the magnetic field we perform a spatially unresolved experiment (i.e., the water in both test tubes resonates at the same frequency). Therefore, we see only one MR signal, which is a quantitative measure of the total amount of water in the two test tubes. Upon application of the field gradient, the water at every spatial location along the direction of that gradient has a different resonance frequency, and therefore we acquire a FID that represents, after Fourier transformation, a one dimensional (1-D) projection (along the direction of the applied gradient) of the amount of water in the two tubes. 2- and 3-D images are acquired by applying gradients in 2 and 3 orthogonal directions, respectively.

A.2. Nuclear Spin Relaxation Times

In the following section, the principles of nuclear spin relaxation processes are summarized and their use in data acquisition discussed. Following the application of the r.f. excitation pulse, the nuclear spin system has excess energy. The system returns to thermal equilibrium by a process known as “relaxation”. A number of different relaxation time constants characterize this process. The most important are the spin–lattice relaxation (T_1) and spin–spin relaxation (T_2) time constants. These time constants characterize the physicochemical environment of the molecules being investigated. T_1 , as the name suggests, characterizes the energy exchange

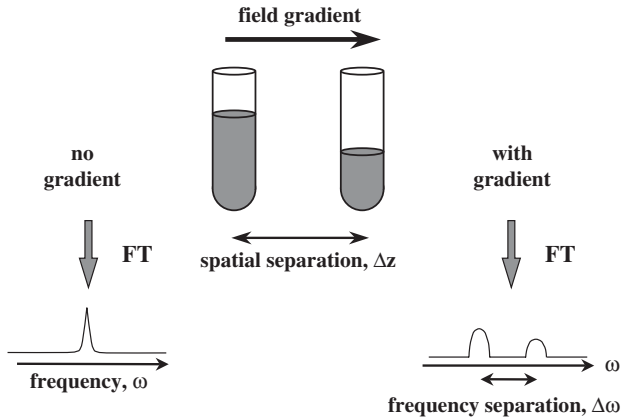


FIG. 3. Consider two test tubes containing different amounts of water. Spatial resolution is obtained by applying a linear gradient in the magnetic field, which makes the resonant frequency of the nucleus of interest a function of its position in real space. Without the presence of the field gradient, the water within the two tubes resonates at the same frequency and a single-peak spectrum is obtained, the area under it being a quantitative measure of the total amount of water in the two tubes. Upon application of the field gradient, the resonant frequency of the water molecules becomes a function of their position along the direction of the applied field gradient. Fourier transformation of the acquired signal yields a 1-D profile of the amount of water present. The area under each peak gives the amount of water in each tube.

between the excited spin and the surrounding physical environment (i.e., the lattice), whereas T_2 characterizes the loss of phase coherence between nuclear spins within the nuclear spin ensemble. If a system is characterized by a very small T_2 (e.g., many solids) it may not be possible to study it using MRI; this is the major limitation in imaging the solid state. Each chemical species will have its own T_1 and T_2 characteristics, and these will vary depending on the physical state in which that species exists.

Spin-lattice relaxation, T_1 . As shown in Fig. 4, before application of the r.f. excitation pulse the net magnetization vector associated with the nuclear spin system is aligned along the direction of the static magnetic field. It is the magnitude of this vector that provides the quantitative measurement of the number of nuclear spins excited within the sample. After excitation by a $\pi/2$ r.f. pulse applied along the x' -axis, the magnetization vector is rotated through $\pi/2$ to lie along the y' -axis. As soon as the excitation stops, the system acts to return to equilibrium; this corresponds to a monotonic increase in the magnitude of the magnetization vector back along z' ($\equiv z$) as a function of time. If we wait a short time, only a fraction of the magnetization will have been re-established along z' . If we wait $\sim 5-7$ times longer than T_1 , the full magnitude of the magnetization will have recovered along z' . The magnitude of the magnetization vector along z' , $M_{z'}$, as a function of the “waiting” time, τ , can be written analytically for any specific r.f. pulse sequence. Equation (3) describes the recovery of the magnetization back along z for a saturation recovery pulse sequence:

$$M_{z'}(\tau) = M_0[1 - \exp(-\tau/T_1)]. \quad (3)$$

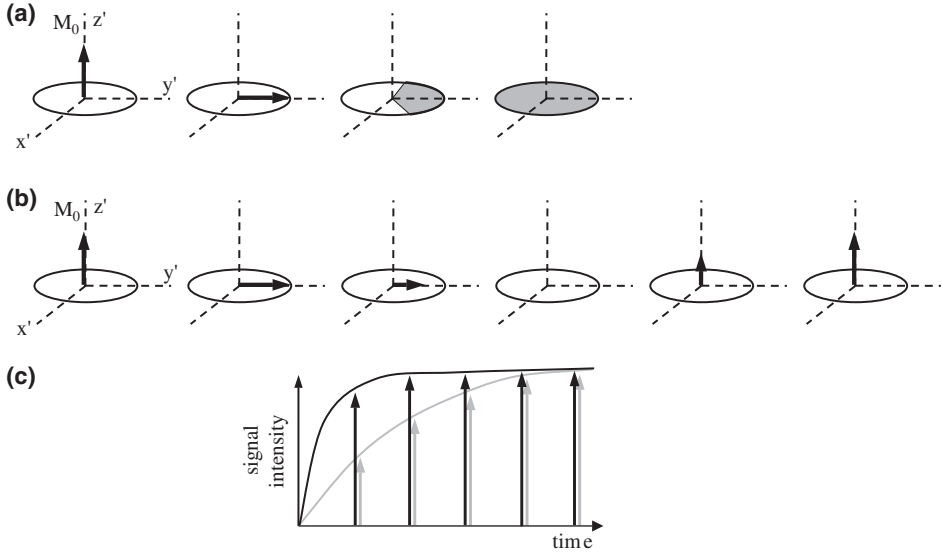


FIG. 4. (a) As described in Fig. 2, the action of the $\pi/2$ pulse (applied along the x' direction) is to rotate the magnetization vector into the $x'-y'$ plane, along the y' direction. The individual spin isochromats then dephase in the $x'-y'$ plane, as shown by the increasing size of the shaded region with time. (b) At time scales longer than T_2 , the magnetization recovers back along the direction of the magnetic field B_0 , with a characteristic time constant T_1 . (c) Two different species within the same sample may have different characteristic T_1 values. In this example, the species associated with the black arrows has a shorter T_1 than the species associated with the gray arrows; the arrows indicate the magnitude of the acquired signal intensity following the initial r.f. excitation. If data are acquired at long times after r.f. excitation, equal signal intensity will be acquired from both species. However, if data are acquired very soon after the excitation pulse, the acquired signal will be predominantly associated with the species characterized by the shorter T_1 . This illustrates the principle of relaxation contrast.

By recording M_z for a number of τ values and fitting these data to Eq. (3), both the T_1 characterizing the system and the value of M_0 (which quantifies the number of initially excited spins) are obtained. In a spatially resolved “relaxometry” experiment, images are acquired at different values of τ , and a fit of Eq. (3) to the intensity as a function of τ , for the equivalent pixel, i , in each image allows a complete map of M_{0i} and T_{1i} to be obtained. Thus spatial variation in T_1 can be mapped throughout the image. Figure 4 also demonstrates that the magnitude of the signal that we acquire depends on the time when we acquire the signal. Thus, if we have two species with different T_1 characteristics, by careful selection of the delay time between excitation and acquisition of the resulting signal, signal can be acquired preferentially from one of the components.

Spin-spin relaxation, T_2 . On time scales less than or equal to that of T_1 , spin-spin relaxation (T_2) processes occur. T_2 characterizes the loss of phase coherence of the individual spin isochromats within the spin ensemble comprising the total magnetization vector M_0 . A spin isochromat represents a group of spins that experiences the same homogeneous magnetic field and that therefore behaves in the same way following the excitation pulse. During the period following excitation, the

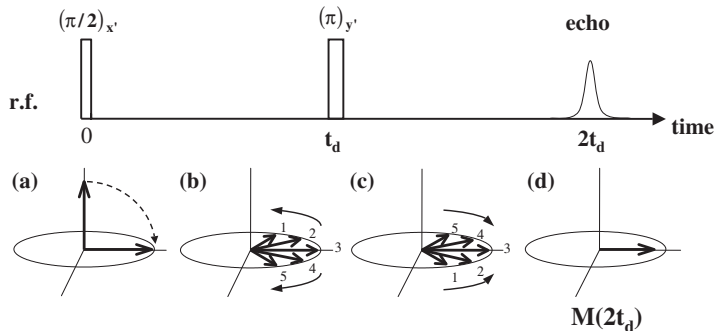


FIG. 5. A spin-echo pulse sequence used to determine T_2 . (a) A $(\pi/2)_{x'}$ pulse puts M_0 into the y' -direction, and (b) the spin isochromats dephase with time. At a time t_d later, a π pulse is applied along the y' -axis, causing the spins to rotate through π radians (c) such that they “refocus” along the y' -axis to form an “echo” at time $2t_d$ (d). The decrease in magnitude of the magnetization vector between stages (a) and (d) provides a measure of T_2 (Eq. (4)). All “reversible” contributions to the T_2 process are removed by the application of the π pulse.

individual isochromats will lose phase coherence with each other as a result of spin-spin interactions and local variations in B_0 . The decay of the coherent magnetization aligned along y' , due to spin-spin interactions but not magnetic field heterogeneities, is characterized by the time constant T_2 and measured by using a “spin-echo” pulse sequence as shown in Fig. 5.

T_2 is defined as follows:

$$M_{y'}(\tau) = M_0 \exp(-\tau/T_2). \quad (4)$$

With reference to Fig. 5, $\tau = 2t_d$ in Eq. (4). The π pulse acts to reverse the de-phasing effects due to the local heterogeneities in B_0 such that the final acquired signal (the “echo”) suffers attenuation resulting from spin-spin interactions only. The spin-echo shown in Fig. 5, or rather “echoes” in general (since they can be produced by actions other than a π pulse) have widespread use in MR methods, far beyond simple measurement of T_2 . In short, by using an echo sequence, instead of exciting the system and then allowing the magnetization to decay to zero as in Fig. 2, the majority of the magnetization can be recovered for use in subsequent measurements. The “echo” sequence shown in Fig. 5 is a common feature of MRI pulse sequences (e.g., Fig. 6).

An additional and important relaxation time constant is T_2^* , which characterizes a faster decay of the magnetization along y' and accounts, in particular, for the additional effects of magnetic field heterogeneities on the loss of phase coherence of the magnetization. Thus, the simple pulse-acquire sequence (with no refocusing), shown in Fig. 2, will give a response in which the envelope of the decay in the time domain and hence the width of the frequency domain signal is characterized by T_2^* .

A.3. The k -Space Raster

Although the schematic of Fig. 3 allows us to appreciate the concept of obtaining spatial resolution in the measurement, it is almost impossible to understand and

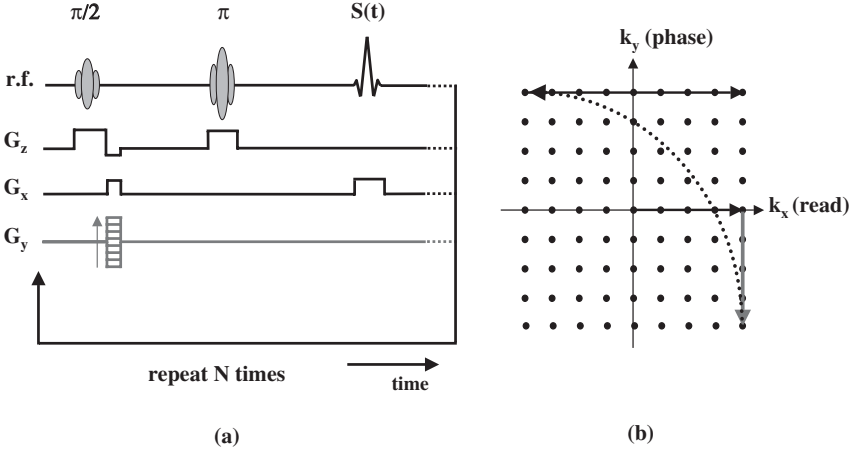


FIG. 6. (a) Schematic representation of a simple slice-selective 2-D spin-echo pulse sequence. In this pulse sequence the magnetic field gradient (G_y) is varied for successive acquisitions of different rows of the \mathbf{k} -space raster. (b) The corresponding \mathbf{k} -space raster used to show how we interpret the pulse sequence. Following a sufficient T_1 -relaxation period, the sequence is repeated to acquire a second row of the \mathbf{k} -space raster. Acquisition of each row of \mathbf{k} -space requires a separate r.f. excitation and application of a G_y -gradient of different magnitude.

design MRI pulse sequences using this approach. Instead, the concept of the so-called \mathbf{k} -space raster, introduced by Mansfield (15), is adopted.

Rewriting Eq. (2) for the general case of the variation of resonance frequency with spatial position \mathbf{r} we find:

$$\omega(\mathbf{r}) = \gamma(B_0 + \mathbf{G} \cdot \mathbf{r}) \quad (5)$$

and neglecting the influence of relaxation on signal intensity, the transverse magnetization—and therefore the acquired signal, dS —in an element of volume $d\mathbf{r}$ at position \mathbf{r} with spin density $\rho(\mathbf{r})$ is given by

$$dS(\mathbf{G}, t) = \rho(\mathbf{r}) \exp[i\omega(\mathbf{r})t] d\mathbf{r}. \quad (6)$$

Inserting Eq. (5) into Eq. (6) gives

$$dS(\mathbf{G}, t) = \rho(\mathbf{r}) \exp[i(\gamma B_0 + \gamma \mathbf{G} \cdot \mathbf{r})t] d\mathbf{r}. \quad (7)$$

A transformation into the rotating frame of reference and integrating over the sample volume allows us to rewrite Eq. (7) as

$$S(t) = \iiint \rho(\mathbf{r}) \exp[i\gamma \mathbf{G} \cdot \mathbf{r}t] d\mathbf{r}. \quad (8)$$

Mansfield and Grannell (16) simplified the interpretation of Eq. (8) and the development of imaging pulse sequences by introducing the concept of \mathbf{k} -space, where the \mathbf{k} -space vector is defined as $\mathbf{k} = (\gamma \mathbf{G}t/2\pi)$. It follows that Eq. (8) can now

be written in terms of the \mathbf{k} -space vector as

$$S(\mathbf{k}) = \iiint \rho(\mathbf{r}) \exp[i2\pi\mathbf{k} \cdot \mathbf{r}] \, d\mathbf{r} \quad (9)$$

and that the spatial distribution of spins is then given by the inverse 3-D Fourier transform:

$$\rho(\mathbf{r}) = \iiint S(\mathbf{k}) \exp[-i2\pi\mathbf{k} \cdot \mathbf{r}] \, d\mathbf{k}. \quad (10)$$

Thus the imaging experiment is seen as acquisition of data in the time domain, sampling the \mathbf{k} -space raster, followed by Fourier transformation to the frequency domain, which in turn is directly related to real space.

Figure 6 shows a schematic of a simple 2-D imaging sequence. In this case let us assume that the sample is cylindrical and oriented along the z -axis, and an xy image is to be recorded. The first component of the pulse sequence is the so-called ‘‘slice selection’’ phase. The procedure comprises the application of a narrow band r.f. excitation simultaneously with a magnetic field gradient imposed along the direction in which the 2-D image is to be taken. The effect of this procedure is that the only spins that will be excited will be those that resonate within the bandwidth $\Delta\omega$ of the r.f. pulse—and therefore only those spins that lie within a certain ‘‘image slice thickness’’ Δz . The rest of the sequence acquires data along a different row of the \mathbf{k} -space raster for successive r.f. excitations, and hence provides spatial resolution in the x - and y -dimensions. With reference to Fig. 6, it is seen that a field gradient is first applied in the x -direction, simultaneously with the maximum magnitude negative field gradient in the y -direction. A slice-selective π ‘‘refocusing’’ pulse is then applied; this is represented on the \mathbf{k} -space raster as a move through the origin from $k_{x,\max}$, $-k_{y,\max}$ to $-k_{x,\max}$, $k_{y,\max}$. A second gradient is then applied along the x -direction while data, typically 128 or 256 complex data points, are acquired at a specified digitization rate. The digitization rate will define the spacing of the points acquired in \mathbf{k} -space. The signal, $S(t)$, that is acquired during application of the second x -gradient is said to be frequency-encoded, because the signal is acquired in the presence of a magnetic field gradient. This gradient along the x -direction is therefore referred to as the frequency-encoding gradient, also being termed the ‘‘read’’ gradient. The acquisition of complex data points in the presence of a constant linear ‘‘read’’ gradient yields a straight-line \mathbf{k} -space data trajectory the direction of which is defined by the Cartesian orientation of the gradient. A straight, equally spaced \mathbf{k} -space trajectory will always result, as long as the read amplitude gradient is kept constant and the digitization (acquisition) rate of the complex data is fixed. The spin system is then allowed to return to equilibrium, via T_1 relaxation, and the pulse sequence is repeated, this time with the second largest negative y -gradient being applied—hence ‘‘reading’’ the next row of \mathbf{k} -space. This process is repeated until the entire raster has been sampled.

In this example, the gradient applied in the y -direction is referred to as the ‘‘phase encoding’’ gradient. Phase encoding refers to the action of an applied gradient that is responsible for moving the acquisition through the \mathbf{k} -space raster. In this case, the

action of the x -gradient is the same in each implementation of the pulse sequence, and it is the y -gradient that enables successive rows of \mathbf{k} -space to be sampled. Therefore, if M complex points are acquired along each row of \mathbf{k} -space and N rows of \mathbf{k} -space are sampled (i.e., there are N phase-encoding steps), the final data matrix will consist of $M \times N$ points on a rectilinear grid. A 2-D Fourier transformation of these data followed by modulus correction gives a 2-D spin-density map. 2-D images are typically acquired in a few minutes using this approach. Although this might be considered slow in that only pseudo steady-state processes can be investigated by using this pulse sequence, it is robust in use and straightforward to implement. It is also easy to minimize, or at least account for, relaxation contrast effects within the acquired image.

In addition to measurements of how much and what type of chemical species are present, modification of the MR experiment allows us to identify the physical state of a given species (e.g., gas, liquid, gel, and solid) and to quantify temperature and any incoherent and/or coherent transport processes within the system. By integrating any of these measurements into an imaging experiment, we can spatially map these quantities or exploit the effect of these characteristics on the magnitude or frequency of the MR signal to preferentially observe sub-populations of spins within the system. In this latter application we are exploiting the so-called “contrast” mechanisms in the image acquisition. These concepts are illustrated in Sections II.B–II.D.

B. MEASUREMENT OF DIFFUSION, DISPERSION, AND FLOW

There are three basic approaches to measuring transport processes, which include diffusion, dispersion, and bulk flow phenomena. These are the following:

- (i) Phase-encoding methods
- (ii) Time-of-flight (TOF) methods
- (iii) Rapid image acquisition

The phase-encoding methods are considered to be the most robust and quantitative but, as demonstrated below, TOF and rapid image acquisition can be particularly useful in specific applications.

B.1. *Phase-Encoding Methods*

Diffusion, dispersion, and flow processes are measured by means of applying pulsed magnetic field gradients to the system, in addition to the normal r.f. pulses. PFG techniques measure molecular displacement as a function of time without the need for introducing tracers into the experiment. The principle of the experiments is easy to understand although the detailed implementation of the experiments is somewhat challenging. The application of a pulsed field gradient at the beginning of an experiment (i.e., immediately after r.f. excitation) encodes a given spin with a “label” describing its position along the direction of that applied field gradient. At a time Δ later, referred to as the observation time, a second pulsed field gradient is applied. The net effect of applying these two gradients separated by the time Δ is

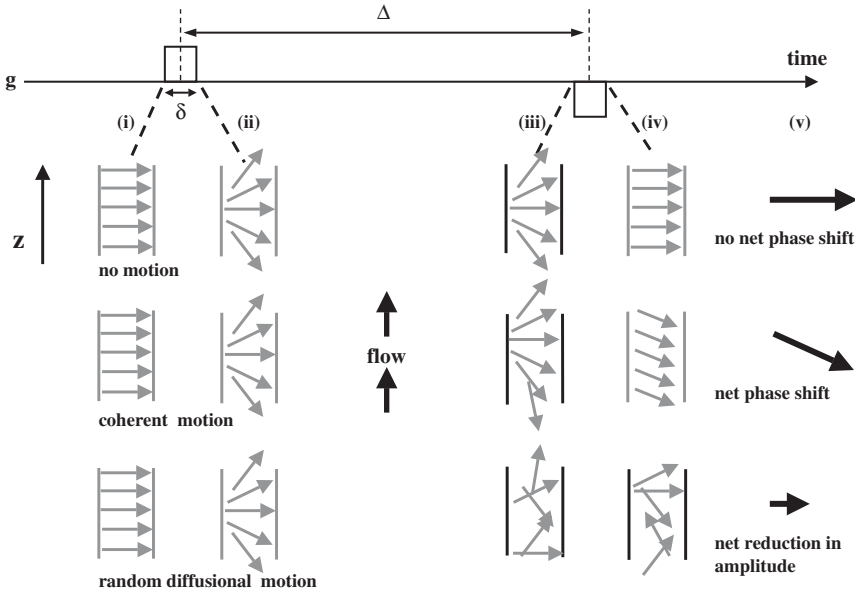


FIG. 7. The principle of transport measurements using the “phase shift” approach. Two-pulsed magnetic field gradients (of magnitude g and duration δ) are applied a time Δ apart. The cases of no motion, coherent motion (i.e., constant velocity), and random diffusional motion are shown. The schematics show the relative phase offsets of the spin isochromats initially at different positions in z along the length of the sample. (i) Initially all the spins are aligned in the rotating frame. (ii) The first gradient pulse applies a phase offset to the spin isochromats depending on their position along the z -direction. (iii) The position of the spin isochromats after the system has evolved for time Δ . (iv) The orientation of the spin isochromats after the action of the second, equal and opposite polarity gradient pulse. (v) The magnitude and phase shift of the net magnetization vector after application of this bipolar gradient pair (i.e., equal and opposite) pulse sequence.

that we can monitor the distance traveled during a known time and hence quantify the transport process of interest.

Figure 7 shows the principles of a measurement. When considering the application of pulsed magnetic field gradients to measure transport processes we use the lower case symbol g , as opposed to G , which is reserved for use in describing the *imaging* gradients (Eq. (2) and Section II.A). Perhaps the most important point to appreciate with respect to MR measurements of transport is that the same measurement methodology is used to quantify incoherent (e.g., diffusion and dispersion) and coherent (e.g., flow) processes occurring within the same system. The basic principle derives directly from Eq. (2).

If the magnetic field gradient is applied for a short time period (i.e., a “pulse”), as opposed to “continuously” during which time data are acquired, instead of imposing a time-independent modified resonance frequency on a nucleus as determined by its spatial position, the nuclear spin is given a *phase offset* (say ϕ_1) after application of the pulse characteristic of its spatial position when the pulse was applied. In the rotating frame of the spin system, this phase offset, ϕ_1 , is equal to $\gamma g \delta z_1$, where δ is the duration of the applied gradient, z_1 the position of the spin,

and g the magnitude of the magnetic field gradient along the z -direction. Although many variations on the theme exist, the basic concept underpinning the vast majority of transport measurements is that after an observation time, Δ , an equal but opposite polarity magnetic field gradient pulse is applied which gives the spins a further phase offset, ϕ_2 , such that the total phase offset is $\phi_1 + \phi_2 = \gamma g \delta (z_1 - z_2)$. Clearly, if the molecule (i.e., spin) has not moved during the time Δ , it will experience a net phase shift of $\phi_1 + \phi_2 = 0$; that is, the magnetization vector will again be aligned along the y' -axis, as it was immediately after application of the initial excitation pulse. However, if the molecule has moved during the time Δ (i.e., $z_1 \neq z_2$) then $\phi_1 + \phi_2 \neq 0$, and observation of the magnetization will show a phase shift that is proportional to the distance moved ($z_1 - z_2$). Since γ , g , and δ are known, the displacement or average velocity over the timescale Δ is obtained. A typical transport measurement would proceed by making several measurements at differing values of δ or g and recording the resulting phase shift and amplitude of the signal.

Let us now consider, in detail, the effect on the acquired signal of a *coherent* transport process (i.e., the molecules move with a velocity v in the direction of the applied pulsed field gradient). With reference to Fig. 7, we see that the effect of the second pulsed gradient is to realign the spin isochromats with each other, but at an increasing angle (phase offset) with respect to the y' -axis. As δ or g increases, the net magnetization will rotate through the x' - y' plane of the rotating frame. This manifests itself as a continuously increasing phase shift while the magnitude of the magnetization vector (i.e., signal amplitude) remains constant (ignoring relaxation effects). If only the real component of the complex signal is recorded (i.e., we observe the magnitude of the magnetization vector projected along y'), an oscillatory signal is recorded as a function of δg , and the period of the oscillation is directly related to the velocity of the moving spins. In the case of an *incoherent* transport process (e.g., diffusion), the random molecular displacements cause a random distribution of phase shifts of the individual spins, and the acquired signal is a vector sum of these phase shifts. As δ or g increases, the magnitude of the acquired signal decreases monotonically. An interesting extension to this example is when the diffusion is occurring within a confined geometry (e.g., an emulsion droplet). In this case the distance traveled is constrained to a maximum value. Therefore, by taking measurements at increasing values of Δ , a value of Δ is reached, above which no further signal attenuation is measured—this value of Δ quantifies the typical dimension of the discrete phase.

When pulsed magnetic field gradients are applied to study diffusive processes, the MR technique is often referred to as pulsed field gradient or pulsed gradient spin echo (PGSE) MR. Application of PGSE MR techniques to quantify molecular diffusion was pioneered by Stejskal and Tanner (17,18), and the techniques typically probe molecular displacements of 10^{-6} – 10^{-5} m over time scales of the order 10^{-3} –1 s.

Transport measurements performed using pulsed magnetic field gradients are most clearly understood in the context of a more mathematical framework. It follows from Eq. (2) that the phase shift (i.e., the instantaneous phase offset in resonance frequency) $\phi(t)$ acquired (in the rotating frame) following application of

a magnetic field gradient, g , along the z -direction, will be:

$$\phi(t) = \gamma \int_0^t g(t)z(t) dt. \quad (11)$$

We also know that the change of position with time of a “spin” or its associated magnetic moment can be written as

$$z(t) = z_0 + vt + \frac{1}{2}at^2 + \dots, \quad (12)$$

where z_0 is the initial position, v the velocity, and a the acceleration in the direction of the applied gradient. Substituting Eq. (12) into Eq. (2) gives

$$\omega(t) = \gamma \left[B_0 + g \left(z_0 + vt + \frac{1}{2}at^2 + \dots \right) \right]. \quad (13)$$

The total relative phase of the MR signal is then calculated by considering the time integrals of the individual terms on the right-hand side of Eq. (13). These integrals are the *moments* of the magnetic field gradient and the zeroth, first, and second are proportional to the following:

$$\text{Zeroth moment : } z_0 \int g(t) dt \quad (14)$$

$$\text{First moment : } v \int g(t)t dt \quad (15)$$

$$\text{Second moment : } \frac{1}{2}a \int g(t)t^2 dt \quad (16)$$

Let us now consider the action of the two equal and opposite pulsed gradients (referred to as a bipolar pair) of amplitude $\pm g$ and length δ , separated by time Δ , as shown in Fig. 7, and in the absence of relaxation. When there is no motion the first pulse, $+g$, will cause a phase shift which is proportional to the zeroth moment (Eq (14)):

$$\int_0^\delta g(t) dt = [gt]_0^\delta = g\delta. \quad (17)$$

The second, equal and opposite, gradient pulse will have a zeroth moment given by

$$\int_\Delta^{\delta+\Delta} g(t) dt = [-gt]_\Delta^{\delta+\Delta} = (-g\delta - g\Delta) - (-g\Delta) = -g\delta. \quad (18)$$

Addition of Eqs. (17) and (18) gives the total relative phase shift which for the case of no motion is clearly zero.

Now consider the phase shift when the spins move at a constant velocity v in the direction of the applied gradient. The total first moment is now non-zero and is

given by

$$\int_0^\delta g(t)t \, dt + \int_\Delta^{\Delta+\delta} g(t)t \, dt = \frac{1}{2}g(\delta^2 - 0 - \Delta^2 - 2\delta\Delta - \delta^2 + \Delta^2) = -g\delta\Delta. \quad (19)$$

Therefore, the residual phase shift of the MR signal for a magnetic moment undergoing uniform motion with velocity v for a set of bipolar gradients, $\pm g$, of duration δ separated by a time Δ is $-\gamma v g \delta \Delta$ (i.e., the measured phase shift is linearly proportional to the velocity).

In practice, we may wish to measure only one of the moments (Eqs. (14)–(16)), thereby removing the sensitivity of the measurement to position, velocity, or acceleration. This measurement is made by modifying the basic transport measurement pulse sequence (Fig. 7) so that the integrals are zero for all moments except the one that is to be measured. These so-called “compensated” pulse sequences have been reviewed in detail by Pope and Yao (19).

Another type of experiment commonly used to characterize transport phenomena is the propagator measurement. The propagator gives a statistical description of the evolution of motion characterizing the system; it provides a complete description of the random (e.g., diffusion) as well as coherent motions. In particular, the propagator $P_s(\mathbf{r}|\mathbf{r}', t)$ gives the probability of finding a spin initially at \mathbf{r} at time $t = 0$, at \mathbf{r}' after a time t . If the propagator depends only on the displacement $\mathbf{R} = \mathbf{r}' - \mathbf{r}$, we can define the average propagator as follows:

$$\bar{P}_s(\mathbf{R}, t) = \int P_s(\mathbf{r}|\mathbf{r} + \mathbf{R}, t)\rho(\mathbf{r}) \, d\mathbf{r} \quad (20)$$

where $\rho(\mathbf{r})$ is the spin density (number density of MR-active nuclei) at position \mathbf{r} . Consider the same pair of gradients as shown in Fig. 7. Let us assume that a molecule moves from z_0 to z' during the time Δ . The first pulse is assumed to be applied for a short time δ and if the displacement of the molecule is negligible during this time then its phase shift is determined by the zeroth moment and is given by $\gamma g \delta z_0$. After a time Δ the molecule has moved to z' and the net phase shift, Φ , following the second gradient pulse is then given by

$$\Phi = \gamma \delta g(z_0 - z'). \quad (21)$$

Defining a dynamic displacement $Z = z' - z_0$, and the average displacement propagator $\bar{P}_s(Z, \Delta)$ as the average probability that any molecule in the sample will move by a displacement Z over time Δ , the acquired signal (relative to that acquired when no magnetic field gradients are used) for a population of spins characterized by a range of displacements is given by the following:

$$\int \bar{P}_s(Z, \Delta) \exp(i2\pi qZ) \, dZ, \quad (22)$$

where $q = ((1/2)\pi)\gamma\delta g_z$ is the reciprocal displacement vector (13). The average displacement propagator distribution, $\bar{P}_s(Z, \Delta)$, is obtained by Fourier inversion of the acquired MR signal. The propagator measurement is equivalent to a tracer

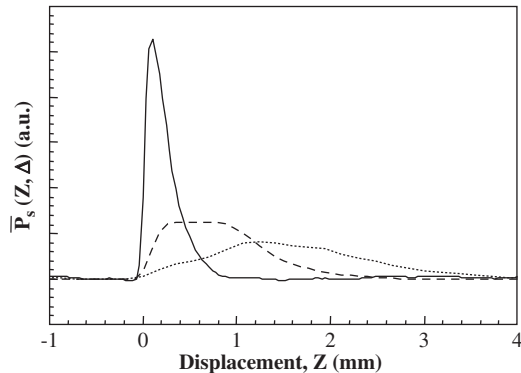


FIG. 8. Displacement propagators recorded for flow of water through a packed bed of 1-mm-diameter glass beads packed within a 10-mm-diameter column. The average flow velocity was 0.77 mm s^{-1} , corresponding to Pe and Re of 350 and 0.77, respectively. Propagators are shown for observation times, $\Delta = 0.3 \text{ s}$ (—), 1 s (---), and 2 s (···).

measurement in which the tracer is introduced into the flow and the average distribution of tracer from its location determined in a completely non-invasive manner. Figure 8 shows propagators determined for water flow within a packed bed of spheres. The major features of the propagator measurement are clearly evident. As the observation time increases the peak in the propagator occurs at a greater displacement, and the width of the propagator distribution increases reflecting the magnitude of molecular diffusion and dispersion phenomena occurring within the bed.

B.2. Time-of-Flight Methods

For obvious reasons, the methods just described are termed “phase shift” measurements of transport, and are considered the most robust and quantitative. Another approach is so-called time-of-flight or TOF imaging. TOF or “spin tagging” methods were first reported in 1959 by Singer (20), and their use has been widespread since then, particularly with respect to velocity measurements, although the same measurements probe other transport processes as well. At its simplest, the TOF approach monitors velocity by the signal attenuation observed in the acquired image—no absolute, direct measure of velocity using pulsed field gradients is employed. The principle is that a set of spins is given an initial excitation pulse—signal is acquired from only these excited spins at a given time later. Thus, if we excite a set of spins in a plane and then acquire signal from that plane a time, Δ , later, the signal will be reduced in the positions at which the fluid has moved fastest. This is because the excited spins will have moved out of the image plane to be replaced by fast moving spins that have moved into the image plane during Δ . The spins that have moved into the image plane will not have received the initial excitation and therefore will not give any signal upon data acquisition. There are many variants on this approach (e.g., (21)) but the principle remains the same. Because these methods often rely on image intensity to determine the fluid velocity, calibration may be

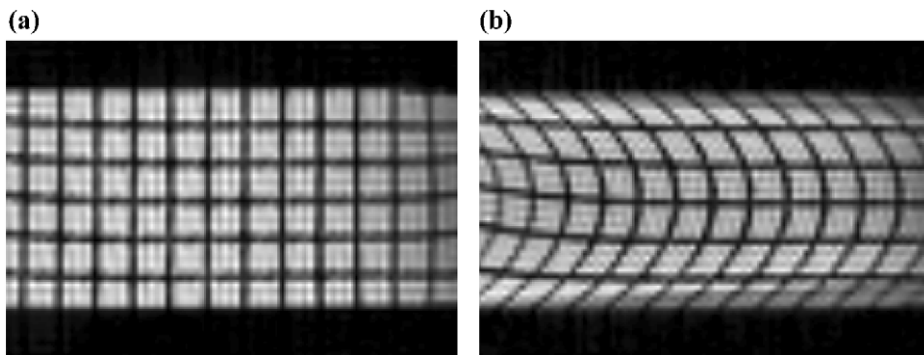


FIG. 9. Example of a DANTE-type velocity image of water flowing through a pipe. ^1H 2-D image of a 2.0 mm-thick longitudinal slice at (a) zero flow rate, and (b) a flow rate of $486\text{ cm}^3\text{ min}^{-1}$. Flow is from left to right.

relaxation dependent, and quantification can be difficult. An extension of this approach is the DANTE method in which a grid of spins is excited in the imaging plane and the motion of the spins observed at a later time (22). An example of a DANTE TOF image of laminar flow in a pipe is shown in Fig. 9.

B.3. Rapid Image Acquisition

MRI can also be used as a high-speed camera such that the movement of particular features over the time scale between successive image acquisitions allows the determination of velocities. These measurements are made using fast imaging techniques (Section II.E) which enable one to acquire images in < 1 s, with images being recorded in immediate succession. For example, Fig. 10 shows images recorded for two-phase co-current downflow of air and water through a ceramic monolith (23). These data were acquired using the SEMI-RARE pulse sequence.

C. CONTRAST MECHANISMS

C.1. Obtaining Chemical Information

In the context of catalysis, being able to make the signal intensity of each image pixel sensitive to chemical species is one of the major motivations for using MR techniques. The most direct way of achieving this goal is to use chemical shift imaging (CSI) techniques. These are introduced below, along with a brief description of the volume-selective spectroscopy method, which integrates spectroscopy and imaging methods in such a way that volume-localized spectra are recorded within the system.

The issues with respect to obtaining chemical information within an imaging experiment are considered next. The description of image acquisition given in Section II.A.1 was based on the assumption that the Larmor frequency of a nuclear spin is directly related to its location in the sample, as determined by the applied magnetic field gradient. As discussed by Callaghan (13), this is precisely true only

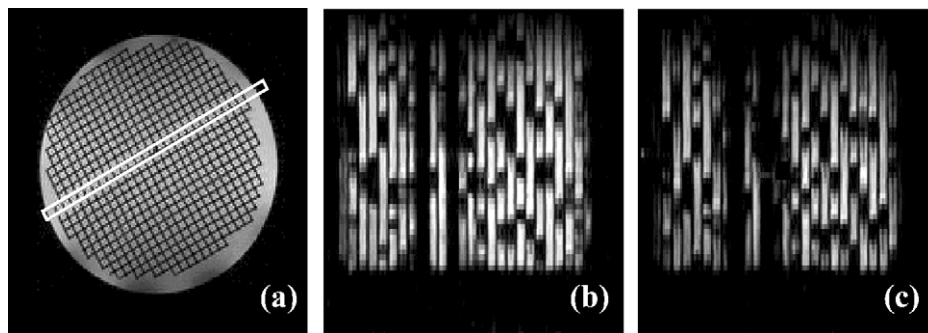


FIG. 10. ^1H MR visualizations within a ceramic monolith. (a) An xy -image of the fully water-saturated monolith showing the array of parallel channels comprising the monolith; each channel has a side length 1.2 mm. The highlighted region identifies the position of the image slice in the xz direction for which the visualizations of gas-liquid distribution during two-phase flow are shown in (b) and (c). The data acquisition time for each image was 160 ms, and there was a period of 160 ms, and between the start of acquisition of each of the images shown in (b) and (c). In all images, the presence of water is indicated by high intensity (white); gas and ceramic are identified by zero intensity (black). The monolith was operated under conditions of co-current downflow with gas and liquid feed flow rates of 1 and 6 L min^{-1} , respectively. The diameter of the monolith was 43 mm and the length was 0.15 m. Reproduced from reference (23), with permission from AIChE, Copyright 2002.

when the NMR spectrum, in the absence of an applied magnetic field gradient, consists of a single, infinitely narrow resonance (spectral peak). When more than one chemical environment is present, leading to two or more spectral peaks, this simple image acquisition strategy will not work. In particular, if the imaging gradients are sufficiently small that the frequency separation of the peaks is larger than one pixel, the simple correspondence between resonance frequency and nuclear position no longer applies and image artifacts appear. In the simplest case of a pair of resonances, the chemical shift leads to two displaced images for the two chemical species of spin. It follows that a way to avoid these artifacts is to increase the magnitude of the applied magnetic field gradients such that the frequency separation is compressed within a single image pixel. However, this approach throws away the chemical information contained in the spectrum. An alternative approach, which retains the chemical information, is to deconvolve the individual contributions of each chemical species to the total signal. In practice, the two most direct approaches to obtaining spatially resolved chemical information, both of which have been used in application to catalytic systems, are (i) n -dimensional CSI, and (ii) volume-selective spectroscopy.

n-Dimensional CSI. This method increases the dimensionality of the acquisition process, so that the acquired NMR spectrum becomes the n th dimension in addition to the $(n-1)$ spatial dimensions of imaging. This procedure is performed by spatially encoding the MR signal prior to reading in the absence of a magnetic field gradient. An example of this pulse sequence is shown in Fig. 11. The major disadvantage of a full CSI experiment is that the acquisition of the additional chemical shift dimension to the $(n-1)$ spatial dimensions is costly in data acquisition time, and therefore one has to consider sacrificing spatial resolution to keep

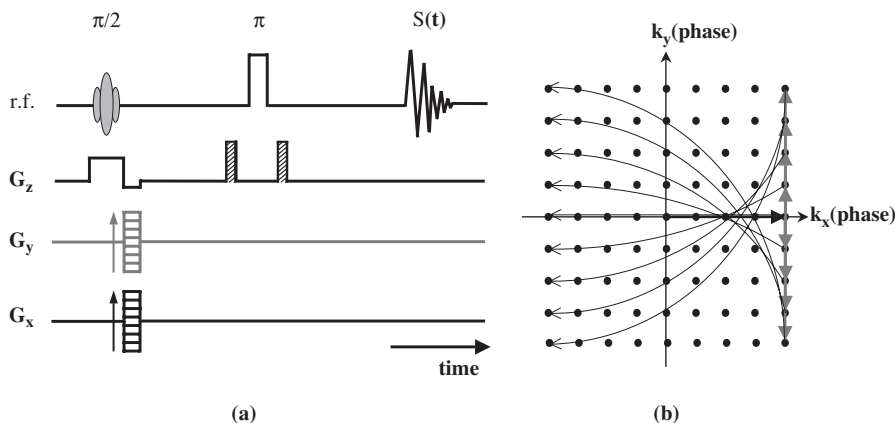


FIG. 11. A CSI pulse sequence. (a) The MR signal is spatially encoded prior to acquiring the spectral signal in the absence of any applied magnetic field gradients. The shaded gradient pulses applied along z either side of the π refocusing pulse are homospoil gradients. For clarity, the action of only one value of the G_x gradient is shown on the k -space raster in (b).

data acquisition times within a practical limit. Figure 12 shows some of the data recorded in a 3-D CSI acquisition (i.e., with two spatial dimensions and one spectral dimension). The experiment was done with a 5-mm diameter tube of acetic acid contained within a larger tube (15 mm diameter) containing water. The ^1H spectral resonances with respect to tetramethylsilane (TMS) occur at 4.8 ppm for the water OH group, 2.7 ppm for the acid CH_3 group, and 12 ppm for the acid OH group. The wealth of information contained within such a data set is illustrated in this example. The projection of the whole data set is shown in Fig. 12a; this image provides a quantitative measure of the amount of acetic acid and water in the two containers. Each pixel in the image has associated with it a full spectrum as shown in Fig. 12b. Figure 12c shows an alternative way of representing the data. In this figure, a full 2-D image is extracted from individual points along the spectral range (2.4–5 ppm). Three series of images are shown; within each series the chemical shift separation between images is 0.065 ppm. This complete data set took approximately 27 h to acquire—as a 128×128 data array with in-plane resolution of $140 \mu\text{m} \times 140 \mu\text{m}$ for an image slice thickness of 1 mm.

A way to reduce the data acquisition time is to use chemically selective excitation. According to this approach, the experimenter may decide that it is not necessary to acquire the full spectrum at each position; instead, one simply acquires data from a particular spectral resonance (i.e., chemical species) within the full spectrum. In this way, the spatial location of just one particular species is mapped in 1-, 2-, or 3-D.

Volume-selective imaging. In this pulse sequence the attributes of MR spectroscopy and MRI are again combined. In this case three slice-selective r.f. pulses are applied in three orthogonal directions to obtain ^1H spectra from pre-determined local volumes within the sample (24). A typical volume-selective spectroscopy pulse sequence is shown in Fig. 13. An example of this pulse sequence used in application

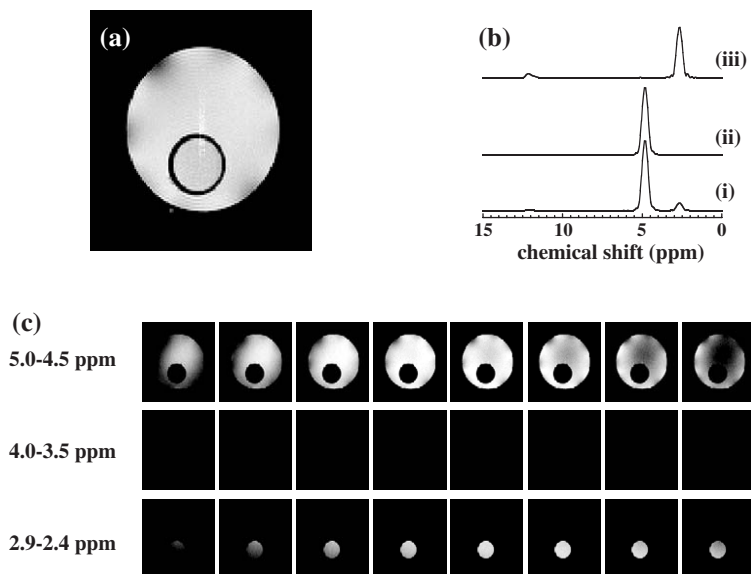


FIG. 12. Example of CSI; the sample used is a 5-mm diameter tube of acetic acid contained within a larger tube (15 mm in diameter) containing water. The spectral resonances, with respect to TMS, occur at 4.8 ppm for the water OH, 2.7 ppm for the acid CH_3 , and 12.0 ppm for the acid OH groups, respectively. The wealth of information contained within such a data set is illustrated in this example. The projection of the whole data set is shown in (a). This image provides a quantitative measure of the amounts of acetic acid and water in the two tubes. Each pixel in the image has a full spectrum associated with it, as shown in (b). (b) The three spectra are taken from (i) the whole sample, (ii) a pixel from the outer region of the image within the larger tube containing water only, (iii) a pixel from inside the inner tube containing acetic acid only. (c) This figure shows an alternative way of representing the data; a full 2-D image is extracted from individual points along the appropriate spectral range (0–15 ppm). Three series of images are shown; within each the chemical shift separation between consecutive images is 0.065 ppm. This complete data set took approximately 27 h to acquire, as a 128×128 data array with in-plane resolution of $140 \mu\text{m} \times 140 \mu\text{m}$ for an image slice thickness of 1 mm.

to the investigation of an *in situ* esterification reaction in a fixed bed of ion-exchange resin catalyst is given in Section V.A.1.

C.2. Relaxation and Transport Contrast

The observation that a specific chemical species existing in a given physicochemical environment is characterized by specific values of T_1 and T_2 is important both in the implementation of imaging pulse sequences to obtain quantitative information and in the modification of the pulse sequences to image selectively one species and/or phase within the sample.

To perform a quantitative imaging or spectroscopy experiment, the relaxation time characteristics of all species (and relevant physical states of those species) must be fully characterized so that the pulse angles and delays between pulses are optimized for that particular system. In particular, if successive repetitions of a pulse sequence are applied at time scales (“recycle delays”) of the order of or

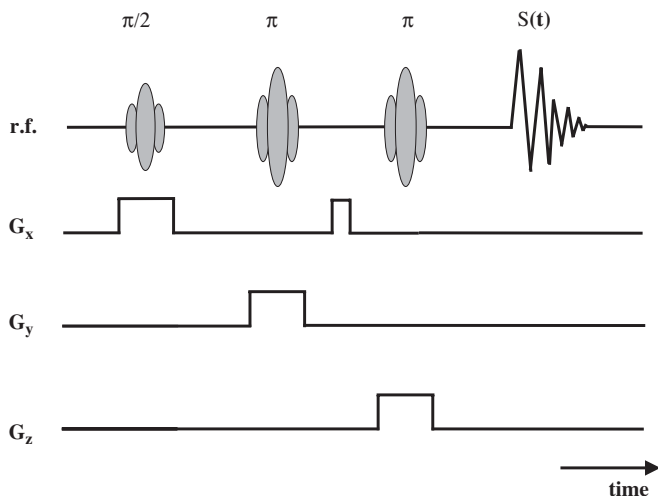


FIG. 13. A volume-selective spectroscopy r.f. pulse sequence. Magnetic field gradients applied along x -, y -, and z -directions enable recording of localized spectra from pre-defined local volume elements within the sample.

significantly faster than T_1 , the data will suffer from T_1 contrast and signal will be lost. If the T_1 of the species of interest is known, the true signal intensity can be recovered in post-acquisition analysis. Alternatively, if we have two species with significantly different values of T_1 , the recycle delay can be set so that signal from one of the species is lost preferentially—that is, we exploit T_1 contrast to make the resulting data selective to the species of interest (Fig. 4). In the case of T_2 , when an imaging pulse sequence is used in which the echo time is of the same duration as or longer than T_2 , then substantial T_2 contrast effects will be introduced. Again, if T_2 is known, the true signal intensity can be recovered in post-acquisition analysis. It follows that contributions to the acquired signal intensity from a particular species can be removed (or at least substantially reduced) by careful selection of recycle and echo times within a given pulse sequence. In a multi-component and/or multi-phase system, each component/phase will be characterized by different relaxation times. Therefore the timings in the MR pulse sequence can be set so that signal is preferentially acquired from one component/phase. Examples illustrating the imposition of relaxation time contrast on an MR image acquisition include investigations of the separation of an oil–water emulsion in which the T_1 characteristics of the oil and water phases are significantly different from each other (25) and the discrimination of liquid and solid phases during crystallization (26). Contrast effects can also be introduced into the image on the basis of differences in molecular mobility within the sample. Thus, if we are imaging two immiscible species of significantly different molecular mobility (i.e., self-diffusion), the image can be made selective to one of the species. This type of “transport” contrast effect can cause problems in quantitative imaging. For example, if a fast-flow/high-shear channel exists within a fixed-bed reactor, signal intensity may decrease as the flow velocity increases. Unless great care is taken to

confirm that the image is not subject to such phenomena, a fast-flow channel may be interpreted as a liquid-free channel!

D. TEMPERATURE

Temperature can be mapped by its effect on nuclear spin relaxation (27,28), resonance frequency (i.e., “chemical shift”) (29,30), and diffusion (31). Because temperature influences so many MR characteristics, great care must be taken to ensure that the effect on the MR signal that we assign to temperature is influenced only by temperature or that other influences can be quantified and hence decoupled from the temperature measurement. For example, if a chemical reaction were occurring within the sample, the chemical shifts of the individual species might be modified slightly by the change in mixture composition as well as by any temperature variation within the sample. Nonetheless, careful studies have shown that MR does offer the opportunity for non-invasive temperature measurement. A recent review of this field by Nott and Hall (32) focuses on food processing applications. MR temperature measurements have not yet been used in any detailed investigations of temperature variation in catalysts or reactors. Perhaps more important than attempting to map temperature within reactors is the awareness of the possible effect of temperature on MR spectra so as to avoid misinterpretation of data recorded during exothermic and endothermic reactions.

E. RECENT DEVELOPMENTS

E.1. *Gas-Phase MR*

MR studies of fluids within catalysts and flow within reactors are not restricted to the liquid phase. Gas-phase MRI can be performed using thermally polarized (“as-received”) or hyper-polarized gas. Gas-phase investigations have lagged behind liquid-phase investigations simply because the signal-to-noise ratio achievable for the same acquisition time is far reduced for gases because of the lower nuclear spin density associated with the gaseous state. The hyperpolarization approach uses laser optical pumping to modify the population distribution between adjacent energy levels such that the polarization of the nuclear spin system is increased by 3–4 orders of magnitude, thereby increasing the signal-to-noise ratio of the measurement by up to factors of 10^4 . Hyperpolarization methods are mostly used for ^3He and ^{129}Xe gases and have found most application in medical imaging, when they are used to image the lung and brain in mammals (33–35). However, Pietraß *et al.* (36) developed cross-polarization techniques using hyperpolarized noble gases to enhance the signals of surface species on catalysts.

Gas-phase MR will undoubtedly find more widespread use in studies of catalysts and catalytic reactors; initial studies have been done with thermally polarized gases. Clearly, it will be of interest to image gas flows in reactors; in this application, the measurement strategies used to image gas and liquid flows will be similar. However, gas- and liquid-phase species diffusing within a porous catalyst will be influenced to differing extents by the physical and chemical characteristics of the catalyst. These

differences arise because gases and liquids have significantly different diffusion coefficients and relaxation time characteristics. Thus, if we consider molecular diffusion within a catalyst pellet, in the case of liquid-phase diffusion, the liquid-phase species exhibit relatively slow diffusion, and their relaxation times are enhanced by interaction with a solid surface. Thus, the MR signal is acquired from molecules traveling relatively short distances (e.g., 50 μm) and hence sampling a relatively small volume of the pore space of the catalyst. In contrast, gas-phase species have high diffusion coefficients and interact less strongly with solid surfaces, thereby allowing investigations with gases to probe larger regions of an internal pore space within a single measurement. It follows that gases also offer greater flexibility in controlling the length scales investigated by changing the temperature and pressure of the probe gas molecules. However, the higher mobility of gas molecules also means that a diffusing gas molecule experiences the effect of internal magnetic field gradients (associated with magnetic susceptibility variations caused by the solid–fluid interface) to a far greater extent than a liquid-phase molecule; this effect gives rise to enhanced diffusion-attenuation phenomena in investigations of gases and may result in poorer spatial resolution in imaging studies. Gas-phase MR has already been used to investigate the pore structures of ceramic materials (Section III.A) and flow in ceramic monoliths (Section IV.C).

E.2. *Fast Data Acquisition*

At the heart of recent developments in applying MR in reaction engineering research has been the implementation and further development of *fast* spatially resolved MR measurements. In this section, the principles of the three main strategies for fast MRI are described. We emphasize that *fast imaging* (the term “fast” is used interchangeably with the terms *ultra-fast* and *rapid*, both in this review and in the wider literature) is considered here to comprise the acquisition of say a 128×128 2-D image in less than 1 s. This section is not a detailed review of fast imaging strategies in general—most of which are employed in medical imaging. Instead we address particular pulse sequences that have been implemented to study magnetically heterogeneous, fast-relaxation-time systems characteristic of catalysts and reactors. Although the data collection strategies will be similar between the medical and engineering fields, the physical and chemical nature of the samples to be investigated, and the nature of the data required, are quite different, and therefore the detail of the implementation will also be different in terms of the hardware and the pulse sequences themselves. In using a fast sequence we will often have to relax our desire for high spatial resolution ($\sim 15\text{--}30 \mu\text{m}$) and take great care, if quantitative data are required, to account for relaxation contrast effects in the final image.

As we have seen, conventional spin–echo imaging (Section II.A.3) typically takes the order of a few minutes. As shown in Fig. 6, an independent r.f. excitation is required for acquisition of each row of \mathbf{k} -space data. Hence sampling of the complete raster is limited by the repetition/recycle time of the pulse sequence used, which in turn is governed by the inherent T_1 relaxation time(s) of the system. In

general, the acquisition speed of an MR image may be improved by two basic methods (37):

- (i) The sampling of more than one line of \mathbf{k} -space for each r.f. excitation of the spin system
- (ii) The use of rapid multiple r.f. excitations (and subsequent acquisitions)

Three sampling strategies are now introduced: echo planar imaging (EPI), rapid acquisition with relaxation enhancement (RARE), and low excitation angle imaging. The first two are based on the sampling of more than one line of \mathbf{k} -space for each r.f. excitation, and the third uses rapid multiple r.f. excitations.

Echo planar imaging. The first example of rapid \mathbf{k} -space imaging was demonstrated by Mansfield (15), who realized that a complete image could be formed by the acquisition of multiple lines in \mathbf{k} -space following a single r.f. excitation in a technique today known as EPI. There are now many EPI-based sequences in use, mostly in the medical field. In applications to reaction engineering research, although these methods acquire data faster than any other sampling strategy, their successful implementation is particularly sensitive to variations in magnetic susceptibility (e.g., as occur at gas/liquid/solid interfaces) within a sample. A common EPI sequence, known as MBEST-EPI or BLIPPED EPI (38), is shown in Fig. 14. Using this sequence, a 128×128 image would typically take 100–130 ms to acquire. In this sequence a single r.f. excitation is used to sample the entire \mathbf{k} -space raster. Following excitation, gradients applied simultaneously in the x - and y -directions take one to the bottom row of \mathbf{k} -space; this row of data is acquired, and then a small (or “blipped”) y -gradient takes one to the next row of \mathbf{k} -space, which is then read in the opposite direction, and so on until the whole raster has been recorded. Post-acquisition data processing techniques address the fact that alternate lines of \mathbf{k} -space are read in opposite directions. The significant step forward made by Mansfield was that he saw it was possible to “refocus” the decaying magnetization

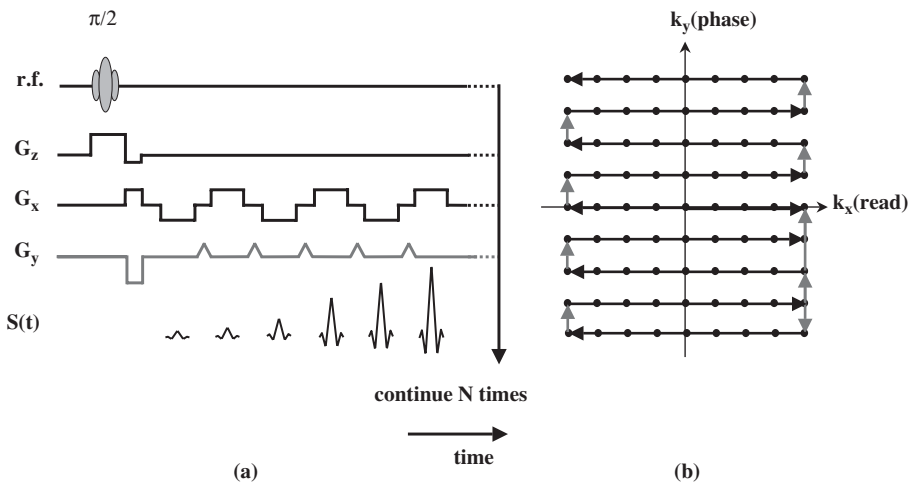


FIG. 14. MBEST-EPI: (a) slice-selective pulse sequence and (b) corresponding \mathbf{k} -space raster.

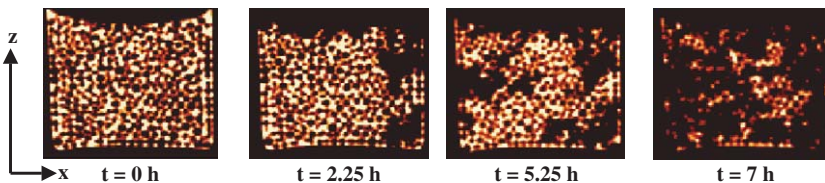


FIG. 15. 2-D slice sections through 3-D MR images of water distribution within an initially water-saturated packing of 500- μm glass spheres. Voxel resolution is $94\ \mu\text{m} \times 94\ \mu\text{m} \times 94\ \mu\text{m}$. Data are shown before drying commenced and at three time intervals during the drying process. Only the water within the inter-particle space of the bead packing was imaged (white pixels). No signal was obtained from the solid and gas phases present.

following r.f. excitation, using the concept of an “echo,” such that it could be used to sample further lines of \mathbf{k} -space (Section II.A.2).

Many variants of EPI have been reported; most have been developed with the aim of reducing potential artifacts in the image. Particular pulse sequences include radial-EPI or REPI (39), π -EPI or PEPI (40), and GRASE (41). Manz *et al.* (42) implemented an EPI-based sequence, which was sufficiently robust to spatially resolve drying within a packed bed of 100- μm glass spheres. Typical data are shown in Fig. 15; although the drying process was characterized by a uniform water mass loss with time, the MR images clearly show the spatial heterogeneity in the drying process. These observations have been used to aid the development of an invasion-percolation modeling strategy, which predicts both the drying rate and the heterogeneity of the drying process (43). The motivation for this investigation was to understand the origins of heterogeneity in the optical properties of pigments dried from a slurry, but such data also provide insights into the effects of drying on the homogeneity of metal loading during catalyst manufacture.

EPI can also be integrated with a transport measurement sequence (e.g., Fig. 7) to provide images of the flow field at timescales of ~ 30 ms or less. Kose (44–46) reported the first EPI MR images of turbulent flow in which individual velocity vectors characterizing the flow were resolved. In particular, the velocity distribution in a cross-sectional plane perpendicular to the direction of superficial flow at a Reynolds number (Re) of 2250 was imaged; clear visualization of a turbulent “puff” was reported. Sederman *et al.* (47) extended the work of Kose to acquire images of three orthogonal velocity components from a single excitation over a time scale of 60 ms, with each velocity component itself being acquired in < 20 ms. Alternatively, in this application, up to 16 velocity images (v_x , v_y , or v_z) can be acquired from a single excitation, at time intervals of 20 ms. Images were acquired in a 2-D data matrix of 64×32 .

The maximum number of images acquired using this approach is limited by the residence time of the moving fluid within the imaging coil. For the system studied here, data acquisition is sufficiently fast that the evolution of turbulent eddies in the flow can be followed. Acquisition of successive velocity images allows the acceleration field to be calculated. In this work, data were acquired over a wide range of Reynolds numbers encompassing the transition from laminar flow into the turbulent flow regime ($1250 < \text{Re} < 5000$). This pulse sequence has been named the

gradient echo rapid velocity and acceleration imaging sequence (GERVAIS) and is based on the MBEST-EPI (or BLIPPED EPI) sequence with the modification that, after the initial excitation pulse, each image is preceded by a velocity encoding gradient pair, separated by a π refocusing pulse.

The GERVAIS pulse sequence is shown in Fig. 16, and the basic combination of transport measurement gradient pair and EPI sequence is clearly seen when one refers to Figs 7 and 14. With reference to Fig. 16, velocities in the x , y , and z directions are acquired by changing the direction of the velocity measurement gradients (g). Figure 17 shows samples of these three Cartesian component velocity images acquired at six different liquid velocities. The velocity component in the superficial direction (v_z) is given by the color scale bar, and the magnitude and direction of the transverse (v_x, v_y) velocity components are indicated by the vector arrows present on each of the images. This pulse sequence has recently been implemented to investigate unsteady state flow phenomena in fixed-bed reactors (Section IV.A.2).

RARE. This type of image acquisition was first realized by Hennig *et al.* (48) and variants such as turbo spin echo (TSE) and fast spin echo (FSE) exist. The k -space sampling strategy appropriate to RARE is shown in Fig. 18, and at first it might not seem so different from the EPI approach—after acquisition of a single line in k -space the coherent signal is refocused and used to acquire further lines in k -space (or averages of the same line). However, there are important differences which

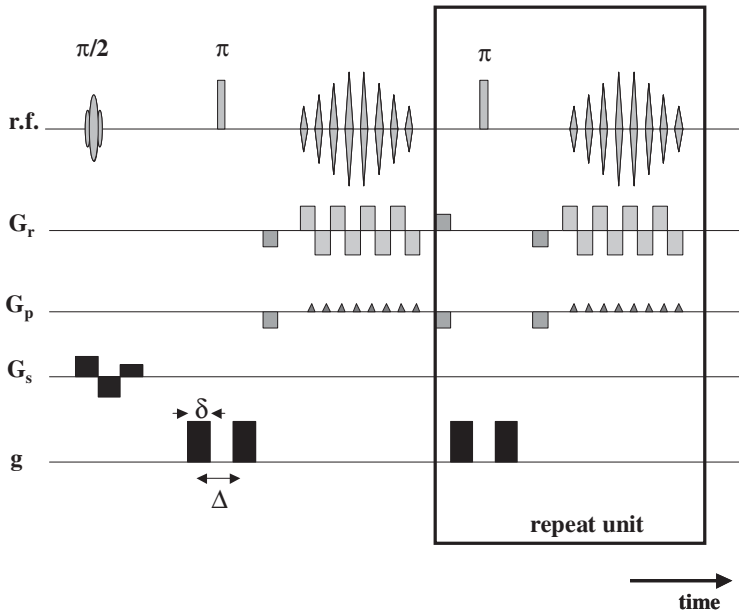


FIG. 16. Schematic representation of the GERVAIS pulse sequence, identifying all pulse and delay timings. The pulse sequence shown is that for acquisition of successive velocity images. The magnitude and orientation of the g -gradient are changed as determined by the velocity or acceleration vector that is to be measured.

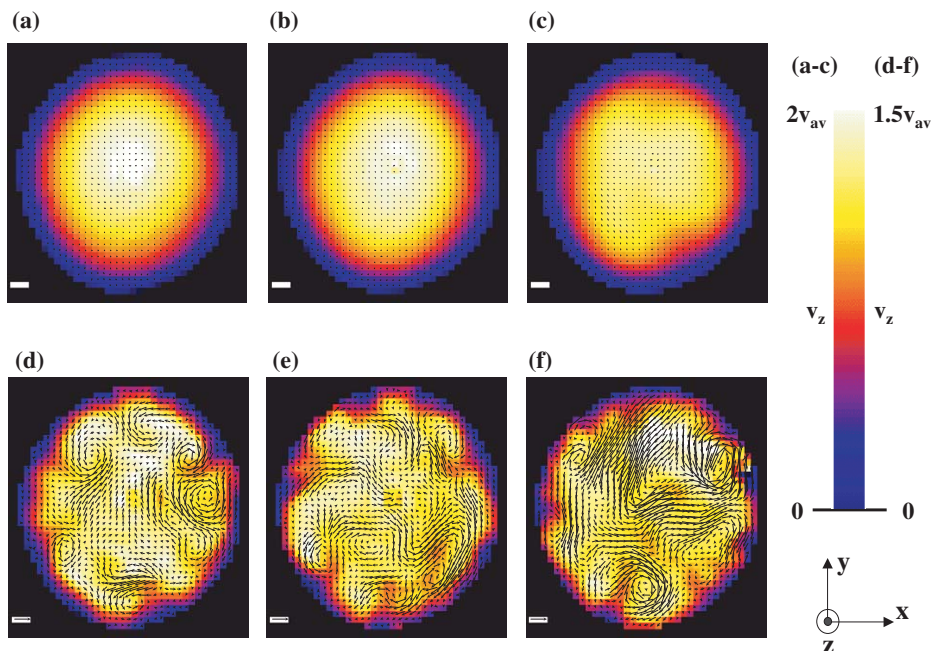


FIG. 17. Imaging unsteady-state and turbulent flow of water within a 29-mm diameter pipe. Three orthogonal component velocity images acquired at increasing Re of (a) 1250, (b) 1700, (c) 2500, (d) 3300, (e) 4200, and (f) 5000 are shown. The color scale identifies the magnitude of the z -velocity, and the flow velocity in the plane of the image (x - y) is shown by the vectors on each image. The vector scale bar on each image corresponds to 1 cm s^{-1} . Reprinted from reference (47), with permission from Elsevier, Copyright (2004).

make RARE much more robust (artifact free) in application to systems characterized by heterogeneous magnetic susceptibility typical of those found in reaction engineering. Furthermore, the decay of the MR signal in a RARE experiment is dependent on T_2 (and, of course, to some extent on T_1) and not T_2^* , as is the case for EPI. In the magnetically heterogeneous systems of interest to us, T_2^* is considerably shorter than T_2 , and therefore RARE allows acquisition of data of higher signal-to-noise ratios over longer time scales, which is important if one wishes to investigate the time evolution of a system.

An example of the application of RARE for rapid image acquisition is shown in Fig. 19, in which a single frame is shown from a series of 2-D images acquired of an oscillatory chemical reaction occurring within a fixed bed. Relaxation contrast is used to discriminate between the reaction products Mn^{2+} and Mn^{3+} (49). In this example, MR offered the opportunity to map the detailed structure of the fixed bed and the product distribution within it. This pulse sequence has also recently been applied to obtain quantitative images of the evolution of a lysozyme–urea separation within a chromatography column (50).

Sederman *et al.* (51) recently implemented a variant of RARE, which yields *multiple images* from full \mathbf{k} -space data at multiple echo times following a single r.f.

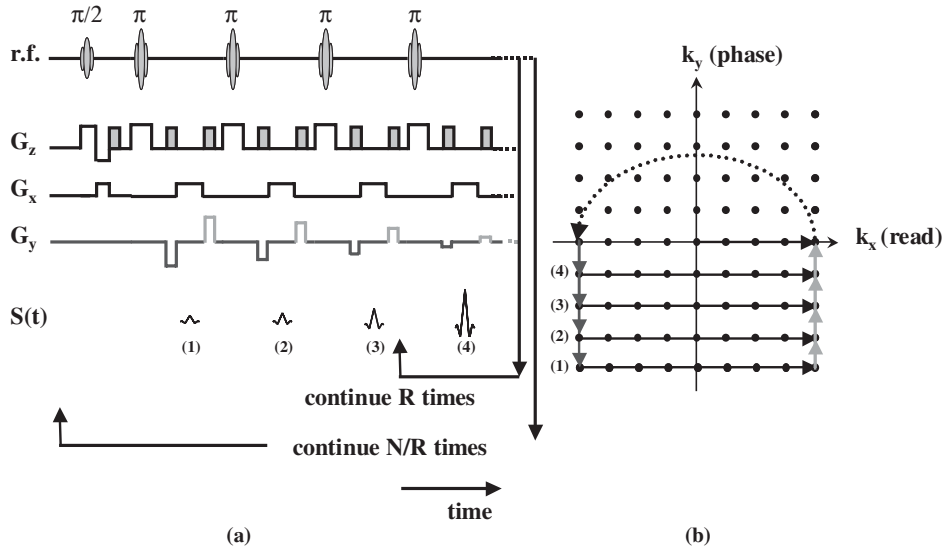


FIG. 18. (a) RARE pulse sequence, and (b) its associated \mathbf{k} -space trajectory. The order of the phase encoding is shown by the numbers to the left of the raster. After each line in \mathbf{k} -space, the spins are returned to the same point on the $k_{x(\text{read})}$ axis prior to the application of the refocusing pulse shown by the dashed line and arrow.

excitation (not just a single complete image from a single excitation). This pulse sequence has been named SEMI-RARE, and it allows acquisition of up to approximately 120 images in immediate acquisition, from a single excitation pulse. The actual number of images acquired from a single excitation is determined by the characteristic nuclear spin relaxation times of the system.

An excellent demonstration of the power of this technique is the visualization of gas–liquid flow within the parallel channels of a ceramic monolith (Fig. 10). To our knowledge, MR is the only technique that has been able to image non-invasively within such a monolith. This is also a fine example of the robustness of the RARE methodology. Not only was there varying magnetic susceptibility across the gas–liquid interface, but there were interfaces of both gas and liquid with the walls of the ceramic channels. In this system, it is not practical to reduce the magnetic susceptibility variations between the gas and liquid by introducing chemical species that modify the magnetic susceptibility of the liquid phase, because they will be adsorbed from the liquid into the porous walls of the monolith. Thus, RARE is probably the only MR method that can be used in this application.

Low excitation angle imaging. The important feature of this technique is that the r.f. excitations are characterized by a low flip angle, θ , typically $5\text{--}10^\circ$, in contrast to the $\pi/2$ pulse discussed in Section II.A.1. For this reason, this technique has been termed fast low-angle shot (FLASH) imaging or SNAPSHOT imaging (52). The signal resulting from small flip angle θ is proportional to $\sin\theta$, and the longitudinal (z -axis) magnetization that remains after the excitation is proportional to $\cos\theta$. Fractions of this remaining magnetization are then used to sample successive

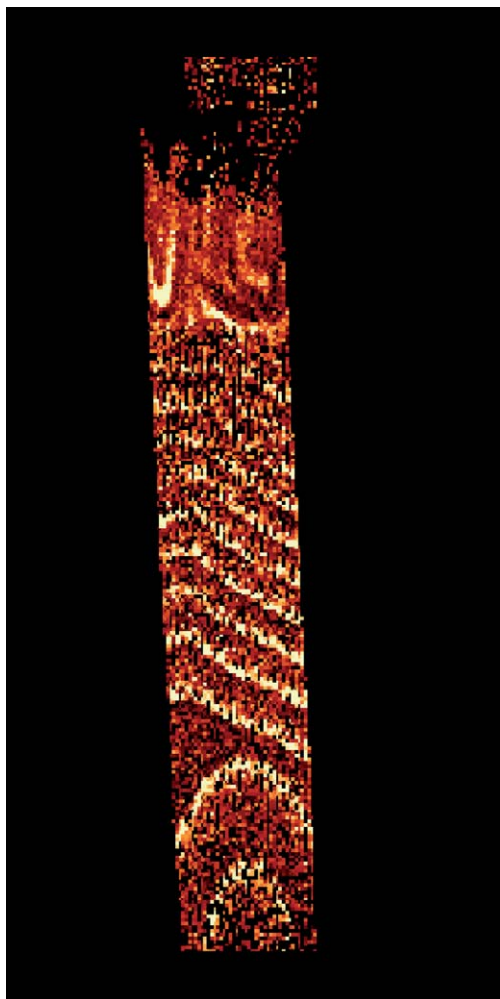


FIG. 19. 2-D MR image of an oscillating chemical reaction occurring within a bed of diameter 15 mm packed with 1-mm-diameter glass beads. In-plane resolution was $195\ \mu\text{m} \times 195\ \mu\text{m}$, and the image slice thickness was 1 mm. A single image was acquired in 1 s. Chemical waves are imaged as a result of the oscillatory production of Mn^{2+} and Mn^{3+} species; the locations of Mn^{2+} and Mn^{3+} are identified as dark and light bands, respectively.

lines of \mathbf{k} -space. A 128×128 image based on a repetition time of 3 ms takes approximately 380 ms to acquire. The disadvantage of this approach is that by using only a proportion of the available magnetization, signal-to-noise in the image is significantly reduced. However, the important advantage is that the acquired signal is not strongly influenced by relaxation contrast effects or artifacts associated with molecular motion and magnetic susceptibility. In short, one is sacrificing temporal (and potentially spatial) resolution (i.e., signal-to-noise ratio) for increased robustness in implementation. Examples of SNAPSHOT

images are given in Section IV.B.2 in application to hydrodynamic transitions in fixed beds.

III. Imaging Individual Catalyst Pellets

The majority of the early MRI studies specific to catalysis addressed the heterogeneity in structure and transport within catalyst pellets. In-plane spatial resolution achieved in these investigations was approximately $30\ \mu\text{m}$, and the pellets themselves were of typical dimension 1–5 mm. In the majority of cases, investigations addressed the pure (usually oxide) support so that the quantitative nature of the data obtained was not lost because of the presence of metal (which introduces an unknown degree of nuclear spin relaxation time contrast into the images).

A. STRUCTURE–TRANSPORT RELATIONSHIPS

Clearly by working with typical spatial resolutions of approximately $30\text{--}50\ \mu\text{m}$, individual pores within the material are not resolved. However, a wealth of information can be obtained even at this lower resolution (53,54,55). Typical data are shown in Fig. 20, which includes images or maps of spin density, nuclear spin–lattice relaxation time (T_1), and self-diffusivity of water within a porous catalyst support pellet. In-plane spatial resolution is $45\ \mu\text{m} \times 45\ \mu\text{m}$, and the image slice thickness is 0.3 mm. The spin-density map is a quantitative measure of the amount of water present within the porous pellet (i.e., it is a spatially resolved map of void volume). Estimates of overall pellet void volume obtained from the MR data agree to within 5% with those obtained by gravimetric analysis.

The spin–lattice relaxation time map (discussed in Section II.A.2) yields information about the spatial distribution of mean pore size within a given image pixel. Lighter shades in the image correspond to larger mean pore size. Even at this coarse

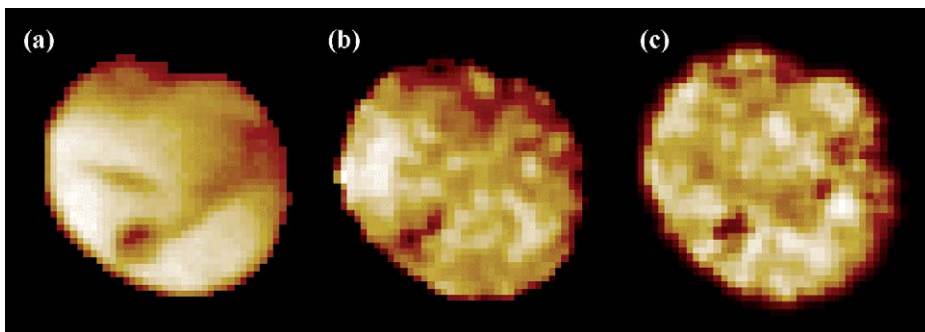


FIG. 20. Spin density, T_1 and water diffusion images for a 2.2-mm-diameter, spherical silica catalyst support pellet. In-plane pixel resolution was $45\ \mu\text{m} \times 45\ \mu\text{m}$; image slice thickness was 0.3 mm. (a) Spin-density map; lighter shades indicate higher liquid content. (b) T_1 map (150–400 ms); lighter shades indicate longer values of T_1 . (c) Diffusivity map ($(0\text{--}1.5) \times 10^{-9}\ \text{m}^2\ \text{s}^{-1}$); lighter shades indicate higher values of water diffusivity within the pellet.

resolution, these data give additional insight beyond that obtainable from a 1-D pore-size distribution as determined, for example, by mercury porosimetry or nitrogen adsorption measurements. Thus by using MR, we can now probe the spatial heterogeneity in porosity within a catalyst pellet introduced during the manufacturing process. Figures 20a and b allow us to discriminate between a region of given void fraction comprising many small pores or a single large pore.

The structure–transport relationship characteristic of the catalyst pellet is shown by comparison of Figs 20a–c; the spatial heterogeneity in the values of the molecular diffusion coefficient is much more consistent with the heterogeneity in the intensity shown in the T_1 map than that of the spin-density map. Thus, we conclude that it is the spatial variation of local pore size that has the dominant influence on molecular transport within the pellet.

There have been a number of investigations exploiting this type of MR measurement. For example, Timonen *et al.* (56) reported water spin-density imaging investigations in which they explored the 3-D structure of activated alumina spheres. The spheres were observed to exhibit a uniform ball structure comprising spherically layered structures and voids. Use of T_1 maps to image spatial variations in locally averaged mean pore size must be performed with caution. T_1 does not provide an absolute measure of the pore size, but it does provide the shape of the pore-size distribution and the spatial distribution of larger and smaller pores. The T_1 values measured are most readily assigned to values of pore size by comparison of the peak in the T_1 population distribution with that of the pore-size distribution determined by nitrogen adsorption measurements.

Simple spin-density imaging has also been used to characterize the tortuosity of catalyst pellets manufactured in various ways (57). This characterization is achieved by initially impregnating the catalyst with deuterated water (invisible in a ^1H MR experiment) and then immersing it in normal protonated water. The diffusive exchange of $^1\text{H}_2\text{O}$ with $^2\text{H}_2\text{O}$ within the pellet is then followed by ^1H imaging. The effective water diffusivity and hence catalyst tortuosity are obtained by fitting the resulting time-resolved $^1\text{H}_2\text{O}$ concentration profiles to a standard (Fick's law) diffusion equation. Measurements of this type are straightforward and give immediate insight into transport anisotropies within the catalyst resulting from the manufacturing process.

When originally recorded, the type of images shown in Fig. 20 suggested a potential dilemma in using this type of information to aid the development of modeling the structure of catalyst pellets and the transport processes occurring within these porous structures. Each pellet that is imaged, even if taken from the same batch, will yield a different image. However, we know that a given batch of pellets is expected to have consistent (typical) properties in use. It therefore follows that there should be some characteristic structural feature of all the pellets taken from a single batch that determines the transport characteristics of that batch.

In an investigation of the spin-density (voidage) and spin–lattice relaxation time maps of many pellets, it was found that it was the heterogeneity in pore size, as characterized by the fractal dimension of the T_1 map, that was consistent between images of pellets drawn from the same batch (58). The fractal dimension of these images identifies a constant perimeter–area relationship for clusters of pixels of

similar intensity (i.e., pore size) in the image. The most natural physical interpretation of this is that a given manufacturing process imposes a common meso-scale (0.1–1 mm) structure characterizing the spatial distribution of pore sizes within the pellet. Numerical modeling strategies employing simulation lattices constructed to have the same fractal dimension as that obtained from the MR images have had some success in predicting mass transfer characteristics in porous catalyst supports (59). Current strategies include combining the characterization of mesoscale structure obtained from MR with characterization of the micropore structure obtained by, say, nitrogen adsorption or mercury porosimetry to construct hierarchical models of the micro- and meso-length scales which control transport processes (60,61).

Although not yet applied to the characterization of catalysts *per se*, MR measurements of thermally polarized gases have been successfully performed using ^{129}Xe and ^{19}F observation (for the case of the ^{19}F nucleus, the molecules CF_4 , C_2F_6 , and SF_6 are usually used) to investigate a variety of inorganic porous media. Mair *et al.* (62) used ^{129}Xe to study the structure of a packed bed of spheres and the gas-phase transport processes occurring within it, with detailed consideration of potential errors in and influences on the measurement. A particularly interesting study is that of Beyea *et al.* (63), who reported a novel application of gas-phase MR was to map the specific surface area and trends in the local adsorption energy within porous materials such as glasses and ceramics. The experiment was done by exposing the porous sample to a gas at a range of pressures and acquiring a spin-density image at each pressure. In this way a spatially resolved Brunauer Emmett Teller (BET) isotherm was generated. In principle this approach could be applied to characterize catalysts in a manner complementary to the aforementioned spin–lattice relaxation time measurements, which also map spatial variations in mean pore size.

B. CATALYST PREPARATION

The ability to image liquid distribution in catalyst support pellets suggests immediate applications in investigations of transport processes occurring during catalyst manufacture and, in particular, wet impregnation methods. Aspects of catalyst preparation, which MR has been used to address include (i) liquid migration, and (ii) ion migration during catalyst drying and synthesis, respectively.

Early work in this field by Hollewand and Gladden (64) used MR relaxation, PFG, and imaging techniques to demonstrate that MR provides a tool for discriminating between uniform and capillary-controlled drying models, even when the bulk-drying curves are similar. Furthermore, the data were used in combination with random pore network modeling studies to estimate the connectivity of the pore structure within the catalyst. More recently, Koptuyg *et al.* (65,66) reported detailed 1-D ^1H imaging studies of acetone, benzene, cyclohexane, and water imbibed within alumina and titania cylinders (of length 1.2 cm and diameter 3.6 mm), and the drying of these liquids under various conditions (different nitrogen flow rates). The 1-D profiles were able to discriminate fast- and slow-drying regimes. Details of the water concentration profiles as a function of time were found to be sensitive to the pore-size distribution of the catalyst support. A numerical analysis of the

quantitative liquid concentration profiles was performed by fitting the profiles to the diffusion equation, allowing for a concentration-dependent diffusivity. It was shown that for liquids characterized by low surface tension, such as acetone, benzene, and cyclohexane, the evolution of the concentration profiles could be modeled adequately on the basis of the assumption of a liquid-independent diffusivity. In contrast, the diffusivity of water in both titania and alumina pellets decreased substantially as the water content decreases.

MRI has also been demonstrated to be a potentially useful tool for characterizing metal ion distributions within catalyst pellets during and after completion of catalyst preparation. To image the metal ion distribution, Khitrina *et al.* (67) exploited the effect of relaxation time contrast within the catalyst resulting from the presence of the hexachloroplatinate dianion. It is non-trivial, and has not yet been attempted, to make such measurements quantitative, but the method does provide a non-destructive method for identifying the positions of metal bands within the catalyst, consistent with the positions identified by an electron probe microanalysis (Fig. 21). The approach uses ^1H microimaging to follow the distribution and spin-lattice relaxation time of cyclohexane imbibed within the catalyst. Cyclohexane interacting with the hexachloroplatinate dianion during the timescale of the measurement is associated with an increased spin-lattice relaxation time, and therefore T_1 -maps of the sample identify the location of the ion within the porous catalyst support. The same methodology was used to follow the dynamics of hexachloroplatinate dianion redistribution during a competitive impregnation of the support with an aqueous solution of $\text{H}_2\text{PtCl}_6 + \text{H}_2\text{C}_2\text{O}_4$ (oxalic acid). It was found that after 5 h of impregnation, the egg-white-type profile transforms into a classic egg-yolk type profile.

C. LIQUID REDISTRIBUTION DURING REACTION

Koptyug *et al.* (68) reported ^1H images of liquid distribution during α -methylstyrene evaporation accompanied by its hydrogenation (with vapor-phase reactants) within a cylindrical $\text{Pt}/\gamma\text{-Al}_2\text{O}_3$ catalyst pellet (diameter and height 4.7 mm). In-plane spatial resolution was $230\ \mu\text{m} \times 140\ \mu\text{m}$, with an image slice thickness of 2 mm. A stream of hydrogen gas heated to 340–342 K and saturated with α -methylstyrene vapor was supplied to the pellet at a flow rate of $18.5\ \text{cm}^3\ \text{s}^{-1}$. A thermocouple implanted in the pellet indicated that the temperature of the pellet increased by 40 K above that of the gas as a result of the exothermic nature of the catalytic reaction. A single image took approximately 4 min to acquire. Figure 22 shows the spatial maps of the liquid phase within the catalyst pellet under catalytic reaction conditions—the MR signal arises from any ^1H containing species within the pores of the pellet that has relaxation time characteristics such that signal from that species can be acquired using the r.f. pulse sequence used. The results suggested that under conditions of the simultaneous evaporation of the reactant and the hydrogenation of its vapor, two regions with very different compositions can form within the catalyst, with one region having a large liquid content and the other filled with the reacting gas mixture.

This work has recently been extended, again with a single $\text{Pd}/\text{Al}_2\text{O}_3$ catalyst pellet (69). The image time was reduced to 34 s by introduction of manganese ions into the

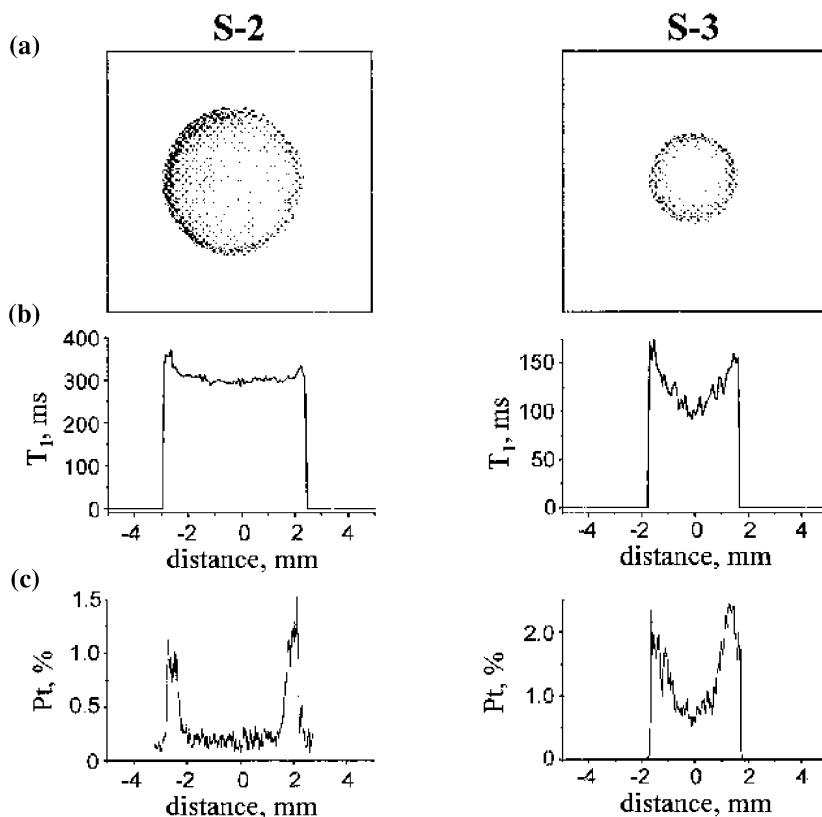


FIG. 21. (a) 2-D T_1 maps, (b) their 1-D central cross sections, and (c) the 1-D profiles of hexachloroplatinate dianion distributions obtained by electron probe analyzer measurements. S2 and S3 identify different porous alumina pellets, both prepared with an eggshell distribution of hexachloroplatinate dianion. S2 and S3 differ in terms of their nominal diameter and their pore size and surface area characteristics. Reprinted from reference (67), with permission from American Chemical Society, Copyright (2000).

pellet such that the relaxation times of the reactant and product molecules were reduced; the manganese ions were not believed to influence the catalytic reaction itself. By decreasing the image time, time-resolved images of the oscillatory movement of the liquid front within the pellet were recorded; such images are consistent with the expected coupling of mass transport and phase transition processes with heat transfer in the reacting system.

To date there have not been any reports of chemically resolved images within oxide-supported catalysts—the ^1H signal in the preceding example did not differentiate between reactants and product species. This limitation results from the severe line broadening that occurs in the ^1H MR resonances associated with individual molecular species when these molecules interact with the catalyst surface, causing a reduction in their nuclear spin relaxation times. However, this is not necessarily an insurmountable problem. Judicious selection of reaction systems may

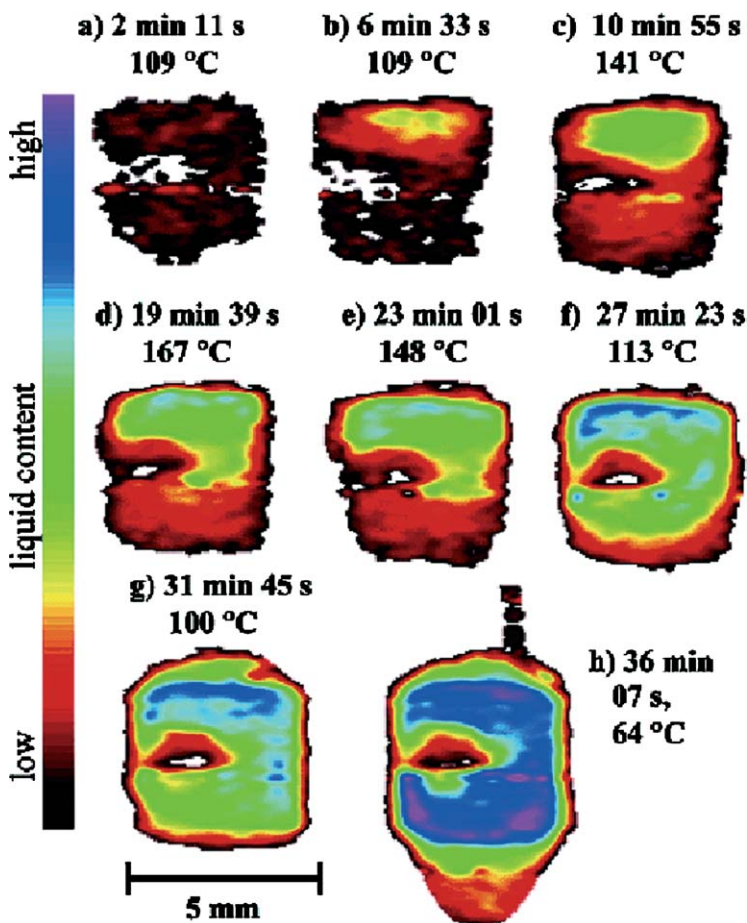


FIG. 22. Spatial maps of the liquid-phase distribution within a catalyst pellet under reactive conditions. For each image, the temperature and time of detection are indicated. The intensity scale is shown on the left-hand side. Reprinted from reference (68), with permission from American Chemical Society, Copyright (2002).

identify specific systems in which the relevant ^1H resonances can be discriminated. Alternatively, imaging of nuclei other than ^1H may provide the solution; ^{13}C is an obvious choice. Although the sensitivity of a ^{13}C measurement is substantially less than that of a ^1H measurement, the existence of fewer, well-separated ^{13}C lines in a typical ^{13}C spectrum of a reaction mixture might make such measurements possible (Section V.A.2). Indeed, preliminary ^1H and ^{13}C measurements of chemical composition within individual catalyst pellets have now been achieved.

D. COKE DEPOSITION

A natural extension of the investigations of single-pellet micro-imaging is to explore the effect of pore structure on the spatial distribution of coke deposition

within the pellet. Cheah *et al.* (70) reported MR images of liquid-saturated coked pellets which clearly showed that even while visual observations of pellets as a function of coking might be consistent with the shrinking-core model commonly employed in chemical engineering, coke deposition actually proceeds in a much more heterogeneous fashion, with regions of coke deposition occurring towards the interior of the pellet ahead of a higher concentration of coke deposition which is well described by the shrinking core model. Furthermore, the length scale over which coke was deposited within isolated regions in the internal pore structure of the catalyst corresponded to that of the length scale of heterogeneities in the pore structure as determined by relaxation time mapping experiments.

Bonardet *et al.* (71) employed a different strategy. These workers imaged the ^1H spin density associated with 2,3-dimethylpentane probe molecules adsorbed on pellets of HY zeolites coked to levels of 7.5 and 10% w/w. The 1-D image profiles of the 7.5% w/w coked sample showed a heterogeneous coke distribution in the pellet at the macroscopic level. The most heavily coked region is that first exposed to reaction, and the heterogeneity in coking was again found to be associated with structural heterogeneities arising from the pellet manufacturing process. Bonardet *et al.* (71) also concluded that the coke is heterogeneous in quality throughout the pellet. By varying the echo time used in the pulse sequence it was found that the T_2 of the probe molecule, which is a function of the aromaticity of the coke with which it interacts, varies within the pellet. In particular, the more heavily coked zones were associated with coke characterized by the shortest T_2 values, indicative of coke of the highest graphitic content. The more highly coked sample had a more homogeneous coke distribution, with the coke being of a homogeneous graphitic content throughout.

A third approach to addressing coke deposition has been demonstrated by Bar *et al.* (72), who investigated the location of coke deposits in industrial HZSM-5 pellets, of diameter 5 mm, contained in a small fixed-bed reactor. The coke distribution was detected directly by use of the SPRITE technique, a special MRI sequence for detecting materials with short T_2 relaxation times. In the example given, SPRITE was used to produce a 1-D coke profile along the axis of the model fixed bed of inner diameter 3 cm, containing two layers of coked pellets (20.5 wt.% coke) separated by a 3.3 cm layer of fresh pellets. A spatial resolution of 0.5 cm was obtained, this being limited by the rapid nuclear spin relaxation times of the sample. These workers also used an approach similar to that of Bonardet *et al.* (71) in which the presence of carbonaceous deposits is observed indirectly by imaging the ^1H spin density of propane loaded within the sample. The different adsorption strengths of propane on the fresh and coked HZSM-5 cause T_2 to vary between the fresh and coked regions, hence allowing the regions of coked and fresh catalyst to be identified.

The effect of coke deposition on pore structure and molecular diffusion within supported metal catalysts has also been investigated (73).

IV. Hydrodynamics in Reactors

So far, MR studies of reactors of relevance to catalytic processes have been restricted to fixed beds and ceramic monoliths. Recently, the first reports of MR being

extended to investigations of fluidized beds have been made, and these are noted briefly for completeness.

A. SINGLE-PHASE FLOW

A.1. High Spatial Resolution of Fluid Flow in Fixed-Bed Reactors

Single-phase flow in porous structures has been investigated extensively by researchers interested in flow within porous rocks and the more fundamental aspects of the effect of the structure of inter-particle space on fluid transport (74–76). High-resolution MRI investigations of fluid flow in packed beds with column-to-particle diameter ratios that are typical of narrow fixed-bed reactors were first reported in the mid-1990s. The first investigations were performed with beds of column-to-particle diameter ratio 10–20, and the packing was non-porous glass spheres. Figure 23 shows 2-D sections through 3-D volume images of the x , y , and z components of flow within a fixed bed of non-porous spherical particles. The map of the z -component of the flow velocity is the most interesting; the $+z$ direction is the direction of superficial flow in the reactor. In this example, the superficial flow velocity was 0.56 mm s^{-1} , corresponding to a Reynolds number of 2.8; hence, flow in much of the bed was dominated by viscous forces, associated with flow velocities less than, or of order of, the superficial velocity. The most striking characteristic of these images is the extent of heterogeneity in the flow field; a relatively small fraction of the inter-particle space carries a high percentage of the liquid flow (77–79).

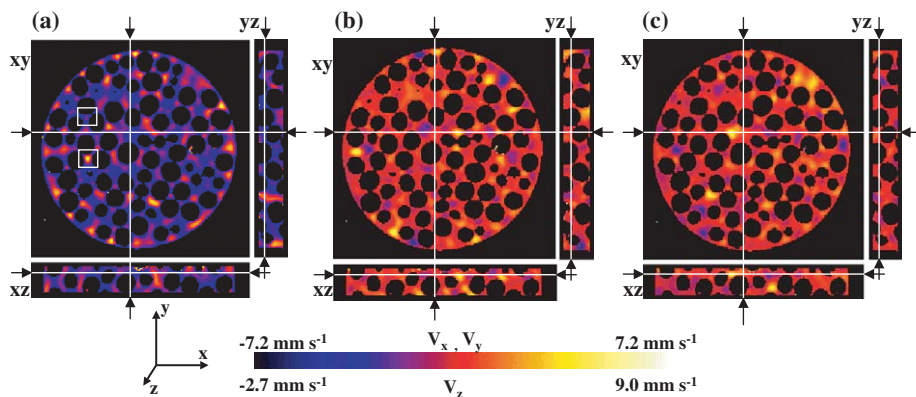


FIG. 23. MR visualization of water flowing within a fixed bed of spherical glass beads; the beads have no MR signal intensity associated with them and are identified as black voxels. Flow velocities in the (a) z -, (b) x -, and (c) y -directions are shown with slices taken in the xy , yz , and xz planes for each of the velocity components. In each xy -image the positions at which the slices in the other two directions were taken are identified. Voxel resolution is $195 \mu\text{m} \times 195 \mu\text{m} \times 195 \mu\text{m}$. The glass beads were of diameter 5 mm and were packed within a column of internal diameter 46 mm. Typically, 40% of the flow was carried by approximately 20% of the inter-particle space within any 2-D slice section through the bed, perpendicular to the direction of superficial flow. Regions of high- and low-flow velocity in the direction of superficial flow are highlighted in (a). Reprinted from reference (77), with permission from Elsevier, Copyright (2001).

Such regions of the bed are associated with high fluid velocities, and inertial effects increasingly influence the flow profile as Reynolds number increases (80). On the basis of these images, it is clear that any theoretical analysis of the flow within such a reactor must account for distinct populations of fast- and slow-moving liquid—channeling does not occur just at the walls of the bed.

The contact time between feed and catalyst varies significantly across the bed (by up to at least an order of magnitude in regions of the bed characterized by the highest and lowest flow velocities), and this variation introduces spatially varying mass transfer characteristics within the bed. The spatial resolution of the flow field is such that the flow profile between individual particles can be extracted from the data. This point is clearly illustrated in Fig. 24, which shows that at low velocities (or, more precisely, below a critical value of a local Reynolds number), parabolic, laminar flow is observed, whereas at higher local velocities the flow profile flattens such that it is much more characteristic of plug flow. The transition in flow regime occurs at a local Reynolds number of approximately 30. Reynolds number is defined as $(\rho dv/\mu)$ where ρ , v , and μ are the density, superficial velocity, and dynamic viscosity of the liquid, respectively, and d the characteristic length scale in the system. The local Reynolds number is defined with d being the length scale of the local void space—which is approximately the diameter of the packing elements.

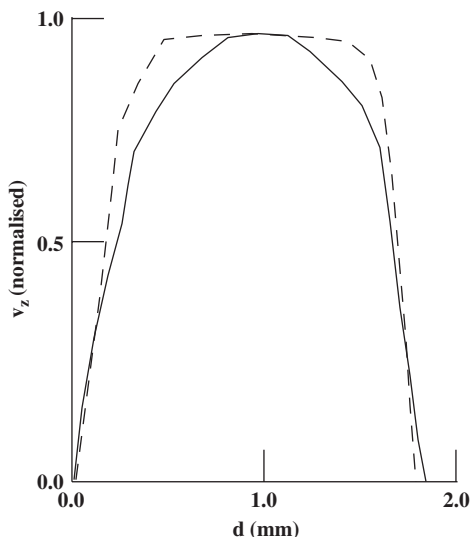


FIG. 24. Velocity profile for flow of water through two different regions (highlighted in Fig. 23a) of the inter-particle space within a fixed bed of spherical glass beads. The velocity profiles are measured across the inter-particle space between two packing elements. Profiles are shown for local regions associated with fast and slow flow velocities, characterized by a local Re of 50 and 12, respectively. At low Reynolds number, a parabolic flow profile typical of Poiseuille flow is evident (—). At the higher Reynolds number, inertial effects in the flow are evident, and the flow approaches plug flow (---). For this particular bed, the Reynolds number based on bed diameter is 15. Reproduced with permission from reference (80). Copyright 2000 AIChE.

MR data of this type have direct use in terms of identifying how catalyst particle size, shape, and method of loading into the reactor influence heterogeneities in hydrodynamics. At a more academic level, the combination of 3-D MR images of the bed structure with flow visualization allows us to explore how the geometry and inter-connectivity of the inter-particle space determines the local flow characteristics within the bed. This field is now receiving increasing interest among academics and catalyst manufacturers interested in investigating how subtle changes in pellet size and shape influence the spatial distribution of porosity and hence hydrodynamics within the reactor (81).

Suekane *et al.* (82) reported MR velocity imaging studies of flow at values of Re up to 205 in a narrow packed bed and investigated the relative importance of inertial to viscous forces as a function of Reynolds number, again using the concept of a local Reynolds number. More recently, Tang *et al.* (83) combined radial MR velocity profiles of single-phase flow within narrow fixed beds (with column-to-particle diameter ratios < 10) with a traditional reaction engineering characterization of the same beds (namely, residence-time distribution analysis). They investigated the influence of column-to-particle diameter and Reynolds number (based on particle diameter) on the dispersion and degree of non-uniformity of the velocity profile.

Figures 25 and 26 show how the combined application of MRI and flow imaging allows us to study deposition of fines within fixed beds. This is a common problem in reaction engineering. For example, during process operation, attrition of the catalyst occurs and the resulting fines are deposited throughout the bed. The deposits then influence the flow paths through the bed, thereby influencing the operating conditions within the bed (e.g., pressure drop) and chemical conversion.

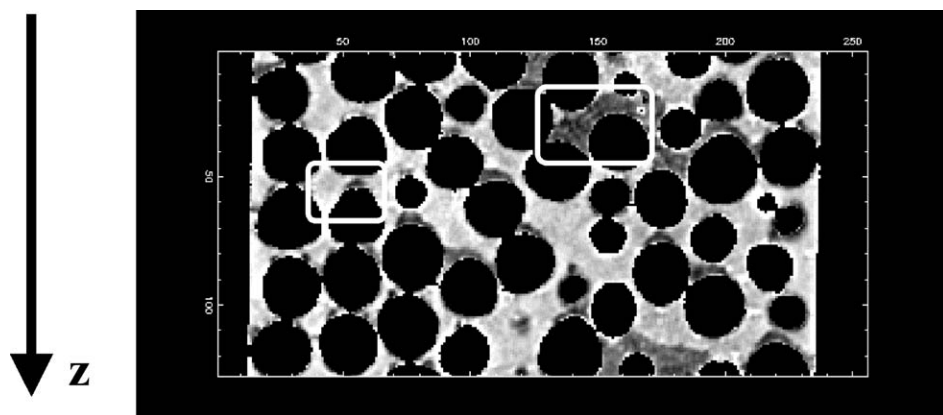


FIG. 25. 2-D MR image of the deposition of 80- μm particles (fines) within a bed packed with 5-mm diameter spherical glass beads. The water flow rate was 300 mL min^{-1} . All images were acquired in 3-D with isotropic spatial resolution of $188\ \mu\text{m} \times 188\ \mu\text{m} \times 188\ \mu\text{m}$. Two local regions associated with a buildup of fines are highlighted and are identified by the low apparent ^1H spin density from these regions resulting from low voidage and relaxation time effects. Flow was in the $+z$ direction. Reprinted from reference (84), with permission of Springer Science and Business Media.

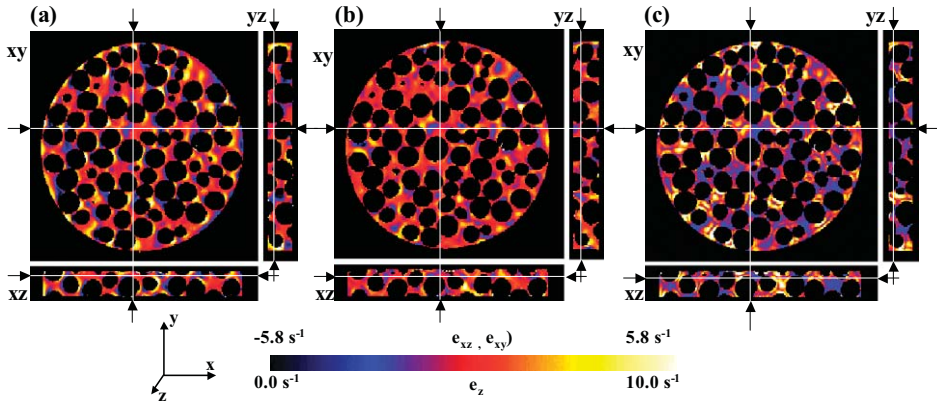


FIG. 26. Images of the liquid stress tensor derived from the data shown in Fig. 23. Data are shown for (a) e_{xz} , (b) e_{xy} , and (c) $|e_z|$ with slices taken in the xy , yz , and xz planes for each of the shear components. Regions of high shear are particularly evident in (c) (i.e., along the direction of superficial flow, z). Reprinted from reference (77) with permission from Elsevier, Copyright (2001).

Figure 25 shows an image of water concentration (or, more precisely, ^1H spin density) within a 2-D slice through a fixed bed of glass beads (84). The beads are evident as black on the color scale and the free water as white. Regions of fines deposition are readily identified as the gray contrast level; when fines are deposited, they pack to produce regions of low voidage and hence are observed as regions of reduced water (^1H) content. The images shown in Fig. 26 explain how the MR flow images shown in Fig. 23 may be used to understand the phenomena leading to deposition. Figure 26 shows maps of the shear stress in the liquid as it moves through the bed. These maps were calculated directly from the flow images shown in Fig. 23 (77). From these maps we see precisely where regions of high liquid-shear stress exist within the bed. Such regions are associated with particle erosion but are not likely to be regions in which significant fines deposition will occur. In contrast, in regions of low shear stress little particle erosion will occur, but we expect them to be particularly susceptible to fines deposition. As regions of particle deposition extend within a bed, the hydrodynamics and pressure drop characteristics also change.

In addition to the immediate practical application of imaging flow fields within reactors, data sets such as these are of use in developing, implementing, and validating numerical codes for the prediction of flow and chemical conversion in process units. In particular, if the 3-D MR image of the internal structure of the reactor is used directly as the simulation lattice in the flow-field simulation code, the subsequent comparison of MR velocity data with the predictions of the code enables a direct evaluation of the ability of the code to predict the flow field. This point is important because often when numerical predictions are compared with experimental results, assumptions have to be made in constructing the simulation lattice itself, which means that the final comparison is influenced not only by the ability of the code to predict the flow field but also the ability to construct a

simulation lattice which captures the essential detail of the internal structure of the reactor.

A demonstration of this approach has been reported to evaluate the ability of a lattice-Boltzmann code to predict both spatially resolved flow fields and MR propagators characterizing flow through random packings of spheres (model fixed beds) for flows defined by Péclet (Pe) and Reynolds numbers in the range $182 < Pe < 350$ and $0.4 < Re < 0.77$ (85). Excellent agreement was found between the numerical predictions and experimental measurements. Current interest in this field addresses the validation and development of numerical codes predicting flows at Reynolds numbers more appropriate to real catalytic reactors.

Other areas in which MR velocity and micro-imaging can be expected to contribute are in optimizing the implementation of a given code. For example, what boundary conditions should be imposed? How many unit cells or layers of the packed bed should be used to give adequate representation of the bed within the simulation. Of course, such methodologies need not be exclusively associated with MR data, but MR is currently the best-placed imaging tool for obtaining images at high spatial resolution of both internal structure (e.g., such that several pixels define each packing element) and transport phenomena within optically opaque media.

A.2. *Imaging Unsteady-State Flows in Fixed-Bed Reactors*

An aspect of reactor design characterized by a lack of sufficient understanding is the operation of a fixed bed under unsteady-state flow conditions. A good example is the design of narrow packed beds, typical of those required for processes requiring high rates of heat or mass transfer (86), exemplified by the steam-cracking process for conversion of long-chain hydrocarbons. Greater rates of heat and mass transfer can be attained by using turbulent flows, but the associated flow fields are difficult to predict. Computational fluid dynamics (CFD) codes are being developed (e.g., (87)), but a technique for imaging the flow fields is required to validate the CFD results.

Until recently, MR flow imaging in fixed beds was limited to imaging pseudo-steady-state phenomena. Data acquisition times for 2-D flow images were typically several minutes, or even tens of minutes, and successful imaging of the velocity field requires the flow field to be stable over the data acquisition time. Therefore, flow imaging studies had been restricted to relatively low flow rates ($Re < 200$ based on the diameter of the packing elements) (82). Figure 27 shows data for a narrow packed bed characterized by a column-to-particle diameter ratio of 2; spheres of diameter 19 mm were packed within a 38-mm-diameter column. Flows at two different values of Reynolds number are shown ($Re = 200$ and 300).

This figure shows the first quantitative images of an unsteady-state flow field within a fixed bed recorded by MR (88). When the flow was steady, a time-averaged acquisition over several minutes was artifact free. This was the case at $Re = 200$, shown in Fig. 27a(i). However at $Re = 300$, when the flow was becoming unsteady, significant artifacts were acquired with the conventional standard spin-echo phase encoding velocity measurement. Images (ii) and (iii) at each value of Reynolds number show the v_z and v_{xy} flow vectors measured using the rapid velocity imaging

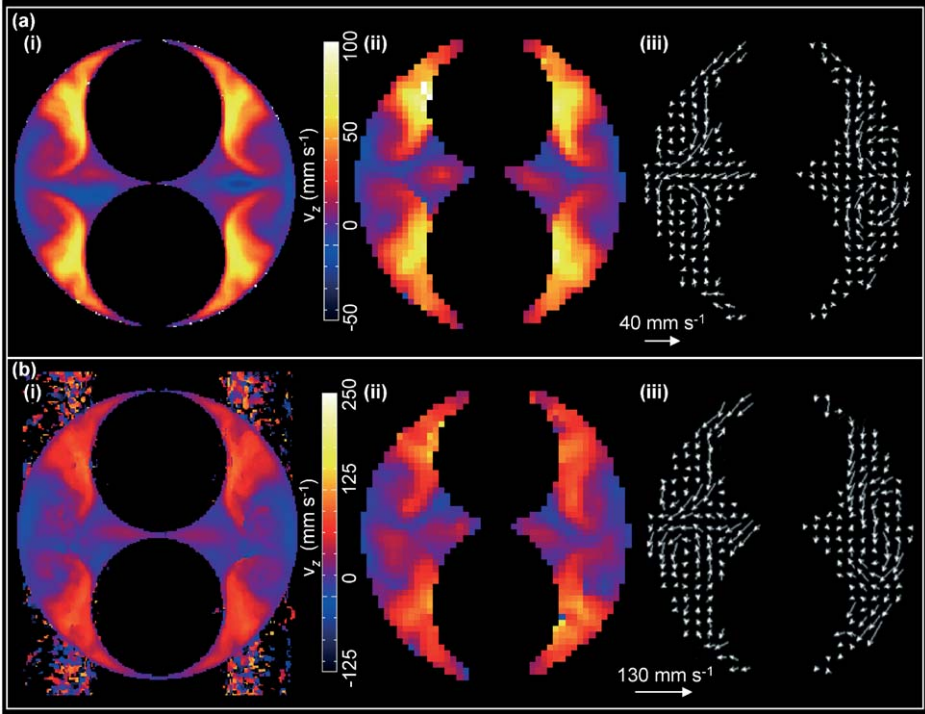


FIG. 27. MR flow images of unsteady-state flow of water through a fixed bed with a column-to-particle diameter ratio of 2. Velocity maps measured by a standard spin-echo phase encoding velocity measurement and the GERVAIS pulse sequence are compared for values of Re of (a) 200 and (b) 300. In each case (i) is the standard spin-echo phase encoding velocity image, and (ii) and (iii) are the v_z and v_{xy} flow vectors measured using GERVAIS.

sequence GERVAIS described in Section II.E.2. In the case of the v_{xy} data, only one in every four flow vectors is shown for clarity. The standard spin-echo phase encoded velocity images were acquired with in-plane spatial resolution of $195 \mu\text{m} \times 195 \mu\text{m}$ in a 256×256 data array, with a data acquisition time of 35 min. GERVAIS data were acquired as a 64×32 raster and Fourier transformed to give a 64×64 image with in-plane pixel size of $781 \mu\text{m} \times 781 \mu\text{m}$. The data acquisition time was 20 ms. All images have a slice thickness of 1 mm. To achieve the reduction in image acquisition time from 35 min to 20 ms, in-plane resolution has been sacrificed ($195 \mu\text{m}$ to $781 \mu\text{m}$) to achieve similar signal-to-noise ratios. In practice, the GERVAIS sequence yields slightly higher signal-to-noise ratios than the standard “slow” imaging sequence.

The results presented in Fig. 27 represent an exciting advance because they demonstrate that the GERVAIS pulse sequence allows direct imaging of regions of liquid recirculation in both the z - and xy -velocity fields. However, a word of caution is needed. Because GERVAIS is an EPI-based technique, it requires that variations in magnetic susceptibility within the sample be minimized. In this system, plastic spheres were used, which were naturally susceptibility-matched with water. If this

had not been the case, chemical agents could instead have been introduced into either phase to satisfy this susceptibility-matching criterion. These investigations have been extended to measure velocity fields up to $Re = 775$ and to investigate the flow in the entrance- and exit-zones of the bed, where highly unsteady-state behavior occurs (89).

B. TWO-PHASE FLOW IN FIXED-BED REACTORS

The natural extension of the single-phase flow studies discussed in Section IV.A is to two-phase flow phenomena. In moving to two-phase flows, it becomes more challenging to retain the quantitative nature of the MR experiment, because typically three or more phases are present, with increased magnetic susceptibility variations within the system. However, as shown below, new insights into reactor operation have been obtained with MRI. Until now such reactors have not been well characterized in terms of their two-phase flow characteristics because of the lack of non-invasive probes of optically opaque systems that can provide data at sufficiently high spatial resolution—along with chemical specificity. There is therefore a strong motivation to employ MRI in this application.

Two-phase flow investigations of fixed-bed reactors fall into two categories: quantification of holdup and wetting characteristics under conditions of trickle flow (Section IV.B.1) and the more recent studies of hydrodynamic transitions and, in particular, the transition from trickle flow to pulse flow in trickle-bed reactors (Section IV.B.2). These investigations have been performed with beds of diameter 40–45 mm filled with packing elements with a typical dimension of 3–5 mm. Given the typical spatial resolution of 100–300 μm , the packing elements and flow field are well resolved in these investigations.

B.1. *Holdup and Wetting in Trickle Flow*

Trickle-bed reactors usually consist of a fixed bed of catalyst particles, contacted by a gas–liquid two-phase flow, with co-current downflow as the most common mode of operation. Such reactors are particularly important in the petroleum industry, where they are used primarily for hydrocracking, hydrodesulfurization, and hydrodenitrogenation; other commercial applications are found in the petrochemical industry, involving mainly hydrogenation and oxidation of organic compounds. Two important quantities used to characterize a trickle-bed reactor are (i) holdup and (ii) wetting efficiency. Holdup is defined as the fraction of (interparticle) void space containing liquid. The wetting efficiency is obtained by calculating the fraction of the surface of the packing, which is in contact with liquid during gas–liquid flow. MRI allows quantification of both holdup and wetting directly at sufficiently high spatial resolution that individual packing elements can be investigated.

Prior to the use of MR to investigate holdup and wetting, while direct measurements of macroscopic holdup could be made gravimetrically, only indirect measurements of surface wetting had been reported. Such indirect measurements of wetting include chemical methods based on reaction rates (90) and tracer (91),

dissolution and dye-adsorption (92–94) techniques. Other non-invasive techniques have been used to characterize flow in trickle beds but, as yet, have not been able to challenge the spatial resolution that MRI offers; however, they can offer faster data acquisition and may be used more readily in large-scale facilities. These techniques include conductance and capacitance methods (95,96), optical methods (97–99), and X-ray tomography (100,101). Initial MRI investigations focused on packings of non-porous glass spheres. Recently, holdup and wetting in beds of porous packings have been reported.

Figure 28 shows the nature of the data obtained (102). In Fig. 28b, the total liquid holdup in the image slice has been partitioned into what we call rivulets, by use of a pore space segmentation algorithm. Application of this algorithm is merely an objective, reproducible procedure to characterize the liquid distribution within the bed. The direct measurement of liquid–solid and gas–liquid contacting is the most important aspect of this work and is still a subject of investigation for beds of porous packing elements, as discussed below. However, even in the case of liquid holdup, which can be measured gravimetrically, MRI can yield new insights. For example, as shown in Fig. 29, the behavior of liquid holdup, χ , as a function of liquid flow velocity, v_l , at constant gas velocity can be impossible to interpret without access to imaging data. The images recorded at these liquid velocities show that the liquid holdup increases relatively sharply at first and then more gradually with increasing v_l . Images recorded at the lower liquid velocities show that only a small proportion of the voxels containing liquid were parts of rivulets, most of the liquid holdup being in the form of surface-wetting films. At the lowest value of liquid superficial velocity of 0.5 mm s^{-1} , only seven rivulets were observed. As v_l increased, the number of rivulets increased sharply to 30 at $v_l = 2.0 \text{ mm s}^{-1}$ and

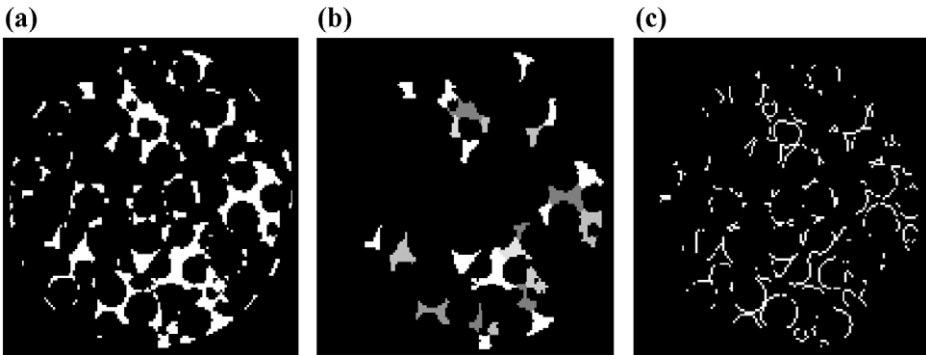


FIG. 28. Identification of rivulets and surface wetting in a packing of 5-mm-diameter glass spheres contained within a column of internal diameter 40 mm. The data were acquired in a 3-D array with an isotropic voxel resolution of $328 \mu\text{m} \times 328 \mu\text{m} \times 328 \mu\text{m}$. (a) The original image of trickle flow is first binary gated, so that only the liquid distribution within the image is evident (white); gas-filled pixels and pixels containing glass spheres are identified as zero intensity (black). (b) The liquid distribution is broken up into individual liquid rivulets, each identified by a different shade on a gray scale. (c) Pixels containing any liquid–solid interface are identified by using image analysis techniques, and “images” of surface wetting are produced. Data are shown for liquid and gas superficial flow velocities of 3 and 66 mm s^{-1} , respectively. Reprinted from reference (102) with permission from Elsevier, Copyright (2001).

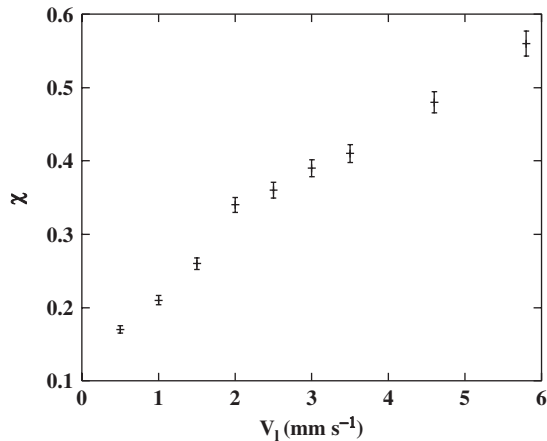


FIG. 29. Plot of the liquid holdup (χ) as a function of increasing liquid velocity (v_l). An increase in the liquid saturation was observed with increasing liquid flow rate. The gas superficial velocity was constant at 66 mm s^{-1} . Data are shown for a bed of 5-mm-diameter ballotini packed within a column of inner diameter 40 mm. Reprinted from reference (102) with permission from Elsevier, Copyright (2001).

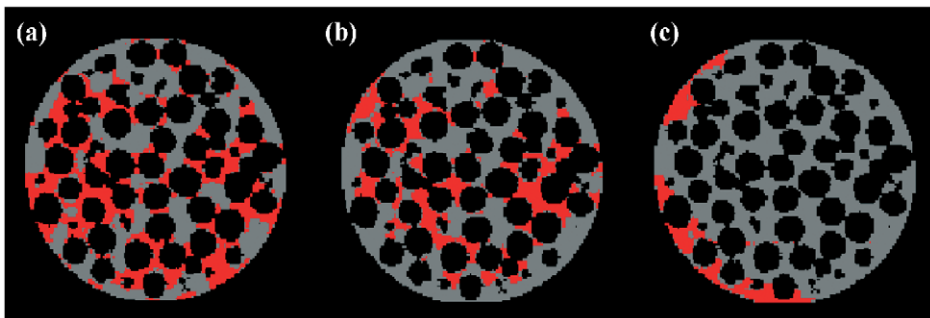


FIG. 30. MR images of gas and liquid distribution within a fixed-bed reactor operating at air and water velocities of 66 and 4.6 mm s^{-1} , respectively. The start-up conditions were different in each case: (a) full pre-wetting; (b) pre-wetting the bed using pulsing flow as in (a) and then allowing the bed to drain for 20 min in the absence of flow prior to establishing trickle flow; (c) no pre-wetting. Red, gray, and black pixels identify water, air, and packing elements, respectively.

then leveled off. As v_l increased beyond 2.0 mm s^{-1} , the existing rivulets increased in size and few, if any, new liquid rivulets were formed.

Images showing the gas–liquid distribution also give important insights into how start-up influences the resulting gas–liquid distribution. Figure 30 shows the gas–liquid distribution for a gas velocity of 66 mm s^{-1} and a liquid velocity of 4.6 mm s^{-1} for start-up conditions of (a) pulsing gas and liquid through the bed for at least 5 min before establishing the trickle flow conditions; (b) pre-wetting of the bed using pulsing flow as in (a) and then allowing the bed to drain for 20 min in the absence of flow prior to establishing trickle flow; and (c) establishing trickle flow directly in a dry bed—this start-up condition clearly caused a very poor gas–liquid

distribution, with the liquid being present primarily in channels at the wall of the bed. Comparison of the images associated with the different start-up conditions shown in (a) and (b) shows that full pre-wetting of the bed followed by immediate establishment of the trickle flow yields significantly greater catalyst wetting and holdup. For gas and liquid velocities of 66 and 3 mm s⁻¹, respectively, the enhancement in adopting the full pre-wetting start-up over that in which the bed is pulsed and then drained is approximately 70% in holdup, surface wetting, and the number of liquid rivulets.

Extension of this methodology to porous packing elements (e.g., catalyst support pellets) is not straightforward. The challenge arises because the signal we wish to measure is associated with the liquid (water) in the bed. However, the signal intensity acquired from a specific region of water depends on its local environment, because the nuclear spin relaxation times of water in different physical environments will vary. In this system, the different environments will be (i) free water in the bulk of the inter-pellet space, (ii) water within the intra-pellet pore space, and (iii) water present in films on the surfaces of the pellets but not part of a rivulet within the inter-pellet space.

Initial investigations have been reported of holdup and wetting during trickle flow in a fixed bed packed with cylindrical, porous alumina extrudate. Data were presented for two packings: (i) packing of diameter 1.5 mm and a distribution of lengths in the range 5 ± 2 mm and (ii) packing of diameter and length equal to 3 mm. A constant gas superficial velocity of 31.3 mm s⁻¹ was used, with liquid superficial velocities in the range 0.1–6 mm s⁻¹. 2-D visualizations of liquid distribution within transverse sections, (of thickness 1 mm) were obtained; the total data acquisition time for each image was 25 min. Data were recorded with a field-of-view of 40 mm × 40 mm and a data array size of 256 × 256, thereby yielding an in-plane spatial resolution of 156 μm × 156 μm (103).

Figure 31 shows plots of dynamic liquid holdup (the dynamic liquid holdup is the total holdup minus the holdup at zero liquid superficial velocity) and wetting efficiency as a function of liquid superficial velocity for a constant gas velocity of 31.3 mm s⁻¹. It is clear that dynamic liquid holdup increases more rapidly as a function of liquid superficial velocity within the 1.5 mm packing, and values of holdup and wetting efficiency are always greater, for a given liquid velocity, for the 1.5-mm diameter packing than for the 3-mm diameter packing. The line through the dynamic liquid holdup data is the best fit of the percolation-based model described by Crine *et al.* (104). The form of the expression for the dynamic liquid holdup is

$$\chi_{\text{dynamic}} = (KQ)^{1/3} \left(\frac{Q}{Q + Q_{\text{min}}} \right)^{2/3}, \quad (23)$$

where Q is the liquid superficial velocity and Q_{min} the minimum liquid superficial velocity; $K = k\mu_L a^2 / \rho_L g$, where k is a proportionality factor depending on the fluid and packing properties, μ_L the liquid dynamic viscosity, ρ_L the liquid mass density, a the specific surface area of the packing, and g the gravitational constant. Equation (23) is fitted to the experimental results, with Q_{min} and K (i.e., k) as variables in the

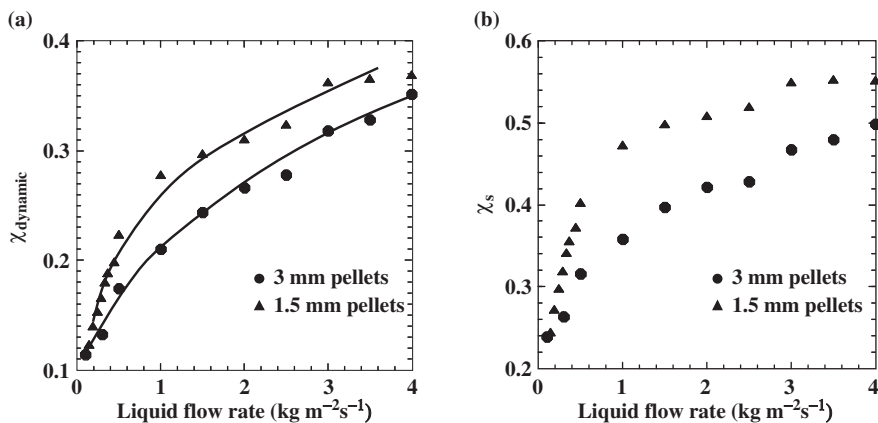


FIG. 31. (a) Dynamic liquid hold-up, and (b) wetting efficiency as a function of liquid superficial velocity for 1.5- and 3-mm cylinders. Gas flow rate was constant at 31.3 mm s^{-1} . The line shows the best fit of the data to the percolation model of Crine *et al.* (104). Reprinted from reference (103) with permission from Elsevier, Copyright (2003).

fit. As shown in Fig. 31, the fit of Eq. (23) to the data is good. The best-fit values of Q_{min} are 3.56×10^{-4} and $12.5 \times 10^{-4} \text{ m s}^{-1}$ for the 1.5- and 3-mm diameter cylinders, respectively. Following the argument of Toye *et al.* (101), Q_{min} characterizes solid-phase (i.e., packing) wettability such that smaller values of Q_{min} are associated with better packing wettability. This statement, as discussed above, is clearly supported by Fig. 31.

These early investigations of trickle flow within beds of porous packing elements identified three general results: (i) values of liquid holdup compare well, typically to within 5%, with gravimetric data; (ii) the general trends in both holdup and wetting data are consistent with the predictions of existing models; and (iii) the absolute value of surface wetting tended to be lower than reported values. Considering (iii), there are, of course, likely to be significant errors in the values of wetting obtained from the range of indirect methods used in the earlier work. However, an underestimate of surface wetting based on data obtained from MRI can be explained as a consequence of not “seeing” liquid layers on the surface when they are not associated with a larger-scale liquid rivulet.

As a result of this concern, improved data acquisition and image analysis strategies have been developed. The key modification to the overall methodology is that we apply an image analysis algorithm which applies a local gating level—this is an objective procedure that accounts for the fact that the gating level we choose must discriminate between intra-pellet water and water bound to the surface as a wetted film. The particular gating level needed to achieve this will be very sensitive to the signal from the intra-pellet water and, since this varies with the characteristics of individual pellets, a global gating level will always introduce inaccuracies into the measurement. With this improved algorithm, MR measurement of both holdup and wetting are in good agreement with the predictions of the neural network analysis of Larachi *et al.* (105).

B.2. The Trickle Flow to Pulse Flow Transition

At higher liquid velocities the hydrodynamics characterizing a trickle bed move into the pulsing regime. Trickle- and pulse-flow regimes account for the contacting patterns most commonly encountered in commercial-scale trickle beds, but yet relatively little is known about the hydrodynamics in the pulsing regime or the mechanism by which the system moves from trickle to pulse operation. The nature of the flow is important because flow patterns significantly influence the performance of a reactor through characteristics such as phase holdups, power consumption, and mass transfer fluxes. Therefore, successful modeling of trickle-bed reactors requires precise tools for the identification of the flow pattern expected for particular operating conditions. As described by Larachi *et al.* (105), there are two conceptually different approaches for describing the onset of the pulsing regime, these being the microscopic and macroscopic models. Microscopic models or single-pore models analyze pore-scale hydrodynamics and are based on the postulate that the macroscopic onset to pulsing flow is an outcome of a statistically large number of local pulsatile occurrences. In contrast, the macroscopic models are used to analyze the onset of pulsing at the reactor scale from a stability analysis of first-principle volume-averaged Navier–Stokes equations.

Results determined by MR to characterize these phenomena suggest that the mechanism for this hydrodynamic transition is best described by local pulsatile events. Data have been recorded for a fixed bed of length 700 mm and diameter 43 mm; 2- and 3-D FLASH (SNAPSHOT) pulse sequences were used to image the temporal stability of liquid distribution within the bed under conditions of gas–liquid two-phase flow (106–108). Typical experiments were carried out with a constant gas velocity as the liquid velocity was increased or decreased. In the case of the 2-D acquisitions, Lim *et al.* (106) investigated the bed under a range of operating conditions, including superficial gas velocities in the range of 27–275 mm s⁻¹ and superficial liquid velocities in the range of 0.4–13.3 mm s⁻¹. For each set of operating conditions, 540 images were acquired for each set of flow velocities. Each image had a data acquisition time of 20 ms, and images were acquired in immediate succession. For the case of the 3-D data, Anadon *et al.* (108) considered 27 liquid velocities between 0.7 and 13.07 mm s⁻¹ at two different gas superficial velocities, namely, 25 and 300 mm s⁻¹. Six series of eight consecutive 3-D images were acquired for each set of flow rates. Each 3-D image was acquired in 280 ms.

The best way of analyzing these time-series data is to calculate the variation in liquid content within each image pixel (voxel) over the complete time-series of images. This is done by calculating the standard deviation in pixel (voxel) intensity on a pixel-by-pixel basis and then displaying the spatially resolved map of standard deviation values in 2- or 3-D. Regions characterized by low values of standard deviation identify stable gas–liquid distribution, whereas values of high standard deviation identify spatial locations in which the liquid content (gas–liquid distribution) is changing with time.

Figure 32 is a summary of the nature of data that can be obtained in 2-D. Under conditions of trickle flow, this analysis shows that the liquid content of any given pixel remains constant, as evidenced by a low value of the standard deviation

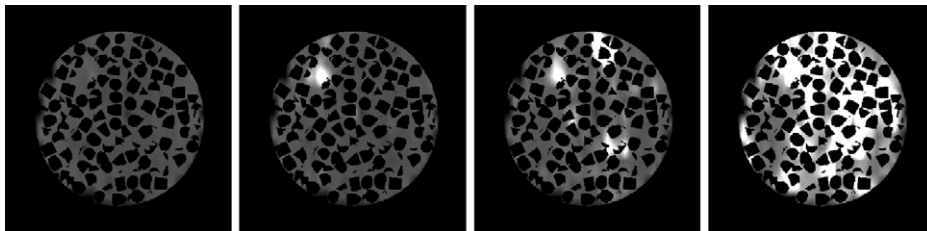


FIG. 32. Identification of location and size of local pulses within a trickle bed. A high spatial resolution image (in-plane spatial resolution $175\ \mu\text{m} \times 175\ \mu\text{m}$; slice thickness $1\ \text{mm}$) is overlaid with a standard deviation map calculated from images acquired at a spatial resolution of in-plane spatial resolution $1.4\ \text{mm} \times 2.8\ \text{mm}$ with a slice thickness of $2\ \text{mm}$. The standard deviation maps have been linearly interpolated to the same in-plane spatial resolution as the high-resolution data. Images are shown for a constant gas velocity of $112\ \text{mm s}^{-1}$. The liquid velocities increase from left to right: 2.8 , 3.7 , 6.1 , and $7.6\ \text{mm s}^{-1}$, with the system existing in the trickle and pulsing regimes at liquid velocities of 2.8 and $7.6\ \text{mm s}^{-1}$, respectively. Data were recorded in order of decreasing liquid velocity. Low and high values of standard deviation are indicated by dark and light shades, respectively. Reprinted from reference (106) with permission from Elsevier, Copyright (2004).

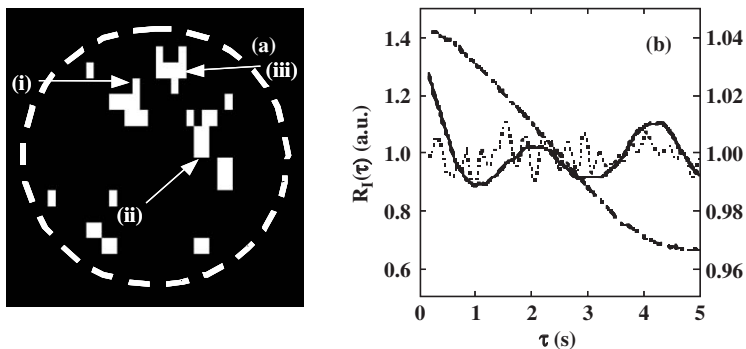


FIG. 33. (a) The binary-gated map derived from a standard deviation map acquired at gas and liquid velocities of 112 and $6.8\ \text{mm s}^{-1}$, respectively, for which the bed was operating in the transition regime between trickle and pulsing flow. The binary gate was applied to identify (in white) only those pixels associated with high values of standard deviation in their signal intensity taken over a series of 540 images (i.e., the position of the local pulses is identified). Pixels associated with a gas-liquid content that does not change with time are identified as black. (b) Local autocorrelation functions calculated from regions (i, ii, iii) identified in (a) reveal well-defined local pulsing frequencies of approximately 10 , 2 , and $0.4\ \text{s}$, respectively. The solid and dashed lines take the values on the left-hand y -axis; the smaller scale intensity fluctuations are associated with the values of standard deviation on the right-hand y -axis. Reprinted from reference (106) with permission from Elsevier, Copyright (2004).

associated with each pixel in the standard deviation maps. As the liquid velocity is increased, instabilities in the liquid content in local regions of the bed are observed. The initial length scale of these instabilities was found to be that of the size scale of the individual packing elements. The timescale over which the local pulses occur is characterized by means of a temporal autocorrelation function of the liquid content within a particular pulsing region. In Fig. 33b, local periodicities of

approximately 0.4, 2, and 10 s are shown for the three local pulsing regions identified in Fig. 33a.

Figure 34 shows standard deviation maps calculated from the 3-D images of time-varying liquid distribution. A cut through half the bed reveals the evolution of the local pulses in a direction parallel to the direction of superficial flow. Standard deviation maps are shown for data recorded at a gas velocity of 75 mm s^{-1} for increasing liquid velocity starting from conditions in the trickle-flow regime, through the transition to pulsing flow. In 3-D, it is clearly shown that the local pulsing regions actually extend to length scales of 2–3 particle diameters in at least one direction. As liquid velocity increases, the number of the local pulsing regions increases until they begin to interconnect. Figure 35 shows an analysis of standard deviation data recorded at two constant gas velocities of 25 and 300 mm s^{-1} . In this figure, the number of individual local pulses (defined as regions having a standard deviation of greater than 1.0) within the full 3-D imaging volume is plotted as a function of liquid velocity. A clear peak is evident in this plot indicating that isolated pulses develop in increasing numbers as liquid velocity increases until a maximum number of such pulses is formed. Combining these data with the 3-D standard deviation maps shown in Fig. 34, leads to the clear recognition that, after this maximum number of pulses is reached, the pulses merge with one another, until the whole bed volume is characterized by a single region of unsteady-state liquid content (i.e., the bed moves into the pulsing regime). It is also clearly evident from Fig. 35 that the peak in the number of isolated local pulsing events occurs at the same liquid velocity at which the standard deviation in pressure drop values taken across the bed begins to rise sharply.

This series of experiments has given us some insight into the mechanism of the hydrodynamic transition, and has also suggested an unambiguous definition of the transition point—that at which the maximum number of independent local pulsatile events exists within the bed. The origin of the local pulses can also be investigated and is the subject of ongoing work. Preliminary MR experiments suggest that fluctuations in the thicknesses of liquid films on the surface of the packing elements increase with increasing liquid velocity prior to the formation of local pulsing events (106,109).

C. TWO-PHASE FLOW IN CERAMIC MONOLITHS

Structured and monolith catalysts and catalytic reactor systems are attracting increasing attention in the chemical and process industries with the expectation that they will provide more uniform, reproducible process performance with greater control over product specification than is possible with conventional fixed-bed processes. In principle, if a multi-channel reactor is used in which each channel is identical, it might be expected that more homogeneous process performance would be achieved. Other potential advantages include the decoupling of heat and mass transfer phenomena, operation under reduced pressure drop conditions and at much higher gas/liquid flow rates, and a greater resistance to attrition (110,111). Metal-loaded ceramic monoliths are already established in use for catalyzing gas-phase reactions, the monolithic exhaust converter used throughout the

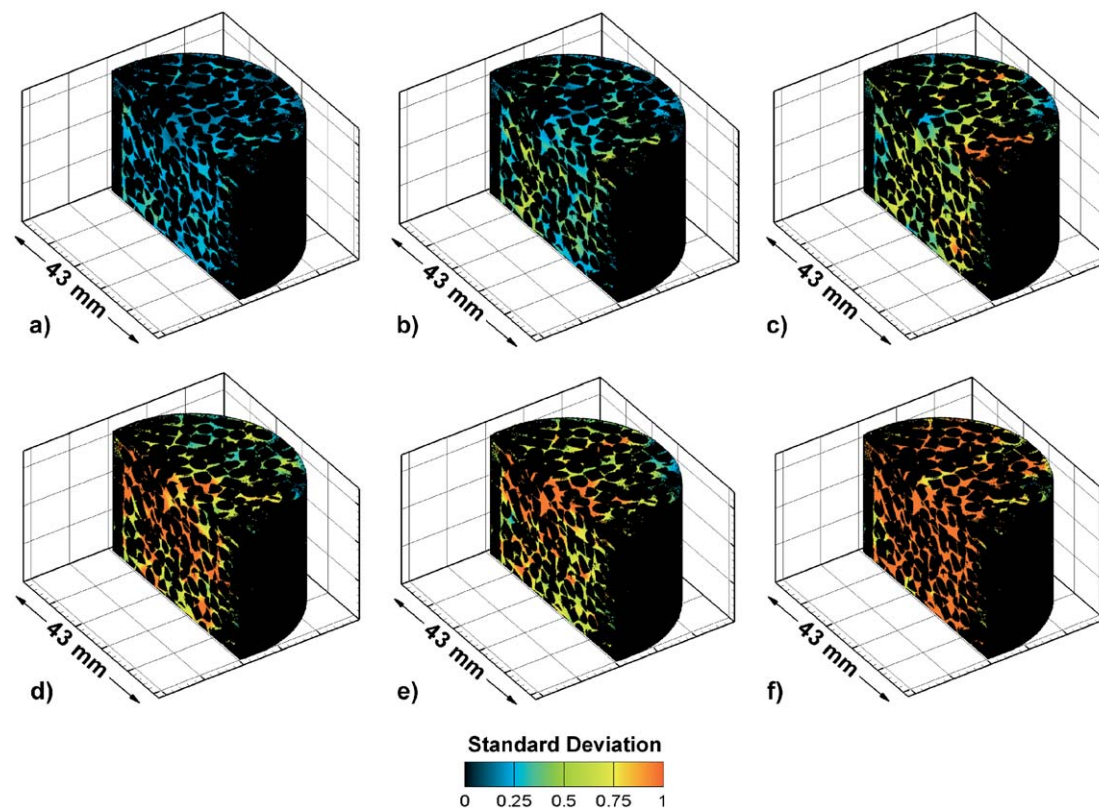


FIG. 34. 3-D standard deviation maps, combined with a RARE image of the trickle bed, calculated from data acquired at a constant gas velocity of 75 mm s^{-1} for increasing liquid velocities of (a) 0.5, (b) 5.0, (c) 7.0, (d) 8.0, (e) 8.5, and (f) 10.0 mm s^{-1} . The height of the bed shown is 28 mm. Data are shown for half of the bed volume imaged. The standard deviation maps ($3.75 \text{ mm} \times 3.75 \text{ mm} \times 1.87 \text{ mm}$) were linearly interpolated to the same resolution as the RARE image ($175 \mu\text{m} \times 175 \mu\text{m} \times 175 \mu\text{m}$) to provide insight into how local pulsing relates to the structure of the bed. Pulsing regions are identified by the highest values of standard deviation (red) (109).

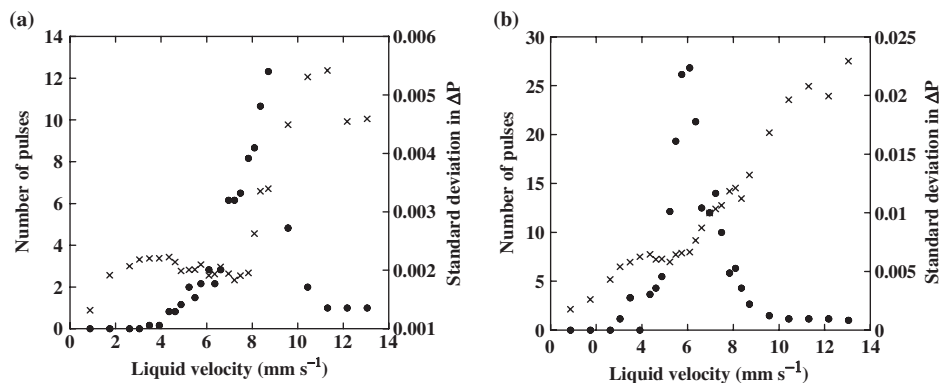


FIG. 35. Analysis of the 3-D standard deviation maps calculated from data acquired with the bed operating at a constant gas velocity of (a) 25 and (b) 300 mm s^{-1} as a function of liquid velocity. The number of independent liquid pulses identified at each liquid velocity (●), and the standard deviation in the pressure drop measurements made over the length of the bed, recorded at 0.5 s intervals over a 10-min period (×), are shown. All data derived from the 3-D MRI standard deviation maps are averaged over six maps acquired for each set of operating conditions.

automotive industry being the obvious example. These multi-channel systems are also of interest in application to multi-phase processes, but their adoption in industry is limited because of a lack of understanding of the transport and reaction phenomena occurring within them (112). As with trickle-bed reactors, imaging of multi-phase flow within monoliths has been attempted with other methods, notably capacitance tomography (113), which has a high temporal resolution (100 images per second can be achieved) but lacks spatial resolution in comparison with MR—typical in-plane resolutions being $5\text{--}10\%$ of the diameter of the system, thereby making visualization of phase distribution within a single channel impossible.

There have already been a number of MRI studies of single- and two-phase flow in ceramic monoliths. Single-phase flow in monoliths was investigated by Koptyug *et al.* (114), who obtained quantitative, spatially resolved velocity maps for the flow of thermally polarized acetylene, propane, butane, and water flowing through the channels of alumina monoliths, with an in-plane spatial resolution of $400 \mu\text{m}$. The monoliths had a channel cross-section of 4.0 mm^2 and a wall channel thickness of 1.0 mm . Axial gas-phase velocities of up to 0.93 m s^{-1} ($\text{Re} = 570$) were investigated. The flow maps showed a highly non-uniform distribution of shear rates within the individual monolith channels.

In a follow-up study, Koptyug *et al.* (115) reported images of both liquid and gas flow and mass transport phenomena in two different cylindrical monolith catalysts (one with triangular channels, the other with square channels) at various axial locations within the monolith. Heibel *et al.* (116,117) addressed two-phase flow in the film flow regime and reported investigations of liquid distributions in the plane perpendicular to the direction of superficial flow, in particular, addressing the accumulation of liquid in the corners of the square channels of the monolith.

Figure 36 shows images recorded from a four-channel array in which the preferential flow of the liquid in the corners of the channels was investigated as a function of the nature of the distributor and the liquid velocity. Non-uniformities of the liquid distribution over the four corners of the square channels were apparent in addition to any maldistribution over the cross-section of the monolith.

Figure 37 illustrates a further approach to imaging two-phase (gas–liquid) flow in monoliths. In this case, Sederman *et al.* (118) investigated Taylor or bubble-train flow, which occurs at higher superficial liquid velocities than film flow and is characterized by gas bubbles separated by liquid slugs passing along the individual channels. These data were recorded by use of the SEMI-RARE technique described in Section II.E.2. In contrast to the data shown in Fig. 10, the monolith was operated with up-flow of air through stagnant water. Ceramic (cordierite) monoliths rated at 300 and 400 channels per square inch (cps) were used. The gas (compressed air) was introduced into the liquid at the bottom of the column through a sparger; gas flow rates of 50–300 mL min⁻¹ were investigated. The SEMI-RARE

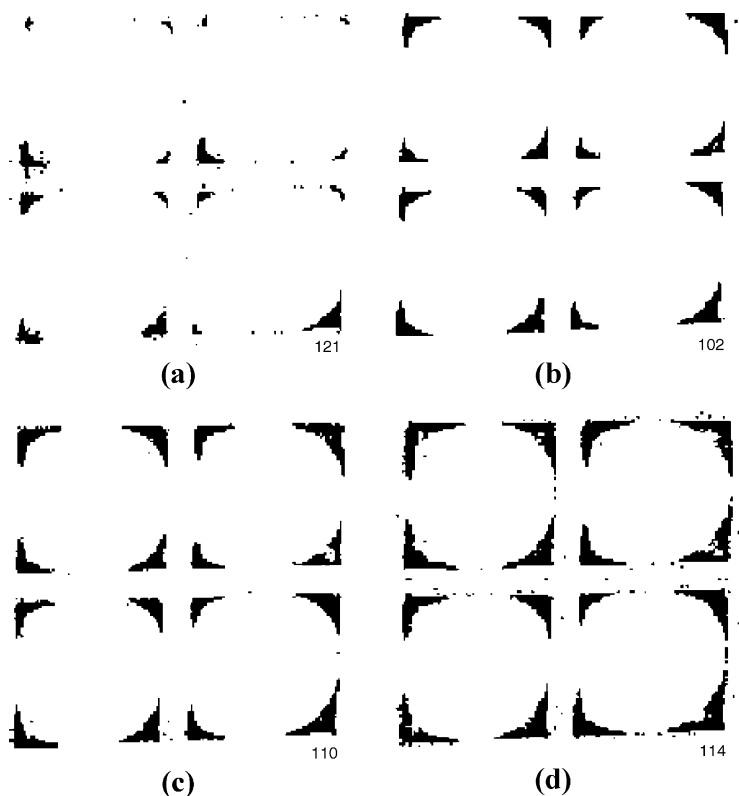


FIG. 36. Liquid distribution within a set of four square channels of hydraulic diameter 4.11 mm and length 500 mm. The monolith was operating under conditions of film flow. The liquid distribution within the channels is shown to depend on both the liquid distributor and the liquid velocity (v_l). (a) Distributor A, $v_l = 0.45 \text{ cm s}^{-1}$. (b) Distributor B, $v_l = 1.1 \text{ cm s}^{-1}$. (c) Distributor C, $v_l = 2.2 \text{ cm s}^{-1}$. (d) Distributor C, $v_l = 4.0 \text{ cm s}^{-1}$. Reprinted from reference (116) with permission from Elsevier, Copyright (2001).

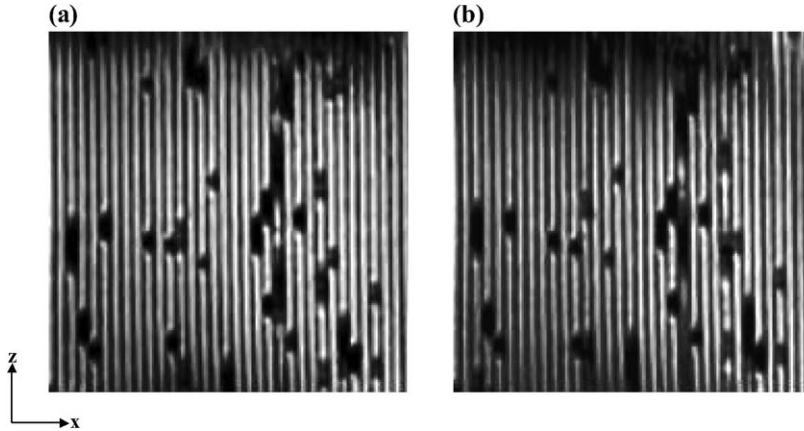


FIG. 37. Two successive 2-D xz images of two-phase flow through the parallel channels of a ceramic monolith rated at 400 cpsi, for a gas flow rate of $200 \text{ cm}^3 \text{ min}^{-1}$: (a) 74 ms after excitation, (b) 220 ms after r.f. excitation. In-plane image resolution is $393 \mu\text{m}$ (x) \times $783 \mu\text{m}$ (z). Reprinted from reference (84) with permission of Springer Science and Business Media.

technique allowed recording of images along the length of the monolith with the slice thickness being smaller than the width of an individual channel; thus, the two-phase flow characteristics (slug and bubble lengths) could be imaged within a set of adjacent channels within the monolith. Four images, each image taking approximately 100 ms to acquire, were recorded in immediate succession. No signal was acquired from the gas phase, and therefore the liquid slugs were imaged directly. By acquiring multiple images in immediate succession, individual gas–liquid interfaces could be followed, and hence slug velocity as well as gas bubble and liquid slug length distributions were obtained.

Another approach to characterizing flow heterogeneity within a monolith has been reported by Heras *et al.* (119). The pulse sequence used to acquire these data combined SEMI-RARE with a time-of-flight experiment, achieved by implementing SEMI-RARE such that only a single line of magnetization (i.e., a line of nuclear spins across the image) was excited and subsequently refocused. These excited spins were then tracked in subsequent image acquisitions using a conventional time-of-flight approach.

The spatial distribution of intensity shown in the images is similar to a probability distribution of displacements (i.e., a displacement propagator convolved with the initial excitation profile). In addition to providing an ultra-fast measurement of flow heterogeneity within the monolith, the method also allows a greater dynamic range of liquid velocities to be investigated than can be achieved by acquiring single velocity images using other time-of-flight techniques. In the example shown in Fig. 38, two-phase flow was studied in a configuration similar to that reported for the application of conventional SEMI-RARE (i.e., up-flow of gas through the liquid-filled monolith). In-plane spatial resolution of $391 \mu\text{m} \times 391 \mu\text{m}$ was achieved with an image slice thickness of 1.7 mm; i.e., flow in a row of adjacent single channels is probed. From Fig. 38 it is clearly seen that as the gas flow rate

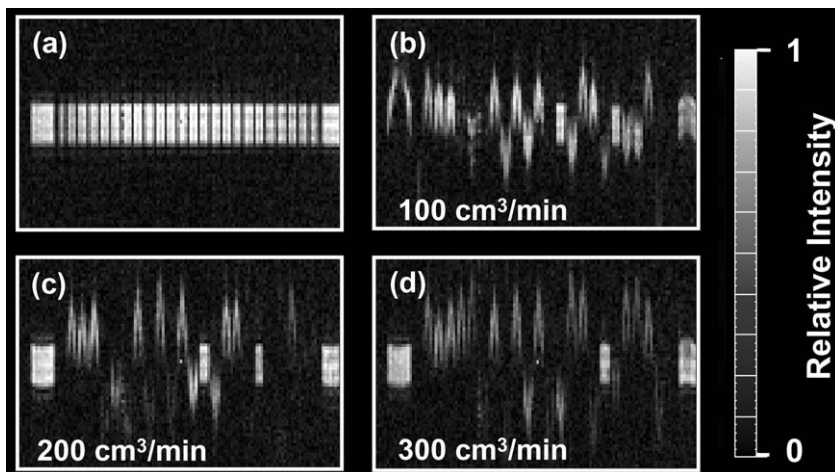


FIG. 38. Line excitation SEMI-RARE images of two-phase flow in a ceramic monolith rated at 200 cpsi. The signal intensity shows how far the initially excited water molecules have traveled in the period between line excitation and the image acquisition. The gas flow rate was (a) 0, (b) 100, (c) 200, and (d) $300 \text{ cm}^3 \text{ min}^{-1}$. Images acquired 78 ms after r.f. excitation are shown. A 5 mm-high “slice” of spins was initially excited along the direction of flow. The field-of-view is 50 mm (x) \times 25 mm (z).

increases, the fluid moves further within the channels, and that the flow is in both positive and negative z directions. Spatial resolution is sufficient that the actual flow profile within an individual channel is imaged.

Thus, we see that in a single image acquisition, the line excitation SEMI-RARE method allows an evaluation of the extent of flow heterogeneity (up- and down-flow) within the monolith. Furthermore, velocities in completely liquid field channels can be measured. This was not possible when SEMI-RARE was used because velocities were measured by following a gas–liquid interface. However, a limitation of the line excitation SEMI-RARE technique is that there needs to be a significant amount of liquid present within the monolith, because the gas phase is not imaged; only liquid captured in the initial line excitation can be followed.

D. FLUIDIZED BEDS

The first report of imaging solids directly in fluidized beds was made by Savelsberg *et al.* (120), who acquired both \mathbf{k} - and \mathbf{q} -space data to monitor the time-averaged density variations and the random motion of granular particles in the presence of gas flow of variable velocity in a model gas-fluidized-bed reactor. Beds of poppy seeds and catalyst particles were studied. The ^1H NMR signal came from the oil component of the seeds and from acetone adsorbed in the pores of the catalyst particles, respectively. Superficial gas velocities up to 55 cm s^{-1} were investigated. The bed was of diameter 21 mm and was filled to a height of 30 mm. The translational behavior of particles in the direction of superficial flow was measured; the data were averaged over the whole bed, with data acquisition times being approximately 1 h. More recently, Fennell *et al.* (121) used an ultra-fast FLASH MRI technique to study

mixing, in real time, within a fluidized bed. In this investigation a batch of poppy seeds was introduced to the top of a fluidized bed of sugar crystals. Since the poppy seeds give an MR signal and sugar crystals do not, it was possible to measure the distribution of poppy seeds within the bed as a function of time. 1-D profiles of the density of poppy seeds along the axial direction of the bed were acquired every 12 ms with a spatial resolution of $625\ \mu\text{m}$; the data were averaged in the x - y plane. Using this method it was possible to measure the mixing time and dispersion coefficient of the poppy seeds within the bed for a range of gas superficial velocities.

Velocity imaging of the solid particles within gas-fluidized beds has now also been achieved. For example, Harms and Stapf (122) acquired a time-averaged velocity map of the motion of poppy seeds (of average diameter $0.8\ \text{mm}$) in a bed filled to a height of $20\ \text{mm}$ inside a column of inner diameter $44\ \text{mm}$. The bed was operated in the bubbling regime. Figure 39 clearly shows that the time-averaged bed dynamics can be approximated by a fountain-like average seed trajectory of upward motion in the central region of the bed, followed by downward motion near the inner cylinder wall. Rees *et al.* (123) have also reported time-averaged maps of the flow of poppy seeds in a bed of diameter $60\ \text{mm}$, the bed being loaded to a pre-fluidization height of approximately $30\ \text{mm}$. It was shown that two distinct fast-flow channels are sometimes observed in the central region of the bed. As expected, downward motion is observed towards the column walls. In the same work, Rees *et al.* report a detailed investigation of the structure of “jets,” which form above each orifice in the distributor plate. These data provide sufficient spatial and temporal resolution that

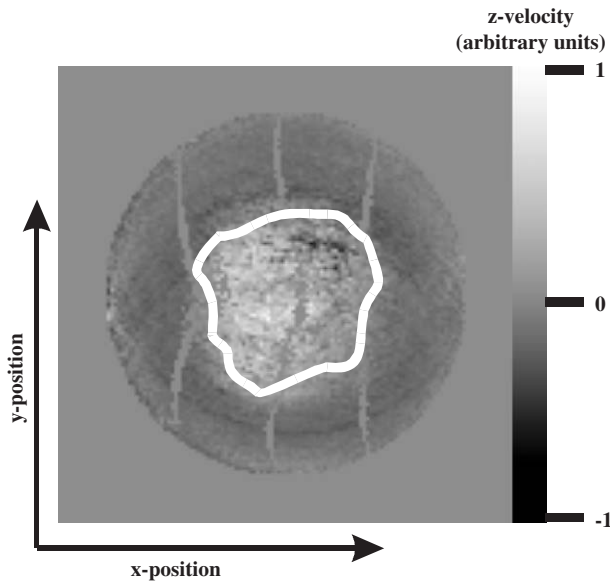


FIG. 39. Velocity imaging of the vertical (v_z) component projected onto the cross-section of a granular bed of poppy seeds. The data are averaged over the height of the bed ($2\ \text{cm}$). Velocities are normalized to the maximum upward motion (which is set to unity). The white line indicates $v_z = 0$ and separates upward (inner part) from downward motion (outer part). Vertical lines are processing artifacts (122).

some of the long-standing assumptions and mathematical analysis underpinning the design of fluidized bed reactors can be critically evaluated for the first time.

V. Imaging of Reactions *In Situ*

Recently there has been increasing interest in this area, but it is important to remember that early studies were reported as far back as 1978—albeit for relatively simple systems. In 1978, Heink *et al.* (124) used 1-D profiling to study the time-resolved concentration profile of butane and water in packings of NaCaA and NaX zeolite crystallites, respectively. Other early investigations include the use of ^{19}F imaging to follow the intercalation of AsF_5 into highly oriented pyrolytic graphite at room temperature (125).

Since this early work, interest has been focused mainly on oscillations and traveling waves during chemical reactions (49, 126–129). Butler *et al.* (130) employed ^1H MRI techniques to investigate the extent of reaction in a single crystal of 4-bromobenzoic acid during exposure to ammonia gas. In a second case study, MRI was used to follow the reaction of a deep bed of powdered toluic acid with ammonia gas flowing over it. The apparent reaction rate constant and the effective diffusivity of ammonia within the bed were obtained from a fit of a diffusion-reaction model to the experimental data. However, these investigations are somewhat removed from mapping chemical conversion within either a catalyst or a catalytic reactor, which is the focus of this section.

As discussed in Section II, all the methods of MR spectroscopy can, in principle, be integrated into a MRI sequence; hence spatially resolved measurements of chemical conversion are possible. However, the practical challenges in achieving this goal are substantial. In particular, as with any measurement, achieving adequate signal-to-noise ratios is key to a successful measurement. This point explains why in the vast majority of MRI experiments, signal from the ^1H nucleus is acquired. The ^1H nucleus has a high MR sensitivity and exists in 100% natural abundance. The problem is that in any reaction mixture there is likely to be a wealth of ^1H resonances, many of which overlap, making it impossible to follow the change in concentration of a particular species. This problem is increased because of the interaction of the fluid phase with the solid catalyst pellets, which causes the relaxation times of the fluid species to decrease. This decrease further reduces the available signal-to-noise ratios in the experiment and also broadens the spectral resonances, hence further increasing the overlap of individual resonances. Therefore, ^1H experiments are likely to be limited to simple reactions in which the ^1H spectral peaks are readily resolved.

Alternatively, we must move, for example, to ^{13}C , ^{31}P , or ^{19}F imaging, if possible. ^{31}P and ^{19}F are commonly used in the medical field and have high abundance and sensitivity. ^{13}C is the most likely candidate species to investigate in heterogeneous catalytic processes, but successful implementation of the technique is not straightforward because of the low abundance and sensitivity of ^{13}C . However, a particular advantage of investigating the ^{13}C nucleus is that it has a much wider chemical shift range than ^1H , therefore enabling better resolution of individual spectral peaks than

is the case with ^1H . A first investigation with ^{13}C to characterize *in situ* reactions, exploiting signal enhancement techniques, is discussed in Section V.A.2. Initial ^1H and ^{13}C experiments have suggested that substantial new insights into the coupling of hydrodynamics and chemical conversion can be obtained by developing the appropriate measurement techniques.

A. SINGLE-PHASE REACTIONS IN FIXED BEDS

A.1. An Esterification Reaction

Albeit for a simple reaction, Yuen *et al.* (131) first demonstrated the nature of the information that can be obtained regarding chemical mapping within a fixed-bed reactor, using the liquid-phase esterification of methanol and acetic acid catalyzed by an ion-exchange resin in the H^+ form (particle size 600–850 μm). Their aim was to demonstrate the link between the heterogeneity in hydrodynamics identified in Section IV.A.1 and possible heterogeneity in conversion within the bed. This investigation is a good example of how the attributes of MR spectroscopy and imaging can be combined.

In principle, there is no reason why the chemical mapping of the reaction cannot be performed at the spatial resolution achieved in the imaging of the structure of the bed. However, in the present example, spectra were acquired from relatively large volumes within the bed (in this case 1.5 mm \times 1.5 mm \times 0.5 mm) to ensure high signal-to-noise ratios in the data. Using this approach, it was possible to characterize quantitatively the extent of conversion at various locations within transverse sections through the bed at several positions along the length of the bed. The technique of volume-selective spectroscopy (Fig. 13) was used to obtain (non-invasively) MR spectra from the well-defined volume elements with the bed (Section II.C.1). The chemical conversion within each volume was obtained directly from the positions of the spectral peaks within each ^1H spectrum. Quantification of chemical composition was achieved by exploiting the phenomenon of fast exchange of the ^1H species associated with hydroxyl groups within the acetic acid, methanol, and water comprising the reaction mixture:



^1H fast-exchange causes the observed chemical shift (i.e., resonance frequency) for the ^1H species associated with OH groups present in the reaction mixture (δ_{observed}) to be determined by an average of the component chemical shifts, weighted by the amount of each molecular species present, as follows from Eq. (24). Thus, the concentration of acetic acid present at any time, and hence the extent of conversion at that time, was determined directly from the value of δ_{observed} identified in the volume-selective spectrum. Figure 40 shows a 2-D slice section through a 3-D RARE image of the bed; the image voxels are of size 97.7 $\mu\text{m} \times 97.7 \mu\text{m} \times 97.7 \mu\text{m}$. ^1H MR spectra were recorded from regions of in-plane dimension 1.5 mm \times 1.5 mm, with a slice thickness of 500 μm in the direction of superficial flow; 10 volume-selective spectra were recorded within each transverse section through the bed.

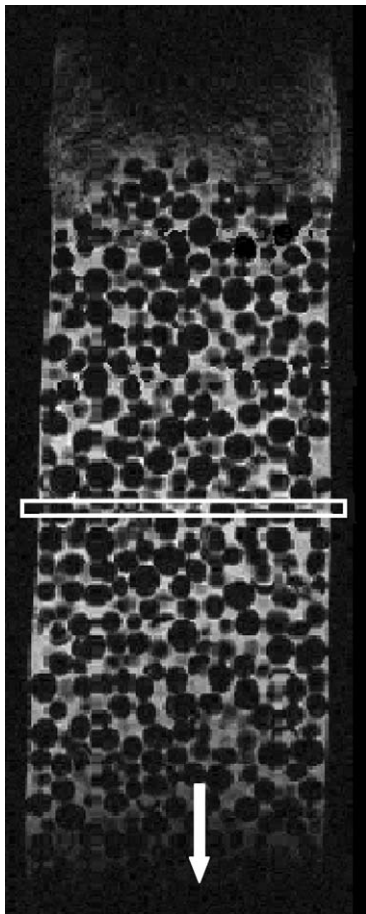


FIG. 40. 2-D slice through a 3-D RARE image of a fixed bed of ion-exchange resin. The image has an isotropic resolution of $97.7 \mu\text{m} \times 97.7 \mu\text{m} \times 97.7 \mu\text{m}$. The image slice in which the local volumes are located for the volume-selective spectroscopy study is identified. The image was acquired by saturating the bed with pure methanol. T_2 -contrast was exploited in the data acquisition so that signal was acquired only from the methanol in the inter-particle space. Reprinted from reference (84) with permission of Springer Science and Business Media.

From each spectrum it is possible to determine, directly and quantitatively, the extent of conversion within that local volume. In Fig. 41, the regions within which the individual volume-selective spectra were acquired are identified and color coded by the extent of conversion as determined from the spectrum recorded from that particular local volume. All images in Fig. 41 show that there is significant heterogeneity in conversion within a single transverse section through the bed, perpendicular to the direction of superficial flow; fractional variations in conversion of up to approximately 20% were found to be typical under steady-state operating conditions.

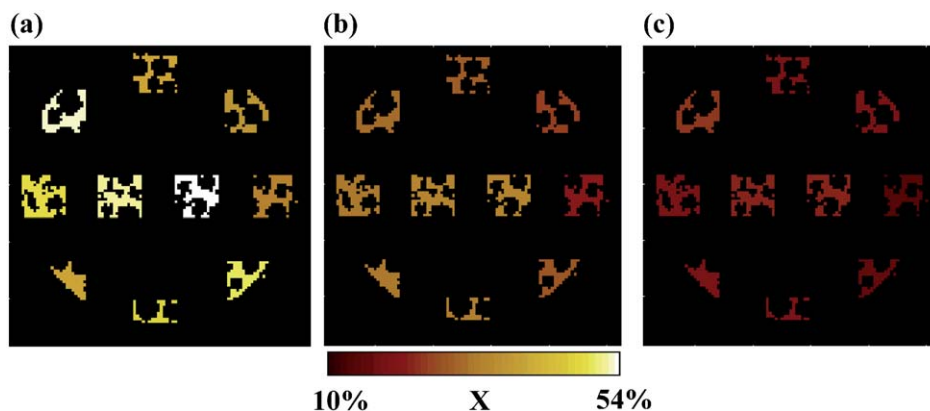


FIG. 41. Visualization of mean conversion, X , within selected volumes located within the slice section identified in Fig. 40. The local volumes have in-plane dimensions of $1.5 \text{ mm} \times 1.5 \text{ mm}$ and a depth (image slice thickness) of $500 \mu\text{m}$. Data are shown for three feed flow rates: (a) 0.025 , (b) 0.05 , and (c) 0.1 mL min^{-1} . As flow rate increases, the residence time characterizing the bed decreases, and it therefore follows that conversion will decrease. Reprinted from reference (84) with permission of Springer Science and Business Media.

Although such studies are in their early stages, this example clearly demonstrates that we have the measurement tools to investigate the complex interaction of hydrodynamics and chemical kinetics in the complex porous medium represented by a fixed bed. Looking to the future, we may expect experiments of this nature to demonstrate how a catalyst with intrinsic high selectivity can produce a far wider product distribution when operated in a fixed-bed environment as a result of the spatial heterogeneity in hydrodynamics and hence, for example, mass transfer characteristics between the inter-pellet space within the bed and the internal pore space of the catalyst.

The ability to estimate mass transfer coefficients *in situ* has also been demonstrated in application to this esterification reaction. Gladden *et al.* (132) showed that mass transfer processes can be quantified by using displacement propagator measurements (Section II.B.1) combined with a relaxation time pre-conditioning pulse sequence (Section II.C.2). Such data acquired for this esterification reaction are shown in Fig. 42. In this propagator measurement, the total propagator measured for the system has been separated into two component propagators by combining the transport measurement pulse sequence with a spin-lattice relaxation time experiment. Since the relaxation time of liquid molecules that have existed only within the inter-particle space during the observation time (100 ms) is significantly longer than that of molecules that have moved between the inter- and intra-particle space, independent propagators characterizing these two populations of liquid molecules can be obtained. In Fig. 42 the broader propagator, which shows two peaks, is that associated with the liquid in the inter-particle space. The two peaks are consistent with there being populations of very slow moving and much faster moving fluid within the bed—note that these observations confirm that the flow heterogeneity observed in beds of lower column-to-particle diameter (Fig. 23) is

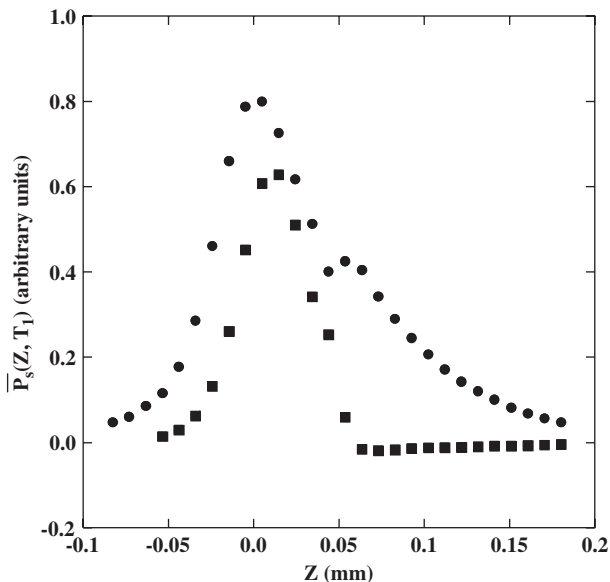


FIG. 42. T_1 -resolved propagators for water flowing within the inter-particle space of a bed packed with ion-exchange resin (●) and for water exchanging between inter- and intra-particle environments (■) during the time scale of the transport measurement. Data are shown for a volumetric feed flow rate of 2 mL min^{-1} , to a column of internal diameter 20 mm. Reprinted from reference (132) with permission from Elsevier, Copyright (2003).

also observed for the bed of significantly higher column-to-particle ratio (~ 20) considered here.

In Fig. 42, the full-width at half maximum of the (narrower) “exchange” propagator provides an estimate of the effective diffusion coefficient of water molecules moving between the pore space of the catalyst and the inter-particle space of the bed. In this example, the value is $\sim 2 \times 10^{-9} \text{ m}^2 \text{ s}^{-1}$, which gives a lower limit to the value for the mass transfer coefficient of $\sim 4 \times 10^{-6} \text{ m s}^{-1}$. This value was obtained by defining a mass transfer coefficient as D/d where d is a typical distance traveled to the surface of the catalyst that we estimate as half a typical bead dimension (approximately $500 \mu\text{m}$). This value of the mass transfer coefficient is consistent with the reaction occurring under conditions of kinetic as opposed to mass transfer control.

The same reaction can be followed in 3-D using CSI (Section II.C.1). In Fig. 43, the color code indicates the extent of conversion. As expected from the 2-D study, conversion is heterogeneous within transverse sections through the bed at any position along the direction of superficial flow.

Küppers *et al.* (133) investigated a similar reaction using a different approach. They investigated the enzymatically catalyzed esterification of propionic acid with 1-butanol to form propionic-acid-butyl-ester and water inside an immobilizing hydrogel. *In situ* reaction within single beads of diameter 3–4 mm was characterized. The beads were made of calcium alginate and prepared with 2-wt.% alginate in a 2-wt.% calcium chloride solution containing 0.2-M NaCl. Both the gel-forming

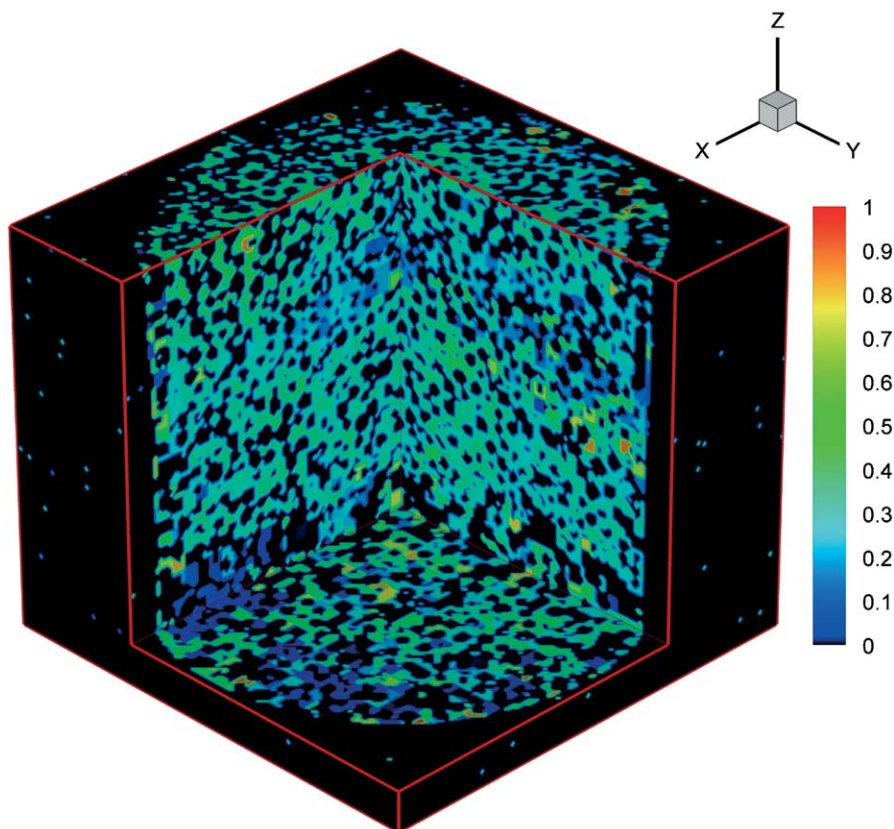


FIG. 43. 3-D cutaway image showing the extent of conversion of the esterification occurring within the fixed bed considered in Figs 40–42. The conversion was calculated from the chemical shift of the OH peak in a 4-D chemical shift image. The chemical shift image was acquired with an isotropic spatial resolution of $625\ \mu\text{m}$. The RARE image of the structure of the bed was acquired at an isotropic spatial resolution of $78\ \mu\text{m}$. Both datasets have been re-interpolated on to a common array giving an effective isotropic spatial resolution of $156\ \mu\text{m}$. The direction of flow is in the negative z direction. The color scale indicates the fractional conversion within the bed.

water and the solvent, cyclohexane, were fully deuterated, so that the ^1H signal from the reactants could be identified. The reaction was followed over a period of 40 h, and the loss of 1-butanol and the production of water inside the gel bead were observed. 2-D images showed that diffusion within the bead was not radially symmetric. 1-D ^1H concentration mapping and 2-D FLASH imaging techniques were used with typically 50–100 images being acquired over a period of 12–24 h. In initial experiments, the time scale of the diffusion process of reactants from the continuous organic phase into the aqueous phase of the gel bead was studied under non-reactive conditions. In a further experiment, the reaction process was followed, reaction being initiated by the addition of enzymes. Conversion was followed by measuring the increase in water and butylpropionate peaks and the decrease of the

1-butanol peak over a period of 40 h. Absolute quantitation of the data in terms of amounts of specific species present was not addressed in this paper, which focused on the MR techniques used and the nature of the data obtained. As in any investigations of phenomena occurring within catalyst particles, care must be taken to ensure that relaxation contrast in the spectral data has been accounted for; gels may hold a particular challenge in this regard, because the degree of hydration and perhaps the composition of the fluid phase within the gel matrix may influence local relaxation times. However, these are first experiments in this field, and again the results are promising.

A.2. Probing Selectivity with ^{13}C Imaging

The investigation of esterification by Yuen *et al.* (131) provided a clear demonstration of the heterogeneity in conversion within a fixed bed. However, this investigation was possible only because the reaction mixture was associated with a relatively simple ^1H NMR spectrum. The spectrum gave only four peaks, with the chemical shift of one being a direct measure of the inter-particle liquid composition and hence the extent of conversion. Recently, Akpa *et al.* (134) used spatially resolved ^{13}C MR spectroscopy to follow a reaction in which competing etherification and hydration reactions took place. As discussed previously, ^{13}C observation may have potential advantages in that the ^{13}C nucleus has a wider chemical shift range than ^1H , making the spectral resonances of individual molecular species better resolved; hence, we can follow the loss of reactants and the formation of products without need for spectral deconvolution.

However, the disadvantage of using ^{13}C is its inherent low abundance and sensitivity, causing low signal-to-noise ratios in the data. These problems are overcome by practitioners of solid-state MR techniques by using isotopically enriched reactants. However, the cost of using these for the larger volumes required for flow-through reactor experiments is prohibitive. Therefore, it is useful to explore the extent to which natural-abundance ^{13}C reactants can be used by employing MR signal enhancement techniques. Typically, such signal enhancement is achieved by transferring polarization from the ^1H spin population to the low-gyromagnetic-ratio, low-natural-abundance species—in this case ^{13}C . In the example considered here, the competing etherification and hydration reactions of 2-methyl-2-butene (2M2B) were followed within a fixed bed of ion-exchange resin in the H^+ form. The reactants were 2M2B, methanol, and water, and the products of the etherification and hydration reactions were *tert*-amyl methyl ether (TAME, 2-methoxy-2-methylbutane) and *tert*-amyl alcohol (TAOH, 2-methyl-butan-2-ol), respectively.

The imaging of conversion within the fixed bed was achieved by using a ^{13}C distortionless enhancement by polarization transfer (DEPT) spectroscopy pulse sequence integrated into an imaging sequence, as shown in Fig. 44. In theory, a signal enhancement of up to a factor of 4 ($\gamma_{\text{H}}/\gamma_{\text{C}}$; γ_i is the gyromagnetic ratio of nucleus *i*) can be achieved with ^{13}C DEPT. In this dual resonance experiment, initial excitation is on the ^1H channel. Consequently, the repetition time for the DEPT experiment is constrained by $T_{1\text{H}} (< T_{1\text{C}})$; where T_{1i} is the T_1 relaxation time of

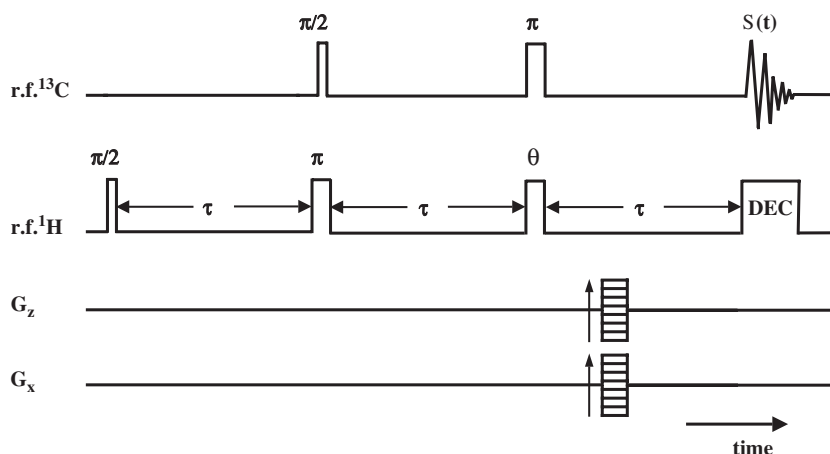


FIG. 44. Spatially resolved ^{13}C DEPT (or ^{13}C DEPT-MRI) pulse sequence. This provides signal enhancement for ^{13}C observation without need for using isotopically enriched materials. The signal is acquired under conditions of ^1H decoupling.

nucleus i . This favorable condition allows increased efficiency of signal averaging, thereby further improving the signal-to-noise ratio for a given acquisition time.

With reference to Fig. 44, the first ^1H pulse generates pure ^1H magnetization, which subsequently evolves under the influence of chemical shift and spin-spin coupling Hamiltonians. At the end of the first evolution period, the ^{13}C $\pi/2$ pulse then converts this magnetization to zero and double quantum coherence. At the same time as the ^{13}C $\pi/2$ pulse, a ^1H π degree pulse is applied to refocus the effects of ^1H chemical shift during the second evolution period. The spin-spin coupling has no effect on the evolution of the multiple quantum coherence during the second evolution period. Finally, a ^{13}C π pulse is applied (again to refocus the effects of ^{13}C chemical shift evolution), while a simultaneous θ pulse is applied to the multiple quantum coherence and converts this to antiphase ^{13}C magnetization. Further evolution converts this (initially unobservable) antiphase magnetization into pure ^{13}C magnetization, the intensity of which is proportional to $\sin\theta$. Note that when a θ pulse is applied some multiple quantum coherence remains at the end of the third evolution period, but is not observed. To achieve spatial resolution of the whole experiment, a double-phase encoding orthogonal pair of gradients is applied during the third evolution period.

A schematic representation of how the double-phase encoded DEPT pulse sequence achieves spatial and spectral resolution within the fixed bed of ion-exchange resin is shown in Fig. 45. Typical data acquired in this experiment are shown in Fig. 46. The data were recorded from a vertical section through the center of the bed. The direction of superficial flow was from the bottom to the top of the bed. The spectra shown were recorded at regular intervals along the length of the bed, with a spatial separation of approximately 2.5 mm. With reference to Fig. 46, the

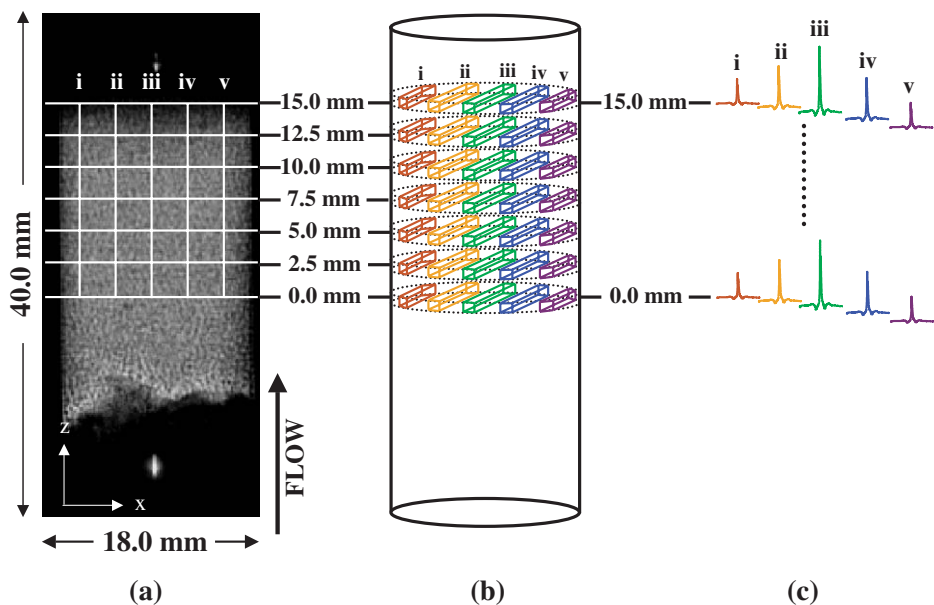


FIG. 45. Schematic representation showing how the double phase-encoded ^{13}C DEPT sequence achieves both spatial and spectral resolution within the fixed-bed reactor. (a) A spin-echo ^1H 2-D image taken through the reactor overlaid with a grid showing the location of the two orthogonal phase-encoded planes (z , along the direction of superficial flow, and x). In-plane spatial resolution was $156\ \mu\text{m}$ (z) \times $141\ \mu\text{m}$ (x) for a 3-mm slice thickness. The center of each volume from which data were acquired is identified by the intersection of the white lines. (b) The corresponding real space volume elements. Note that the individual volume elements have been separated for clarity but actually form a continuous array. (c) ^{13}C DEPT spectra associated with the volume elements shown in (b). The decreasing signal intensity towards the walls of the bed arises from the smaller volumes from which data were acquired in these regions.

conversion and selectivity were quantified *in situ* as follows. Conversion was measured by taking the ratio of the peak areas corresponding to the products and reactants. The spectral resonances of the same carbon group needs to be compared between species, since the degree of polarization transfer (i.e., signal enhancement) is dependent on the chemical environment of each specific carbon atom. In this case the CH_3 resonances have been compared; for the products TAME and TAOH these occur at approximately 8 ppm (CH_3 resonances for TAME and TAOH occur at 7.8 and 8.7 ppm, respectively), whereas those of the reactant 2M2B occur at 13.4, 17.3, and 25.7 ppm. (All chemical shifts are quoted with respect to the ^{13}C resonance of TMS.) Selectivity to TAME was quantified by comparing the intensity of the CH_3 resonances of TAME and TAOH, which occur at 25 and 28 ppm, respectively. Analysis of the data shown in Fig. 46 indicates that over the 15 mm height of the bed for which spectra are shown, conversion increased by approximately 25% while selectivity remained approximately constant at 75–80%. This MR method has now been successfully applied to investigate alkene hydrogenation in a trickle-bed reactor (Section V. B).

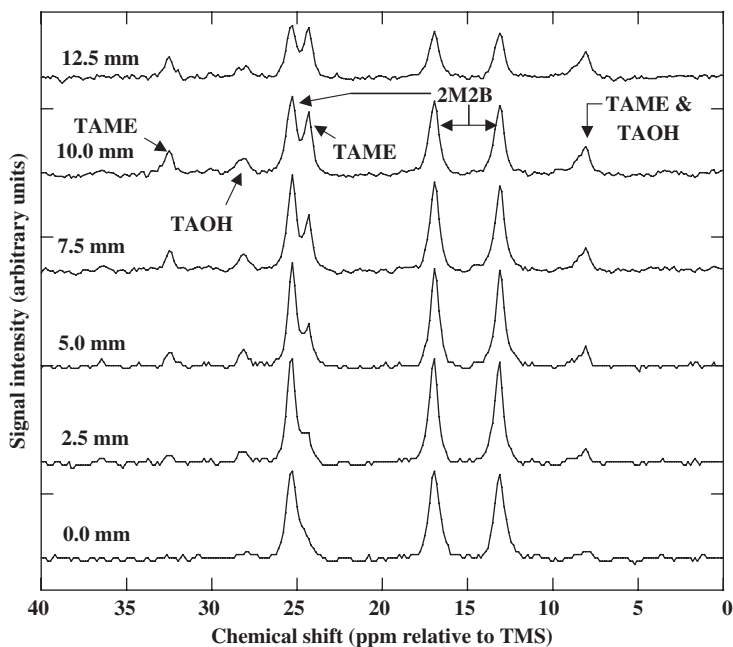


FIG. 46. Spatially resolved ^{13}C DEPT spectra recorded for the competitive etherification and hydration reactions of 2M2B to give 2-methoxy-2-methylbutane (TAME) and 2-methyl-butane-2-ol (TAOH), respectively. The molar composition of the feed was in the ratio 2:10:1 for 2M2B/methanol/water. The spectral assignments, relative to TMS, are as follows: 2M2B (CH_3 : 13.4, 17.3, and 25.7 ppm; CH : 118.7 ppm); TAME (CH_3 : 7.8, 24.1, and 48.5 ppm; CH_2 : 32.2 ppm); and TAOH (CH_3 : 8.7, 28.7 ppm; CH_2 : 36.5 ppm). Spectra are shown for a vertical section of the bed (i.e., column (iii) in Fig. 45) at six different positions along the direction of superficial flow.

B. TWO-PHASE FLOW AND REACTION IN FIXED BEDS

Koptyug *et al.* (69) extended their work on the catalytic hydrogenation of α -methylstyrene from the single-pellet study discussed in Section III.C to the environment of a catalytic fixed bed. The bed was packed with spherical $\text{Pd}/\text{Al}_2\text{O}_3$ catalyst pellets (1 wt.% Pd). The bed was 10.5 mm in diameter and 3–4 cm long. Feed flow rates to the top of the bed were 10^{-2} g s^{-1} and $10.5 \text{ cm}^3 \text{ s}^{-1}$ for α -methylstyrene and pre-heated hydrogen, respectively. The temperature measured at the bottom of the bed was constant at 403 K. Importantly, to protect the MR hardware (in particular, the gradient coils which can easily be damaged by heating to temperatures above 323–333 K) from the elevated temperatures within the reaction zone, an evacuated cylindrical glass dewar surrounded the reaction volume. Axial slices of thickness 2 mm were imaged with a spatial resolution of $230 \mu\text{m} \times 311 \mu\text{m}$. As shown in Fig. 47, the pulse sequence used yielded a map of liquid distribution within the axial slice, with a ^1H MR spectrum associated with each image pixel. The spectra clearly show a decrease in the intensity of the peak at ~ 5.5 ppm and the formation of a peak at ~ 1.25 ppm (relative to TMS), consistent with the formation of cumene as reaction proceeds.

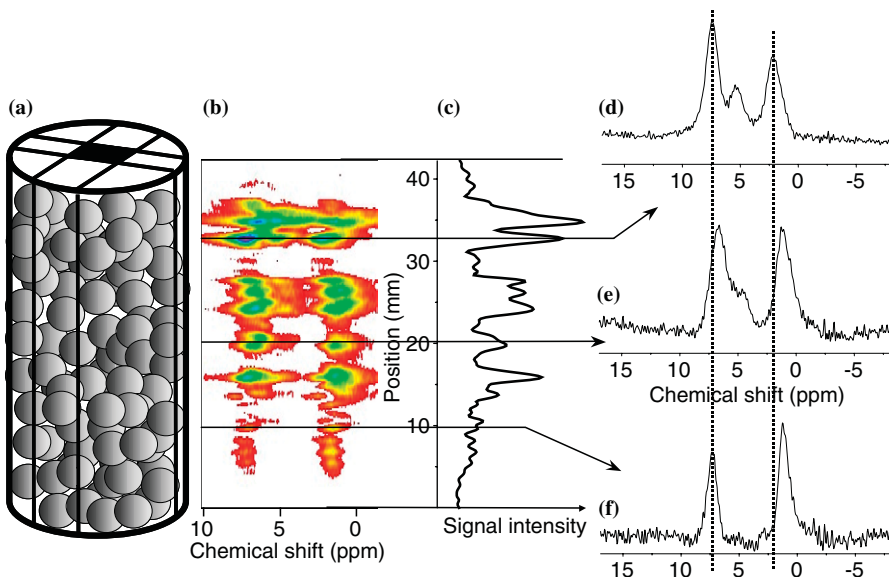


FIG. 47. *In situ* study of α -methylstyrene hydrogenation in a fixed bed of Pd/Al₂O₃ catalyst. (a) Schematic representation of the bed and the chosen axial bar. (b) A mixed spatial-spectral 2-D map which corresponds to that axial bar. (c) The distribution of the liquid phase along the axial bar obtained as an integral projection of (b) on its vertical (coordinate) axis. (d–f) NMR spectra of the liquid phase at various heights along the bar obtained as horizontal cross-sections of the map in (b). The location of these cross-sections is indicated in (b,c) with horizontal lines. Each spectrum corresponds to a volume of 0.66 mm \times 1.3 mm \times 2 mm. The two vertical dotted lines are drawn to show the differences in relative positions of the external peaks in the spectra. Reprinted from reference (69) with permission from Elsevier, Copyright (2004).

Recently, Sederman and co-workers (135) used the ¹³C DEPT MRI pulse sequence described in Section V.A.2 to investigate 1-octene hydrogenation occurring over a 1-wt.% Pd/Al₂O₃ catalyst in a trickle-bed reactor. The reactor was of inner diameter 2.5 cm and the catalyst was loaded to a bed height of 3 cm. Gas and 1-octene (liquid) flow rates were 32 and 1.0 mL min⁻¹, respectively. By employing ¹³C observation it was possible to spatially map not only 1-octene and octane species but also the formation of 2-, 3- and 4-octene isomers. This would not have been possible using ¹H MR; the only information that could have been obtained was the loss of 1-octene as reaction proceeded. Figure 48 shows 2-D maps of the ¹³C DEPT MR datasets recorded along the length of the trickle bed; ¹³C DEPT spectra are acquired separately for (a) the olefinic and (b) the aliphatic regions of the ¹³C spectrum. The intensities shown in the 2-D map are those of the spectral peaks in the ¹³C DEPT spectrum. Any horizontal cut through the 2-D map recovers an individual ¹³C DEPT spectrum. In Fig. 48 the spectra shown below each 2-D map were acquired just above the upper white line on the 2-D map; this line identifies the interface between the pure catalyst support and the catalyst. Therefore in the olefinic spectrum only two peaks occurring at 114 and 139 ppm with respect to TMS are seen. These peaks are associated with 1-octene. No other peaks are seen at this position in the bed because no reaction has occurred at this point. As the reactants move down the bed (i.e., below the upper

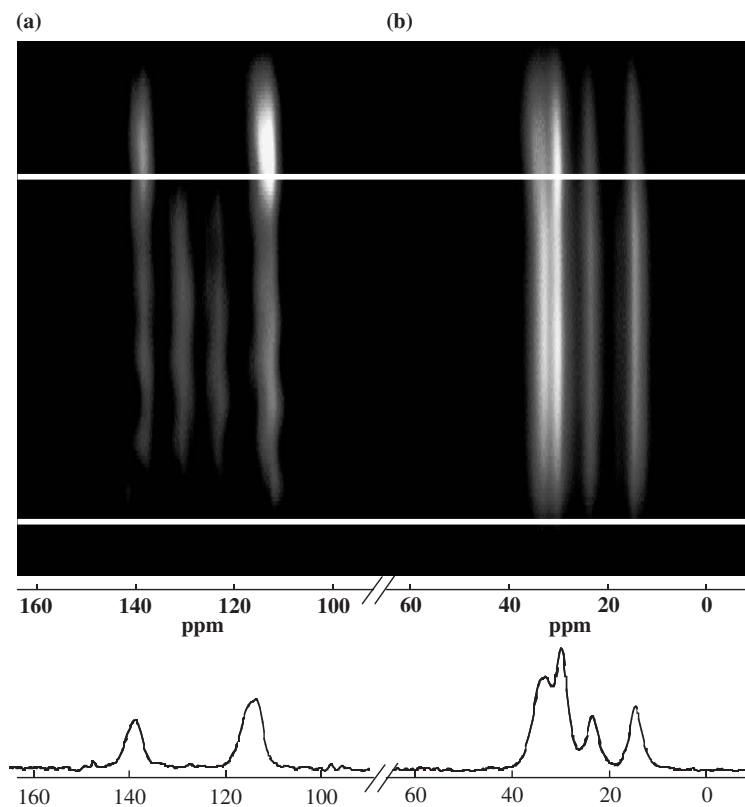


FIG. 48. 2-D map of ^{13}C DEPT-MRI spectra recorded along the length of the trickle bed. Separate acquisitions were made for each of the (a) olefinic and (b) aliphatic regions of the spectrum. The white, horizontal lines indicate the limits of the catalyst packing. Below each 2-D map, the 1-D ^{13}C DEPT NMR spectrum recorded at an axial location just before the reactants reach the catalyst (i.e., just above the upper white line) is shown. The peaks at 114 and 139 ppm indicate that only unreacted 1-octene exists within the bed at this location as expected.

white line) additional peaks are seen at 124 and 131 ppm indicating the formation of 2-octene. More detailed analysis of the relative intensities of peaks within the olefinic region provides evidence that small amounts of 3- and 4-octene isomers are also formed. This MR technique has been used to investigate the influence of feed composition on the product distribution along the length of the reactor.

In summary, many of the foundations for performing *in situ* imaging of catalytic processes in the reactor environment have now been put in place, and we can expect this to be an active area of research for many years to come.

VI. Future Directions

In the preceding 5–10 years there has been increasing recognition of the insights into both catalyst and reactor performance offered by MRI methods. The application of

MRI to characterize hydrodynamics within reactors is already established. The extent to which the potential of MR to study both hydrodynamics and chemical conversion is fully realized will depend on our ability to integrate the well-established MR spectroscopy techniques in liquid- and solid-state NMR into imaging pulse sequences, and still provide quantitative data in the magnetically heterogeneous environments typical of catalysts and reactors.

Where does MRI fit into the landscape of catalyst and reactor research and development? In the context of large-scale chemical processes, MR will only ever be a tool for helping to *understand* phenomena that may occur in the large commercial reactors. However, it is worth noting that the reactors of diameter 4–6 cm, which are typically studied by MR techniques, are the same size as those used in industrial research and catalyst testing. More important, with the current interest in the use of smaller reactor units, many reactors can be investigated at the size at which they will be used commercially. Regardless of the particular application, it is important to remember that MR methods offer the opportunity to measure directly quantities such as catalyst wetting and mass transfer coefficients for the first time. Furthermore, MR provides techniques for studying chemistry and hydrodynamics in 3-D within optically opaque systems; these techniques are enormously powerful.

Many of the foundations of chemical reaction engineering have to some extent been based on investigations of 2-D systems designed to represent the real 3-D problem. The need to do this has arisen because of the lack of non-invasive measurement techniques capable of imaging inside optically opaque structures. Notwithstanding this simplification, our ability to design reactors is remarkably good. However, the ability to image in 3-D, non-invasively and with chemical specificity, over a range of length scales characterizing the integrated catalyst/reactor system suggests that MR may yield important new insights in catalyst and reactor performance, which may have immediate impact on catalyst design and use. Quite apart from the industrial relevance of this research, we should not forget that MR is providing, in many cases, the first *in situ* images of hydrodynamics and chemical conversion in many porous media, of which catalysts and reactors are but two examples. These measurements are providing a wealth of data with which to develop and test theories and numerical models of the interaction of hydrodynamics, chemical kinetics, and heat and mass transfer processes. Further, with the advent of ultra-fast MRI that allows the investigation of unsteady-state phenomena, MRI is set to have an increasing impact in many fields of scientific research.

Acknowledgment

We thank Dr. P. Alexander for his help in the preparation of this manuscript.

References

1. Packer, K.J., *Top. Catal.* **3**, 249 (1996).
2. Dybowski, C., Bansal, N., and Duncan, T.M., *Annu. Rev. Phys. Chem.* **42**, 433 (1991).

3. Roe, D.C., Kating, P.M., Krusic, P.J., and Smart, B.E., *Top. Catal.* **5**, 133 (1998).
4. Baba, T., and Ono, Y., *Ann. Rep. NMR Spectr.* **38**, 355 (1999).
5. Fraissard, F., *Catal. Today* **51**, 481 (1999).
6. Haw, J.F., *Top. Catal.* **8**, 81 (1999).
7. Ivanova, I.I., *Colloid Surface A* **158**, 189 (1999).
8. Parker, W.O., *Comment Inorg. Chem.* **A 22**, 31 (2000).
9. van der Klink, J.J., *Adv. Catal.* **44**, 1 (2000).
10. Hunger, M., and Weitkamp, J., *Angew. Chem. Int. Edit.* **40**, 2954 (2001).
11. Han, H.W., Yan, Z.M., Zhang, W.P., and Bao, X.H., *Curr. Org. Chem.* **5**, 1017 (2001).
12. Karger, J., and Freude, D., *Chem. Eng. Technol.* **25**, 769 (2002).
13. Callaghan, P.T., "Principles of Nuclear Magnetic Resonance Microscopy." Clarendon, Oxford, 1991.
14. Kimmich, R., "NMR Tomography, Diffusometry, Relaxometry." Springer-Verlag, Berlin, Heidelberg, 1997.
15. Mansfield, P., *J. Phys. C Solid State* **10**, L55 (1977).
16. Mansfield, P., and Grannell, P.K., *J. Phys. C Solid State* **6**, L422 (1973).
17. Stejskal, E.O., and Tanner, J.E., *J. Chem. Phys.* **42**, 288 (1965).
18. Stejskal, E.O., *J. Chem. Phys.* **43**, 3597 (1965).
19. Pope, J.M., and Yao, S., *Concept Magn. Res.* **5**, 281 (1993).
20. Singer, J.R., *Science* **130**, 1652 (1959).
21. Pope, J.M., and Yao, S., *Magn. Reson. Imaging* **11**, 585 (1993).
22. Mosher, T.J., and Smith, M.B., *Magn. Reson. Med.* **15**, 334 (1990).
23. Mantle, M.D., Sederman, A.J., Raymahasay, S., Stitt, E.H., Winterbottom, J.M., and Gladden, L.F., *AIChE J.* **48**, 909 (2002).
24. Kimmich, R., and Hoepfel, D., *J. Magn. Reson.* **72**, 379 (1987).
25. Kauten, R.J., Maneval, J.E., and McCarthy, M.J., *J. Food Sci.* **56**, 799 (1991).
26. Simoneau, C., McCarthy, M.J., Kauten, R.J., and German, J.B., *J. Am. Oil Chem. Soc.* **68**, 481 (1991).
27. Doran, S.J., Carpenter, T.A., and Hall, L.D., *Rev. Sci. Instrum.* **65**, 2231 (1994).
28. Jezzard, P., Carpenter, T.A., Hall, L.D., Clayden, N.J., and Jackson, P., *J. Polym. Sci. Pol. Phys.* **30**, 1423 (1992).
29. Hall, L.D., Amin, M.H.G., Evans, S., Nott, K.P., and Sun, L., *J. Electron. Imaging* **10**, 601 (2001).
30. Bertsch, F., Mattner, J., Stehling, M.K., Muller-Lisse, U., Peller, M., Loeffler, R., Weber, J., Messmer, K., Wilmanns, W., Issels, R., and Reiser, M., *Magn. Reson. Imaging* **16**, 393 (1998).
31. Le Bihan, D., Delannoy, J., and Levin, R.L., *Radiology* **171**, 853 (1989).
32. Nott, K.P., and Hall, L.D., *Trends Food Sci. Tech.* **10**, 366 (1999).
33. Albert, M.S., and Balamore, B., *Nucl. Instrum. Meth. A* **402**, 441 (1998).
34. Kober, F., Koenigsberg, B., Belle, V., Viallon, M., Levieil, J.L., Delon, A., Ziegler, A., and Decorps, M., *J. Magn. Reson.* **138**, 308 (1999).
35. Wong, G.P., Tseng, C.H., Pomeroy, V.R., Mair, R.W., Hinton, D.P., Hoffmann, D., Stoner, R.E., and Hersman, F.W., *J. Magn. Reson.* **141**, 217 (1999).
36. Pietraß, T., Seydoux, R., and Pines, A., *J. Magn. Reson.* **133**, 299 (1998).
37. Mantle, M.D., and Sederman, A.J., *Prog. Nucl. Mag. Res. Sp.* **43**, 3 (2003).
38. Howseman, A.M., Stehling, M.K., Chapman, B., Coxon, R., Turner, R., Ordidge, R.J., Cawley, M.G., Glover, P., Mansfield, P., and Coupland, R.E., *Br. J. Radiol.* **61**, 822 (1988).
39. Silva, A.C., Barbier, E.L., Lowe, I.J., and Koretsky, A.P., *J. Magn. Reson.* **135**, 242 (1998).
40. Guilfoyle, D.N., Mansfield, P., and Packer, K.J., *J. Magn. Reson.* **97**, 342 (1992).
41. Oshio, K., and Feinberg, D.A., *Magnet. Reson. Med.* **20**, 344 (1991).
42. Manz, B., Chow, P.S., and Gladden, L.F., *J. Magn. Reson.* **136**, 226 (1999).
43. Gladden, L.F., Buckley, C., Chow, P.S., Davidson, J.F., Mantle, M.D., and Sederman, A.J., *Curr. Appl. Phys.* **4**, 93 (2004).
44. Kose, K., *Phys. Rev. A* **44**, 2495 (1991).
45. Kose, K., *J. Magn. Reson.* **92**, 631 (1991).
46. Kose, K., *J. Magn. Reson.* **96**, 596 (1992).

47. Sederman, A.J., Mantle, M.D., Buckley, C., and Gladden, L.F., *J. Magn. Reson.* **166**, 182 (2004).
48. Hennig, J., Nauwerth, A., and Friedburg, H., *Magnet. Reson. Med.* **3**, 823 (1986).
49. Britton, M.M., Sederman, A.J., Taylor, A.F., Scott, S.K., and Gladden, L.F., *J. Phys. Chem. A* **109**, 8306 (2005).
50. Holland, D.J., Sederman, A.J., Mantle, M.D., Gladden, L.F., and Middelberg, A.P.J., *J. Chromatogr. A* **1033**, 311 (2004).
51. Sederman, A.J., Mantle, M.D., and Gladden, L.F., *J. Magn. Reson.* **161**, 15 (2003).
52. Haase, A., Frahm, J., Matthaei, D., Hanicke, W., and Merboldt, K.D., *J. Magn. Reson.* **67**, 258 (1986).
53. Hollewand, M.P., and Gladden, L.F., *J. Catal.* **144**, 254 (1993).
54. Hollewand, M.P., and Gladden, L.F., *Chem. Eng. Sci.* **50**, 309 (1995).
55. Hollewand, M.P., and Gladden, L.F., *Chem. Eng. Sci.* **50**, 327 (1995).
56. Timonen, J., Alvila, L., Hirva, P., Pakkanen, T.T., Gross, D., and Lehmann, V., *Appl. Catal. A Gen.* **129**, 117 (1995).
57. Rigby, S.P., Cheah, K.Y., and Gladden, L.F., *Appl. Catal. A Gen.* **144**, 377 (1996).
58. Gladden, L.F., Alexander, P., and Hollewand, M.P., *AIChE J.* **41**, 894 (1995).
59. Rigby, S.P., and Gladden, L.F., *J. Catal.* **173**, 484 (1998).
60. Rigby, S.P., and Gladden, L.F., *Chem. Eng. Sci.* **54**, 3503 (1999).
61. Rigby, S.P., and Daut, S., *Adv. Colloid Interface* **98**, 87 (2002).
62. Mair, R.W., Sen, P.N., Hürlimann, M.D., Patz, S., Cory, D.G., and Walsworth, R.L., *J. Magn. Reson.* **156**, 202 (2002).
63. Beyea, S.D., Caprihan, A., Clewett, C.F.M., and Glass, S.J., *Appl. Magn. Reson.* **22**, 175 (2002).
64. Hollewand, M.P., and Gladden, L.F., *Magn. Reson. Imaging* **12**, 291 (1994).
65. Koptyug, I.V., Fenelonov, V.B., Khitrina, L.Y., Sagdeev, R.Z., and Parmon, V.N., *J. Phys. Chem. B* **102**, 3090 (1998).
66. Koptyug, I.V., Khitrina, L.Y., Arsitov, Y.I., Tokarev, M.M., Iskakov, K.T., Parmon, V.N., and Sagdeev, R.Z., *J. Phys. Chem. B* **104**, 1695 (2000).
67. Khitrina, L.Y., Koptyug, I.V., Pakhomov, N.A., Sagdeev, R.Z., and Parmon, V.N., *J. Phys. Chem. B* **104**, 1966 (2000).
68. Koptyug, I.V., Kulikov, A.V., Lysova, A.A., Kirillov, V.A., Parmon, V.N., and Sagdeev, R.Z., *J. Am. Chem. Soc.* **124**, 9684 (2002).
69. Koptyug, I.V., Lysova, A.A., Kulikov, A.V., Kirillov, V.A., Parmon, V.N., and Sagdeev, R.Z., *Appl. Catal. A Gen.* **267**, 143 (2004).
70. Cheah, K.Y., Chiaranussati, N., Hollewand, M.P., and Gladden, L.F., *Appl. Catal. A Gen.* **115**, 147 (1994).
71. Bonardet, J.-L., Domeniconi, T., N'Gokoli-Kékélé, P., Spinguel-Huet, M.-A., and Fraissard, J., *Langmuir* **15**, 5836 (1999).
72. Bar, N.-K., Bauer, F., Ruthven, D.M., and Balcom, B., *J. Catal.* **208**, 224 (2002).
73. Wood, J., and Gladden, L.F., *Appl. Catal. A Gen.* **249**, 241 (2003).
74. Seymour, J.D., and Callaghan, P.T., *AIChE J.* **43**, 2096 (1997).
75. Stapf, S., Packer, K.J., Graham, R.G., Thovert, J.F., and Adler, P.M., *Phys. Rev. E* **58**, 6206 (1998).
76. Manz, B., Alexander, P., and Gladden, L.F., *Phys. Fluids* **11**, 259 (1999).
77. Sederman, A.J., and Gladden, L.F., *Magn. Reson. Imaging* **19**, 339 (2001).
78. Sederman, A.J., Johns, M.L., Bramley, A.S., Alexander, P., and Gladden, L.F., *Chem. Eng. Sci.* **52**, 2239 (1997).
79. Sederman, A.J., Johns, M.L., Alexander, P., and Gladden, L.F., *Chem. Eng. Sci.* **53**, 2117 (1998).
80. Johns, M.L., Sederman, A.J., Bramley, A.S., Alexander, P., and Gladden, L.F., *AIChE J.* **46**, 2151 (2000).
81. Gotz, J., Zick, K., Heinen, C., and Konig, T., *Chem. Eng. Process.* **41**, 611 (2002).
82. Suekane, T., Yokouchi, Y., and Hirai, S., *AIChE J.* **49**, 10 (2003).
83. Tang, D., Jess, A., Ren, X., Blumich, B., and Stapf, S., *Chem. Eng. Technol.* **27**, 866 (2004).
84. Gladden, L.F., *Top. Catal.* **24**, 19 (2003).
85. Manz, B., Gladden, L.F., and Warren, P.B., *AIChE J.* **45**, 1845 (1999).

86. Dixon, A.G., *Ind. Eng. Chem. Res.* **36**, 3053 (1997).
87. Dixon, A.G., and Nijemeisland, M., *Ind. Eng. Chem. Res.* **40**, 5246 (2001).
88. Sains, M.C., El-Bachir, M.S., Sederman, A.J., and Gladden, L.F., *Magn. Reson. Imaging* **23**, 391 (2005).
89. Sains, M.C., El-Bachir, M.S., Sederman, A.J., and Gladden, L.F., *Exp. Fluids* (2005, submitted).
90. Satterfield, C.N., *AIChE J.* **21**, 209 (1975).
91. Mills, P.L., and Dudukovic, M.P., *AIChE J.* **27**, 893 (1981).
92. Lakota, A., and Levec, J., *Ind. Eng. Chem. Res.* **36**, 1444 (1990).
93. Lazzaroni, C.L., Keselman, H.R., and Figoli, N.S., *Ind. Eng. Chem. Res.* **27**, 1132 (1988).
94. Ravindra, P.V., Rao, D.P., and Rao, M.S., *Ind. Eng. Chem. Res.* **36**, 5133 (1997).
95. Helwick, J.A., Dillon, P.O., and McCreedy, M.J., *Chem. Eng. Sci.* **47**, 3249 (1992).
96. Reinecke, N., and Mewes, D., *Chem. Eng. Sci.* **52**, 2111 (1997).
97. Melli, T.R., de Santos, J.M., Kolb, W.B., and Scriven, L.E., *Ind. Eng. Chem. Res.* **29**, 2367 (1990).
98. Kolb, W.B., Melli, T.R., de Santos, J.M., and Scriven, L.E., *Ind. Eng. Chem. Res.* **29**, 2380 (1990).
99. Tsochatzidis, N.A., and Karabelas, A.J., *Ind. Eng. Chem. Res.* **33**, 1299 (1994).
100. Kantzas, A., *AIChE J.* **40**, 1254 (1994).
101. Toye, D., Marchot, P., Crine, M., and L'Homme, G., *Meas. Sci. Technol.* **7**, 436 (1996).
102. Sederman, A.J., and Gladden, L.F., *Chem. Eng. Sci.* **56**, 2615 (2001).
103. Gladden, L.F., Lim, M.H.M., Mantle, M.D., Sederman, A.J., and Stitt, E.H., *Catal. Today* **79**, 203 (2003).
104. Crine, M., Marchot, P., Lekhlif, B., and L'Homme, G., *Chem. Eng. Sci.* **47**, 2263 (1992).
105. Larachi, F., Iliuta, I., Chen, M., and Grandjean, B.P.A., *Can. J. Chem. Eng.* **77**, 751 (1999).
106. Lim, M.H.M., Sederman, A.J., Gladden, L.F., and Stitt, E.H., *Chem. Eng. Sci.* **59**, 5403 (2004).
107. Anadon, L.D., Lim, M.H.M., Sederman, A.J., and Gladden, L.F., *Magn. Reson. Imaging* **23**, 291 (2005).
108. Anadon, L.D., Sederman, A.J., and Gladden, L.F., *AIChE J.* (2005, in press).
109. Gladden, L.F., Anadon, L.D., Lim, M.H.M., Sederman, A.J., and Stitt, E.H., *Ind. Eng. Chem. Res.* **44**, 6320 (2005).
110. Irandoust, S., and Andersson, B., *Catal. Rev.* **30**, 341 (1988).
111. Kapteijn, F., Heiszwolf, J.J., Nijhuis, T.A., and Moulijn, J.A., *CatTech* **5**, 24 (1999).
112. Nijhuis, T.A., Kreutzer, M.T., Romijn, A.C.J., Kapteijn, F., and Moulijn, J.A., *Chem. Eng. Sci.* **56**, 823 (2001).
113. Mewes, D., Loser, T., and Millies, M., *Chem. Eng. Sci.* **54**, 4729 (1999).
114. Koptug, I.V., Altobelli, S.A., Fukushima, E., Matveev, A.V., and Sagdeev, R.Z., *J. Magn. Reson.* **147**, 36 (2000).
115. Koptug, I.V., Ilyina, L.Y., Matveev, A.V., Sagdeev, R.Z., Parmon, V.N., and Altobelli, S.A., *Catal. Today* **69**, 385 (2001).
116. Heibel, A.K., Scheenen, T.W.J., Heiszwolf, J.J., van As, H.J., Kapteijn, F., and Moulijn, J.A., *Chem. Eng. Sci.* **56**, 5935 (2001).
117. Heibel, A.K., Vergeldt, F.J., and van As, H., *AIChE J.* **49**, 3007 (2003).
118. Sederman, A.J., Mantle, M.D., and Gladden, L.F., *Magn. Reson. Imaging* **21**, 359 (2003).
119. Heras, J.J., Sederman, A.J., and Gladden, L.F., *Magn. Reson. Imaging* **23**, 387 (2005).
120. Savelsberg, R., Demco, D.E., Blumich, B., and Stapf, S., *Phys. Rev. E* **56**, Art. no. 020301(R) (2002).
121. Fennell, P.S., Davidson, J.F., Dennis, J.S., Gladden, L.F., Hayhurst, A.N., Mantle, M.D., Müller, C.R., Rees, A.C., Scott, S.A., and Sederman, A.J., *Chem. Eng. Sci.* **60**, 2085 (2005).
122. Harms, S., and Stapf, S., Private Communication, 2004.
123. Rees, A.C., Davidson, J.F., Dennis, J. S., Fennell, P. S., Gladden, L.F., Hayhurst, A.N., Mantle, M.D., Müller, C.R., and Sederman, A.J., *Chem. Eng. Sci.* (2005, in press).
124. Heink, W., Kärger, J., and Pfeifer, H., *Chem. Eng. Sci.* **33**, 1019 (1978).
125. Chingas, G.C., Miller, J.B., and Garroway, A.N., *J. Magn. Reson.* **66**, 530 (1986).
126. Tzalmona, A., Armstrong, R.L., Menzinger, M., Cross, A., and Lemaire, C., *Chem. Phys. Lett.* **188**, 457 (1992).
127. Menzinger, M., Tzalmona, A., Armstrong, R.L., Cross, A., and Lemaire, C., *J. Phys. Chem.* **96**, 4725 (1992).

128. Balcom, B.J., Carpenter, T.A., and Hall, L.D., *Macromolecules* **25**, 6818 (1992).
129. Koptug, I.V., Lysova, A.A., Parmon, V.N., and Sagdeev, R.Z., *Kinet. Catal+* **44**, 401 (2003).
130. Butler, L.G., Cory, D.G., Dooley, K.M., Miller, J.B., and Garroway, A.N., *J. Am. Chem. Soc.* **114**, 125 (1992).
131. Yuen, E.H.L., Sederman, A.J., and Gladden, L.F., *Appl. Catal. A Gen.* **232**, 29 (2002).
132. Gladden, L.F., Alexander, P., Britton, M.M., Mantle, M.D., Sederman, A.J., and Yuen, E.H.L., *Magn. Reson. Imaging* **21**, 213 (2003).
133. Küppers, K., Heine, C., Han, S., Stapf, S., and Blümich, B., *Appl. Magn. Reson.* **22**, 235 (2002).
134. Akpa, B.S., Mantle, M.D., Sederman, A.J., and Gladden, L.F., *Chem. Commun.* **21**, 2741 (2005).
135. Sederman, A.J., Mantle, M.D., Dunckley, C.P., Huang, Z., and Gladden, L.F., *Catal. Lett.* **103**, 1 (2005).

Atomic-Scale Imaging of Supported Metal Nanocluster Catalysts in the Working State

P.L. HANSEN and S. HELVEG

Haldor Topsøe A/S, Nymøllevvej 55, DK-2800 Kgs. Lyngby, Denmark

and

A.K. DATYE

Department of Chemical and Nuclear Engineering, University of New Mexico, MSC 01-1120, Albuquerque, NM 87131-0001, USA

Recent developments in high-resolution transmission electron microscopy (HRTEM) provide new possibilities for imaging—with atomic resolution—transition metal catalysts during exposure to reactive gases at elevated temperatures. The capability provides unprecedented insight into the structure, morphology, and dynamics of complex supported metal nanocluster catalysts with various surfaces and interfaces, even as they are functioning. Here we review recent work that exploits this capability of HRTEM to elucidate the nature of the exposed surfaces in such catalysts. The observations provide information about the exposed metal–surface sites, metal–support interface, and surface dynamic processes induced by changes in the gas environment. Examples include the location of a barium promoter in a ruthenium catalyst for the ammonia synthesis catalyst, gas-induced shape changes in supported copper nanocrystals for the methanol synthesis, and carbon nanofiber formation in steam reforming catalysts.

Abbreviations: CCD; Charge-coupled device; DFT; Density functional theory; EDS; Energy dispersive spectroscopy; EELS; Electron energy loss spectroscopy; ELNES; Electron energy loss near-edge structure; EXAFS; Extended X-ray absorption fine structure; eV; Electron volts; FEG; Field emission gun; HRTEM; High-resolution transmission electron microscopy; kV; Kilovolts; mbar; Millibar; MeV; Mega electron volts; Min; Minutes; mL; Millilitres; nm; Nanometers; STEM; Scanning transmission electron microscopy (or microscope); TEM; Transmission electron microscopy (or microscope); μm ; Micrometers; 2D; Two-dimensional; 3D; Three-dimensional.

I. Introduction

The state of the surface of a solid catalyst may change markedly with changes in the reactive environment. The realization that catalyst surface structures, and therefore catalytic properties, depend on the reaction conditions has spurred tremendous

interest in obtaining atomic-scale structural, electronic, and chemical information about solid catalysts during exposure to reactive gas atmospheres. Over the past four decades, the development of methods for determining such information has mainly focused on spectroscopic methods providing information averaged over length scales considerably larger than the characteristic nanostructures in the catalysts. Complementary atomic-level, real-space images obtained under catalytic reaction conditions have not previously been available.

Transmission electron microscopy (TEM) and scanning transmission electron microscopy (STEM) are recognized as powerful and versatile tools for the characterization of supported metal catalysts, because real-space images of catalysts with spatial resolution down to 0.1 nm can be recorded and combined with high-spatially resolved spectroscopic information. However, TEM has been used mainly for *ex situ* characterization, for example, of catalysts after gas treatments.

The application of TEM to *in situ* investigations is challenging, in part because of the strong interactions between the high-energy electron beam of the microscope and the gas atmosphere. Consequently, although *in situ* TEM for investigation of catalysts was pioneered about three decades ago, it is only as a result of developments in the preceding decade that the technique has matured enough to allow atomic-level imaging of many different types of solid catalysts in their working states (1–3). However, to obtain *in situ* high-resolution TEM (HRTEM) images of important industrial catalysts incorporating 3d transition metals, such as iron, nickel, and copper, a resolution of at least 0.18 nm is required, and this has been achieved only recently as a result of further instrumental developments (4).

This capability opens up new possibilities for exploring the structure and morphology of complex supported metal nanocluster catalysts. Metal nanoclusters may expose various types of surface sites to their environments, and if they are large enough, they expose well-defined crystal facets. From fundamental investigations of elementary gas–surface interactions, it is known that steps and other defect sites are more reactive than sites on metal facets (5,6). Recent advances in surface science show that the enhanced reactivities of step sites originate from the reduced metal coordination, resulting in stronger adsorption through changes in the metal valence *d*-electron properties, or from a unique local atomic geometry that is well-suited to bond-breaking or -formation processes (7).

With the ability to obtain information about the concentrations of various types of metal surface sites in complex metal nanocluster catalysts, HRTEM provides new opportunities to include nanoparticle structure and dynamics into fundamental descriptions of the catalyst properties. This chapter is a survey of recent HRTEM investigations that illustrate the possibilities for characterization of catalysts in the functioning state. This chapter is not intended to be a comprehensive review of the applications of TEM to characterize catalysts in reactive atmospheres; such reviews are available elsewhere (e.g., (1,8,9)). Rather, the aim here is to demonstrate the future potential of the technique used in combination with surface science techniques, density functional theory (DFT), other characterization techniques, and catalyst testing.

II. Transmission Electron Microscopy (Limitations of Conventional TEM in the Characterization of Catalysts)

Modern TEM combines high-resolution imaging and electron diffraction with local elemental analysis and electronic structure information (10). Images can be recorded by use of either a parallel electron beam (in HRTEM) or a focused probe that is scanned across the specimen (in STEM). In either case, a spatial resolution down to about 0.1 nm was demonstrated allowing, for example, atomic columns to be resolved in images of crystalline materials (11,12). The transmission geometry provides 2D images representing projections of the 3D atomic arrangement in the sample. Images showing the crystal lattice can therefore be obtained only if the crystalline structures are aligned with a zone axis close to the direction of the electron beam.

Local chemical composition from areas less than 1 nm in diameter can be measured by energy dispersive X-ray spectroscopy (EDS) or electron energy loss spectroscopy (EELS). Such spectroscopic information may be presented in 2D maps showing the spatial element distribution in the specimen (13). Furthermore, information about the local density of unoccupied electron states of a specific element can be extracted from EELS data and used to estimate the oxidation state and the local coordination geometry of the excited atoms (14). In some favorable cases, electronic structure information with a resolution of about 1 eV from individual atomic columns has been attained (15,16). Recent developments of monochromators and spectrometers have brought the resolution down to 0.1 eV (17,18), and this capability may offer new opportunities to determine relationships between electronic structure information, the atomic arrangements and the catalytic activities of solids.

Conventional HRTEM of supported nanocluster catalysts is often hampered by the lack of control of the gas environment surrounding the catalyst. As a consequence of the strong interaction between the electron beam and a solid phase, the thickness of the sample has to be less than about 50 nm to allow imaging on the atomic scale. Sample specimens are therefore typically prepared under ambient conditions by crushing and grinding of the catalyst powder in a mortar and distributing small amounts of the resultant fine powder onto a bare metal grid or on a holey carbon film supported on a metal grid, which is mounted in the sample holder and inserted into the TEM vacuum. As the catalyst is exposed to air, this procedure inevitably leads to oxidation of reactive metal nanoclusters, which may have been formed during reductive treatments, for example, in a catalytic reactor. One way to prevent reoxidation of the metal is to handle and store the catalysts under an inert gas by use of sealed reactors and TEM sample holders for transferring samples, and a glove box with controlled inert atmospheres for preparation of the TEM specimens.

This so-called *ex situ* or *quasi in situ* TEM approach has allowed researchers to determine important structural information about catalysts containing, for

example, metal sulfides (19), metallic nickel (20), and iron-containing phases (21). However, we emphasize that the approach does not exclude the possibility of undetermined structural or morphological changes of the supported species that are present under catalytic reaction conditions. The catalysts encounter various residual gases during transfer from a catalytic reactor to the TEM vacuum, depending on the cleanness of the inert gas atmosphere. Even at the background pressure of about 10^{-7} mbar in a TEM instrument, adsorption of residual gas components (mainly H_2 , H_2O , CO , and CO_2) may result in significant adsorbate coverages of a catalyst surface kept at room temperature. The surface contaminants perturb the surface free energies, to a degree that depends on the adsorbate coverages and bond strengths, and, with sufficient coverage, the contaminants will eventually cause changes in the shape and thus the distribution of exposed surface sites of supported metal nanoclusters.

Furthermore, we emphasize the importance of using low electron beam current intensities to avoid beam-induced artifacts such as oxidization of metals, reduction of oxides, and carbon deposition on samples, which may occur even under the high-vacuum conditions in the TEM instrument. For optimal HRTEM imaging, an electron dose in the range $0.1\text{--}1\text{ C/cm}^2$ is typically needed (22). The actual dose is, however, set as a trade-off between maintaining a signal-to-noise ratio in the images and avoiding beam-induced artifacts. To determine the optimal electron beam intensity, the specimen is imaged with varying beam intensities and the range of intensities where no changes in the specimens are detected is used for characterization of other regions of the specimen.

III. Approaches to Characterization of Catalysts in Reactive Atmospheres

The central challenge in constructing an HRTEM instrument for investigation of catalysts in reactive atmospheres is to avoid degradation of the electron beam coherence, and, thus, loss of spatial resolution resulting from the scattering of the electron beam by the gas molecules in the column. The goal can be achieved by minimizing the extent of the gas phase along the TEM column. Constructions facilitating investigations of samples in reactive atmospheres began to appear around the 1960s (e.g., (23)). So far, two fundamentally different approaches have been taken to realize such HRTEM investigations, employing either (i) differentially pumped microscope columns or (ii) thin-window cells placed on the sample holder. In the following these two approaches are reviewed separately.

A. DIFFERENTIALLY PUMPED TEM INSTRUMENTS

The first instruments applying differentially pumped vacuum columns were mainly used for low-magnification imaging and electron diffraction investigations

(24–26). The pioneering applications of this TEM design to problems related to catalysis were the work of Baker and co-workers in the early 1970s (1). The instrument was a 100-kV JEOL 7A, equipped with a resistively heated tungsten filament as the electron source; the image resolution was about 3 nm. In this microscope, the catalyst specimens could be exposed to temperatures in the range of 870–1470 K and gas pressures in the range of 10–100 mbar (25).

In the 1990s, several differentially pumped high-resolution TEMs for investigations of samples in reactive atmospheres were developed on the basis of 300–400-kV instruments with LaB₆ electron sources (2,3,27,28). These instruments achieved an improved resolution of down to 0.26–0.23 nm, allowing imaging of the lattice structures of several oxide materials. Furthermore, the first image of the (111) lattice planes in platinum catalysts was presented (2), demonstrating the resolution of 0.23 nm. Typical operating gas pressures in these instruments are 1–10 mbar. Moreover, electron energy loss spectrometers and image filters were added to the TEM columns, and it was demonstrated that spectroscopy data characterizing functioning catalysts could be obtained as well (3).

The most recent developments have made the differentially pumped HRTEM even more versatile, with an image resolution of down to 0.14 nm. This allows imaging of the lattice structures of most transition metal catalysts under reaction conditions (4). The instruments are based on a modern 300-kV CM300 FEG TEM (4) (or a 200-kV Tecnai (29)) from FEI. The main reason for the improved image resolution is the implementation of a field emission gun (FEG) as the electron source and the incorporation of the “SuperTwin” objective lens. The differential pumping system is based on the design of Boyes and Gai (2), but an extra pumping stage is introduced to better protect the FEG. Investigations can be conducted with gas pressures of up to 15 mbar and flow rates up to 10 mL/min for single gases or gas mixtures containing, for example, H₂, O₂, CO, CO₂, H₂O, N₂, He, and CH₄. In the following, the design of the differential pumping system and the sample holders used in this instrument are described in detail.

Figure 1 includes an image and a schematic outline of the microscope column, with emphasis on the differential pumping system. Reactive gases can be introduced into the sample area through a needle valve. Two apertures with diameter of 200 μm are mounted in small metal tubes and inserted into the holes in the upper and lower pole pieces of the objective lens; the enclosed volume around the sample corresponds to the cell where the sample is exposed to the reactive atmosphere. The distance between the two apertures is about 5 mm. From the cell, gases can diffuse away through the apertures. A second set of apertures (with a diameter of 400 μm) is mounted at the other ends of the tubes to set up the first pumping stage, and the volume between the 200- and the 400-μm apertures in the tubes is connected to a molecular drag pump through cylindrical paths drilled in the magnetic objective lens material. The second part of the differential pumping system is evacuated by a turbo molecular pump, which is connected to the upper part of the TEM column at the second condenser aperture. In the upper part of the column, an ion-getter pump (IGP) is connected to the first condenser aperture assembly, which is also constructed to operate as a differential pumping aperture. Two further IGPs are part of the standard vacuum system in the FEG unit.

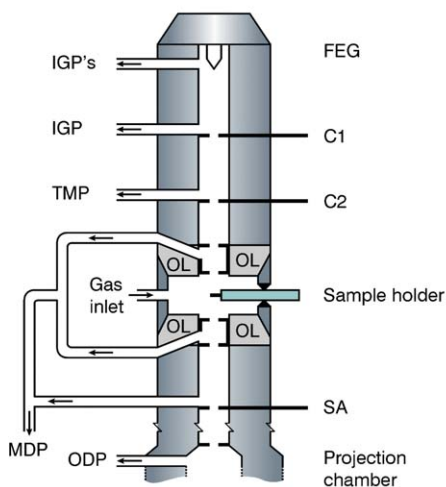
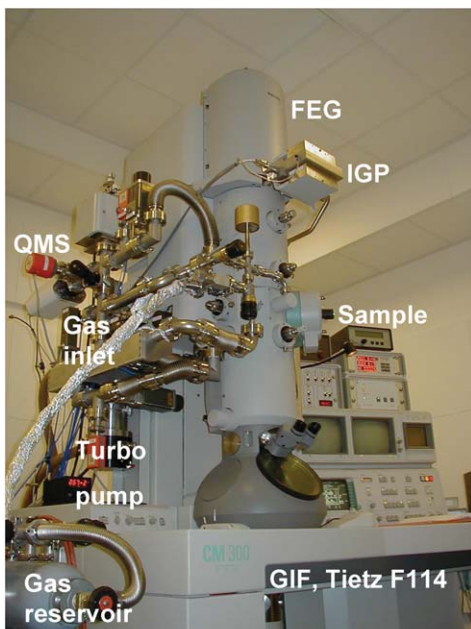


FIG. 1. Photo and illustration of the HRTEM allowing acquisition of images of catalysts under working conditions (4). The microscope is equipped with an FEG, a quadrupole mass spectrometer (QMS), a Gatan image filter (GIF), and a Tietz F144 CCD for data acquisition. The differential pumping system consists of IGPs, turbo molecular pump units (TMP, MDP), and an oil diffusion pump (ODP). The differential pumping stages are set up by apertures inside the TEM column (denoted by black bars) at the objective lens (OL), the first (C1) condenser aperture, the second (C2) condenser aperture, and the selected area aperture (SA).

With this design, a pressure of about 15 mbar in the cell can be obtained while the high vacuum needed for operating the FEG is maintained and the electrons can be transmitted through the column with a minimal amount of scattering. The lower part of the TEM column is pumped differentially by one stage centered at the selected area aperture and one stage including the viewing screen area and the detectors (a Gatan image filter (GIF2000) and a Tietz F114 Fastscan CCD). The latter is pumped by the oil diffusion pump, which is part of the standard vacuum system of the microscope.

Specially designed sample holders are needed for heating of the sample in a reactive gas. Figure 2 shows an example of such a holder (30). A tungsten filament covered with alumina is used as the heating element. This element is placed inside a cup, which acts as a support for the metal grid holding the sample and as a distributor of the heat from the tungsten filament. The cup is suspended by alumina or zirconia spheres to isolate it thermally from the frame of the holder. The 3-mm metal grid supporting the sample is clamped between rings made, for example, of tungsten by a circlip of steel. For measurement of the sample temperature, a thermocouple is spot-welded onto the cup.

The construction materials of all the heated parts of the holder are of utmost importance, as not all materials remain stable when exposed to gas atmospheres of varying composition at elevated temperatures. For example, the tungsten heating element breaks when used in oxidizing gases, and heaters constructed from other materials (e.g., steel) and with different thermal connections to the cup must be applied instead. Moreover, it is also important to choose the materials for construction and for the holder design so that drift of the cup (and drift of the sample) is minimized when the temperature of the holder is changed.

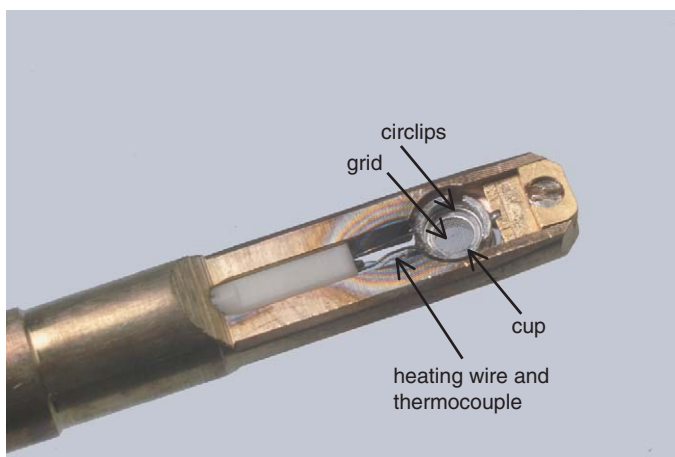


FIG. 2. Photo of tip of a sample holder for heating the catalyst specimen during exposure to reactive gases. The holder body suspends a cup with the TEM specimen grid. The cup is thermally and electrically isolated from the holder body and can be heated by a tungsten filament located inside the cup. The temperature is measured by a thermocouple mounted on the outside of the cup.

B. THIN-WINDOW CELLS

Specially designed sample holders allowing the sample to be enclosed between two gas-tight electron-transparent thin films have been used for investigations of samples in gases (mainly water-saturated air) at pressures up to 200 mbar (31,32). Heating of these samples was limited to temperatures of about 470 K. The advantages of this type of cell compared to the differentially pumped cell are associated with the very small volume of gas around the sample and the control of the flow geometry for the gas passing over the sample. A mass spectrometer can be connected to the gas outlet for analysis of reaction products, and thus the thin-window cells provide the opportunity for a direct coupling between structure data determined by TEM and reactivity data determined by mass spectrometric analysis of gas-phase products of a catalytic reaction. The main disadvantage of the thin-window cells is the scattering of the electron beam on the windows. The contrast from two 10–15-nm thick windows of amorphous carbon is large enough to make interpretations of atomic-scale features difficult. The construction of thin-window cells including O-ring seals limits the possibility to heat the sample to high temperatures. This limitation may, however, be remedied to some degree by the use of soft metal gaskets instead of conventional O-rings. We note that a combination of the differential pumping system with a thin holey film window cell may combine the advantages of the two different systems.

VI. Examples of HRTEM Characterization of Catalysts in Reactive Atmospheres

Atomic-scale imaging of supported metal nanocluster catalysts has provided unprecedented insight into structural and morphological dynamics induced by reactive gas environments. In the following, a survey of recent HRTEM investigations of samples in reactive atmospheres is presented. Specifically, we focus on recent work that has been performed with HRTEM imaging of supported metal nanocluster catalysts to understand the role of gas–surface interactions on the working catalysts. We also discuss the possibilities for including insight into nanocluster dynamics into the description of catalyst properties.

A. THE COMPLEX NANOSTRUCTURE OF AN AMMONIA SYNTHESIS CATALYST

A complex nanostructured catalyst for ammonia synthesis consists of ruthenium nanoclusters dispersed on a boron nitride support (Ru/BN) with barium added as a promoter (33). It was observed that the introduction of barium promoters results in an increase of the catalytic activity by 2–3 orders of magnitude. The multi-phase catalyst was first investigated by means of conventional HRTEM, but this technique did not succeed in identifying a barium-rich phase (34). It was even difficult to determine how the catalyst could be active, because the ruthenium clusters were encapsulated by layers of the boron nitride support. By HRTEM imaging of the catalyst during exposure to ammonia synthesis conditions, it was found that the

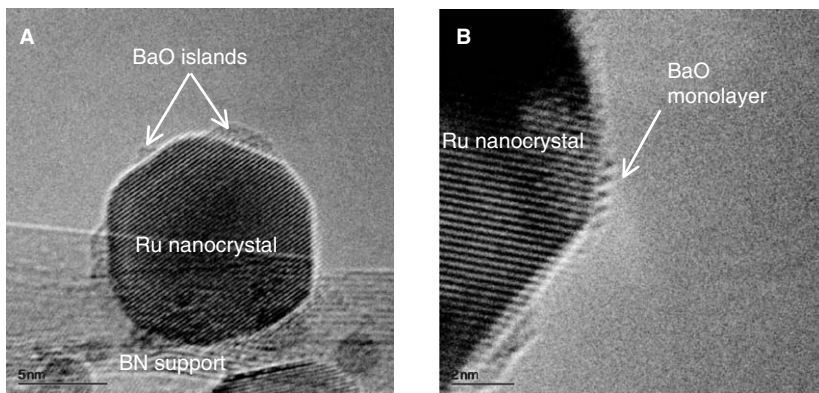


FIG. 3. HRTEM images of barium-promoted ruthenium nanocrystals on BN support. The images were recorded with the catalyst exposed to 5.2 mbar of a gas mixture of H_2/N_2 of 3:1 at 825 K. (A) Patches of a barium-containing phase are found on several ruthenium nanocrystal surfaces. The lattice fringe spacing in the ruthenium nanocrystal is 0.21 nm corresponding to the (101) lattice planes. (B) Image of the edge of a ruthenium nanocrystal. The lattice fringe spacing is 0.23 nm corresponding to the (100) planes in ruthenium. On the edge, a monolayer patch of the barium oxide phase is evident. The distance between the dark spots, representing barium atoms, is 0.48 nm. Reprinted with permission from Reference (34).

catalyst was restructured, and ruthenium nanocrystals appeared with hexagonal crystal shapes freed of the support (Fig. 3) (34). The HRTEM images allowed a comparison of the unpromoted and promoted ruthenium catalysts, which showed that the shape of the ruthenium clusters were unaltered in the presence of barium, suggesting that the number of active site was not substantially changed and that the barium acts as an electronic promoter. Furthermore, HRTEM images indicated two distinctly new phases at the exterior surfaces of the ruthenium nanocrystals in the barium-promoted catalyst: An amorphous phase covering mainly some facets of the ruthenium nanocrystals and another well-dispersed monolayer phase (Fig. 3).

To elucidate the state of the barium promoter phase, EELS data were obtained in addition to the images. The spectroscopic data obtained at the oxygen K-edge and the barium $M_{4,5}$ -edge demonstrate that barium is present as an oxide. From HRTEM images alone it was not possible to conclude which of the two phases is related to the increased activity. However, recent DFT calculations have shown that the activity of both the promoted and unpromoted ammonia synthesis catalysts is predominantly associated with B_5 -type sites (35–38). Such sites are located near the edges of the nanocrystals. The finding that step edge sites dominate the ammonia synthesis activity is supported by results of investigations with single crystals showing that the rate-limiting step of N_2 dissociation is nine orders of magnitude faster at step sites than at facet sites (6).

On the basis of these results, the increased activity of the promoted catalyst was attributed to a two-dimensional barium–oxygen overlayer on the ruthenium nanocrystals, located in the vicinity of the crystal edges (B_5 -type sites). The ability to

directly image the atomic-scale structure of the complex multi-phase nanocluster system under ammonia synthesis conditions by means of HRTEM was decisive for obtaining insight into the structure and location of the promoter phase. The example also demonstrates the necessity of combining such HRTEM results with results of theoretical modeling and/or other characterization methods to understand the dramatic influence of the promoters on the catalytic properties.

B. GAS-INDUCED SHAPE CHANGES IN Cu/ZnO-CONTAINING METHANOL SYNTHESIS CATALYSTS

In the description of adsorption of atoms and molecules and in particular of chemical reactions between the adsorbates at metal surfaces, the surface is often considered to be static, providing a fixed number of sites. Because adsorption energies are often comparable to metal-metal bond strengths, changes in the surface free energy of the exposed surface may therefore occur and, depending on the gas composition and conditions, perhaps eventually result in structural transformations of the nanometer-sized metal particles—with dramatic consequences for their catalytic properties. Clearly, these considerations emphasize the need for characterizing the supported metal nanoparticles under relevant conditions and for obtaining real-space information about the dynamic structures and shapes of the nanoclusters.

A recent example of such dynamic behavior involves the Cu/ZnO-containing methanol synthesis catalyst (4). Figure 4 shows HRTEM images of copper particles supported on ZnO in the presence of various gases. The copper nanoclusters are produced by reduction of the CuO/ZnO precursor in H₂ at 550 K. The lattice fringes in the nanoclusters, as well as EELS data, confirm the presence of metallic copper in these structures. In an investigation of the response of the nanoclusters to variations in the gas composition, the catalyst was exposed to more oxidizing conditions (by addition of water to the H₂ gas) or to more reducing conditions (by addition of CO to the H₂ gas). Upon each change in gas atmosphere, the copper nanoclusters changed shape. The images (Fig. 4) represent equilibrium shapes attained by these clusters on the ZnO support.

The images provide direct insight into the gas-induced shape changes and help to elucidate the main driving force for the transformations: Addition of water results in copper nanoclusters with a more spherical shape, which means that the copper nanocrystals are terminated by a higher fraction of (1 1 0) and (1 0 0) facets, relative to the more close-packed (1 1 1) facet, than in pure hydrogen. Hence, the surface free energies of the more open (1 1 0) and (1 0 0) facets tend to stabilize with respect to the (1 1 1) facet. The contact area between the copper and ZnO did not change significantly. This observation points to the fact that water adsorption on the various exposed copper facets is the main driving force for the gas-induced surface reconstructions and the resulting reshaping of the copper clusters. On the other hand, addition of the more reducing CO/H₂ mixture induced a transformation of the copper nanoclusters into disc-like structures, corresponding to an increase in the interface area by about 50%. The increased wetting of the ZnO support by copper suggests a large change in the interface energy. Previously, a

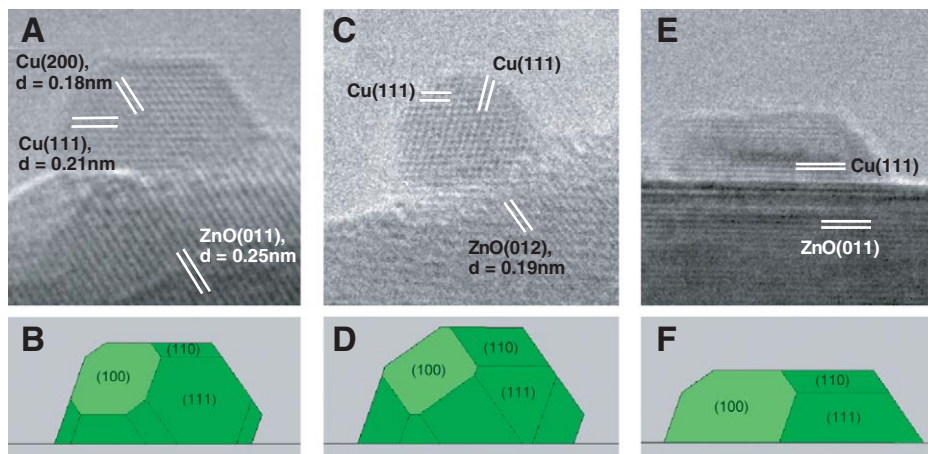


FIG. 4. High-resolution TEM images of a Cu/ZnO model catalyst in various gas environments together with their corresponding Wulff construction. (A, B) A metallic copper nanocrystal with facets corresponding to the (1 0 0), (1 1 0), and (1 1 1) surfaces. The image was obtained at a pressure of 1.5 mbar of H_2 at 493 K. The electron beam was parallel to the (0 1 1) zone axis of copper. (C, D) A metallic copper nanocrystal in a gas mixture of H_2 and H_2O , H_2 : H_2O = 3:1 at a total pressure of 1.5 mbar at 493 K. (E, F) A metallic copper nanocrystal in a gas mixture of H_2 (95%) and CO (5%) at a total pressure of 5 mbar at 493 K. Reprinted with permission from Reference (4).

decrease in the interface energy was attributed to lower oxygen content in the ZnO surfaces resulting from an increase in the reduction potential of the gas phase (39–41).

Combining these HRTEM results with EELS measurements provided some support for this interpretation (42). As the reduction potential in the gas phase was increased, the wetting of the ZnO by copper was accompanied by a slight intensity increase in the energy loss near edge structure (ELNES) of Cu L_3 -ionization edge (Fig. 5). The variations in the ELNES of the L_3 -edge mainly reflect changes in the density of electronic states for copper above the Fermi level. By comparison of these observations with spectral simulations, the increase in the ELNES intensity (caused by the increase in the reduction potential of the gas phase) was interpreted as a consequence of Cu–Zn alloy formation at the Cu–ZnO interface or the copper surface, in accord with previous suggestions (39–41,43). The results illustrate how complex gas-dependent metal–support interactions involving changes in both morphology and electronic interactions in supported metal catalysts can be addressed by the combination of HRTEM and EELS.

The microscopy results characterizing the Cu/ZnO catalyst are in accord with EXAFS data representing the dynamic morphology changes (39–41), and they also provide an important additional insight: On the basis of the lattice-resolved images, the nature of the exposed facets of the projected copper nanoclusters and the epitaxial relationship between the copper and ZnO can be identified. The majority of the copper nanocrystals appear to be in contact with the ZnO support with their (1 1 1) facets, as was also observed for copper particles prepared by vapor

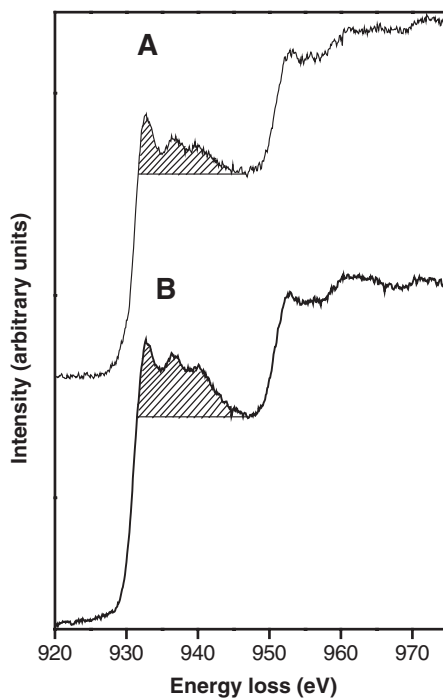


FIG. 5. Normalized EEL spectra of the Cu/ZnO catalyst Cu $L_{2,3}$ -edges. The spectra were acquired from the Cu/ZnO catalyst (A) in 1.5 mbar of H_2 at 493 K and (B) in a H_2 (85%)/CO (15%) mixture at a total pressure of 1.5 mbar at 493 K (after heating to 723 K for 1 h). The hatched areas indicate changes in the ELNES intensity at the L_3 -edge by variations in the gas environment. Reprinted in part with permission of the American Chemical Society from Reference (42).

deposition under ultra-high vacuum conditions onto various atomically clean ZnO surfaces (44). The detailed structural insight led to Wulff constructions for the copper nanocrystals and a quantitative determination of the relative metal surface free energies and the interface free energy of the sample in the various gas environments (4). Previously, such quantitative information characterizing solid catalysts could only be obtained from *ex situ* electron microscopy observations (45) or scanning tunneling microscopy studies under ultra-high vacuum conditions (46,47). This information allows a reconstruction of the full 3D shape of the supported copper nanocrystals, which in turn may provide important information regarding the concentrations of the various types of surface sites (low-index planes, corners, steps, etc.) under reaction conditions. Understanding at this level allows a direct incorporation of the dynamic morphology into a representation of the microkinetics of the catalytic reaction using the approach discussed earlier (41). Previous descriptions of catalysis have relied largely on assumptions regarding the nature of the exposed surfaces, the interface energy, and their dependence on the gas composition.

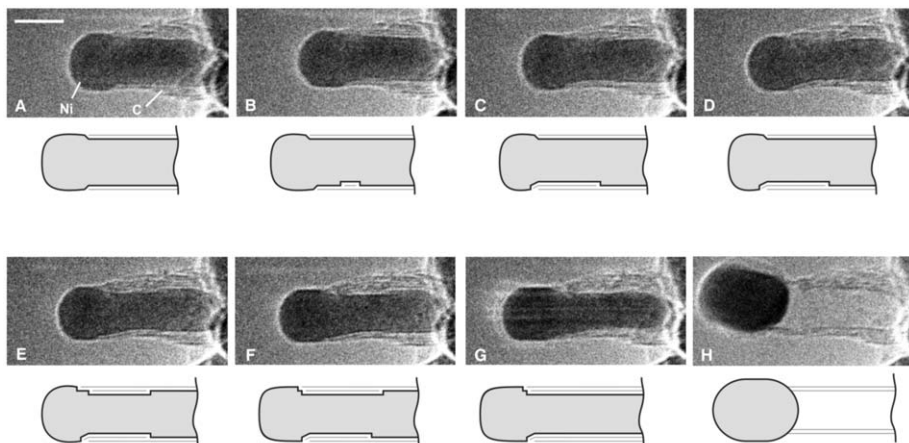


FIG. 6. Image sequence of a growing carbon nanofiber (movies are available as supplementary information to Reference (52) and can be found in Reference (57)). Images (A)–(H) illustrate one cycle in the elongation/contraction process. Drawings are included to guide the eye in locating the positions of mono-atomic nickel step edges at the carbon–nickel interface. The images are acquired *in situ* with CH_4 : $\text{H}_2 = 1:1$ at a total pressure of 2.1 mbar with the sample heated to 809 K. All images were obtained at a rate of 2 frames/s. Scale bar = 5 nm. Reprinted with permission from Reference (52).

C. ATOMIC-SCALE MONITORING OF CARBON NANOFIBER GROWTH IN STEAM REFORMING CATALYSTS

TEM imaging can also provide atomic-scale insight into dynamic processes associated with restructuring of supported metal catalysts that may be induced in response to changes in the gas composition or the course of a catalytic reaction under steady-state conditions. The information emerges from acquisition of many consecutive images from the same area of the catalyst obtained either with a television camera coupled to a video recorder or a CCD with suitable digital acquisition software. When the time-resolved images are played back as in the form of a movie, they provide a direct visualization of the structural changes in time. This capability has led to unprecedented new insights into mechanisms involved in phase transformations, crystallization, oxidation/reduction processes, morphology changes, sintering, and vapor deposition (48–51).

A recent dynamic study focused on oxide-supported nickel nanoclusters (52), which are widely used in industrial processes for methane steam reforming to produce synthesis gas or hydrogen (53). Under some reaction conditions, the formation of carbon nanofibers is induced in the catalyst, and this process presents a deactivation mechanism that eventually destroys the catalyst (53,54). In their pioneering work, Baker et al. (55,56) used TEM to investigate carbon nanofiber growth by catalytic decomposition of acetylene on nickel nanoclusters. Figure 6 shows a time-resolved series of HRTEM images of the growth of a carbon nanofiber by catalytic decomposition of methane on a supported nickel nanocluster (57). The images show

that the initial compact equilibrium shape of the nickel nanocluster transforms into a highly elongated shape. The elongation of the clusters appears to be correlated with the formation of more graphene sheets at the graphene–nickel interface, with their basal (002) planes oriented parallel to the nickel surface. Hence, the reshaping of a nickel nanocluster assists in the alignment of a graphene layer into a tubular structure. The elongation of a nanocluster continues until it achieves an aspect (length/width) ratio of up to approximately 4, before it abruptly contracts to a spherical shape within less than approximately 0.5 s (Fig. 6H). The contraction is attributed to the fact that the increase in the nickel surface energy can no longer be compensated for by the energy gained when binding the graphitic fiber to the nickel surface. The elongation/contraction scenario continues in a periodic manner as the nanofiber grows. Furthermore, the growth stops if the graphene layers eventually encapsulate the nickel particle, indicating that part of the nickel surface must be in direct contact with the gas phase.

The HRTEM images furthermore reveal that mono-atomic steps are present at the nickel surfaces and that a graphene sheet terminates at each of these steps. Such nickel step edges play a key role in the nucleation and growth of graphene sheets: Nickel step edges are induced spontaneously in the course of the reaction, even at the graphene–nickel interface (Figs 6B–G). Between a pair of such step edges, an additional graphene layer grows as the nickel steps move toward the ends of the nickel cluster and vanish. It is clear that this process involves transport of carbon atoms toward and nickel atoms away from the graphene–nickel interface. The flux of nickel atoms is directed toward the free nickel surface, producing the observed elongation. Carbon atoms, resulting from methane decomposition at the free surface, must diffuse to the interface to account for the growth of the graphene layer.

Although the HRTEM movies provide important information about the atomic-scale surface dynamics, they capture only the result of the atomic diffusion events and not directly the individual atomic displacements. To understand the origin of the transport mechanisms, the observations have been complemented with results based on DFT calculations. The calculations show that step edges facilitate methane dissociation and that carbon atoms bind more strongly to step edges than

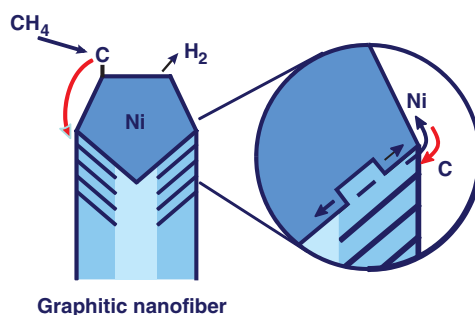


FIG. 7. Growth mechanism of graphitic carbon nanofibers. The illustration highlights the observation of spontaneous nickel step edge formation at the carbon–nickel interface. The observations in Reference (52) are consistent with a growth mechanism involving surface transport of carbon and nickel atoms along the graphene–nickel interface.

to facet sites (58). This result suggests that step sites act as preferential nucleation sites for graphene. The extra binding energy of carbon to a step site is larger than the energy cost for step formation, which explains the spontaneous step formation at the nickel surface (52,58). Moreover, the DFT calculations show that carbon atoms are more stable in a graphene layer than at a step site, showing that there is an energetic driving force for graphene growth.

Furthermore, the interfacial dynamics can be explained by a novel interfacial transport mechanism (Fig. 7). The experiments clearly point to the need for interfacial transport of nickel atoms toward the graphene-free part of the nickel surface, because the transport definitely cannot take place through the bulk crystal of these clusters. The DFT calculations of transport of atomic nickel along the graphene-free surface, modeled by a Ni(111) surface, and the graphene–nickel interface, modeled by a graphene–Ni(111) interface, show that nickel interface transport is possible. It has been suggested (54,55,59–61) that carbon transport could proceed through the bulk of the nickel particles. Although bulk diffusion may occur under some growth conditions, DFT calculations show (52) that it is not necessary to include bulk diffusion to obtain a consistent growth mechanism and that carbon can migrate along the graphene-free surfaces and the graphene–nickel interface. The DFT calculations show that carbon migration along the graphene-free surface, modeled by a Ni(111) surface, and the graphene–nickel interface, modeled by the graphene–Ni(111) interface, is also possible. The maximum activation energy barrier for surface transport of carbon atoms from sites at the graphene-free nickel surface to sites at the graphene–nickel interface was estimated on the basis of the DFT calculations to be 1.6 eV. This estimate is in satisfactory agreement with the measured activation barrier for carbon nanofiber growth, in the range 1.3–1.5 eV (55,56,59), suggesting that surface transport of carbon atoms confined to the nickel surface could be the rate-limiting step for carbon nanofiber growth.

These results demonstrate that step sites play an important role as centers for carbon growth, and, thus, that the properties and dynamic behavior of step sites are crucial for the stability of nickel-containing catalysts. On the basis of this knowledge, a more general understanding of the effects of many different promoters has been developed: Potassium, sulfur, and gold promoter atoms have been found to bind preferentially to step edges of nickel, suggesting that these elements suppress graphite formation through a step blocking mechanism (53,58).

V. Outlook

High-resolution transmission electron microscopy (HRTEM) has matured markedly in the preceding decade and has emerged as a powerful technique for investigation of nanostructured metal catalysts at the atomic level, even under working conditions. The ability to image the dynamic structure and morphology of supported metal nanocluster catalysts in such detail makes HRTEM an essential complement to the arsenal of spectroscopic techniques used for characterization of

working catalysts. When these methods are used in concert, new possibilities open up for developing fundamental insight into supported metal catalysts. HRTEM provides the crucial information identifying structures of surfaces and interfaces and opportunities to relate fundamental information about gas–surface interactions measured or calculated with simple samples such as single crystals to more complex supported metal nanocluster catalysts exposed to high temperatures and pressures. Thus, HRTEM images help to bridge what have been referred to as the materials and pressure gaps in catalysis (62). Specifically, the interplay of HRTEM with atomic-scale modeling of possible elementary processes at the exposed surfaces provides an important approach for rationalizing the complex dynamic phenomena occurring in catalysis.

Important ongoing developments in HRTEM that are expected to be valuable in catalysis research include the correction of spherical aberrations in electron microscope lenses and monochromatization of the electron beam for improvement of the spatial and spectral resolution. Recently, scanning-TEM (STEM) of atomically dispersed lanthanum atoms on alumina (63) has provided *ex situ* aberration-corrected images, but it is noteworthy that there is no technical limitation in applying the correction devices to instruments used for making measurements of samples in reactive environments.

Combining the improved spatial resolution with monochromatic electron sources may open up the possibility of obtaining spectroscopic characterization of single atoms. EELS data could provide the ability to probe the local electronic fine structure with atomic-scale resolution and thus establish links between the detailed electronic properties and local atomic geometry of a particular type of surface site. This point is important in light of recent advances in surface science, which show that low-coordinated metal surface sites, such as steps or corners, generally are associated with a higher activity than sites on metal facets and that the higher activity originates from the reduced metal coordination, resulting in stronger adsorption through a change in the metal valence *d*-electron properties, or from a characteristic local atomic geometry that is well-suited to bond-breaking or -formation processes (7).

Another advance in HRTEM will be the implementation of drift-compensation systems. Drift of the specimen in the heated sample holder hampers the HRTEM monitoring of rapid transient behavior of the catalyst during temperature variations and HRTEM imaging of specific catalyst areas over extended periods. Commercially available sample holders, even after modest temperature changes of about 10 K, typically require a period of 15 min before the specimen drift is leveled out to an extent that allows the catalyst structure to be imaged with atomic-scale resolution. The developments of more sensitive CCDs for recording images will also be an important improvement, as specific catalyst areas can be monitored over long periods without inducing beam damage.

A major challenge that remains is to link the structural insight provided by HRTEM to simultaneous measurements of the catalytic activity and selectivity at ambient pressures or higher. At the moment, this seems to be a daunting task, as the amount of catalyst used for TEM imaging is significantly smaller than the amount of heated material in contact with the gas within a microscope. One way to

accomplish higher-pressure investigations could be to integrate the differential pumping systems and the thin-window cell approach in such a way that the thin windows act as an extra set of differential pumping apertures to the extent that the high-pressure region is further confined around the catalyst specimen. Miniaturization of thin-window cells by use of advanced semiconductor preparation technology and careful selection of the construction materials in contact with the reactive gases may lead to the construction of microreactors allowing measurements of catalytic activity by mass spectrometric analysis of product gases concurrently with the HRTEM analysis of the catalyst structure at high temperature and pressures up to 1 bar (64,65). Such a device would allow the active structure and its catalytic properties to be scrutinized directly at the atomic level.

Acknowledgments

The authors gratefully acknowledge J. B. Wagner, T. W. Hansen, C. López-Cartes, J. Sehested, S. Dahl, C. H. J. Jacobsen, A. M. Molenbroek, H. Topsøe, B. S. Clausen, J. R. Rostrup-Nielsen, F. Abild-Pedersen, and J. K. Nørskov for contributions to the research included in the present article. We thank the China Technical Consultants Foundation, Taiwan, for financial support and the FEI Company for a fruitful collaboration on the development of the *in situ* HRTEM facility at Haldor Topsøe A/S.

References

1. Baker, R.T., *Catal. Rev.—Sci. Eng.* **19**, 161 (1979).
2. Boyes, E., and Gai, P.L., *Ultramicroscopy* **67**, 219 (1997).
3. Sharma, R., and Weiss, K., *Microsc. Res. Tech.* **42**, 270 (1998).
4. Hansen, P.L., Wagner, J.B., Helveg, S., Rostrup-Nielsen, J.R., Clausen, B.S., and Topsøe, H., *Science* **295**, 2053 (2002).
5. Zambelli, T., Wintterlin, J., Trost, J., and Ertl, G., *Science* **273**, 1688 (1996).
6. Dahl, S., Logadóttir, Á., Egeberg, R.C., Larsen, J.H., Chorkendorff, I., Törnqvist, E., and Nørskov, J.K., *Phys. Rev. Lett.* **83**, 1814 (1999).
7. Hammer, B., and Nørskov, J.K., *Adv. Catal.* **45**, 71 (2000).
8. Sharma, R., *Microsc. Microanal.* **7**(6), 494 (2001).
9. Thomas, J.M., and Gai, P.L., *Adv. Catal.* **48**, 174 (2004).
10. Datye, A.K., in "Handbook of Heterogeneous Catalysis" (G. Ertl, H. Knözinger, and J. Weitkamp, Eds.), Wiley-VCH, New York, p. 493–512, 1997.
11. Tang, D., Zandbergen, H., Jansen, J., Op de Beck, M., and Van Dyck, D., *Ultramicroscopy* **64**, 265 (1996).
12. Nellist, P., and Pennycook, S., *Phys. Rev. Lett.* **81**, 4156 (1998).
13. Thomas, P.J., and Midley, P.A., *Top. Catal.* **21**, 109 (2002).
14. Egerton, R.F., *Top. Catal.* **21**, 185 (2002).
15. Batson, P.E., *Ultramicroscopy* **59**, 63 (1995).
16. Browning, N.D., and Pennycook, S.J., *J. Microsc.* **180**, 230 (1995).
17. Brink, H.A., Barfels, M.M.G., Burgner, R.P., and Edwards, B.N., *Ultramicroscopy* **96**, 367 (2003).
18. Mitterbauer, C., Kothleitner, G., Grogger, W., Zandbergen, H., Freitag, B., Tiemeijer, P., and Hofer, F., *Ultramicroscopy* **96**, 469 (2003).

19. Sun, M., Kooyman, P.J., and Prins, R., *J. Catal.* **206**, 368 (2002).
20. Sehested, J., Carlson, A., Janssens, T.V.W., Hansen, P.L., and Datye, A.K., *J. Catal.* **197**, 200 (2001).
21. Shroff, M.D., Kalakkad, D.S., Köhler, S., Jackson, N.B., Sault, A.G., and Datye, A.K., *J. Catal.* **156**, 185 (1995).
22. Reimer, L., "Transmission Electron Microscopy." Springer, Berlin, 1993.
23. Butler, E.P., and Hale, K.F., "Dynamic Experiments in the Electron Microscope." pp. 239–308 North-Holland, Amsterdam, 1981.
24. Hashimoto, H., Naiki, T., Eto, T., and Fujiwara, K., *Jpn. J. Appl. Phys.* **7**, 946 (1968).
25. Baker, R.T., and Harris, P.S., *J. Phys. E Sci. Instrum.* **5**(8), 793 (1970).
26. Swann, P.R., and Tighe, N.J., *Proc. 5th Eur. Micros. Congr.* **I**, 306 (1972).
27. Doole, R.C., Parkinson, G., and Steed, J.M., *Inst. Phys. Conf. Ser.* **119**, 161 (1991).
28. Lee, T.C., Dewald, D., Eades, J., Robertson, I.M., and Birnbaum, H.K., *Rev. Sci. Instrum.* **62**, 1438 (1991).
29. Sharma, R., and Crozier, P., in "Handbook of Microscopy for Nanotechnology" (N. Yao, and Z.L. Wang, Eds.), Springer and Tsinghua University Press, Berlin, p. 531–565, 2005.
30. Heating Holder (PW6592) Obtained from the FEI Company (<http://www.feicompany.com>).
31. Daulton, T.L., Little, J.L., Kim, J.W., Newell, S., Lowe, K., Furukawa, Y., Jones-Mehan, J., and Lavoie, D.L., *JEOL News* **37**, E no. 1, 6 (2002).
32. Sao-Joao, S., Giorgio, S., Nietche, S., and Henry, C.R., *Proc. 13th Eur. Micros. Congr.* **II**, 101 (2004).
33. Jacobsen, C.J.H., Dahl, S., Hansen, P.L., Törnqvist, E., Jensen, L., Topsøe, H., Prip, D.V., Møenhau, P.B., and Chorkendorff, I., *J. Mol. Catal. A* **163**, 19 (2000).
34. Hansen, T.W., Hansen, P.L., Wagner, J.B., Dahl, S., Topsøe, H., and Jacobsen, C.H.J., *Science* **294**, 1508 (2001).
35. Logadóttir, Á., Rod, T.H., Nørskov, J.K., Hammer, B., Dahl, S., and Jacobsen, C.H.J., *J. Catal.* **197**, 229 (2001).
36. Mortensen, J.J., Hansen, L.B., Hammer, B., and Nørskov, J.K., *J. Catal.* **182**, 479 (1999).
37. Dahl, S., Logadóttir, Á., Jacobsen, C.H.J., and Nørskov, J.K., *Appl. Catal.* **222**, 19 (2001).
38. Honkala, K., Hellman, A., Remediakis, I.N., Logadóttir, Á., Carlsson, A., Dahl, S., Christensen, C.H., and Nørskov, J.K., *Science* **307**, 555 (2005).
39. Clausen, B.S., Schiøtz, J., Gråbæk, L., Ovesen, C.V., Jacobsen, K.W., Nørskov, J.K., and Topsøe, H., *Top. Catal.* **1**, 367 (1994).
40. Grunwaldt, J.-D., Molenbroek, A.M., Topsøe, N.-Y., Topsøe, H., and Clausen, B.S., *J. Catal.* **194**, 452 (2000).
41. Ovesen, C.V., Clausen, B.S., Schiøtz, J., Stoltze, P., Topsøe, H., and Nørskov, J.K., *J. Catal.* **168**, 133 (1997).
42. Wagner, J.B., Hansen, P.L., Molenbroek, A.M., Topsøe, H., Clausen, B.S., and Helveg, S., *J. Phys. Chem. B* **107**, 7753 (2003).
43. Topsøe, N.-Y., and Topsøe, H., *Top. Catal.* **8**, 267 (1999).
44. Campbell, C., *Surf. Sci. Rep.* **27**, 1 (1997).
45. Henry, C.R., *Surf. Sci. Rep.* **31**, 231 (1998).
46. Hansen, K., Worren, T., Stempel, S., Lægsgaard, E., Bäumer, M., Freund, H.-J., Besenbacher, F., and Stensgaard, I., *Phys. Rev. Lett.* **83**, 4120 (1999).
47. Koplitz, L.V., Dulub, O., and Diebold, U., *J. Phys. Chem. B* **107**, 10583 (2003).
48. Derouane, E., Baker, R.T.K., Dumesic, J.A., and Sherwood, R.D., *J. Catal.* **69**, 101 (1981).
49. Baker, R.T.K., Harris, P.S., and Thomas, R.B., *Surf. Sci.* **46**, 311 (1974).
50. Crozier, P.A., and Datye, A.K., *Stud. Surf. Sci. Catal.* **130**, 3119 (2000).
51. Sharma, R., and Iqbal, Z., *Appl. Phys. Lett.* **84**, 990 (2004).
52. Helveg, S., López-Cartes, C., Sehested, J., Hansen, P.L., Clausen, B.S., Rostrup-Nielsen, J.R., Abild-Pedersen, F., and Nørskov, J.K., *Nature* **427**, 426 (2004).
53. Rostrup-Nielsen, J.R., Sehested, J., and Nørskov, J.K., *Adv. Catal.* **47**, 65 (2002).
54. De Jong, K.P., and Geus, J.W., *Catal. Rev.—Sci. Eng.* **42**, 481 (2000).
55. Baker, R.T.K., Harris, P.S., Thomas, R.B., and Waite, R.J., *J. Catal.* **26**, 5 (1972).
56. Baker, R.T.K., Harris, P.S., Thomas, R.B., and Waite, R.J., *J. Catal.* **30**, 86 (1973).

57. Examples of HRTEM movies of the carbon nanofiber growth from Reference (52) can be found at <http://www.haldortopsoe.com/site.nsf/pages/nanotechnology>.
58. Bengaard, H.S., Nørskov, J.K., Sehested, J., Clausen, B.S., Nielsen, L.P., Molenbroek, A.M., and Rostrup-Nielsen, J.R., *J. Catal.* **209**, 365 (2002).
59. Trimm, D.L., *Catal. Rev.—Sci. Eng.* **16**, 155 (1977).
60. Alstrup, I., *J. Catal.* **109**, 241 (1988).
61. Rostrup-Nielsen, J.R., and Trimm, D.L., *J. Catal.* **48**, 155 (1977).
62. Jaeger, N.I., *Science* **294**, 1601 (2001).
63. Wang, S., Borisevich, A.Y., Rashkeev, S.N., Glazoff, M.V., Sohlberg, K., Pennycook, S.J., and Pantelides, S.T., *Nat. Mater.* **3**, 143 (2004).
64. Creemer, J.F., Sarro, P.M., Laros, M., Schellevis, H., Nathoeni, T., Steenweg, L., Svetchnikov, V., and Zandbergen, H.W., “Proceedings Semiconductor Advances for Future Electronics (SAFE)”, Veldhoven, The Netherlands, 2004, pp. 742–746.
65. Williamson, M.J., Tromp, R.M., Vereecken, P.M., Hull, R., and Ross, F.M., *Nat. Mater.* **2**, 532 (2003).

Model Catalyst Surfaces Investigated by Scanning Tunneling Microscopy

J.V. LAURITSEN and F. BESENBACHER

Interdisciplinary Nanoscience Center (iNANO), Department of Physics and Astronomy, University of Aarhus, DK-8000 Aarhus C, Denmark

Scanning tunneling microscopy (STM) has become established as a versatile technique for direct, real-space investigations and characterization of matter at the atomic level. Recent progress in STM studies of model systems relevant to heterogeneous catalysis has shown that it is possible to resolve fundamental issues related to catalytic processes by atomic-scale imaging of catalytically active surfaces and nanostructures. In this chapter, we briefly introduce the basics of the STM technique and the framework needed to understand the electronic and geometrical information contained in STM images. We highlight recent developments of the STM technique that will help further the elucidation of understanding of catalysts in the working state, and illustrate how the level of insight gained from characterizing model systems has advanced to a stage where the insight and ideas may lead to the design of new and improved high-surface-area catalysts.

Abbreviations: AFM, atomic force microscopy; CUS, coordinatively unsaturated site; DFT, density functional theory; E_a , activation energy; E_{ads} , adsorption energy; E_{H} , adsorption energy of H; ϵ_F , Fermi energy; EXAFS, extended X-ray absorption fine structure; fcc, face-centered cubic; hcp, hexagonal close packed; HDN, hydrodenitrogenation; HDS, hydrodesulfurization; I_t , tunneling current; LDOS, local density of states; $\rho_s(\epsilon_F, \vec{r}_0)$, local density of states at the Fermi level evaluated at a point \vec{r}_0 in the tip; \vec{r}_0 , center of the tip; STM, scanning tunneling microscopy; scanning tunneling microscope; UHV, ultra-high vacuum; V_t , tunneling bias; ϵ_s , energy of sample electronic states ψ_s ; κ , decay length of the electronic states from the sample; ψ_{tip} , wave function representing the STM tip; ψ_s , wave function representing the sample.

1. Introduction

Notwithstanding the great importance of catalysis in society and the fact that its application has expanded dramatically throughout the preceding century, the detailed principles governing catalyzed chemical reactions are in general far from established. This lack is a consequence of the immense complexity of catalyst structures and their dependence on external parameters (temperature, pressure, etc.). Fundamental understanding of catalytic processes requires the ability to characterize the structure and location of catalytically active sites at the single-molecule level. The active sites are the docking sites, which temporarily bind reactants, thereby offering an alternative and energetically favorable reaction pathway. The level of insight

needed to understand catalysis requires characterization of the catalyst and individual reactants with high spatial and temporal resolution.

To understand heterogeneous catalysis it is necessary to characterize the surface of the catalyst, where reactants bond and chemical transformations subsequently take place. The activity of a solid catalyst scales directly with the number of exposed active sites on the surface, and the activity is optimized by dispersing the active material as nanometer-sized particles onto highly porous supports with surface areas often in excess of $500 \text{ m}^2/\text{g}$. When the dimensions of the catalytic material become sufficiently small, the properties become size-dependent, and it is often insufficient to model a catalytically active material from its macroscopic properties. The structural complexity of the materials, combined with the high temperatures and pressures of catalysis, may limit the possibilities for detailed structural characterization of real catalysts.

Such limitations explain why current catalytic processes have been developed almost entirely through costly trial-and-error experimentation. In many respects, solid catalysts have been treated as black boxes, characterized only by their activity, selectivity, and stability. However, recent developments of new, improved catalyst characterization tools have made the investigation of the fundamentals of catalysis possible (1,2), and a detailed understanding has thus been obtained for some catalysts. The growing interest in advancing to more selective and energy-efficient catalytic processes has motivated researchers to pursue investigations of the fundamentals of catalysis (3). The ultimate goal of catalysis research is to achieve full understanding and control of the constituents at the molecular and atomic levels. With this ability, it may be possible to construct tailor-made, high-performance catalysts for even highly specialized reactions, with obvious benefits for the chemical industry and consumers of the countless products made in catalytic processes.

One approach to a detailed atomic-scale understanding of catalysts is to investigate well-characterized model systems under well-controlled conditions (2,4–10). Within this surface-science approach, the investigation of a catalyst is broken down into simplified components that can be dealt with in detail. The active catalyst particles have typically been represented by idealized flat single-crystal surfaces kept under well-controlled ultra-high vacuum (UHV) conditions at pressures of 10^{-10} mbar or less. This approach allows for a detailed characterization of the surface structures by application of a wide range of surface-science tools. Such fundamental and idealized investigations have provided valuable information about a number of catalytic reactions, with a prominent example being the synthesis of ammonia on an iron-containing catalyst (11–15).

Although surface scientists have thus come a long way in understanding the basic elementary steps of some catalytic reactions, large phenomenological gaps still separate the idealized surfaces under vacuum and complex catalysts operating at high temperatures and pressures; one refers to a pressure gap and a materials gap, respectively (16). Under the idealized conditions, the high-pressure situation is imitated by exposing surfaces to high incoming fluxes of molecules to facilitate high adsorbate coverages. For a few thoroughly investigated samples it was shown that it is legitimate to extrapolate results obtained under the rarefied UHV conditions to high pressures and temperatures (17–19)—that is, raising the pressure is often

equivalent to lowering the temperature as long as the thermodynamic equilibrium structure remains kinetically accessible. However, it is still not clear to what extent this statement may be of general validity.

The materials gap refers to the discrepancy between catalytically active clusters on supports and the corresponding model systems. A description based on investigations of single-crystal surfaces has often been shown to work very well, but only if the nanoclusters in the real catalyst expose the same facet as in the model and only if this facet is the catalytically active part of the cluster. In some cases (as in the hydrodesulfurization (HDS) catalysts referred to below), the properties of the catalytically active material in the form of nanoclusters are quite different from those of the bulk material, and geometric or electronic features in the microscopic clusters control the reactivity on the macroscale (20,21). A fully functional oxidation catalyst consisting of TiO₂-supported gold nanoclusters is a good example of how the properties of the materials may change as the dimensions are reduced, inasmuch as bulk gold is known to be noble and notoriously inert (22). To bridge the materials gap, efforts have recently been focused on the investigation of new and more realistic model systems, those consisting of particles on flat supports (21,23–29).

A number of techniques have been developed that provide detailed atomic-scale structural and chemical insight into both real and model catalysts in realistic environments (5,30). Investigations of these samples in reactive atmospheres have been made possible by major developments and refinement of the techniques used in X-ray absorption spectroscopy, X-ray diffraction, infrared and UV spectroscopy, and high-resolution electron spectroscopy (31–35). These techniques have provided valuable new insight, but they are in general averaging techniques, and information about individual particles is not obtained. Consequently, these techniques have limited applicability for analyzing complex model systems containing, for example, nanoclusters. This limitation makes the attempts to characterize and understand the active structures in catalysts a great challenge to researchers. Currently, only transmission electron microscopy (TEM) provides the means to resolve individual nanoclusters in real catalysts, even with atomic resolution and with samples in reactive gaseous atmospheres (36–38).

It is, however, generally impossible with these techniques to image adsorbates and single defects, which often turn out to be important in catalysis. Here we focus on an alternative approach involving investigations of model catalysts with the scanning tunneling microscope (STM). The STM technique is indispensable for exploring the atomic structure of matter. In the preceding two decades following the development of the STM (39–41), the technique has provided much information about the structures and electronic properties of surfaces, and because it also resolves individual signatures of adsorbed species, it has become a valuable tool for monitoring chemical reactions on surfaces (42–45).

The ability of the STM to achieve atom-resolved real-space images of localized regions of a surface and to directly resolve the local atomic-scale structure has provided essential insight into the active sites on catalysts and emphasized the importance of edges, kinks, atom vacancies, and other defects, which often are difficult to detect with other techniques (46–49). It is evident, however, that STM cannot be used to image real catalysts supported on high-surface-area, porous oxide carriers,

because STM requires flat and conductive samples. Nonetheless, STM has provided unprecedented new insight into model systems that, as shown below, has in some cases even triggered new ideas that have facilitated the development of new catalysts.

In this chapter we discuss how the STM may be applied in fundamental catalysis research. The examples are numerous, and it is beyond the scope of this review to present an exhaustive review of the field; several reviews have already appeared (50–52). Instead we mainly focus on three illustrative examples in which STM investigations have played an important role, not only for a better fundamental understanding of the geometrical and electronic structure of model catalysts, but also for the design and development of new and improved catalysts to operate under technologically relevant conditions. First, however, we summarize the working concepts of the STM.

II. Scanning Tunneling Microscopy

The fundamental principle of STM is conceptually simple. When an atomically sharp metal tip (typically tungsten) is brought into close proximity (3–5 Å) to a surface, electronic wave functions of the tip and surface start to overlap (Fig. 1c). This overlap enables electron exchange in the vacuum gap between the tip and surface—the phenomenon described in quantum physics as *tunneling*. If a small bias voltage (V_t) is applied across this tunnel junction, the Fermi levels of the tip and sample are shifted relative to each other, allowing for electrons to tunnel elastically from filled sample states into empty tip states (or *vice versa*, depending on V_t). This vacuum tunneling, lending its name to the microscope, thus establishes a small tunnel current (I_t) within the nano-ampere range.

In the usual mode of operation, the STM tip is raster-scanned across the surface at a fixed bias voltage with a piezo-scanner used to control the x – y – z motion of the tip (Fig. 1a). Because the tunnel current depends strongly (exponentially) on the distance z between the tip and surface, the individual atoms in the surface will give rise to current variations as the tip is scanned across the corrugated surface; that is, the tunneling current will increase (or decrease) as the separation (z) between the tip and sample decreases (or increases). In the so-called *constant-current* mode, the z position of the tip is allowed to vary to keep the tunnel current at a constant preset value, because this procedure generally gives a good sensitivity. As the tip sweeps over surface structures, a feedback circuit regulates the tip–sample z separation in such a manner that the tunneling current is kept at the constant preset value, and the z position of the tip (or in reality the feedback signal) is recorded, to produce a topographic map of the surface.

Alternatively, the STM may be operated in the *constant-height* mode, whereby the z -position is kept constant, and direct variations in the tunneling current are recorded as surface corrugation. Generally, constant-current operation yields better resolution, and the constant-height mode might be used for faster data acquisition.

The ability of the STM to achieve atomic resolution on the sample is explained in a simple manner by the strong exponential dependence of the tunnel current on the actual tip–sample separation z . One can estimate that a variation in tip–sample

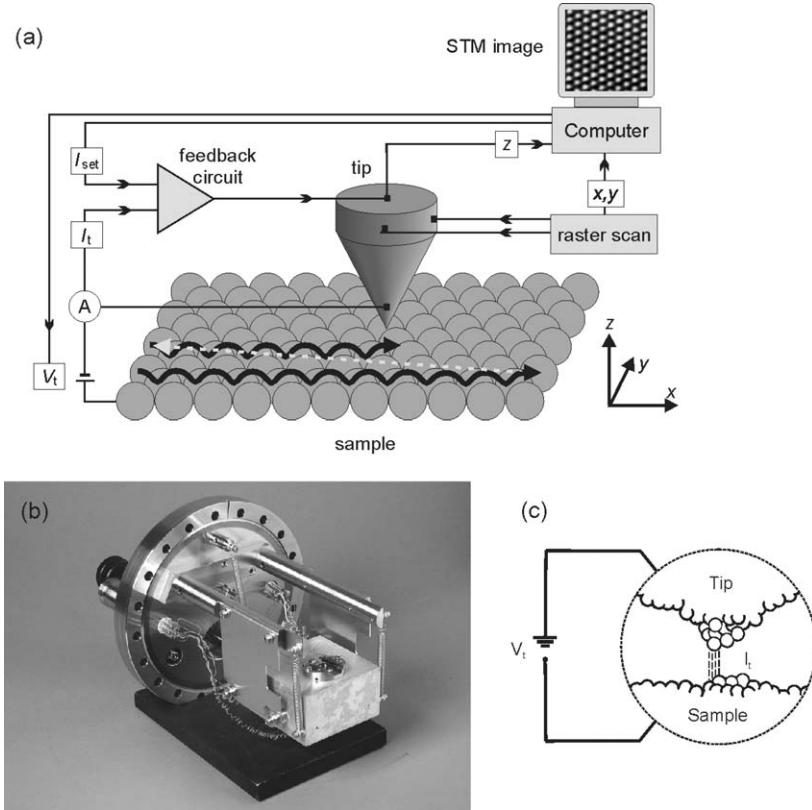


FIG. 1. (a) Basic operational principle of an STM. The tip is positioned in x - y - z space with atomic precision using piezo-ceramic elements (not shown). The tunnel bias (V_t) is measured on the sample relative to the tip, which is on virtual ground. While the tip raster-scans the surface, the tunnel current is recorded at a predefined number of points. The feedback controls the height of the tip above the surface (z) by comparing the measured tunneling current I_t to a preset value to ensure *constant-current* operation, and the position of the tip is recorded at every point to construct a map of the surface beneath the tip. (b) UHV-compatible STM microscope. (c) Schematic illustration of the tip-sample tunnel junction during STM operation. The tip (upper part) is lowered toward the sample to a distance less than 1 nm, and by application of a voltage, electrons can tunnel through the vacuum junction. The ability of the STM to achieve atomic resolution is explained by a strong z -dependence of the tunnel current, whereby essentially all the current flows to or from a single atom protruding from the tip.

distance of only 1 \AA results in an order of magnitude variation in the tunneling current. This means that essentially the entire tunnel current is localized in the junction between a single atom protruding from the tip and the sample, thereby making atomic resolution intuitively plausible (Fig. 1c).

A. STM DESIGN CONSIDERATIONS

Although the concept is simple, the actual realization of an STM apparatus is a major challenge. The mechanical design of an STM instrument has the inherent

complication that the tip-to-sample distance has to be stabilized on a picometer scale by construction elements with dimensions in the centimeter range (53,54). This mismatch of more than nine orders of magnitude is a major difficulty, because construction elements such as tip, scan unit, sample, sample holder, manipulator, and interconnecting base systems are affected by vibrations and thermal drift. The coarse mechanical positioning of the tip relative to the specimen—for example, bringing the tip from a distance of a millimeter to a distance of 10 \AA without “crashing” into the surface, is another major challenge in many STM designs.

Today, the technical difficulties have largely been overcome, and STM instruments that routinely provide atomic resolution on surfaces have been built (41,54–56). This capability has greatly facilitated the applications of the microscope in surface science, and recently the technique has been improved even further, allowing investigations of more complex samples such as model catalysts consisting of nanoclusters on flat single-crystal surfaces.

In most of the research summarized here, a homebuilt UHV-compatible Aarhus STM instrument (Fig. 1b) was used, which represents a successful solution to the problem of designing a stable high-resolution microscope (55). It features state-of-the-art atomic resolution, and the compact, rigid design with a high mechanical frequency also allows for high sampling frequencies (i.e., fast data acquisition that enables observation of dynamic processes on the surface) (57).

B. THEORY OF THE STM

In the early days of STM, most researchers were satisfied when it was possible to obtain nice images with atomic resolution of the nano-scale morphology of surfaces, with the STM providing unique information about geometrical features on the nanometer scale, such as atomic steps, kinks, and defects. Today, there is an increasing demand for extracting as much quantitative information as possible from STM images, and therefore it is important to understand that the contrast in atom-resolved STM images does not in general reflect the geometry of, for example, the adsorbed atoms on the surface, nor does it provide direct information about the chemical specificity of adsorbates. Because we are dealing with tunneling between the tip and the surface by conduction electrons energetically near the Fermi level, the atomic details obtained with STM are connected with the density of electronic states at the Fermi level, rather than the total electron charge density. Indeed, the following theoretical description of constant-current STM images shows that constant-current STM images represent contours of constant local density of states (LDOS) at the Fermi level projected to the tip apex. Consequently, STM images often reflect a rather complicated convolution of electronic and geometric features of the surface. Although this complexity may present some difficulties in the direct interpretation of STM images, the additional information gained about the electronic structure of the surface turns out to reveal further and essential insight in many cases. In this section, we briefly summarize some of the theoretical STM models that construct the framework needed to properly understand the information present in STM images and obtain new insights. The reader familiar with the tunneling theory of the STM may skip the next section without loss of generality.

B.1. Tersoff–Hamann STM Theory

The task of modeling the exact tunnel current in STM is huge as a consequence of the inherent difficulties that lie in a description of the exact geometry of the junction. A complete calculation of the tunneling current requires both knowledge of the electronic structure of the sample and of the STM tip, which generally is in some undefined state, chemically and structurally. Even if the characteristics of the sample and the tip were both known in exact detail, the problem of modeling the tunnel junction in a complete quantum mechanical description is quite intractable for this strongly correlated system, and one must resort to descriptions with various levels of approximations.

In the perturbative “transfer Hamiltonian” approach developed by Bardeen (58), the tip and sample are treated as two non-interacting subsystems. Instead of trying to solve the problem of the combined system, each separate component is described by its wave function, ψ_{tip} and ψ_s , respectively. The tunneling current is then calculated by considering the overlap of these in the tunnel junction. This approach has the advantage that the solutions can be found, for many practical systems, at least approximately, by solution of the stationary Schrödinger equation.

The purpose of doing STM is to learn about surface structures, and the tip as such is regarded as an uninteresting probe. In this sense, it is a problem that the electronic structure of the tip is contained in the formula for the tunnel current in the original work by Bardeen (58). Tersoff and Hamann (59,60), however, extended Bardeen’s formalism and showed by simple, yet relevant approximations that the impact of the unwanted electronic structure of the tip is in many cases less pronounced for typical tunneling parameters. Fortunately, the Tersoff–Hamann model provides a simple conceptual framework for interpreting STM images, and therefore it is still the most widely used model.

The difficulty of evaluating the effect on the tunneling current of the tip electronic structure was approached by Tersoff–Hamann by assuming a simple s -wave tip model with wave functions centered at a point \vec{r}_0 in the tip. In the limit of low-bias voltages, the total tunnel current can then be expressed as follows:

$$I_t \propto V_t \sum_s |\psi_s(\vec{r}_0)|^2 \delta(\epsilon_s - \epsilon_F) = V_t \rho_s(\epsilon_F, \vec{r}_0), \quad (1)$$

in which the sum extends over sample states (ψ_s) evaluated at \vec{r}_0 , and the delta function reflects that only states at the Fermi level contribute. The term on the right-hand side of Eq. (1) represents a quite tractable property of the surface, the so-called LDOS at the Fermi level, $\rho_s(\epsilon_F, \vec{r}_0)$ (i.e., the charge density from states at the Fermi level for the bare surface evaluated at the position \vec{r}_0 of the tip). Thus, the tunnel current scales to a first approximation only with this property of the surface, and low-bias constant-current STM images can then be considered a reflection of contours of constant surface LDOS.

The strength of the Tersoff–Hamann theory is that it provides a simple interpretation of the tunnel current in terms of a physical quantity, representing the surface alone. However, it also explains the exponential dependence of the tunneling bias on the tip–sample separation. All electronic states decay exponentially into

the vacuum, and because $|\psi_s(\vec{r}_0)|^2 \propto \exp(-2\kappa(z))$, where κ is the decay length of the electronic states, the tunnel current will, according to Eq. (1), have the same exponential behavior. For typical metals, $\kappa \sim 1 \text{ \AA}^{-1}$, and I_t will thus decrease by roughly an order of magnitude over a distance of only 1 \AA .

Features of the LDOS of a metal surface, measured at some distance from the surface, generally coincide with the total electron charge density, and the contours in STM images are therefore interpreted as simple topographic maps of the surface. When adsorbates are present on the surface, they alter the LDOS in the surrounding area and are in general found to be imaged either as protrusions or, counter-intuitively, as depressions with respect to the bare surface (Fig. 2). The contrast is decided by the way the adsorbates change the LDOS at the Fermi level; that is, if the LDOS is enhanced (or depleted), the tip moves away from (or closer to) the surface when the affected area is scanned (61).

Consequently, one cannot in general assume that maxima expected from the surface topography coincide with maxima observed in STM images. This effect becomes especially evident on semiconductor surfaces (e.g., those of MoS_2 or TiO_2), for several reasons. In contrast to metals, semiconductors show a very strong

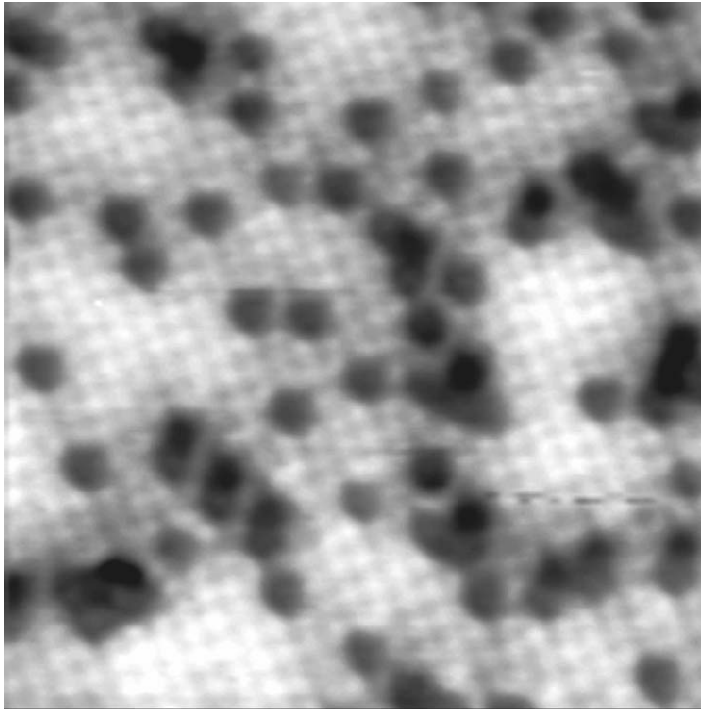


FIG. 2. STM image ($78 \text{ \AA} \times 76 \text{ \AA}$) of nitrogen atom adsorbates on an Fe(100) surface. Because the nitrogen adsorbates deplete the LDOS at the Fermi level, the nitrogen atoms are imaged as depressions in accord with the Tersoff–Hamann model. From the STM image it is concluded that nitrogen atoms adsorb in fourfold hollow sites on Fe(100). This is just one of many examples illustrating how the STM contrast may depend on the details of the LDOS around an adsorbate and produce a somewhat counter-intuitive picture. Adapted from Reference (65).

variation of the LDOS with bias voltage. In particular, this quantity changes discontinuously at the band edges. Adding to the complexity of the contrast in STM images, the electronic structure may also be dominated by spatially localized states or dangling bonds, which generally change the picture relative to what would be expected on geometric grounds.

Therefore, the interpretation of such structures should be performed carefully and preferably in combination with other experimental or theoretical techniques. Nevertheless, the large database of STM results, which in combination with other experimental and theoretical surface science investigations have solved many problems correctly, often rely on the Tersoff–Hamann interpretation (62–65). In this sense, the Tersoff–Hamann theory has proved itself very successful, but when applying it to STM characterizations of more complicated samples, one has to be aware of the limitations of the model. The sample wave functions may be distorted by the close proximity of the tip to the surface, and the forces between the tip and sample may lead to geometric relaxations of the atoms in the surface layer beneath the tip (66). Moreover, the tip is in this model represented by a simple s -wave, so that the chemical composition of the tip is neglected. In reality the nature of the tip may, however, differ significantly from this situation because of adsorbates or other contaminants present on the tip apex (53).

B.2. *Simulation of STM Images*

As mentioned above, the information contained in STM images pertains principally to the electronic structure of the surface, and (as for most types of microscopy) STM provides no direct insight into the chemical identities of structures. This lack of chemical specificity often makes it difficult to relate the observed structures of complex clusters, molecular adsorbates, or reaction intermediates to their chemical nature and conformation on the surface. Theoretical electronic-structure calculations are therefore commonly employed to assist in the interpretation of STM results. The theoretical calculations provide complementary information about the possible ground-state configurations of samples and can be used to generate fairly accurate simulations of STM images.

One of the major advantages of the Tersoff–Hamann theory is that simulated images can be generated directly from first-principles electronic-structure calculations. One approach to modeling the electronic structure of a sample involves the application of density functional theory (DFT), which has become a main theoretical technique employed for the elucidation of energetics, geometrical structures, and electronic structures related to surfaces and catalysis (67,68). From the output of a DFT calculation, it is a rather straightforward matter to extract the LDOS at the Fermi level of the sample, and constant-current STM images can be simulated by plotting contours projected at an appropriate distance from the surface. Such an approach makes no attempt to remedy the limitations of the inherent approximations of the Tersoff–Hamann theory, but it has nevertheless been found to be sufficiently detailed to account qualitatively for the experimental observations in most investigations.

For a more detailed and quantitative description of STM images, another class of methods has been developed, in which attempts are made to include tip effects in a more realistic way (69). These methods go beyond perturbation theory and include a proper description of the interacting sample and tip within a scattering-theory formalism. In one implementation, the tunneling process is considered to be a scattering process and the sample–tip junction is modeled by two semi-infinite bulk solids connected by a cluster of 1–15 atoms to model the tip apex (70,71). Tip effects and tip–sample interactions are thus included, and, specifically, the influence of imaging conditions such as tip structure or bias voltage dependence can be systematically varied. In some cases, the resulting STM simulations have allowed for extraction of quantitative structural information from experimental images. The price to pay for this more elaborate simulation scheme is the large computational expense associated with modeling the tunnel junction, and therefore the Tersoff–Hamann approach still dominates in the analysis of the majority of experimental STM images.

III. New Au/Ni Surface Alloy Catalyst for Steam Reforming

The following sections illustrate by three selected examples the capabilities of STM in catalyst characterization. The examples describe fundamental STM investigations of model catalysts and illustrate how we have reached a stage where it is possible to take the step from atomistic surface-science investigations of model systems to the design of new, high-surface-area catalysts. The jump to catalyst design is made possible by combining the detailed new fundamental atomic-scale insight gained from STM investigations with results from first-principles theoretical DFT calculations and investigations of real high-surface-area industrial catalysts. In this respect, the three examples illustrate that we are on the verge of moving from an era in heterogeneous catalysis research dominated by trial and error to one of rational nanoscale design.

In the first example we are dealing with the steam reforming process, whereby hydrocarbon molecules (mainly CH_4) and water are converted into synthesis gas (consisting principally of H_2 and CO). The usual catalyst for this reaction includes nickel as the active component (72). The main problem with the reaction is that nickel is highly active and also catalyzes the formation of graphite, which may lead to the growth of carbon filaments and subsequently to an accelerated deactivation and eventual complete breakdown of the catalyst (a process referred to as coking) (73,74). One solution to this problem has been to add minute amounts of H_2S to the reactants. The adsorbed sulfur acts as a poison of the nickel catalyst, which on the one hand inhibits the reforming process, but on the other, poisons the graphite formation even more. The overall result is a better selectivity, and thus a longer life cycle of the catalyst. This solution is, however, not ideal because sulfur is also a strong poison for most other transition-metal containing catalysts that are used downstream to catalyze the formation of products; the presence of sulfur in the reactant stream is therefore generally undesirable.

On the basis of fundamental STM investigations of flat single-crystal nickel surfaces, the idea originated to design a new catalyst incorporating gold/nickel alloy nanoparticles with improved reforming selectivity. It is known that alloys in some cases have catalytic properties superior to those of single metals (75), but typically the focus has been on the class of binary metal systems that form ordered or random bulk alloys. STM investigations, in combination with DFT calculations, showed that a new class of surface alloys exists for two-component metal systems that do not mix in the bulk but do form stable alloy-like structures in the outermost surface (76–78).

The gold/nickel system belongs to this category of surface alloys. STM investigations show that a surface alloy is formed when gold is deposited on a nickel(111) surface (or on any other low-index nickel surface); the gold atoms squeeze out surface nickel atoms and are subsequently substituted into nickel atom lattice positions, as depicted in the atom-resolved STM image of Fig. 3 (79). The gold atoms are imaged as depressions although they are substituted into the nickel(111) surface lattice. This is a result of the fact that we are imaging the LDOS, which is lower at the positions of the substituted gold atoms than on the adjacent nickel sites. Figure 3 was recorded after deposition of gold atoms at room temperature and annealing of the surface to 800 K. When gold is deposited at room temperature, the gold atoms preferentially nucleate as islands at the step edges, but after annealing to 800 K a random alloyed gold–nickel phase is formed, as shown in Fig. 3. In this case also the step edges of the nickel crystal are saturated with a thin brim of gold atoms in this phase.

An explanation of why a gold/nickel surface alloy is formed, whereas no bulk three-dimensional gold/nickel alloy exists (reflecting the fact that the heat of

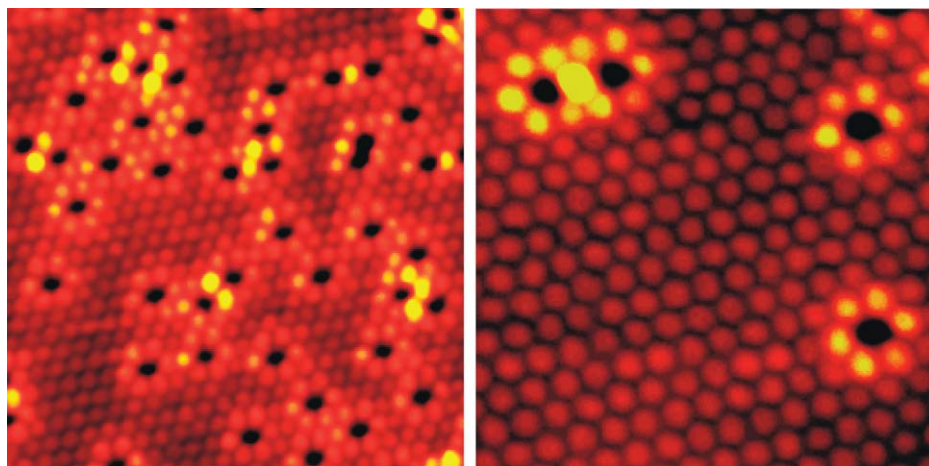


FIG. 3. Two STM images of the nickel(111) surface with 2% (right) and 7% (left) gold coverage, respectively. Au is imaged as dark depressions in the surface. The nickel atoms surrounding the gold appear brighter owing to a local modification of the electronic structure, indicating a changed chemical reactivity of these. Adapted from Reference (79).

formation of a solution of gold and nickel is large and positive, 27 kJ/mol) is as follows. The nickel atoms in the surface layer are under-coordinated relative to the nickel atoms in the bulk. The gold atoms have an electron density that is more extended than that of the nickel atoms, and when the gold atoms are alloyed into the surface layer, the neighboring nickel atoms experience a higher electron density or, equivalently, a higher effective coordination number. The gold atoms alloyed into the surface layer thus help to lower the nickel surface energy. This simple reasoning is confirmed by extended theoretical calculations (79).

The idea that the gold–nickel surface could have interesting catalytic properties for steam reforming originated from three fundamental findings:

- (a) It was observed directly from the high-resolution STM images that the gold atoms alloyed into the nickel surface layer perturb the electronic structure of the nearby nickel atoms, as all six nickel atoms next to the gold atoms substituted into the nickel surface layer were imaged brighter. DFT calculations showed that this observation cannot be explained by a geometrical outward relaxation; instead it reflects a higher LDOS at ϵ_F for the nickel atoms surrounding the gold. From the STM images it can furthermore be observed that when a nickel atom has two gold atoms as its nearest neighbors, it is imaged even brighter, corresponding to an even more perturbed electronic structure. Thus, the nickel surface layer consists basically of three different types of nickel atoms, namely, those which only have nickel neighbors, those which have one gold neighbor, and those which have two gold neighbors.
- (b) DFT calculations showed that these three different types of nickel atoms have different reactivities for activation of hydrocarbon molecules such as methane.
- (c) Both the DFT calculations (Fig. 4) and the STM investigations showed that the tendency of the surface to bind carbon and form graphite is strongly impeded by the presence of the substituted gold in the surface. Although the activation energy for methane dissociation is increased by the presence of surface alloyed gold, this effect is compensated by an even stronger tendency of the gold to impede the binding of carbon.

These findings led us to suggest that nanoclusters with a nickel–gold surface alloy may be a superior steam reforming catalyst and, thus, a high-surface-area MgAl_2O_4 supported nickel catalyst (with 16.5 wt% Ni), which was modified with 0.3 wt% Au, was synthesized (79). The structure and composition of the active catalyst were characterized by extended X-ray absorption fine structure (EXAFS) spectroscopy, and the results showed that the gold was indeed alloyed into the first layer of the nickel catalyst. The steam reforming activity of this catalyst was measured, and the results are shown in Fig. 5.

The only difference between the two samples is the gold modification of the nickel nanoclusters. In these investigations, *n*-butane was used to test the activity, because it is known to cause the most severe graphite formation problems. Whereas the pure nickel catalyst was deactivated rapidly as a result of the formation of graphite, as confirmed by electron microscopy, for example, it was found that the conversion catalyzed by the gold/nickel sample was maintained almost constant. This comparison is consistent with the inference that the novel gold/nickel catalyst did not

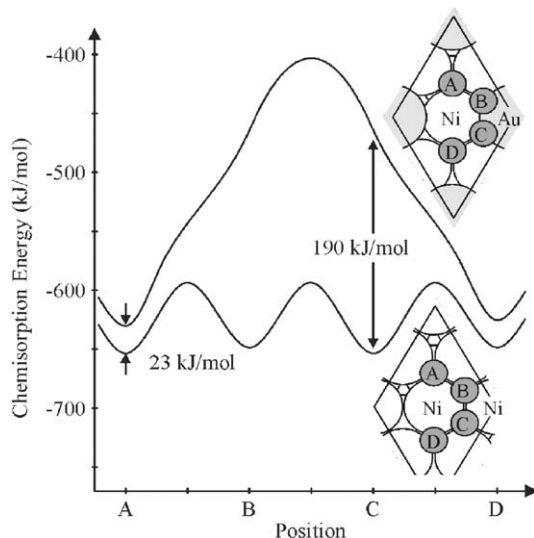


FIG. 4. Stability of carbon on different sites (A–D) on a pure nickel(111) surface (below) and a gold-alloyed nickel(111) surface (above). The probability of nucleation of graphite is determined by the stability of the adsorbed carbon atoms. The less stable the adsorbed carbon, the larger the tendency to react with adsorbed oxygen to form CO and the lower the coverage. On the pure nickel(111) surface, the most stable adsorption configuration of carbon is in the threefold (hcp) site (lower curve). The upper graph shows that carbon adsorption in threefold sites next to a gold atom is completely unstable (sites B and C), and even the threefold sites that are next-nearest neighbors (sites A and D) to the gold atoms are led to a substantial destabilization of the carbon. From Reference (79).

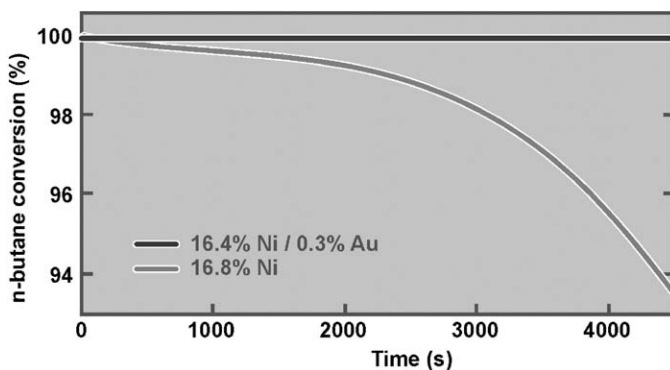


FIG. 5. Conversion of *n*-butane as a function of time-on-stream during steam reforming in a flow reactor. The gray curve shows the conversion of the pure nickel catalyst, and the black curve represents the gold/nickel catalyst. From Reference (79).

produce graphite under the catalytic reaction conditions, and the results therefore illustrate how fundamental insight into surface structure and reactivity has been applied to the design of a new steam reforming catalyst that operates under technologically relevant conditions.

IV. Designing New Nickel Catalysts by Step Blocking

It is rare that the entire surface area of a nanocluster is uniformly responsible for its catalytic activity. For many reactions the catalysis takes place on active sites that may occupy only a small fraction of the total surface, as was pointed out by Taylor (80). In the past, the catalytic importance of step edges as active sites has been investigated by comparing the reactivities of the planar and stepped surfaces, using averaging and integrating techniques (2,81). Recently, STM has provided unique new atomic-scale information by allowing identification of the active sites on metal surfaces, as demonstrated, for example, by the investigations of NO dissociation on Ru(0001) by Zambelli *et al.* (42). DFT calculations have also shown that the difference in reactivity between terrace sites and step edges can be immense, and it has been shown experimentally that the rate of N₂ dissociation is at least nine orders of magnitude greater at steps than on close-packed terraces on Ru(0001) (82). Similar effects have been predicted for a number of other diatomic molecules (83).

In Chapter 2 (Section VI. C) of this volume, Hansen *et al.* also discuss detailed TEM results that show how the steps of a supported nickel cluster play an important role as centers for carbon growth in a real supported catalyst (73).

Although the activity of a catalyst is often a distinguishing characteristic of a good catalyst, the selectivity is often more important. Only little information is available illustrating how the selectivity can be controlled by active sites such as step edges or kinks. In an investigation with STM and DFT used in combination, the initial steps of the decomposition of ethene on nickel(111) surfaces were characterized. The results provide information about the role of step edges in C–H and C–C bond breaking, reactions that take place in dehydrogenation and hydrogenolysis reactions of hydrocarbons.

Figure 6 is an STM image of a nickel(111) surface after exposure to ethene at room temperature. The ethene adsorption induces the formation of a rim along the step edges, with a significantly higher corrugation than that of the (111) facets of the clean nickel(111) surface. It was concluded that the formation of the rim was caused by ethene that had partly or fully decomposed at the step sites. As no rim was observed when the sample was exposed to ethene at low temperatures (<200 K), it was concluded that a significant activation barrier must be associated with the formation of carbon residues on the rim. The width of the ethene-induced rim structure did not increase when the exposure to ethene was increased significantly, from which it was concluded that the ethene decomposition process was self-poisoning (84).

These results were supplemented by DFT calculations of the activation barriers for the dissociation (C–H bond breaking) and dehydrogenation (C–H bond breaking) in ethene on both the flat nickel(111) and the stepped nickel(211) surfaces. It was found that the energies of the transition states both for the ethene dissociation and dehydrogenation on nickel(211) were lower by more than 50 kJ/mol than those of the most stable transition state on the flat nickel surface, consistent with the high reactivity of the step sites observed in the STM investigation. The DFT results comparing the step sites to terrace sites further showed that the reduction in the

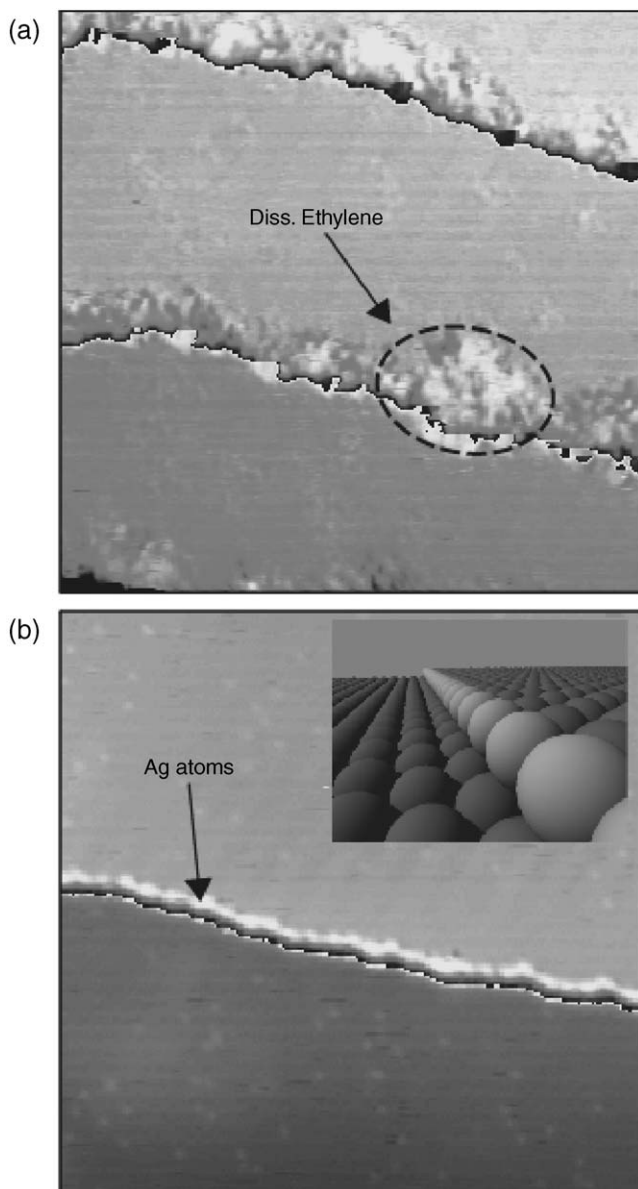


FIG. 6. (a) STM image ($200 \text{ \AA} \times 200 \text{ \AA}$) of a nickel (111) surface after exposure to ethene (1.3×10^{-11} bar; 100 s) at room temperature. (b) STM image ($400 \text{ \AA} \times 400 \text{ \AA}$) of a nickel(111) surface with the step edges blocked by silver atoms.

height of the activation barrier was much more pronounced for dissociation than for dehydrogenation, indicating that the selectivity of the nickel(111) surface for ethene dissociation vs. dehydrogenation is determined to a great extent by the ratio of the number of step sites to the number of terrace sites.

The selectivity of the nickel(1 1 1) surface may thus be controlled by modification of the number of free step sites, and this notion was tested experimentally by blocking the steps with small amounts of silver (84). In other STM investigations it was found that when silver was deposited on nickel(1 1 1) at room temperature, the silver preferentially nucleated and grew as islands at the step edges. When this system was post-annealed to 800 K, the silver atoms were observed to become highly mobile and decorate all the step edges of nickel(1 1 1), as shown in Fig. 6b.

To test the altered selectivity, this silver/nickel-modified surface was exposed to ethene at room temperature. When all the step edges were decorated with silver, STM showed no evidence of an ethene-induced brim structure, either at the step edges or at the terrace sites. This result clearly indicates that the step sites are indeed the active sites for the decomposition of ethene, and the experiments showed that addition of silver effectively blocks these sites and changes the overall selectivity of the stepped nickel(1 1 1) surface.

To bridge the gap from the fundamental investigations of model systems and exploit the new knowledge in the design of a real catalyst, a new oxide-supported silver/nickel catalyst was synthesized (84). The silver-doped catalyst was tested for hydrogenolysis of ethane, which is the simplest possible reaction to probe the activity for C–C bond breaking. The integral flow-reactor measurements performed on both a pure and a silver-modified nickel high-surface-area catalyst, depicted in Fig. 7, show that the addition of silver to the nickel catalyst led to a decrease in the rate constant for ethane hydrogenolysis by an order of magnitude. The fact that the apparent activation energy (the slope of the curves in Fig. 7) was the same for the nickel and silver–nickel catalysts indicates that the active sites on the two catalysts are the same. It was therefore concluded that the decrease in the rate constant was caused by silver atoms partly covering the nickel step edges. This example indicates that not only are step sites in general more reactive but the steps also control the selectivity for certain catalytic processes to a high degree. We thus have in hand a new route for nanoscale design of new, improved catalysts.

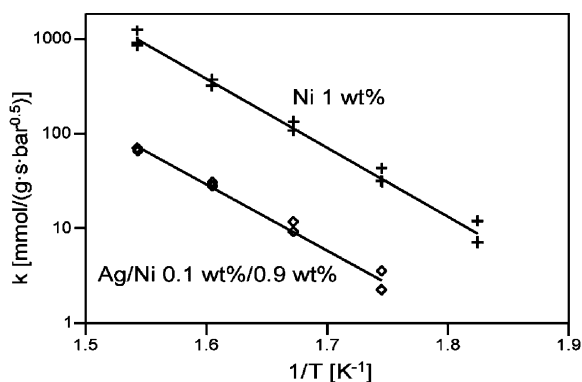


FIG. 7. Arrhenius plot of the rate constant for hydrogenolysis on nickel/ MgAl_2O_4 and silver/nickel/ MgAl_2O_4 . The rate constant (k) for ethane hydrogenolysis is one order of magnitude lower on the silver/nickel catalyst than on the nickel catalyst, and the activation energies (determined by the slopes of the Arrhenius plots) are similar for the two.

V. Investigations of an HDS Model Catalyst with STM

Hydrotreating catalysts are applied in a wide range of processes to upgrade petroleum fractions. Hydrotreating processes are reductive hydrogen treatments of compounds in petroleum, with the primary goal of removing the heteroatoms sulfur, nitrogen, and oxygen. Sulfur and nitrogen are removed to minimize the environmentally harmful SO_2 and NO_x , resulting from combustion of fuel. Furthermore, sulfur and nitrogen are removed because compounds of these elements are harmful to the performance of transition-metal containing catalysts used in downstream treatment of the petroleum fractions.

Hydrotreating catalysts provide an excellent example of the improvement of technological catalysts that has resulted from the application of new and better catalyst characterization tools. The traditional catalyst characterization techniques (2,5) that have made these advances possible seem now, however, to be reaching a limit in the understanding that they can provide. Nonetheless, severe legislation is forcing refiners to further upgrade and purify petroleum fuels, requiring further improved catalysts. In particular, the removal of sulfur by the HDS process is the subject of increasing attention, as new legislation in the EU and the USA has imposed severe limits on the sulfur impurity concentrations in transportation fuels. According to the new specifications for diesel fuel, the amount of sulfur must be reduced from 350 to less than 50 ppm by 2005 (85–87). The aim of deep HDS for the next decade is to reduce the sulfur content of diesel fuels to less than 10 ppm.

To meet the continuing research needs, researchers in surface science have taken up the challenge of understanding the fundamentals of operation of hydrotreating catalysts on the atomic scale, using all the available experimental and theoretical techniques. The challenge is great because the catalysts are complex in composition and structure. In previous investigations, important aspects of morphology, atomic-scale structure, and positions of active sites have been addressed only indirectly, limited by the lack of appropriate characterization tools.

A. HYDROTREATING CATALYST STRUCTURE AND REACTIVITY

HDS catalysts have been characterized extensively with a wide variety of tools, and several extensive reviews of the subject have been presented (85,88–91). Substantial effort has been aimed at relating catalytic activity and selectivity to microscopic properties such as catalyst composition, electronic structure, and geometric structure. EXAFS investigations of working catalysts have provided information about the composition, average local coordination, and interatomic distances of atoms in the catalyst clusters. It has been concluded that the active phase under operating conditions is MoS_2 -like particles with a dimension of 10–20 Å (92–94).

Notwithstanding the impressive number of investigations of HDS catalysts, many fundamental questions remain unanswered, and most of them are obviously related to the fact that traditional spectroscopic techniques are not capable of unequivocally mapping the real-space atomic structure. For instance, what is the preferential shape of the MoS_2 crystallites? The basal planes of the MoS_2 slabs are chemically inert, and it is therefore clear that the HDS activity is associated with the

edges terminating the clusters (85,95,96). Because the morphology of the clusters ultimately determines the nature of the exposed edges, the shape is an important characteristic of the clusters.

MoS₂ has a layer structure consisting of S–Mo–S slabs held together by weak van der Waals forces. The unit cell of the MoS₂ structure is illustrated in Fig. 8a. Each slab consists of a tri-layer with two close-packed hexagonal (0001) planes of sulfur atoms and an intermediate hexagonal plane of molybdenum atoms, which are coordinated in a trigonal prismatic fashion to the six surrounding sulfur atoms. In the catalyst, the MoS₂ crystallites exist as slabs with dimensions parallel to the (0001) basal plane that are relatively large in comparison with the height of the crystallites perpendicular to the basal plane. A ball model of a hypothetical, hexagonal, single-layer cluster with the stoichiometry of MoS₂ is depicted in Fig. 9. The hexagon is terminated by the two different, low-index edge terminations of MoS₂, the (10 $\bar{1}$ 0) Mo edge, and the ($\bar{1}$ 010) S edge. The actual shape of the single-layer MoS₂ cluster is in principle governed by the relative stabilities of these two different low-index edge terminations. Depending on the exact edge free energies of the molybdenum and sulfur edges, single-layer clusters can thus adopt various shapes—as hexagons if the edges are of equal stability, as truncated structures with the most stable edge termination dominating, or as triangles terminated exclusively by one type of edge. The distribution of the various facets within the MoS₂ clusters can be addressed directly by STM.

Earlier investigations led to the suggestion that the active sites are located at the edges of the MoS₂ clusters (97,98), but the question remains, what are the detailed atomic-scale structures of the edges? And what are the active sites, and just where on the edges are they located? Often the edge structure has been modeled on the basis of the bulk structure of MoS₂ (Fig. 9). However, as of the coordination of the

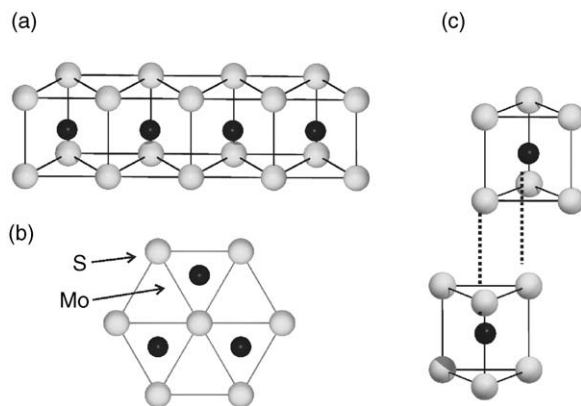


FIG. 8. Crystal structure of MoS₂. (a) Side view of a single-layer S–Mo–S slab of MoS₂. The molybdenum atoms (dark) are coordinated to six sulfur atoms (bright) in a trigonal prismatic coordination. (b) Within each layer, the sulfur lattice (and the molybdenum lattice) are hexagonally arranged with in-plane interatomic distances d_{S-S} or d_{Mo-Mo} equal to 3.15 Å. (c) Illustration of the 2H-MoS₂ stacking sequence of successive layers in bulk MoS₂. The distance between the molybdenum layers is 6.15 Å.

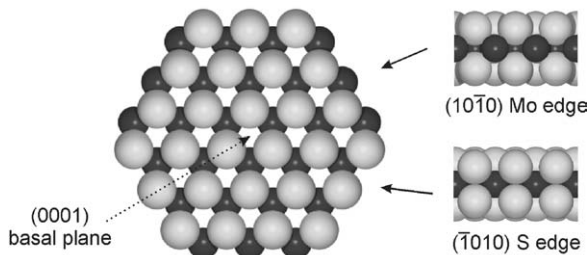


FIG. 9. Ball model of a hexagonal MoS_2 cluster, obtained from a simple truncation of a bulk $\text{MoS}_2(0001)$ slab. Left: The cluster is oriented with the (0001) basal plane in parallel with the paper, and it exposes the two different fundamental low-index edge terminations, the $(10\bar{1}0)$ molybdenum edge and the $(\bar{1}010)$ sulfur edge. Right: Side view of the edges. The molybdenum atoms (dark) are coordinated to six sulfur atoms (bright) at the sulfur edge, whereas at the molybdenum edge the coordination to sulfur is only four.

edge atoms does not match that of the bulk, reconstructions of the edges are likely. Obviously, a detailed understanding of the edge structure is essential, and only local probes such as the STM can provide it.

According to a simple model, sulfur vacancies created at the edges of the clusters are considered to be the active sites for HDS (99–101). Evidently, such coordinatively unsaturated sites (CUS) will be prone to interact strongly with sulfur atoms in organic molecules. The vacancies are thought to be created by a reaction with hydrogen, which strips off sulfur from the edges. Although the number of vacancies at edge sites (or corner sites) has been considered to be a key measure of the catalytic activity in many investigations, it is noteworthy that the exact nature of such sites is far from established. In particular, the structural configuration of the vacancy is debated (i.e., do vacancies form preferentially on the molybdenum or on the sulfur edges of MoS_2 , or do they perhaps even form on both?). Similarly, the adsorption modes of sulfur-bearing molecules on the catalytic clusters are controversial, and the literature contains a number of suggestions for the mechanisms and sites governing the adsorption of typical molecules found in petroleum.

B. HDS MODEL CATALYST

To address the unresolved issues related to the HDS catalyst, a number of model studies have been performed with single-crystal surfaces under well-defined vacuum conditions (e.g., with $\text{MoS}_2(0001)$ (95,102–104), $\text{Mo}(110)$ (105–108), and $\text{Mo}(100)$ (109–111)). Although substantial understanding can be derived from such investigations, they have not provided a major breakthrough in the microscopic understanding of hydrotreating catalysts. It is especially difficult to relate the information determined in single-crystal investigations to the real catalysts because the reactivity is exclusively associated with sites on the edges of single-layer MoS_2 -like nanoclusters. Therefore, we investigated a new type of HDS model catalyst, consisting of single-layer MoS_2 nanoclusters grown on a gold substrate.

B.1. HDS Model Catalyst: MoS₂ Nanoclusters Supported on Au (111)

Alumina supports are preferred for industrial HDS catalysts. Because alumina is an electrically insulating material, it does not permit tunneling of the electrons necessary for STM imaging, and the high band gap of this material thus excludes its use as a carrier in model investigations. Instead, a Au(111) single crystal was chosen, because it is relatively inert and allows for investigation of the intrinsic properties of MoS₂ nanoclusters supported on it. Furthermore, gold belongs to the class of metals having surfaces that reconstruct in the clean state (112,113). The clean Au(111) surface reconstructs into the characteristic herringbone form (114), which provides an ideal, regular array of nucleation sites for epitaxial growth of highly dispersed metal islands (115). The reconstruction is characterized by a $22 \times \sqrt{3}$ unit cell, in which the gold atoms in the topmost surface layer are compressed gradually by approximately 4.5% along the $[1\bar{1}0]$ direction. As a consequence of this contraction, 23 surface gold atoms are distributed among 22 bulk sites in the unit cell, resulting in alternating fcc and hcp stacking regions, which run in a parallel fashion along the $[1\ 1\bar{2}]$ direction. Brighter dislocation lines of gold atoms located near bridge positions separate the fcc and hcp areas, as shown in the STM image of Fig. 10. Long-range elastic interactions introduce domain boundaries, approximately every 140 Å. At these boundary lines, the domains bend by alternating $\pm 120^\circ$, and a zigzag pattern often referred to as the herringbone reconstruction forms. At the domain walls, two types of elbows are observed, a pinched and a bulged elbow. The latter, which is associated with a surface dislocation, acts as the preferential nucleation site for the epitaxial growth of a number of different metals or molecules (116,117). The surface thus provides a periodic network of nucleation sites.

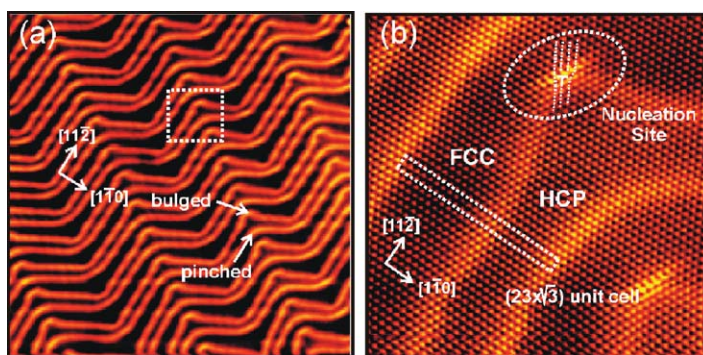


FIG. 10. STM images of the Au(111) surface. (a) A large-scale STM image of the Au(111) herringbone surface reconstruction ($802 \text{ \AA} \times 795 \text{ \AA}$). The bulged and the pinched elbow sites are indicated together with the directions of the crystal. (b) The surface imaged with atomic resolution, $141 \text{ \AA} \times 135 \text{ \AA}$. The surface is characterized by a $22 \times \sqrt{3}$ unit cell (indicated with a rectangle), in which the positions of the topmost gold atoms are gradually shifted from fcc to hcp sites. The bright lines reflect gold atoms in bridge sites in the transition region, which have a corrugation of 0.2 \AA . The bulged elbows (white circles) are associated with a surface dislocation (indicated with the symbol \perp), which is the preferential nucleation site of a wide range of metals, including molybdenum and cobalt.

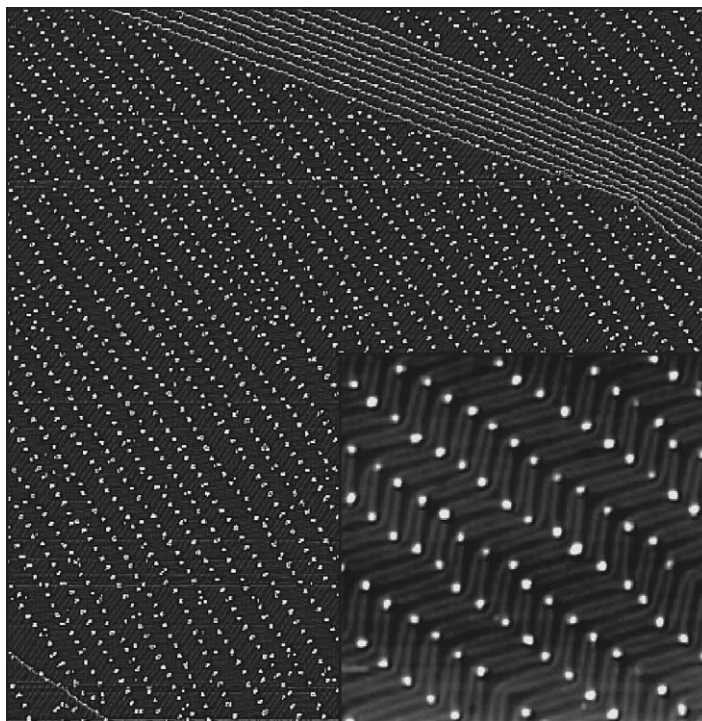


FIG. 11. STM images $4035 \text{ \AA} \times 4090 \text{ \AA}$ of molybdenum deposited on the Au(111) surface at room temperature and under UHV conditions. The inset ($890 \text{ \AA} \times 920 \text{ \AA}$) shows the location in the bulged elbows of the herringbone reconstruction of 20-\AA wide molybdenum nanoclusters.

In this investigation, the herringbone reconstruction was used as a template to disperse, in a parallel fashion, deposited metals (molybdenum or cobalt) into nanoclusters of similar size and with a well-defined nanometer separation (*118,119*). Figure 11 shows STM images of molybdenum deposited at a sub-monolayer coverage on the Au(111) surface. Indeed, molybdenum is observed to belong to the category of metals that nucleate in a regular fashion at the herringbone elbows. The deposited molybdenum self-organizes into equally sized 20-\AA wide nanoclusters dispersed over the entire surface. For the subsequent synthesis of MoS_2 nanoclusters, the high degree of dispersion and narrow particle size distribution constitute a favorable situation, because they enable direct access of gaseous H_2S and ensure a homogeneous sulfidation of the clusters during crystallization.

B.2. Preparation of MoS_2 Nanoclusters

Several approaches were investigated for the synthesis of the model catalyst, and the procedure resulting in the most homogeneous sample in terms of cluster size and morphology can essentially be divided into two steps: Initially, metallic molybdenum is deposited on a single-crystal Au(111) substrate in an atmosphere of H_2S at

a pressure of 1×10^{-6} mbar. Thus, the template effect of the reconstructed Au(111) is exploited to synthesize partially sulfided molybdenum nanoclusters with a high dispersion on the surface. STM images recorded at this stage show that the clusters form preferentially in the herringbone elbows as in Fig. 11, although they appear more irregular (i.e., the clusters seem to be in an amorphous state of sulfided molybdenum). Next, the substrate was annealed to 673–723 K for 15 min while the flux of H_2S was maintained to form the clusters. This procedure transformed the majority of the clusters into crystalline MoS_2 nanoclusters (Fig. 12).

The morphology of the structures was characterized in detail by STM. Analysis of images such as the one in Fig. 12 shows that the morphology of the nanoclusters is remarkably homogeneous with respect to both size and shape. Of the synthesized structures, the majority ($> 95\%$) are characterized as crystalline MoS_2 clusters. The remaining ones are either amorphous structures, resulting from incomplete sulfidation, or clusters too small to be characterized. Of the crystalline structures, the predominant shape is the triangle, and triangles constitute 93.7% of the total. The remaining clusters also reflect the hexagonal symmetry of MoS_2 , but they have shapes of rhomboids, trapezoids, pentagons, hexagons, or structures resulting from the merge of these simpler forms. Thus, under the sulfiding conditions applied, the triangular structure of MoS_2 clusters is strongly favored.

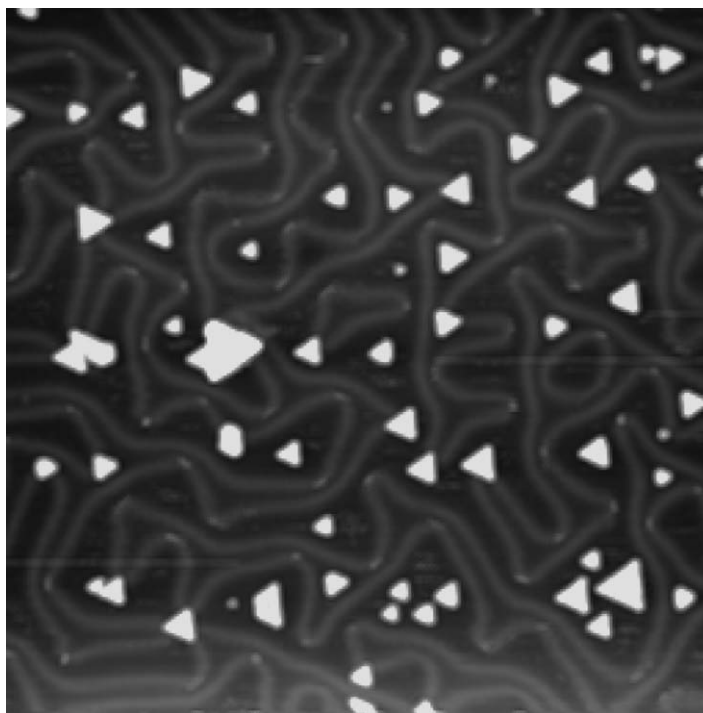


FIG. 12. STM image of MoS_2 nanoclusters synthesized on a Au(111) surface at 673 K in a sulfiding atmosphere. The size is $744 \text{ \AA} \times 721 \text{ \AA}$. Reprinted with permission from Reference (118). Copyright (2000) by the American Physical Society.

The clusters are also very similar to each other in size, with an average area of 500 \AA^2 . This area corresponds to a side length of a triangle of approximately 30 \AA , which corresponds well to the dimensions of the active clusters in typical HDS catalysts. As a model system for the HDS catalyst, the clusters are therefore a well-characterized reference for further experiments to elucidate details of the structure of the active edges and the reactivity with adsorbed molecules.

C. ATOMIC-SCALE STRUCTURE OF MoS_2 NANOCCLUSERS

C.1. *Fundamental Characterization*

An atomically resolved STM image of a triangular MoS_2 nanocluster is illustrated in Fig. 13. The cluster incorporates a plane of hexagonally arranged protrusions with an average interatomic distance of $3.15 \pm 0.05 \text{ \AA}$. This distance matches exactly the value found for the lattice on the basal plane of $\text{MoS}_2(0001)$ (120).

As discussed in Section II, STM images generally represent a rather complicated convolution of both electronic and geometric structures on the surface. This is especially true for oxides or sulfides such as MoS_2 , which generally exhibit a band gap. In light of this fact, it cannot *a priori* be determined whether the hexagonally

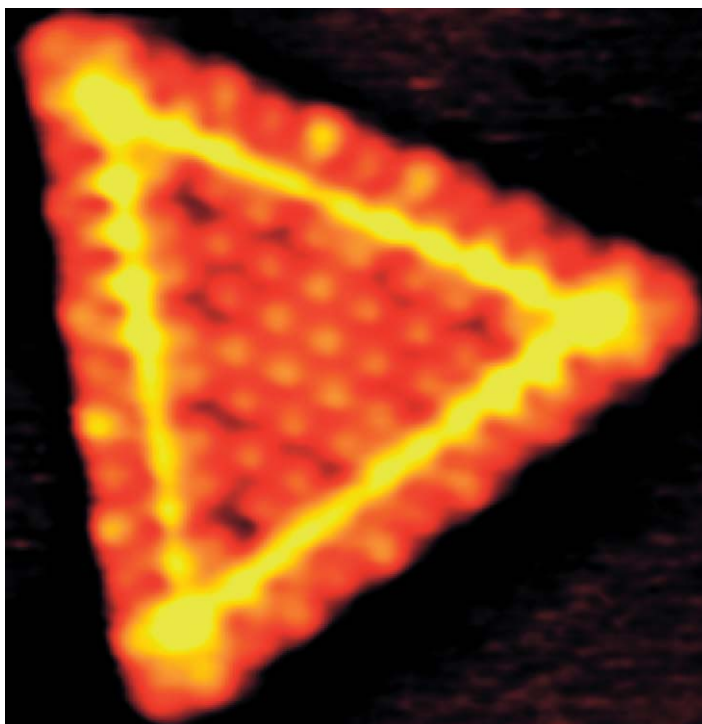


FIG. 13. Atomically resolved STM image ($V_t = 5.2 \text{ mV}$, $I_t = 1.28 \text{ nA}$) of a triangular single-layer MoS_2 nanocluster on $\text{Au}(111)$. The size of the image is $41 \text{ \AA} \times 42 \text{ \AA}$. Reprinted with permission from Reference (118). Copyright (2000) by the American Physical Society.

arranged protrusions on the basal plane of MoS₂ reflect either the sulfur atoms in the surface layer or molybdenum atoms in the second layer (Fig. 8), because the lattices of sulfur and molybdenum atoms are identical. However, it was shown elsewhere (121,122) by means of detailed STM simulations that the lattice of protrusions on the MoS₂ basal plane can be attributed to the topmost layers of sulfur atoms in the clusters in low-bias STM images. This inference is also in accord with previous theoretical investigations of layered MoS₂ slabs (123,124). The hexagonal arrangement of protrusions on the basal plane of the clusters does not change in STM images and as a result of changes in the tunneling parameters, the triangular-shaped islands are thus interpreted as MoS₂ nanocrystals with their (0001) basal planes oriented parallel to the gold substrate, with the protrusions reflecting the hexagonally arranged sulfur atoms in the topmost layer.

The cluster height and stacking were determined from STM line scans performed across the clusters. In STM images, the cluster height exhibits a slight variation as a function of the exact tunneling voltage, but it increases asymptotically toward values near 3.0 Å under the highest stable tunneling conditions, and this distance is close to the geometrical distance of 3.16 Å between sulfur nuclei in the top and bottom sulfur layer in a single layer of MoS₂, and it is therefore concluded that the clusters are present as MoS₂ single-layer slabs.

C.2. Morphology and Edge Structure

The predominant triangular shape of the single-layer MoS₂ islands implies that only one of the two low-indexed edges is present in the equilibrium structures. As is evident from a detailed analysis of the edge structures, all of the triangles are terminated by the same type of edge, which further implies that one of the two types of edge termination (the (10 $\bar{1}$ 0) molybdenum edge or the ($\bar{1}$ 010) sulfur edge) must be far more stable than the other.

The identity of the edges that terminate the triangular MoS₂ clusters was addressed in work with atom-resolved STM images of the clusters. In Fig. 14 a single-layer MoS₂ nanocluster is displayed with a grid superimposed on the positions of the basal-plane sulfur atoms. At the edges, the protrusions are imaged out of registry with the basal plane sulfur atoms. Indeed, the protrusions are shifted half a lattice constant along the edge but they retain their interatomic distance of 3.15 Å. This is a feature of the edges that is representative of all the investigated single-layer MoS₂ triangles.

The question of which type of edge terminates the triangular MoS₂ clusters is complicated by the fact that under the sulfiding conditions of the experiment, the edges may not be simple terminations of the stoichiometric MoS₂, as depicted in Fig. 9a. In the hypothetical bulk-truncated MoS₂ hexagon, sulfur edges are terminated by a row of sulfur atoms positioned at bridge positions close to the bulk-terminated case, and every molybdenum atom retains the bulk coordination to six sulfur atoms. The molybdenum edges, on the other hand, are terminated by a row of fourfold coordinated molybdenum cations (Fig. 15a) (i.e., they are undercoordinated with respect to bulk MoS₂).

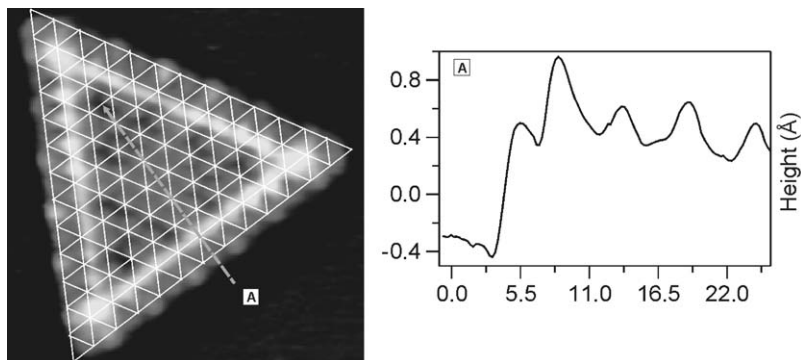


FIG. 14. A grid superimposed on the basal plane of a triangular single-layer MoS_2 nanocluster. The intersections of the white lines indicate the sulfur atomic positions on the basal plane. At the edges, the protrusions are observed to be shifted out of registry with the basal plane lattice. An STM line scan across the bright brim of the single-layer MoS_2 nanocluster is illustrated on the right. The arrow indicates the direction and position of the scan in the image.

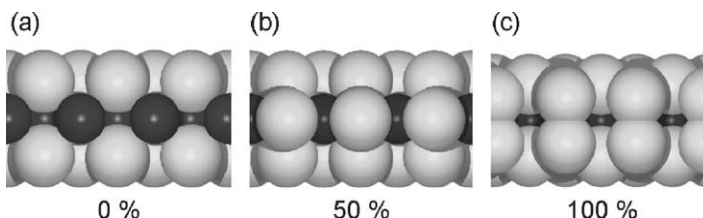


FIG. 15. Side view of ball models of the molybdenum edge of MoS_2 with various coverages (0, 50, and 100%). (a) Molybdenum edge exposing a row of under-coordinated molybdenum atoms (dark). Under sulfiding conditions, the most stable structures are saturated with sulfur atoms (light) adsorbed on the edge. This occurs in two configurations that have almost equal stability, but with different total coverages of sulfur. (b) Molybdenum edge with sulfur monomers, corresponding to a coverage of 50%. (c) Molybdenum edge with sulfur dimers, with 100% coverage. In both configurations (b) and (c) the edge molybdenum atoms keep the coordination to six sulfur atoms, but structurally the edges are reconstructed relative to the bulk configuration.

DFT calculations have shown that under sulfiding conditions, sulfur will adsorb in two almost equally stable configurations (125–127), in which either one or two sulfur atoms adsorb per molybdenum edge atom. In both cases, the molybdenum atoms achieve a sixfold coordination to sulfur, as in the bulk, but, as illustrated in the ball models of Fig. 15, significant reconstructions occur. When only one sulfur atom is adsorbed per molybdenum atom on the edge (configuration b), the position of the sulfur monomer is shifted relative to the bulk position, and it moves down to a bridging position in-plane with the molybdenum lattice. When the molybdenum edge is fully covered (Fig. 15c), the sulfur atoms keep their lateral positions along the edge, but in the direction perpendicular to the edge there is a tendency for the sulfur atoms to contract and form S–S dimers (128).

An intuitively simple way of interpreting the edge structure in the STM image of the single-layer MoS₂ nanoclusters would be to assign it to the reconstructed monomer molybdenum edge (Fig. 15b), because geometrically this seems to be consistent with the observed shift of half a lattice constant in the STM image. However, this purely geometrical model is valid only if the protrusions at the edges directly reflect the positions of sulfur atoms, and it does not account for several other edge features in the STM images. Specifically, a pronounced bright brim of high electron state density extends all the way around the cluster edge adjacent to the edge protrusions (Fig. 13). A line scan across the cluster edge (Fig. 14b) shows the bright brim imaged with an intensity corresponding to an increase of approximately 0.4 Å above the basal plane. In atom-resolved images, this value is independent of the bias voltage. Rather than a geometrical effect, this is attributed to an electronic effect probed by the STM, reflecting subtle changes at the edges (i.e., the existence of localized electron states at the cluster perimeter, so-called *edge states*). A line scan parallel to and directly on top of the bright brim reveals no systematic corrugations in this direction. This result suggests that electrons are localized strongly within one-dimensional edge states perpendicular to the MoS₂ edges—but delocalized along the direction of the edges.

The electronic structure of the clusters is important, because bulk MoS₂, consisting of infinite sheets of S–Mo–S, is semiconducting and displays a band gap of approximately 1.2 eV (129). The absence of electronic states available for tunneling in bulk MoS₂ thus implies that the clusters should be impossible to image at bias voltages less than half the value of the band gap. However, STM images of the MoS₂ clusters obtained by tunneling at low-bias voltages ($V_t = 5.2$ mV in Fig. 13) are clearly possible, and this again suggests that the electronic structure of the clusters is perturbed relative to bulk MoS₂.

DFT calculations by Bollinger *et al.* (121,122) show that electronic structure near step edges of MoS₂ is indeed significantly perturbed relative to that of the bulk, and they show that the triangular MoS₂ nanoclusters observed with STM have two types of metallic edge state. In Fig. 16b, the band structure (full lines) is shown for a MoS₂ slab terminated by the fully saturated sulfur edge and the molybdenum edge covered with sulfur dimers (Fig. 15c). Three bands protrude into the semiconducting gap of MoS₂ and cross the Fermi level. This observation implies the existence of three electronic edge states with metallic properties, labeled I, II, and III. The corresponding Kohn-Sham wave functions (Fig. 16b) show that the metallic edge states I and II are localized entirely on the molybdenum edge with sulfur dimers, whereas edge state III is associated with the fully covered sulfur edge (not shown).

An STM simulation based on the Tersoff–Hamann model (i.e., a contour map of constant-surface LDOS) shows that both the bright brim and the apparent shifted registry of the edge protrusions can be traced back to the existence of the two edge states (I and II) on the fully sulfided molybdenum edges. Edge state I has a Fermi wave vector of $k_F \approx 0.39 \text{ \AA}^{-1}$, and it is seen almost completely localized at the sulfur dimers (Fig. 16b); it is a superposition of p_x orbitals, extending in two parallel chains along the edge. Edge state II extends over the first three rows, having $k_F \approx 0.67 \text{ \AA}^{-1}$.

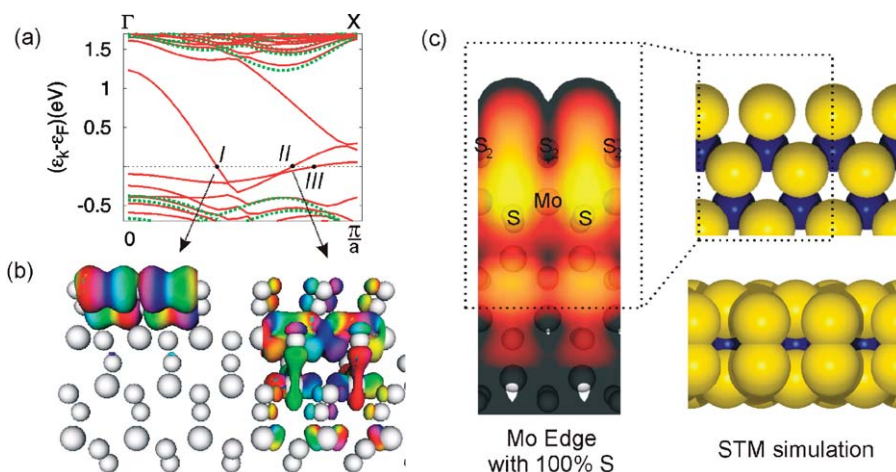


FIG. 16. (a) Energy bands associated with the MoS_2 slab exposing the sulfur edge and the molybdenum edge (full lines), and the corresponding plots for an infinite MoS_2 layer of the same size (dotted lines). The band gap of approximately 1.2 eV for the infinite layer is clearly outlined. The edge-terminated system was calculated with a 100% sulfur coverage on both edges, and by inspection of the energy bands in the band diagram, three bands pertaining to electronic edge states (denoted as I, II, and III) are seen to cross the Fermi level. (b) Edge states I and II are localized entirely at the molybdenum edge, and the illustration shows the contours of the electronic wave functions associated with the edge states. (c) Simulated STM image of the molybdenum edge with sulfur dimers. The positions of the individual atoms in the simulated image are represented as shadowed atom balls (small: sulfur, large: molybdenum). Accompanying the simulation to the right are ball models of the molybdenum edge with 100% sulfur coverage shown in top (upper part) and front view (lower part).

The nature of this state is somewhat more complicated than that of state I. It is primarily constituted of two bonds: (a) the $d-d$ bond between the first row of molybdenum atoms, and (b) the $p-d$ bond between the second row of sulfur atoms and the molybdenum atom behind. A simulated section of the slab exposing the molybdenum edge with sulfur dimers is shown in Fig. 16c. The simulation evidently reproduces all the prominent features of the experimental STM image. Notably, the bright brim is reproduced in the row adjacent to the edge protrusion and is therefore inferred to be associated with edge state II. Significantly, the protrusions on the edge are not associated with the position of the sulfur dimers, but rather reflect the interstitial region between pairs of sulfur dimers. This behavior is attributed to edge state I and reproduces the shifted geometry along the edges, as shown by the STM image (Fig. 14). It is therefore concluded that under the sulfiding conditions of the experiment, triangular single-layer MoS_2 nanoclusters are terminated with the molybdenum edge fully covered with sulfur dimers, and that the electronic structure of these edges is dominated by one-dimensional edge states that give the edge a metallic character. Such fully sulfur-saturated edges are not considered to be particularly reactive, but as shown in the next sections, the edges of the MoS_2 nanoclusters can be considered to be metallic in some respect and therefore have properties with respect to adsorption different from what is assumed from the traditional coordination chemistry of MoS_2 .

D. THE CHEMISTRY OF SINGLE-LAYER MoS_2 NANOCCLUSERS

D.1. *Thiophene on Fully Sulfided MoS_2 Nanoclusters*

Observations of the sample after room temperature exposure to thiophene ($\text{C}_4\text{H}_4\text{S}$) seem at first to confirm the simple expectation that the fully sulfided single-layer MoS_2 nanoclusters (Fig. 13) are quite unreactive toward sulfur-containing molecules. At room temperature STM images show no signatures on the (0001) basal plane that can be ascribed to adsorbed thiophene molecules, in agreement with the results of TPD investigations of thiophene on single-crystal $\text{MoS}_2(0001)$ (95). Furthermore, the edges of the MoS_2 nanoclusters appear unchanged by the exposure to thiophene.

This situation, however, changes when the temperature of the sample is reduced below 200 K. As illustrated in the STM image of Fig. 17, chain-like structures consisting of elliptical protrusions are evident, attributed to individual molecules adsorbed near the edges of the single-layer MoS_2 nanoclusters. At these tunneling parameters, the individual molecules are imaged as protrusions, the dimensions of which ($\sim 4 \text{ \AA} \times 5 \text{ \AA}$) agree well with the expected van der Waals radius of thiophene lying flat on the surface. As illustrated in the first STM image, the molecules adsorb at the lowest temperatures at two different sites near the cluster: In addition to the chains of molecules adsorbed on top of sites toward the edges of the triangular

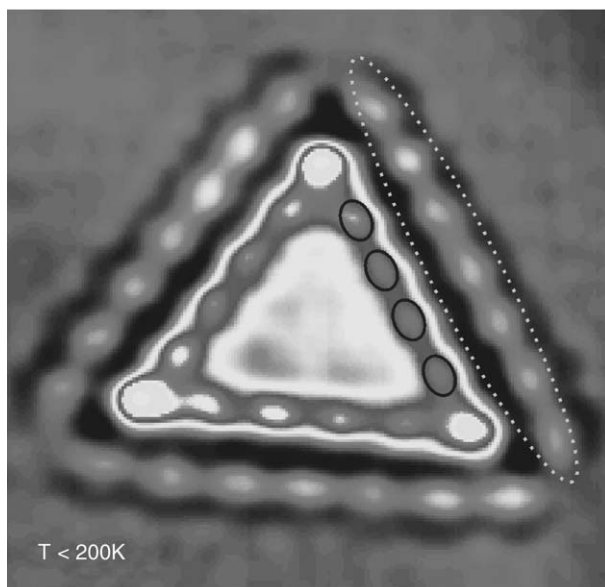


FIG. 17. STM image of thiophene on the triangular MoS_2 nanoclusters at a sample temperature below 200 K. Thiophene molecules are evident in positions on top of the bright brim associated with an edge state (dark circles), and additionally thiophene decorates the perimeter of the cluster (gray striped circle). For clarity, the color scale in this image is circled twice to enhance contrast. At temperatures $> 240 \text{ K}$, no indications of adsorbed thiophene were observed with STM.

clusters, thiophene is also found to decorate the cluster periphery by forming rows of adsorbed molecules. The latter is attributed to thiophene lying flat on the Au(111) substrate next to the clusters. It is possible that this adsorption mode is a result of dipole–dipole interactions with the cluster edge and a weak bonding of the π -electron system of thiophene to the gold substrate; the thiophene can be regarded as in a physisorbed state of little significance to the catalytic properties of the clusters. The molecules adsorbed on top of the cluster are, however, the result of a direct bonding between thiophene and the MoS₂ nanoclusters. The adsorption site is significant, as it shows that the molecules seem to adsorb on sites near the bright brims associated with a metallic one-dimensional edge state of MoS₂ (Fig. 14). In contrast to the common assumption that the fully saturated edges generally do not bind thiophene, the results clearly suggest that the unique electronic environment may facilitate the formation of stable chemical bonds. Again, a rather low corrugation and the position and dimension of the protrusions associated with the molecules suggest π -bonding of the thiophene at sites on top of the edge state.

In the terminology of organometallic chemistry, this corresponds to a flat η^5 -adsorption geometry, but in this case the term does not refer to coordination to a single metal atom but rather to the metallic edge state. A rough estimate of the adsorption strength of the thiophene on the clusters could be found in terms of the apparent desorption temperature by heating the sample slightly in the sample manipulator, followed by its imaging in the still-cooled STM. It was observed that the molecules initially bound near the bright brim all had desorbed at temperatures slightly above 200 K, and it is therefore concluded that thiophene is relatively weakly bonded in this configuration. The thiophene molecules bind, however, considerably more strongly to the metallic edge state than to internal regions of the MoS₂ basal plane, and the low-temperature STM results thus provide information about possible initial adsorption geometries of thiophene on the edges, which under the right conditions may lead to further reactions.

D.2. *Reactions of Hydrogen-Activated MoS₂ Nanoclusters*

When the triangular MoS₂ nanoclusters were pre-treated with hydrogen, a much stronger chemisorbed state of thiophene was observed in the atom-resolved STM images (Fig. 20). We return to the discussion of such an interaction in the next section, but first emphasize that the exact procedure for this experiment is important, because exposure to molecular hydrogen (H₂) does not seem to initiate the reaction directly. Generally, most types of reactions with molecular hydrogen are inhibited under the conditions of the experiment. We associate this behavior with a rather high activation barrier of H₂ and the low pressures used in the experiment. If, instead, the sample is dosed with pre-dissociated (atomic) hydrogen at elevated temperatures, several changes in the clusters are observed, which can be ascribed to reactions with hydrogen. First, the exposure of atomic hydrogen to the MoS₂ nanocluster leads to the formation of single sulfur vacancies on the edges of the clusters (118). Typically, one or two vacancies are formed in each cluster. This point is illustrated in Fig. 18, where the vacancies are associated with regions on the edge

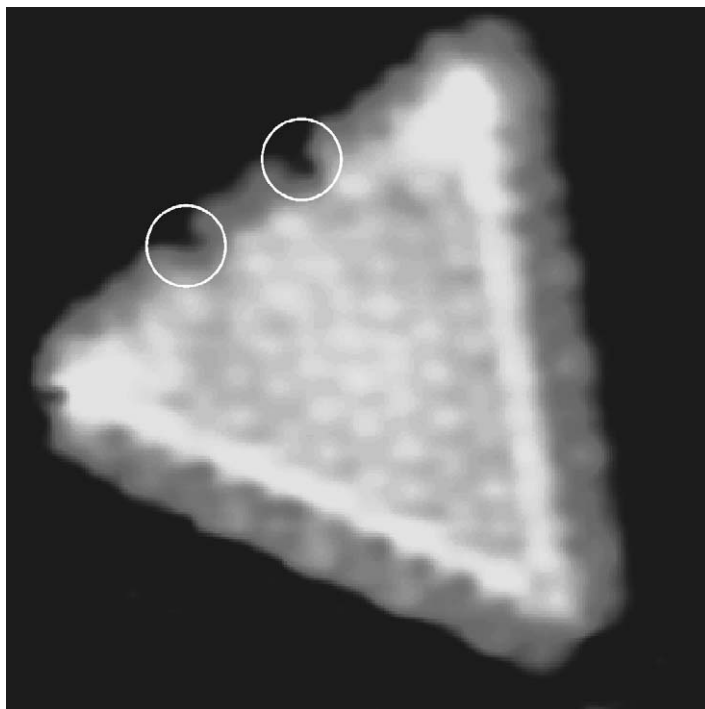


FIG. 18. Atom-resolved STM image ($V_t = -8.5$ mV, $I_t = 1.12$ nA) of a triangular single-layer MoS₂ nanocluster after reduction with atomic hydrogen atoms at 673 K in 5 min. Image size $46 \text{ \AA} \times 47 \text{ \AA}$. The location of two sulfur vacancies is illustrated with circles. Reprinted with permission from Reference (118). Copyright (2000) by the American Physical Society.

with a depleted intensity, and the experimental results thus provide the first direct evidence that it is possible to sustain a population of sulfur vacancies on the edges of the single-layer MoS₂ nanoclusters—and these vacancies are believed to be similar to what is present in the active state of the HDS catalyst.

In addition to the formation of sulfur vacancies on the molybdenum edge, the STM images furthermore reveal that the exposure to atomic hydrogen also changes the regions of the edges that do not have sulfur vacancies in the near vicinity. After exposure to atomic hydrogen, little qualitative change was observed in these regions on the edges, which retained the characteristics of the fully sulfided molybdenum edges (two lower edges of the triangle in Fig. 18; i.e., the protrusions were still out of registry, and the 0.4-\AA -high bright brims seem unaltered). A detailed analysis of the edges showed that the fully sulfided edges in clusters display a small intensity shift of the outermost edge protrusions after exposure to atomic hydrogen.

This result is illustrated with STM line scans, as shown in Fig. 19, where data characterizing the edge of the freshly prepared, fully sulfided structures are compared with a similar line scan for an atomic hydrogen pre-treated cluster. The average height of the edge protrusions shifted down relative to the basal plane by approximately 0.2 \AA in the hydrogen-treated cluster. This downshift occurs as a

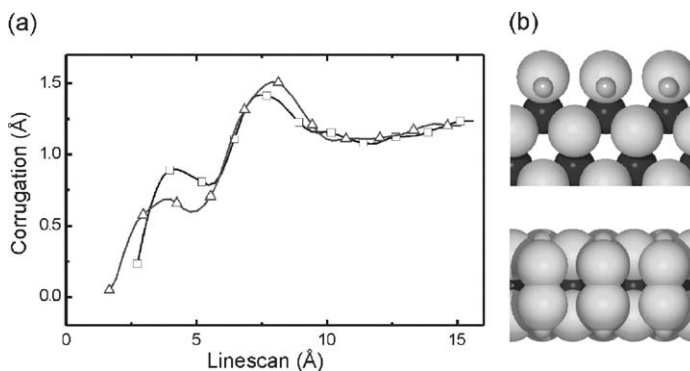


FIG. 19. (a) STM line scans drawn perpendicularly to the fully sulfided molybdenum edge of the single-layer MoS₂ nanocluster prior to (squares) and after (triangles) exposure to atomic hydrogen. The down-shifted intensity of the outermost edge protrusions, corresponding to approximately 0.2 Å, is associated with a change in the electronic structure when hydrogen is adsorbed on the edges. (b) Ball models of the configuration of hydrogen in which hydrogen adsorbs on the fully sulfided molybdenum edges shown in a top- and side-view representation. Adapted from Reference (130).

result of the treatment in atomic hydrogen, and it therefore suggests that the observations are related to the formation of S–H groups on the fully sulfided edges.

We interpret the intensity reduction in the STM images as a modification of the LDOS at the Fermi level in the interstitial regions between sulfur dimers when hydrogen species saturate the edges. This interpretation is also supported by recent DFT-based theoretical investigations of various hydrogen configurations of hydrogen on MoS₂ edges (122), which furthermore show that the hydrogen atoms adsorbed on the sulfur dimers are in fact marginally unstable (less than 17 kJ/mol) relative to molecular H₂. It is suggested that an energy barrier exists, which inhibits desorption of hydrogen under the conditions of the experiments, and because this interpretation implies a similar barrier for the dissociative adsorption of H₂, it also explains the need experimentally to pre-dissociate H₂. Under real reaction conditions, however, the high temperatures and high partial pressure of hydrogen gas are expected to allow for rapid hydrogen dissociation, and the edges are expected to maintain a substantial coverage of S–H groups.

Thus, the use of atomic hydrogen in this experiment can therefore be viewed as a simple way of providing hydrogen atoms at the high chemical potential found under realistic reaction conditions. On the basis of the STM experiments, it is therefore concluded that exposure to atomic hydrogen leads to the formation of sulfur vacancies on the single-layer MoS₂ nanoclusters, and that the increased chemical potential of hydrogen leads to a high population of hydrogen atoms adsorbed on the remaining sites that form edge S–H groups under the conditions of the experiment.

D.3. Reaction of Thiophene on Hydrogen-Activated MoS₂ Nanoclusters

The atomically resolved STM image of Fig. 20 shows one of the triangular single-layer MoS₂ nanoclusters following the exposure to, first, atomic hydrogen, and,

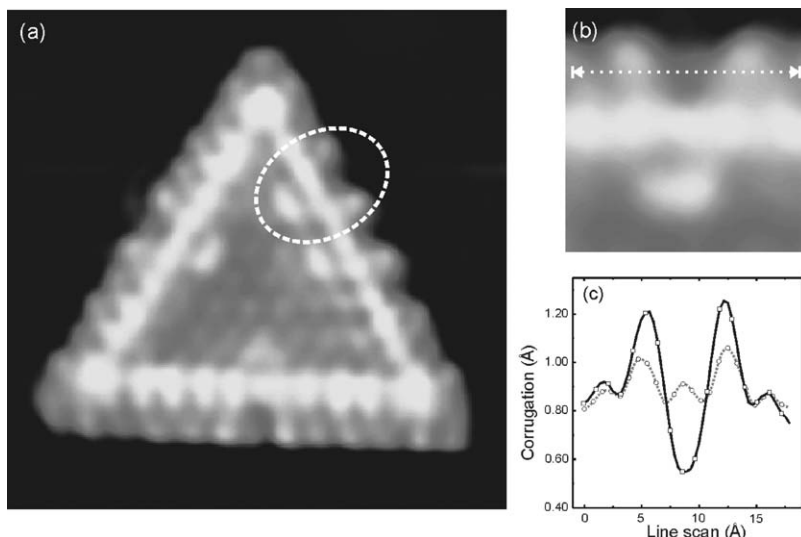


FIG. 20. (a) Atom-resolved STM image ($V_t = -331$ mV, $I_t = 0.50$ nA) of an atomic-hydrogen-pretreated MoS₂ cluster subsequently exposed to thiophene. Image dimensions are $50 \text{ \AA} \times 54 \text{ \AA}$. The dashed circle indicates the features associated with individual adsorbed molecules. (b) A close-up view that illustrates in detail the features associated with the adsorption of individual thiophene-derived species at the edge of a MoS₂ nanocluster. These are (i) a bean-like structure adjacent to the bright brim and (ii) an intensity shift of the three outermost edge protrusions. (c) STM line scan along the edge protrusions of a cluster (black), corresponding to the line in (b). A line scan of an equal section of an unreacted, fully sulfided edge (gray dashed) is also shown. Adapted from Reference (180).

subsequently, thiophene. The room-temperature STM image now indicates several bean-like structures protruding approximately 0.4 \AA from the basal plane in the row adjacent to the bright brim toward the basal plane of the MoS₂ cluster. These features can be ascribed to signatures of distinct molecules bonded to sites on the metallic edge state. STM images generally reflect a rather complex convolution of the electronic and geometric structure, and when this combination is complicated by the highly perturbed electronic structure that already dominates the edges of the triangular MoS₂ clusters, it becomes difficult to relate the observed new structures in Fig. 20 to the molecular structure of reaction products or intermediates formed in an HDS reaction. Most likely, the shifted intensity of the protrusions near the adsorption site is the result of a slight quenching of the metallic edge state that is associated with the sulfur dimers. The bean-like features adjacent to the brim are, however, attributed to parts of the structure of the adsorbed molecules, which are located in a position spanning the bright brim associated with a metallic edge state.

The experiment was performed with a quench-and-look approach, whereby the model system was first heated to 673 K and exposed to low amounts of atomic hydrogen produced by dissociating H₂ on a glowing tungsten filament. The flux of hydrogen was then terminated, and the clusters were exposed to thiophene at an elevated sample temperature of about 500 K. Subsequently, the model system was

quenched to room temperature and imaged with the STM. As shown in the previous section, the atomic hydrogen pre-treatment was found to produce both S–H groups and sulfur vacancies on the fully sulfided single-layer MoS₂ nanoclusters, but we can rule out the possibility that the observed adsorbates in Fig. 20 reflect intact thiophene molecules coordinated end-on to either one or more sulfur vacancy sites. First, the cluster edges in Fig. 20 display every characteristic of the fully sulfided molybdenum edge and retain the 0.4-Å high bright brim and edge protrusions, which are shifted exactly half a lattice constant out of registry. Molybdenum edges that are partially or completely reduced with respect to sulfur coverage do exist under different conditions, but they are imaged with a quite different structure in STM (130). Second, the adsorbed molecules were found to be quite mobile; that is, they were observed in consecutive STM images to jump from one site to the next. In no instance were vacancies such as those in Fig. 18 found to exhibit the same mobility in STM images at room temperature.

On the basis of these observations and the fact that hydrogen is necessary for a strong interaction, the molecular species observed in Fig. 20 are proposed to be the result of thiophene molecules that have undergone a hydrogenation reaction on the brim sites near the edges. It is proposed that S–H groups formed during the exposure to atomic hydrogen play an essential role in a reaction with thiophene occurring on sites on the metallic brim. Presumably, the combination of having hydrogen atoms adsorbed at the edges in the form of S–H groups, and the unusual sites for thiophene adsorption on the metallic brim in Fig. 20 presents a favorable situation for a hydrogenation reaction. Thus, the STM results suggest that the most likely candidates for the adsorbed intermediate species are molecules formed from thiophene in which either one or both of the double bonds have become hydrogenated.

D.4. Energetics and Reaction Pathways: Metallic Edge States as Active Sites

To identify the nature and conformation of the species observed in the STM experiments, extensive DFT calculations were performed by Nyberg *et al.* (131). In this investigation, the molybdenum edge was again modeled as a single slab of MoS₂, and various molecules were adsorbed in a repeated geometry along the edges. In accord with results of the low-temperature STM experiments (Fig. 17) and earlier estimates temperatures of desorption of thiophene from supported MoS₂ catalyst particles (132), it was found that pure thiophene indeed interacts very weakly with the fully sulfided edges of MoS₂. However, DFT calculations of several hydrogenated species derived from thiophene show that in particular a C₄H₇S (*cis*-but-2-ene-thiolate) compound coordinated through the terminal sulfur atom to the edge sulfur atoms near the brim is found to be quite stable and shows a good agreement with the STM results. The adsorbed thiolates are illustrated in a simulated STM image in Fig. 21(a), and the features associated with each molecule reproduce the signatures found in the STM image of Fig. 21(b), including the shifted intensity of the three outermost protrusions near the molecular adsorption site. The bean-like structure behind the brim is also reproduced in the simulated

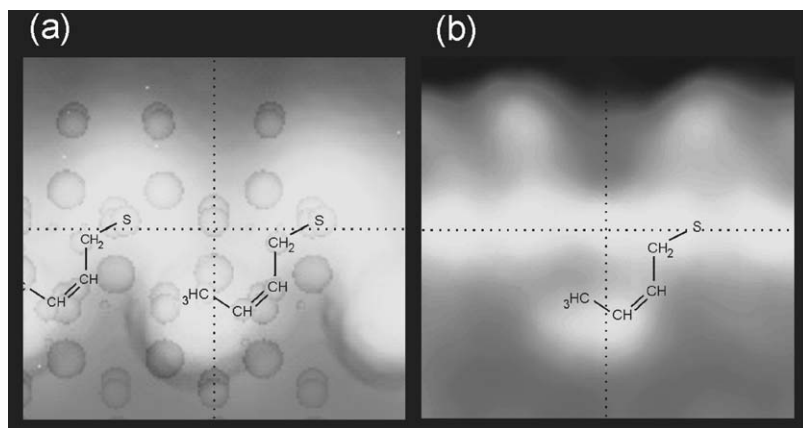


FIG. 21. (a) Simulated STM image of C_4H_7S molecules (*cis*-but-2-ene-thiolate) adsorbed in stable positions across the metallic brim state of MoS_2 . The simulated STM image was calculated with the Tersoff–Hamann scheme and is based on DFT calculations employing a periodic unit cell. Adapted from Reference (180). (b) For a direct comparison, the corresponding experimental STM image is illustrated here, with a schematic representation indicating the position of a single molecule.

STM images and is evidently associated with the ring-opened carbon chain of the thiolate, the end-group of which is imaged with a higher intensity.

Figure 22 illustrates the proposed reaction pathway leading to the adsorbed C_4H_7S state. Starting from the physisorbed thiophene (i) molecules (bound by an energy of less than 20 kJ/mol), one of the double bonds in thiophene is hydrogenated, causing the other double bond to move; that is, 2,5-dihydrothiophene (ii) adsorbed to the cluster edge is formed. A calculation of the activation barrier in the next step is included in Fig. 22 for what is assumed to be the most difficult step in the reaction, the C–S bond cleavage. The associated barrier is rather modest ($E_a \approx 107$ kJ/mol). At the temperature at which thiophene reacts (500 K), this means that equilibrium between C_4H_7S and thiophene in the gas phase is easily achieved. The same is of course true under industrial hydrotreating conditions. The barrier for the reverse reaction is, however, large enough for thiophene not to be desorbed during imaging at room temperature, in accord with the experimental observations.

The final configuration (iii) in Fig. 22, associated with the ring-opened thiolate structure on the cluster edge, corresponds to a simple adsorbed thiol. The observation of these thiolate intermediates is significant, because thiols are much more reactive than thiophenes under real HDS conditions. This observation is, however, fully explained by the conditions of the STM experiment and the barrier to desorption of the thiolates. The final C–S bond breakage is, however, likely to require a site capable of accepting sulfur and may thus take place at another site on the cluster. Such sites are presumably sulfur vacancies located at the edges, such as the one illustrated in Fig. 18. It is thus likely that surface diffusion of the thiolates along the edge or through the gas phase (after recombination with adsorbed H) to vacancies is needed for the final step in the overall reaction. From a consecutive series of STM images, a mobility of the adsorbed thiolate species was indeed observed,

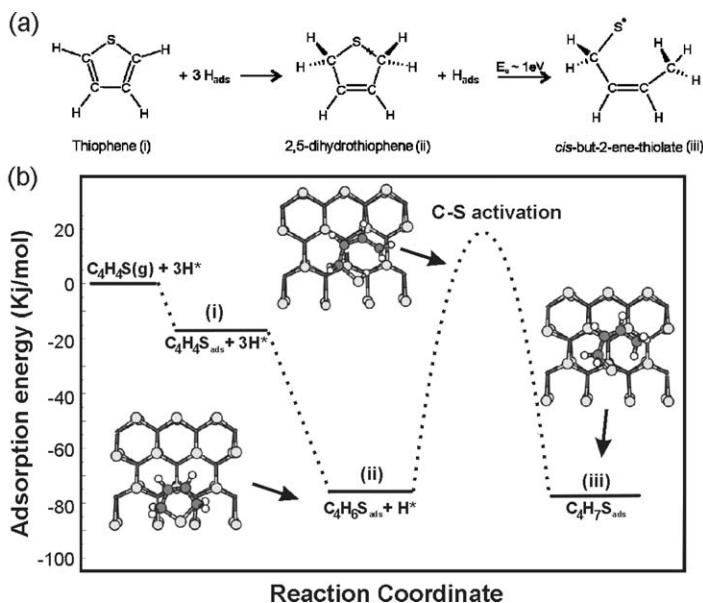


FIG. 22. (a) The proposed reaction scheme of thiophene leading to the thiolate intermediates observed with STM. All processes occur while the reactants are adsorbed on the fully sulfided molybdenum edge of the MoS_2 nanoclusters. For clarity, only thiophene and H reactants are shown. (b) The calculated energies associated with the individual steps in the reaction path (above) of thiophene species adsorbed on sites on the metallic edge state of MoS_2 . The energies are in kJ/mol and were calculated relative to gas-phase thiophene and H adsorbed on the fully sulfided molybdenum edge ($E_{\text{H}} \approx 17$ kJ/mol). The diagram displays the most relevant intermediate steps in the hydrogenation of thiophene and subsequent C–S bond cleavage. Labels refer to the schematic representation above. The ball-and-stick models illustrate the geometric configurations associated with adsorbed species before, during, and after C–S bond cleavage. The final configuration is $\text{C}_4\text{H}_7\text{S}$ (*cis*-but-2-ene-thiolate). The position and geometry of the molecule adsorbed on the cluster are also illustrated in Fig. 5. Note the modest activation barrier associated with the last step, (ii) to (iii); $E_a = 107$ kJ/mol. From Reference (131) copyright (2004) with permission from Elsevier.

supporting the notion that the reactivity can be explained by a two-step process in which the thiophene is first hydrogenated, the first C–S bond is cleaved on the brim sites, and the ring-opened molecule is subsequently transported to a sulfur vacancy on the cluster edge, where the second C–S bond can be broken. The final sulfur extrusion on a vacancy was not observed directly in these dynamic STM investigations, because the present experiments, performed under UHV at room temperature, capture the model catalyst in a fully sulfur-saturated situation, disabling the continued reaction of thiolates. In contrast to the situation under real continuous HDS, the number of available sulfur vacancies is depleted in experiment once the flux of atomic hydrogen is terminated owing to the recombination with sulfur from dosed molecules prior to imaging. By quickly cooling the sample in the STM to temperatures below 240 K after the thiophene flux had been terminated, it was, however, possible to capture species attached to the edge in a configuration that indicated a direct end-on bonding in a very few instances. This bonding is illustrated

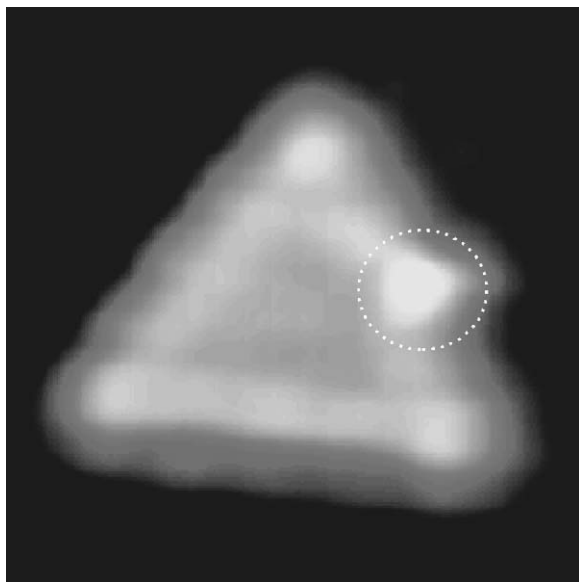


FIG. 23. STM image of a MoS₂ nanocluster first exposed to atomic hydrogen, then thiophene and subsequently imaged at 240 K in cold STM. The protrusion in the circle may represent a thiophene molecule or a hydrogenated derivative coordinated through the terminal sulfur atom to a sulfur vacancy. Reproduced from Reference (131) copyright (2004) with permission from Elsevier.

in Fig. 23. In view of the spherical appearance of the adsorbate on the cluster edge, we associate the species with η^1 -coordinated thiophene rather than a thiolate.

The STM investigations thus reveal the first direct atomic-scale information of thiophene HDS reaction pathways on MoS₂ nanoclusters, and the results have several important implications in terms of explaining the reactivity of MoS₂ nanoclusters. On the basis of identification of reaction intermediates, a new route is identified for activating a sulfur-containing molecule such as thiophene, which takes place by hydrogenation of the double bonds followed by a C–S bond breaking. Remarkably, the brim sites adjacent to the completely sulfur-saturated molybdenum edge are capable not only of catalyzing the hydrogenation of the carbon–carbon double bonds in the presence of neighboring C–S groups, but also of activating and breaking the first C–S bond of the hydrogenated thiophene. All of these processes take place on top of specific sulfur atoms of the MoS₂ nanoclusters, with no direct interaction with the molybdenum atoms. The interesting chemistry is clearly associated with the metallic brim sites located adjacent to the MoS₂ edges. No indication of chemical reactivity is found experimentally or theoretically at the interior sulfur atoms on the MoS₂ basal plane. The metallic states associated with the brim sites, on the other hand, have the ability to donate and accept electrons and thus act as catalytic sites. In this respect they are much like ordinary catalytically active metal surfaces. Whereas many catalytically active metals (iron, nickel, and molybdenum, for example) are poisoned by H₂S and strongly bonded sulfur residues, the fully sulfur-coordinated brim sites of the MoS₂ nanoclusters are clearly

not. In comparison to the reactive metals and the inert basal plane of the MoS_2 nanoclusters the metallic brim sites seem to offer a more nearly optimum bonding strength for the adsorption of thiophene. This kind of interaction represents a compromise, with an intermediate adsorption strength of the reactant, and such a compromise generally characterizes a good catalyst (83,133).

D.5. Atomic-Scale Structure of the Cobalt-Promoted Catalyst

Upon addition of cobalt in the preparation of the MoS_2 -containing HDS catalysts, the HDS activity increases by more than an order of magnitude relative to that of the unpromoted MoS_2 (85). Because it has been established that small amounts of cobalt can dramatically change the activities of the catalysts, the cobalt is considered to be a promoter rather than a catalyst in its own right, and the enhanced activity has previously been shown to be correlated uniquely with the formation of bimetallic sulfided Co–Mo structures, termed CoMoS as originally proposed by Topsøe, Clausen, and co-workers (134–136). The CoMoS clusters are characterized as MoS_2 -like nanoclusters with molybdenum substituted by cobalt at edge sites.

By applying an approach similar to the one taken with the unpromoted MoS_2 nanoclusters, we recently managed to synthesize a model system for the promoted CoMoS catalyst (119). As a result of co-deposition of molybdenum and cobalt onto the Au(111) crystal during exposure to an H_2S atmosphere and subsequent annealing, crystalline CoMoS clusters formed on the Au(111) terraces. As shown in Fig. 24, the main new finding is that the CoMoS nanoclusters now adopt a

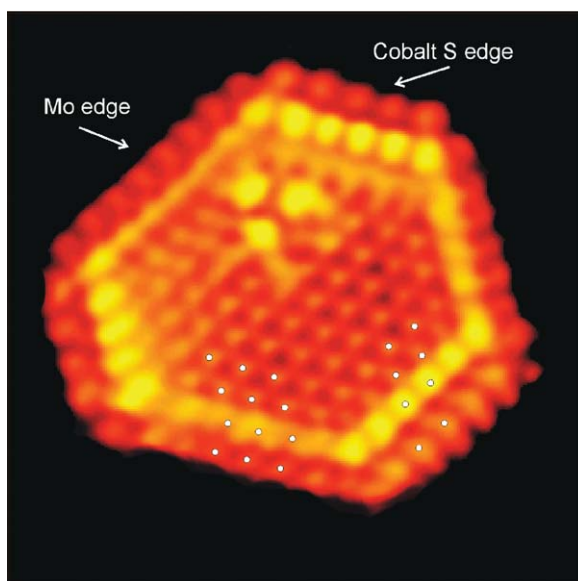


FIG. 24. Atom-resolved STM image of a CoMoS nanocluster. The size is $51 \text{ \AA} \times 52 \text{ \AA}$, and $V_t = -95.2 \text{ mV}$ and $I_t = 0.81 \text{ nA}$. Note the intense brim associated with the cobalt-substituted sulfur edge (shorter edges).

hexagonal shape, as opposed to the triangular morphology of unpromoted MoS_2 (Fig. 13) observed when only molybdenum was deposited and sulfided. This change in the equilibrium shape is therefore attributed to the incorporation of cobalt into the MoS_2 structure (i.e., the formation of the CoMoS phase (119)).

The predominant hexagonal morphology implies that both fundamental types of low-indexed edge terminations of MoS_2 must be present (i.e., the molybdenum edge and the sulfur edge). One edge type in the CoMoS structure is found to be similar to that observed for the MoS_2 triangles (Fig. 13), with the edge protrusions clearly imaged *out* of registry with the lattice of sulfur atoms on the basal plane and the bright brim along the edge. These edges are therefore identified as molybdenum edges, fully sulfided with two sulfur dimers per molybdenum edge atom (Fig. 25b). From the symmetry of MoS_2 , the other, shorter edges are consequently attributed to sulfur edges. Significantly, these edges are observed in the low-bias STM images to exhibit an even brighter brim, implying the existence of one-dimensional edge states in the promoted structures as well. This observation suggests that the promoting role of cobalt may be explained by a change of the electronic structure on the sulfur edge together with a possible change of the interaction strength of sulfur with the cobalt.

On the basis of the detailed atomic-scale information provided by the STM images, a structural model of the CoMoS nanoclusters is proposed in which cobalt atoms have replaced molybdenum atoms along the sulfur edges of hexagonally truncated nanoclusters. As depicted in the ball model in Fig. 25(a) and (c), a tetrahedral environment of the cobalt atoms is produced if the outermost protrusions are assumed to be sulfur monomers, which agrees well with spectroscopic results reported for supported CoMoS catalysts (93,137–139) and previous DFT investigations (128,140).

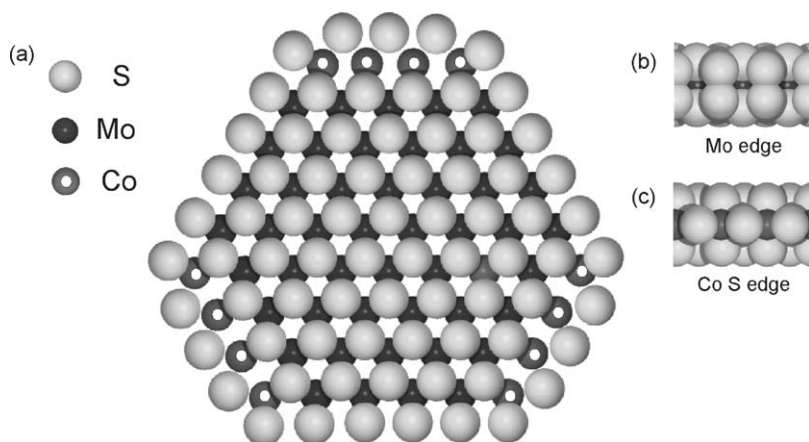


FIG. 25. (a) Ball model of the proposed CoMoS structure. The CoMoS cluster is shown in top view, exposing the unpromoted molybdenum edge and a cobalt-promoted sulfur edge (molybdenum: dark; sulfur: bright; cobalt: dark with white spot). Also shown on the basal plane is a single cobalt inclusion. (b) The molybdenum edge (shown in side view) is unaffected by cobalt and is covered with sulfur dimers. (c) Cobalt fully substitutes for molybdenum on the sulfur edge. Sulfur monomers adsorbed on the edge produce a tetrahedral coordination of each cobalt atom.

D.6. *Metallic Brim States as Active Sites in Hydrotreating Catalysts*

The existence of metallic sites on the brim in promoted and unpromoted MoS₂-containing catalysts and their role in hydrogenation reactions may explain the results of many other investigations reporting the kinetics and mechanisms of HDS catalysis (131). For example, the lack of strong inhibition by H₂S on the hydrogenation activity (in contrast to the HDS activity (141)) of the catalyst was difficult to understand in previous models, which incorporated active sites only in the form of one or more sulfur vacancies on the edges. This observation is now readily understood, because the metallic brim sites are fully coordinated by sulfur and do not readily adsorb more H₂S, as confirmed in STM experiments.

On the other hand, the hydrogenation activity in the reaction of thiophene is severely inhibited by more electronegative nitrogen-containing aromatic compounds such as pyridine (C₅H₅N) or quinoline (C₉H₇N) (which were converted simultaneously with the thiophene), implying that these molecules adsorb initially on sites similar to those where thiophene adsorbs on the bright brim (142). As the hydrogenation of such nitrogen-containing aromatics is also an integral part of hydrotreating catalysis (in the hydrodenitrogenation (HDN) process (143)), it is therefore inferred to be likely that the catalytic activity associated with sites on the metallic brim sites of MoS₂ may be of importance for a wide variety of compounds in petroleum.

On the basis of the fundamental insight about the role of metallic edge states in the MoS₂-containing hydrotreating catalyst, combined with new knowledge about support interactions (144), it recently became possible to manufacture a new generation of hydrotreating catalysts which optimize the number of brim sites and enhance the hydrogenation properties (145). Again, this accomplishment shows that information gained from fundamental STM investigations of idealized systems can generate ideas that are required for the manufacture of better industrial catalysts. It is doubtful whether any experimental technique other than STM could unequivocally indicate the presence of electronic states on the edges of highly dispersed MoS₂ nanoclusters of this size, and beyond this to determine their roles in the adsorption of reactant molecules.

VI. Toward more Realistic Model Systems and Imaging of Surfaces during Reaction

A. TIME-RESOLVED STM INVESTIGATIONS

The development of fast-scanning STMs with highly compact designs, exceptionally high vibration and drift stability, and dedicated electronics has today made it possible to visualize dynamic phenomena on surfaces at speeds near video rate (50 Hz), compared to a typical STM frame rate of one image per minute (146,147). In time-resolved STM investigations, images of surfaces are recorded in a consecutive manner and stored in a so-called STM movie that may be replayed at a desired higher or lower rate to reveal dynamic changes of the surface with atomic precision

(examples can be found on <http://www.phys.au.dk/spm/stmmovies.shtml>). The application of fast-scanning STM has several important implications for fundamental catalysis research, because with this tool in hand it is in principle possible to monitor the progress of chemical reactions, including the diffusion of adsorbed molecules or the intramolecular transformations involved in bond activation. This powerful application of STM has thus already provided important atomic-scale information on the diffusion pathways of particles, molecules, and surface defects under non-equilibrium conditions (44,48,148–150). The subject was recently reviewed in *Advances in Catalysis* by Winterlin (50). It is, however, important to point out that STM investigations performed even at video rate will never provide real-time images of chemical reactions, because such events occur on a time-scale of the order of 10^{-9} – 10^{-12} s. The STM movies rather provide snap-shots of intermediate steps in such chemical reactions.

Winterlin *et al.* (151,152) used time-resolved STM to follow the propagation of reaction fronts for the catalytic oxidation of hydrogen on platinum(1 1 1) in great detail. Figure 26 shows STM images taken from Ref. (151), in which a reaction front is seen to propagate on the initially oxygen terminated surface during the

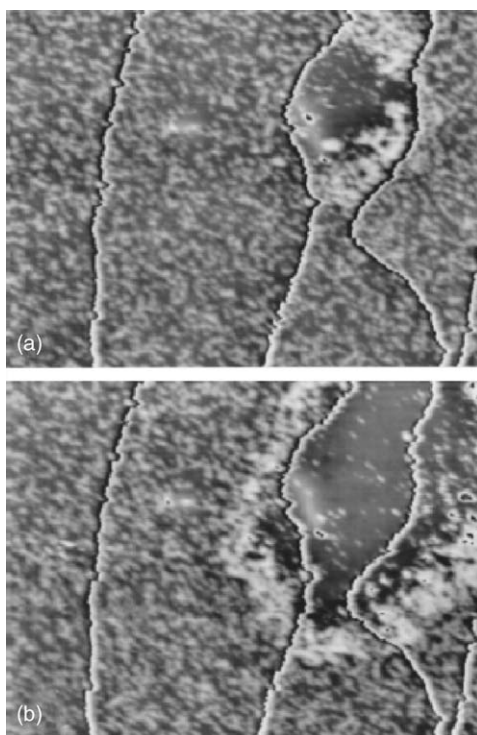


FIG. 26. STM images of the oxygen pre-covered platinum(1 1 1) surface during reaction with hydrogen. Images were recorded at a temperature of $T = 111$ K with a time interval of 625 K. The white ring in the upper right corner is associated with a reaction front of OH intermediates from the autocatalytic reaction. The outside is characterized by an oxygen-terminated surface, whereas water molecules from the reaction are identified inside the ring. Adapted with permission from Reference (151).

reaction with hydrogen provided from the gas phase. The appearance of the reaction front (white ring) was explained by an autocatalytic reaction involving OH intermediates formed by the fast reaction of H_2O with adsorbed O, which is initiated at low temperatures or high pressures, where the residence time of adsorbed H_2O on the surface is high. The detailed insight from the STM investigations that combine high spatial and temporal resolution and the observation of an autocatalytic reaction could explain a number of controversial observations related to the kinetics of hydrogen oxidation on this particular system.

In another recent investigation, Mitsui *et al.* (45) applied the time-resolved STM to investigate the reaction pathways for hydrogen dissociation on palladium(111). By imaging hydrogen dissociation events on an almost fully hydrogen-saturated palladium(111) surface in consecutive STM images, these authors were able to shed new light on the role of palladium as a hydrogenation catalyst. Hydrogen adsorbs in a dissociative manner on the clean palladium(111) surface, and in these investigations an almost fully hydrogen-covered surface was imaged at low temperature (Fig. 27). Static STM images revealed a surface with a small concentration of vacancies, assigned to empty sites on the surface with no hydrogen adsorbed. As a result of an inversion of contrast for this system, the sites which are missing

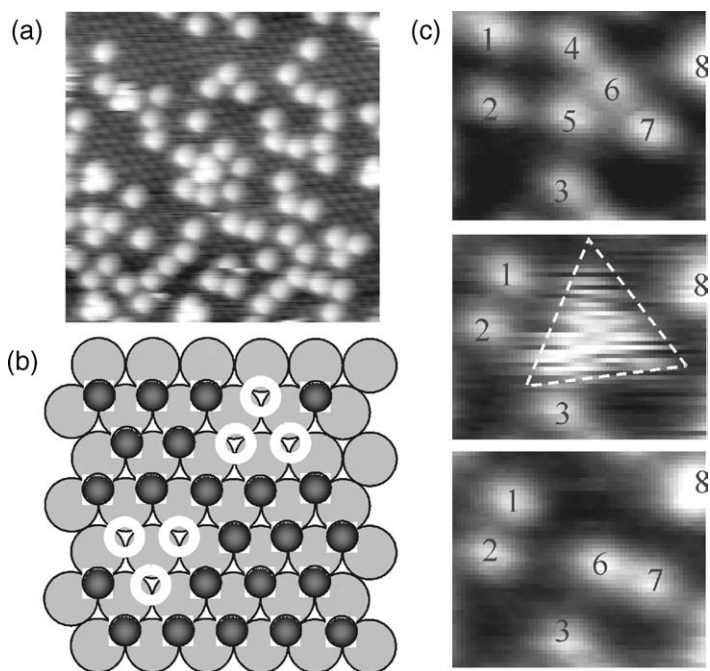


FIG. 27. (a) An STM image of a nearly fully hydrogen-saturated Pd(111) surface imaged at 65 K at 2×10^{-7} Torr of H_2 . The vacancies in the 1×1 hydrogen adlayer are imaged as bright protrusions. (b) Ball model of the surface illustrating agglomeration of three vacancies on the surface. (c) Three consecutive STM images showing a dissociation event of hydrogen on the palladium surface. From top to bottom, the STM images first show the agglomeration of four vacancy sites followed by the disappearance of two vacancies. With permission from Reference (45).

hydrogen ad-atoms are imaged as protrusions, as shown in Fig. 27a. By monitoring the movement of the hydrogen vacancies in STM movies at low temperature, the authors observed that only when an agglomeration of three or more empty sites occurred could hydrogen dissociate and fill the vacancies. This is shown in the sequence of STM images in Fig. 27c, where the triangular feature represents an agglomeration of four vacancies. On the basis of such STM observations, the authors concluded that three or more empty palladium sites (Fig. 27b) were necessary for the dissociation of further hydrogen molecules. This finding is rather surprising in view of the conventional Langmuir adsorption model, according to which two empty palladium sites should be sufficient to dissociate a diatomic molecule. These investigations nicely illustrate the application of time-resolved STM to investigate the progress of a chemical reaction on a surface with atomic precision.

B. IMAGING OF SURFACES DURING REACTION

One of the simplifying assumptions behind the descriptions of adsorption of atoms and molecules, and in particular chemical reactions between adsorbates on catalytically active surfaces, has often been that the surface can be considered as a static “checkerboard” providing adsorption sites for, and bonds to, the adsorbing atoms and molecules. However, it has been found for several materials that this is rather the exception, and the surface structure and composition may instead depend intimately surface coverage of adsorbates and thus on the applied gas pressure. The difference between a surface observed under well-controlled vacuum or low-pressure conditions and the same surface exposed to the high pressures relevant in catalysis is referred to as the “pressure gap,” and several groups are currently exploring catalysts by *in situ* techniques such as HRTEM (37,38) and sum frequency generation (SFG) spectroscopy (35,153,154). The STM can be operated over a wide pressure range ranging from UHV to high pressure (~1 bar), and STM is thus an appropriate technique for the characterization of the pressure gap at the atomic scale.

Today, a number of groups have taken up the challenge of building an STM capable of operating in a high-pressure cell (155–160). A major challenge in imaging surfaces with the STM over a wide pressure range is the sensitivity of the tunneling current to minute changes at the tunneling junction resulting from tip and/or sample instabilities associated with the ambient gas. Furthermore, the gas atmosphere and gas flow transmit vibrations from the surroundings to the STM, in contrast to the situation under vacuum conditions, and thus care must be taken to reduce vibrational noise. Gas purification is another important issue, as the STM gives *a priori* no direct clues regarding the chemical nature of adsorbates, and even highly diluted impurities may entirely pollute the surface when the surface is exposed to high pressures.

Notwithstanding the challenges involved in the design and operation of STM under high gas pressure, it has been possible to image adsorbate structures on single-crystal surfaces, even with atomic resolution at pressures ranging from the idealized UHV conditions to pressures of 1 bar (161,162). Hendriksen and Frenken (163) went one step further and implemented a reactor cell in connection with the STM, which allowed investigations of a platinum(1 1 0) surface while it was exposed

to a flow of CO and O₂, with varying concentrations. By recording the partial pressures of the reactants and the CO₂ formation, the authors were able to correlate an observed surface roughening of the platinum(1 1 0) in an O₂-rich atmosphere directly to an increase in oxidation activity, as shown in Fig. 28. The surface roughening was attributed to the formation of a platinum oxide in the topmost layer. According to the Mars-van Krevelen mechanism, the platinum oxide serves as an oxygen reservoir, which is continuously reduced by reaction with CO and re-oxidized under the O₂-rich conditions to produce a steady-state reaction.

In this context, it is noteworthy that Over and co-workers (46,164–167) found the same types of Mars-van Krevelen mechanism for CO oxidation for ruthenium. Although the active surface was not characterized directly under high-pressure conditions in these investigations, it was found for the ruthenium(0001) surface, which forms a RuO₂(1 1 0) thin film in an oxygen-rich environment, that the activity of ruthenium as an oxidation catalyst is in fact primarily related to the RuO₂ phase.

Novel types of oxidation catalysts currently attract much attention both in industrial processes and in organic synthesis for the oxidation of alcohols to carbonyl

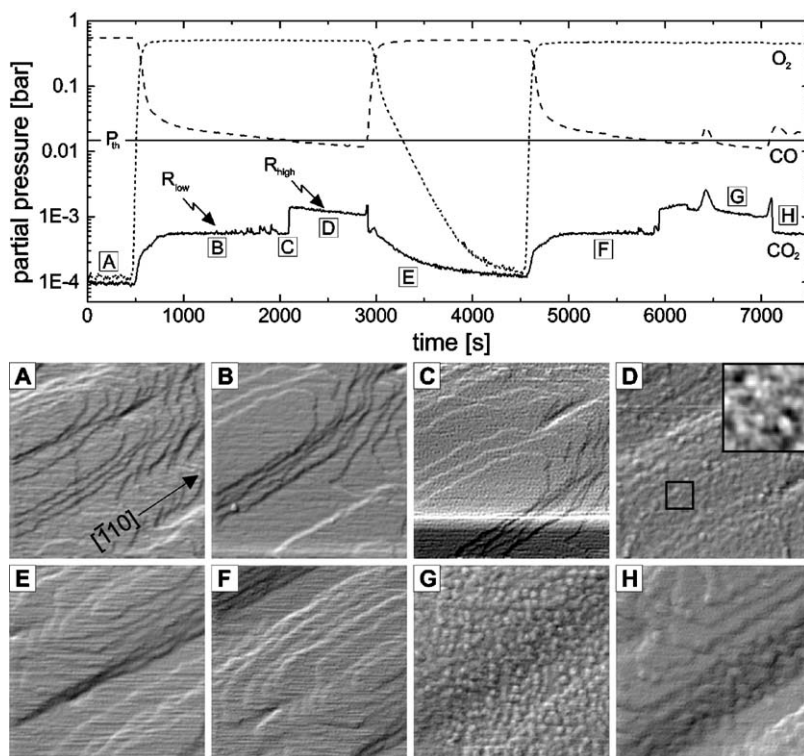
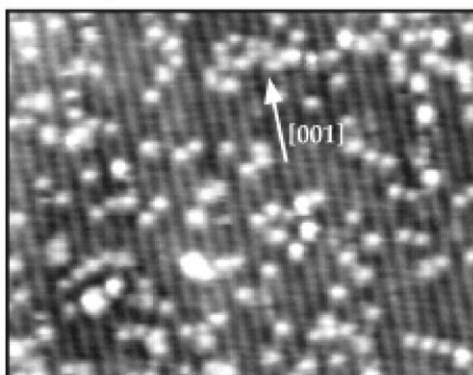


FIG. 28. Data recorded for CO oxidation on platinum(1 1 0) with an STM in a flow reactor. The upper panel shows mass spectrometer signals recorded directly from the reactor cell. The STM images show the surface morphology at different stages, corresponding to the curves in the mass spectrometer signal. High CO oxidation activity was correlated with the observation of a rough, oxidic platinum surface. With permission from Reference (163).

compounds, for which non-catalytic methods based on stoichiometric oxidants are mostly used today (168). It has been proposed that the oxidation of larger molecules may be controlled by the morphology of the RuO_2 surface, that is, by tuning the distance between adsorption site and the reactive oxygen for various facets of the RuO_2 surface (166). In investigations of the $\text{RuO}_2(1\ 1\ 0)$ surface, in particular, STM images (Fig. 29a) showed that CO spontaneously reacted with surface oxygen atoms (Fig 29a). After a subsequent annealing to 600 K, it was observed that the surface was even further reduced, and it was concluded that the CO had extracted oxygen from the rows to form CO_2 . The fully oxidized surface could subsequently be restored by exposure to O_2 to complete the cycle, and it was concluded that the close vicinity of adsorbed CO and reactive oxygen from the surface presents a favorable situation for the reaction, as no diffusion step would be involved in the

(a) Dosing of 10L CO at RT



(b) Annealing to 600K

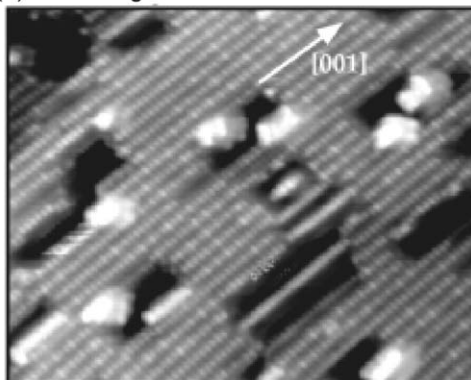


FIG. 29. (a) Atom-resolved STM images ($200\ \text{\AA} \times 200\ \text{\AA}$) of an ultrathin $\text{RuO}_2(1\ 1\ 0)$ film grown on a ruthenium(0001) surface after exposure to 10 L of CO at room temperature. The bright rows in the image reflect CO atoms that have replaced bridging oxygen atoms on the rutile RuO_2 surface, and the bright protrusions between rows reflect single CO molecules sitting on top of ruthenium atoms. (b) STM image ($200\ \text{\AA} \times 200\ \text{\AA}$) of the CO-dosed $\text{RuO}_2(1\ 1\ 0)$ surface after a subsequent annealing to 600 K. The adsorbed CO reduces surface even further thus creating holes (dark stripes). Images taken with permission from Reference (167).

reaction. It is, however, important to point out that this is yet another example for which it seems that the catalytically active surface is best characterized as a metal oxide rather than the pure metallic phase.

For many other systems, it has been shown that the traditional surface-science approach is applicable, that is, that raising the pressure is equivalent to lowering the temperature as long as the equilibrium structure remains kinetically accessible. This criterion implies that it is legitimate to extrapolate results obtained under the well-characterized and well-controlled UHV conditions to high pressures (17). For example, it was found for CO adsorption on platinum(110) and platinum(111) (18,161,169) and NO on palladium(111) (170) that high-coverage adsorbate structures formed under high-pressure conditions (1 bar) were also formed under low-temperature and low-pressure conditions.

C. ATOMIC FORCE MICROSCOPY OF INSULATING MATERIALS

Concurrent with the continued development of STM as a versatile tool for fundamental catalysis research, the atomic force microscope (AFM) is also beginning to find significant applications in catalysis research. The principle of the AFM is quite similar to that of the STM. Instead of taking advantage of the exponential decay of the tunneling current, the AFM responds to the forces between a sharp probe and the surface, and therefore the AFM does not require that the surface be conducting (171,172). Consequently, AFM seems to have some advantages as compared to the STM in the area of catalysis, because a range of insulating oxide materials, used as integral parts of many catalysts, can now be imaged in some cases even with atomic resolution (173–177). The AFM is thus ideally suited to the investigation of model catalysts on real insulating metal oxide supports, and by deposition of nanoclusters on these types of supports, it will eventually become possible to learn much more about the sintering of nanoparticles and metal–support interactions in general. So far, the stability and versatility of the AFM is, however, lacking relative to those characterizing the STM. By applying the AFM in the so-called non-contact mode (178), it recently became possible to obtain genuinely atom-resolved AFM images of point defects and molecules on metal and oxide surfaces. Many groups are today investigating how information about the chemical specificity and defects can be extracted from AFM images. There is no doubt that this breakthrough will come from an interplay between high-resolution AFM data and simulations of AFM images based on theoretical calculations (69,179).

VII. Synopsis and Perspective

STM has matured enormously since the development of the first microscope 20 years ago, an achievement for which Binnig and Rohrer were awarded the Nobel Prize in physics in 1986 (39,41). STM has emerged as a powerful technique for exploring surfaces at the atomic scale. This ability makes the STM unique in comparison to other surface-sensitive analytical techniques, and the progress of

STM for the investigation of surface phenomena has been quite astonishing in numerous areas of physical, chemical, and biological research.

STM instruments have evolved from a complicated homebuilt instrument sensitive to vibrations into a compact, rigid, stable variable-temperature microscope, available commercially at fairly low cost. The availability of the instrumentation for STM has led to a tremendous diversification of the application of the technique, and new areas of applications are constantly being developed.

One area in which STM has turned out to be a powerful and versatile tool is surface catalysis. According to the so-called surface-science approach, detailed investigations are made by applying the arsenal of modern physical methods to well-defined single-crystal surfaces as model systems, often under well-controlled high-vacuum conditions. This approach is capable of providing fundamental microscopic insight into the principles underlying the elementary steps of heterogeneous catalysis. The development of the STM has in particular enabled a direct atomic-scale view of active sites such as edges, kinks, or atomic defects, which turn out to be present in only low densities but nonetheless to dominate the catalytic properties in many cases. STM investigations of model systems more complex than single crystals have enabled us to bridge the materials gap; in particular, samples consisting of nanoclusters supported on flat conducting surfaces (e.g., thin oxide films) have pushed the model systems closer to real solid catalysis. The results of these investigations demonstrate that one cannot neglect the dispersed character of the active materials in catalysts and model them from the usually well-known bulk properties. Atomic-scale insight is essential, and the STM is an excellent tool to resolve structures on this scale of nanoclusters deposited on conducting substrates in general.

In this review, we have selected a few examples to illustrate how information at the atomic scale obtained by STM concerning the formation of surface alloys, wetting, and blocking of reactive step edges, and the identification of unique electronic states at the edges of nanoclusters, have provided sufficient insight to guide the preparation of new high-surface-area catalysts. This progress indicates that a new era in heterogeneous catalysis is within reach in the sense that the novel high-surface-area catalysts may be designed not only on the basis of traditional trial and error, but rather on the basis of detailed fundamental science. However, one should be aware of the fact that catalyst model systems investigated under well-controlled conditions may differ significantly from the real high-surface-area catalysts, both with regard to the nature of the surface morphology and the applied pressure range. Today, various routes are being developed to overcome the materials and pressure gaps, and it is likely that the STM will play a central role in the progress ahead. A number of new developments of the STM and AFM techniques are under way, and they have already shown promising results with great significance for fundamental investigations of catalysis.

Acknowledgments

We would like to thank our colleagues who have contributed in various ways to the work presented in this article, including M. Bollinger, I. Chorkendorff, B. S.

Clausen, S. Dahl, B. Hammer, K. Honkala, S. Helveg, E. Lægsgaard, M. Nyberg, J. K. Nørskov, J. Schnadt, I. Stensgaard, H. Topsøe, R. T. Vang, and E. K. Vestergaard. We also thank M. Salmeron, H. Over, J. Wintterlin, B. L. M. Hendriksen and J. W. M. Frenken for providing us with copies of their figures. The work was financed in part by the Danish Research Councils through a grant to iNANO, the Velux Foundation, and the Danish National Research Foundation. J.V.L. acknowledges financial support from the Danish Technical Research Council and the Carlsberg Foundation.

References

1. Ertl, G., Knözinger, H., and Weitkamp, J. (Eds.), "Handbook of Heterogeneous Catalysis." Vols. 1–5, VCH, Weinheim, 1997.
2. Somorjai, G.A., "Surface Chemistry and Catalysis." Wiley, New York, 1994.
3. Derouane, E.G., *Cattech* **5**, 214 (2001).
4. Ertl, G., and Freund, H.-J., *Phys. Today* **52**(1), 32 (1999).
5. Niemantsverdriet, J.W., "Spectroscopy in Catalysis." 2nd Edition, Wiley-VCH, Weinheim, 2000.
6. Goodman, D.W., *J. Phys. Chem.* **100**, 13090 (1996).
7. King, D.A., *Surf. Sci.* **299/300**, 678 (1994).
8. King, D.A., in "Dynamics of Surfaces and Reaction Kinetics in Heterogeneous Catalysis" (G.F. Froment, and K.C. Waugh, Eds.), Elsevier Science, Amsterdam, p. 79, 1997.
9. Gunter, P.L.J., Niemantsverdriet, J.W., Ribeiro, F.H., and Somorjai, G.A., *Catal. Rev.-Sci. Eng.* **39**, 77 (1997).
10. Sinfelt, J.H., *Surf. Sci.* **500**, 923 (2002).
11. Ertl, G., *Angew. Chem. Int. Ed.* **29**, 1219 (1990).
12. Ertl, G., Lee, S.B., and Weiss, M., *Surf. Sci.* **114**, 515 (1982).
13. Strongin, D.R., and Somorjai, G.A., *J. Catal.* **109**, 51 (1988).
14. Dumesic, J.A., and Trevino, A.A., *J. Catal.* **116**, 119 (1989).
15. Logadottir, A., Rod, T.H., Nørskov, J.K., Hammer, B., Dahl, S., and Jacobsen, C.J.H., *J. Catal.* **197**, 229 (2001).
16. Freund, H.-J., Kuhlenbeck, H., Libuda, J., Rupprechter, G., Bäumer, M., and Hamann, H., *Top. Catal.* **15**, 201 (2001).
17. Österlund, L., Rasmussen, P.B., Thostrup, P., Lægsgaard, E., Stensgaard, I., and Besenbacher, F., *Phys. Rev. Lett.* **86**, 460 (2001).
18. Vestergaard, E.K., Thostrup, P., An, T., Lægsgaard, E., Stensgaard, I., Hammer, B., and Besenbacher, F., *Phys. Rev. Lett.* **88**, 259601 (2002).
19. Stoltze, P., and Nørskov, J.K., *Phys. Rev. Lett.* **55**, 2502 (1985).
20. Valden, M., Lai, X., and Goodman, D.W., *Science* **281**, 1647 (1998).
21. Henry, C.R., *Surf. Sci. Rep.* **31**, 231 (1998).
22. Haruta, M., *Catal. Today* **36**, 153 (1997).
23. Campbell, C.T., *Surf. Sci. Rep.* **27**, 3 (1997).
24. Hansen, K.H., Worren, T., Stempel, S., Lægsgaard, E., Bäumer, M., Freund, H.-J., Besenbacher, F., and Stensgaard, I., *Phys. Rev. Lett.* **83**, 4120 (1999).
25. Bäumer, M., and Freund, H.-J., *Prog. Surf. Sci.* **61**, 127 (1999).
26. Freund, H.-J., *Surf. Sci.* **500**, 271 (2002).
27. Campbell, C.T., Parker, S.C., and Starr, D.E., *Science* **298**, 811 (2002).
28. Becker, C., von Bergmann, K., Rosenhahn, A., Schneider, J., and Wandelt, K., *Surf. Sci.* **486**, L443 (2001).
29. Perrot, E., Humbert, A., Piednoir, A., Chapon, C., and Henry, C.R., *Surf. Sci.* **445**, 407 (2000).
30. Topsøe, H., *Stud. Surf. Sci. Catal.* **130**, 1 (2000).
31. Hunger, M., and Weitkamp, J., *Angew. Chem. Int. Ed.* **40**, 2954 (2001).
32. Grunwaldt, J.D., and Clausen, B.S., *Top. Catal.* **18**, 37 (2002).

33. Banares, M.A., *Catal. Today* **100**, 71 (2005).
34. Koningsberger, D.C., Mojet, B.L., van Dorssen, G.E., and Ramaker, D.E., *Top. Catal.* **10**, 143 (2000).
35. Dellwig, T., Rupprechter, G., Unterhalt, H., and Freund, H.J., *Phys. Rev. Lett.* **85**, 776 (2000).
36. Boyes, E.D., and Gai, P.L., *Ultramicroscopy* **67**, 219 (1997).
37. Hansen, P.L., Wagner, J.B., Helveg, S., Rostrup-Nielsen, J.R., Clausen, B.S., and Topsøe, H., *Science* **295**, 2053 (2002).
38. Hansen, T.W., Wagner, J.B., Hansen, P.L., Dahl, S., Topsøe, H., and Jacobsen, C.J.H., *Science* **294**, 1508 (2001).
39. Binnig, G., Rohrer, H., Gerber, C., and Weibel, E., *Phys. Rev. Lett.* **49**, 57 (1982).
40. Binnig, G., Rohrer, H., Gerber, C., and Weibel, E., *Surf. Sci.* **131**, L379 (1983).
41. Binnig, G., and Rohrer, H., *Rev. Mod. Phys.* **59**, 615 (1987).
42. Zambelli, T., Wintterlin, J., Trost, J., and Ertl, G., *Science* **273**, 1688 (1996).
43. Wintterlin, J., Völkening, S., Janssens, T.V.W., Zambelli, T., and Ertl, G., *Science* **278**, 1931 (1997).
44. Renisch, S., Schuster, R., Wintterlin, J., and Ertl, G., *Phys. Rev. Lett.* **82**, 3839 (1999).
45. Mitsui, T., Rose, M.K., Fomin, E., Ogletree, D.F., and Salmeron, M., *Nature* **422**, 705 (2003).
46. Over, H., Kim, Y.D., Seitsonen, A.P., Wendt, S., Lundgren, E., Schmid, M., Varga, P., Morgante, A., and Ertl, G., *Science* **287**, 1474 (2000).
47. Zambelli, T., Barth, J.V., Wintterlin, J., and Ertl, G., *Nature* **390**, 495 (1997).
48. Schaub, R., Wahlström, E., Rønna, A., Lægsgaard, E., Stensgaard, I., and Besenbacher, F., *Science* **299**, 377 (2003).
49. Schaub, R., Thosttrup, R., Lopez, N., Lægsgaard, E., Stensgaard, I., Nørskov, J.K., and Besenbacher, F., *Phys. Rev. Lett.* **87**, 6104 (2001).
50. Wintterlin, J., *Adv. Catal.* **45**, 131 (2000).
51. Yeung, K.L., and Yao, N., *J. Nanosci. Nanotechnol.* **4**, 647 (2004).
52. Santra, A.K., and Goodman, D.W., *J. Phys. Cond. Matt.* **15**, R31 (2003).
53. Chen, J.C., "Introduction to Scanning Tunneling Microscopy." Oxford University Press, Oxford, 1993.
54. Wiesendanger, R., "Scanning Probe Microscopy and Spectroscopy." Cambridge University Press, Cambridge, 1994.
55. Lægsgaard, E., Besenbacher, F., Mortensen, K., and Stensgaard, I., *J. Microsc.* **152**, 663 (1988).
56. Bonnell, D.A. (Ed.), "Scanning Tunneling Microscopy and Spectroscopy.", 2nd Edition, Wiley-VCH, New York, 2001.
57. Besenbacher, F., *Rep. Prog. Phys.* **59**, 1737 (1996).
58. Bardeen, J., *Phys. Rev. Lett.* **6**, 57 (1961).
59. Tersoff, J., and Hamann, D.R., *Phys. Rev. B* **31**, 805 (1985).
60. Tersoff, J., and Hamann, D.R., *Phys. Rev. Lett.* **50**, 1998 (1983).
61. Lang, N.D., *Phys. Rev. Lett.* **55**, 230 (1985).
62. Klink, C., Olesen, L., Besenbacher, F., Stensgaard, I., Lægsgaard, E., and Lang, N.D., *Phys. Rev. Lett.* **71**, 4350 (1993).
63. Eigler, D.M., Weiss, P.S., Schweizer, E.K., and Lang, N.D., *Phys. Rev. Lett.* **66**, 1189 (1991).
64. Helveg, S., Lorensen, H.T., Horch, S., Lægsgaard, E., Stensgaard, I., Jacobsen, K.W., Nørskov, J.K., and Besenbacher, F., *Surf. Sci.* **430**, L533 (1999).
65. Pedersen, M.Ø., Österlund, L., Mortensen, J.J., Mavrikakis, M., Hansen, L.B., Stensgaard, I., Lægsgaard, E., Nørskov, J.K., and Besenbacher, F., *Phys. Rev. Lett.* **84**, 4898 (2000).
66. Hofer, W.A., Fisher, A.J., Wolkow, R.A., and Grütter, P., *Phys. Rev. Lett.* **87**, 236104 (2001).
67. Hammer, B., and Nørskov, J.K., in "Chemisorption and Reactivity on Supported Clusters and Thin Films" (R.M. Lambert and G. Pacchioni, Eds.), Kluwer Academic Publishers, Dordrecht, The Netherlands, p. 285, 1997.
68. Hammer, B., and Nørskov, J.K., *Adv. Catal.* **45**, 71 (2000).
69. Hofer, W.A., Foster, A.S., and Shluger, A.L., *Rev. Mod. Phys.* **75**, 1287 (2003).
70. Sautet, P., *Chem. Rev.* **97**, 1097 (1997).
71. Sarid, D., Henson, T.D., Armstrong, N.R., and Bell, L.S., *Appl. Phys. Lett.* **52**, 2252 (1988).
72. Rostrup-Nielsen, J.R., Sehested, J., and Nørskov, J.K., *Adv. Catal.* **47**, 65 (2002).

73. Helveg, S., Lopez-Cartes, C., Sehested, J., Hansen, P.L., Clausen, B.S., Rostrup-Nielsen, J.R., Abild-Pedersen, F., and Nørskov, J.K., *Nature* **427**, 426 (2004).
74. Bengaard, H.S., Nørskov, J.K., Sehested, J., Clausen, B.S., Nielsen, L.P., Molenbroek, A.M., and Rostrup-Nielsen, J.R., *J. Catal.* **209**, 365 (2002).
75. Ponec, V., *Appl. Catal. A* **222**, 31 (2001).
76. Nielsen, L.P., Besenbacher, F., Stensgaard, I., Lægsgaard, E., Engdahl, C., Stoltze, P., Jacobsen, K.W., and Nørskov, J.K., *Phys. Rev. Lett.* **71**, 754 (1993).
77. Besenbacher, F., Nielsen, L.P., and Sprunger, P.T., in "The Chemical Physics of Solid Surfaces and Heterogeneous Catalysis" (D.A. King, and D.P. Woodruff, Eds.), Elsevier, Amsterdam, 1996.
78. Jacobsen, J., Nielsen, L.P., Besenbacher, F., Stensgaard, I., Lægsgaard, E., Rasmussen, T., Jacobsen, K.W., and Nørskov, J.K., *Phys. Rev. Lett.* **75**, 489 (1995).
79. Besenbacher, F., Chorkendorff, I., Clausen, B.S., Hammer, B., Molenbroek, A.M., Nørskov, J.K., and Stensgaard, I., *Science* **279**, 1913 (1998).
80. Taylor, H.S., *Proc. R Soc. London, Ser. A* **108**, 105 (1925).
81. Yates, J.T., *J. Vac. Sci. Technol. A* **13**, 1359 (1995).
82. Dahl, S., Logadottir, A., Egeberg, R.C., Larsen, J.H., Chorkendorff, I., Törnquist, E., and Nørskov, J.K., *Phys. Rev. Lett.* **83**, 1814 (1999).
83. Nørskov, J.K., Bligaard, T., Logadottir, A., Bahn, S., Hansen, L.B., Bollinger, M., Bengaard, H., Hammer, B., Sljivancanin, Z., Mavrikakis, M., Xu, Y., Dahl, S., and Jacobsen, C.J.H., *J. Catal.* **209**, 275 (2002).
84. Vang, R.T., Honkala, K., Dahl, S., Vestergaard, E.K., Schnadt, J., Lægsgaard, E., Clausen, B.S., Nørskov, J.K., and Besenbacher, F., *Nat. Mater.* **4**, 160 (2005).
85. Topsøe, H., Clausen, B.S., and Massoth, F.E., in "Hydrotreating Catalysis. Catalysis—Science and Technology." (J.R. Anderson, and M. Boudart, Eds.), Vol. 11, Springer, Berlin, 1996.
86. Landau, M.V., *Catal. Today* **36**, 393 (1997).
87. Grisham, J.L., *Chem. Eng. News* **23**, 21 (1999).
88. Prins, R., in "Handbook of Heterogeneous Catalysis" (G. Ertl, H. Knözinger, and J. Weitkamp, Eds.), VHC, Weinheim, p. 1908, 1997.
89. Whitehurst, D.D., Isoda, T., and Mochida, I., *Adv. Catal.* **42**, 345 (1998).
90. Kabe, T., Ishihara, A., and Qian, W., "Hydrodesulfurization and Hydrogenation—Chemistry and Engineering." Wiley-VCH, Kodansha, 1999.
91. Gosselink, J.W., *Cattech* **4**, 127 (1998).
92. Parham, T.G., and Merrill, R.P., *J. Catal.* **85**, 295 (1984).
93. Clausen, B.S., Lengeler, B., Candia, R., Als-Nielsen, J., and Topsøe, H., *Bull. Soc. Chim. Belg.* **90**, 1249 (1981).
94. Boudart, M., Dalla Betta, R.A., Fogger, K., Löffler, D.G., and Samant, M.G., *Science* **228**, 717 (1985).
95. Salmeron, M., Somorjai, G.A., Wold, A., Chianelli, R., and Liang, K.S., *Chem. Phys. Lett.* **90**, 105 (1982).
96. Daage, M., and Chianelli, R.R., *J. Catal.* **149**, 414 (1994).
97. Topsøe, H., and Clausen, B.S., *Appl. Catal.* **25**, 273 (1986).
98. Prins, R., de Beer, V.H.J., and Somorjai, G.A., *Catal. Rev.-Sci. Eng.* **31**, 1 (1989).
99. Lipsch, J.M.J., and Schuit, G.C.A., *J. Catal.* **15**, 179 (1969).
100. Schuit, G.C.A., and Gates, B.C., *AIChE J.* **19**, 417 (1973).
101. Topsøe, H., Clausen, B.S., Topsøe, N.Y., Nørskov, J.K., Ovesen, C.V., and Jacobsen, C.J.H., *Bull. Soc. Chim. Belg.* **104**, 283 (1995).
102. Kushmerick, J.G., and Weiss, P.S., *J. Phys. Chem. B* **102**, 10094 (1998).
103. Kushmerick, J.G., Kandel, S.A., Johnson, J.A., and Weiss, P.S., *J. Phys. Chem. B* **104**, 2980 (2000).
104. Komiyama, M., Kiyohara, K., Li, Y.J., Fujikawa, T., Ebihara, T., Kubota, T., and Okamoto, Y., *J. Mol. Catal. A* **215**, 143 (2004).
105. Chen, D.A., and Friend, C.M., *Surf. Sci.* **371**, 131 (1997).
106. Li, S.Y., Rodriguez, J.A., Hrbek, J., Huang, H.H., and Xu, G.-Q., *Surf. Sci.* **366**, 29 (1996).
107. Kuhn, M., and Rodriguez, J.A., *Surf. Sci.* **355**, 85 (1996).
108. Clark, P.G. Jr., and Friend, C.M., *J. Chem. Phys.* **111**, 6991 (1999).

109. Gellman, A.J., Farias, M.H., Salmeron, M., and Somorjai, G.A., *Surf. Sci.* **136**, 217 (1984).
110. Dunphy, J.C., Sautet, P., Ogletree, D.F., and Salmeron, M., *J. Vac. Sci. Tech. A* **11**, 1975 (1993).
111. Salmeron, M., Somorjai, G.A., and Chianelli, R.R., *Surf. Sci.* **127**, 526 (1983).
112. Ho, K.-M., and Bohnen, K.P., *Phys. Rev. Lett.* **59**, 1833 (1987).
113. Fiorentini, V., Methfessel, M., and Scheffler, M., *Phys. Rev. Lett.* **71**, 1051 (1993).
114. Barth, J.V., Brune, H., Ertl, G., and Behm, R., *Phys. Rev. B* **42**, 9307 (1990).
115. Chambliss, D.D., Wilson, R.J., and Chiang, S., *Phys. Rev. Lett.* **66**, 1721 (1991).
116. Meyer, J.A., Baikie, I.D., Kopatzki, E., and Behm, R.J., *Surf. Sci.* **365**, L647 (1996).
117. Böhringer, M., Morgenstern, K., Schneider, W.-D., Berndt, R., Mauri, F., Vita, A.D., and Car, R., *Phys. Rev. Lett.* **83**, 324 (1999).
118. Helveg, S., Lauritsen, J.V., Lægsgaard, E., Stensgaard, I., Nørskov, J.K., Clausen, B.S., Topsøe, H., and Besenbacher, F., *Phys. Rev. Lett.* **84**, 951 (2000).
119. Lauritsen, J.V., Helveg, S., Lægsgaard, E., Stensgaard, I., Clausen, B.S., Topsøe, H., and Besenbacher, F., *J. Catal.* **197**, 1 (2001).
120. Dickinson, R.G., and Pauling, L., *J. Am. Chem. Soc.* **45**, 1466 (1923).
121. Bollinger, M.V., Lauritsen, J.V., Jacobsen, K.W., Nørskov, J.K., Helveg, S., and Besenbacher, F., *Phys. Rev. Lett.* **87**, 196803 (2001).
122. Bollinger, M.V., Jacobsen, K.W., and Nørskov, J.K., *Phys. Rev. B* **67**, 085410 (2003).
123. Altibelli, A., Joachim, C., and Sautet, P., *Surf. Sci.* **367**, 209 (1996).
124. Kobayashi, K., and Yamauchi, J., *Phys. Rev. B* **51**, 17085 (1995).
125. Byskov, L.S., Hammer, B., Nørskov, J.K., Clausen, B.S., and Topsøe, H., *Catal. Lett.* **47**, 177 (1997).
126. Raybaud, P., Hafner, J., Kresse, G., Kasztelan, S., and Toulhoat, H., *J. Catal.* **189**, 129 (2000).
127. Raybaud, P., Hafner, J., Kresse, G., and Toulhoat, H., *Surf. Sci.* **407**, 237 (1998).
128. Byskov, L.S., Nørskov, J.K., Clausen, B.S., and Topsøe, H., *J. Catal.* **187**, 109 (1999).
129. Kam, K.K., and Parkinson, B.A., *J. Phys. Chem.* **86**, 463 (1982).
130. Lauritsen, J.V., Bollinger, M.V., Lægsgaard, E., Jacobsen, K.W., Nørskov, J.K., Clausen, B.S., Topsøe, H., and Besenbacher, F., *J. Catal.* **221**, 510 (2004).
131. Lauritsen, J.V., Nyberg, M., Nørskov, J.K., Clausen, B.S., Topsøe, H., Lægsgaard, E., and Besenbacher, F., *J. Catal.* **224**, 94 (2004).
132. Tarbuck, T.L., McCrea, K.R., Logan, J.W., Heiser, J.L., and Bussell, M.E., *J. Phys. Chem. B* **102**, 7845 (1998).
133. Chianelli, R.R., Berhault, G., Raybaud, P., Kasztelan, S., Hafner, J., and Toulhoat, H., *Appl. Catal. A* **227**, 83 (2002).
134. Wivel, C., Candia, R., Clausen, B.S., Mørup, S., and Topsøe, H., *J. Catal.* **68**, 453 (1981).
135. Topsøe, H., Clausen, B.S., Candia, R., Wivel, C., and Mørup, S., *J. Catal.* **68**, 433 (1981).
136. Topsøe, H., and Clausen, B.S., *Catal. Rev.-Sci. Eng.* **26**, 395 (1984).
137. Niemann, W., Clausen, B.S., and Topsøe, H., *Catal. Lett.* **4**, 355 (1990).
138. Louwers, S.P.A., and Prins, R., *J. Catal.* **133**, 94 (1992).
139. Bouwens, S.M.A.M., van Veen, J.A.R., Koningsberger, D.C., de Beer, V.H.J., and Prins, R., *J. Phys. Chem.* **95**, 123 (1991).
140. Raybaud, P., Hafner, J., Kresse, G., Kasztelan, S., and Toulhoat, H., *J. Catal.* **190**, 128 (2000).
141. Lee, H.C., and Butt, J.B., *J. Catal.* **49**, 320 (1977).
142. LaVopa, V., and Satterfield, C.N., *J. Catal.* **110**, 375 (1988).
143. Prins, R., *Adv. Catal.* **46**, 399 (2002).
144. Hinnemann, B., Nørskov, J.K., and Topsøe, H., *J. Phys. Chem. B* **109**, 2245 (2005).
145. Zeuthen, P., and Skyum, L., *Hydrocarbon Eng.* **11**, 65 (2004).
146. Besenbacher, F., Lægsgaard, E., and Stensgaard, I., *Mater. Today* **26** (2005).
147. Rot, M.J., Crama, L., Schakel, P., van Tol, E., van Velzen-Williams, G., Overgauw, C.F., ter Horst, H., Dekker, H., Okhuijsen, B., Seynen, M., Vijftigchild, A., Han, P., Katan, A.J., Schoots, K., Schumm, R., van Loo, W., Oosterkamp, T.H., and Frenken, J.W.M., *Rev. Sci. Instrum.* **5**, 76 (2005).
148. Wintterlin, J., Trost, J., Renisch, S., Schuster, R., Zambelli, T., and Ertl, G., *Surf. Sci.* **394**, 159 (1997).
149. Linderoth, T.R., Horch, S., Lægsgaard, E., Stensgaard, I., and Besenbacher, F., *Phys. Rev. Lett.* **78**, 4978 (1997).

150. Horch, S., Lorenzen, H.T., Helveg, S., Lægsgaard, E., Stensgaard, I., Nørskov, J.K., Jacobsen, K.W., and Besenbacher, F., *Nature* **398**, 134 (1999).
151. Völkening, S., Bedürftig, K., Jacobi, K., Wintterlin, J., and Ertl, G., *Phys. Rev. Lett.* **83**, 2672 (1999).
152. Sachs, C., Hildebrand, M., Völkening, S., Wintterlin, J., and Ertl, G., *Science* **293**, 1635 (2001).
153. Su, X., Cremer, P.S., Shen, Y.R., and Somorjai, G.A., *J. Am. Chem. Soc.* **119**, 3994 (1997).
154. Cremer, P.S., Su, X.C., Somorjai, G.A., and Shen, Y.R., *J. Mol. Catal. A* **131**, 225 (1998).
155. McIntyre, B.J., Salmeron, M., and Somorjai, G.A., *J. Vac. Sci. Technol. A* **11**, 1964 (1993).
156. Rasmussen, P.B., Hendriksen, B.L.M., Zeijlemaker, H., Ficke, H.G., and Frenken, J.W.M., *Rev. Sci. Instrum.* **69**, 3879 (1998).
157. Jensen, J.A., Rider, K.B., Chen, Y., Salmeron, M., and Somorjai, G.A., *J. Vac. Sci. Technol. B* **17**, 1080 (1999).
158. Lægsgaard, E., Österlund, L., Thostrup, P., Rasmussen, P.B., Stensgaard, I., and Besenbacher, F., *Rev. Sci. Instrum.* **72**, 3537 (2001).
159. Kolmakov, A., and Goodman, D.W., *Rev. Sci. Instrum.* **74**, 2444 (2003).
160. Rössler, M., Geng, P., and Wintterlin, J., *Rev. Sci. Instrum.* **76**, 023705 (2005).
161. Thostrup, P., Vestergaard, E.K., An, T., Laegsgaard, E., and Besenbacher, F., *J. Chem. Phys.* **118**, 3724 (2003).
162. Rider, K.B., Hwang, K.S., Salmeron, M., and Somorjai, G.A., *J. Am. Chem. Soc.* **124**, 5588 (2002).
163. Hendriksen, B.L.M., and Frenken, J.W.M., *Phys. Rev. Lett.* **89**, 046101 (2002).
164. Over, H., Seitsonen, A.P., Lundgren, E., Schmid, M., and Varga, P., *J. Am. Chem. Soc.* **123**, 11807 (2001).
165. Over, H., and Muhler, M., *Prog. Surf. Sci.* **72**, 3 (2003).
166. Over, H., Knapp, M., Lundgren, E., Seitsonen, A.P., Schmid, M., and Varga, P., *ChemPhysChem* **5**, 167 (2004).
167. Over, H., Seitsonen, A.P., Lundgren, E., Schmid, M., and Varga, P., *Surf. Sci.* **515**, 143 (2002).
168. Yamaguchi, K., and Mizuno, N., *Angew Chem. Int. Ed.* **41**, 4538 (2002).
169. Longwitz, S.R., Schnadt, J., Vestergaard, E.K., Vang, R.T., Lægsgaard, E., Stensgaard, I., Brune, H., and Besenbacher, F., *J. Phys. Chem. B* **108**, 14497 (2004).
170. Vang, R.T., Wang, J.G., Knudsen, J., Schnadt, J., Lægsgaard, E., Stensgaard, I., and Besenbacher, F., *J. Phys. Chem. B* **109**, 14262 (2005).
171. Binnig, G., Quate, C.F., and Gerber, C., *Phys. Rev. Lett.* **56**, 930 (1986).
172. García, R., and Pérez, R., *Surf. Sci. Rep.* **47**, 197 (2002).
173. Barth, C., and Reichling, M., *Nature* **414**, 54 (2001).
174. Barth, C., and Henry, C.R., *Phys. Rev. Lett.* **91**, 196102 (2003).
175. Namai, Y., Fukui, K.I., and Iwasawa, Y., *Catal. Today* **85**, 79 (2003).
176. Fukui, K., Onishi, H., and Iwasawa, Y., *Phys. Rev. Lett.* **79**, 4202 (1997).
177. Gritschneider, S., Namai, Y., Iwasawa, Y., and Reichling, M., *Nanotechnology* **16**, S41 (2005).
178. Giessibl, F.J., *Science* **267**, 68 (1995).
179. Foster, A.S., Gal, A.Y., Airaksinen, J.M., Pakarinen, O.H., Lee, Y.J., Gale, J.D., Shluger, A.L., and Nieminen, R.M., *Phys. Rev. B* **68**, 195420 (2003).
180. Lauritsen, J.V., Nyberg, M., Vang, R.T., Bollinger, M.V., Clausen, B.S., Topsøe, H., Jacobsen, K.W., Besenbacher, F., Lægsgaard, E., Nørskov, J.K., and Besenbacher, F., *Nanotechnology* **14**, 385 (2003).

Characterization of Solid Catalysts in the Functioning State by Nuclear Magnetic Resonance Spectroscopy

M. HUNGER

Institute of Chemical Technology, University of Stuttgart, D-70550 Stuttgart, Germany

and

W. WANG

State Key Laboratory of Applied Organic Chemistry, Lanzhou University, 730000 Gansu, P.R. China

This chapter is a review of techniques and applications of solid-state nuclear magnetic resonance (NMR) spectroscopy for investigations of solid catalysts, with a strong emphasis on investigations of catalysts in the functioning state. The techniques allow investigations of both the chemical reactions as well as changes in the catalysts taking place inside the NMR spectrometer. The experimental techniques are suitable for magic-angle spinning (MAS) NMR spectroscopy under batch reaction conditions, for example, with a sample of catalyst powder in a sealed glass ampoule or a gas-tight MAS NMR rotor, or under flow conditions, for example, with the catalyst particles in an MAS NMR rotor reactor. The former technique has the advantage of low cost and commercially accessible equipment, and the latter technique allows measurements under conditions close to those of industrial processes. Representative applications described in this review include investigations of the fate of isotopic labels allowing the indirect characterization of the nature of transition states and reaction pathways by isotope scrambling and the determination of activation energies of the reactions in the pathways. Other examples include investigations of organic deposits, surface complexes, and reaction intermediates formed in the pores of zeolite catalysts under continuous- and stopped-flow reaction conditions. Further applications include investigations of changes in the local structure of framework atoms and surface sites in microporous catalysts resulting from adsorption and desorption of probe molecules and reactants.

Abbreviations: CAVERN, cryogenic adsorption vessel enabling rotor nestling; CF, continuous-flow; CRAMPS, combined rotation and multiple-pulse spectroscopy; Cs,NaY, zeolite Na-Y (FAU) exchanged with cesium cations; CP, cross polarization; CT, central transition; DABCO, 1,4-diazabicyclo-(2,2,2)-octane; DCAA, dichloroacetic acid; DCAC, dichloroacetyl chloride; DFT, density functional theory; DME, dimethyl ether; DOR, double-oriented rotation; GRASSHopper, gas reactor and solid sample hopper; H-EMT, H-form of zeolite with structure type EMT; H-GaMFI, H-form of gallosilicate with structure type MFI; HPDEC, high-power proton decoupling; H-SAPO-5, H-form of a microporous silicoaluminophosphate with structure type AFI; H-SAPO-11, H-form of a microporous silicoaluminophosphate with structure type AEL; H-SAPO-34, H-form of a microporous silicoaluminophosphate with structure type CHA; HY, H-form of zeolite with structure type FAU; HZSM-5, H-form of zeolite with structure type MFI; HZSM-11, H-form of zeolite with structure type MEL; HZSM-12, H-form of

zeolite with structure type MTW; HZSM-23, H-form of zeolite with structure type MTT; MAH, magic-angle hopping; MAS, magic-angle spinning; MPi, methylpiperidine; MPy, methylpyrrolidine; MQMAS, multiple-quantum magic-angle spinning; MTBE, methyl *tert*-butyl ether; MTHC, methanol to hydrocarbons; MTO, methanol to olefin; MTG, methanol to gasoline; NaY, Na-form of zeolite with structure type FAU; NMR, nuclear magnetic resonance; NMA, *N*-methylaniline; NNDMA, *N*, *N*-dimethylaniline; PA, proton affinity; ppm, parts per million; PVG, porous Vycor[®] glass; SF, stopped-flow; SPINOE, spin polarization-induced nuclear Overhauser effect; SZA, sulfated zirconia; TCE, trichloroethylene; TEA, triethylamine; TRAPDOR, transfer of population in double resonance; TTAA, tetramethyldibenzotetraaza annulene; USY, ultra-stabilized zeolite with structure type FAU; UV/Vis, ultraviolet visible; Y, zeolite with structure type FAU; A_{CP} , intensity of the signal of the spins S measured with cross polarization; A_{SP} , intensity of the signal of the spins S measured with single-pulse excitation; B_0 , flux density of the external magnetic field; C_{QCC} , quadrupole coupling constant; E_A , activation energy; eQ , electric quadrupole moment; $f(v)$, normalized line shape function; \mathbf{H} , Hamiltonian; h , Planck's constant; \hbar , Planck's constant h divided by 2π ; I , spin I ; k , order of the spinning sideband; k , Boltzmann constant; m , magnetic spin quantum number; M_0 , magnetization of a spin ensemble; M_2 , second moment; N_I , N_S , numbers of nuclei with spins I and S , respectively; r_{ij} , internuclear distance between the nuclei i and j ; S , spin S ; t_{hop} , hop time in an MAH experiment; T , temperature; T_1 , spin-lattice relaxation time; V_{ii} , principal values of the tensor of the electric field gradient; α_I , parameter given by the value of spin I and its magnetic spin quantum number; γ , magnetogyric ratio; δ , chemical shift; ϵ , parameter given by the numbers of spins I and S and their parameters α_I and α_S ; δ_{ii} , principal values of the chemical shift tensor; $\Delta\sigma$, asymmetry parameter of the chemical shift tensor; $\Delta v_{1/2}$, full-width at half-maximum of a statically recorded signal; $\Delta v_{1/2}^{MAS}$, residual linewidth for magic-angle spinning; η_{CSA} , anisotropy of the chemical shift tensor; η_Q , asymmetry parameter of the electric field gradient tensor; θ , angle between the external magnetic field and the sample spinning axis; θ_m , magic angle of $\theta = 54.74^\circ$; μ_0 , permeability of vacuum; ν , frequency; ν_{cg} , frequency at the center of gravity; ν_{qs} , second-order quadrupole shift; ν_0 , Larmor frequency; σ , shielding constant; τ_{CP} , duration of the contact period during a cross polarization experiment.

I. Introduction

Many of the atoms in the frameworks of solid catalysts and in the reactants adsorbed on them have isotopes with nuclear spin, which renders these isotopes NMR-active. ^1H , ^{13}C , ^{15}N , and ^{31}P are suitable isotopes allowing the investigation of a wide variety of reactants. As a consequence of their nuclear spin of $I = 1/2$, sufficient line narrowing is reached by the conventional magic-angle spinning (MAS) NMR technique. Similar conditions exist for isotopes such as ^1H , ^{29}Si , and ^{31}P occurring in the frameworks and in surface sites of solid catalysts. Isotopes with a nuclear spin of $I > 1/2$, such as ^{17}O , ^{23}Na , ^{27}Al , and ^{31}Ga , are characterized by an electric quadrupole moment. These nuclei are involved in quadrupolar interactions with the electric field gradient caused by the surrounding atoms. The averaging of interactions may require the application of sophisticated solid-state NMR techniques, such as double-oriented rotation (DOR) or multiple-quantum MAS (MQMAS) NMR, making the investigation of quadrupole nuclei more complicated than that of ^1H , ^{13}C , ^{15}N , and ^{31}P . In all the above-mentioned cases, however, NMR spectroscopy is a powerful tool for studies of working catalysts, their surface sites, and the reactants and adsorbates occurring on their surface under reaction conditions.

This review starts with an introduction to the principles and techniques of solid-state NMR spectroscopy and the description of the most important experimental approaches for NMR investigations of solid catalysts in the working state (Sections II and III). Section IV is a summary of experimental approaches to the characterization of transition states of acid-catalyzed reactions under batch reaction conditions.

Section V is focused on the activation of saturated hydrocarbons on solid catalysts, and Section VI is a description of the application of a more sophisticated batch approach for NMR spectroscopic investigations of photocatalytic reactions on solid catalysts. The application of NMR spectroscopy to investigate working catalysts under flow conditions for the characterization of surface sites and framework atoms in zeolites during adsorption and desorption or dehydration processes is described in Section VII. The work presented in Sections VIII–X has the goal of explaining the synthesis of methyl *tert*-butyl ether (MTBE), the alkylation of aromatic compounds, and the conversion of methanol into hydrocarbons on zeolite catalysts. These investigations were performed with modern techniques of NMR spectroscopy by use of continuous- (CF) and stopped-flow (SF) protocols. Industrial processes are frequently operated under flow conditions. To cope with such continuous process schemes, a growing number of research groups are developing novel NMR techniques allowing investigations of working catalyts under flow conditions.

In view of the breadth of NMR spectroscopy in heterogeneous catalysis, no attempt has been made in this review to cover the field comprehensively; the reader is directed to other reviews for complementary information (1–9). This review is focused on zeolite catalysts, in part because of their crystalline structures and in part because of their widespread use in industrial catalysis.

II. Principles of Solid-State NMR Spectroscopy

NMR spectroscopy in heterogeneous catalysis requires the application of solid-state techniques. In general, liquids and gases cause narrow NMR signals, because the influence of spatially anisotropic magnetic interactions on the linewidth is averaged to zero by thermal motions, leading to an isotropic reorientation of the compounds under investigation. In contrast, materials such as solid catalysts and adsorbate complexes exhibit NMR signals that are strongly broadened by magnetic interactions. Informative structural information can be obtained by the analysis of these spectra, but resolution of the NMR signals of nuclei in various compounds and local structures requires sophisticated experimental techniques allowing the averaging of these interactions.

A. SOLID-STATE INTERACTIONS OF NUCLEAR SPINS

The dominant interactions of nuclei having spin I that are responsible for the broadening of solid-state NMR lines and for their characteristic line shapes are described by the total Hamiltonian:

$$\widehat{H} = \widehat{H}_{\text{II}} + \widehat{H}_{\text{IS}} + \widehat{H}_{\text{CSA}} + \widehat{H}_{\text{Q}} \quad (1)$$

where \widehat{H}_{II} , \widehat{H}_{IS} , \widehat{H}_{CSA} , and \widehat{H}_{Q} are the Hamiltonians of the homonuclear and the heteronuclear magnetic dipole–dipole interaction, the chemical shift anisotropy, and the quadrupolar interaction, respectively. Analytical expressions for these Hamiltonians are given, for example, in refs. (10–14). For nuclei with a spin $I = 1/2$, only the first three Hamiltonians are valid. For nuclei with a spin $I > 1/2$, which

exhibit an electric quadrupole moment interacting with the electric field gradient at the site of the nuclei, the Hamiltonian $\hat{\mathbf{H}}_Q$ also affects the solid-state NMR signals.

The center of gravity, ν_{cg} , of an NMR signal occurs at the frequency of

$$\nu_{\text{cg}} = \int_0^{\infty} \nu f(\nu) d\nu \quad (2)$$

where $f(\nu)$ is the normalized line shape function. The value of the frequency ν_{cg} may deviate from the Larmor frequency,

$$\nu_0 = \frac{\gamma_I}{2\pi} B_0, \quad (3)$$

which is the resonance frequency of an isolated and non-shielded nucleus with the magnetogyric ratio γ_I . B_0 denotes the magnetic flux density of the external magnetic field.

The superposition of the different magnetic interactions complicates the interpretation and calculation of the resulting normalized line shape function, $f(\nu)$. It is therefore advantageous to make use of the so-called second moment M_2 as a measure of the linewidth of the solid-state NMR signals. The full-width at half-maximum of an NMR signal in frequency units, also called the static linewidth, is

$$\Delta\nu_{1/2} = \frac{1}{\pi} \sqrt{2 \ln 2} \sqrt{M_2} \quad (4)$$

for Gaussian lines. The second moment, M_2 , with respect to the center of gravity, ν_{cg} , of the signal is defined by

$$M_2 = 4\pi^2 \int_0^{\infty} (\nu - \nu_{\text{cg}})^2 f(\nu) d\nu. \quad (5)$$

The second moments of NMR signals in the observable spectral range can be calculated, provided that the local structure and the type of the internal magnetic interactions of the spin ensemble under study are known. According to the total Hamiltonian given in Eq. (1), it follows that

$$M_2 = M_2^{\text{II}} + M_2^{\text{IS}} + M_2^{\text{CSA}} + M_2^{\text{Q,CT}} \quad (6)$$

with

$$M_2^{\text{II}} = \frac{3}{5} \left(\frac{\mu_0}{4\pi} \right)^2 \gamma_I^4 \hbar^2 I(I+1) \frac{1}{N_I} \sum_{i \neq j}^{N_I} r_{ij}^{-6}, \quad (7)$$

$$M_2^{\text{IS}} = \frac{4}{15} \left(\frac{\mu_0}{4\pi} \right)^2 \gamma_I^2 \gamma_S^2 \hbar^2 S(S+1) \frac{1}{N_I} \sum_{j=1}^{N_I} \sum_{k=1}^{N_S} r_{ij}^{-6}, \quad (8)$$

$$M_2^{\text{CSA}} = \frac{4}{45} \gamma_I^2 B_0^2 \Delta\sigma^2 \left(1 + \frac{1}{3} \eta_{\text{CSA}}^2 \right), \quad (9)$$

$$M_2^{\text{Q,CT}} = \frac{92\pi^2}{7} \nu_{\text{qs}}^2. \quad (10)$$

Here, h denotes Planck's constant h divided by 2π , and μ_0 is the permeability of vacuum. I and S are the nuclear spins of the resonating spins I and non-resonating spins S , respectively. N_I and N_S denote the numbers of resonating and non-resonating nuclei in the sample, respectively; γ_S the magnetogyric ratio of the non-resonating spins S , and r_{ij} and r_{jk} the internuclear distances.

In the case of spins $I = 1/2$ and assuming that the sample does not contain paramagnetic impurities and that other susceptibility effects can also be neglected, the relationship between ν_{cg} and ν_0 is given by the following:

$$\nu_{cg} = \nu_0(1 - \sigma) \quad (11)$$

Here, σ denotes the shielding constant caused by the anisotropic shielding of the external magnetic field by the electron shell around the resonating nuclei. The so-called isotropic chemical shift, δ , is defined as $\delta = \sigma_{ref} - \sigma$, where σ_{ref} is the shielding constant of the nuclei in a reference material, and δ is defined by the following:

$$\delta = \frac{1}{3}(\delta_{xx} + \delta_{yy} + \delta_{zz}) \quad (12)$$

where δ_{xx} , δ_{yy} , and δ_{zz} are the principal values of the chemical shift tensor, which are denoted such that the inequality $\delta_{xx} \geq \delta_{yy} \geq \delta_{zz}$ is fulfilled. The unit of the chemical shift δ is "ppm," which means parts per million of the resonance frequency. The anisotropy, $\Delta\sigma$, and the asymmetry parameter, η_{CSA} , of the chemical shift tensor, used in Eq. (9), are defined by the following:

$$\Delta\sigma = \frac{1}{2}(\delta_{xx} + \delta_{yy}) - \delta_{zz} \quad (13)$$

and

$$\eta_{CSA} = \frac{3}{2} \frac{\delta_{xx} - \delta_{yy}}{\Delta\sigma}. \quad (14)$$

The NMR spectra of quadrupole nuclei with half-integer nuclear spins $I > 1/2$ consist of the central transition (CT), $\{+1/2 \leftrightarrow -1/2\}$, and the so-called satellite transitions, $\{\pm 1/2 \leftrightarrow \pm 3/2\}$, $\{\pm 3/2 \leftrightarrow \pm 5/2\}$, etc. In the case of strong quadrupolar interactions, it is practically impossible to excite the whole spectrum non-selectively (i.e., the CT is often selectively observed). Therefore, the second moments, $M_2^{Q,CT}$, caused by quadrupolar interactions in Eqs. (6) and (10), are those of the CT only.

In the case of quadrupole nuclei with spin $I > 1/2$, the frequency at the center of gravity, ν_{cg} , of the CT is shifted by the second-order quadrupole shift:

$$\nu_{qs} = \nu_{cg} - \nu_0(1 - \sigma) = -\frac{I(I+1) - 3/4}{30} \frac{\nu_Q^2}{\nu_0} \left(1 + \frac{1}{3}\eta_Q^2\right) \quad (15)$$

with respect to the line position given in Eq. (11). The second-order quadrupole shift, ν_{qs} , also affects the value of the second moment of the CT, $M_2^{Q,CT}$, in Eq. (10). The quadrupole frequency is given by the following:

$$\nu_Q = \frac{3}{2I(2I-1)} C_{QCC} \quad (16)$$

with the quadrupole coupling constant being C_{QCC} . Often, the quadrupole coupling constant

$$C_{\text{QCC}} = \frac{V_{zz}eQ}{h} \quad (17)$$

is used to describe strength of quadrupolar interactions; eQ is the electric quadrupole moment of the nuclei with spin $I > 1/2$. The asymmetry parameter, η_Q , of the electric field gradient tensor, used in Eq. (15), is defined by

$$\eta_Q = \frac{V_{yy} - V_{xx}}{V_{zz}}. \quad (18)$$

The principal values V_{xx} , V_{yy} , and V_{zz} of the electric field gradient tensor in the molecular frame at the site of the resonating nuclei are denoted in such a manner that $|V_{xx}| \leq |V_{yy}| \leq |V_{zz}|$.

B. SOLID-STATE NMR TECHNIQUES

The most frequently applied technique for the averaging of magnetic interactions in solid-state NMR spectroscopy is the MAS technique (15). This technique is based on a rapid rotation of the sample with the frequency ν_{rot} . For the limiting case of rapid sample spinning, $\nu_{\text{rot}} \gg \Delta\nu_{1/2}$, the total Hamiltonian $\hat{\mathbf{H}}$ in Eq. (1) can be replaced by the mean Hamiltonian $\langle \hat{\mathbf{H}} \rangle_t$. In the first-order of perturbation theory, the mean Hamiltonian $\langle \hat{\mathbf{H}} \rangle_t$ includes the geometric term $(3\cos^2\theta - 1)$, where θ denotes the angle between the direction of the external magnetic field and the sample spinning axis (Fig. 1). The maximum averaging of solid-state interactions (i.e., best line narrowing), is achieved for the magic angle $\theta_m = 54.74^\circ$, when $(3\cos^2\theta_m - 1)$ becomes zero.

If an NMR signal is broadened by inhomogeneous interactions (16), such as the heteronuclear magnetic dipole-dipole interaction, the chemical shift anisotropy or the quadrupolar interaction, MAS leads to an MAS NMR signal consisting of a narrow central line at the center of gravity of the signal, ν_{cg} , and spinning sidebands at the frequencies

$$\nu_k = \nu_{\text{cg}} + k\nu_{\text{rot}} \quad (19)$$

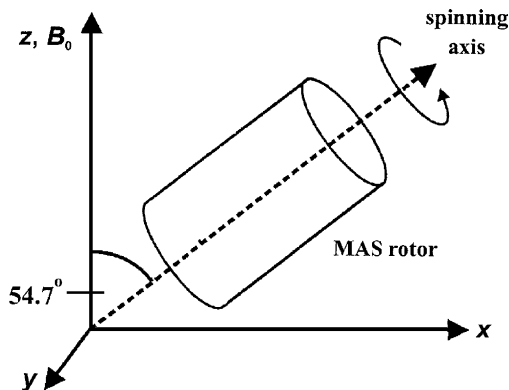


FIG. 1. Schematic representation of MAS.

where $k = \pm 1, \pm 2, \dots$ is the order of the spinning sideband (Fig. 2). In the present work, spinning sidebands are denoted by the asterisk symbol (*) in all figures. The full-width at half-maximum of the central line of an MAS NMR signal is denoted as the residual linewidth, $\Delta\nu_{1/2}^{\text{MAS}}$. In the presence of a homogeneous interaction, such as the homonuclear magnetic dipole–dipole interaction between more than two nuclei, the central line as well as the spinning sidebands exhibit a residual broadening, which is approximately given by the following:

$$\Delta\nu_{1/2}^{\text{MAS}} = \frac{1}{A} \frac{(\Delta\nu_{\text{II}})^2}{\nu_{\text{rot}}} \quad (20)$$

with $10 \leq A \leq 40$ (17,18). The term $\Delta\nu_{\text{II}}$ denotes the so-called homonuclear linewidth, which can be calculated from M_2^{II} according to Eq. (7), and the parameter A depends on the spatial arrangement of the spins and the line shape of the central line (17).

The influence of the homonuclear magnetic dipole–dipole interaction on $\Delta\nu_{1/2}^{\text{MAS}}$ can be reduced either by an increase of the sample spinning frequency, ν_{rot} , (Eq. (20)) or by the application of a multiple-pulse sequence causing an additional averaging of this interaction (combined rotation and multiple-pulse spectroscopy, CRAMPS (19–21)). With today's instruments, sample spinning frequencies of up to 40 kHz can be reached using MAS NMR rotors with an outer diameter of 2.0 mm.

Further effects that may cause a residual linewidth of MAS NMR signals are inhomogeneity of the external magnetic field, bad adjustment of the magic angle, thermal motions and exchange processes (22), heteronuclear magnetic dipole–dipole interaction with quadrupole nuclei (23), anisotropy of the magnetic susceptibility (24), and distribution of the isotropic chemical shift (25). Furthermore, the residual linewidth of MAS NMR signals of quadrupole nuclei (spin $I > 1/2$) is determined by the second-order quadrupole broadening of the CT, which is not completely suppressed by the MAS technique. The second moment, $M_2^{\text{Q,CT,MAS}}$, of

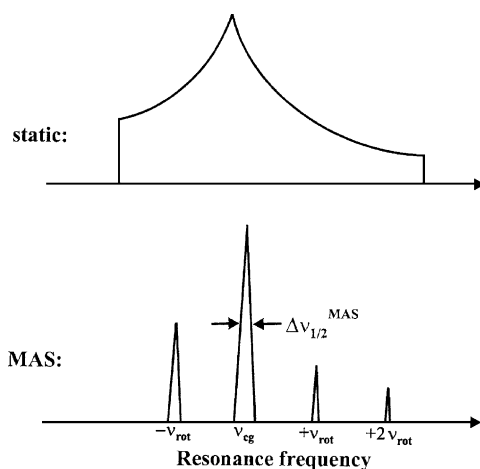


FIG. 2. Effect of line narrowing by MAS.

the CT under MAS conditions is given by the following (26):

$$M_2^{Q,CT,MAS} = \frac{7}{92} M_2^{Q,CT} = \pi^2 v_{qs}^2. \quad (21)$$

Hence, application of the MAS technique for the investigation of quadrupole nuclei leads to a decrease of the linewidth of the CT by a factor of about 3.6. A further improvement of the resolution of the NMR spectra of quadrupole nuclei requires the application of more sophisticated techniques, such as the DOR (27) or the more recently developed MQMAS NMR spectroscopy (26,28). Until now, however, neither of these techniques has been applied for investigations of working solid catalysts, and they are therefore not considered in this review.

C. TECHNIQUES FOR SIGNAL ENHANCEMENT AND DISCRIMINATION IN SOLID-STATE NMR SPECTROSCOPY

Signal enhancement, if performed as a selective method, is very helpful for the assignment of NMR lines. In a more general manner, the application of signal enhancement techniques may improve the signal-to-noise ratio of the NMR spectrum, which is important for investigations of samples at elevated temperatures (Section II.D).

The transfer of population in double resonance (TRAPDOR) experiments are a method allowing the discrimination of NMR signals (e.g., of spin $I = 1/2$ nuclei involved in a heteronuclear dipolar interaction with quadrupole nuclei with a nuclear spin $S > 1/2$) (29). In a TRAPDOR experiment, an adiabatic irradiation at the spin S is applied during the evolution period of an echo pulse sequence of spins I , and the loss of the intensity at the echo signal of the spins I is analyzed (Fig. 3). ^{27}Al irradiation during the ^1H echo, for example, results in a dephasing of the heteronuclear dipolar coupling between the ^1H and ^{27}Al nuclei in a solid. Therefore, $^1\text{H}/^{27}\text{Al}$ spin pairs, which are coupled by dipolar interactions, do not contribute to the ^1H echo intensity in the case of ^{27}Al irradiation. The TRAPDOR effect can only be used if the ^{27}Al irradiation frequency lies within the boundaries given by the first-order quadrupolar broadening (i.e., in a frequency range of $\nu_0 \pm 2\nu_Q = \nu_0 \pm (3/10) C_{QCC}$ for ^{27}Al nuclei (spin $S = 5/2$)). The TRAPDOR technique allows, for example, a discrimination of aluminum-connected and aluminum-unconnected surface complexes or hydroxyl groups on calcined catalysts.

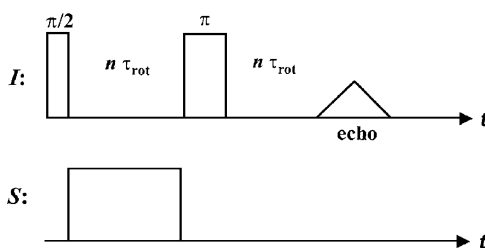


FIG. 3. Schematic representation of a TRAPDOR pulse sequence.

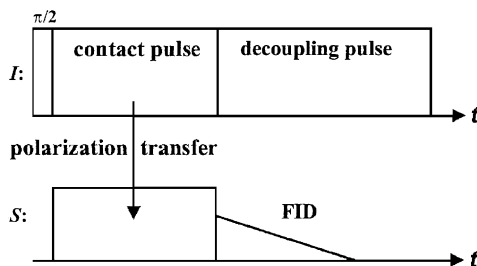


FIG. 4. Schematic representation of a CP pulse sequence.

A suitable way to enhance NMR signals of nuclei with small magnetogyric ratios or low concentrations (rare spins S) interacting with abundant spins I is the polarization transfer from the spin I to the spin S ensemble via a cross polarization (CP) experiment. This experiment is based on a double resonance technique, which can be applied in combination with MAS for the characterization of surface sites of solid catalysts and rigidly bound surface complexes. The pulse sequence used for CP experiments is demonstrated in Fig. 4.

The experiment starts with a $\pi/2$ pulse applied to the spins I . Spin polarization is transferred from the spins I to the spins S in the rotating frame during the contact pulse of the duration τ_{CP} if the condition

$$\alpha_I \gamma_I B_{1I} = \alpha_S \gamma_S B_{1S} \quad (22)$$

is fulfilled (13); B_{1I} and B_{1S} denote the amplitude of the magnetic fields of the contact pulses applied to the spins I and S , respectively. The parameter α_I is equal to $(I(I+1)-m(m-1))^{1/2}$, provided that the radio frequency pulse, applied to spins I , selectively induces transitions between the levels with the magnetic spin quantum numbers $m-1$ and m . The analogous expression holds for α_S . The parameters α_I and α_S are equal to one for $I = S = 1/2$ (i.e., if Eq. (22) corresponds to the Hartmann-Hahn condition) (30). If polarization transfer from spins I to spins S occurs, a free-induction decay of the spins S is observed after the contact period, τ_{CP} . During the observation of this induction decay, the dipolar interaction between the spins I and S is often averaged by a decoupling pulse applied on the spin I system. The maximum signal enhancement achievable by the CP experiment amounts to the following (31):

$$\frac{A_{CP}}{A_{SP}} = \frac{\gamma_I}{\gamma_S} \frac{1}{1 + \varepsilon} \quad (23)$$

with

$$\varepsilon = \frac{N_S}{N_I} \left(\frac{\alpha_S}{\alpha_I} \right)^2, \quad (24)$$

where A_{CP} and A_{SP} denote the intensity of the signal of the spins S measured with CP and single-pulse excitation and N_S and N_I the numbers of spins S and I , respectively. For a review on the theory of CP, see refs. (13,31).

A very new approach to improve the sensitivity of NMR spectroscopy is the injection of laser-polarized ^{129}Xe isotopes into the sample volume of the NMR

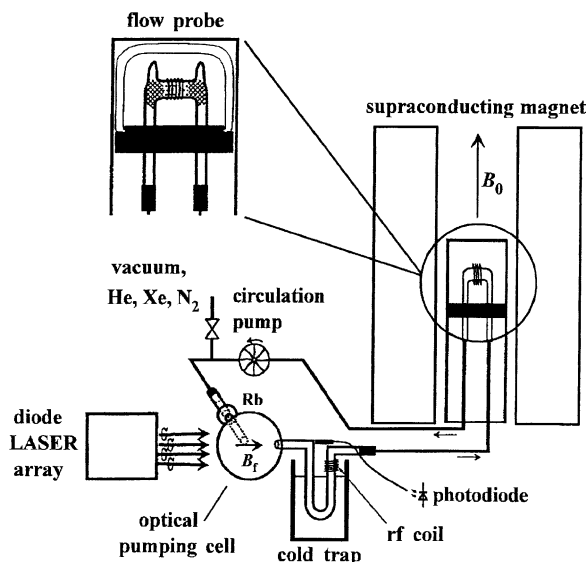


FIG. 5. Schematic representation of equipment for laser-polarized ^{129}Xe in NMR spectroscopy. Reproduced with permission from (36). Copyright 1999 American Chemical Society.

probe (Fig. 5). With this technique, a selective enhancement of the magnetization of spins located at the surfaces of solid materials can be achieved. The principle of this technique consists of an optical pumping of rubidium vapor at the wavelength of the Rb D1 transition (794.8 nm) with circularly polarized light from a diode laser (32–36). After passing the optical pump cell, the excited rubidium atoms are in contact with Xe atoms, and a polarization transfer from rubidium to xenon is performed. This mixture is led through a rubidium trap and, subsequently, the laser-polarized xenon is injected into the sample volume of the NMR probe. There, a polarization transfer occurs via the spin polarization-induced nuclear Overhauser effect (SPINOE), provided that a coupling exists between the laser-polarized ^{129}Xe spins and the nuclei to be polarized at the catalyst surface. Applications of this technique, for example, for a selective enhancement of the NMR signals of surface OH groups on solid materials, are described in refs. (32–36).

Because of the limitations of NMR spectroscopy by the decrease of the signal-to-noise ratio at elevated temperatures, the application of laser-polarized ^{129}Xe isotopes for enhancing the polarization of resonating nuclei may help to expand the accessible temperature range in the future.

D. SOLID-STATE NMR SPECTROSCOPY AT ELEVATED TEMPERATURES

D.1. Effect of Temperature on Signal-to-Noise Ratio

In an external magnetic field, B_0 , the magnetization, M_0 , of an ensemble of spins I is given by Curie's equation (10–13):

$$M_0 = \frac{\gamma_I^2 \hbar^2 I(I+1)}{3kT} B_0 \quad (25)$$

where k is the Boltzmann constant and T the thermodynamic temperature. Hence, the increase of the sample temperature during an NMR experiment is accompanied by a linear decrease of the signal-to-noise ratio. To measure a ^1H MAS NMR spectrum with suitable signal-to-noise ratio at room temperature, a concentration of ^1H nuclei with a minimum of *ca.* 0.1 mmol/g is necessary. According to Eq. (25), an NMR experiment performed at 673 K requires a minimum concentration that is a factor of 2.5 greater than this value. In comparison with ^1H nuclei (relative sensitivity of 1), the relative sensitivities for equal numbers of spins are, for example, 9.65×10^{-3} for ^2H , 1.59×10^{-2} for ^{13}C , and 1.04×10^{-3} for ^{15}N nuclei (37). Hence, for most of the ^2H , ^{13}C , and ^{15}N NMR investigations of reactants and adsorbates on solid catalysts, an isotopic enrichment is necessary. NMR experiments of working catalysts at elevated temperatures thus require the application of isotopically enriched reactants.

D.2. Temperature Calibration

An important prerequisite for the reproducibility of NMR experiments at elevated temperatures is the accurate determination of the temperature inside the sample volume of the probe. Often, there is a systematic error in the temperature displayed by the controller unit. Therefore, methods for the temperature calibration of MAS NMR probes under various working conditions, such as various heating rates, sample spinning frequencies, etc., are required for experiments at elevated temperatures.

A simple method for determining the temperature inside the sample volume of an NMR probe is the quantitative evaluation of the absolute intensity using Curie's law (Eq. (25)). However, this approach is limited to systems that heat the sample volume only and not the radio frequency coil or other electronic parts of the probe. A heating of the radio frequency coil strongly influences the quality factor of the NMR probe and leads to an additional change of the signal intensity and, therefore, renders the quantification of intensity more complicated.

A more suitable method to calibrate the temperature behavior of an NMR probe involves the characterization of temperature-dependent melting points and phase transitions. Table 1 is a list of materials that can be applied for the calibration of variable-temperature NMR probes in the temperature range of 279–791 K.

Another way to calibrate temperatures in NMR spectroscopy consists of investigating materials that lead to signals with temperature-dependent chemical shifts (shift thermometers). For the development of shift thermometers, the temperature-dependent chemical shift is compared with the occurrence of melting and phase transitions, allowing a temperature calibration with high accuracy over a broad temperature range.

On the basis of the calibration by melting points and phase transitions, a number of shift thermometers have been developed for solid-state NMR spectroscopy in various temperature ranges. Wehrle *et al.* (44), for example, used the line splitting in the ^{15}N CP/MAS NMR spectrum of the organic dye molecule tetramethyldibenzotetraaza annulene (TTAA) in the temperature range 123–405 K. A high-temperature shift thermometer for temperatures of up to 790 K was developed by van Moorsel *et al.* (40) on the basis of ^{119}Sn MAS NMR spectroscopic

TABLE I

Melting Points and Phase Transition Temperatures of Materials Used for the Calibration of NMR Probes at Elevated Temperatures (8)

Material	Melting point (K)	Phase transition temperature (K)	References
Benzene	279		(38)
2,2-Dimethylpropane-1,3-diol		315	(39)
Carbon tetrabromide		320	(40)
4-Cyano-4'-7-alkoxybiphenyls	347	327	(41)
Samarium acetate tetrahydrate		343	(42)
1,4-Diazabicyclo-(2,2,2)-octane (DABCO)		351	(40,43)
4-Cyano-4''-5-terphenyl		404	(41)
Citric acid	426		(38,41)
Rubidium nitrate		447	(40)
Sodium nitrate	580		(41)
Lithium iodide	742		(41)
Lithium sodium sulfate		791	(40)

investigations of $\text{Pr}_2\text{Sn}_2\text{O}_7$. Pan and Gerstein (45) characterized the temperature dependence of the ^{31}P NMR shift of paramagnetic $(\text{VO})_2\text{P}_2\text{O}_7$ and found a Curie-type behavior in the temperature range of 285–353 K.

A number of groups (38,41,46–48) used the temperature-dependent chemical shift of $\text{Pb}(\text{NO}_3)_2$ as a ^{207}Pb NMR shift thermometer. A detailed evaluation of the temperature dependence of the ^{207}Pb NMR shift of this material in the temperature range of 303–673 K led to Eq. (26):

$$T = -5.2 \times 10^{-4} \delta^2 + 1.3\delta + 303.1 \quad (26)$$

with T in K. By evaluating the line broadening of the ^{207}Pb NMR signal of $\text{Pb}(\text{NO}_3)_2$, filled into the sample chamber of a variable-temperature MAS NMR probe, one can use Eq. (26) to determine the temperature gradient, ΔT , over the sample volume under working conditions (38,47,49).

III. Experimental Techniques for MAS NMR Spectroscopy of Working Catalysts

As a consequence of the line broadening effects of internal magnetic interactions on solid-state NMR spectra (Section II.A), experiments that characterize working solid catalysis require the application of the MAS technique. Because of the salient feature of MAS NMR spectroscopy (rapid sample spinning during the measurement), specific techniques had to be developed to allow characterization of solids in sealed vessels under batch reaction conditions and in fixed-bed reactors under flow conditions.

An important advantage of NMR spectroscopy under batch reaction conditions is that most of the materials and equipment are commercially accessible. Furthermore, a number of homemade instruments were developed that allow a pre-treatment of catalyst samples in gas-tight MAS NMR rotors (Section III.A). In contrast, NMR

techniques used for investigations of catalysts under flow conditions were mostly developed and built by the individual research groups (Section III.B).

A. BATCH CONDITIONS

The first NMR investigations of catalyzed reactions taking place under batch reaction conditions were performed in the early 1980s with homemade glass ampoules, which fit as inserts into commercial MAS NMR rotors. Figure 6 shows the scheme of a turning-lathe applied for the preparation of glass ampoules applied as inserts for MAS NMR rotors (22). A glass tube is fixed by two chucks, which rotate at a rate of *ca.* 0.5 s^{-1} . For 4-mm Bruker DB MAS NMR rotors, for example, the glass tube No. 327-pp-1 produced by Wilmad Glass Company is used. With a twofold flame burner, the glass tube is closed at the bottom. Then a waist with an inner diameter of *ca.* 1 mm is made at a distance of *ca.* 12 mm from the bottom.

An alternative, and more expensive, technique involves the application of commercial glass inserts, which are offered by Wilmad for all commercial MAS NMR rotor types. Approximately 60 or 200 mg of catalyst powder can be filled into a 4-mm or 7-mm glass insert, respectively. After calcination of the catalyst and adsorption of reactant molecules introduced from a vacuum line, the glass insert is sealed at the waist (Fig. 7). To prevent heating of the sample, the glass ampoule is clamped in one of the chucks and cooled by liquid nitrogen.

Another, frequently applied, approach is based on the preparation of the solid catalyst directly inside the sample volume of an MAS NMR rotor. After filling the MAS NMR rotor with the catalyst, the rotor is placed into a fitting at the bottom of a piece of specialized vacuum equipment, which is shown schematically in Fig. 8. After calcination of the catalyst under vacuum and loading with reactant molecules, the MAS NMR rotor is sealed with a gas-tight rotor cap inside the vacuum equipment.

In 1989, Haw *et al.* (50) introduced the so-called cryogenic adsorption vessel enabling rotor nestling (CAVERN) equipment. Inside this equipment, the catalyst can be cooled during the adsorption of molecules and the sealing of the rotor with the gas-tight cap. The CAVERN is suitable for the investigation of highly reactive compounds at low temperatures.

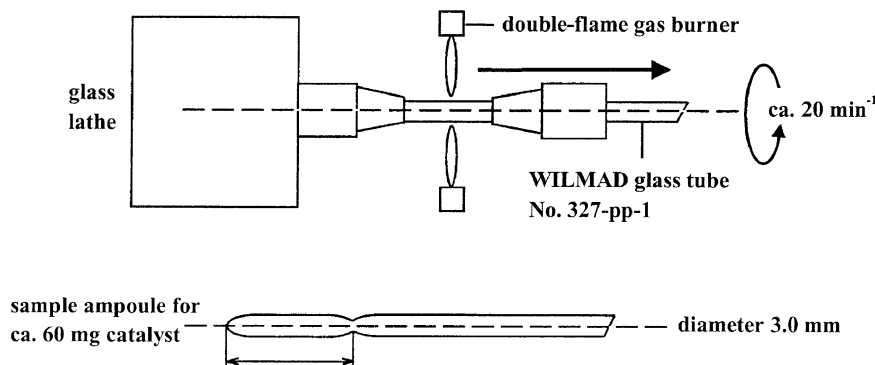


FIG. 6. Equipment for the preparation of glass ampoules for MAS NMR investigations under batch reaction conditions.

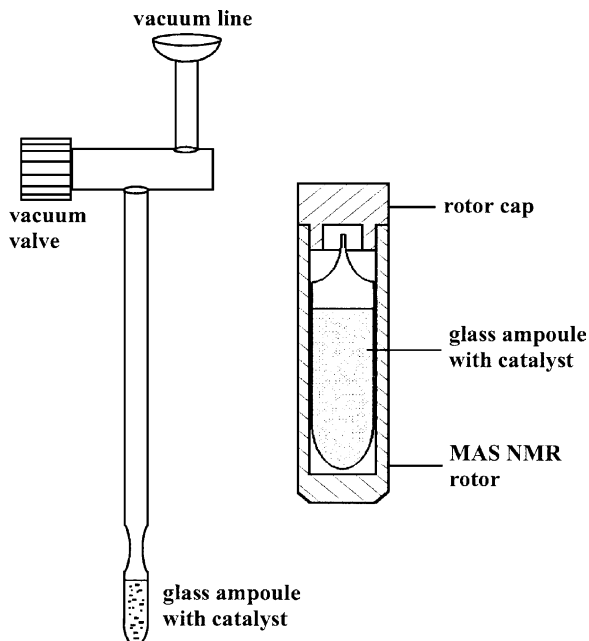


FIG. 7. Schematic representation of the preparation and application of catalyst samples for MAS NMR investigations under batch reaction conditions.

In more recently introduced equipment, the calcination and loading of the catalyst samples can be performed under shallow-bed conditions. For example, the equipment developed by Zhang *et al.* (51) (Fig. 9) allows a calcination of the powder in a horizontal tube inside a heater at temperatures of up to 1000 K. After loading of the catalyst with probe molecules or reactants, the powder is added to an MAS NMR rotor at the bottom of the equipment, sealed with a rotor cap from a plug rack, and transferred to the NMR spectrometer. As in the case of the former approaches, the samples prepared in the equipment of Zhang *et al.* (51) can be used for *ex situ* as well as *in situ* NMR investigations under batch reaction conditions. Furthermore, this equipment is suitable for *ex situ* investigations of solid-catalyzed reactions under flow conditions. In this case, the horizontal tube inside the heater is used as a fixed-bed reactor.

Rafty and co-workers (52) developed an *in situ* MAS NMR probe for photocatalytic experiments under batch reaction conditions. The probe based on a MAS NMR turbine of the Gay design can have sample spinning frequencies of 2–3 kHz (53). On top of the turbine, a light pipe is inserted into the stator to bring ultraviolet light to the sample via a 10-mm long gap in the radio frequency coil (Fig. 10). A 300-W xenon arc lamp is used as the ultraviolet light source. After filtering the near infrared light, the remaining ultraviolet light is delivered to the sample region inside the magnet using a liquid-filled optical light guide that has a polished 70-mm long suprasil quartz rod attached to its end. The quartz rod reduces the effects of radio frequency pickup by the probe coil from the aluminum-encased

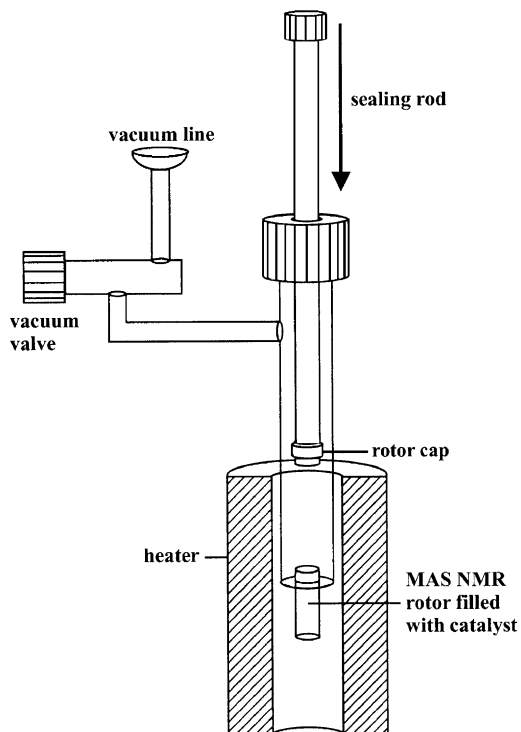


FIG. 8. Schematic representation of equipment for the direct preparation of catalyst samples inside an MAS NMR rotor.

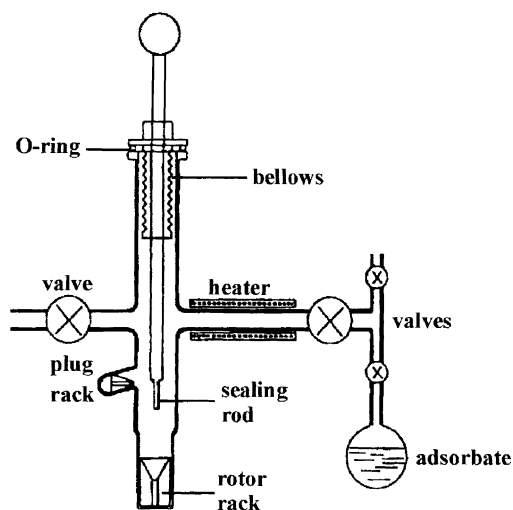


FIG. 9. Schematic representation of equipment for the preparation of catalyst samples under shallow-bed conditions. Reproduced with permission from (51). Copyright 1999 The Royal Society of Chemistry.

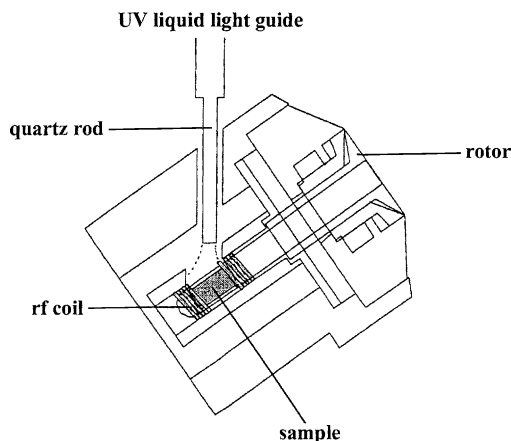


FIG. 10. Schematic representation of optical/MAS NMR probe for photocatalytic investigations under batch reaction conditions. Reproduced with permission from (52). Copyright 1998 American Chemical Society.

liquid-light guide. The power of the ultraviolet light that reaches the sample was measured to be 5 mW.

Generally, several protocols are used for the characterization of solid-catalyzed reactions under batch reaction conditions by NMR spectroscopy. In *ex situ* experiments, the conversion of reactants adsorbed on the catalyst is carried out in an external oven and stopped after a given reaction time by quenching, for example, in liquid nitrogen. Subsequently, the reaction products formed on the catalyst surface are investigated at room temperature by use of a standard MAS NMR probe. This protocol is repeated with a stepwise increment of the reaction time at the same temperature or with a stepwise increment of the reaction temperature for the same duration. In an *in situ* experiment, the catalytic conversion of the reactants is measured inside the NMR spectrometer by use of a high-temperature MAS NMR probe.

Often, the latter experiments are carried out with a high-temperature MAS NMR probe with a gas heating system for the bearing and driving gas of the MAS NMR turbine. As a consequence of the heat transfer from the bearing and driving gas via the rotor wall to the powder in the sample volume, temperatures of up to 923 K can be reached. Another approach that was applied for such experiments under batch reaction conditions takes advantage of heating of the sample in the MAS NMR rotor by a laser beam. In this case, a CO₂-laser beam with a power of 50–100 W is reflected via a mirror to the bottom of a boron nitrate sample container inside the MAS NMR rotor (Fig. 11) (54). Depending on the laser power, temperatures of the sample of up to 773 K can be reached. An important advantage of this heating system is that only the MAS NMR rotor is heated, and not the radio frequency coil inside the stator. Hence, there is no decrease in the quality factor of the NMR probe that would cause an additional decrease of the signal-to-noise ratio at elevated temperatures. An important disadvantage of the laser heating system is the larger temperature gradient over the sample volume, which can reach 50 K at a mean temperature of 673 K.

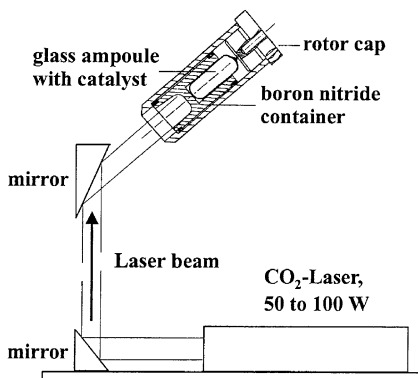


FIG. 11. Schematic representation of a laser heating system for high-temperature MAS NMR investigations under batch reaction conditions. Reproduced with permission from (54). Copyright 1996 Elsevier Science.

The laser heating technique can be applied to perform temperature jumps by irradiating short laser pulses at the sample container. Ernst *et al.* (54) used such a temperature jump protocol to perform “stop-and-go” experiments. After the start of the laser pulse, the temperature inside the sample volume is raised to the reaction temperature, the conversion of the adsorbed reactants proceeds, and the ¹H MAS NMR measurement is performed. After the laser pulse is stopped, the temperature inside the sample volume decreases to ambient temperature, and the ¹³C MAS NMR measurement is made. Subsequently, the next laser pulse is started and, in this way, the reaction is recorded as a function of the reaction time. By use of the free-induction decay and the reaction time as time domains t_1 and t_2 , respectively, a two-dimensional Fourier transformation leads to a two-dimensional spectrum, which contains the NMR spectrum in the F_1 -dimension and the reaction rate information in the F_2 -dimension (54,55).

B. FLOW CONDITIONS

The first NMR investigations of working solid catalysts under CF conditions were reported by Haddix *et al.* (56) and Davis *et al.* (57). However, these experiments were made without application of the MAS technique, which led to problems with the spectral resolution and interpretation of the spectra. Today, two experimental approaches to CF MAS NMR spectroscopy are distinguished: (i) *ex situ* approaches with the catalytic reaction performed in an external fixed-bed reactor and a subsequent transfer of the catalyst into an MAS NMR rotor after quenching of the reaction and (ii) *in situ* approaches utilizing the MAS NMR rotor directly as a fixed-bed reactor situated inside a high-temperature MAS NMR probe. The NMR investigations under flow conditions described in Sections VII–X are performed exclusively by approach (ii) and, therefore, the following description focuses on the latter technique.

The most frequently applied technique for *in situ* MAS NMR investigations of heterogeneously catalyzed reactions under flow conditions is based on the injection

of a carrier gas loaded with vapors of the reactants into the spinning MAS NMR rotor via an injection tube (58,59). For this purpose, a glass tube is inserted into the sample volume up to the bottom of the MAS NMR rotor reactor via an axially placed hole in the rotor cap (Fig. 12). With a specially constructed tool, the solid catalyst is pressed into a hollow cylinder. The feed is injected into the inner space of this cylinder and flows from the bottom to the top of the sample volume inside the MAS NMR rotor reactor. The product stream leaves the sample volume via an annular gap in the rotor cap.

For the modification of a 4-mm MAS NMR probe, an injection tube with an outer diameter of 1 mm is used, and the hole in the rotor cap has an inner diameter of 1.4 mm. This 4-mm CF MAS NMR probe reaches sample spinning frequencies of 12 kHz and is suitable for the investigations of atoms in the framework of solid catalysts, such as ^{23}Na , ^{27}Al , and ^{31}P nuclei. Approximately 50 mg of catalyst powder can fit in the rotor reactor of a 4-mm CF MAS NMR probe.

In ^{13}C CF MAS NMR investigations of adsorbate complexes and reactants, modified 7-mm MAS NMR probes are used. The injection tube has an outer diameter of 1.5 mm, and the hole in the rotor cap has an inner diameter of 2.5 mm. The maximum sample spinning frequency of 7-mm CF MAS NMR probes is *ca.* 3.5 kHz. Approximately 200 mg of catalyst powder fits in the rotor reactors of a 7-mm CF MAS NMR probe (60).

A disadvantage of CF MAS NMR probes with injection tubes is that these systems are not gas tight at the outlet in the rotor cap. Hence, they are limited to catalytic investigations at atmospheric pressure. On the other hand, because pure

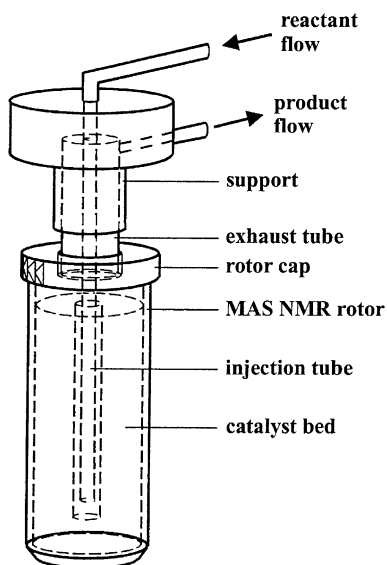


FIG. 12. Schematic representation of an MAS NMR rotor reactor for MAS NMR investigations under CF reaction conditions. Reproduced with permission from (60). Copyright 1999 Kluwer Academic.

carrier gas is used for the bearing and driving of the MAS NMR rotor in injection probes, no humidity can penetrate into the sample volume filled with the catalyst.

In some applications, the reaction products leaving the CF MAS NMR probe were led to the sampling loop of an on-line gas chromatograph (Fig. 13) (60). In such an application, a second glass tube with an outer diameter of 3 mm is inserted into the rotor cap having a hole with an inner diameter of 3.5 mm. The reaction products leave the sample volume of the MAS NMR rotor reactor via the gap between the outer 3-mm and the inner 1.5-mm glass tube (Fig. 12). An exhaust pump is needed to ensure a constant exhaust flow for various sample spinning frequencies and temperatures (Fig. 13). For a quantitative analysis of the reaction products, a flow of an internal standard gas, such as methane, is added to the feed gas continuously injected into the spinning MAS NMR rotor reactor. With a DSI-740 7-mm STD MAS NMR probe manufactured by Doty Scientific Instruments, Columbia, TX, USA, modified with the above-mentioned injection system, NMR investigations of solid-catalyzed reactions can be performed under flow conditions at atmospheric pressure and temperatures up to 873 K, with spinning rates of up to 3.5 kHz (49). Recently, this experimental approach was adopted with slight modifications by a number of groups and by the Bruker BioSpin Company (34,35,61–64).

CF MAS NMR probes allowing a separation of the reactant flow and the gas flow used for driving the rotor are based on mechanical bearings (46,65,66). The CF MAS NMR probe shown in Fig. 14 consists of the module body, the bearing and driving cartridge, the reactant gas endcap, the product gas endcap, and the rotor (46,65). The bearing and driving cartridge made by Vespel[®] is press-fitted into the module body. The cartridge supports two Si₃N₄ ball bearings and two sets of

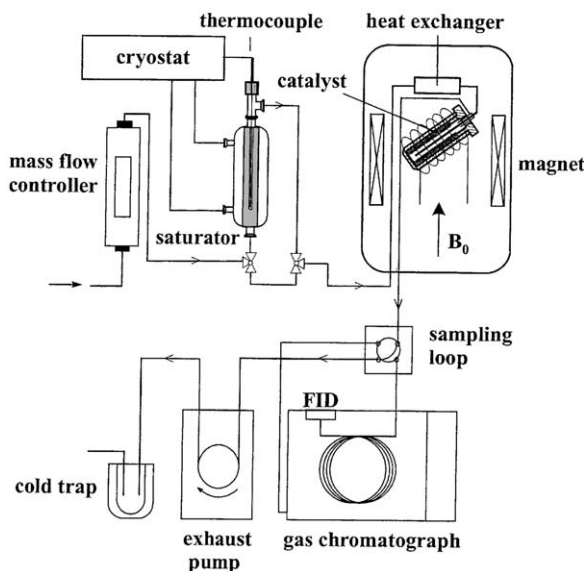


FIG. 13. Schematic representation of the coupling of a CF MAS NMR probe with an on-line gas chromatograph. Reproduced with permission from (60). Copyright 1999 Kluwer Academic.

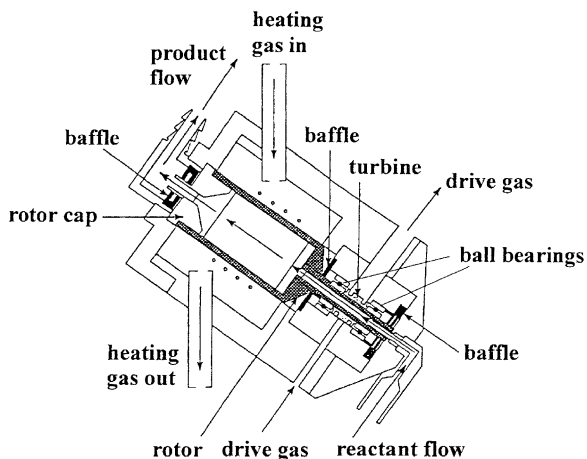


FIG. 14. Schematic representation of a CF MAS NMR probe with ball bearings and separate gas flows. Reproduced with permission from (46). Copyright 1999 Elsevier Science.

Vespel[®] baffles. The baffles are located at both ends of the cartridge, and are designed to isolate the drive gas from the reactant flow gas. The rotor is exclusively supported by the two ball bearings of the cartridge. A turbine is press-fitted onto the rotor and is located inside the cartridge between the two ball bearings. Unlike conventional MAS rotors, which are typically a hollow cylinder with plastic end-caps and drive tips, the mechanical flow rotor is one piece of boron nitride with two distinct parts, a hollow axis and a sample chamber. The axis supports and propels the rotor. The reactant gas enters the hollow axis and flows into the sample volume. The large end of the sample volume is press-fitted in the rotor cap. The rotor cap constructed of boron nitride is used to seal the rotor and to direct the product gas into the product gas endcap. A series of baffles is located in the endcap to isolate the product gas stream and the surrounding gas. The above-mentioned mechanical CF MAS NMR probe allows experiments of catalysts under working conditions at temperatures of up to 608 K with sample spinning frequencies of 1–2 kHz (46).

Maciel and co-workers (66) introduced a technique based on the hopping of the flow reactor about an axis in the magic angle. This system was called gas reactor and solid sample hopper (GRASSHopper). The principles of magic-angle hopping (MAH) were developed 1985 by the same group (67). In an MAH experiment, the sample chamber hops by 120° around the axis of the magic angle. Between these jumps, the sample chamber is stationary for the NMR experiment. The hopping is implemented by a suitable controlled step motor, which drives a shaft that is coupled via a gear system to the sample cell (Fig. 15).

An important advantage of the GRASSHopper device is the fact that after a complete MAH cycle of three orientations, the MAH device can be re-initialized by rotating backward to the initial orientation. For this reason, a number of flexible input and output lines to the sample chamber of the GRASSHopper device exist and allow a rotation of the fixed-bed reactor about an axis in the magic-angle while the system is gas-tight (Fig. 16). In the reported experiments (66), the 120° hop time

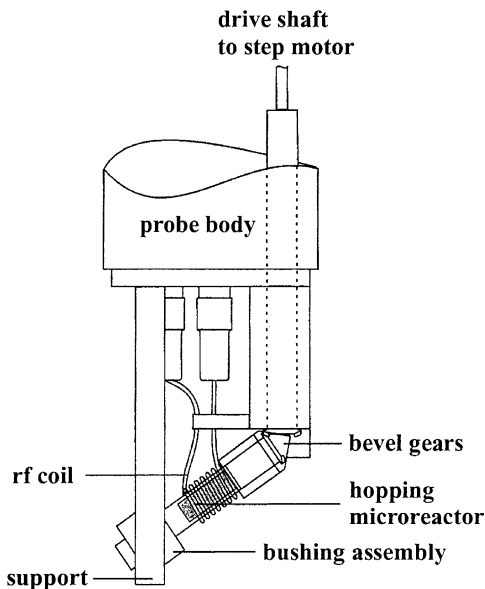


FIG. 15. Schematic representation of a CF MAS NMR probe with a hopping microreactor (GRASS-Hopper II). Reproduced with permission from (66). Copyright 1999 Elsevier Science.

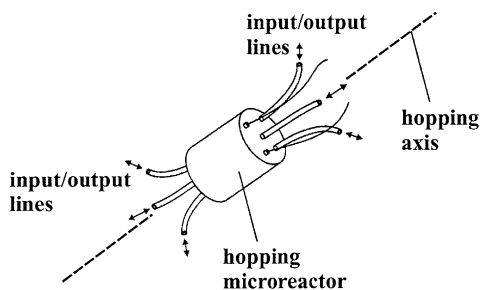


FIG. 16. Schematic representation of the reaction cell with flexible gas-tight input/output lines allowing the hopping of a microreactor around a hopping axis (GRASSHopper II). Reproduced with permission from (66). Copyright 1999 Elsevier Science.

was $t_{\text{hop}} = 30$ ms. A requirement of the MAH technique is that t_{hop} be small in comparison with the spin-lattice relaxation time T_1 of the resonating nuclei. Furthermore, the hopping must be accomplished in such a manner that it does not induce slippage of the particles in the sample chamber. The experiments are performed with a pulse sequence based on an eight-pulse refocusing cycle (66). This pulse sequence is applied to reach a refocusing of the x and y components of the nuclear magnetization.

A recent development is the direct coupling of UV/Vis and CF MAS NMR spectroscopy under flow conditions (68). The CF MAS NMR–UV/Vis probe is

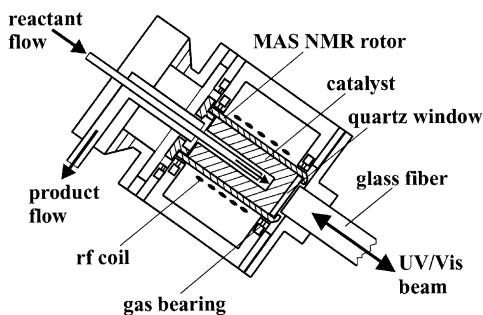


FIG. 17. Schematic representation of a CF MAS NMR probe coupled with a fiber optic for UV/Vis spectroscopy. Reproduced with permission from (68). Copyright 2004 The Royal Society of Chemistry.

based on the injection technique (Fig. 12). In the 7-mm CF MAS NMR probe shown in Fig. 17, a glass fiber is attached to the bottom of the stator. The rotor is equipped at the bottom with a quartz window. Via this quartz window and with a glass fiber, the catalyst in the sample volume can be investigated by a fiber-optic UV/Vis spectrometer. In recent work (68), the UV/Vis spectra were recorded with an AvaSpec-2048 Fiber Optic spectrometer, an AvaLight-DH-S deuterium light source, and a glass fiber reflection probe FCR-7UV20-3-SR-S1, allowing UV/Vis investigations in the spectral range of 200–800 nm. This technique is suitable for simultaneous CF MAS NMR and UV/Vis investigations of the formation of aromatic compounds and carbenium ions on the surfaces of solid catalysts (68).

C. LIMITATIONS AND ADVANTAGES OF SOLID-STATE NMR SPECTROSCOPY FOR INVESTIGATIONS OF WORKING CATALYSTS

C.1. General Aspects

A general problem of NMR spectroscopy is its low sensitivity in comparison with other spectroscopic methods, such as EPR, FTIR, and UV/Vis. Especially for experiments at elevated temperatures, this is a significant limitation. According to Curie's law (Eq. (25)), the magnetization of a spin ensemble decreases linearly with increasing temperature. An isotopic enrichment can improve the signal-to-noise ratio, but it is expensive and often not sufficient. On the other hand, because the magnetization of a spin ensemble is a function of the flux density B_0 of the external magnetic field (Eq. (25)), experiments in high magnetic fields are advantageous. As shown in Section II.C, an additional method for enhancing the signal intensity of rare nuclei is the application of the CP technique. This technique requires an internal coupling between the rare spins S and abundant spins I . A high mobility of the compounds containing the rare and abundant spins, however, averages this coupling, and no polarization transfer occurs. At elevated temperatures, therefore, the effect of the CP technique for the enhancement of the signal-to-noise ratio is limited.

An additional limitation of NMR spectroscopy is the long observation time. Depending on the technique applied, observation times of *ca.* 100 ms to some hours may be needed. Hence, only structures that are stable during the observation time

can be investigated by NMR spectroscopy. The investigation of the transition state of a chemical reaction by NMR spectroscopy is as limited as for all other spectroscopic methods. In Section IV, NMR techniques are described that allow the study of reaction pathways and transition states by investigation of the fate of isotopic labels. The determination of the ^{13}C scrambling path and dynamics in hydrocarbons and of the rate and selectivity of the H/D exchange between surface OH groups on solid catalysts and adsorbate molecules helps to understand the reaction mechanisms.

An important advantage of NMR spectroscopy is the availability of a large number of isotopes with NMR-active nuclear spins. Most of the atoms incorporated in the framework and in surface sites of solid catalysts and in adsorbate complexes and reactants comprise NMR-sensitive isotopes. This is the reason for the increasing application of solid-state NMR spectroscopy in the field of heterogeneous catalysis during the preceding decades. As a consequence of the large chemical shift ranges of the most interesting nuclei, a suitable separation of signals attributed to atoms in different chemical environments is possible (69).

Unlike other spectroscopic methods requiring samples under vacuum or very low gas pressures, NMR spectroscopy of working catalysts is not limited by the so-called pressure gap. The flow techniques described in Section III.B are suitable for catalytic reaction experiments under atmospheric pressure. If necessary, a higher pressure inside the MAS NMR rotor reactor can be used. The gas pressure inside batch samples may be limited by the strength of the walls of the glass inserts or the type of the cap used to seal the MAS NMR rotor after the preparation of the reaction system. In both cases, at least atmospheric pressure can be reached inside the sample volume.

A significant advantage of the methodology of NMR spectroscopy is that it allows application of pulse sequences for the discrimination of nuclei in specific local structures, if these nuclei are characterized by a coupling with other nuclei. Examples are dipolar-dephasing techniques such as those used in TRAPDOR experiments (Section II.C). CP experiments can be applied for the discrimination of nuclei in various structures, for example, for the identification and investigation of strongly adsorbed species with low mobility.

It is important to note the quantitative character of NMR spectroscopy. By use of an internal or external intensity standard, a spin counting via the comparison of the signal intensities can be performed. In the case of an external intensity standard, the same spectroscopic parameters must be used, and the effect of Curie's law (Eq. (25)) in experiments at elevated temperatures has to be taken into account.

C.2. Comparison of Batch and Flow Techniques

Considering the various approaches of solid-state NMR spectroscopy, contrasting advantages and limitations must be mentioned for batch and flow techniques. MAS NMR spectroscopy under batch reaction conditions with glass inserts for the preparation of the catalyst samples has the advantage that all the materials and equipment are commercially available. Because the amounts of reactants necessary for these experiments are small, only low costs for isotopically enriched materials

are incurred. A limitation of NMR spectroscopy under batch reaction conditions is the observation time. During a batch experiment, the lifetime of the intermediate species must be longer than the NMR detection period of up to some hours (e.g., in the case of ^{13}C nuclei). As was mentioned above for species with very short lifetimes, therefore, the fate of isotopic labels before and after a chemical conversion under batch reaction conditions should be investigated.

MAS NMR experiments characterizing catalysts in reaction environments in flow systems may be carried out under conditions close to those of industrial processes. The formation of catalytically active surface species and the cause of the deactivation of catalysts can be characterized best under flow conditions. When flow techniques are used for the investigation of reactions under steady-state conditions, a continuous formation and transformation of intermediates occurs. The lifetime of the species under study must be of the order of the length of the free-induction decay, which is *ca.* 100 ms for ^{13}C MAS NMR spectroscopy.

Another valuable approach used with the flow technique is the application of SF protocols, which allow the isolation and characterization of intermediates with longer lifetimes and the investigation of their further conversions (Sections VIII and X). The most significant advantage of the flow techniques consists in their combination with other analytical methods such as UV/Vis spectroscopy or on-line gas chromatography. In the latter case, simultaneous investigation of species adsorbed on the working catalyst and volatile products leaving the reactor is possible.

A significant limitation of NMR experiments of working catalysts in flow systems is the necessity of using isotopically enriched materials as reactants, which leads to high costs. Furthermore, most of the flow approaches described in Section III.B are based on homemade equipments requiring large efforts to make the techniques feasible.

IV. Study of Transition States of Acid-Catalyzed Reactions

A. INDIRECT EXPERIMENTAL EVIDENCE OF REACTIVE CARBENIUM IONS

Knowledge of the mechanisms of surface-catalyzed reactions is of fundamental interest and may also be of value for optimization of existing industrial processes and the development of new ones. In the preceding decade, a number of reviews have been published that summarize the recent progress in mechanistic studies of the heterogeneously catalyzed reactions by *in situ* MAS NMR spectroscopy (1–9). Carbenium ions are assumed to be transition states or intermediates in a variety of reactions catalyzed by acidic solids. However, the attempts to verify the existence of small alkyl cations, such as isopropyl cations or *tert*-butyl cations, on acidic zeolites, have not been successful. Until now, identification of carbenium ions persistent in zeolites is still rarely reported. Today, it is generally accepted that carbenium cations exist mostly as transition states rather than as long-lived intermediates in acid-catalyzed reactions on zeolites (70). Consequently, these species cannot be observed directly by NMR spectroscopy. However, several experimental attempts were undertaken in an endeavor to enable indirect NMR characterization of transition states occurring in acid catalysis on solid materials.

A.1. Formation of Surface Alkoxy Species with Carbenium-Ion-Like Properties

So far, fewer than 10 types of carbenium ions have been reported to be persistent species formed upon adsorption of olefins or alcohols on acidic zeolites. Instead, surface alkoxy (alkoxide) species with carbenium-ion-like properties are suggested to act, most likely, as catalytic intermediates in reactions catalyzed by acidic zeolites. Various groups have observed that, upon adsorption of olefins or alcohols on acidic zeolites, alkoxy species are formed; the observations are based on both *in situ* and *ex situ* ^{13}C MAS NMR spectroscopy (49,50,71–80).

In Table 2, the ^{13}C chemical shifts of the carbon atoms of alkoxy species attached to zeolite framework oxygen atoms are summarized. In general, the ^{13}C spins of surface alkoxy species are characterized by relatively long T_1 times (2–5 s), an efficient ^1H – ^{13}C CP, and broad spinning sideband patterns. The adsorption and evacuation conditions (72,79) used for preparing these alkoxy species have been found to be important, because these intermediates are highly reactive. The chemistry of these surface-bound alkoxy species is similar to that of carbenium ions (79). For example, upon exposure to water at ambient temperature, they undergo hydrolysis to the corresponding alcohols (50,79). The preparation and reactivity of surface methoxy intermediates and their role in the methanol-to-olefin (MTO) process are discussed in detail in Section X.

As an example, Fig. 18 shows ^{13}C CP/MAS NMR spectra recorded during the investigation of surface ethoxy species (78) formed on acidic zeolite HY ($n_{\text{Si}}/n_{\text{Al}} = 2.7$) by a SF protocol. Figure 18a shows the ^{13}C CP/MAS NMR spectrum recorded after a continuous injection of ^{13}C -1-enriched ethanol, $\text{CH}_3^{13}\text{CH}_2\text{OH}$, into the MAS NMR rotor reactor containing calcined zeolite HY. The ethanol was injected at room temperature for 10 min. Subsequently, the loaded zeolite was purged with dry nitrogen (200 mL/min) at room temperature for 2 h.

The spectrum in Fig. 18a is dominated by a signal at 60.5 ppm assigned to the ^{13}C -enriched methylene carbon of ethanol. The signal marked by an asterisk is assigned to a spinning sideband of the signal at 60.5 ppm, and this assignment was confirmed by changing the spinning speeds. The weak signal at 15.8 ppm was caused by the methyl carbon atoms of ethanol. Hence, no reaction was observed at room temperature. After further purging of the working catalyst with dry nitrogen (200 mL/min) at 453 K for 2 h to remove water and excess ethanol, the ^{13}C CP/MAS

TABLE 2
 ^{13}C MAS NMR Chemical Shifts of Surface Alkoxy Species Observed upon the Adsorption of Alkenes or Alcohols on Acidic Zeolites

Surface alkoxy species	Chemical shift ^a (ppm)	Adsorbate	Zeolite	References
Methoxy	56	Methanol	HY	(71–74)
	58–60	Methanol	HZSM-5	(49,72,74,75)
	56	Methanol	H-SAPO-34	(74,76,77)
Ethoxy	73	Ethanol	HY	(78)
<i>sec</i> -Propoxy	87	Propene	HY	(50)
<i>tert</i> -Butoxy	77–81	2-Methyl-2-propanol	HZSM-5	(79,80)

^a The ^{13}C chemical shift for the carbon atoms attached to zeolite framework oxygen.

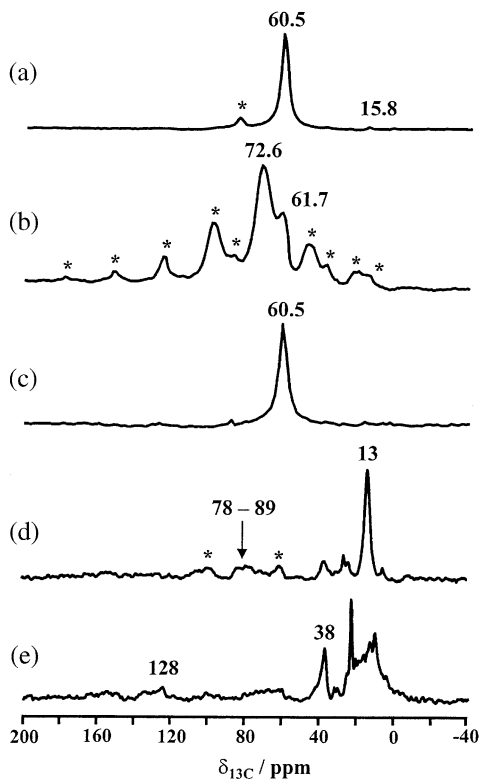
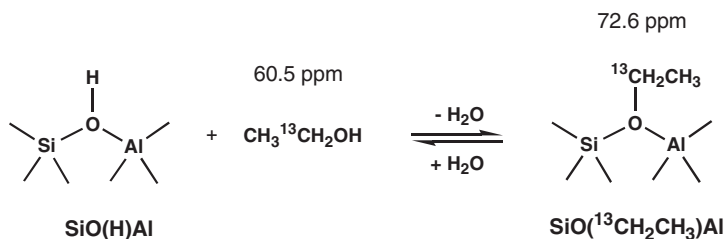


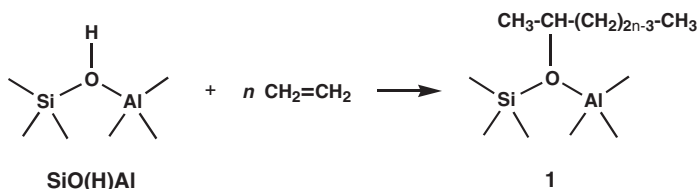
FIG. 18. ^{13}C CP/MAS NMR spectra of zeolite HY ($n_{\text{Si}}/n_{\text{Al}} = 2.7$) recorded after a continuous injection of $\text{CH}_3^{13}\text{CH}_2\text{OH}$ into the MAS NMR rotor reactor at room temperature and subsequent purging with dry nitrogen at room temperature (a); after a subsequent purging with dry nitrogen at 453 K (b); and after water had been injected into the MAS NMR rotor reactor at room temperature (c). The ^{13}C CP/MAS NMR spectra of ethylated zeolite Y ($\text{CH}_3^{13}\text{CH}_2\text{-Y}$) were recorded after thermal treatments at 523 K (d) and 623 K (e). Asterisks denote spinning sidebands.

NMR spectrum shown in Fig. 18b was recorded. The spectrum is dominated by a signal at 72.6 ppm assigned to surface ethoxy species $[\text{SiO}(\text{}^{13}\text{CH}_2\text{CH}_3)\text{Al}]$ with a characteristic spinning sideband pattern indicating the presence of strongly bonded surface species. The signal at 61.7 ppm with spinning sidebands originates from terminal ethoxy species ($\text{SiO}^{13}\text{CH}_2\text{CH}_3$) or strongly bonded ethanol. The assignments of surface ethoxy species are further supported by the reaction of these species with water. Figure 18c shows the ^{13}C CP/MAS NMR spectrum recorded after water was injected onto the working catalyst. The reappearance of the ethanol signal at 60.5 ppm confirms the formation of surface ethoxy species via the SF protocol. The reversible transformation between ethanol and surface ethoxy species on acidic zeolites is explained in Scheme 1.

Surface ethoxy species were also formed on acidic zeolite HY ($n_{\text{Si}}/n_{\text{Al}} = 2.7$) with the conventional vacuum technique, that is, with the adsorption of ^{13}C -1-enriched ethanol, $\text{CH}_3^{13}\text{CH}_2\text{OH}$, and subsequent evacuation at 453 K for 24 h (78). The further transformation of surface ethoxy species into hydrocarbons at elevated



SCHEME 1.

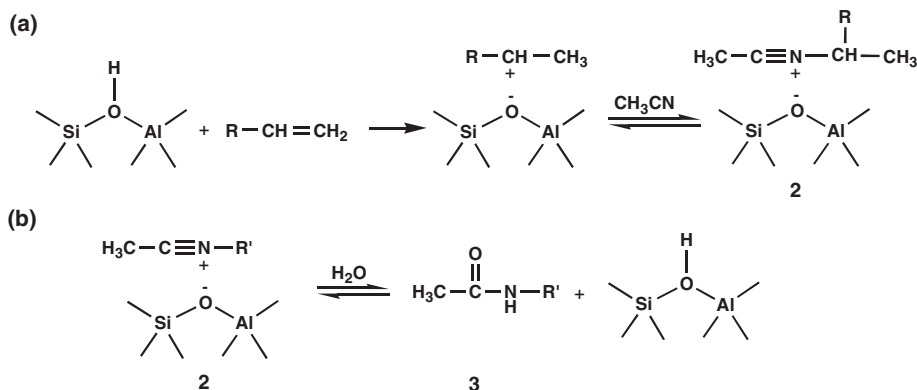


SCHEME 2.

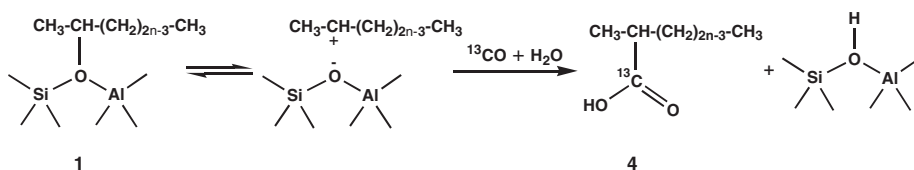
temperatures was investigated by *in situ* ^{13}C CP/MAS NMR spectroscopy under batch reaction conditions (78). Figure 18d shows the ^{13}C CP/MAS NMR spectrum of the surface ethoxy species on zeolite HY recorded after thermal treatment at 523 K for 20 min. At this temperature, a decomposition of surface ethoxy species occurred, which was indicated by the appearance of new signals at 78–89 and 13 ppm. The broad signals at 78–89 ppm may be assigned to oligomeric alkoxy species similar to **1** in Scheme 2, which were also observed by Stepanov and coworkers (81) upon adsorption of ^{13}C -1-ethylene on calcined zeolite HZSM-5 at 296 K. At a reaction temperature of 523 K (Fig. 18d), the initial ethoxy species may decompose first to ethylene, followed by the fast oligomerization of ethylene as shown in Scheme 2. At temperatures higher than 523 K, secondary reactions occur. Figure 18e shows the ^{13}C CP/MAS NMR spectrum recorded after a thermal treatment at 623 K for 20 min. Signals in the aliphatic shift range of 0–50 ppm and trace signals indicative of olefins or, most probably, aromatics appear at *ca.* 120–150 ppm.

A.2. Evidence for the Existence of Carbenium Ions by Trapping Experiments

Trapped by a suitable compound, a transient intermediate can be converted into a more stable species for unequivocal identification. Stepanov and Luzgin (82) investigated the reaction of acetonitrile with 1-octene or *tert*-butyl alcohol on acidic zeolite HZSM-5 ($n_{\text{Si}}/n_{\text{Al}} = 49$) at 296 K by *in situ* MAS NMR spectroscopy under batch reaction conditions. Upon coadsorption of acetonitrile and 1-octene, a ^{13}C MAS NMR signal at 108 ppm was observed, indicative of *N*-alkylnitrilium ions **2** in Scheme 3. As depicted in Scheme 3a, the formation of these cations was explained by trapping the chemically unstable alkylcarbenium ions (formed from the adsorbed



SCHEME 3.



SCHEME 4.

olefin) with the acetonitrile molecules. In accordance with the classic Ritter reaction, the *N*-alkylnitrilium cations **2** are slowly converted to *N*-alkylamide **3** in the presence of water (Scheme 3b). In the case of acetonitrile and alcohol coadsorbed on zeolite HZSM-5, for example, the intermediate *N*-alkylnitrilium ion and the final product *N*-alkylamide were observed simultaneously by MAS NMR spectroscopy under batch reaction conditions (82). These results were confirmed by Barich *et al.* (83), who used an *ex situ* pulse-quench technique. The parameters of the ^{13}C shielding of the alkylnitrilium ion, calculated by the density functional theory (DFT) method, agree very well with the values determined experimentally (83).

The classic Koch reaction between olefins or alcohols and CO in the presence of water provides evidence for the existence of carbenium ions in superacidic solutions (84). Accordingly, indirect NMR spectroscopic evidence for the presence of carbenium ions on solid acid catalysts has been obtained from trapping experiments with carbon monoxide. Stepanov *et al.* (81) studied the oligomerization reaction of ethylene on zeolite HZSM-5 ($n_{\text{Si}}/n_{\text{Al}} = 44$) at 296 K by *in situ* ^{13}C MAS NMR spectroscopy under batch reaction conditions. ^{13}C NMR signals assigned to carbenium ions (300–330 ppm (85,86)) were not observed. At a 32-fold amplification of the spectrum, however, a weak and broad signal at 89 ppm was observed, which is assigned to oligomeric alkoxy species **1** (Scheme 4). Upon further co-adsorption of ^{13}C -enriched carbon monoxide and water, the oligomeric carboxylic acids **4** were formed, causing the appearance of a ^{13}C MAS NMR signal at 189 ppm attributed

to the ^{13}C -enriched carboxyl groups and accompanied by a disappearance of the broad alkoxy signal at 89 ppm. This experiment provided evidence for the equilibrium between carbenium ions and oligomeric alkoxy species. These alkoxy species are transformed into carboxylic acids via the interaction of the equilibrated carbenium ions with carbon monoxide and water (Scheme 4).

By *in situ* ^{13}C MAS NMR spectroscopy, the Koch reaction was also observed upon co-adsorption of butyl alcohols (*tert*-butyl, isobutyl, and *n*-butyl) and carbon monoxide or of olefins (*iso*-butylene and 1-octene), carbon monoxide, and water on HZSM-5 ($n_{\text{Si}}/n_{\text{Al}} = 49$) under mild conditions (87,88). Under the same conditions, but in the absence of water (89), it was shown that ethylene, isobutylene, and 1-octene undergo the Friedel–Crafts acylation (90) to form unsaturated ketones and stable cyclic five-membered ring carboxonium ions instead of carboxylic acids. Carbonylation of benzene by the direct reaction of benzene and carbon monoxide on solid catalysts was reported by Clingenpeel *et al.* (91,92). By ^{13}C MAS NMR spectroscopy, the formation of benzoic acid (178 ppm) and benzaldehyde (206 ppm) was observed on zeolite HY (91), AlCl_3 -doped HY (91), and sulfated zirconia (SZA) (92).

Carboxylic acids can also be formed by a reaction of small alkanes, carbon monoxide, and water on solid acid catalysts (93,94). By *in situ* ^{13}C MAS NMR spectroscopy (93), the activation of propane and isobutane on acidic zeolite HZSM-5 was investigated in the presence of carbon monoxide and water. Propane was converted to isobutyric acid at 373–473 K, while isobutane was transformed into pivalic acid with a simultaneous production of hydrogen. On SZA, methyl isopropyl ketone was observed as evidence for the carbonylation of isobutane with carbon monoxide after the sample was held at 343 K for 1 h (94). When the reaction of isobutane and carbon monoxide was carried out in the presence of water, pivalic acid was identified as the main reaction product (94). These observations are rationalized by the existence of a small number of sites capable of generating carbenium ions, which can be further trapped by carbon monoxide (93).

A.3. Isotope Scrambling

Isotopic labeling is a powerful tool being used to understand the nature of transition states as well as the mechanisms of surface-catalyzed reactions. By *in situ* ^{13}C MAS NMR spectroscopy, the scrambling of ^{13}C labels at room temperature was investigated upon adsorption of [^{13}C -1]-1-octene on calcined zeolite HZSM-5 ($n_{\text{Si}}/n_{\text{Al}} = 44$) (81). Figure 19 shows the ^{13}C CP/MAS NMR spectra recorded 10 min to 53 h after adsorption of [^{13}C -1]-1-octene on zeolite HZSM-5. The spectra indicate that the ^{13}C -labeled terminal olefinic $=\text{CH}_2$ groups evident in the spectra at *ca.* 113 ppm are transformed into terminal ^{13}C -labeled paraffinic CH_3 groups, evident at 14.3 ppm. Furthermore, the selective ^{13}C label penetrates into internal $-\text{CH}_2-$ groups of the octene hydrocarbon skeleton, characterized by resonances occurring at 33.0 ppm.

A possible pathway for this scrambling is presented in Scheme 5. First, protons from acidic bridging OH groups of the zeolite catalyst are transferred to the adsorbed octene molecules. Subsequently, carbenium ions are formed, and the $=\text{CH}_2$ groups are transformed into CH_3 groups. The further scrambling of the ^{13}C label over the hydrocarbon chain can proceed via species incorporating protonated

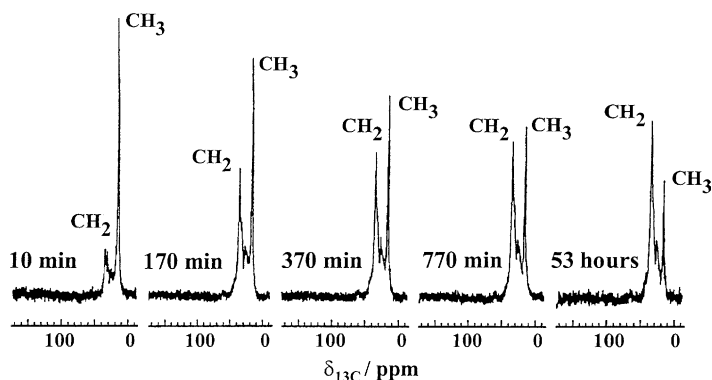
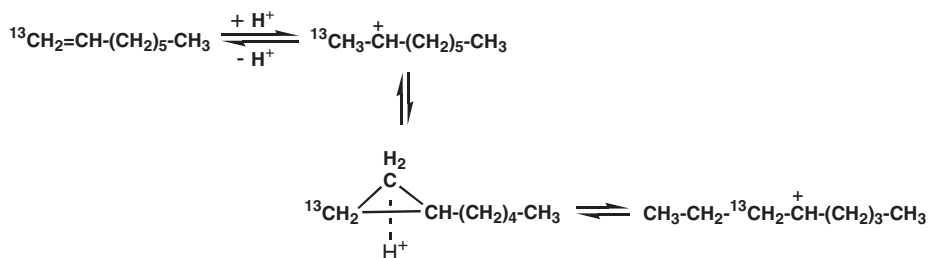


FIG. 19. ^{13}C CP/MAS NMR spectra of zeolite HZSM-5 ($n_{\text{Si}}/n_{\text{Al}} = 44$) loaded with [^{13}C -1]-1-octene and recorded at 296 K after various times. Reproduced with permission from (81). Copyright 1998 Elsevier Science.



SCHEME 5.

cyclopropane rings, which are well accepted for organic compounds in superacidic solutions (70,85,95) and for the alkane isomerization on bifunctional catalysts (96). Hence, the observed scrambling of the selective ^{13}C label in adsorbed [^{13}C -1]-1-octene provides indirect experimental evidence for the existence of alkylcarbenium ions as transition states on acidic zeolites.

In situ ^{13}C MAS NMR spectroscopy has also been applied to characterize the ^{13}C scrambling in *n*-butene conversion on zeolite H-ferrierite (97), *n*-butane conversion on SZA (98), *n*-butane isomerization on $\text{Cs}_{2.5}\text{H}_{0.5}\text{PW}_{12}\text{O}_{40}$ (99), *n*-pentane conversion on SZA (100), isopropylation of benzene by propene on HZSM-11 (101,102), and propane activation on HZSM-5 (103–105) and on Al_2O_3 -promoted SZA (106,107). The existence of carbenium ions was proposed to rationalize the experimental ^{13}C scrambling results observed by *in situ* ^{13}C MAS NMR spectroscopy.

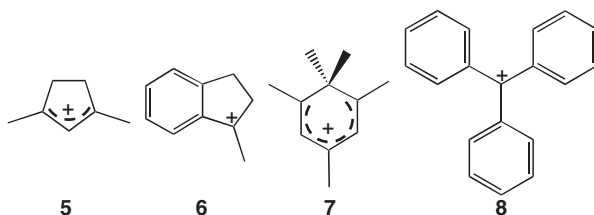
On the other hand, ^1H MAS NMR spectroscopy offers the possibility for investigations of transition states of acid-catalyzed reactions via an H/D exchange between acidic surface OH groups of the solid catalyst and adsorbate molecules. For example, Beck *et al.* (108) studied the H/D exchange between deuterated benzene molecules and bridging OH groups on various acidic zeolites in the temperature range of 333–393 K. As in the case of ^{13}C label scrambling, the investigation of the H/D exchange dynamics at various temperatures and an Arrhenius plot of

the measured rates allow the determination of activation energies. For the H/D exchange of benzene on zeolites H,NaY, USY, and HZSM-5, activation energies E_A of 107, 85, and 60 kJ/mol, respectively, were obtained (108). Mildner and Freude (109) confirmed these results by using a high-temperature MAS NMR probe with a laser heating system (Fig. 11, Section III.A). Activation energies E_A of 102 and 93 kJ/mol were calculated for the H/D exchange of benzene on zeolites HY with cation-exchange degrees of 85 and 92%, respectively (109). According to theoretical investigations of Beck *et al.* (108), the experimentally obtained activation energies agree with those characteristic of benzene molecules adsorbed at the acidic bridging OH groups via van der Waals interactions. These authors concluded that the H/D exchange between benzene molecules and bridging OH groups does not occur via free benzenium ions as intermediates.

H/D exchange and ^{13}C scrambling occurring during the activation of small alkanes on solid acid catalysts is discussed in detail in Section V.

A.4. Persistent Carbenium Ions in Zeolites Characterized by NMR Spectroscopy

The capability of acidic zeolites to generate and stabilize carbenium ions has been a matter of extensive discussion for years. Primarily on the basis of solid-state NMR investigations, zeolites were reclassified from solid superacids to solid acids that are slightly weaker than 100% sulfuric acid (110). Haw and coworkers (111) suggested, therefore, that the gas-phase proton affinity (PA) of the corresponding neutral olefin or aromatic could predict whether the carbenium ion under study is persistent or not in an acidic zeolite. If the PA value of the hydrocarbon is higher than *ca.* 874 kJ/mol, the proton transfer from zeolite to hydrocarbon would result in a carbenium ion (111). In the case of zeolite HY loaded with ^{13}C -enriched propene, for example, Haw *et al.* (50) observed ^{13}C MAS NMR signals at 47, 145, and 249 ppm, which they assigned to 1,3-dimethyl cyclopentadienyl cation **5** (Scheme 6). The parent compound of this carbenium ion, 1,3-dimethyl cyclopentadiene, has the theoretical PA value of 902 kJ/mol, which is greater than the threshold for a protonation by acidic zeolites. The formation of alkyl-substituted cyclopentadienyl cations was also observed in the reaction of methanol or acetone on zeolite HZSM-5 when an *ex situ* pulse-quench technique was applied (112–114). Among other persistent carbenium ions in zeolites, characterized by solid-state NMR spectroscopy, are the methylindanyl cation **6** (115), *gem*-dimethyl benzenium ions (116,117), such as the 1,1,2,4,6-pentamethyl benzenium ion **7**, and triarylmethyl cations (118–120), such as the triphenylmethyl cation **8**.



SCHEME 6.

B. KETO–ENOL ISOMERIZATION ON ACIDIC ZEOLITE HZSM-5 EVIDENCED BY H/D EXCHANGE

The aldol condensation is an important reaction in organic synthesis leading to the formation of C–C bonds. This reaction is catalyzed by zeolites (121–127). To understand the mechanisms involved, various spectroscopic methods (122–125, 128–130) and theoretical calculations (131,132) have been employed, mainly to investigate the nature of the adsorbed aldehydes and ketones on various zeolite catalysts. It was suggested that the keto–enol isomerization is the first step of this reaction (132). *In situ* MAS NMR spectroscopy has been applied to characterize the chemical state of acetone adsorbed on zeolite HZSM-5 (133). The observed H/D exchange between Brønsted acid sites and adsorbed acetone molecules indicates the formation of an enol via a concerted action of bridging hydroxyl protons and neighboring framework oxygen atoms in zeolite HZSM-5 (133).

Figure 20 shows the ^1H MAS NMR spectra of zeolite HZSM-5 ($n_{\text{Si}}/n_{\text{Al}} = 21.5$) before (a) and after (b) adsorption of acetone- d_6 at room temperature. The ^1H MAS NMR signals at 4.0 and 1.8 ppm are attributed to bridging OH groups (SiOHAl) and silanol groups (SiOH), respectively (Fig. 20a). Upon adsorption of 0.33 mmol

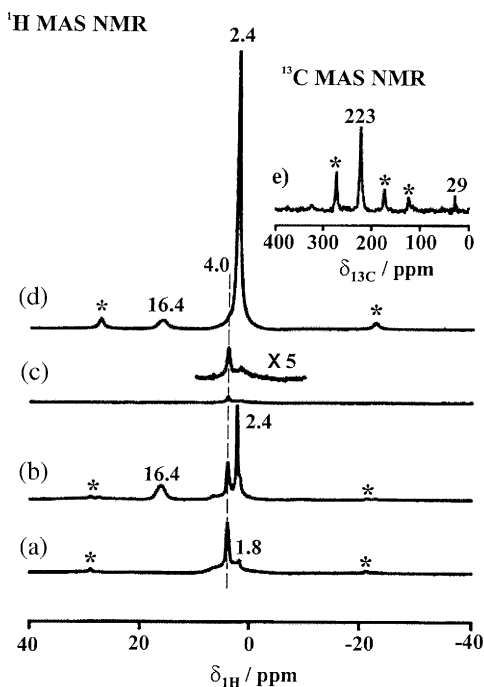
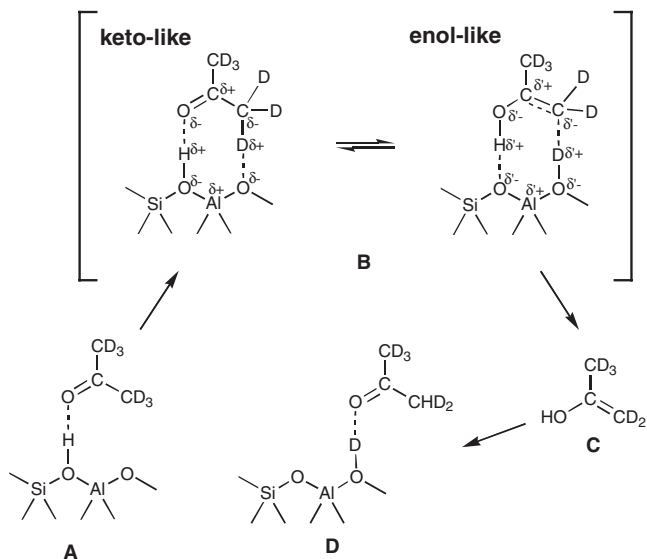


FIG. 20. ^1H MAS NMR spectra of zeolite HZSM-5 ($n_{\text{Si}}/n_{\text{Al}} = 21.5$) before (a) and after (b) adsorption of 0.33 mmol acetone- d_6 per gram. In (c) and (d), the ^1H MAS NMR spectra of zeolite D,HZSM-5 recorded before and after loading, respectively, with 0.34 mmol acetone- ^{13}C -2 per gram of zeolite are shown. The inset (e) is the ^{13}C MAS NMR spectrum of the sample in (d). Asterisks denote spinning sidebands. Reproduced with permission from (133). Copyright 2003 The Royal Society of Chemistry.



SCHEME 7.

of acetone- d_6 per gram of calcined zeolite HZSM-5, new signals appeared at 2.4 and 16.4 ppm. As verified by $^1H\{^{27}Al\}$ TRAPDOR NMR spectroscopy (Section II.C), the signal at 16.4 ppm originates from hydrogen-bonded bridging hydroxyl protons in complexes with adsorbed acetone molecules. The signal at 2.4 ppm is attributed to protons of methyl groups in adsorbed acetone molecules.

As depicted in Scheme 7, this observation hints at an H/D exchange between SiOHAl groups and adsorbed acetone- d_6 molecules via a monomolecular mechanism. The H/D exchange involving more than one acetone molecule at one SiOHAl group can be excluded, because only a small amount of acetone- d_6 was adsorbed on zeolite HZSM-5 (≤ 0.5 acetone- d_6 per SiOHAl group) (133). As shown in Scheme 7(A), the acetone molecule is first adsorbed at a bridging hydroxyl group via a hydrogen bond. This hydrogen bond induces a partial charge transfer from the framework to the carbonyl group. As a result of the charge redistribution, the adjacent framework oxygen becomes more basic. The keto-enol isomerization is achieved as shown in Scheme 7(B). A subsequent or simultaneous transfer of the hydrogen-bonded bridging hydroxyl proton produces the acetone enol (C). Finally, the unstable acetone enol is converted to an acetone molecule (D). By this mechanism, the H/D exchange is realized without the formation of other reaction products. The keto-enol isomerization in Scheme 7 is therefore also responsible for the observed aldol condensation on acidic solid catalysts.

The H/D exchange between the methyl groups of adsorbed acetone molecules and the Brønsted acid sites of zeolite HZSM-5 was also observed upon adsorption of ^{13}C -2-acetone on a deuterated catalyst (D,HZSM-5, $n_{Si}/n_{Al} = 21.5$) at room temperature (Figs 20c and d). The ^{13}C MAS NMR spectrum of ^{13}C -2-acetone adsorbed on zeolite D,HZSM-5 (Fig. 20e) consists of the carbonyl signal at 223 ppm with a featured sideband pattern and a methyl signal at 29 ppm. No significant

conversion of acetone can be identified, which further supports the monomolecular mechanism shown in [Scheme 7](#).

V. Activation of Saturated Hydrocarbons on Solid Catalysts

Activation of C–H bonds of alkanes on the surfaces of solid acid catalysts such as zeolites, heteropolyacids, or SZA can lead to various reactions including cracking, isomerization, dehydrogenation, and oligomerization ([134–137](#)). Hydrogen exchange between alkanes and acidic groups of solid acids occurs in early stages of the reaction, which implies the activation of these saturated hydrocarbons ([138–149](#)). By investigating the isotopic labeling (H/D exchange and ^{13}C scrambling) of the reactants, useful information concerning the reaction mechanisms can be obtained.

A. CATALYTIC TRANSFORMATION OF METHANE INTO AROMATICS UNDER NON-OXIDATIVE CONDITIONS

As the simplest hydride of carbon and the major constituent of natural gas, methane has attracted increasing attention in recent years. The transformation of methane into higher hydrocarbons ([150](#)) has been a topic of broad and ongoing interest in view of the limited oil resources. In 1993, Xu and co-workers ([151](#)) reported the catalytic transformation of methane into aromatics under non-oxidative conditions. The reaction occurs at 973 K at atmospheric pressure on transition-metal-ion-modified catalysts, such as zeolite Mo/HZSM-5. Solid-state NMR spectroscopy has been used to demonstrate the nature of the catalytically active sites in molybdenum-modified zeolites applied for this reaction ([152,153](#)). The investigations were performed by using the equipment shown in [Fig. 9](#) (Section III.A). This technique allows the preparation of catalyst samples under *ex situ* flow conditions, transfer of the powder material into the MAS NMR rotor, and a sealing in a gas-tight MAS NMR rotor without contacting with air ([51](#)).

Zeolite Mo/HZSM-5 was found to be a suitable catalyst for methane dehydroaromatization. Methane conversions of *ca.* 10% and benzene selectivities of 50–60% could be reached at 973 K ([154–156](#)). To prepare the catalyst, a modification of the micron-sized and, alternatively, nanometer-sized zeolite HZSM-5 crystallites was performed with an aqueous solution of ammonium heptamolybdate and a subsequent calcination in air at 773 K ([152](#)). The ^{27}Al MAS NMR spectra of these catalysts, recorded after rehydration, consist of signals at –14, 0, 30, and 52 ppm. The ^{27}Al MAS NMR signal at 52 ppm was assigned to tetrahedrally coordinated framework Al atoms. The intensity of this signal decreased with increasing molybdenum loading ([152](#)). The broad signals at 0 and 30 ppm were assigned to octahedrally coordinated and penta-coordinated extra-framework aluminum species, respectively ([157,158](#)). The signal at –14 ppm was attributed to octahedrally coordinated aluminum in crystalline $\text{Al}_2(\text{MoO}_4)_3$ species ([159,160](#)).

The intensities of signals at –14, 0, and 30 ppm increased with increasing molybdenum loading ([152](#)). A series of ^{27}Al MAS NMR spectra indicated that, with increasing amounts of ammonium heptamolybdate, a dealumination occurred as a

consequence of interactions of the molybdenum species with the framework of the zeolite. On the nanometer-sized zeolite crystallites, this effect was stronger, resulting in larger amounts of $\text{Al}_2(\text{MoO}_4)_3$ species. By correlation of the ^{27}Al MAS NMR results and the catalytic data, it was shown that the presence of large amounts of $\text{Al}_2(\text{MoO}_4)_3$ species makes the zeolite catalysts less active for methane dehydroaromatization (3).

^1H MAS NMR investigations of zeolites Mo/HZSM-5 indicated that the molybdenum species preferentially react with silanol groups (1.7 ppm) and extra-framework AlOH groups (2.4 ppm) on the outer surface of the zeolite (51). After methane conversion on zeolites Mo/HZSM-5 at a temperature of 873 K or less under flow conditions, the ^1H MAS NMR spectra of the working catalyst contained signals of silanol and bridging OH groups at 1.7 and 4.1 ppm, respectively. An additional sharp line at -0.1 ppm was explained by residual methane remaining in the zeolite pores (161). After the temperature had been raised to 973 K and held for 10 min, the ^1H MAS NMR signal of bridging OH groups at 4.1 ppm decreased drastically, and two new signals appeared at 6.8 and 7.9 ppm, which emerged clearly with prolonged reaction times. The signal at 6.8 ppm was assigned to water molecules caused by the formation of Mo_2C (161). The signal at 7.9 ppm was assigned to hydrogen atoms of aromatic adsorbates formed at the Brønsted acid sites. The decrease of the signal intensity of Brønsted acid sites indicates that these sites take part in the aromatization or the hydrogen transfer process of the reaction. Direct observation of the ^1H MAS NMR signals during the methane dehydroaromatization provided strong support for an acid-induced aromatization process (161).

Methane dehydroaromatization on zeolites Mo/HZSM-5 was also investigated by solid-state ^{13}C MAS NMR spectroscopy (162). Both variation of the state of the transition metal component and products (such as ethane, benzene, and ethylene) adsorbed in zeolite were observed after reaction at high temperature (900–1000 K). Molybdenum carbide species, dispersed on the external surface or in the internal channels of the zeolite catalysts, had formed during the reaction (162).

B. ACTIVATION AND AROMATIZATION OF PROPANE ON SOLID ACID CATALYSTS

The activation and functionalization of light alkanes are drawing increasing attention because of the large interest in commercially attractive routes for the replacement of expensive raw materials by cheap alkanes. In recent years, propane aromatization has been investigated extensively on a variety of Ga-containing zeolites, for example, Ga-exchanged or Ga-impregnated zeolite HZSM-5 (Ga/HZSM-5) (163–167), H-gallosilicates (H-GaMFI) (168–174), and H-galloaluminosilicate (H-GaAlMFI) (175). The aromatization of propane on zeolite Ga/HZSM-5 occurs at temperatures of 773–823 K. During this process, a number of reactions (i.e., cracking, dehydrogenation, aromatization, and hydrogenolysis) occur. The thermodynamic feasibility of these reactions is controlled primarily by the temperature. Because the mechanism of propane activation at low temperatures remained a matter of debate, this reaction was intensively investigated by NMR spectroscopy (105,176–184).

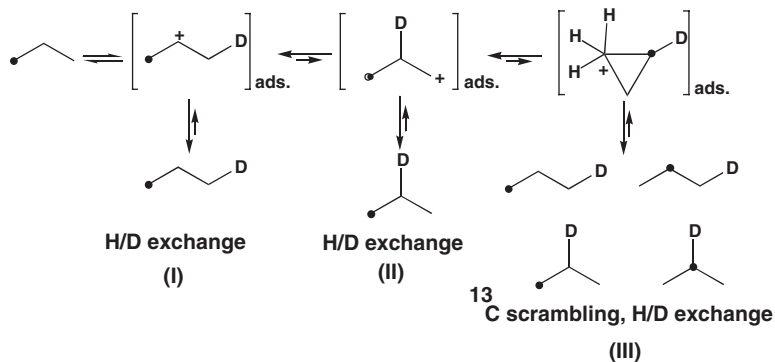
Using labeled ^{13}C -2-propane as reactant and gallium-modified silicalite-1 ($n_{\text{Si}}/n_{\text{Al}} = 480$, 0.96 wt.% Ga) and zeolites Ga/HZSM-5 ($n_{\text{Si}}/n_{\text{Al}} = 35$, 1.02 wt.% Ga) and HZSM-5 ($n_{\text{Si}}/n_{\text{Al}} = 35$) as catalysts, Derouane *et al.* (105,178–181) and Ivanova *et al.* (103,104,177,182,183) investigated the activation of propane by solid-state ^{13}C MAS NMR spectroscopy. The NMR experiments were performed under batch reaction conditions with samples fused in glass inserts. NMR data characterizing zeolites Ga/HZSM-5 loaded with ^{13}C -2-propane were recorded after heating of the sample for various times at 573 K in an external oven (179,181). The ^{13}C MAS NMR spectrum taken at time $t = 0$ consisted of a single line at 17 ppm (not shown). This signal is attributed to ^{13}C -labeled methylene groups of the reactant ^{13}C -2-propane. After 5 min at 573 K, an additional ^{13}C MAS NMR signal was observed at 16 ppm, attributed to the methyl groups of propane. A complete ^{13}C scrambling leading to the theoretical 2:1 ratio of the methyl (16 ppm) and methylene (17 ppm) signals was reached after 20 min at 573 K. No other signal occurred in the ^{13}C MAS NMR spectrum in this step.

In contrast, an extremely low activity was observed for the gallium-modified silicalite-1. ^{13}C scrambling started first at 723 K, which clearly indicates that Brønsted acid sites are necessary to activate propane adsorbed on zeolites Ga/HZSM-5 (179,181). A low activity was also observed for ^{13}C -2-propane adsorbed on zeolite HZSM-5 in the absence of gallium. On this catalyst, ^{13}C scrambling was observed after heating at 573 K for 20 min, and the theoretical 2:1 ratio of the signal intensities of methyl and methylene groups was reached after 80 min at 573 K.

The finding of the low-temperature activation of propane on zeolite Ga/HZSM-5 indicates a bifunctional reaction mechanism (179,181). The highly dispersed gallium oxide species in close vicinity to the Brønsted acid sites promote the initial activation of propane. Derouane *et al.* (179,181) further showed that hydrogen inhibits the activation of propane. This effect was explained by a competitive adsorption of hydrogen on the gallium species or even by a reduction of Ga^{3+} to Ga^+ species.

Stepanov *et al.* (184) investigated the H/D exchange between deuterated propane and acidic bridging OH groups of zeolite HZSM-5 by ^1H MAS NMR spectroscopy in the temperature range of 457–543 K. These authors determined activation energies of E_{A} of 108 kJ/mol for the exchange of acidic bridging OH groups with the methyl groups of propane, and of value of E_{A} of 117 kJ/mol for the exchange with the methylene groups of propane. These values agree with the activation energies obtained theoretically for the hydrogen exchange with methane ($E_{\text{A}} = 122$ kJ/mol (143)) and ethane ($E_{\text{A}} = 118$ kJ/mol (144)). A transition state of carbonium ions (with pentacoordinated carbon atoms) was proposed for the hydrogen exchange. A further argument against the assumption of propyl cations as transition state was the finding of a non-regiospecific H/D exchange (184). In contrast, Sommer *et al.* (145) and Haouas *et al.* (106) reported that only methyl hydrogen of propane was isotopically exchanged during the initial stages of the H/D exchange process, and the H/D regioselectivity was, however, lost at longer contact times.

Internal hydrogen scrambling and isotope redistribution between propane and solid catalysts may proceed by a rather complex mechanism involving several pathways with different rates and activation energies. The competitive pathways cannot be distinguished if the temperature for activating propane on zeolites is



SCHEME 8.

higher than those necessary for crossing the activation barriers of all the above-mentioned pathways. Taking this point into account, Haouas *et al.* (107) applied *in situ* MAS NMR spectroscopy to investigate the initial stage of propane activation on an Al_2O_3 -promoted SZA catalyst in the temperature range of 303–375 K. In this case, the samples were prepared in gas-tight MAS NMR rotors and heated in a variable-temperature MAS NMR probe. The sequence of reaction steps was established in terms of reaction rates. Three competitive pathways of isotope redistribution was demonstrated during the reaction: (i) a regioselective H/D exchange between acidic groups of the solid surface and the deuterons of the methyl group of propane-1,1,1,3,3,3- d_6 , monitored by ^1H MAS NMR spectroscopy, (ii) an intramolecular H/D exchange between methyl deuterons and protons of the methylene group, without exchange with the catalyst surface, monitored by ^2H MAS NMR spectroscopy, and (iii) an intramolecular ^{13}C scrambling, by a skeletal rearrangement process, favored at higher temperatures, monitored by ^{13}C MAS NMR.

The selective H/D exchange between the catalyst and the methyl hydrogen atoms of the propane occurred first. The H/D scrambling between methyl and methylene hydrogen atoms occurred at higher temperatures. A third, much slower, process resulted in a complete H/D and ^{13}C isotope scrambling via a skeletal rearrangement. The apparent activation energy for the H/D exchange with the catalyst is significantly lower than that of each of the scrambling processes. The activation energy characteristic of the ^{13}C scrambling was estimated to be very close to that of the H/D exchange. This finding suggests that the two processes imply a common transition state responsible for both vicinal hydride migration and protonated cyclopropane formation. All pathways are consistent with a classical carbenium ion-type mechanism, as shown in Scheme 8.

VI. Photocatalytic Reactions on Solid Catalysts

In 1972, Fujishima and Honda (185–187) opened a new research field in heterogeneous photocatalysis with their discovery of the photocatalytic splitting of water on TiO_2 electrodes. Thereafter, TiO_2 , in part because of its high stability and lack of

toxicity, has been applied frequently for the catalytic degradation of a variety of environmentally harmful organic compounds (188,189). As a new approach to the study of heterogeneous photocatalysis on TiO_2 , an *in situ* optical/MAS NMR method was introduced in 1997 by Raftery and co-workers (52,190). By a light pipe, which was incorporated into the solid-state NMR probe, the near UV light could be brought to the sample via a 10-mm gap between the two radio-frequency Helmholtz coils (Fig. 10, Section III.A). This technique allows the recording of ^1H and ^{13}C MAS NMR spectra under reaction conditions during a photocatalytic process (52).

A. PHOTOCATALYTIC CONVERSION OF CHLORINE-CONTAINING ORGANIC COMPOUNDS ON TITANIUM OXIDE

A noteworthy application of the *in situ* optical/MAS NMR technique was reported in an investigation of the photocatalytic oxidation of trichloroethylene (TCE: $\text{CHCl}=\text{CCl}_2$) on TiO_2 -containing catalysts (190). Figure 21 shows the ^{13}C MAS NMR spectra obtained during photooxidation of TCE on a TiO_2 powder (Degussa P-25) in the presence of oxygen. The UV irradiation time is given in minutes. The ^{13}C MAS NMR spectra indicate the degradation of TCE (117 and 124 ppm), the formation of dichloroacetyl chloride (DCAC: Cl_2CHCOCl , 70 and 167 ppm), carbon monoxide (CO, 184 ppm), phosgene (Cl_2CO , 144 ppm), and pentachloroethane ($\text{CHCl}_2\text{CCl}_3$, 79 and 100 ppm), and their final conversion to carbon dioxide (CO_2 , 124 ppm) (190).

To minimize the problem of UV light scattering by the powder catalyst, a TiO_2 photocatalyst consisting of highly dispersed TiO_2 on the surface of transparent porous Vycor glass (PVG) was employed. The influence of water on the photooxidation of TCE was investigated by introducing water before TCE and oxygen were loaded onto the TiO_2 /PVG catalyst. Figure 22 shows ^{13}C MAS NMR spectra

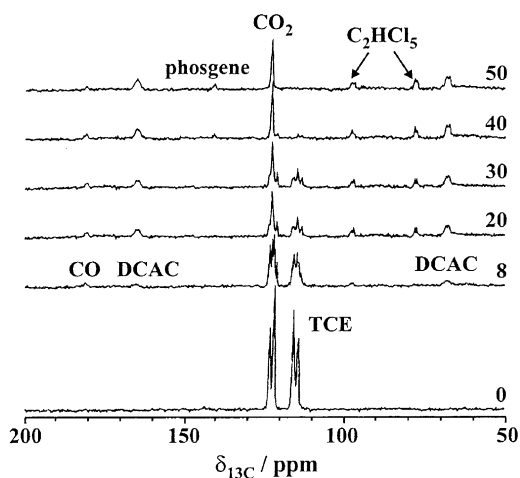


FIG. 21. ^{13}C MAS NMR spectra recorded during the photocatalytic oxidation of TCE ($48\ \mu\text{mol}$) on $170\ \text{mg}$ of TiO_2 in the presence of gaseous oxygen ($60\ \mu\text{mol}$). The UV irradiation time is indicated in minutes (right). Reproduced with permission from (190). Copyright 1997 American Chemical Society.

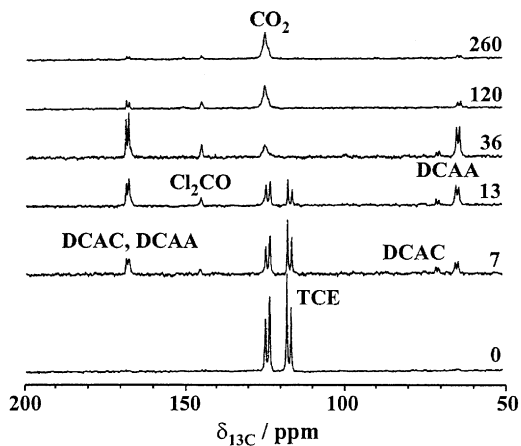


FIG. 22. ^{13}C MAS NMR spectra recorded during the photocatalytic oxidation of TCE ($48\ \mu\text{mol}$) with gaseous oxygen ($96\ \mu\text{mol}$) and water ($0.1\ \text{mmol}$) as co-reactants on a TiO_2/PVG catalyst. The UV irradiation time is indicated in minutes (right). Reproduced with permission from (52). Copyright 1998 American Chemical Society.

recorded as a function of the UV irradiation time. The degradation of TCE upon UV illumination occurs in a very similar fashion to that observed under dry conditions. However, the formation of dichloroacetic acid (DCAA: Cl_2CHCOOH , 63 and 167 ppm) was observed as a major intermediate. It is evident that the degradation of TCE leads to formation of DCAC and an immediate hydrolysis of DCAC to DCAA. DCAA could be further photooxidized, but its degradation rate was found to be low. The formation of phosgene was almost suppressed in the presence of water.

The photocatalysis of TCE on the TiO_2 -coated optical microfibers in the presence of oxygen was further investigated by *in situ* ^{13}C MAS NMR spectroscopy (191). The major products are phosgene and carbon dioxide, with small quantities of DCAA and trichloroacetaldehyde remaining on the catalyst at the end of the reaction. Solid-state NMR spectroscopy has also been applied successfully for the investigation of the photocatalytic degradation of dichloromethane (192,193).

B. PHOTOCATALYTIC CONVERSION OF OXYGENATES ON TITANIUM OXIDE

A further application of the solid-state NMR technique was the investigation of the photocatalytic oxidation of ethanol on various TiO_2 -containing catalysts, such as Degussa P-25 (194), TiO_2/PVG (194), TiO_2 -coated optical microfibers (195), and V-doped TiO_2 (196). Two adsorption sites were identified for ethanol: (i) a chemisorbed ethoxide species and (ii) a hydrogen-bonded species. Long-lived intermediates, including acetaldehyde (CH_3CHO), acetic acid (CH_3COOH), formic acid (HCOOH), acetate (CH_3COO^-), and carbon monoxide were observed, and the surface-bound ethoxide species was determined to be the photocatalytically reactive surface ethanol species. Carbon dioxide was produced as a final product of photocatalytic oxidation of ethanol. It was found that the presence of water decreases

the rate of ethanol photodegradation, because water and ethanol compete for the same adsorption sites on the surface of the TiO_2 catalysts (195).

Other photocatalytic reactions that have been successfully investigated by *in situ* solid-state NMR spectroscopy are the oxidation of 2-propanol (197) and the oxidation of acetone (198).

VII. Investigations of Chemical Behavior and Local Structure of Surface Sites in Zeolites and Microporous Silicoaluminophosphates

In general, it is of interest to investigate the surface sites on calcined catalysts and adsorbates as a complementary approach to elucidation of the nature of surface complexes formed by adsorbate molecules. In comparison with the large number of *in situ* NMR investigations of the mechanisms of reactions catalyzed by solids, only a few investigations have been performed to clarify the chemical behavior and local structure of the surface sites during the solid-catalyzed reactions. Most of the atoms contributing to surface sites of dehydrated catalysts are involved in strong solid-state interactions. The strong line broadening that is a result of quadrupolar interactions, for example, may hinder NMR investigations of these surface sites by the MAS technique. Therefore, the application of sophisticated solid-state NMR techniques is necessary (Section II.B).

A. CHEMICAL BEHAVIOR AND LOCAL STRUCTURE OF SURFACE SITES IN ZEOLITES

The incorporation of Al atoms into the framework of zeolites occurs in a tetrahedral oxygen coordination and leads to negative framework charges. These framework charges are compensated by protons in acidic hydroxyl groups or by extra-framework cations such as Li^+ , Na^+ , Cs^+ , Mg^{2+} , etc. Accordingly, these surface sites are responsible for the chemical behavior of zeolites in separation processes and in catalysis (199,200).

^{27}Al spin-echo NMR spectroscopy is a suitable technique for investigating the local structure of Al atoms in dehydrated zeolites. To overcome problems with the length of the ring-down time of the probe in comparison with the rapid decay of the NMR signal, often a $\pi/6-\tau-\pi/6-\tau$ -echo sequence with the pulse delay τ is applied (201). The samples used for these investigations have to be fused in quartz glass inserts or sealed in gas-tight capsules. ^{27}Al spin-echo NMR spectra of dehydrated and unloaded zeolites HY, H-mordenite, and HZSM-5 consist of signals with line broadenings according to quadrupole coupling constants of $C_{\text{QCC}} = 13\text{--}16$ MHz (Table 3). In contrast, framework Al atoms in calcined zeolites in the Na^+ or NH_4^+ form are characterized by significantly lower C_{QCC} values of 5–9 MHz.

Adsorption of strongly basic molecules, such as pyridine, on dehydrated H-form zeolites also results in a significant narrowing of the ^{27}Al spin-echo NMR signal of framework Al atoms (202). This narrowing is a consequence of a transfer of the hydroxyl protons from the zeolite framework to the basic adsorbate molecules, which causes a higher local symmetry of the AlO_4 tetrahedron, leading to a decrease of the electric field gradient and the quadrupolar interactions. In contrast, adsorption

TABLE 3

²⁷Al Quadrupole Coupling Constant, C_{QCC} , and Asymmetry Parameter, η , of Framework Al Atoms in Dehydrated Zeolites Y (faujasite), MOR (mordenite), and ZSM-5

Compound or zeolite	C_{QCC} /MHz	η	References
Unloaded zeolites			
NaY	5.5	0.3	(201)
NH ₄ Y	9.0	0.8	(204)
HY	13.1	0.75	(201)
HY	13.5	0.4	(204)
HY	15.3	0.4	(205)
NH ₄ MOR	5.0	0.7	(204)
HMOR	15.0	0.35	(204)
NH ₄ ZSM-5	9.0	0.8	(204)
HZSM-5	16.0	0.1	(201)
HZSM-5	15.5	0.5	(204)
Loaded zeolites (with added material designated following slash)			
HZSM-5/1 CH ₃ OH/SiOHAl	8.0	0.9	(206)
HZSM-5/3 CH ₃ OH/SiOHAl	2.5	0.9	(206)
HZSM-5/1 CH ₃ OCH ₃ /SiOHAl	11.2	0.2	(207)
SiOHAl/methoxonium ion ^a	8.2	0.85	(208)
SiOHAl/methoxy group ^a	16.2	0.16	(208)

^a Results of theoretical DFT calculations.

of benzene molecules interacting with bridging OH groups via hydrogen bonding only does not bring about a significant change of the ²⁷Al spin-echo NMR signal of framework Al atoms (202), because no hydrogen transfer occurs from the zeolite framework to these adsorbate molecules (202). Hence, the ²⁷Al quadrupole coupling constant is a parameter that is sensitive to the chemical interaction of adsorbate molecules and reactants with bridging OH groups acting as Brønsted acid sites in zeolite catalysts (203).

The conversion of methanol to hydrocarbons (MTHC) on acidic zeolites is of industrial interest for the production of gasoline or light olefins (see also Section X). Upon adsorption and conversion of methanol on calcined zeolites in the H-form, various adsorbate complexes are formed on the catalyst surface. Identification of these surface complexes significantly improves the understanding of the reaction mechanism. As demonstrated in Table 3, methanol, dimethyl ether (DME), and methoxy groups influence in a characteristic manner the quadrupole parameters of the framework Al atoms in the local structure of bridging OH groups. NMR spectroscopy of these framework atoms under reaction conditions, therefore, helps to identify the nature of surface complexes formed.

In a recent work (207), *in situ* ¹H and ²⁷Al MAS NMR spectroscopy was used to investigate the Brønsted acid sites of zeolite HZSM-5 during the conversion of methanol under CF conditions. As a consequence of the application of MAS instead of the spin-echo technique, only framework Al atoms involved in quadrupolar interactions according to $C_{QCC} \leq 5$ MHz could be observed. Upon injection of methanol into the MAS NMR rotor reactor filled with calcined zeolite HZSM-5, a single ²⁷Al MAS NMR signal arose at 54 ppm at reaction temperatures up to

473 K. This signal was assigned to framework Al atoms contributing to the local structure of bridging OH groups, which interact with methanol molecules. At reaction temperatures of $T > 473$ K, no ^{27}Al MAS NMR signal of framework Al atoms with a quadrupole coupling constant of $C_{\text{QCC}} \leq 5$ MHz was observed. Therefore, the presence of adsorption complexes consisting of bridging OH groups interacting with methanol ($C_{\text{QCC}} = 2.5$ MHz (206)) or water molecules ($C_{\text{QCC}} = 2.2$ MHz (209)) could be excluded under these reaction conditions (207).

B. CHEMICAL BEHAVIOR AND LOCAL STRUCTURE OF SURFACE SITES IN MICROPOROUS SILICOALUMINOPHOSPHATES

In the preceding decade, microporous silicoaluminophosphates have drawn increasing interest as solid catalysts in chemical technology, because of their acidic and shape-selective properties. H-SAPO-34 with the chabasite structure, for example, is a suitable catalyst for the conversion of MTO (210). H-SAPO-37 with the faujasite structure was applied for the isomerization of *n*-decane (211) and the isobutylene/2-butene alkylation (212).

Replacement of phosphorus sites by silicon atoms in the aluminophosphate framework ($\text{P} \rightarrow \text{Si}$) leads to the formation of $\equiv\text{Si}-\text{O}-\text{Al}\equiv$ bridges. As in crystalline aluminosilicates, negative charges are formed at the tetrahedrally coordinated framework Al atoms, and these charges are compensated by the hydroxyl protons of bridging OH groups (213). A replacement of a pair of neighboring Al and P sites by two Si atoms ($\text{Al}, \text{P} \rightarrow \text{Si}, \text{Si}$) causes the formation of $\equiv\text{Si}-\text{O}-\text{Si}\equiv$ bridges, which are free of framework charges and can lead to the formation of siliceous islands (214).

Investigations performed by Minchev *et al.* (215) indicated that the framework of crystalline silicoaluminophosphates can be damaged upon the rehydration of the template-free material. In the case of rehydrated template-free H-SAPO-5 and H-SAPO-34, for example, a strong loss of the crystallinity occurs in the presence of water. However, the crystallinity can be completely restored after an additional dehydration at 823 K. Hydration of H-SAPO-37 at room temperature causes irreversible structural changes and leads to a material that is totally amorphous to X-ray diffraction (216). At temperatures of more than 345 K, template-free H-SAPO-37 exhibits a high stability toward hydration (216).

To investigate the hydration and dehydration processes of H-SAPO-34 and H-SAPO-37, ^1H and ^{27}Al MAS NMR spectroscopy was applied under CF conditions with the equipment shown in Fig. 12 (217). The chemical behavior and the change of the silicoaluminophosphate framework were monitored as nitrogen loaded with water or dry nitrogen was injected into the MAS NMR rotor filled with the silicoaluminophosphates. By this approach, the primary adsorption sites of water in silicoaluminophosphates and the variation of the aluminum coordination were observed. Furthermore, the formation of framework defects and the conditions of water desorption were characterized.

Figure 23 shows ^1H and ^{27}Al CF MAS NMR spectra recorded during the hydration of calcined H-SAPO-34. The ^1H MAS NMR spectrum of the calcined material recorded before the start of the hydration is dominated by a signal of

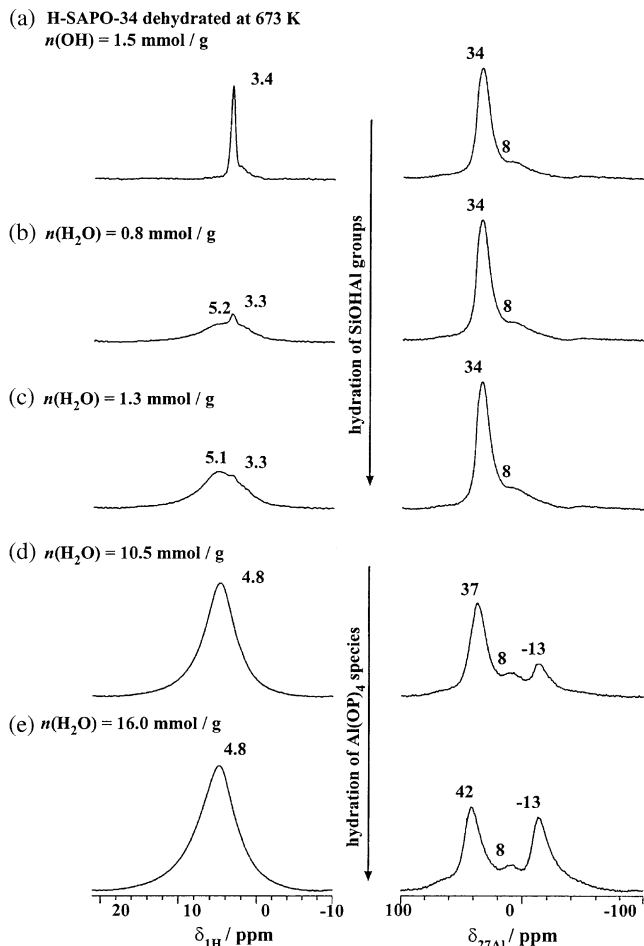


FIG. 23. ^1H (left) and ^{27}Al MAS NMR spectra (right) of silicoaluminophosphate H-SAPO-34 recorded during the hydration of the calcined sample in a flow of nitrogen loaded with water. Reproduced with permission from (217). Copyright 2003 Elsevier Science.

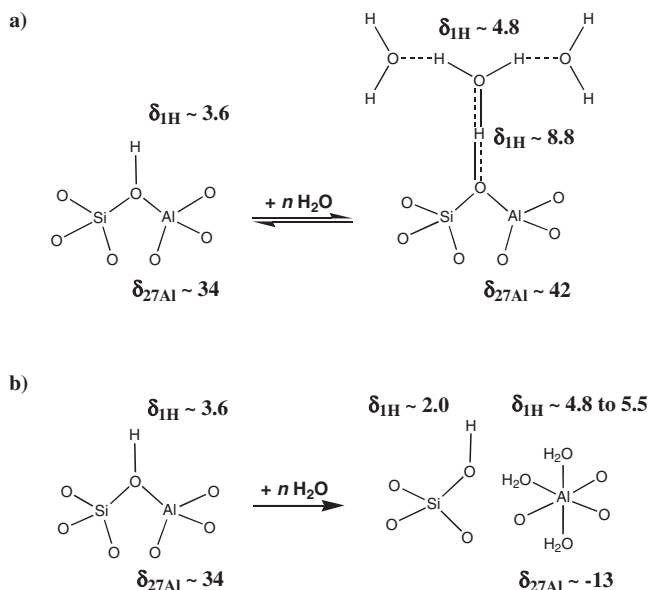
bridging OH groups (SiOHAl) at 3.4 ppm, and the weak high-field shoulder is attributed to a small number of SiOH groups (Fig. 23a, left). The ^1H spin counting verified that each Si atom in the framework of H-SAPO-34 resulted in one bridging OH group. The ^{27}Al MAS NMR spectrum in Fig. 23a, right, is dominated by a strong signal at 34 ppm attributed to tetrahedrally coordinated framework Al atoms. The weak high-field shoulder at *ca.* 8 ppm is caused by a small number of pentacoordinated Al atoms (217).

At the beginning of the hydration of calcined H-SAPO-34 (i.e., after the start of the injection of nitrogen loaded with water vapor into the spinning MAS NMR rotor), only a change in the ^1H MAS NMR spectra was observed (Figs 23b and c, left). After a water adsorption of 0.8 mmol/g, a significant decrease of the signal of

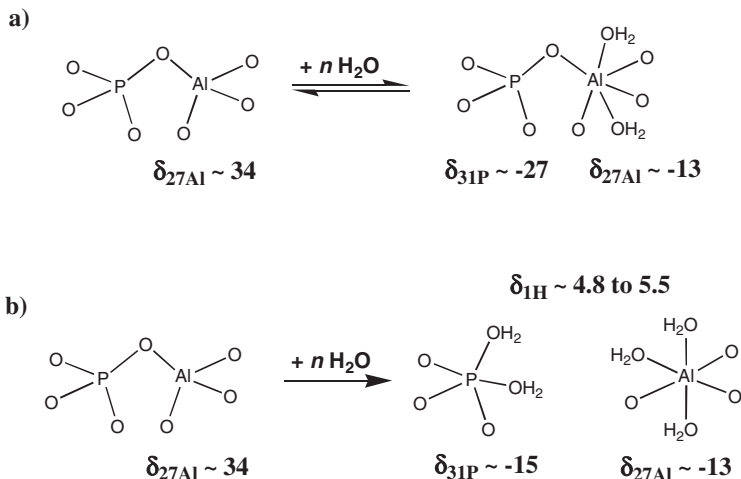
SiOHAl groups occurred, accompanied by the appearance of a broad signal assigned to water molecules. The resonance position of this broad water signal indicates the presence of hydrogen-bonded water molecules and the formation of hydroxonium ions, which are involved in a rapid chemical exchange (218,219). Until a water adsorption of *ca.* 5 mmol/g, no change of the ^{27}Al MAS NMR signals was found. Hence, the hydration of calcined H-SAPO-34 is inferred to start with an adsorption of water molecules exclusively at Brønsted acidic bridging OH groups (Scheme 9a).

The ^1H MAS NMR spectrum of H-SAPO-34 loaded with more than *ca.* 10 mmol of water per gram (Figs 23d and e, left) is dominated by a broad signal of bulk water at *ca.* 4.8 ppm. In the ^{27}Al MAS NMR spectra, a weak signal appears at -13 ppm, which indicates the formation of octahedrally coordinated Al atoms (Figs 23d and e, right). After adsorption of more than three water molecules per bridging OH group, therefore, a second hydration step starts, which leads to a coordination of water to Al atoms (Scheme 10). Neither for weakly hydrated H-SAPO-34 nor for strongly hydrated H-SAPO-34, were ^1H MAS NMR signals of defect SiOH groups observed. This result indicates that the adsorption of water molecules at bridging OH groups does not lead to the breakage of $\equiv\text{Si}-\text{O}-\text{Al}\equiv$ bonds as depicted in Scheme 9b.

As found for H-SAPO-34, the hydration of H-SAPO-37 is separated into two successive steps. At a water adsorption of more than 6 mmol/g, only a hydration of Brønsted acidic bridging OH groups occurred, whereas upon further hydration, a coordination of water molecules to Al atoms was found (217). In contrast to the adsorption of water in H-SAPO-34, the adsorption of water at framework Al atoms



SCHEME 9.



SCHEME 10.

in H-SAPO-37 is accompanied by a strong hydrolysis of $\equiv\text{P}-\text{O}-\text{Al}\equiv$ bonds. Hydration of H-SAPO-37 at elevated temperatures ($T \geq 353 \text{ K}$), however, was found to lead to hydration of bridging OH groups only and not to a coordination of water molecules to framework Al atoms (217). This adsorption behavior occurring at elevated temperatures hinders the above-mentioned hydrolysis of $\equiv\text{P}-\text{O}-\text{Al}\equiv$ bonds in H-SAPO-37, which is responsible for the damage of the structure observed upon hydration at room temperature.

CF MAS NMR investigations (217) of the dehydration of H-SAPO-34 indicated that this process also consists of two successive steps. Even at 298 K, desorption of water molecules coordinated to Al atoms occurs. The hydration of the $\equiv\text{P}-\text{O}-\text{Al}\equiv$ bonds in H-SAPO-34 occurs as a reversible process on the time scale of the NMR experiments. The second dehydration step, that is, the dehydration of bridging OH groups, requires temperatures of at least 373 K. No breakage of $\equiv\text{Si}-\text{O}-\text{Al}\equiv$ bonds and formation of defect SiOH groups was found in H-SAPO-34. In contrast, no significant desorption of water molecules coordinated to Al atoms was observed upon purging of H-SAPO-37 with dry nitrogen at 298 K. The significantly stronger coordination of water molecules in H-SAPO-37 in comparison with H-SAPO-34 indicates an immediate hydrolysis of the H-SAPO-37 framework. In the case of H-SAPO-37, the hydrolysis of the framework starts with a breakage of $\equiv\text{P}-\text{O}-\text{Al}\equiv$ bonds, and $\equiv\text{Si}-\text{O}-\text{Al}\equiv$ bonds are not affected (217).

Another application of ^1H and ^{27}Al MAS NMR spectroscopy under CF conditions was an investigation of the ammoniation and deammoniation of the silicoaluminophosphates H-SAPO-34 and H-SAPO-37 (220). During the solid-state NMR measurements, the silicoaluminophosphates were purged by nitrogen gas loaded with ammonia and by dry nitrogen gas. Again, a two-step adsorption process was found. The first ammoniation step, an adsorption of ammonia exclusively at Brønsted acidic bridging OH groups (SiOHAl), leads to the formation of ammonium ions (NH_4 -form). The second ammoniation step, a coordination of

ammonia molecules to framework Al atoms in $\equiv\text{P}-\text{O}-\text{Al}\equiv$ bridges, occurred at higher ammonia coverages. The first adsorption step is a chemisorption of ammonia molecules on surface OH groups, which has no influence on the local structure of framework Al atoms, and the second ammoniation step is a weak physisorption accompanied by a transformation of tetrahedrally coordinated framework Al atoms to octahedrally coordinated aluminum species. Upon purging of strongly ammoniated H-SAPO-34 and H-SAPO-37 with dry nitrogen at 413 K, it was found that the second ammoniation step is a reversible process.

Hydration of the NH_4 -form of SAPO-34 and SAPO-37, that is, of materials that were ammoniated at the bridging OH groups, caused a coordination of water molecules exclusively to Al atoms in $\equiv\text{P}-\text{O}-\text{Al}\equiv$ bridges. This process led to a hydrolysis of the framework (220). No hydrolysis of the silicoaluminophosphate framework occurred, provided that not only the bridging OH groups (SiOHAl), but also the aluminophosphate framework ($\equiv\text{P}-\text{O}-\text{Al}\equiv$) was covered by ammonia. The latter finding may explain the stabilizing effect of preloaded ammonia on silicoaluminophosphates toward hydration and weak hydrothermal treatments as recently observed for H-SAPO-34 (221).

VIII. Synthesis of MTBE on Acidic Zeolites

MTBE is used on a large scale as an octane number boosting additive in unleaded gasoline. Sulfonic acid resins are applied as efficient catalysts for the industrial production of MTBE from methanol and isobutylene (222). Since 1987, investigations of the synthesis of MTBE with reactants in the gas phase have been performed with zeolites HY (223–225), H-Beta (226), HZSM-5 (224,225), and H-BZSM-5 (227) as catalysts.

A. REVERSIBLE CONVERSION OF MTBE ON BORON-MODIFIED PENTASIL UNDER BATCH CONDITIONS

The first *in situ* MAS NMR investigation of the synthesis of MTBE on acidic zeolites was performed by Mildner *et al.* (228) under batch reaction conditions. In this investigation, the temperature-jump MAS NMR technique (stop-and-go experiment, see Section III.A) was applied to characterize the reaction dynamics under non-equilibrium conditions on a boron-modified pentasil zeolite ($n_{\text{Si}}/n_{\text{B}} = 80$). The catalyst was calcined in a glass insert, which was sealed after the loading with MTBE. ^1H MAS NMR spectra were recorded during the heating period of 100 s. Then the laser power was switched off and the temperature of the samples fell back to room temperature within about 60 s. During the stop period of 1 h, when the reaction state was frozen, a ^{13}C MAS NMR spectrum was recorded. By repetition of the stop-and-go periods for several times, the complete reaction could be measured by both ^1H and ^{13}C MAS NMR spectroscopy.

Using the above-mentioned experimental approach, Mildner *et al.* (228) recorded ^1H MAS NMR spectra of the MTBE/B-pentasil system at 373, 389, 405, and 421 K. These spectra were obtained with the sample in thermal equilibrium after the

samples were held for more than 10 min at the given temperature. The spectra consisted of four lines indicative of the CH₂ groups of isobutylene (4.8 ppm), the OCH₃ groups of MTBE (3.4 ppm), the *tert*-butyl CH₃ groups of MTBE (1.4 ppm), and the CH₃ groups of isobutylene (1.8–2.3 ppm). The rate constants of the MTBE decomposition and formation were determined by evaluation of the intensities of these signals. The corresponding apparent activation energies of MTBE decomposition and formation were found to be 51 ± 5 and 32 ± 3 kJ/mol, respectively, in the temperature range of 373–421 K.

B. MTBE SYNTHESIS ON ZEOLITE H-BETA UNDER CF CONDITIONS

A number of investigations were performed to characterize the synthesis of MTBE from isobutylene and methanol on acidic zeolites HY, HZSM-5, and H-Beta by the ¹³C MAS NMR technique under CF conditions (60,229,230). For example, Fig. 24 shows the ¹³C MAS NMR spectra recorded in the steady state of the synthesis of MTBE from methanol and isobutylene (both with ¹³C isotopes in natural abundance) on calcined zeolite H-beta ($n_{\text{Si}}/n_{\text{Al}} = 16$) at 333 K. The signal at 52 ppm was assigned to adsorbed methanol molecules, and that at 32 ppm to methyl groups of isobutylene dimers and oligomers. The signals at *ca.* 80 ppm were assigned to alkoxy species (230). Methyl groups of butoxy species were inferred to be responsible for the signal at 29 ppm.

Applying the equipment shown in Fig. 13 (Section III.B) the authors performed a simultaneous analysis of the reaction products leaving the MAS NMR rotor reactor by on-line gas chromatography and an NMR characterization of the compounds adsorbed on the catalyst under steady-state conditions. These investigations showed that the intensity of the signals at *ca.* 80 ppm correlates with the yields of MTBE determined by gas chromatography (60). An increase of the reaction temperature of the exothermic synthesis of MTBE from 333 to 353 K, led to a simultaneous

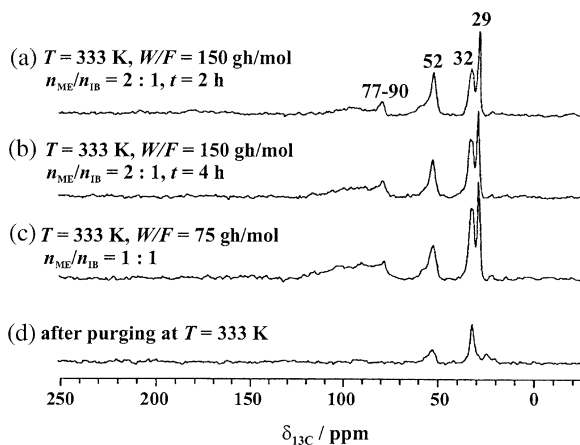


FIG. 24. ¹³C MAS NMR spectra recorded in the steady state of the synthesis of MTBE by isobutylene and methanol on calcined zeolite H-Beta ($n_{\text{Si}}/n_{\text{Al}} = 16$) (a–c) and after purging of the catalyst with dry nitrogen (d). Reproduced with permission from (230). Copyright 2000 Elsevier Science.

decrease of the ^{13}C MAS NMR signal at *ca.* 80 ppm and of the yield of MTBE, from 27 to 12% (60).

By characterizing various zeolite catalysts under the same reaction conditions, the authors found weaker ^{13}C MAS NMR signals of alkoxy species for the less active zeolites HY and HZSM-5 than for the more active zeolite H-beta (230). This observation suggests that the alkoxy species observed under steady-state conditions act as reactive surface species in the MTBE synthesis from isobutylene and methanol on acidic zeolite catalysts.

IX. Alkylation of Aromatic Compounds on Acidic and Basic Zeolites

A. ALKYLATION OF TOLUENE

Investigating the side-chain methylation of toluene by methanol on basic zeolites such as Cs,NaX and Cs,NaY, Yashima *et al.* (231) suggested that the basic catalyst has two functions: (i) an adsorption of toluene at cesium cations, which enhances the polarization of the methyl group and (ii) the dehydrogenation of methanol to formaldehyde, which acts as the alkylating agent. Formaldehyde was suggested to react with toluene to form styrene, which is further hydrogenated to ethylbenzene (Fig. 25a). Figure 25b describes the surface species formed by methanol on basic solids. The ^{13}C MAS NMR chemical shifts of these surface species are indicated beneath the respective structures in the figure.

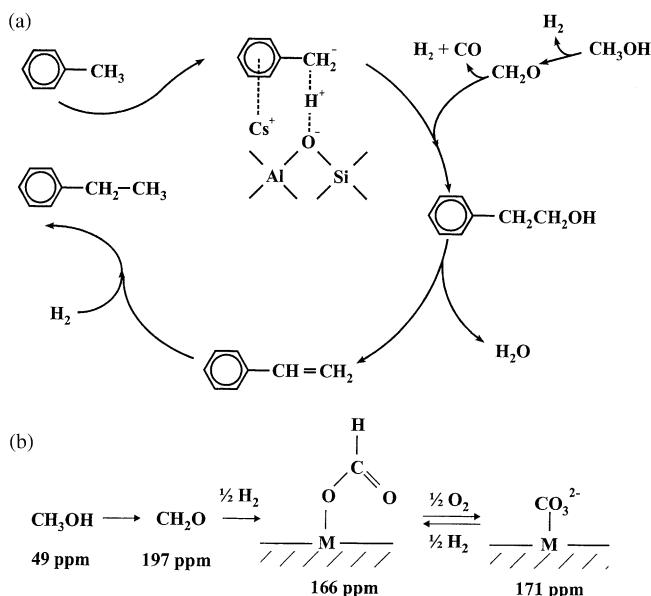


FIG. 25. Proposed mechanism of the side-chain alkylation of toluene by methanol on basic zeolites (a) and the surface species formed during the decomposition of methanol on basic zeolites (b).

The first ^{13}C MAS NMR spectroscopic investigations of the side-chain methylation of toluene with methanol were performed under batch reaction conditions with a basic cesium-exchanged zeolite X (Cs,NaX) catalyst (232). In more recent work (233), the impregnation of zeolites Cs,NaX and Cs,NaY with cesium hydroxide or acetate was described. A subsequent calcination leads to strongly basic sites, which are well dispersed in the zeolite pores (233). These sites govern the catalytic behavior of basic zeolites X and Y. Impregnated zeolites Cs,NaY (CsOH/Cs,Na-Y) (234) and Cs,NaX (CsOH/Cs,Na-X) (235,236) were used to investigate the side-chain methylation of toluene with methanol by MAS NMR spectroscopy under batch reaction conditions as well as under CF conditions. For example, Fig. 26 shows the ^{13}C MAS NMR spectra of zeolite CsOH/Cs,NaX recorded under batch reaction conditions after loading of a mixture of ^{13}C -enriched methanol and of selectively ^{13}C -enriched toluene ($\text{C}_6\text{H}_5^{13}\text{CH}_3$) in a molar ratio of 3:1. The spectrum obtained at 295 K (Fig. 26a) consists of the CH_3 signals of the reactants methanol (49 ppm) and toluene (21 ppm). The absence of the signal at 49 ppm and the appearance of a new signal at 166 ppm, observed after heating the loaded zeolites to 573 K (Fig. 26b), indicate a complete conversion of methanol into formate species formed by conversion of methanol (237,238). Formaldehyde, which could have been formed by dehydrogenation of methanol, was not detected. After heating of the zeolite catalyst to 723 K, the signal of formate species at 166 ppm decreased, and an additional line appeared at 171 ppm, which is assigned to surface carbonates (Fig. 26c). Furthermore, signals of the reaction product ethylbenzene (15 and 29 ppm) were observed. Ethylbenzene was formed first after heating of the catalyst to 723 K, that is, after the methanol had already been fully converted to formate species. This result indicates that formate species formed from methanol may act as reactive surface species contributing to the side-chain alkylation of toluene on zeolite CsOH/Cs,NaY.

The inference of reactive surface formate species formed on zeolite CsOH/Cs,NaX was further supported by ^{13}C CF MAS NMR spectroscopy (Fig. 27) (235,236). This *in situ* investigation was performed under CF conditions at a

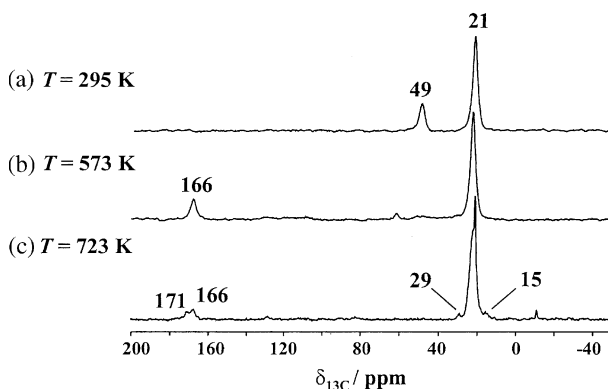


FIG. 26. ^{13}C MAS NMR spectra of calcined zeolite CsOH/Cs,NaX recorded after loading with a mixture of selectively ^{13}C -enriched toluene ($\text{C}_6\text{H}_5^{13}\text{CH}_3$) and ^{13}C -enriched methanol in a molar ratio of 3:1 at 295 K (a) and upon heating to 573 K (b) and 723 K (c). Reproduced with permission from (235). Copyright 2000 Elsevier Science.

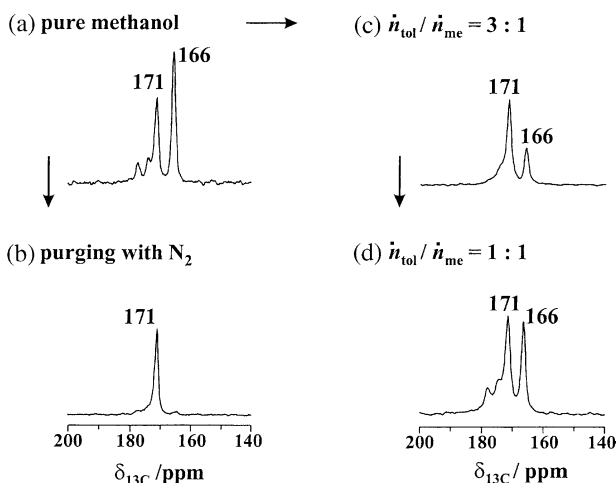


FIG. 27. ^{13}C CF MAS NMR spectra recorded at 723 K during the conversion of pure ^{13}C -enriched methanol on zeolite CsOH/Cs,NaX (a), after purging with dry nitrogen (b), and during the conversion of mixtures of toluene and ^{13}C -enriched methanol with molar ratios of 3:1 (c) and 1:1 (d). Reproduced with permission from (235). Copyright 2000 Elsevier Science.

reaction temperature of 723 K and by injecting reactant flows with various feed ratios into the spinning MAS NMR rotor reactor filled with the calcined catalyst. The spectral range shown in Fig. 27 is restricted and shows only the signals of surface formate (166 ppm) and carbonate species (171 ppm). The aim was to characterize the response of the surface formate signal to the changes of the reactant flow.

The ^{13}C CF MAS NMR spectrum recorded during the conversion of pure ^{13}C -enriched methanol on zeolite CsOH/Cs,NaX is dominated by the signal of surface formate species at 166 ppm, accompanied by signals of carbonate species at 171–175 ppm (Fig. 27a). After purging of the used catalyst for 1 h with dry nitrogen, the spectrum was reduced to the signal of carbonate species (Fig. 27b), which indicates that the previously existing surface formate species are chemically unstable. On the other hand, after switching of the reactant flow from pure ^{13}C -enriched methanol to a toluene/ ^{13}C CH₃OH mixture with a molar ratio of 3:1, a strong decrease of the formate signal (166 ppm) was observed (Fig. 27c). This finding indicates that the surface formate species were consumed by the reactant toluene. To corroborate this inference, the toluene/methanol molar ratio in the reactant mixture was decreased to 1:1, whereupon the signal of formate species increased again (Fig. 27d). Hence, the lower toluene content in the reactant flow decreases the consumption of the surface formate species. These findings are evidence for the reactivity of the surface formate species in the side-chain alkylation of toluene on zeolite CsOH/Cs,NaX.

B. ALKYLATION OF ANILINE

Mono- and di-*N*-methylation of aniline are important reactions for the synthesis of intermediates in fine chemicals manufacture. Aniline methylation by methanol

has been performed on a number of catalysts, and the products were found to be *N*-methylaniline (NMA), *N,N*-dimethylaniline (NNDMA), and toluidines (239–241). The product distribution is influenced by the reaction temperature, the residence time in the reactor, the methanol to aniline feed ratio, and the nature of the catalyst. To understand the reaction mechanisms, the reaction was studied almost exclusively by analyzing the product distribution in the gas phase by using gas chromatography. The spectroscopic investigation of the working catalyst is an approach to reaching a deeper insight into the reaction mechanism.

B.1. Alkylation of Aniline on Basic Zeolite CsOH/Cs,NaY

To investigate the methylation of aniline by methanol on basic zeolite CsOH/Cs,NaY, the CF MAS NMR technique was combined with SF protocols (242). In the first period, these protocols allowed the observation of adsorbate complexes formed on solid catalysts under steady-state conditions. In subsequent periods, an identification of adsorbates acting as intermediates of the further reaction was carried out.

The left-hand side of Figs 28a–c shows ^{13}C CF MAS NMR spectra which were recorded during the conversion of pure ^{13}C -enriched methanol on zeolite CsOH/Cs,NaY under CF conditions at reaction temperatures of 473–523 K (242). As was observed previously (234–236), the conversion of methanol (49 ppm) on the basic zeolite catalysts caused the formation of surface formate species, leading to a ^{13}C MAS NMR signal at 166 ppm. Upon cessation of the methanol flow at the reaction

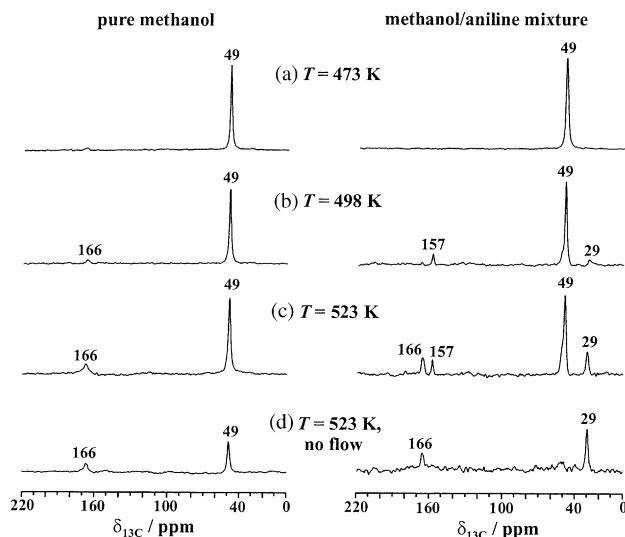


FIG. 28. ^{13}C CF MAS NMR spectra recorded during the conversion of pure $^{13}\text{CH}_3\text{OH}$ (left) and an aniline/ $^{13}\text{CH}_3\text{OH}$ mixture (right) on calcined zeolite CsOH/Cs,NaY ($W/F = 40$ g h/mol, molar aniline/ $^{13}\text{CH}_3\text{OH}$ ratio of 1:4) at reaction temperatures of 473 K (a), 498 K (b), and 523 K (c) and at 523 K after stopping the reactant flow (d). Reproduced with permission from (242). Copyright 2001 The Royal Society of Chemistry.

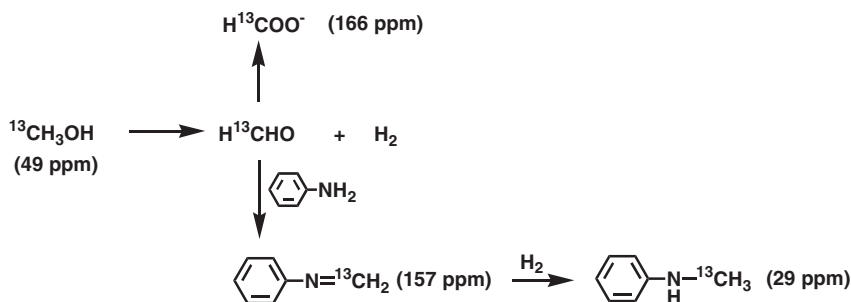
temperature of 523 K, the signals of methanol and formate species at 49 and 166 ppm, respectively, decreased (Fig. 28d, left).

The spectra on the right-hand side of Fig. 28 were obtained during the conversion of a reactant mixture consisting of aniline and methanol in a molar ratio of 1:4. The spectrum obtained at 473 K consists of a single signal assigned to methanol, and the spectrum obtained at 498 K includes additional signals at 29 and 157 ppm. That at 29 ppm was assigned to the reaction product NMA and that at 157 ppm to *N*-methyleneaniline. A further increase of the reaction temperature to 523 K led to the formation of surface formate species, with a signal at 166 ppm, and a strong increase of the signal at 29 ppm caused by an increase of the concentration of the reaction product NMA.

To decide whether the *N*-methyleneaniline formed on the working catalyst acts as intermediate in the formation of NMA, a SF experiment was performed, and a spectrum was recorded at 523 K after the reactant flow had been stopped (242). In the spectrum (Fig. 28d, right), the signals of methanol (49 ppm) and of *N*-methyleneaniline (157 ppm) disappeared completely, while the signal of the reaction product NMA (29 ppm) had increased significantly in intensity. Hence, not only methanol, but also the *N*-methyleneaniline species are consumed by the formation of NMA. This result is evidence of the role of *N*-methyleneaniline as an intermediate in the methylation of aniline according to Scheme 11. In the first reaction in the sequence, the reactant methanol is converted on the basic catalyst to formaldehyde and/or surface formate species acting as alkylating species. Subsequently, the alkylation of aniline leads to the formation of *N*-methyleneaniline, which is hydrogenated in a final reaction to NMA (242).

B.2. Alkylation of Aniline on Acidic Zeolite HY

Recently, a novel reaction mechanism was proposed for the alkylation of aniline with methanol on acidic zeolite HY (243). By SF MAS NMR spectroscopy, the formation and decomposition of *N,N,N*-trimethylanilinium ions on the working catalyst were observed. Figure 29 shows the ^{13}C MAS NMR spectra recorded under CF conditions during methylation of aniline by methanol at reaction temperatures of 473–523 K. In these experiments, a mixture of aniline and ^{13}C -enriched methanol ($W/F = 40 \text{ g h/mol}$) in a molar ratio of 1:2 was injected into the MAS NMR rotor



SCHEME 11.

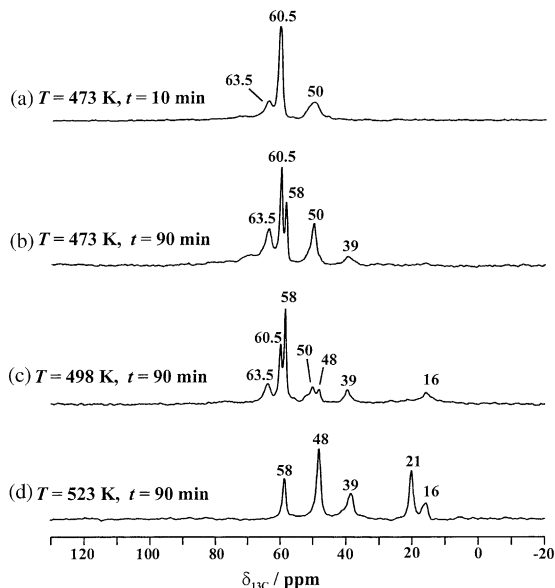


FIG. 29. ^{13}C MAS NMR spectra recorded during the methylation of aniline by ^{13}C -enriched methanol on zeolite HY ($n_{\text{Si}}/n_{\text{Al}} = 2.7$) under CF reaction conditions ($W/F = 40$ g h/mol, molar aniline/ ^{13}C methanol ratio of 1:2) at temperatures of 473 K for 10 min (a), 473 K for 90 min (b), 498 K for 90 min (c), and 523 K for 90 min (d). Reproduced with permission from (243). Copyright 2002 American Chemical Society.

reactor. The signal at 50 ppm in Fig. 29a is caused by methanol adsorbed on zeolite HY. The signals observed at 63.5 and 60.5 ppm indicate the formation of DME adsorbed in side-on and end-on conformations, respectively (244,245). After a reaction time of 90 min at 473 K, a signal of protonated NMA, i.e., *N*-methyl-anilinium ions ($[\text{PhNH}_2\text{CH}_3]^+$), appeared at 39 ppm (Fig. 29b). The protonation of NMA by Brønsted acid sites (73) was evidenced by the significant low-field shift of the methyl signal from *ca.* 30 ppm to the position of 39 ppm. Furthermore, another new signal appeared at 58 ppm, which was assigned to *N,N,N*-trimethylanilinium ions ($[\text{PhN}(\text{CH}_3)_3]^+$). Similar quaternary ammonium ions, such as tetramethylammonium ions, give a narrow ^{13}C MAS NMR signal at *ca.* 56 ppm (246).

Upon a further increase in the reaction temperature to 498 K, the intensity of the signal at 58 ppm attributed to *N,N,N*-trimethylanilinium ions increased, while the intensities of the methanol signal at 50 ppm and of the DME signals at 60.5 and 63.5 ppm decreased, and eventually disappeared (Figs 29c and d). During aniline methylation at 498–523 K, additional signals appeared at 48, 21, and 16 ppm. The signal at 48 ppm is assigned to protonated NNDMA (i.e., *N,N*-dimethylanilinium ions ($[\text{PhNH}(\text{CH}_3)_2]^+$)). The signals at 16 and 21 ppm originate from ring-alkylated anilines, that is, *ortho*- and *para*-toluidine, either in their neutral or in their protonated states. Except for *N,N,N*-trimethylanilinium ions, all the adsorbates on the working catalyst existed in their adsorption/desorption equilibrium with the desorbed state in the gas phase.

The role of the *N,N,N*-trimethylanilinium ions in the overall reaction was further investigated by SF experiments. After *N,N,N*-trimethylanilinium ions had been formed on zeolite HY under CF conditions, the reactant flow was stopped and an

MAS NMR investigation of the progressive reaction on the working catalyst was performed at various reaction temperatures.

The ^{13}C MAS NMR spectrum shown in Fig. 30a was recorded after the continuous injection of the reactants at 473 K for 1 h with a molar aniline: ^{13}C CH₃OH ratio of 1:4 and a modified residence time of ^{13}C CH₃OH of $W/F = 75$ g h/mol. Subsequently, the flow was stopped and the catalyst purged with dry nitrogen at ambient temperature for 1 h. The spectrum recorded at ambient temperature thereafter consisted only of a single signal of *N,N,N*-trimethylanilinium ions at 58 ppm (Fig. 30b). After the temperature had been raised to 498 K without starting the flow of reactants, the signals at 48 and 39 ppm recurred, accompanied by a decrease of the signal at 58 ppm (Fig. 30c). This observation indicates a decomposition of *N,N,N*-trimethylanilinium ions into *N,N*-dimethylanilinium and *N*-methylanilinium ions. At 523 K, additional signals appeared at 16 and 21 ppm, indicative of ring-alkylated anilines (Fig. 30d).

On the basis of results of ^{13}C NMR investigations performed under CF and SF conditions, a new mechanism for the alkylation of aniline by methanol on acidic zeolite HY was proposed (Scheme 12). In the first reaction in the sequence, methanol is converted to surface methoxy groups and DME, which are further involved in the methylation as alkylating agents, along with methanol. The alkylation of aniline starts at 473 K and leads to a consecutive and reversible formation of *N*-methylanilinium (39 ppm), *N,N*-dimethylanilinium (48 ppm), and *N,N,N*-trimethylanilinium ions (58 ppm) on the working catalyst. The products of *N*-alkylation of aniline, that is, NMA and NNDMA are further formed via the deprotonation of the corresponding *N*-methylanilinium and *N,N*-dimethylanilinium ions. The product distribution in the

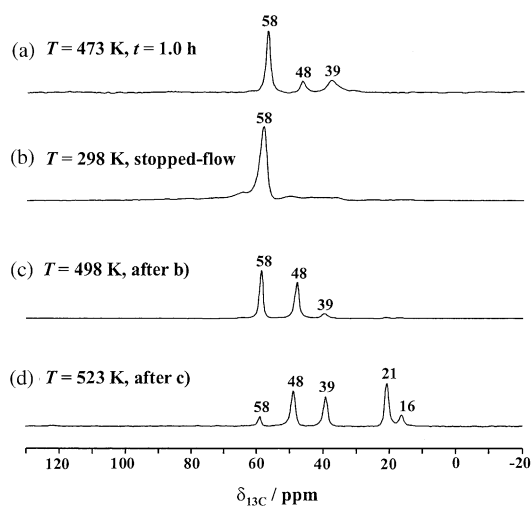
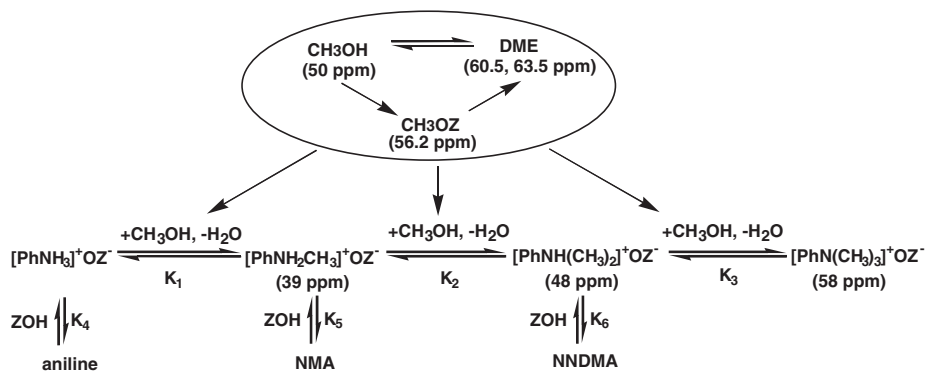


FIG. 30. ^{13}C MAS NMR spectra recorded during the methylation of aniline by ^{13}C -enriched methanol on zeolite HY ($n_{\text{Si}}/n_{\text{Al}} = 2.7$) under CF reaction conditions ($W/F = 75$ g h/mol, molar aniline/ ^{13}C CH₃OH ratio of 1:4) at a reaction temperature of 473 K for 1.0 h (a), at 298 K after stopping the flow of reactants and purging the catalyst with dry nitrogen (b), and, subsequently, at reaction temperatures of 498 K (c) and 523 K (d) without purging the catalyst. Reproduced with permission from (243). Copyright 2002 American Chemical Society.



SCHEME 12.

gas phase is, therefore, determined by the chemical equilibria between the different methylanilinium ions, which in turn is affected by the reaction conditions (temperature, methanol to aniline ratio, etc.). C-alkylated products are formed via further transformation of methylanilinium ions at temperatures higher than 523 K.

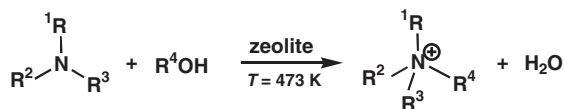
The reaction mechanism including the formation and decomposition of quaternary cations may be a general pathway in amine alkylation processes on acidic zeolites. Pouilloux *et al.* (247), for example, synthesized dimethylethylamine from ethylamine and methanol on an acidic catalyst. At the reaction temperature of 503 K, trimethylamine was determined by gas chromatographic analysis, which can be explained by the formation and decomposition of trimethylethylammonium ions, (CH₃)₃N⁺CH₂CH₃.

Furthermore, investigations of template decomposition in zeolites upon calcination of the as-synthesized materials have received much attention by researchers (248–250). However, the decomposition mechanisms of quaternary ammonium salts, which are commonly used as templates for zeolite synthesis, are still not well understood. Thus, ¹³C MAS NMR investigations of the decomposition of quaternary ammonium ions in zeolites bear the potential of significantly improving the understanding of these processes (243,251). For this purpose, a general method was developed for the synthesis of ¹³C-labeled quaternary ammonium ions in zeolites (Section IX.C).

C. SYNTHESIS AND IMMOBILIZATION OF QUARternary AMMONIUM IONS IN ZEOLITES

Zeolites and zeolite-related porous solids are ideal inorganic hosts for accommodating a wide variety of guest species (252). Bulky carbon-centered ionic intermediates, such as triarylmethyl cations, can be encapsulated within zeolite supercages via a “ship-in-a-bottle” synthesis (118,253). Some nitrogen-centered ionic species, for example, quaternary ammonium ions, are readily occluded in as-synthesized zeolites when these compounds originally act as template molecules during zeolite crystallization (254). Furthermore, a general method has been developed for the post-synthesis of quaternary ammonium ions in acidic zeolites (251,255).

As depicted in Scheme 13, quaternary ammonium ions can be post-synthesized by a direct reaction of tertiary amines and alcohols in the pores of acidic zeolites. By



SCHEME 13.

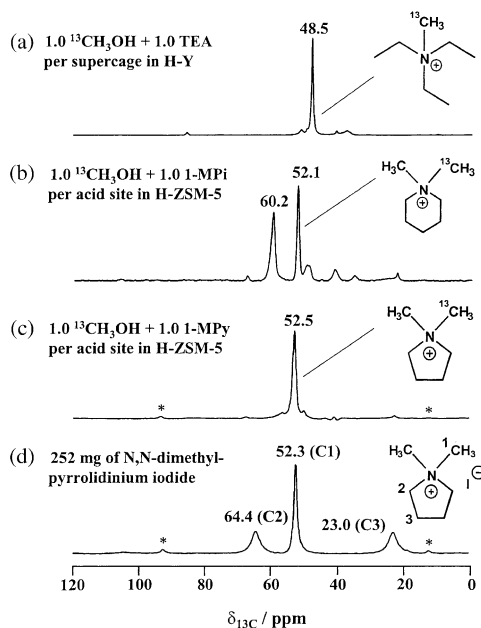


FIG. 31. ^{13}C MAS NMR spectra recorded after the reaction of ^{13}C -enriched methanol with TEA on zeolite HY ($n_{\text{Si}}/n_{\text{Al}} = 2.7$) at 493 K (a), with 1-MPi on zeolite HZSM-5 ($n_{\text{Si}}/n_{\text{Al}} = 22$) at 493 K (b), and with 1-methylpyrrolidine (1-MPy) on zeolite HZSM-5 ($n_{\text{Si}}/n_{\text{Al}} = 22$) at 483 K (c). The assignment of the signal at 52.5 ppm to *N,N*-dimethylpyrrolidinium ions was confirmed by ^{13}C MAS NMR spectroscopy of *N,N*-dimethylpyrrolidinium iodide (d). Asterisks denote spinning sidebands. Reproduced with permission from (251). Copyright 2003 The Royal Society of Chemistry.

use of ^{13}C -labeled methanol as a methylating agent, the formation of quaternary ammonium ions was verified by ^{13}C MAS NMR spectroscopy.

For example, Fig. 31a shows the ^{13}C MAS NMR spectrum recorded after the reaction of triethylamine (TEA) and ^{13}C -enriched methanol on zeolite HY at 493 K for 1 h under batch reaction conditions (251). The signal at 48.5 ppm is assigned to the ^{13}C -enriched methyl group of the methyl triethyl ammonium ions that were synthesized. The ^{13}C MAS NMR spectrum of 1-methylpiperidine (1-MPi) converted with ^{13}C -enriched methanol on zeolite HZSM-5 ($n_{\text{Si}}/n_{\text{Al}} = 22$) at 493 K consists of a signal at 52.1 ppm, assigned to *N,N*-dimethylpiperidinium ions, and a signal at 60.2 ppm is attributed to DME (Fig. 31b) (74). Figure 31c shows the ^{13}C MAS NMR spectrum recorded after the reaction of 1-methylpyrrolidine and ^{13}C -enriched methanol on zeolite HZSM-5, leading to a strong signal at 52.5 ppm. The assignment of this signal to the methyl groups of *N,N*-dimethylpyrrolidinium ions

was verified by the ^{13}C NMR shift of the C1 signal (52.3 ppm) of *N,N*-dimethylpyrrolidinium iodide salt shown in Fig. 31d (251).

When the above-mentioned approach was used, a variety of quaternary ammonium ions were synthesized in high yields under both batch and flow conditions on calcined acidic zeolites HY and HZSM-5 (251). The reaction parameters were optimized by investigation of the conversion with ^{13}C MAS NMR spectroscopy. The reaction temperatures and the ^{13}C NMR shifts of the cationic species formed are summarized in Table 4.

The above-mentioned route to the preparation of quaternary ammonium ions in acidic zeolites is remarkable for the following reasons: an immobilization of quaternary ammonium ions in a well-controlled concentration is an approach to modification of zeolite catalysts. Furthermore, the synthesis of isotopically labeled compounds is of importance in organic, pharmaceutical, and agricultural chemistry. This method is an approach to the synthesis of ^{13}C -labeled (or ^{13}C , ^{15}N -labeled) tertiary amines via a thermal decomposition (243,251) of the corresponding quaternary ammonium ions in zeolites.

Investigations of template-related issues by solid-state NMR spectroscopy have suffered from the low NMR sensitivity associated with the low natural abundance of ^{13}C -isotopes. The formation of selectively ^{13}C -labeled (or ^{15}N -labeled) quaternary ammonium ions offers possibilities to overcome this limitation.

X. MTHC Conversion on Acidic Zeolites

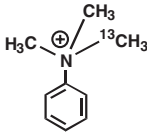
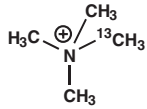
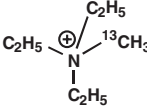
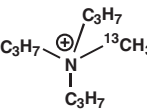
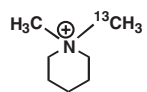
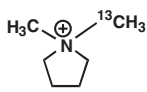
The development of a synthetic gasoline process by Mobil Oil Corporation was based on the MTHC conversion on acidic zeolite catalysts (210,256,257). The MTHC technology, mainly the conversion of methanol to gasoline (MTG) and of MTO, was regarded as a means to convert coal or natural gas into high-octane-number gasoline and chemicals in general. As a consequence of the increasing demands for light alkenes, the catalytic conversion of methanol to alkenes on solid acid catalysts continues to be an industrially interesting process (210).

The main reactions of the MTG/MTO process can be summarized as follows: the first is the dehydration of methanol to DME on acidic zeolite catalysts. The equilibrium mixture of methanol, DME, and water is then converted to light alkenes, which react further to form higher alkenes, *n*- and *iso*-alkanes, aromatics, and naphthenes by hydrogen transfer, alkylation, polycondensation, isomerization, and other secondary reactions.

Until now, the detailed mechanism involved in the MTG/MTO process has been a matter of debate. Two key aspects considered in mechanistic investigations are the following: the first is the mechanism of the dehydration of methanol to DME. It has been a matter of discussion whether surface methoxy species formed from methanol at acidic bridging OH groups act as reactive intermediates in this conversion. The second is the initial C–C bond formation from the C_1 reactants. More than 20 possible mechanistic proposals have been reported for the first C–C bond formation in the MTO process. Some of these are based on roles of surface-bound alkoxy species, oxonium ylides, carbenes, carbocations, or free radicals as intermediates (210).

TABLE 4

Synthesis of Quaternary Ammonium Ions (Column 1) on Acidic Zeolites (Column 2) by a Methylation of the Corresponding Tertiary Amines (Column 3) with ^{13}C -Enriched Methanol at the Reaction Temperatures Given in Column 4 (251)

Quaternary ammonium ion	Zeolite	Tertiary amine	Reaction temperature (K)	^{13}C NMR shift ^a (ppm)
	HY	<i>N,N</i> -Dimethylaniline	473	58.2
	HZSM-5	Trimethylamine	473	56.5
	HY		473	55.9
	HZSM-5	Triethylamine	483	48.3
	HY		493	48.5
	HY	Tripropylamine	503	50.6
	HZSM-5	1-Methylpiperidine	503	51.6
	HY		503	52.1
	HZSM-5	1-Methylpyrrolidine	483	52.5
	HY		503	52.7

^a Chemical shifts of ^{13}C -labeled carbon atoms were compared with the data either reported in the literature or obtained from the corresponding quaternary ammonium iodides which were synthesized separately.

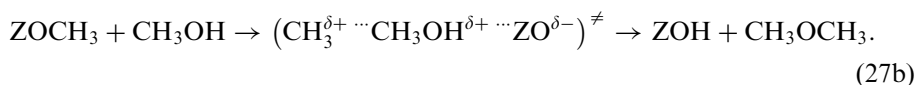
Various NMR spectroscopic techniques have been applied to investigate the conversion of methanol on acidic zeolites in the low-temperature ($T \leq 523$ K) formation of DME and the high-temperature ($T \geq 523$ K) formation of alkenes and gasoline. Techniques successfully applied were the stop-and-go method under batch reaction conditions (258,259), the pulse-quench method (113), and various flow techniques (46,49,74,207,260–263). This section is a summary of the recent progress in investigations of the mechanism of the MTO process by NMR techniques.

A. REACTIVITY OF SURFACE METHOXY SPECIES

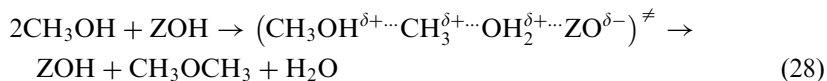
A.1. Formation of Surface Methoxy Species during the Conversion of Methanol to DME on Acidic Zeolites

Among the early investigations of methanol adsorption and conversion on acidic zeolites, most of the ^1H and ^{13}C MAS NMR experiments were performed under batch reaction conditions with glass inserts in which the catalyst samples were fused. Zeolites HZSM-5 (76a,204,206,264–272), HY (71,72), H-EMT (273), HZSM-12 (274), HZSM-23 (275), H-erionite (275), H-mordenite (271,272), and H-offretite (275,276), silicoaluminophosphates H-SAPO-5 (271,274), H-SAPO-11 (274), and H-SAPO-34 (76,277,278), as well as montemorillonite (279) and saponite (279) were investigated as catalysts.

At reaction temperatures of $T \leq 523$ K, the conversion of methanol on acidic zeolites is dominated by a dehydration of methanol to DME (210). Two mechanisms have been proposed for the formation of DME. In the indirect pathway (Eqs. (27a, b)), methanol molecules adsorbed on bridging OH groups react first to give methoxy species (ZOCH_3), which subsequently react with another methanol molecule to give DME (280,281):



Z stands for the zeolite framework. In the direct pathway (Eq. (28)), two methanol molecules react with each other on one Brønsted acid site (282). This pathway involves the simultaneous adsorption and reaction of two methanol molecules, with the formation of one DME and one water molecule in a single step:



A number of theoretical studies have been performed to improve our understanding of the adsorption and conversion of methanol on acidic zeolites (245,283–288). Applying non-local periodic density functional calculations, Gale and co-workers (284) suggested that both pathways, described in Eqs. (27a, b) and (28), are energetically reasonable routes. By contrast, Blaszkowski and van Santen (286) found

that the pathway described by Eqs. (27a, b) is less preferred, because of the high-energy barrier for the formation of methoxy groups.

To characterize the conversion of methanol to DME on acidic zeolites, ^{13}C MAS NMR experiments under CF and SF conditions were performed. Figure 32 shows ^{13}C CF MAS NMR and ^{13}C CF CP/MAS NMR spectra recorded at 393, 433, and 473 K during the methanol conversion on zeolite HY ($n_{\text{Si}}/n_{\text{Al}} = 2.7$) under flow conditions (74). In these experiments, a flow of ^{13}C -enriched methanol with a modified residence time of $W/F = 100$ g h/mol was continuously injected into the spinning MAS NMR rotor reactor. Simultaneously, the yields of DME, Y_{DME} , were determined by on-line gas chromatography (Fig. 32, middle).

The ^{13}C CF MAS NMR spectrum obtained at 393 K (Fig. 32a, left) consists of a single signal at 50 ppm assigned to unconverted methanol. In the spectrum recorded with CP (Fig. 32a, right), an additional signal at 63.5 ppm was observed, attributed to DME strongly adsorbed with a side-on conformation (244,245). After the reaction temperature had been raised to 433 K, the conversion of methanol to DME was detected by on-line gas chromatography ($Y_{\text{DME}} = 0.04$). At this reaction temperature, the ^{13}C MAS NMR spectrum showed a decrease of the signal of adsorbed methanol molecules (50 ppm), and the presence of DME (60.5 ppm) adsorbed with an end-on conformation (Fig. 32b, left). The low intensity of the latter species in the spectrum recorded with the CP technique (Fig. 32b, right) is inferred to have been caused by the high mobility of these end-on adsorbed DME species. An additional signal appeared at 56.2 ppm indicating the formation of surface methoxy groups (71–74). With an increasing yield of DME at 473 K ($Y_{\text{DME}} = 0.23$), an increase of the signal of surface methoxy groups (56.2 ppm) was also observed by ^{13}C CF CP/MAS NMR spectroscopy (Fig. 32c, right).

In summary, the results of this experiment indicate that methoxy species do occur during the conversion of methanol to DME. However, the temperatures for the formation of surface methoxy groups and DME are very close. Therefore, it is difficult to determine whether the methoxy groups are significant intermediates in DME

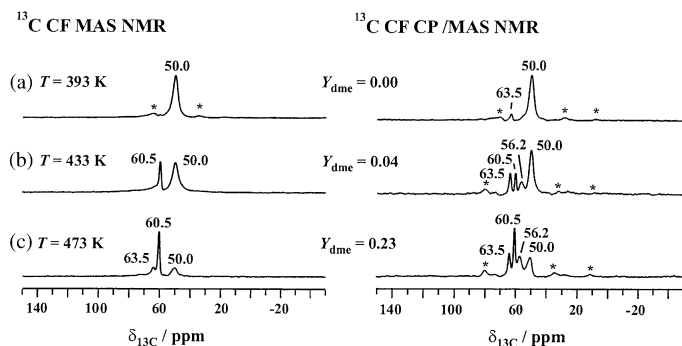


FIG. 32. ^{13}C CF MAS NMR spectra recorded during the conversion of ^{13}C -enriched methanol ($W/F = 100$ g h/mol) on calcined zeolite HY ($n_{\text{Si}}/n_{\text{Al}} = 2.7$) at reaction temperatures of 393 K (a), 433 K (b), and 473 K (c). The spectra on the left-hand side were obtained with MAS NMR and proton decoupling (HPDEC), and the spectra on the right-hand side were recorded with the CP technique. Asterisks denote spinning sidebands. Reproduced with permission from (74). Copyright 2001 American Chemical Society.

formation or only spectator species. A suitable experiment starting with a catalyst that was initially covered by methoxy species only, is described below (Section X.A.2).

A.2. Preparation of Methoxy Species on Acidic Zeolites by the SF Technique

To unambiguously elucidate the reactivity of surface methoxy species, the preparation of pure methoxy species on the catalyst surface is an important prerequisite. This preparation can be achieved by a SF protocol, which starts with a flow of ^{13}C -enriched methanol into acidic zeolites at room temperature, followed by a purging of the catalyst with dry nitrogen at room temperature and subsequently at higher temperatures (74,262). The latter step progressively removes the surplus of methanol and DME, together with water produced by the conversion of methanol.

Figure 33 shows ^{13}C HPDEC MAS NMR (left) and ^{13}C CP/MAS NMR spectra (right), which were recorded to monitor the formation of methoxy species on zeolite HY ($n_{\text{Si}}/n_{\text{Al}} = 2.7$). The signal at 50.2 ppm, assigned to methanol molecules adsorbed on zeolite HY, dominates the ^{13}C MAS NMR spectra recorded after adsorption of $^{13}\text{CH}_3\text{OH}$ at room temperature and purging at temperatures $T \leq 373$ K (Figs 33a–c). The signal of methoxy species at 56.2 ppm was observed after purging of the sample at 413 K (Fig. 33d), and finally it dominated the ^{13}C MAS NMR spectra after purging at 473 K (Figs 33e–g). The weak signal at 63.5 ppm is attributed to side-on adsorbed DME. In contrast to the spectra obtained under CF conditions (Fig. 32), the signal of end-on adsorbed DME at 60.5 ppm is absent as a

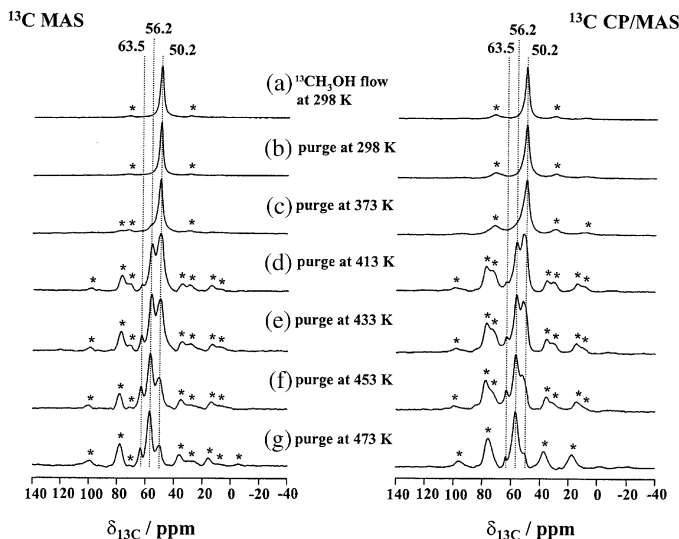
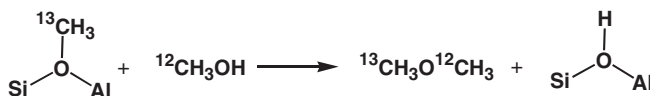


FIG. 33. ^{13}C HPDEC/MAS NMR (left) and CP/MAS NMR (right) spectra of zeolite HY ($n_{\text{Si}}/n_{\text{Al}} = 2.7$) recorded during the formation of methoxy species (56.2 ppm) at various temperatures. The spectra were obtained after a continuous injection of ^{13}C -enriched methanol into the MAS NMR rotor reactor at room temperature for 20 min (a) and after a subsequent purging with dry nitrogen (200 mL/min) at 298 K (b), 373 K (c), 413 K (d), 433 K (e), 453 K (f), and 473 K (g). The temperature treatments were performed for 2 h at each step. Asterisks denote spinning sidebands. Reproduced with permission from (262). Copyright 2003 Elsevier Science.

result of a rapid purging of these weakly bound DME species by nitrogen. With the application of the above-mentioned SF protocol, up to 0.72 methoxy species per SiOHAl group of calcined zeolite HY could be prepared (262). With similar SF protocols, surface methoxy species were also successfully prepared on zeolite HZSM-5 ($n_{\text{Si}}/n_{\text{Al}} = 22.0$) and H-SAPO-34 ($n_{\text{Si}}/(n_{\text{Al}} + n_{\text{Si}} + n_{\text{P}}) = 0.088$) (74).

A.3. Role of Surface Methoxy Species in the Formation of DME

The role of surface methoxy species during the conversion of methanol to DME was investigated by SF MAS NMR spectroscopy (74). After the preparation of pure surface methoxy species by conversion of ^{13}C -enriched methanol on zeolite HY ($n_{\text{Si}}/n_{\text{Al}} = 2.7$) (Fig. 34a), a flow of methanol with a natural abundance of ^{13}C -isotopes ($^{12}\text{CH}_3\text{OH}$) was injected at 433 K for 10 min into the spinning MAS NMR rotor reactor. In the ^{13}C CP/MAS NMR spectrum shown in Fig. 34b, weak signals are evident at 60.5 and 63.5 ppm, indicating the formation of DME accompanied by a decrease of the signal of surface methoxy groups at 56.2 ppm. This finding indicates a reaction of ^{13}C -enriched surface methoxy groups with $^{12}\text{CH}_3\text{OH}$ leading to $^{13}\text{CH}_3\text{O}^{12}\text{CH}_3$, as shown in Scheme 14. After the injection of a flow of $^{12}\text{CH}_3\text{OH}$ at 433 K for 1.0 h (Fig. 34c), all signals disappeared except that of the DME at 63.5 ppm. The results of this experiment demonstrate that surface methoxy groups prepared on zeolite HY are reactive and contribute to the formation of DME by the mechanism described in Eqs. (27a, b).



SCHEME 14.

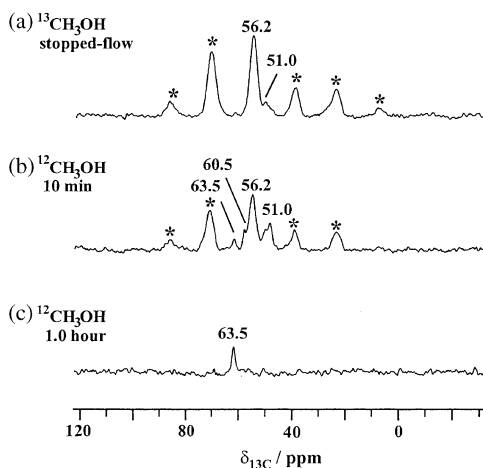


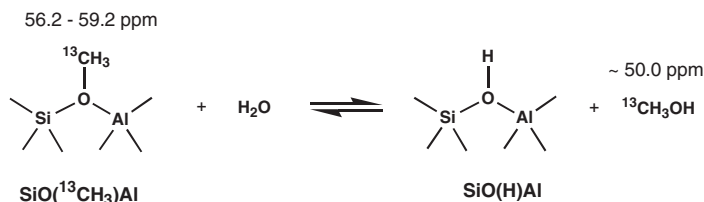
FIG. 34. ^{13}C SF CP/MAS NMR spectra recorded at 433 K after stopping the conversion of ^{13}C -enriched methanol ($W/F = 40$ g h/mol) on zeolite HY ($n_{\text{Si}}/n_{\text{Al}} = 2.7$) at 423 K and purging the catalyst with dry carrier gas (a). Spectra (b) and (c) were obtained 10 min and 1.0 h, respectively, after starting the flow of ^{12}C -enriched methanol ($W/F = 40$ g h/mol) at 433 K. Asterisks denote spinning sidebands. Reproduced with permission from (74). Copyright 2001 American Chemical Society.

A.4. Formation of Higher Hydrocarbons by Surface Methoxy Species

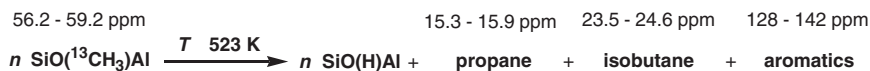
The reactivity of surface methoxy species was further investigated with various probe molecules that were thought to possibly be involved in the MTO process, including water, toluene (representing aromatics), and cyclohexane (representing saturated hydrocarbons) (263). It was found that surface methoxy species react at room temperature with water to form methanol, which indicates the occurrence of a chemical equilibrium between these species at low reaction temperatures (Scheme 15) (263).

Surface methoxy groups react with aromatics and alkanes at temperatures of *ca.* 433 and 493 K, respectively (263). Figure 35 shows the reaction of surface methoxy species with toluene (with a natural abundance of ^{13}C -isotopes) on a methylated zeolite Y ($^{13}\text{CH}_3\text{-Y}$) at elevated temperatures. After surface methoxy species were prepared *in situ* under flow conditions, the zeolite $^{13}\text{CH}_3\text{-Y}$ was loaded with toluene via a vacuum line and sealed in a glass insert. Figure 35a shows the ^{13}C MAS NMR spectrum recorded directly after adsorption of toluene at room temperature. The spectrum is dominated by methoxy species at 56.2 ppm, with spinning sidebands, and the weak signals at 19.2, 125.6, 129.6, and 140.2 ppm are assigned to toluene. The toluene methylation by surface methoxy species starts at *ca.* 433 K, as documented in Fig. 35b by the decrease in intensity of the signals representing surface methoxy species and the appearance of the signal at 18.3 ppm assigned to *o*-xylene (Scheme 16). At the reaction temperature of 453 K, ethylbenzene ($\text{C}_6\text{H}_5\text{CH}_2^{13}\text{CH}_3$) was formed, as indicated by the signal at 15.0 ppm (Fig. 35c). Upon heating of the sample to 473 K, a new signal appeared at 22.8 ppm caused by *p*- and/or *m*-xylenes (Fig. 35d). After a further increase in the reaction temperature to 493 K, all the surface methoxy species and the residual DME and methanol molecules were consumed by the reaction with toluene, and the resulting spectrum is dominated by the signals of ethylbenzene, xylenes, and/or polymethylbenzenes (Fig. 35e). These results indicate that surface methoxy species formed on acidic zeolite catalysts react readily with aromatic compounds such as toluene, leading to ring and/or side-chain methylations at temperatures lower than those in the steady state of the MTO process ($T \geq 573$ K).

In a similar way, the reaction of surface methoxy species with cyclohexane on zeolite $^{13}\text{CH}_3\text{-Y}$ was investigated (263). At temperatures $T \geq 493$ K, surface methoxy species most probably act as precursors of carbene intermediates, which can undergo the sp^3 insertion into C–H single bonds. In the absence of water and other organic species, conversion of methoxy groups alone to alkanes and aromatics was observed at temperatures $T \geq 523$ K (Scheme 17) (263). This observation indicates a



SCHEME 15.



SCHEME 17.

“hydrocarbon pool” route is the dominant pathway. Reactive organic species, such as large alkenes, polymethylbenzenes, cyclic carbenium ions, and probably methylbenzenium ions, are methylated by methanol and DME. By elimination of the alkyl chains of these organic species, light alkenes are formed.

To shed more light on this issue, the steady state of methanol conversion on zeolites HZSM-5, H-SAPO-34, and H-SAPO-18 was characterized by CF MAS NMR spectroscopy under CF reaction conditions (49,261).

B.1. Characterization of the Hydrocarbon Pool

To ensure that meaningful results were obtained by ^{13}C CF MAS NMR spectroscopy, catalytic experiments were performed with a conventional fixed-bed reactor and, under the same conditions, a spinning MAS NMR rotor reactor. The reaction products from both reactors were analyzed by on-line gas chromatography (261). A comparison of the results showed a reasonably good agreement; in particular, the methanol conversion takes place in the same temperature range, and the same qualitative behaviors of the conversion and yield curves were found for the two reactors (261).

To investigate the methanol conversion under steady-state conditions by CF MAS NMR spectroscopy, a flow of ^{13}C -enriched methanol ($W/F = 25 \text{ g h/mol}$) was injected into a spinning 7-mm MAS NMR rotor reactor filled with 100 mg of a calcined zeolite (HZSM-5, H-SAPO-18, or H-SAPO-34) (49,261). In the low-temperature range (i.e., at $T \leq 523 \text{ K}$), the ^{13}C MAS NMR signals occurring at 50 and 61 ppm indicate the conversion of methanol to DME. This result agrees with the high yield of DME ($Y_{\text{DME}} = 58\%$) observed for reaction at 523 K by on-line gas chromatography. After the reaction temperature had been increased to 548 K or higher, ^{13}C MAS NMR signals first appeared in the alkyl region, at 10–35 ppm, accompanied by broad signals in the regions indicating alkenes and aromatics, at 129–134 ppm. Simultaneously, a strong increase in the yields of light alkenes, such as $\text{C}_2 =$ and $\text{C}_3 =$, was observed by on-line gas chromatography.

For a detailed analysis of the hydrocarbon pool formed under steady-state conditions, a line separation of the ^{13}C MAS NMR spectra was performed with commercial software such as BRUKER WINFIT (261). The ^{13}C CF MAS NMR signals observed during methanol conversion on H-SAPO-34 at reaction temperatures of 548–673 K were attributed to a mixture of C_6 to C_{12} alkenes and aromatics, such as 3-hexene (131–133, 21 and 15 ppm), 2,5-dimethyl-3-hexene (134–136, 32, and 22 ppm), 2,3-hexadiene (132–134, 126–128, and 18 ppm), alkylated octadienes (133–135, 25, 23, and 15 ppm), cyclopentene (131–133, 33, and 23 ppm), diethylcyclopentene (133–135 ppm and various signals at 14–33 ppm), and *p*-xylene (134, 129, and 21 ppm) (261). Signals at *ca.* 22 and 129 ppm, retained at 673 K and after purging of the used catalyst at 673 K with dry carrier gas, indicated

the presence of aromatic compounds, such as *p*-xylene (134, 129, and 21 ppm, intensity ratio of 1:2:1), occluded in the pores of H-SAPO-34 (261).

In an attempt to identify the catalytic role of the hydrocarbon pool, the MTO process was further studied by ^{13}C CF MAS NMR spectroscopy with an alternating flow of $^{13}\text{CH}_3\text{OH}$ and $^{12}\text{CH}_3\text{OH}$. After the conversion of $^{13}\text{CH}_3\text{OH}$ under steady-state conditions, the reactant flow was switched to $^{12}\text{CH}_3\text{OH}$ without a change the reaction parameters. If the alkyl groups of the hydrocarbon pool were involved in the conversion of methanol, for example, by adding reactant molecules and splitting off product molecules, the ^{13}C -isotope abundance of these groups would be expected to decrease strongly after the switch from $^{13}\text{CH}_3\text{OH}$ to $^{12}\text{CH}_3\text{OH}$.

Figure 36 shows the ^{13}C and ^1H CF MAS NMR spectra recorded during the conversion of methanol on zeolite HZSM-5 ($n_{\text{Si}}/n_{\text{Al}} = 22$) at temperatures of 548 and 573 K (300). The characteristic features of these spectra agree with those observed in earlier investigations of the MTO process catalyzed by HZSM-5 (49). To quantify the ^{13}C isotopic abundance of the alkyl groups contributing to the hydrocarbon pool, the spectral range of 0–40 ppm was integrated using spectra that were Fourier-transformed in the absolute intensity mode. These integrals were set to 100% for the spectra recorded during the conversion of ^{13}C -enriched methanol. At both reaction temperatures and 1 h after switching the reactant flow from $^{13}\text{CH}_3\text{OH}$ to $^{12}\text{CH}_3\text{OH}$, the ^{13}C -isotopic abundance of the alkyl groups contributing to the hydrocarbon pool decreased by *ca.* 40% (Fig. 36, left). Simultaneously recorded ^1H CF MAS NMR spectra, on the other hand, showed no change of the

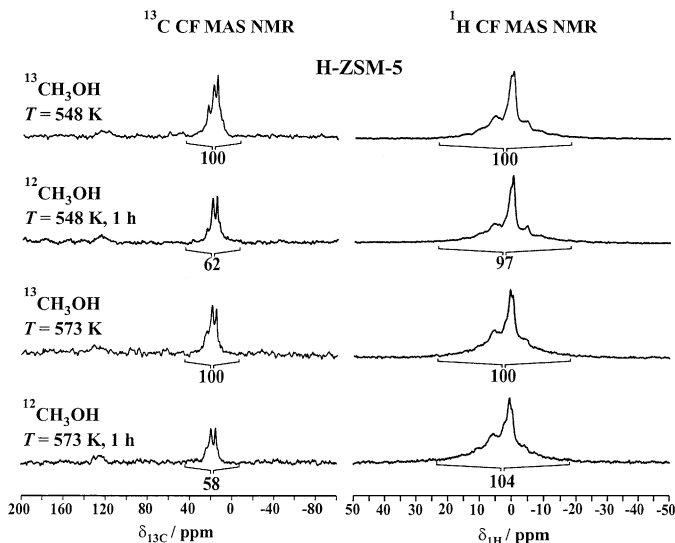


FIG. 36. ^{13}C and ^1H CF MAS NMR spectra recorded during the alternating conversion of ^{13}C -enriched and non-enriched methanol ($W/F = 25$ g h/mol) on calcined zeolite HZSM-5 ($n_{\text{Si}}/n_{\text{Al}} = 22$) at reaction temperatures of 548 and 573 K. The relative intensities given below the spectra were determined by integration in the absolute intensity mode by using the spectra obtained during the conversion of ^{13}C -enriched methanol as intensity standard. Reproduced with permission from (300). Copyright 2003 Kluwer Academic.

total intensities of the hydrogen atoms contributing to the organic deposits on the zeolite catalyst within the experimental accuracy of $\pm 5\%$. Hence, it was inferred that the replacement of the ^{13}C -enriched alkyl groups of the hydrocarbon pool by alkyl groups with a natural abundance of ^{13}C -isotopes is the result of an alkylation of the compounds in the hydrocarbon pool by $^{12}\text{CH}_3\text{OH}$. This observation provides direct evidence that the alkenic and aromatic species of the hydrocarbon pool play an active role in the MTO process under steady-state conditions.

B.2. Simultaneous Characterization of the Formation of Hydrocarbon Pool Compounds on Acidic Zeolites by MAS NMR–UV/Vis Spectroscopy

Recently, a novel CF MAS NMR–UV/Vis technique (Fig. 17, Section III.B) was applied to characterize the formation of hydrocarbons by the conversion of methanol on a weakly dealuminated zeolite HZSM-5 (68). The ^{13}C MAS NMR spectrum recorded at 413 K during the continuous conversion of ^{13}C -enriched methanol (Fig. 37a, left) consists of signals at 51 and 61 ppm attributed to methanol and DME, respectively. The very weak signal at *ca.* 23 ppm is probably an indication of alkanes or alkylated cyclic compounds. The appearance of the signals at 23 and 61 ppm indicates that the conversion of methanol on weakly dealuminated zeolites HZSM-5 starts even at 413 K. The simultaneously recorded UV/Vis spectrum (Fig. 37a, right) consists of bands at 275, 315, and 375 nm. The band at 275 nm indicates the formation of neutral aromatic compounds (301,302), and those at 315 and 375 nm may be assigned to mono- and dienylic carbenium ions (301,302), respectively. Because the UV/Vis spectrum of the non-dealuminated zeolite HZSM-5, that

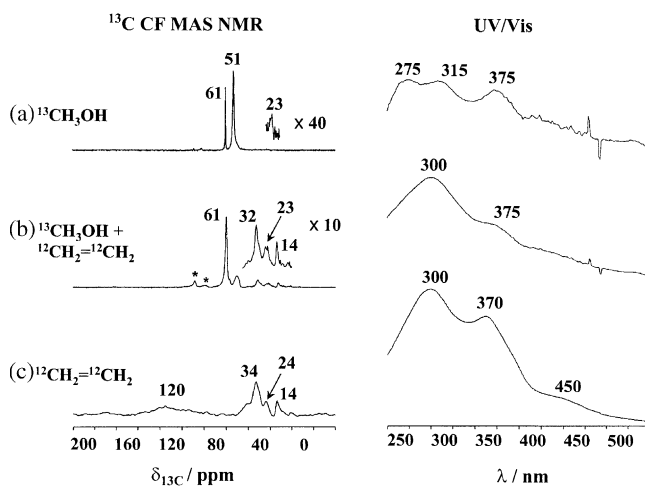


FIG. 37. ^{13}C CF MAS NMR (left) and UV/Vis (right) spectra of a dealuminated zeolite HZSM-5 recorded during conversion of ^{13}C -enriched methanol ($W/F = 25$ g h/mol) at 413 K for 2 h (a), during a subsequent conversion of $^{12}\text{CH}_2 = ^{12}\text{CH}_2$ ($W/F = 10$ g h/mol) at 413 K for 1 h (b), and during conversion of $^{12}\text{CH}_2 = ^{12}\text{CH}_2$ ($W/F = 10$ g h/mol) at 413 K on a fresh catalyst for 2 h (c). Asterisks denote spinning sidebands. The narrow peaks at *ca.* 500 nm in UV spectra were caused by the equipment. Reproduced with permission from (68). Copyright 2004 The Royal Society of Chemistry.

is, of the parent zeolite HZSM-5, recorded under the same reaction conditions, consists only of a very weak band at *ca.* 300 nm, the formation of the first hydrocarbons and carbenium ions, even at 413 K, may be influenced by the presence of extra-framework aluminum species acting as Lewis acid sites (68).

The weakly dealuminated zeolite HZSM-5 used to convert methanol was subsequently applied to investigate the conversion of ethylene (^{13}C -isotopes in natural abundance) (Fig. 37b). ^{13}C MAS NMR signals, appearing at 14, 23, and 32 ppm during conversion of ethylene at 413 K for 1 h (Fig. 37b, left), are assigned to alkyl groups of small amounts of alkylated cyclic compounds, such as cyclopentene, cyclohexene, cyclohexadiene, and/or benzene. The simultaneously recorded UV/Vis spectrum (Fig. 37b, right) shows bands at 300 and 375 nm, which characterize the formation of neutral cyclic compounds and dienyl carbenium ions, respectively (301).

The conversion of ethylene on a fresh zeolite HZSM-5 catalyst, which had not been used beforehand for methanol conversion, led to the spectra shown in Fig. 37c. The ^{13}C MAS NMR spectrum consists of signals at 14, 24, and 34 ppm caused by alkyl groups of cyclic compounds. Furthermore, a broad signal in the chemical shift range of alkenic and aromatic compounds appeared at *ca.* 120 ppm. The UV/Vis spectrum consists of bands similar to those shown in Fig. 37b and an additional weak band at *ca.* 450 nm. The latter may be attributed to condensed aromatics or trienyl carbenium ions (301). A weak shoulder observed at *ca.* 400 nm is an indication for the formation of hexamethylbenzenium ions (302).

The simultaneous investigation of the methanol conversion on weakly dealuminated zeolite HZSM-5 by ^{13}C CF MAS NMR and UV/Vis spectroscopy has shown that the first cyclic compounds and carbenium ions are formed even at 413 K. This result is in agreement with UV/Vis investigations of the methanol conversion on dealuminated zeolite HZSM-5 performed by Karge *et al.* (303). It is probably that extra-framework aluminum species acting as Lewis acid sites are responsible for the formation of hydrocarbons and carbenium ions at low reaction temperatures. NMR spectroscopy allows the identification of alkyl signals in more detail, and UV/Vis spectroscopy gives hints to the formation of low amounts of cyclic compounds and carbenium ions.

XI. Conclusions and Outlook

In the preceding decade, solid-state NMR spectroscopy has provided important and novel information about the nature and properties of surface sites on working solid catalysts and the mechanisms of these surface reactions. This spectroscopic method offers the advantages of operation close to the conditions of industrial catalysis. A number of new techniques have been introduced and applied that allow investigations of surface reactions by solid-state NMR spectroscopy under both batch and flow conditions. Depending on the problems to be solved, both of these experimental approaches are useful for the investigation of calcined solid catalysts and surface compounds formed on these materials under reaction conditions. Problems with the time scale of NMR spectroscopy in comparison with the time scale of the catalytic reactions can be overcome by sophisticated experimental

approaches such as the study of isotope scrambling dynamics and the application of SF experiments.

In the future, we can expect the development of novel experimental techniques in solid-state NMR spectroscopy for investigation of functioning catalysts. Important goals are (i) the enhancement of the sensitivity of solid-state NMR spectroscopy, for example, by a selective enhancement of the nuclear polarization taking advantage of laser-polarized xenon, (ii) increases in the temperature range accessible for the characterization of solid-catalyzed reactions, and (iii) the coupling of NMR spectroscopy with other techniques such as mass spectrometry. Furthermore, modern two-dimensional techniques of solid-state NMR spectroscopy such as MQMAS NMR spectroscopy will be applied to improve the resolution of the spectra.

Acknowledgments

The Deutsche Forschungsgemeinschaft, the Max-Buchner-Forschungsförderung, and the Volkswagen-Stiftung provided financial support, which the authors gratefully acknowledge.

References

1. Anderson, M.W., *Top. Catal.* **3**, 195 (1996).
2. Derouane, E.G., He, H., Derouane-Abd Hamid, S.B., and Ivanova, I.I., *Catal. Lett.* **58**, 1 (1999).
3. Han, X., Yan, Z., Zhang, W., and Bao, X., *Curr. Org. Chem.* **5**, 1017 (2001).
4. Hunger, M., and Weitkamp, J., *Angew. Chem. Int. Ed.* **40**, 2954 (2001).
5. Parker, W.O., *Comments Inorg. Chem.* **22**, 31 (2000).
6. (a) Haw, J.F., Nicholas, J.B., Xu, T., Beck, L.W., and Ferguson, D.B., *Acc. Chem. Res.* **29**, 259 (1996);
(b) Haw, J.F., and Xu, T., *Adv. Catal.* **42**, 115 (1998);
(c) Haw, J.F., in "In-situ Spectroscopy in Heterogeneous Catalysis" (J.F. Haw, Ed.), Wiley-VCH, Weinheim, p. 53, 2002;
(d) Haw, J.F., Song, W.G., Marcus, D.M., and Nicholas, J.B., *Acc. Chem. Res.* **36**, 317 (2003).
7. Weckhuysen, B.M., *Chem. Commun.* 97 (2002).
8. Hunger, M., and Weitkamp, J., in "In-situ Spectroscopy of Catalysts" (B.M. Weckhuysen, Ed.), American Scientific Publishers, Stevenson Ranch, CA, p. 177, 2004.
9. Hunger, M., *Catal. Today* **97**, 3 (2004).
10. Abragam, A., "The Principles of Nuclear Magnetism." Clarendon Press, Oxford, 1962.
11. Haeberlen, U., "High Resolution NMR in Solids." Academic Press, New York, 1976.
12. Slichter, C.P., "Principles of Magnetic Resonance." 2nd Edition, Springer, Berlin, 1978.
13. Mehring, M., "Principles of High-Resolution NMR in Solids." 2nd Edition, Springer, Berlin, 1983.
14. Stejskal, E.O., and Memory, J.D., "High Resolution NMR in the Solid State." Oxford University Press, Oxford, 1994.
15. Andrew, E.R., Bradbury, A., and Eades, R.G., *Nature* **182**, 1659 (1958).
16. Maricq, M.M., and Waugh, J.S., *J. Chem. Phys.* **70**, 3300 (1979).
17. Brunner, E., Fenzke, D., Freude, D., and Pfeifer, H., *Chem. Phys. Lett.* **169**, 591 (1990).
18. Wind, R.A., in "Modern NMR Techniques and their Application in Chemistry" (A.I. Popov, and K. Hallenga, Eds.), Marcel Dekker, New York, Basel, Hongkong, p. 125, 1991.
19. Haeberlen, U., and Waugh, J.S., *Phys. Rev.* **175**, 453 (1968).
20. Ryan, L.M., Taylor, R.E., Paff, A.J., and Gerstein, B.C., *J. Chem. Phys.* **72**, 508 (1980).

21. Scheler, G., Haubenreisser, U., and Rosenberger, H., *J. Magn. Reson.* **44**, 134 (1981).
22. Hunger, M., *Catal. Rev. Sci. Eng.* **39**, 345 (1997).
23. Olivieri, A.C., *J. Magn. Reson. A* **101**, 313 (1993).
24. Alla, M., and Lippmaa, E., *Chem. Phys. Lett.* **87**, 30 (1982).
25. Brunner, E., *J. Chem. Soc. Faraday Trans.* **89**, 165 (1993).
26. Freude, D., in "Encyclopedia of Analytical Chemistry" (R.A. Meyers, Ed.), Wiley, Chichester, p. 12188, 2000.
27. Samoson, A., Lippmaa, E., and Pines, A., *Mol. Phys.* **65**, 1013 (1988).
28. Frydman, L., and Harwood, J.S., *J. Am. Chem. Soc.* **117**, 5367 (1995).
29. (a) van Eck, E.R.H., Janssen, R., Maas, W.E.J.R., and Veeman, W.S., *Chem. Phys. Lett.* **174**, 428 (1990);
(b) Fyfe, C.A., Mueller, K.T., Grondey, H., and Wong-Moon, K.C., *J. Phys. Chem.* **97**, 13484 (1993).
30. Hartmann, S.R., and Hahn, E.L., *Phys. Rev.* **128**, 2042 (1962).
31. Michel, D., and Engelke, F., in "NMR Basic Principles and Progress." (P. Diehl, E. Fluck, H. Guenther, R. Kosfeld, and J. Seelig, Eds.), Vol. 32, p. 69. Springer, Berlin, 1994.
32. Raftery, D., MacNamara, E., Fisher, G., Rice, C.V., and Smith, J., *J. Am. Chem. Soc.* **119**, 8746 (1997).
33. Haake, M., Pines, A., Reimer, J.A., and Seydoux, R., *J. Am. Chem. Soc.* **119**, 11711 (1997).
34. Brunner, E., Seydoux, R., Haake, M., Pines, A., and Reimer, J.A., *J. Magn. Reson.* **130**, 145 (1998).
35. MacNamara, E., Fisher, G., Smith, J., Rice, C.V., Hwang, S. -J., and Raftery, D., *J. Phys. Chem. B* **103**, 1158 (1999).
36. Seydoux, R., Pines, A., Haake, M., and Reimer, J.A., *J. Phys. Chem. B* **103**, 4629 (1999).
37. Michel, D., "Grundlagen und Methoden der kernmagnetischen Resonanz," p. 40. Akademie-Verlag, Berlin, 1981.
38. Bielecki, A., and Burum, D.P., *J. Magn. Reson. A* **116**, 215 (1995).
39. Aliev, A.E., and Harris, K.D.M., *Magn. Reson. Chem.* **32**, 366 (1994).
40. van Moorsel, G.-J.M.P., van Eck, E.R.H., and Grey, C.P., *J. Magn. Reson. A* **113**, 159 (1995).
41. Takahashi, T., Kawashima, H., Sugisawa, H., and Baba, T., *Solid State Nucl. Magn. Reson.* **15**, 119 (1999).
42. Campbell, G.C., Crosby, R.C., and Haw, J.F., *J. Magn. Reson.* **69**, 191 (1986).
43. Haw, J.F., Crook, R.A., and Crosby, R.C., *J. Magn. Reson.* **66**, 551 (1986).
44. Wehrle, B.B., Aguilar-Parrilla, F., and Limbach, H.-H., *J. Magn. Reson.* **87**, 584 (1990).
45. Pan, H.-J., and Gerstein, B.C., *J. Magn. Reson.* **92**, 618 (1991).
46. Isbester, P.K., Zalusky, A., Lewis, D.H., Douskey, M.C., Pomije, M.J., Mann, K.R., and Munson, E.J., *Catal. Today* **49**, 363 (1999).
47. Mildner, T., Ernst, H., and Freude, D., *Solid State Nucl. Magn. Reson.* **5**, 269 (1995).
48. Ferguson, D.B., and Haw, J.F., *Anal. Chem.* **67**, 3342 (1995).
49. Seiler, M., Schenk, U., and Hunger, M., *Catal. Lett.* **62**, 139 (1999).
50. Haw, J.F., Richardson, B.R., Oshiro, I.S., Lazo, N.D., and Speed, J.A., *J. Am. Chem. Soc.* **111**, 2052 (1989).
51. Zhang, W., Ma, D., Liu, X., Liu, X., and Bao, X., *Chem. Commun.* 1091 (1999).
52. Hwang, S.-J., Petucci, C., and Raftery, D., *J. Am. Chem. Soc.* **120**, 4388 (1998).
53. Gay, I.D., *J. Magn. Reson.* **58**, 413 (1984).
54. Ernst, H., Freude, D., Mildner, T., and Wolf, I., *Solid State Nucl. Magn. Reson.* **6**, 147 (1996).
55. Ernst, H., Freude, D., Mildner, T., and Wolf, I., in "Catalysis by Microporous Materials" (H.K. Beyer, H.G. Karge, I. Kiricsi, and J.B. Nagy, Eds.), "Stud. Surf. Sci. Catal.," Vol. 94, p. 413. Elsevier, Amsterdam, 1995.
56. (a) Haddix, G.W., Reimer, J.A., and Bell, A.T., *J. Catal.* **106**, 111 (1987);
(b) Haddix, G.W., Reimer, J.A., and Bell, A.T., *J. Catal.* **108**, 50 (1987).
57. Davis, M.E., Hathaway, P., Morgan, D., Glass, T., and Dorn, H., in "Catalysis 1987" (J.W. Ward, Ed.), "Stud. Surf. Sci. Catal.," Vol. 38, p. 263. Elsevier, Amsterdam, 1988.
58. Hunger, M., and Horvath, T., *J. Chem. Soc., Chem. Commun.* 1423 (1995).
59. Hunger, M., and Horvath, T., *J. Catal.* **167**, 187 (1997).

60. Hunger, M., Seiler, M., and Horvath, T., *Catal. Lett.* **57**, 199 (1999).
61. Mori, H., Kono, H., Terano, M., Nossov, A., and Zakharov, V.A., *Macromol. Rapid Commun.* **20**, 536 (1999).
62. Mori, H., Kono, H., Terano, M., Nossov, A., and Zakharov, V.A., *J. Mol. Catal. A: Chem.* **164**, 235 (2000).
63. Moudrakovski, I.L., Nossov, A., Lang, S., Breeze, S.R., Ratcliffe, C.I., Simard, B., Santyr, G., and Ripmeester, J.A., *Chem. Mater.* **12**, 1181 (2000).
64. Nossov, A., Guenneau, F., Springuel-Huet, M.-A., Haddad, E., Montouillout, V., Knott, B., Engelke, F., Fernandez, C., and Gedeon, A., *Phys. Chem. Chem. Phys.* **5**, 4479 (2003).
65. Isbester, P.K., Kaune, L., and Munson, E.J., *Chem. Tech. (November)* 40 (1999).
66. Keeler, C., Xiong, J., Lock, H., Dec, S., Tao, T., and Maciel, G.E., *Catal. Today* **49**, 377 (1999).
67. Szeverenyi, N.M., Bax, A., and Maciel, G.E., *J. Magn. Reson.* **61**, 440 (1985).
68. Hunger, M., and Wang, W., *Chem. Commun.* 584 (2004).
69. Breitmaier, E., and Voelter, W., "Carbon-13 NMR Spectroscopy." VCH Verlagsgesellschaft, Weinheim, 1990.
70. (a) Kazansky, V.B., *Catal. Today* **51**, 419 (1999);
(b) Boronat, M., Viruela, P.M., and Corma, A., *J. Am. Chem. Soc.* **126**, 3300 (2004).
71. Bronnimann, C.E., and Maciel, G.E., *J. Am. Chem. Soc.* **108**, 7154 (1986).
72. (a) Bosacek, V., *J. Phys. Chem.* **97**, 10732 (1993);
(b) Bosacek, V., *Z. Phys. Chem.* **189**, 241 (1995);
(c) Bosacek, V., Ernst, H., Freude, D., and Mildner, T., *Zeolites* **18**, 196 (1997);
(d) Bosacek, V., Klik, R., Genoni, F., Spano, G., Rivetti, F., and Figueras, F., *Magn. Reson. Chem.* **37**, S135 (1999).
73. Ivanova, I.I., Pomakhina, E.B., Rebrov, A.I., Hunger, M., Kolyagin, Y.G., and Weitkamp, J., *J. Catal.* **203**, 375 (2001).
74. Wang, W., Seiler, M., and Hunger, M., *J. Phys. Chem. B* **105**, 12553 (2001).
75. Campbell, S.M., Jiang, X.Z., and Howe, R.F., *Microporous Mesoporous Mater.* **29**, 91 (1999).
76. (a) Salehirad, F., and Anderson, M.W., *J. Catal.* **177**, 189 (1998);
(b) Philippou, A., Salehirad, F., Luigi, D.P., and Anderson, M.W., *J. Chem. Soc., Faraday Trans.* **94**, 2851 (1998).
77. (a) Song, W., Haw, J.F., Nicholas, J.B., and Heneghan, C.S., *J. Am. Chem. Soc.* **122**, 10726 (2000);
(b) Fu, H., Song, W., Marcus, D.M., and Haw, J.F., *J. Phys. Chem. B* **106**, 5648 (2002).
78. Wang, W., Jiao, J., Jiang, Y., Ray, S., and Hunger, M., *ChemPhysChem* **6**, 1467 (2005).
79. Aronson, M.T., Gorte, R.J., Farneth, W.E., and White, D., *J. Am. Chem. Soc.* **111**, 840 (1989).
80. Lazo, N.D., Richardson, B.R., Schettler, P.D., White, J.L., Munson, E.J., and Haw, J.F., *J. Phys. Chem.* **95**, 9420 (1991).
81. Stepanov, A.G., Luzgin, M.V., Romannikov, V.N., Sidelnikov, V.N., and Paukshtis, E.A., *J. Catal.* **178**, 466 (1998).
82. Stepanov, A.G., and Luzgin, M.V., *Chem. Eur. J.* **3**, 47 (1997).
83. Barich, D.H., Xu, T., Song, W., Wang, Z., Deng, F., and Haw, J.F., *J. Phys. Chem. B* **102**, 7163 (1998).
84. Bahrman, H., in "New Syntheses with Carbon Monoxide" (J. Falbe, Ed.), Springer, Berlin, p. 372, 1980.
85. Olah, G.A., *Angew. Chem. Int. Ed.* **12**, 173 (1973).
86. Olah, G.A., and Donovan, D.J., *J. Am. Chem. Soc.* **99**, 5026 (1977).
87. Stepanov, A.G., Luzgin, M.V., Romannikov, V.N., and Zamaraev, K.I., *J. Am. Chem. Soc.* **117**, 3615 (1995).
88. Stepanov, A.G., Luzgin, M.V., Romannikov, V.N., Sidelnikov, V.N., and Zamaraev, K.I., *J. Catal.* **164**, 411 (1996).
89. Luzgin, M.V., Romannikov, V.N., Stepanov, A.G., and Zamaraev, K.I., *J. Am. Chem. Soc.* **118**, 10890 (1996).
90. (a) Olah, G.A., "Friedel-Crafts and Related Reactions." Vol. 1, Wiley, New York, 1963;
(b) Olah, G.A., "Friedel-Crafts Chemistry." Wiley, New York, 1973;
(c) Groves, J.K., *Chem. Soc. Rev.* **1**, 73 (1972).

91. Clingenpeel, T.H., and Biaglow, A.I., *J. Am. Chem. Soc.* **119**, 5077 (1997).
92. Clingenpeel, T.H., Wessel, T.E., and Biaglow, A.I., *J. Am. Chem. Soc.* **119**, 5469 (1997).
93. Luzgin, M.V., Stepanov, A.G., Sassi, A., and Sommer, J., *Chem. Eur. J.* **6**, 2368 (2000).
94. Stepanov, A.G., Luzgin, M.V., Krasnoslobodtsev, A.V., Shmachkova, V.P., and Kotsarenko, N.S., *Angew. Chem. Int. Ed.* **39**, 3658 (2000).
95. Saunders, M., Vogel, P., Hagen, E.L., and Rosenfeld, J., *Acc. Chem. Res.* **6**, 53 (1973).
96. Weitkamp, J., *Ind. Eng. Chem., Prod. Res. Dev.* **21**, 550 (1982).
97. Stepanov, A.G., Luzgin, M.V., Arzumanov, S.S., Ernst, H., and Freude, D., *J. Catal.* **211**, 165 (2002).
98. Luzgin, M.V., Arzumanov, S.S., Shmachkova, V.P., Kotsarenko, N.S., Rogov, V.A., and Stepanov, A.G., *J. Catal.* **220**, 233 (2003).
99. Ma, Z., Hua, W., Ren, Y., He, H., and Gao, Z., *Appl. Catal. A: Gen.* **256**, 243 (2003).
100. Luzgin, M.V., Stepanov, A.G., Shmachkova, V.P., and Kotsarenko, N.S., *J. Catal.* **203**, 273 (2001).
101. Ivanova, I.I., Brunel, D., Nagy, J.B., Daelen, G., and Derouane, E.G., in "Heterogeneous Catalysis and Fine Chemistry III" (M. Guisnet, J. Barbier, J. Barrault, C. Bouchoule, D. Duprez, G. Perot, and C. Montassier, Eds.), "Stud. Surf. Sci. Catal.." Vol. 78, p. 587. Elsevier, Amsterdam, 1993.
102. Ivanova, I.I., Brunel, D., Nagy, J.B., and Derouane, E.G., *J. Mol. Catal.* **95**, 243 (1995).
103. Ivanova, I.I., Blom, N., and Derogane, E.G., in "Catalysis by Microporous Materials" (H.K. Beyer, H.G. Karge, I.I. Kiricsi, and J.B. Nagy, Eds.), "Stud. Surf. Sci. Catal.." Vol. 94, p. 419. Elsevier, Amsterdam, 1995.
104. Ivanova, I.I., Pomakhina, E.B., Rebrov, A.I., and Derouane, E.G., *Top. Catal.* **6**, 49 (1998).
105. Derouane, E.G., Abdul-Hamid, S.B., Ivanova, I.I., Blom, N., and Højlund-Nielsen, P.E., *J. Mol. Catal.* **86**, 371 (1994).
106. Haouas, M., Walspurger, S., and Sommer, J., *J. Catal.* **215**, 122 (2003).
107. Haouas, M., Walspurger, S., Taulelle, F., and Sommer, J., *J. Am. Chem. Soc.* **126**, 599 (2004).
108. Beck, L.W., Xu, T., Nicholas, J.B., and Haw, J.F., *J. Am. Chem. Soc.* **117**, 11594 (1995).
109. Mildner, T., and Freude, D., *J. Catal.* **178**, 309 (1998).
110. Haw, J.F., *Phys. Chem. Chem. Phys.* **4**, 5431 (2002).
111. Nicholas, J.B., and Haw, J.F., *J. Am. Chem. Soc.* **120**, 11804 (1998).
112. Haw, J.F., Goguen, P.W., Xu, T., Skloss, T.W., Song, W., and Wang, Z., *Angew. Chem. Int. Ed.* **37**, 948 (1998).
113. Goguen, P.W., Xu, T., Barich, D.H., Skloss, T.W., Song, W., Wang, Z., Nicholas, J.B., and Haw, J.F., *J. Am. Chem. Soc.* **120**, 2650 (1998).
114. Haw, J.F., Nicholas, J.B., Song, W., Deng, F., Wang, Z., Xu, T., and Heneghan, C.S., *J. Am. Chem. Soc.* **122**, 4763 (2000).
115. Xu, T., and Haw, J.F., *J. Am. Chem. Soc.* **116**, 10188 (1994).
116. Xu, T., Barich, D.H., Goguen, P.W., Song, W.G., Wang, Z.K., Nicholas, J.B., and Haw, J.F., *J. Am. Chem. Soc.* **120**, 4025 (1998).
117. Song, W., Nicholas, J.B., Sassi, A., and Haw, J.F., *Catal. Lett.* **81**, 49 (2002).
118. Tao, T., and Maciel, G.E., *J. Am. Chem. Soc.* **117**, 12889 (1995).
119. Tao, T., and Maciel, G.E., *Macromolecules* **30**, 8226 (1997).
120. Tao, T., and Maciel, G.E., *Langmuir* **15**, 1236 (1999).
121. Hölderich, W., Hesse, M., and Naeumann, F., *Angew. Chem. Int. Ed. Engl.* **27**, 226 (1988).
122. Kubelkova, L., and Novakova, J., *Zeolites* **11**, 822 (1991).
123. Chavez-Diaz, C.D., Locatelli, S., and Gonzo, E.E., *Zeolites* **12**, 851 (1992).
124. Xu, T., Munson, E.J., and Haw, J.F., *J. Am. Chem. Soc.* **116**, 1962 (1994).
125. Biaglow, A.I., Sepa, J., Gorte, R.J., and White, D., *J. Catal.* **151**, 373 (1995).
126. Gorte, R.J., and White, D., *Top. Catal.* **4**, 57 (1997).
127. Dumitriu, E., Hulea, V., Fecete, I., Auroux, A., Lacaze, J.-F., and Guimon, C., *Microporous Mesoporous Mater.* **43**, 341 (2001).
128. Florian, J., and Kubelkova, L., *J. Phys. Chem.* **98**, 8734 (1994).
129. Sepa, J., Lee, C., Gorte, R.J., White, D., Kassab, E., Evleth, E.M., Jessri, H., and Allavena, M., *J. Phys. Chem.* **100**, 18515 (1996).
130. Hutchings, G.J., Johnston, P., Lee, D.F., and Williams, C.D., *Catal. Lett.* **21**, 49 (1993).

131. Kassab, E., Jessri, H., Allavena, M., and White, D., *J. Phys. Chem. A* **103**, 2766 (1999).
132. Solans-Monfort, X., Bertran, J., Branchadell, V., and Sodupe, M., *J. Phys. Chem. B* **106**, 10220 (2002).
133. Xu, M., Wang, W., and Hunger, M., *Chem. Commun.* 722 (2003).
134. Pines, H., "The Chemistry of Catalytic Hydrocarbon Conversion." Academic Press, New York, 1981.
135. Olah, G.A., and Molnar, A., "Hydrocarbon Chemistry." Wiley, New York, 1995.
136. Corma, A., *Chem. Rev.* **95**, 559 (1995).
137. Corma, A., and Orchilles, A.V., *Microporous Mesoporous Mater.* **35-36**, 21 (2000).
138. Ozaki, A., "Isotopic Studies of Heterogeneous Catalysis." Kodansha, Tokyo, 1977.
139. Hindin, S.G., Mills, G.A., and Oblad, A.G., *J. Am. Chem. Soc.* **73**, 278 (1951).
140. Freude, D., Oehme, W., Schmiedel, H., and Staudte, B., *J. Catal.* **49**, 123 (1977).
141. Mota, C.J.A., and Martins, R.L., *J. Chem. Soc. Chem. Commun.* 171 (1991).
142. Mota, C.J.A., Nogueira, L., and Kover, W.B., *J. Am. Chem. Soc.* **114**, 1121 (1992).
143. Kramer, G.J., van Santen, R.A., Emeis, C.A., and Nowak, A.K., *Nature* **363**, 529 (1993).
144. Kramer, G.J., and van Santen, R.A., *J. Am. Chem. Soc.* **117**, 1766 (1995).
145. Sommer, J., Hachoumy, M., Garin, F., Barthomeuf, D., and Vedrine, J., *J. Am. Chem. Soc.* **117**, 1135 (1995).
146. Engelhardt, J., and Hall, W.K., *J. Catal.* **151**, 1 (1995).
147. Sommer, J., Habermacher, D., Hachoumy, M., Jost, R., and Reynaud, A., *Appl. Catal.* **146**, 193 (1996).
148. Narbeshuber, T.F., Stockenhuber, M., Brait, A., Seshan, K., and Lercher, J.A., *J. Catal.* **160**, 183 (1996).
149. Blaszkowski, S.R., Nascimento, M.A.C., and van Santen, R.A., *J. Phys. Chem.* **100**, 3463 (1996).
150. Crabtree, R.H., *Chem. Rev.* **95**, 987 (1995).
151. Wang, L., Tao, L., Xie, M., Xu, G., Huang, J., and Xu, Y., *Catal. Lett.* **21**, 35 (1993).
152. Zhang, W., Ma, D., Han, X., Liu, X., Bao, X., Guo, X., and Wang, X., *J. Catal.* **188**, 393 (1999).
153. Shu, Y., Ma, D., Liu, X., Han, X., Xu, Y., and Bao, X., *J. Phys. Chem. B* **104**, 8245 (2000).
154. Shu, Y., Xu, Y., Wong, S.-T., Wang, L., and Guo, X., *J. Catal.* **170**, 11 (1997).
155. Ma, D., Shu, Y., Bao, X., and Xu, Y., *J. Catal.* **189**, 314 (2000).
156. Solymosi, F., Szoke, A., and Cserenyi, J., *Catal. Lett.* **39**, 157 (1996).
157. Klinowski, J., *Chem. Rev.* **91**, 1459 (1991).
158. Klinowski, J., *Anal. Chim. Acta* **283**, 929 (1993).
159. Liu, W., Xu, Y., Wong, S., Wang, L., Qin, J., and Yang, N., *J. Mol. Catal. A: Chem.* **120**, 257 (1997).
160. Zhang, J.Z., Long, M.A., and Howe, R.F., *Catal. Today* **44**, 293 (1998).
161. Ma, D., Shu, Y., Zhang, W., Han, X., Xu, Y., and Bao, X., *Angew. Chem. Int. Ed.* **39**, 2928 (2000).
162. Yang, J., Ma, D., Deng, F., Luo, Q., Zhang, M., Bao, X., and Ye, C., *Chem. Commun.* 3046 (2002).
163. Engelhardt, J., and Hall, W.K., *J. Catal.* **125**, 472 (1990).
164. Abbot, J., *Appl. Catal.* **57**, 105 (1990).
165. Guisnet, M., Gnep, N.S., and Alario, F., *Appl. Catal. A: Gen.* **89**, 1 (1992).
166. Ono, Y., *Catal. Rev.-Sci. Eng.* **34**, 179 (1992).
167. Giannetto, G., Monque, R., and Galiasso, R., *Catal. Rev.-Sci. Eng.* **36**, 271 (1994).
168. Bayense, C.R., van der Pol, A.J.H.P., and van Hoof, J.H.C., *Appl. Catal.* **72**, 81 (1991).
169. Bayense, C.R., and van Hoof, J.H.C., *Appl. Catal. A: Gen.* **79**, 127 (1991).
170. Giannetto, G., Montes, A., Gnep, N.S., Florentino, A., Cartraud, P., and Guisnet, M., *J. Catal.* **145**, 86 (1993).
171. Choudhary, V.R., Kinage, A.K., Sivadinarayana, C., Sansare, S.D., and Guisnet, M., *Catal. Lett.* **33**, 401 (1995).
172. Choudhary, V.R., Kinage, A.K., Sivadinarayana, C., Devadas, P., Sansare, S.D., and Guisnet, M., *J. Catal.* **158**, 34 (1996).
173. Choudhary, V.R., Devadas, P., Kinage, A.K., Sivadinarayana, C., and Guisnet, M., *J. Catal.* **158**, 537 (1996).
174. Choudhary, V.R., Sivadinarayana, C., Kinage, A.K., Devadas, P., and Guisnet, M., *Appl. Catal. A: Gen.* **136**, 125 (1996).
175. Doolan, P.C., and Pujado, P.R., *Hydrocarbon Process.* **68**, 72 (1989).
176. Ivanova, I.I., Blom, N., Abdul-Hamid, S.B., and Derouane, E.G., *J. Neth. Chem. Soc.* **113**, 454 (1994).

177. Ivanova, I.I., Blom, N., and Derouane, E.G., *J. Mol. Catal. A: Chem.* **109**, 157 (1996).
178. Derouane, E.G., Hamid, S.B.A., Pasau-Claerbout, A., Seivert, M., and Ivanova, I.I., in "Science and Technology in Catalysis 1994" (Y. Izumi, H. Arai, and M. Iwamoto, Eds.), "Stud. Surf. Sci. Catal.." Vol. 92, p. 123. Elsevier, Amsterdam, 1995.
179. Derouane, E.G., He, H., Derouane-Abd Hamid, S.B., Lambert, D., and Ivanova, I.I., *J. Mol. Catal. A: Chem.* **158**, 5 (2000).
180. Derouane-Abd Hamid, S.B., Pal, P., He, H., and Derouane, E.G., *Catal. Today* **64**, 129 (2001).
181. Derouane, E.G., He, H., Derouane-Abd Hamid, S.B., and Ivanova, I.I., *Catal. Lett.* **58**, 1 (1999).
182. Ivanova, I.I., and Derouane, E.G., in "Advanced Zeolite Science and Applications" (J.C. Jansen, M. Stöcker, H.G. Karge, and J. Weitkamp, Eds.), "Stud. Surf. Sci. Catal.." Vol. 85, p. 357. Elsevier, Amsterdam, 1994.
183. Ivanova, I.I., Rebrov, A.I., Pomakhina, E.B., and Derouane, E.G., *J. Mol. Catal. A: Chem.* **141**, 107 (1999).
184. Stepanov, A.G., Ernst, H., and Freude, D., *Catal. Lett.* **54**, 1 (1998).
185. Fujishima, A., and Honda, K., *Kog. Kagaku. Zasshi.* **74**, 355 (1971).
186. Fujishima, A., Inoue, T., and Honda, K., *J. Am. Soc. Chem.* **101**, 5582 (1979).
187. Fujishima, A., and Honda, K., *Nature* **37**, 238 (1972).
188. Linsebigler, A.L., Lu, G., and Yates, J.T. Jr., *Chem. Rev.* **95**, 735 (1995).
189. Heller, A., *Acc. Chem. Res.* **28**, 503 (1995).
190. Hwang, S.-J., Petucci, C., and Raftery, D., *J. Am. Chem. Soc.* **119**, 7877 (1997).
191. Rice, C.V., and Raftery, D., *Chem. Commun.* **895** (1999).
192. Pradhan, A.R., Macnaughtan, M.A., and Raftery, D., *J. Am. Chem. Soc.* **122**, 404 (2000).
193. Borisch, J., Pilkenton, S., Miller, M.L., Raftery, D., and Francisco, J.S., *J. Phys. Chem. B* **108**, 5640 (2004).
194. Hwang, S.-J., and Raftery, D., *Catal. Today* **49**, 353 (1999).
195. Pilkenton, S., Hwang, S.-J., and Raftery, D., *J. Phys. Chem. B* **103**, 11152 (1999).
196. Klosek, S., and Raftery, D., *J. Phys. Chem. B* **105**, 2815 (2001).
197. Xu, W., and Raftery, D., *J. Phys. Chem. B* **105**, 4343 (2001).
198. Xu, W., and Raftery, D., *J. Catal.* **204**, 110 (2001).
199. (a) Weitkamp, J., Ernst, S., and Puppe, L., in "Catalysis and Zeolites, Fundamentals and Applications" (J. Weitkamp, and L. Puppe, Eds.), Springer, Berlin, p. 327, 1999;
(b) Espeel, P., Parton, R., Toufar, H., Martens, J., Hölderich, W., and Jacobs, P., in "Catalysis and Zeolites, Fundamentals and Applications" (J. Weitkamp, and L. Puppe, Eds.), Springer, Berlin, p. 377, 1999;
(c) Blauwhoff, P.M.M., Gosselink, J.W., Kieffer, E.P., Sie, S.T., and Stork, W.H.J., in "Catalysis and Zeolites, Fundamentals and Applications" (J. Weitkamp, and L. Puppe, Eds.), Springer, Berlin, p. 437, 1999.
200. (a) Rees, L.V.C., and Shen, D., in "Introduction to Zeolite Science and Practice" (H. van Bekkum, E.M. Flanigen, P.A. Jacobs, and J.C. Jansen, Eds.), "Stud. Surf. Sci. Catal.." Vol. 137, p. 579. Elsevier, Amsterdam, 2001;
(b) Martens, J.A., and Jacobs, P.A., in "Introduction to Zeolite Science and Practice" (H. van Bekkum, E.M. Flanigen, P.A. Jacobs, and J.C. Jansen, Eds.), "Stud. Surf. Sci. Catal.." Vol. 137, p. 633. Elsevier, Amsterdam, 2001;
(c) Maxwell, I.E., and Stork, W.H.J., in "Introduction to Zeolite Science and Practice" (H. van Bekkum, E.M. Flanigen, P.A. Jacobs, and J.C. Jansen, Eds.), "Stud. Surf. Sci. Catal.." Vol. 137, p. 747. Elsevier, Amsterdam, 2001;
(d) Hölderich, W.F., and van Bekkum, H., in "Introduction to Zeolite Science and Practice" (H. van Bekkum, E.M. Flanigen, P.A. Jacobs, and J.C. Jansen, Eds.), "Stud. Surf. Sci. Catal.." Vol. 137, p. 821. Elsevier, Amsterdam, 2001.
201. Freude, D., Ernst, H., and Wolf, I., *Solid State Nucl. Magn. Reson.* **3**, 271 (1994).
202. Hunger, M., Horvath, T., Engelhardt, G., and Karge, H.G., in "Catalysis by Microporous Materials" (H.K. Beyer, H.G. Karge, I. Kiricsi, and J.B. Nagy, Eds.), "Stud. Surf. Sci. Catal.." Vol. 94, p. 756. Elsevier, Amsterdam, 1995.
203. Ehresmann, J.O., Wang, W., Herreros, B., Luigi, D.-P., Venkatraman, T.N., Song, W., Nicholas, J.B., and Haw, J.F., *J. Am. Chem. Soc.* **124**, 10868 (2002).

204. Hunger, M., and Horvath, T., *Ber. Bunsenges. Phys. Chem.* **99**, 1316 (1995).
205. Grey, C.P., and Vega, A.J., *J. Am. Chem. Soc.* **117**, 8232 (1995).
206. Hunger, M., and Horvath, T., *J. Am. Chem. Soc.* **118**, 12302 (1996).
207. Seiler, M., Wang, W., and Hunger, M., *J. Phys. Chem. B* **105**, 8143 (2001).
208. Koller, H., Meijer, E.L., and van Santen, R.A., *Solid State Nucl. Magn. Reson.* **9**, 165 (1997).
209. van Bokhoven, J.A., Roest, A.L., Koningsberger, D.C., Miller, J.T., Nachttegaal, G.H., and Kentgens, A.P.M., *J. Phys. Chem. B* **104**, 6743 (2000).
210. Stöcker, M., *Microporous Mesoporous Mater.* **29**, 3 (1999).
211. Martens, J.A., Grobet, P.J., and Jacobs, P.A., *J. Catal.* **126**, 299 (1990).
212. Mostad, H.B., Stöcker, M., Karlsson, A., and Rorvik, T., *Appl. Catal. A: Gen.* **144**, 305 (1996).
213. Hunger, M., Anderson, M., Ojo, A., and Pfeifer, H., *Microporous Mater.* **1**, 17 (1993).
214. Chen, Q., Springuel-Huet, M.A., Fraissard, J., Smith, M.L., Corbin, D.R., and Dybowski, C., *J. Phys. Chem.* **96**, 10914 (1992).
215. Minchev, C., Neinska, Y., Valtchev, V., Minkov, V., Tsoncheva, T., Penchev, V., Lechert, H., and Hess, M., *Catal. Lett.* **18**, 125 (1993).
216. Briend, M., Shikholeslami, A., Peltre, M.J., Delafosse, D., and Barthomeuf, D., *J. Chem. Soc. Dalton Trans.* 1361 (1989).
217. Buchholz, A., Wang, W., Arnold, A., Xu, M., and Hunger, M., *Microporous Mesoporous Mater.* **57**, 157 (2003).
218. Hunger, M., Freude, D., and Pfeifer, H., *J. Chem. Soc., Faraday Trans.* **87**, 657 (1991).
219. Batamack, P., Doremieux-Morin, C., Fraissard, J., and Freude, D., *J. Phys. Chem.* **95**, 3790 (1991).
220. Buchholz, A., Wang, W., Xu, M., Arnold, A., and Hunger, M., *J. Phys. Chem. B* **108**, 3107 (2004).
221. Mees, F.D.P., Martens, L.R.M., Janssen, M.J.G., Verberckmoes, A.A., and Vasant, E.F., *Chem. Commun.* **44** (2003).
222. (a) Lee, A.K.K., and Al-Jarallah, A., *Chem. Econ. Eng. Rev.* **18**, 25 (1986);
(b) Goodwin, J.G., Natesakhawat, S., Nikolopoulos, A.A., and Kim, S.Y., *Catal. Rev.-Sci. Eng.* **44**, 287 (2002).
223. Kogelbauer, A., Goodwin, J.G., and Lercher, J.A., *J. Phys. Chem.* **99**, 8777 (1995).
224. Kogelbauer, A., Nikolopoulos, A.A., Goodwin, J.G., and Marcelin, G., *J. Catal.* **152**, 122 (1995).
225. Nikolopoulos, A.A., Oukaci, R., Goodwin, J.G., and Marcelin, G., *Catal. Lett.* **27**, 149 (1994).
226. Collignon, F., Mariani, M., Moreno, S., Remy, M., and Poncelet, G., *J. Catal.* **166**, 53 (1997).
227. Hölderich, W.F., in "Catalytic Science and Technology." (S. Yoshida, Ed.), Vol. 1, p. 31. Kodansha Ltd., Tokyo, 1991.
228. Mildner, T., Ernst, H., Freude, D., and Hölderich, W.F., *J. Am. Chem. Soc.* **119**, 4258 (1997).
229. Hunger, M., Horvath, T., and Weitkamp, J., *Microporous Mesoporous Mater.* **22**, 357 (1998).
230. Horvath, T., Seiler, M., and Hunger, M., *Appl. Catal. A: Gen.* **193**, 227 (2000).
231. Yashima, T., Sato, K., Hayasaka, T., and Hara, N., *J. Catal.* **26**, 303 (1972).
232. Philippou, A., and Anderson, M.W., *J. Am. Chem. Soc.* **116**, 5774 (1994).
233. (a) Hathaway, P.E., and Davis, M.E., *J. Catal.* **116**, 263 (1989);
(b) Hathaway, P.E., and Davis, M.E., *J. Catal.* **116**, 279 (1989);
(c) Hathaway, P.E., and Davis, M.E., *J. Catal.* **119**, 497 (1989).
234. Hunger, M., Schenk, U., and Weitkamp, J., *J. Mol. Catal. A: Chem.* **134**, 97 (1998).
235. Hunger, M., Schenk, U., Seiler, M., and Weitkamp, J., *J. Mol. Catal. A: Chem.* **156**, 153 (2000).
236. Schenk, U., Ph.D. thesis, Department of Chemistry, Stuttgart, University of Stuttgart, 2001.
237. Lazo, N.D., Murray, D.K., Kieke, M.L., and Haw, J.F., *J. Am. Chem. Soc.* **114**, 8552 (1992).
238. Murray, D.K., Chang, J.-W., and Haw, J.F., *J. Am. Chem. Soc.* **115**, 4732 (1993).
239. (a) Bautista, F.M., Campelo, J.M., Garcia, A., Luna, D., Marinas, J.M., Romero, A.A., and Urbano, M.R., *J. Catal.* **172**, 103 (1997);
(b) Bautista, F.M., Campelo, J.M., Garcia, A., Luna, D., Marinas, J.M., and Romero, A.A., in "Heterogeneous Catalysis and Fine Chemistry IV" (H.U. Blaser, A. Baiker, and R. Prins, Eds.), "Stud. Surf. Sci. Catal.," Vol. 108, p. 123. Elsevier, Amsterdam, 1997;
(c) Bautista, F.M., Campelo, J.M., Garcia, A., Luna, D., Marinas, J.M., and Romero, A.A., *Appl. Catal. A: Gen.* **166**, 39 (1998).

240. Shaikh, R.A., Singh, P.S., Bandyopadhyay, R., Kavedia, C.V., Mirajkar, S.P., and Rao, B.S., in "Recent Advances in Basic and Applied Aspects of Industrial Catalysis" (T.S.R. Prasad Rao, and G. Murali Dhar, Eds.), "Stud. Surf. Sci. Catal.," Vol. 113, p. 637. Elsevier, Amsterdam, 1998.
241. Narayanan, S., and Deshpande, K., *Appl. Catal. A: Gen.* **199**, 1 (2000).
242. Wang, W., Seiler, M., Ivanova, I.I., Weitkamp, J., and Hunger, M., *Chem. Commun.* 1362 (2001).
243. Wang, W., Seiler, M., Ivanova, I.I., Sternberg, U., Weitkamp, J., and Hunger, M., *J. Am. Chem. Soc.* **124**, 7548 (2002).
244. Ivanova, I.I., and Corma, A., *J. Phys. Chem. B* **101**, 547 (1997).
245. Blaszkowski, S.R., and van Santen, R.A., *J. Phys. Chem. B* **101**, 2292 (1997).
246. Ernst, H., and Pfeifer, H., *J. Catal.* **136**, 202 (1992).
247. Pouilloux, Y., Doidy, V., Hub, S., Kervennal, J., and Barrault, J., in "Heterogeneous Catalysis and Fine Chemicals IV" (H.U. Blaser, A. Baiker, and R. Prins, Eds.), "Stud. Surf. Sci. Catal.," Vol. 108, p. 139. Elsevier, Amsterdam, 1997.
248. Kongshaug, K.O., Fjellvag, H., Klewe, B., and Lillerud, K.P., *Microporous Mesoporous Mater.* **39**, 333 (2000).
249. Kruk, M., and Jaroniec, M., *J. Phys. Chem. B* **103**, 4590 (1999).
250. Kleitz, F., Schmidt, W., and Schüth, F., *Microporous Mesoporous Mater.* **44/45**, 95 (2001).
251. Wang, W., Buchholz, A., Ivanova, I.I., Weitkamp, J., and Hunger, M., *Chem. Commun.* 2600 (2003).
252. Weitkamp, J., Fritz, M., and Ernst, S., in "Proceedings from the Ninth International Zeolite Conference, Montreal 1992" (R. von Ballmoos, J.B. Higgins, and M.M.J. Treacy, Eds.), Butterworth-Heinemann, Stoneham, MA, p. 13, 1993.
253. Cano, M.L., Corma, A., Fornes, V., Garcia, H., Mirando, M.A., Baerlocher, C., and Lengauer, C., *J. Am. Chem. Soc.* **118**, 11006 (1996).
254. Jansen, J.C., and Wilson, S.T., in "Introduction to Zeolite Science and Practice" (H. van Bekkum, E.M. Flanigen, P.A. Jacobs, and J.C. Jansen, Eds.), "Stud. Surf. Sci. Catal.," Vol. 137, p. 175. Elsevier, Amsterdam, 2001.
255. Wang, W., Xu, M., Buchholz, A., Arnold, A., and Hunger, M., *Magn. Reson. Imaging* **21**, 329 (2003).
256. Chang, C.D., *Catal. Rev. Sci. Eng.* **25**, 1 (1983).
257. Chang, C.D., *Catal. Rev. Sci. Eng.* **26**, 323 (1984).
258. Ernst, H., Freude, D., and Mildner, T., *Chem. Phys. Lett.* **229**, 291 (1994).
259. Mildner, T., Ernst, H., Freude, D., Kärger, J., and Winkler, U., *Magn. Reson. Chem.* **37**, S38 (1999).
260. Carlson, L.K., Isbester, P.K., and Munson, E.J., *Solid State Nucl. Magn. Reson.* **16**, 93 (2000).
261. Hunger, M., Seiler, M., and Buchholz, A., *Catal. Lett.* **74**, 61 (2001).
262. Wang, W., Buchholz, A., Arnold, A., Xu, M., and Hunger, M., *Chem. Phys. Lett.* **370**, 88 (2003).
263. Wang, W., Buchholz, A., Seiler, M., and Hunger, M., *J. Am. Chem. Soc.* **125**, 15260 (2003).
264. Anderson, M.W., and Klinowski, J., *Nature* **339**, 200 (1989).
265. Reiss, G., *Gas Sep. Purif.* **8**, 95 (1994).
266. Anderson, M.W., Barrie, P.J., and Klinowski, J., *J. Phys. Chem.* **95**, 235 (1991).
267. Klinowski, J., and Anderson, M.W., *Magn. Reson. Chem.* **28**, S68 (1990).
268. Anderson, M.W., and Klinowski, J., *J. Am. Chem. Soc.* **112**, 10 (1990).
269. Tsiao, C., Corbin, D.R., and Dybowski, C., *J. Am. Chem. Soc.* **112**, 7140 (1990).
270. Mirth, G., Lercher, J.A., Anderson, M.W., and Klinowski, J., *J. Chem. Soc., Faraday Trans.* **86**, 3039 (1990).
271. Thursfield, A., and Anderson, M.W., *J. Phys. Chem.* **100**, 6698 (1996).
272. Kotrla, J., Nachtigallova, D., Kubelkova, L., Heeribout, L., Doremieux-Morin, C., and Fraissard, J., *J. Phys. Chem. B* **102**, 2454 (1998).
273. Salehirad, F., and Anderson, M.W., *J. Chem. Soc., Faraday Trans.* **94**, 1911 (1998).
274. Salehirad, F., and Anderson, M.W., *J. Chem. Soc., Faraday Trans.* **94**, 2857 (1998).
275. Anderson, M.W., Ocelli, M.L., and Klinowski, J., *J. Phys. Chem.* **96**, 388 (1992).
276. Alba, M.D., Romero, A.A., Ocelli, M.L., and Klinowski, J., *J. Phys. Chem. B* **101**, 5166 (1997).
277. Anderson, M.W., Sulikowski, B., Barrie, P.J., and Klinowski, J., *J. Phys. Chem.* **94**, 2730 (1990).

278. Salehirad, F., and Anderson, M.W., *J. Catal.* **164**, 301 (1996).
279. He, H., Zhang, L., Klinowski, J., and Occelli, M.L., *J. Phys. Chem.* **99**, 6980 (1995).
280. Ono, Y., and Mori, T., *J. Chem. Soc., Faraday Trans.* **77**, 2209 (1981).
281. Forester, T.R., and Howe, R.F., *J. Am. Chem. Soc.* **109**, 5076 (1987).
282. Bandiera, J., and Naccache, C., *Appl. Catal.* **69**, 139 (1991).
283. Sinclair, P.E., and Catlow, C.R.A., *J. Chem. Soc., Faraday Trans.* **93**, 333 (1997).
284. (a) Shah, R., Payne, M.C., Lee, M.H., and Gale, J.D., *Science* **271**, 1395 (1996);
(b) Shah, R., Gale, J.D., and Payne, M.C., *J. Phys. Chem. B* **101**, 4787 (1997);
(c) Stich, I., Gale, J.D., Terakura, K., and Payne, M.C., *J. Am. Chem. Soc.* **121**, 3292 (1999).
285. Pelmenchikov, A.G., Morosi, G., Gamba, A., and Coluccia, S., *J. Phys. Chem.* **99**, 15018 (1995).
286. (a) Blaszkowski, S.R., and van Santen, R.A., *J. Phys. Chem.* **99**, 11728 (1995);
(b) Blaszkowski, S.R., and van Santen, R.A., *J. Am. Chem. Soc.* **118**, 5152 (1996).
287. Haase, F., Sauer, J., and Hutter, J., *Chem. Phys. Lett.* **266**, 397 (1997).
288. Nusterer, E., Bloechl, P.E., and Schwarz, K., *Angew. Chem. Int. Ed.* **35**, 175 (1996).
289. Haag, W.O., in "Proceedings of the 6th International Zeolite Conference" (R.A. Bisio, and D.G. Olson, Eds.), Butterworths, Guildford, p. 466, 1984.
290. Hölderich, W., Eichhorn, H., Lehnert, R., Marosi, L., Mross, W., Reinke, R., Ruppel, W., and Schlimper, H., in "Proceedings of the 6th International Zeolite Conference" (R.A. Bisio, and D.G. Olson, Eds.), Butterworths, Guildford, p. 545, 1984.
291. Dessau, R.M., *J. Catal.* **99**, 111 (1986).
292. Kolboe, S., *Acta Chem. Scand. A* **40**, 711 (1986).
293. Dahl, I.M., and Kolboe, S., *J. Catal.* **149**, 458 (1994).
294. Dahl, I.M., and Kolboe, S., *J. Catal.* **161**, 304 (1996).
295. Mikkelsen, O., Ronning, P.O., and Kolboe, S., *Microporous Mesoporous Mater.* **40**, 95 (2000).
296. Arstad, B., and Kolboe, S., *J. Am. Chem. Soc.* **123**, 8137 (2001).
297. Arstad, B., and Kolboe, S., *Catal. Lett.* **71**, 209 (2001).
298. Song, W., Marcus, D.M., Fu, H., Ehresmann, J.O., and Haw, J.F., *J. Am. Chem. Soc.* **124**, 3844 (2002).
299. Sassi, A., Wildman, M.A., Ahn, H.J., Prasad, P., Nicholas, N.B., and Haw, J.F., *J. Phys. Chem. B* **106**, 2294 (2002).
300. Seiler, M., Wang, W., Buchholz, A., and Hunger, M., *Catal. Lett.* **88**, 187 (2003).
301. Kiricsi, I., Förster, H., Tasi, G., and Nagy, J.B., *Chem. Rev.* **99**, 2085 (1999). *Chem. Rev.* **99**, 3367.
302. Bjørgen, M., Bonino, F., Kolboe, S., Lillerud, K.P., Zecchina, A., and Bordiga, S., *J. Am. Chem. Soc.* **125**, 15863 (2003).
303. Karge, H.G., Laniecki, M., Ziolk, M., Onyestyak, G., Kiss, A., Kleinschmit, P., and Siray, M., in "Zeolites: Facts, Figures, Future" (P.A. Jacobs, and R.A. van Santen, Eds.), "Stud. Surf. Sci. Catal.," Vol. 49, p. 1327. Elsevier, Amsterdam, 1989.

Attenuated Total Reflection Infrared Spectroscopy of Solid Catalysts Functioning in the Presence of Liquid-Phase Reactants

T. BÜRGI

Institut de Microtechnique, Université de Neuchâtel, Rue Emile-Argand 11, 2009 Neuchâtel, Switzerland

and

A. BAIKER

Institute for Chemical and Bioengineering, Department of Chemistry and Applied Biosciences, ETH Zürich, Hönggerberg, HCI, CH-8093 Zürich, Switzerland

Attenuated total reflection (ATR) infrared (IR) spectroscopy is a powerful tool for investigation of solid catalysts, allowing the detection of liquid-phase products (for on-line reaction monitoring) and the investigation of species adsorbed on the catalyst, during reaction and in the presence of strongly absorbing solvents. Flat model catalysts such as metal films as well as powder catalysts can be investigated. In favorable situations, even changes of the catalyst structure can be followed. In this review, some fundamental concepts of ATR spectroscopy are summarized, and practical aspects, such as cell design and sample preparation, are discussed. The potential and limitations of the method are illustrated with examples. Furthermore, powerful techniques aimed at enhancing signal-to-noise ratios and long-term stability are described, which make use of phase-sensitive detection of periodically varying signals and accurate reference measurements. Until now, only a rather limited number of investigations have been reported that use the ATR technique to study heterogeneous catalytic reactions at solid–liquid interfaces, but the method holds good promise because it is comparatively inexpensive and versatile and can provide a large amount of information.

Abbreviations: ATR, attenuated total reflection; CD, cinchonidine; DFT, density functional theory; FT, Fourier transform; GC, gas chromatography; HPLC, high-performance liquid chromatography; IR, infrared; IRE, internal reflection element; IRRAS, infrared reflection absorption spectroscopy; KPL, ketopantolactone; MES, modulation excitation spectroscopy; MS, mass spectrometry; NMR, nuclear magnetic resonance; PM-IRRAS, polarization modulation infrared reflection absorption spectroscopy; PSD, phase-sensitive detection; SBSR, single-beam signal reference; SEIRA, surface enhanced infrared absorption; SFG, sum frequency generation; TBHP, t-butyl hydroperoxide; TOF, turnover frequency; UHV, ultrahigh vacuum; A , absorbance; B , constant defining band intensity of a damped harmonic oscillator (Eq. (23)); c , concentration; d_p , penetration depth (Eq. (2)); d_e , effective thickness (Eq. (3)); E , electric field amplitude; E_0 , electric field amplitude at interface; E_{\parallel} , electric field amplitude parallel to

the plane of incidence; E_{\perp} , electric field amplitude perpendicular to the plane of incidence; e , base of natural logarithm; k , extinction coefficient; m^* , effective electron mass; M , characteristic matrix defining reflectance properties of a layer (Eqs. (13) and (14)); m , elements of characteristic matrix defining reflectance properties of a layer (Eqs. (20) and (21)); n , refractive index; \tilde{n} , complex refractive index; p , angle-dependent refractive index (Eq. (16)); q , angle-dependent refractive index (Eq. (17)); R , reflectance; r , Fresnel reflection coefficient; T , modulation period; U , tangential component of the field amplitude (Eq. (12)); V , tangential component of the field amplitude (Eq. (12)); β , angle-dependent refractive index (Eq. (18)); γ , damping constant of damped harmonic oscillator (Eq. (23)); ϵ , dielectric constant; ϵ_m , molar absorption coefficient; $\tilde{\nu}$, wavenumber; θ , angle of incidence; θ_c , critical angle; ϕ , demodulation phase angle (Eq. (26)); λ , wavelength; τ , relaxation time of electron (Eq. (24)); ω_p , plasma frequency (Eq. (24)); ω , angular frequency; ζ , angle-dependent refractive index (Eq. (15)).

I. Introduction

Many important heterogeneous catalytic reactions occur at the interface between a solid catalyst and liquid or liquid–gas reactants. Notwithstanding the importance of solid-catalyzed reactions in the presence of liquid reactants, relatively little attention has been paid to spectroscopic methods that allow researchers to follow the processes occurring at the solid–liquid interface during reaction. This lack can be explained in part by the fact that there are only a few techniques that give access to information about solid–liquid interfaces, the most prominent of them being attenuated total reflection infrared spectroscopy (ATR-IR) and X-ray absorption fine structure (XAFS) spectroscopy.

The vibrational spectrum of a molecule adsorbed on a metal surface contains detailed information about the metal–adsorbate bonds, the local orientation of the molecule, and intermolecular interactions within the adsorbate layer. It is this detailed information about the adsorbate layer that makes vibrational spectroscopy and most prominently IR spectroscopy an important tool in heterogeneous catalysis research.

In recent years IR spectroscopy has become a powerful method to probe catalytic solid–gas interfaces *in situ* (1). In contrast, catalytic solid–liquid interfaces have hardly been investigated *in situ* by vibrational spectroscopy or other techniques. An exception to this statement is represented by extensive work in electrochemistry, whereby vibrational spectroscopy has been used for many years to probe solid–liquid interfaces at electrodes (2).

In this contribution, we discuss the potential of ATR-IR spectroscopy for the investigation of heterogeneous catalytic reactions. Although ATR has been applied for some time in various fields of research, its application in heterogeneous catalysis has gained significant attention only recently, mainly because of its promising features for *in situ* investigation of catalytic solid–liquid interfaces. Notwithstanding the growing attention given to ATR, its applications in investigations of heterogeneous catalysis are still quite limited in number.

The aim of this review is to provide an assessment of the state of this field. After a summary of some basic theoretical results, the focus is on experimental aspects, ranging from cell design to specialized techniques such as modulation excitation spectroscopy (MES). We emphasize the opportunities and limitations of ATR-IR spectroscopy in catalysis research.

II. Fundamentals of ATR Spectroscopy

The phenomenon of internal reflection was already known by Newton (3), but the fundamentals of ATR spectroscopy or internal reflection spectroscopy were elaborated only 40 years ago (4-6). Recent monographs deal with its application in various fields of science (7-9), such as polymer science (10) and the science of biological interfaces (11,12). The principle is shown schematically in Fig. 1. An internal reflection element (IRE), which is a transparent optical element with a high refractive index n_1 , is in contact with an optically thinner medium, the sample, with refractive index n_2 . When electromagnetic radiation propagating through the IRE strikes the interface at an angle of incidence (θ) larger than the critical angle (θ_c), given by $\sin(\theta_c) = n_2/n_1$, total reflection occurs at the interface.

A. EVANESCENT FIELD, PENETRATION DEPTH, AND EFFECTIVE THICKNESS

Calculation of the propagation of a plane wave from a medium 1 with higher refractive index (IRE) into a non-absorbing medium 2 with lower refractive index (rarer medium) under conditions of total reflection yields

$$E = E_0 e^{-z/d_p}, \quad (1)$$

where E_0 is the electric field amplitude at the interface, which depends on the angle of incidence, the refractive indices, and the polarization of the field (5). The electric field components of the evanescent wave fall off exponentially with the distance z from the interface. There is no net flux of energy in the evanescent field, whereas in a light beam there is a flux of energy in the direction of propagation. According to Eq. (1), d_p , the penetration depth of the evanescent wave, is defined as the distance from the interface at which the electric field amplitude E has decayed to $1/e$ of its

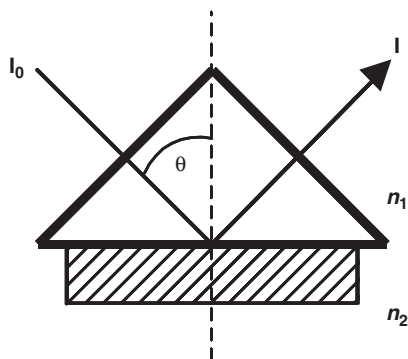


FIG. 1. Experimental geometry for attenuated total reflection (ATR) IR spectroscopy. I_0 and I are the intensities of the incident and transmitted (reflected) radiation, respectively; θ is the angle of incidence, and n_1 and n_2 are the refractive indices of the IRE and sample, respectively.

value at the interface, E_0 . The penetration depth d_p is given by

$$d_p = \frac{\lambda_1}{2\pi\sqrt{\sin^2\theta - n_{21}^2}}, \quad (2)$$

where $\lambda_1 = \lambda/n_1$ is the wavelength in the optically denser medium and $n_{21} = n_2/n_1$. The penetration depth depends on the wavelength of the light and thus changes across the spectrum.

Harrick (5) introduced the concept of the effective thickness d_e , which is the equivalent path in a hypothetical transmission experiment that results in the same absorption signal $A = \epsilon_m c d_e$ as in the ATR experiment under identical conditions, where A is absorbance; ϵ_m the molar absorption coefficient; and c the concentration of dissolved molecules:

$$d_e = \frac{n_{21} E_0^2 d_p}{2 \cos \theta}. \quad (3)$$

For a Ge IRE ($n_1 = 4$) in contact with water ($n_2 = 1.33$) at an angle of incidence of $\theta = 45^\circ$, the effective thickness at 1640 cm^{-1} is $0.44 \mu\text{m}$ for parallel polarized light (polarized in the plane of incidence of the light) and $0.22 \mu\text{m}$ for perpendicular-polarized light. For a ZnSe IRE the corresponding values are 1.12 and $0.56 \mu\text{m}$. The sensitivity of ATR experiments can be increased by multiple internal reflections.

B. ELECTRIC FIELD COMPONENTS IN BULK RARE (OPTICALLY THIN) MEDIUM

The incident plane wave has only field components perpendicular to the direction of propagation. In contrast, the evanescent field has components along all directions x , y , and z of a Cartesian coordinate system attached to the IRE, as shown in Fig. 2. The direction of the incident field vector can be selected by use of a polarizer. The symbols \parallel and \perp denote electric field vectors parallel and perpendicular to the

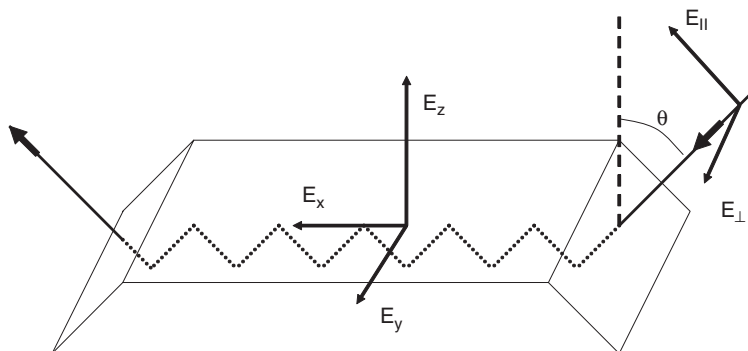


FIG. 2. ATR equipment: θ is the angle of incidence. E_{\parallel} (parallel) and E_{\perp} (perpendicular) denote the direction of the electric field components of the incident light with respect to the plane of incidence ((x, z) plane). E_x , E_y , and E_z denote the electric field components with respect to a coordinate system fixed on the IRE.

plane of incidence (Fig. 2). A parallel polarized electric field E_{\parallel} results in field components E_x and E_z along the x - and z -axis. A perpendicular-polarized incident electric field E_{\perp} results in a y component E_y of the evanescent field. The relative electric field components in medium 2 at the phase boundary $z = 0$ (i.e., the ratio between the absolute field components in medium 2 at $z = 0$ and medium 1) are given by Fresnel's equations (13).

$$E_{0x2}^r = \frac{E_{0x2}}{E_{1\parallel}} = \frac{2 \cos(\theta) (\sin^2(\theta) - n_{21}^2)^{1/2}}{(1 - n_{21}^2)^{1/2} ((1 + n_{21}^2) \sin^2(\theta) - n_{21}^2)^{1/2}}, \quad (4)$$

$$E_{0z2}^r = \frac{E_{0z2}}{E_{1\parallel}} = \frac{2 \sin(\theta) \cos(\theta)}{(1 - n_{21}^2)^{1/2} ((1 + n_{21}^2) \sin^2(\theta) - n_{21}^2)^{1/2}}, \quad (5)$$

$$E_{0y2}^r = \frac{E_{0y2}}{E_{1\perp}} = \frac{2 \cos(\theta)}{(1 - n_{21}^2)^{1/2}}, \quad (6)$$

$$E_{02\parallel}^r = \left(E_{0x2}^r{}^2 + E_{0z2}^r{}^2 \right)^{1/2}, \quad (7)$$

$$E_{02\perp}^r = E_{0y2}^r. \quad (8)$$

The above equations are exact only for non-absorbing rare media, but are very good approximations for weakly absorbing samples. Note that E_{0x2}^r , E_{0y2}^r , and E_{0z2}^r are in general not equal!

Equations (4)–(6) hold for a bulk (non- or weakly absorbing) rare medium 2 (case (a) in Fig. 3). In the case of a thin film with thickness $d \ll d_p$ in contact with the IRE (case (b) in Fig. 3), the thin-layer approximation gives good results (5). Here it is assumed that the electric field is determined by the IRE and the bulk medium above the thin film. The thin film is then considered as a dielectric in this field, and equations similar to Eqs. (4)–(6) can be derived.

Equations (7) and (8) have to be used to calculate the effective thickness (for a bulk medium 2), according to the following:

$$d_e = \frac{n_{21} E_{02}^r d_p}{2 \cos \theta}, \quad (9)$$

where the relative electric field in the sample E_{02}^r stands for either parallel-polarized $E_{02\parallel}^r$ or perpendicular-polarized $E_{02\perp}^r$ incident light according to Eqs. (7) and (8). The effective thickness of an isotropic sample for the two polarizations differ by the factor

$$\frac{d_{e\parallel}}{d_{e\perp}} = \frac{A_{\parallel}}{A_{\perp}} = \frac{E_{0x}^r{}^2 + E_{0z}^r{}^2}{E_{0y}^r{}^2}, \quad (10)$$

which is called the dichroic ratio. This ratio is experimentally accessible by measuring the absorbance A of a vibrational band for the two polarizations of the incident light

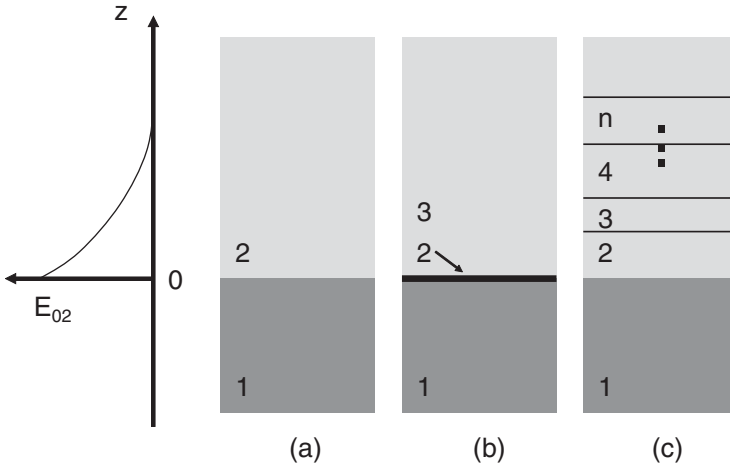


FIG. 3. Various situations encountered in ATR spectroscopy. Medium 1 represents the IRE. (a) Bulk rare (optically thin) medium 2. (b) Thin film with thickness d much less than the penetration depth d_p . (c) General case with N layers of different optical properties and thickness. The electric field depicted schematically on the left decays exponentially into the rare medium. This situation applies for case (a). In the more general case (c), the electric field does not decay smoothly.

beam. The dichroic ratio is 2.0 for an isotropic bulk medium at an angle of incidence θ of 45° . Note that in a transmission experiment this quantity is unity for isotropic media. Equation (10) forms the basis for orientation measurements in oriented samples (9,14).

C. SIMULATION OF SPECTRA OF STRATIFIED MEDIA

For the more general case (c) in Fig. 3 a formalism has been developed. The overall reflectance of plane-polarized light of a system of N parallel, optically isotropic layers can be calculated from Maxwell's equations by considering the continuity requirements for the electric and magnetic field vectors at the phase boundaries. The matrix method developed by Abelès and Hansen (15,16) allows calculation of the overall reflectance of any combination of absorbing and non-absorbing isotropic layers at any angle of incidence. Although the derived equations do not readily make clear the underlying physics, they facilitate numerical calculations. In this way, plots of the reflectance versus various parameters can be used to clarify unknown optical behavior. The method has been described in (16–18).

The calculations assume semi-infinite first and last layers and a non-absorbing first layer. The complex refractive index of the j th layer is given by the following:

$$\tilde{n}_j = n_j + ik_j, \tag{11}$$

where n_j is the refractive index and k_j the extinction coefficient. For a general system containing N phases, there are $N-1$ surfaces of discontinuities at z_j ($j = 1, 2, \dots, N-1$).

For each layer $z_{j-1} < z < z_j$ and for the semi-infinite space $z > z_{N-1}$ there is a characteristic matrix \mathbf{M} . The latter can be used to relate the tangential fields at the first phase boundary at $z = z_1 = 0$ to those at the final phase boundary at $z = z_{N-1}$ by use of the following equation:

$$\begin{pmatrix} U_1 \\ V_1 \end{pmatrix} = M_2, M_3, \dots, M_{N-1} \begin{pmatrix} U_{N-1} \\ V_{N-1} \end{pmatrix}, \quad (12)$$

where U_j and V_j represent the tangential components of the field amplitudes at boundary j . The characteristic matrices of the j th layer for parallel and perpendicular-polarized light are as follows:

$$M_{j(\parallel)} = \begin{pmatrix} \cos \beta_j & \frac{-i}{q_j} \sin \beta_j \\ -iq_j \sin \beta_j & \cos \beta_j \end{pmatrix}, \quad (13)$$

$$M_{j(\perp)} = \begin{pmatrix} \cos \beta_j & \frac{-i}{p_j} \sin \beta_j \\ -ip_j \sin \beta_j & \cos \beta_j \end{pmatrix}. \quad (14)$$

With the definition of an angle-dependent refractive index term ζ_j is as follows:

$$\zeta_j = \tilde{n}_j \cos \theta_j = \left(\tilde{n}_j^2 - n_1^2 \sin^2 \theta_1 \right)^{1/2}, \quad (15)$$

one can write the following:

$$p_j = \zeta_j, \quad (16)$$

$$q_j = \frac{\zeta_j}{\tilde{n}_j^2}, \quad (17)$$

$$\beta_j = 2\pi \left(\frac{d_j}{\lambda} \right) \zeta_j, \quad (18)$$

where d_j is the thickness of the j th layer and λ is the wavelength.

The characteristic matrix \mathbf{M} for the whole system is simply obtained by multiplication of the characteristic matrices for the individual layers:

$$\mathbf{M} = M_2, M_3, \dots, M_{N-1}. \quad (19)$$

The Fresnel reflection coefficients r for the overall system can be obtained from the elements m of the characteristic matrix \mathbf{M} associated with the overall system:

$$r_{\parallel} = \frac{(m_{11} + m_{12}q_N)q_1 - (m_{21} + m_{22}q_N)}{(m_{11} + m_{12}q_N)q_1 + (m_{21} + m_{22}q_N)}, \quad (20)$$

$$r_{\perp} = \frac{(m_{11} + m_{12}p_N)p_1 - (m_{21} + m_{22}p_N)}{(m_{11} + m_{12}p_N)p_1 + (m_{21} + m_{22}p_N)}. \quad (21)$$

The overall reflectance R for parallel- and perpendicular-polarized light can be calculated from the Fresnel reflection coefficient:

$$\begin{aligned} R_{\parallel} &= |r_{\parallel}|^2 = R_{\parallel}(n_1, \tilde{n}_2, d_2, \dots, \tilde{n}_{p-1}, d_{p-1}, \tilde{n}_p, \tilde{\nu}, \theta_1), \\ R_{\perp} &= |r_{\perp}|^2 = R_{\perp}(n_1, \tilde{n}_2, d_2, \dots, \tilde{n}_{p-1}, d_{p-1}, \tilde{n}_p, \tilde{\nu}, \theta_1). \end{aligned} \quad (22)$$

The overall reflectance is a function of the complex refractive indices \tilde{n} and thicknesses d of the layers as well as the wavenumber of the light and the angle of incidence θ_1 .

ATR spectra of stratified isotropic media can be calculated by use of the above formalism (18). This formalism has also been generalized for anisotropic layers (19), which makes it possible to carry out simulations of uniaxial layers ($\tilde{n}_x = \tilde{n}_y \neq \tilde{n}_z$) and biaxial layers ($\tilde{n}_x \neq \tilde{n}_y \neq \tilde{n}_z$).

III. ATR Spectroscopy for *In situ* Investigations in Catalysis

Attenuated total reflection IR spectroscopy can be used to investigate model as well as powder catalysts.

A. THIN METAL FILMS

Model catalysts have to be prepared directly on the IRE, which can be a challenging task. Thin metal films are an important type of model catalyst and can be made, for example, by physical vapor deposition or sputtering of the metal onto the IRE. Most suitable IRE materials for such applications are Ge and Si. The former has a high refractive index of 4.0, which results in a small penetration depth and therefore good discrimination against bulk solvent. The metal film should not be too thick, so that the evanescent field can reach the outer interface of the metal film.

Figure 4 shows the reflectance for a system Ge/Pt/vacuum as a function of the thickness d of the platinum film. The plot was calculated by using the formalism described above (Eqs. (11)–(22)) for an angle of incidence θ of 45° , assuming an isotropic platinum layer with bulk optical constants. For $d = 0$, the reflectivity is unity. For increasing platinum layer thicknesses d , the reflectance first decreases (platinum and metals in general are strong IR absorbers). However, at some thickness the curve has a minimum. In this regime, the film starts to act as a mirror, and eventually the evanescent field no longer reaches the outer surface of the metal film.

This situation is obviously useless for spectroscopy. Hence, valuable films are very thin, on the order of few nanometers, depending on the material. Figure 4 shows that even for a thin metal film the overall reflectivity of the system can be severely reduced. This characteristic is even more important for multiple reflection elements, for which the total reflectivity R_{tot} is the reflectivity for a single reflection R to the power of the number of reflections N : $R_{\text{tot}} = R^N$. For a reflectivity R of 90% (90% of the incident intensity is reflected), only 35% of the incident intensity will reach the detector after 10 reflections ($N = 10$). The smaller the reflectivity R_{tot} , the smaller is the signal at the detector and the larger the noise. On the other hand, the intensity of an absorption

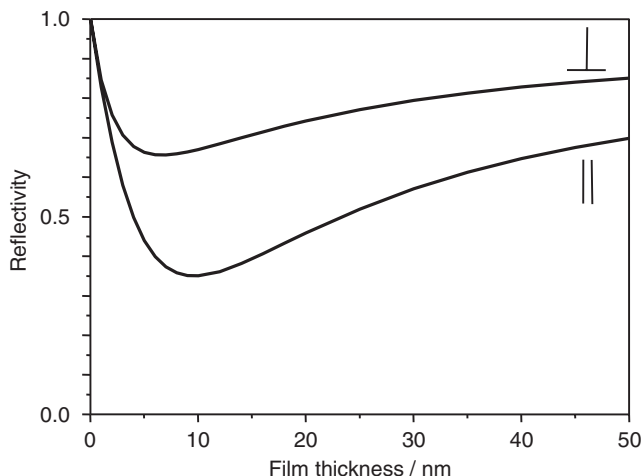


FIG. 4. Reflectivity of parallel- and perpendicular-polarized light at 1600 cm^{-1} for the system Ge/Pt/vacuum determined for platinum films of various thicknesses. In the calculations, the optical constants of bulk platinum were used: $n_{\text{Ge}} = 4.0$, $\tilde{n}_{\text{Pt}} = 5.71 + i23.35$. The angle of incidence was 45° . Calculations were performed according to the matrix formalism described in the text.

band will of course increase with the number of reflections. For weak absorption bands, the absorbance increases as $A_{\text{tot}} = A_{\text{single reflection}} \times N$. Hence, the optimal signal-to-noise ratio depends on the number of reflections and makes the latter an important parameter for the design of suitable experimental equipment.

It becomes clear from the above discussion that metal catalyst films suitable for ATR spectroscopy must be very thin. Such films are generally not homogeneous. In many cases physical vapor deposition leads to films composed of metal islands. The morphology depends on the substrate (IRE), the metal, and preparation conditions such as evaporation rate, substrate temperature, and background gas.

Figure 5 shows an STM image of a platinum film evaporated on a Ge IRE. The metal particles or islands have a diameter of about 6 nm. Au, Ag, and Cu tend to form larger islands than platinum. Metal films consisting of islands have an important property for ATR spectroscopy; absorption signals of molecules in contact with the metal film can be considerably enhanced relative to the absorption signals in the absence of the metal film. This... phenomenon is sometimes called surface-enhanced IR absorption (SEIRA) (20). Within the metal film, the electric field is enhanced, leading to an enhanced IR absorption for molecules in close contact with the film, similar to the enhancement found for Raman scattering from rough metal surfaces. The enhancement depends strongly on the morphology of the film (i.e., the size and shape of the metal particles and the interparticle distance) (21,22) and is restricted to molecules very near the metal film (23). Enhancement factors of up to 1000 have been reported for Au films (24). Enhancement is also found for platinum films (25,26), although considerably smaller factors are usually found for this metal. SEIRA has been applied successfully for spectroelectrochemical applications, whereby the thin metal film directly serves as the working electrode (27–34).

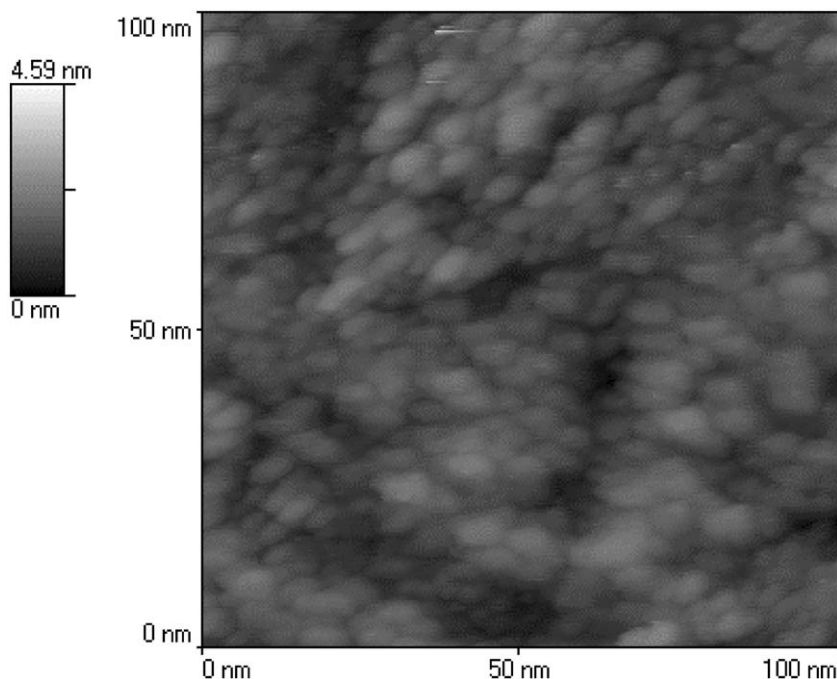


FIG. 5. STM image (100×100 nm) of a 1-nm-thick platinum film electron beam evaporated onto Ge. Evaporation conditions: pressure, 1.5×10^{-5} mbar; room temperature; 0.5 \AA/s evaporation rate (26).

The system IRE/metal/adsorbate/solvent, one example of case (c) in Fig. 3, has interesting optical properties relevant to ATR spectroscopy of thin metal films (18). Depending on the thickness and the optical constants of the thin metal film, the spectrum of the adsorbate can change drastically. Simulations show that strongly distorted lines are expected for strong absorbers even far away from the critical angle. (Distorted line shapes can occur near the critical angle in the absence of a metal (5).) Figure 6 shows the line shape calculated for a thin adsorbate film on a 20-nm-thick metal film as a function of the optical constants of the metal film. The optical constants characterizing the adsorbate film were calculated from a damped harmonic oscillator model.

$$\tilde{\epsilon}(\tilde{\nu}) = \tilde{n}_3(\tilde{\nu})^2 = n_e^2(\tilde{\nu}) + \frac{B}{\tilde{\nu}_0^2 - \tilde{\nu}^2 - i\gamma\tilde{\nu}}. \quad (23)$$

In the above equation, $\tilde{\nu}$ (cm^{-1}) is the wavenumber, $\tilde{\nu}_0$ (cm^{-1}) the wavenumber of the absorption band center, γ (cm^{-1}) the damping constant (which gives the band width), B (cm^{-2}) determines the intensity of the band, and n_e the refractive index far away from resonance. The properties of the adsorbate film are those of CO on platinum. For the middle spectrum, the complex refractive index ($\tilde{n} = 5 + 20i$) is close to that of platinum at 2000 cm^{-1} ; n and k were varied between 2.5 and 10 and between 10 and 40, respectively, in view of the fact that n and k vary drastically over the mid-IR region and from metal to metal (35).

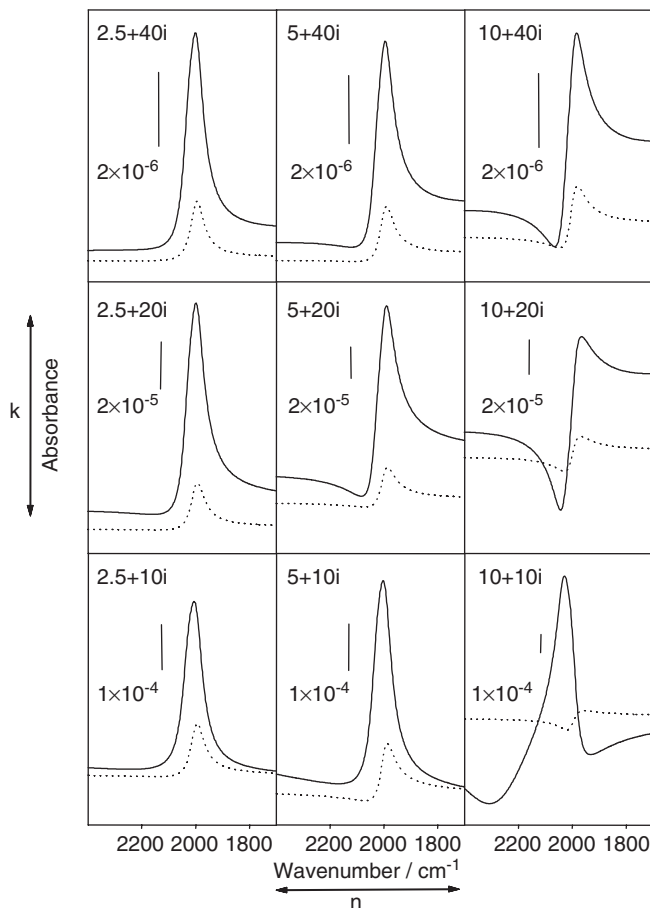


FIG. 6. Calculated ATR spectra (angle of incidence 45°) for a monolayer adsorbate (thickness $d_3 = 3 \text{ \AA}$) on a 20-nm-thick metal film in contact with a solvent as a function of the complex refractive index \tilde{n}_2 of the metal film. Solid line: parallel polarized light; dotted line: perpendicular-polarized light. The appropriate complex refractive index \tilde{n}_2 is given at the top of each spectrum. The vertical bars indicate the scale for the absorbance, which is different for each spectrum. Parameters: $n_1 = 4.01$ (Ge), $n_4 = 1.4$ (organic solvent), $d_3 = 3 \text{ \AA}$, $n_c = 1.6$, $B = 280\,000 \text{ cm}^{-2}$, $\nu_0 = 2000 \text{ cm}^{-1}$, $\gamma = 60 \text{ cm}^{-1}$. The parameters correspond to adsorbed CO. The calculations were performed by using the formalism proposed by Hansen (16), and the results are given in terms of absorbance $A = -\log_{10}(R/R_0)$, where R is the reflectivity of the system Ge/Pt/adsorbate/solvent and R_0 is the reflectivity of the system Ge/Pt/solvent (18).

The values of both n and k of the metal film have an influence on the line shape of the adsorbate. With the middle spectrum as the reference, Fig. 6 shows that increasing n leads to a more distorted line shape, whereas increasing k leads to a less distorted line shape. Increasing k (use of a more absorbing metal) also leads to a decreased absorbance. Without a metallic film, the absorption band is symmetric (not shown). Dispersive line shapes such as shown in Fig. 6 were also observed experimentally for CO on platinum films (26).

Although the reflectivity calculations using the formalism outlined above give results in qualitative agreement with ATR experiments, a quantitative description is in many cases restricted by the limited knowledge of the effective optical constants of the thin metal film. The latter differ significantly from (known) bulk values below about 10-nm thickness as a consequence of the island morphology of the film. For thicker films (10 nm), spectral simulations assuming bulk optical constants for the platinum film were found to be in excellent agreement with experiment (18).

Reproducibility of film preparation and stability of the resulting films are important issues for practical applications. Cleanliness of the IRE before metal deposition can play a decisive role in determining reproducibility. Depending on the conditions, metal films may not be stable and may peel off (36,37). The stability and reproducibility of metal films can be enhanced by evaporating a metal oxide support material (such as Al_2O_3) prior to evaporation of the desired metal. Contaminants on the IRE are covered or displaced by evaporation of the metal oxide. It was reported that a 50–100-nm-thick Al_2O_3 layer deposited on a Ge IRE by electron beam physical vapor deposition hardly affected the reflectivity in an ATR experiment. Thin platinum films directly deposited onto it were found to be rather stable under catalytic reaction conditions (26,38).

When using metal films as model catalysts in a conducting fluid, one should bear in mind that an electrode is formed. When using a metal cell, such as a steel cell, unwanted electrochemical processes may occur, induced by the potential difference between the steel surface (which also acts as an electrode) and the metal film.

Thin metal films have been used as model catalysts not only in electrocatalysis (27–34) but also to study enantioselective hydrogenation catalyzed by supported platinum and palladium catalysts modified by adsorbed chiral compounds (39–44).

B. POWDER CATALYSTS

Investigation of high-area powder catalysts requires that they be immobilized on the IRE. Several methods can be used to accomplish this task. For some materials, stable catalyst films can be prepared by dropping a slurry of the catalyst onto the IRE followed by drying. The procedure can be applied several times in order to attain the desired thickness of the film. The stability of such films in the presence of a flowing solvent depends on the catalyst, and also on the IRE material, preparation conditions, and solvent. For the investigation of powder catalysts, ZnSe IREs have advantages relative to Ge IREs because of their larger penetration depth, as a consequence of the smaller refractive index of ZnSe (2.4 for ZnSe and 4.0 for Ge). These values lead to stronger signals when ZnSe IREs are used. Stable catalyst films on ZnSe and Ge IREs were reported for catalysts supported on Al_2O_3 (45–47) and TiO_2 (48,49), for Ti–Si mixed oxide aerogel catalysts (50,51), and some materials such as modified silica (52–54), chromium oxide hydroxide (55,56), zirconium oxide, and tantalum oxide (57,58). Such films are not mechanically stable and can easily be wiped off the IRE. Still, they were found to be stable for many hours in a flow-through cell. Removal of the films from the volume probed by the evanescent fields during ATR experiments would result in the disappearance of the corresponding catalyst signals. The amount of catalyst used for such experiments is

typically very small. For an area of about 3 cm^2 of covered IRE, a catalyst mass of 1–10 mg is typical.

Depending on interfacial properties, some catalyst powder films are not stable in flowing solvent. For example, SiO_2 -containing materials have been reported to stick badly to the IRE in flowing solvent (59). In such a situation, the catalyst particles may be fixed to the IRE by addition of a small amount of a polymer such as polyethylene before contacting of the slurry with the IRE (59,60). Films can also be prepared by dip- and spin coating.

Quantitative simulation of spectra as outlined above is complicated for particle films. The material within the volume probed by the evanescent field is heterogeneous, composed of solvent entrapped in the void space, support material, and active catalyst, for example a metal. If the particles involved are considerably smaller than the penetration depth of the IR radiation, the radiation probes an “effective medium.” Still, in such a situation the formalism outlined above can be applied. The challenge is associated with the determination of the effective optical constants of the composite layer. Effective medium theories have been developed, such as Maxwell-Garnett (61), Bruggeman (62), and other effective medium theories (63), which predict the optical constants of a composite layer. Such theories were applied to metal-particle thin films on IREs to predict enhanced IR absorption within such films. The results were in qualitative agreement with experiment (30). However, quantitative results of these theories depend not only on the bulk optical constants of the materials (which in most cases are known precisely), but also critically on the size and shape (aspect ratio) of the metal particles and the distance between them. Accurate information of this kind is seldom available for powder catalysts.

An important issue to consider when probing powders with ATR spectroscopy is the match between particle size and penetration depth of the evanescent wave, as outlined schematically in Fig. 7. For large particles (Fig. 7, case (a)), only the part closest to the IRE is probed by the evanescent field. For large spherical particles, the overlap between the particle and the evanescent field is reduced for geometrical reasons. As shown by Fig. 7(a), the point of contact (the point of highest density) of

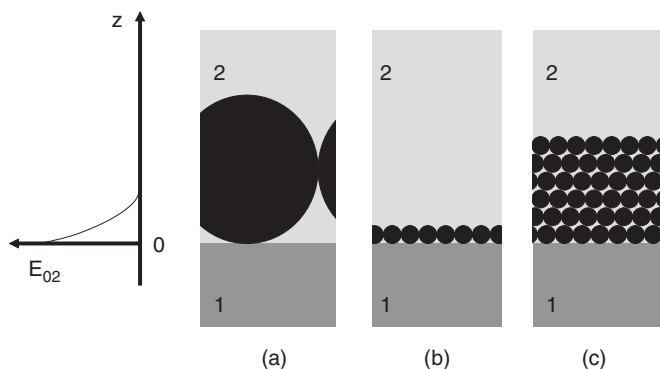


FIG. 7. Matching of penetration depth d_p and particle size of the catalyst. (a) Particle diameter of catalyst is larger than penetration depth d_p . (b) Particle diameter is smaller than d_p . (c) Thick film of particles with small diameters.

the particles is out of reach for the evanescent field, whereas the evanescent field probes a large part of the void volume (solvent).

The fraction of the volume not occupied by the catalyst particle (void fraction) determines how much bulk fluid will be probed by the evanescent field. For a film consisting of a 5-wt% Pt/Al₂O₃ catalyst, this fraction was estimated (47). The support particles had a mean diameter of 37 nm. The film was prepared by spreading a suspension of the catalyst onto a Ge IRE. Figure 8 shows the relative absorbance of ethanol at 2974 cm⁻¹ as a function of the number of coatings. The reference is the signal without a coating. The absorbance decreases up to three coatings and is approximately constant for more than three coatings. After six coatings had been applied, the thickness of the film was measured by optical microscopy to be 10 ± 2 μm. For this system, a penetration depth d_p of about 0.2 μm was calculated for a wavelength of 2974 cm⁻¹. This result means that even after one coating, the film thickness should be large enough to minimize the signal from the liquid. The observation that the ethanol signal decreased until three coatings had been applied was explained by an increased packing density of the film closest to the IRE.

From the limiting value of 55% of the ethanol signal without coating, a void fraction can be estimated. However, this number does not directly correspond to the void fraction. One has to consider the fact that the effective thickness d_e is affected by the presence of the catalyst. Equation (3) shows that the influence is

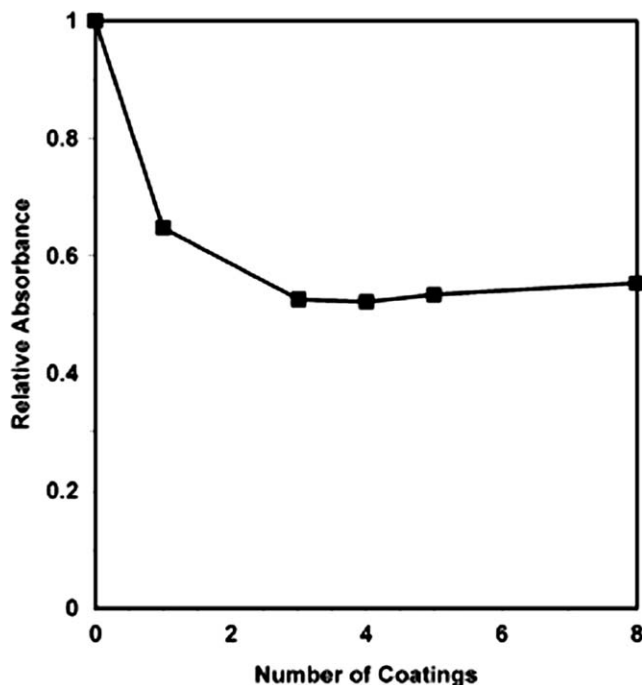


FIG. 8. Dependence of the 2974-cm⁻¹ band of liquid ethanol on the number of catalyst coatings on an IRE. Intensities were normalized with respect to the ethanol signal measured on the uncoated Ge IRE (47).

through a change of the relative refractive index n_{21} and through the electric field amplitude E_0 (Eqs. (4)–(6)). Considering these factors (Ge IRE and large angle of incidence of 60°), it was found that the intensity of the ethanol signal as shown in Fig. 8 overestimates the void fraction by 5–10%. The estimate of the void fraction could therefore be taken to be about 50%. Of course the void fraction depends on particle size distribution and particle shape. For uniform particles and ideal packing, the void fraction is 0.26 for a face-centered cubic packing geometry, 0.32 for a body-centered cubic packing, and 0.48 for a simple cubic packing (47).

The size of the particles is also critical if gradients exist within the particles, caused, for example, by diffusion limitations. An interesting case is a fast reaction on a porous film or a film of porous particles. In such a situation, concentration gradients may exist within the film or particles (64). An example of such a reaction is alcohol oxidation. The concentration gradient of oxygen has important consequences, because the activity of the catalyst in alcohol oxidation critically depends on the oxygen concentration at the surface, as discussed below. The gradients depend on the diffusion and reaction rates. At the outer surface of the film (away from the IRE), the concentration of the reactant and rate of the catalytic reaction are high, but these decrease within the film, closer to the IRE. Of course in such a situation the thickness of the film with respect to the penetration depth is important.

Compared to transmission IR techniques, according to which the signal is averaged over concentration gradients, only the region closest to the IRE is probed in the ATR experiment. These situations are represented schematically in Fig. 9. The investigation of systems accounting for the concentration gradients could be an interesting application of the ATR method. However, such an investigation would require adequate modeling of the mass transport and chemical reaction (65). ATR

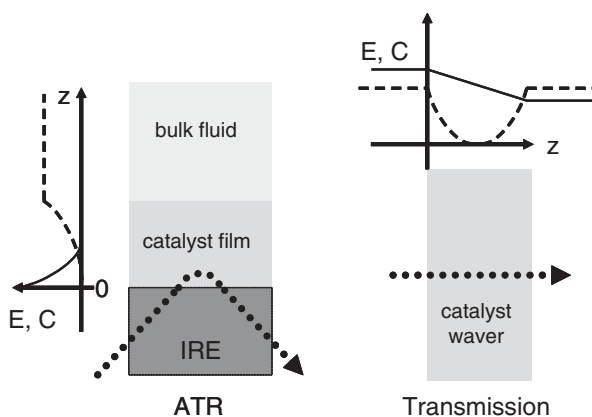


FIG. 9. Electric field E and concentration C of a reactant for a fast reaction catalyzed by a porous solid for transmission and ATR geometries. The dotted line represents the IR beam path. The electric field E is represented as a solid line, and the concentration C of a hypothetical reactant is represented as a dashed line. In the ATR experiment, the electric field is evanescent and decays exponentially with distance z from the surface of the IRE. In the transmission experiment, the electric field decreases as a consequence of absorption. The two techniques sample the catalyst differently.

has already been applied to characterize diffusion in the liquid phase (65) and in porous materials (50,66–68).

IV. Cell Design

A variety of cell designs for internal reflection or attenuated total reflection spectroscopy have been reported, demonstrating the flexibility of the technique. In the following, we describe only a few examples in some detail.

A. ON-LINE PROCESS CONTROL AND REACTION MONITORING

Internal reflection spectroscopy is widely applied for on-line process control. In this type of application, the chemical reactor is equipped with an internal reflection probe or an IRE. The goal of this type of application is the quantification of reactant and/or product concentrations to provide real-time information about the conversion within the reactor. In comparison with other analytical methods such as gas chromatography, high-pressure liquid chromatography, mass spectrometry, and NMR spectroscopy, ATR spectroscopy is considerably faster and does not require withdrawal of sample, which can be detrimental for monitoring of labile compounds and for some other applications.

For example, a high yield of an intermediate in a consecutive reaction depends sensitively on the instant in time when the reaction is quenched. For such applications, the fast response of the ATR method more than compensates for deficiencies related to sensitivity when the ATR technique is compared with other methods. The design of the equipment depends on the specific requirements of the application.

Similar equipment for applications on the laboratory scale has been reported (and has recently been commercialized) (69–72). Most of the reported applications had the aim of investigating kinetics of chemical reactions as indicated by changes in liquid-phase concentrations. The equipment can typically be used at elevated temperatures and pressures. Applications to heterogeneous catalytic reactions include investigations of the enantioselective hydrogenation of exocyclic α,β -unsaturated ketones catalyzed by Pd/C in the presence of (*S*)-proline (73) and the esterification of hexanoic acid with octanol catalyzed by a solid acid (the resin Nafion on silica) (74).

The latter reaction was performed at temperatures in the range of 427–447 K at atmospheric pressure in the presence of cumene or *n*-decane. Figure 10 shows the experimental set-up of the open reflux batch reactor with the IR probe. Because the reactants (acid and alcohol) and products (ester) have distinctly different IR spectra, their concentration profiles within the reactor can be followed conveniently. Figure 11 depicts the concentration profiles for ester formation and acid conversion as determined by ATR spectroscopy, including a comparison of them with the profiles determined *ex situ* by GC analysis. Very good agreement is apparent. Both the acid and the ester concentrations were quantified through their C = O stretching vibrations at 1720 and 1745 cm^{-1} , respectively. These vibrations are both

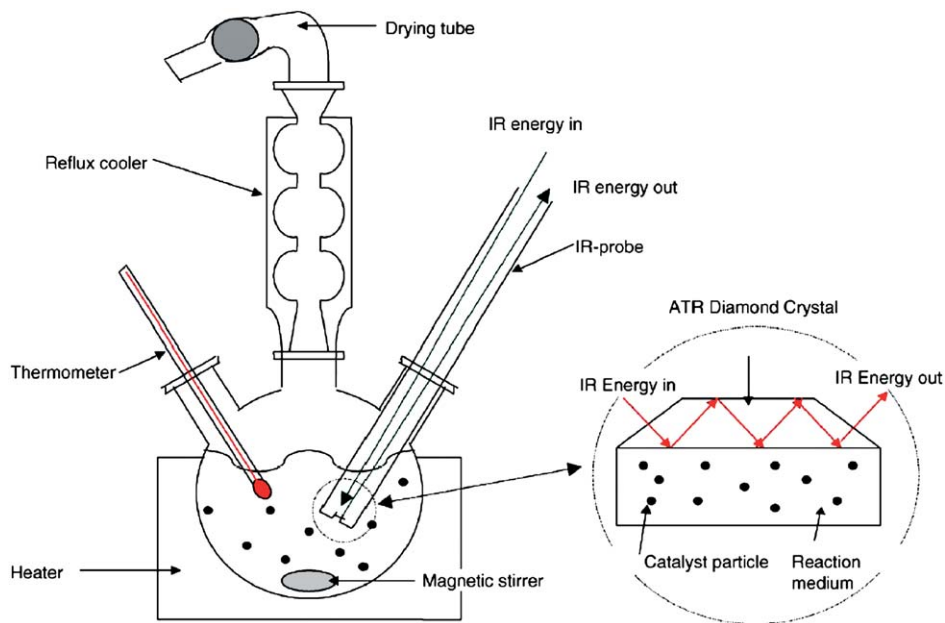


FIG. 10. ATR equipment for on-line monitoring of catalytic reactions in a reflux reactor (74).

associated with relatively large transition dipole moments, resulting in strong signals, which simplify the analysis. The ATR spectra were recorded with a six-reflection diamond composite ATR probe, and the absorbance signals characterizing the C = O vibrations were of the order of 5% for 0.4 molar concentration of the dissolved reactants and products. This procedure allows estimation of the detection limit of the ATR method for reaction monitoring using the described approach: Assuming a signal detection limit of 0.0001 absorbance units (0.01%), one would arrive at a detection limit for the described procedure (six internal reflections with a diamond probe) of $(0.4 \text{ mol/L} \times 0.01\%) / 5\% = 0.0008 \text{ mol/L}$.

Thus, concentrations of about 1 mM can be detected. Of course the detection limit is worse for more weakly absorbing analytes. The above estimate of the detection is based on the assumption of a signal detection limit of 0.0001 absorbance units. This value depends prominently on the design of the optical equipment (IR spectrometer, energy throughput, source, detector, and stability) and the number of scans that are averaged for one spectrum. The latter also determines the achievable time resolution. In the application described above, one spectrum was recorded every two minutes. The noise evident in the curves shown in Fig. 11 at longer reaction times is less than 0.01 mol/L. Pintar and co-workers (73) reported a detection limit of 0.2 mmol/L for α,β -unsaturated ketones using similar equipment.

The combination of an ATR probe and a slurry reactor depicted in Fig. 10 yields IR spectra of the fluid containing dissolved reactants and products. However, if catalyst particles are found within the volume probed by the evanescent field, the catalyst itself and molecules adsorbed on it may be monitored as well. Indeed,

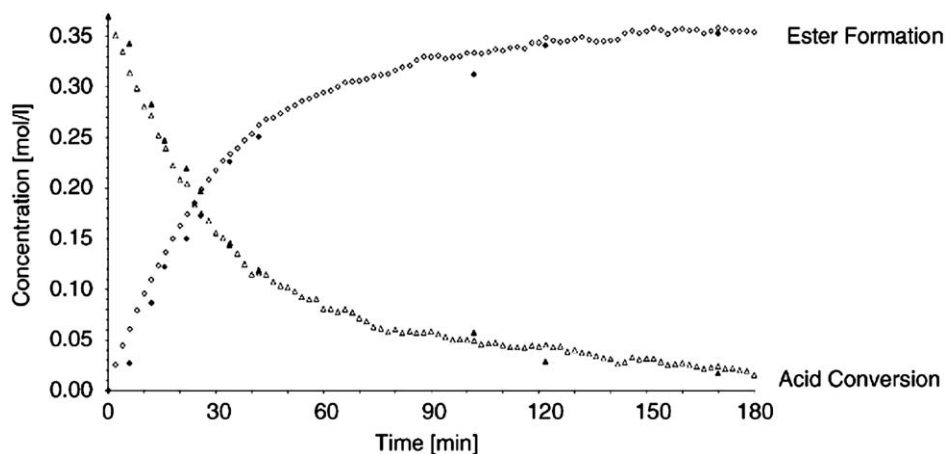


FIG. 11. Concentration profiles as measured with the equipment depicted in Fig. 10 (open symbols) and by GC analysis (closed symbols) for an esterification reaction between octanol and hexanoic acid. Conditions: 200 mL of reactant, 0.4 mol/L of octanol, 0.4 mol/L of hexanoic acid, 1.0 g Nafion[®] resin/silica, 447 K. The profiles were constructed from signals at 1720 and 1745 cm^{-1} , and the spectra were corrected for solvent, octanol, and catalyst (74).

Mul *et al.* (74) observed a band at approximately 1100 cm^{-1} in the esterification of hexanoic acid with octanol catalyzed by Nafion on silica, which was not associated with solvent, reactants, or products. It was shown that this band resulted from the reaction of silica with octanol, yielding Si–O–R groups. Whether the signal was a consequence of leaching of silica into the solution or the silica particles itself could not yet be determined conclusively, although the strength of the signal supports the latter possibility.

This latter interpretation would mean that with the approach depicted in Fig. 10, the catalyst itself could be monitored. The authors reported that the silica-supported Nafion could not be observed in the beginning of their experiments and appeared in the spectra only after the catalyst interacted with octanol. This observation may indicate that the octyl groups promote the sticking of the catalyst particles onto the ATR probe, within the evanescent field. However, the example also shows that this approach may not be without problems, because it depends on the adsorption of the particles from the slurry reactor onto the ATR element. This process is accompanied by the adsorption of molecules on the catalyst surface and complicates the analysis. More important, as also indicated by the work of Mul *et al.* (74), this adsorption depends on the surface properties of the catalyst particles and the ATR element. These properties are prone to change as a function of conversion in a batch process and are therefore hardly predictable.

Significantly, for the enantioselective hydrogenation of α,β -unsaturated ketones catalyzed by Pd/C (occurring in a three-phase system), it was concluded that the measurement of dissolved species was unaffected by the presence and fouling of Pd/C catalyst particles or other solids in the suspension on the diamond ATR

sensor (73). Whether the approach depicted in Fig. 10 is well suited to the investigation of the solid catalyst in a slurry reactor will have to be determined in future investigations.

B. FLOW-THROUGH CELL

The equipment described in the preceding paragraphs was designed to follow reactions in batch reactors. ATR spectroscopy, however, is also well suited to continuous reactors. In this case, the IRE can be used as one wall of the reactor. Solid catalysts can be immobilized directly on the IRE, as described above. In this way the response of the catalytic system to changes of reactant concentration can be investigated, and such information has turned out to be a powerful tool for mechanistic investigations (45,48,49,75). This approach matches in an ideal way the power of modern Fourier transform IR (FTIR) spectrometers with their excellent time resolution. Furthermore, modern FTIR spectrometers are single-beam spectrometers and are therefore most sensitive to spectral *changes*.

An example of a flow-through cell is depicted in Fig. 12 (65). The upper part of the figure is a schematic representation of the experimental set-up. In the lower part, a photograph shows the cell, in which the IRE was replaced by a glass slide. The IRE is fixed between two steel parts (one is shown in Fig. 12). The gap between the polished steel cell and the IRE is about $265\ \mu\text{m}$ and defined by an O-ring fit into a precision electroeroded nut. The volume of the cell is only 0.077 mL, which allows a fast exchange of the fluid. The cell can be heated and cooled by attaching metal plates, which are kept at constant temperature by means of a thermostat. The whole cell is then fixed onto an optical device within the sample compartment in the FTIR spectrometer. The cell in Fig. 12 was specially designed for fast exchange of two fluids and has two inlet tubes that meet at a single inlet hole above the IRE. With this design, backmixing upstream of the cell can be minimized. In the design of a flow-through cell, care has to be taken to minimize regions where the fluid stagnates.

When fluid is pumped through a cell such as that shown in Fig. 12, transport of dissolved molecules from the cell inlet to the IRE by convection and diffusion is an important issue. The ATR method probes only the volume just above the IRE, which is well within the stagnant boundary layer where diffusion prevails. Figure 13 shows this situation schematically for a diffusion model and a convection–diffusion model (65). The former model assumes that a stagnant boundary layer exists above the IRE, within which mass transport occurs solely by diffusion and that there are no concentration gradients in the convection flow. A more realistic model of the flow-through cell accounts for both convection and diffusion. As a consequence of the relatively narrow gap between the cell walls, the convection leads to a laminar flow profile and consequently to concentration gradients between the cell walls.

Figure 14 shows a series of concentration profiles within an ATR flow-through cell as calculated by a convection–diffusion model that has been described elsewhere (65) for a small, rapidly diffusing molecule (acetonitrile) and a large, slowly diffusing molecule (hemoglobin). At time $t = 0$, the concentrations of the molecules at the inlet were switched from zero to non-zero values. The laminar flow profile is established due to relatively low flow rates (low Reynolds numbers), which is clearly

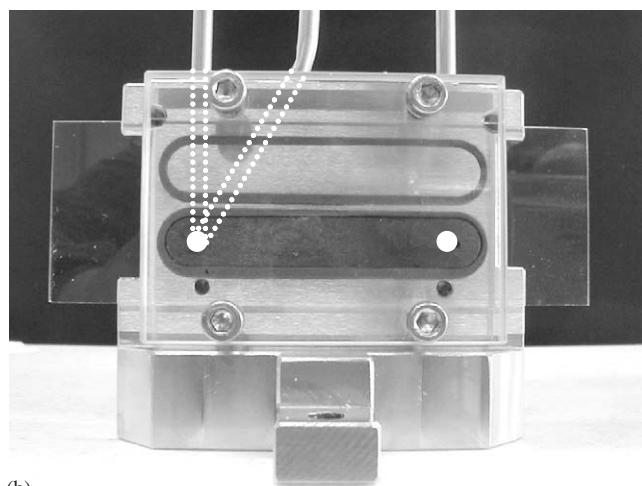
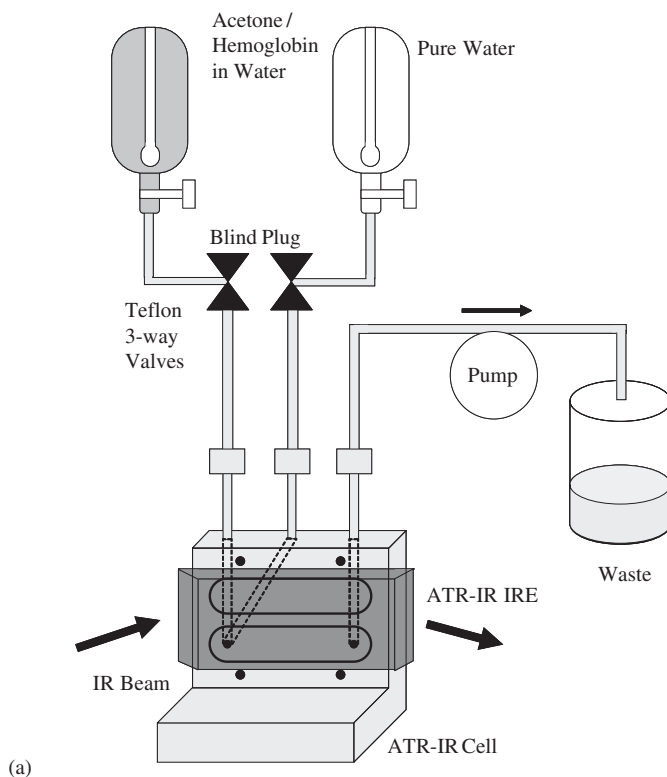


FIG. 12. (a) Schematic representation of equipment for an ATR experiment using a flow-through cell. (b) Picture of the cell with a glass slide instead of the IRE (65).

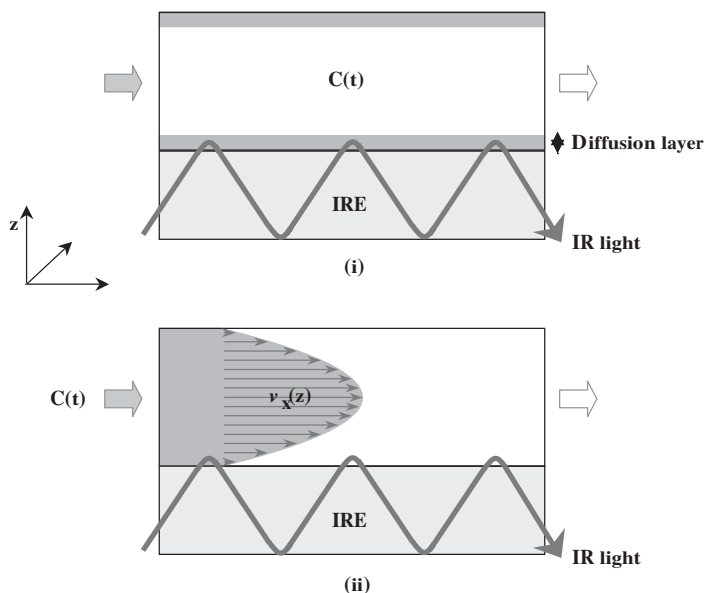


FIG. 13. Concentration profiles within an ATR flow-trough cell for a (i) diffusion layer model and (ii) convection–diffusion model (65). The models are described in the text.

visible, and it is apparent that the diffusion behavior of the two molecules is significantly different.

Figure 15 shows a comparison between the performance simulated (with the convection diffusion model) and that measured, in terms of absorption signals of acetonitrile and hemoglobin as a function of time. The measurements were performed with the cell depicted in Fig. 12 by switching back and forth between water and aqueous solutions containing both acetonitrile and hemoglobin. The experiment was performed for three different switching (modulation) frequencies. Both the simulation and the experimental results indicate a clear difference in the diffusion behavior of the two molecules. The good agreement between simulation and experiment shows that the convection–diffusion model describes the combined mass transport by convection and diffusion within the ATR cell well. The results also show that the fluid in the cell can be exchanged within a few seconds (about 3 s in the example) (and this time evidently depends on the flow rate).

The example furthermore shows that diffusion from the bulk fluid phase toward the volume near the IRE, which is probed by the evanescent field, has to be accounted for because it may be the limiting step when fast processes are investigated. The importance of diffusion is more pronounced when a catalyst layer is present on the IRE, because of the diffusion in the porous film is much slower than that in the stagnant liquid film. Indeed, the ATR method, because of the measurement geometry, is ideally suited to characterization of diffusion within films (50,66–68). Figure 16 shows the time dependence of absorption signals associated with cyclohexene (top) and *t*-butyl hydroperoxide (TBHP, bottom). Solutions (with concentrations of 3 mmol/L) of the two molecules in cyclohexane and neat cyclohexane were alternately admitted once to

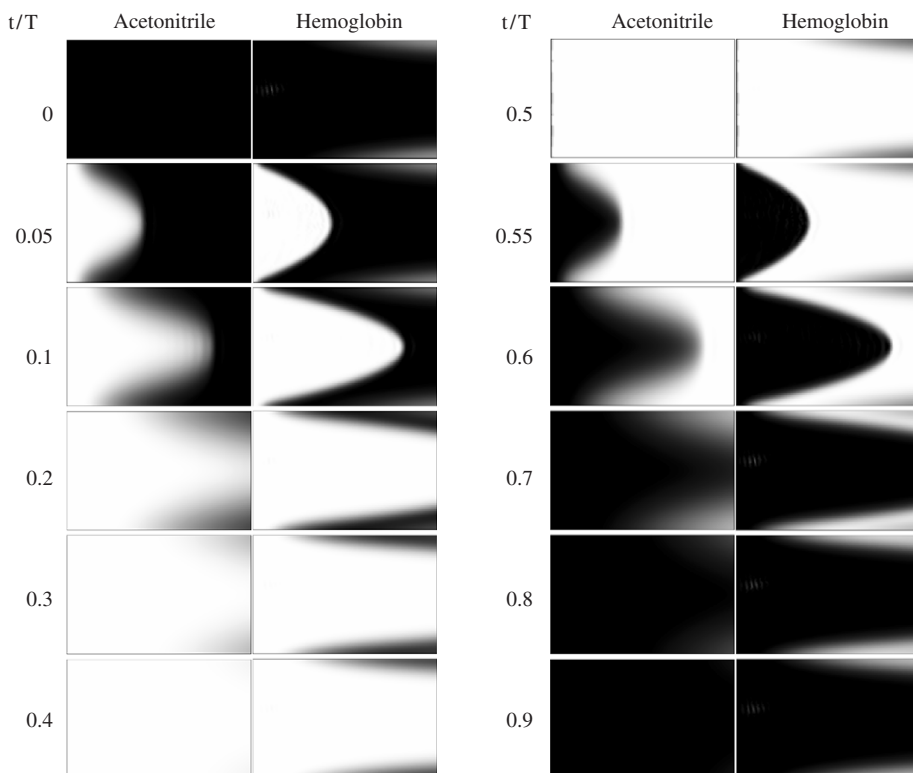


FIG. 14. Comparison of the convection–diffusion behavior of acetonitrile and hemoglobin within an ATR flow-through cell as calculated by the convection–diffusion model described in the text. The concentrations of the two molecules were periodically varied between zero and a non-zero value with a frequency of 67 mHz; the flow rate was 1.5 mL/min. Dark areas represent high concentrations of the solute molecules (65).

a clean ZnSe IRE and once to a ZnSe IRE coated with a modified Ti–Si mixed oxide aerogel catalyst (51). As a consequence of the slow diffusion of TBHP within the catalyst film, the time behavior of the ATR signals is significantly different in the presence and in the absence of the porous film.

C. HIGH-PRESSURE VIEW CELL

The last ATR cell described here in detail was designed for the study of catalytic reactions at high pressures and in particular in supercritical fluids. A schematic representation of the design is shown in Fig. 17 (76). An important issue in this type of reaction is the phase behavior of the system, which can have a large influence on the catalytic reaction (77,78). The cell consists of a horizontal stainless-steel cylinder. It is designed to allow monitoring of the phase behavior via a video camera. For this purpose, one end of the cylinder is sealed with a sapphire window, behind

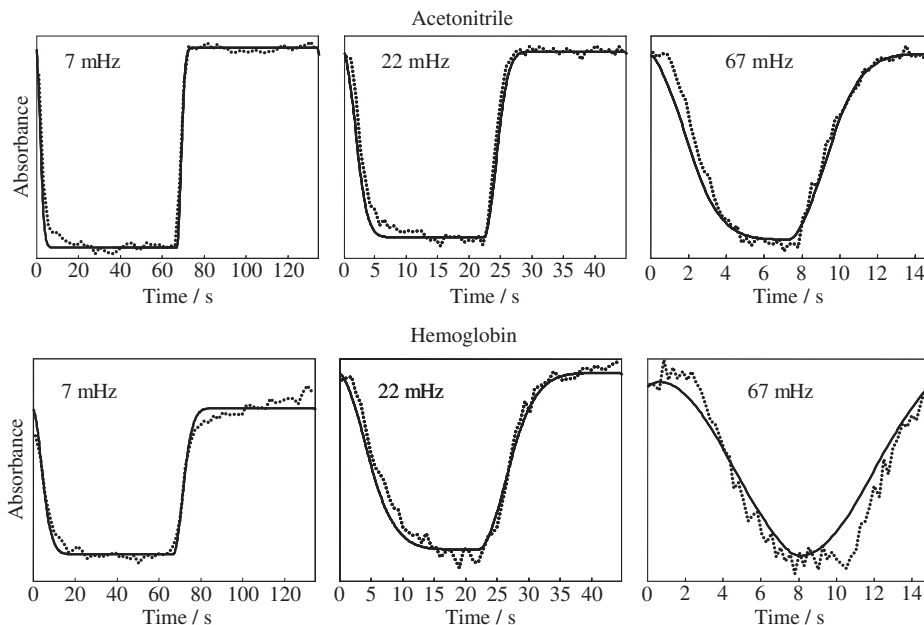


FIG. 15. Response comparison between experiment and prediction of the convection–diffusion model described in the text for acetoneitrile and hemoglobin at three different modulation frequencies. Solid line, simulated response; dotted line, experimental response (65).

which a CCD camera is installed. The other end of the cylinder is equipped with a piston containing a second sapphire window that serves for illumination purposes. The piston allows variation of the volume and thus pressure.

Under subcritical conditions, several phases coexist in the reactor. The cell allows the measurement almost simultaneously of IR spectra of the denser phase by ATR spectroscopy and of the lighter phase by transmission spectroscopy. A set of mirrors directs the IR beam either through the ZnSe IRE for ATR measurements or through cylindrical ZnSe windows for transmission measurements. The path length for the transmission measurements can be adjusted in the range between 0.3 and 38 mm by variation of the length of the cylindrical windows. The design depicted in Fig. 17 requires careful attention to the details and machining. In particular, sealing of the brittle optical components, which have to withstand temperatures up to 473 K and pressures up to 200 bar, is a challenge. Furthermore, the mechanical stability of the optical equipment is a prerequisite for the measurement of accurate, reproducible results.

A powerful characteristic of the cell described above is the opportunities it affords for the determination of the compositions of both the lower (denser) and upper (lighter) phases. In particular, the combination of ATR and transmission IR spectroscopy shows the distribution of the catalyst between the two phases. For example, in the homogeneously catalyzed formylation of morpholine with carbon dioxide and hydrogen by a ruthenium catalyst, a two-phase system was found at a

conversion of 50% at 353 K and 50 bar. A comparison of transmission and ATR spectra showed that the catalyst was confined to the liquid phase under these conditions (76).

The equipment depicted in Fig. 17 also allows monitoring of species adsorbed on a solid catalyst. For this application, the ZnSe IRE is coated with a layer of the catalyst before assembly of the cell and the start of the reaction. This approach was chosen for investigation, for example, of the interaction of the reactant with the catalyst during the asymmetric hydrogenation of ethyl pyruvate catalyzed by cinchonidine (CD)-modified Pt/Al₂O₃ in the presence of supercritical ethane (79).

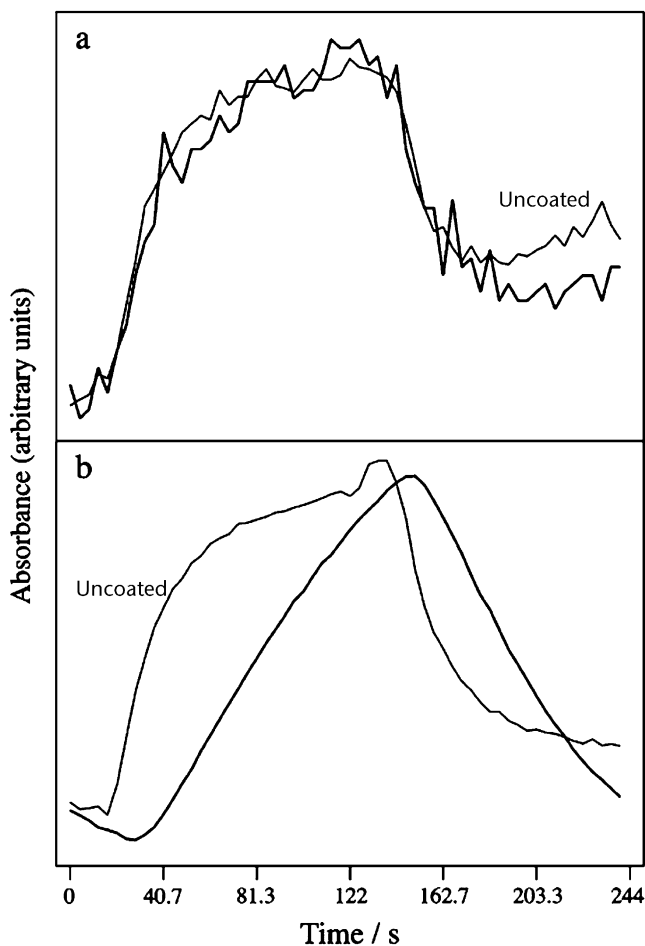


FIG. 16. Change of the absorbance signal as a function of time for (a) cyclohexene and (b) TBHP on an uncoated ZnSe IRE (thin line) and on a ZnSe IRE coated with a methyl-modified Ti-Si aerogel catalyst (solid line). At time $t = 0$, the concentration at the inlet of the ATR flow-through cell was switched from 0 to 3 mmol/L, and at $t = 122$ s, it was switched back again (50).

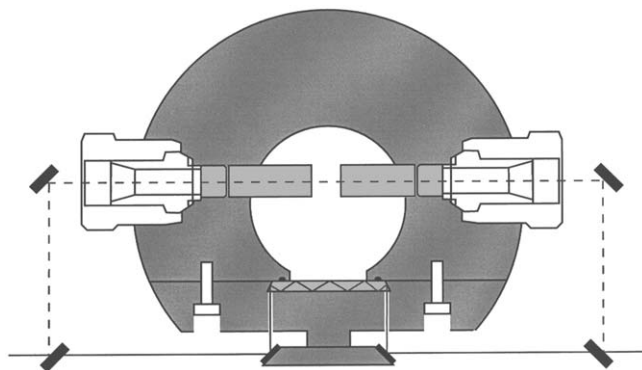


FIG. 17. Cross-section of the view cell at the spectroscopic level. The IR beam is directed either through the ATR crystal (bottom, solid lines) or through the transmission windows (upper part, dashed lines). The four mirrors are mounted on a motor-driven mobile attachment (76).

V. Potential and Limitations

What can we expect to learn about heterogeneous solid–liquid catalytic reactions from the ATR technique? Figure 18 shows schematically the situation typically encountered in an ATR experiment. The ATR can provide information about dissolved species, such as reactants and products in the bulk liquid (void volume). The great advantage of the method is that it can provide insight into the species adsorbed on the catalyst during reaction, such as reaction intermediates—even in the presence of strongly absorbing solvents. In some cases, information about the catalyst itself can be obtained. For example, oxide catalysts have characteristic IR spectra. In contrast, metal catalyst particles do not exhibit vibrations in the mid-IR region that is typically accessible in ATR spectroscopy. Nevertheless, metals strongly absorb IR radiation, and in some circumstances the observations can provide useful information characterizing the state of a supported metal catalyst as a consequence of different reflectivity caused by, for example, oxidation (49), as described in detail below.

Thus, the ATR technique yields much information—which may be one of its greatest limitations. An ATR spectrum of a working heterogeneous catalytic system *simultaneously* provides information about dissolved and adsorbed reactants and products, adsorbed intermediates, byproducts, spectators, and the catalyst itself. The technique is unspecific in the sense that a signal cannot *a priori* be assigned to dissolved or adsorbed species or the catalyst itself. Thus, analysis of the data requires more effort and specific techniques, such as the ones discussed in detail below. In the following we illustrate the points raised above by some examples.

The real-time monitoring of dissolved molecules has already been demonstrated above for a batch reactor (Fig. 10). Figure 19 gives an example of data obtained with a continuous reactor of the type shown in Fig. 12. The example was chosen to illustrate the excellent time resolution of the method, which is limited by mass

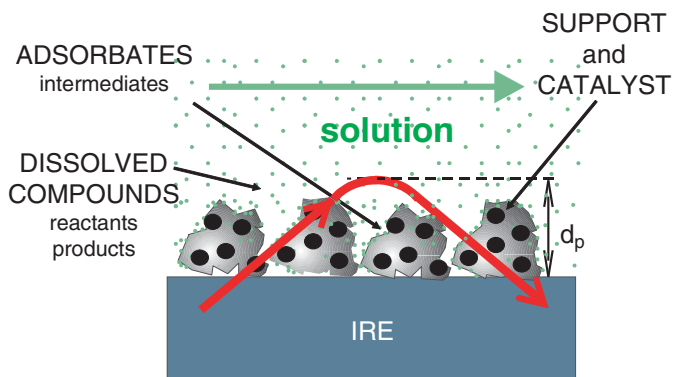


FIG. 18. *In situ* ATR-IR spectroscopy of heterogeneous solid-liquid catalytic reactions gives simultaneous information about dissolved species and species adsorbed on the catalyst.

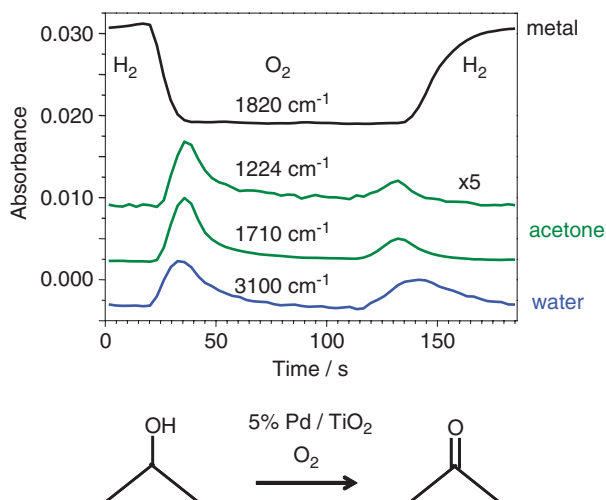


FIG. 19. ATR signals as a function of time for 2-propanol oxidation at 298 K catalyzed by 5% Pd/TiO₂ immobilized on a ZnSe IRE. At time $t = 20$ s, the solvent flow was switched from hydrogen-saturated 2-propanol to oxygen-saturated 2-propanol. At $t = 120$ s, the flow was switched again to hydrogen-saturated 2-propanol. Signals associated with the oxidation product of 2-propanol, acetone, and water are shown. The signal at 1820 cm^{-1} is associated with changes occurring on the metal catalyst (see text for details) (49).

transport (convection and diffusion). A Pd/TiO₂ catalyst was immobilized on a ZnSe IRE, and 2-propanol flowed over it. 2-Propanol can be oxidized to acetone on the supported palladium catalyst in the presence of oxygen under mild conditions, at room temperature or slightly higher temperatures. The 2-propanol was provided to the ATR cell from two separate saturators through which gas was sparged. In one of them, the 2-propanol was saturated with hydrogen; in the other it was

saturated with oxygen. The two fluids alternately flowed over the sample. In the presence of hydrogen, the oxidation reaction does not occur. When the stream was switched to oxygen-saturated 2-propanol (at time $t = 20$ s), acetone was observed in the ATR spectra. The traces shown in Fig. 19 correspond to the absorbance signals at 1224, 1710, and 3100 cm^{-1} associated with the carbonyl and C–C stretching vibrations of dissolved acetone and the O–H stretching vibrations of water. The concentration of acetone decreased sharply after a short time. This observation was attributed to the “over-oxidation” of the Pd catalyst, characterized by a high coverage of oxygen, preventing adsorption of the reactant (80,81). The traces in Fig. 19 show that relatively fast concentration variations on the order of a few seconds can easily be measured by ATR, which allows the determination of fast kinetics in continuous reactors.

2-Propanol oxidation under mild conditions takes place with high selectivity. No products other than acetone were observed in the ATR spectra recorded *in situ*. The situation is more complex for the oxidation of primary alcohols such as ethanol. The first oxidation step produces acetaldehyde, which is prone to further reactions, as is apparent in the ATR spectra. Figure 20, left, shows ATR spectra recorded *in situ* during ethanol oxidation. Figure 20, right, shows some signals as a function of time. The experiment was performed in a manner similar to that of the one

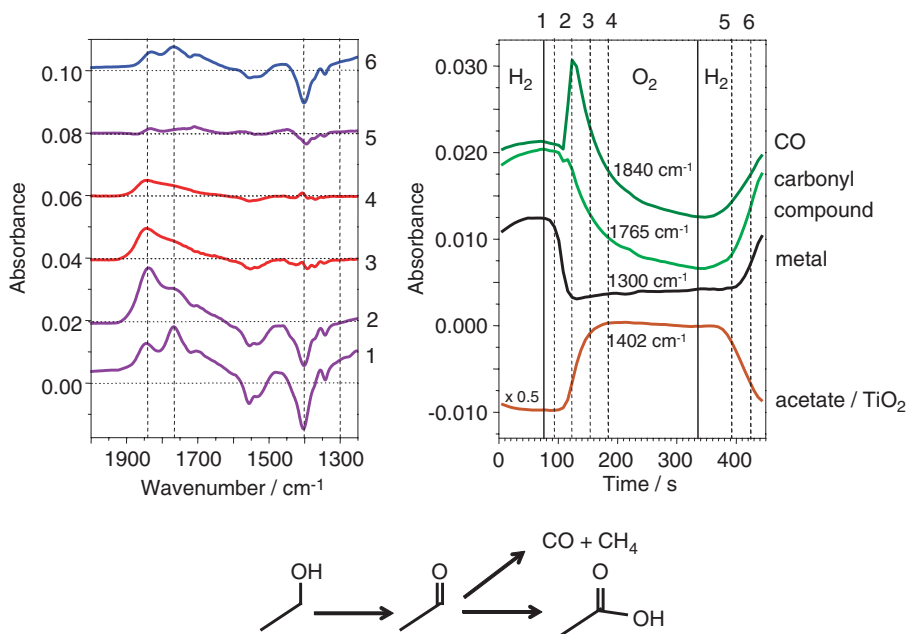


FIG. 20. ATR spectra (left) and ATR signals as a function of time (right) for ethanol oxidation catalyzed by 5% Pd/TiO₂ immobilized on a ZnSe IRE. At time $t = 75$ s, the solvent flow was switched from hydrogen-saturated ethanol to oxygen-saturated ethanol. At $t = 335$ s, the flow was switched again to hydrogen-saturated ethanol. The signal at 1300 cm^{-1} is associated with changes occurring on the metal catalyst (see text for details). The numbered dashed lines on the graph at the right indicate the time at which the spectra shown in the left graph were recorded (49).

described above for 2-propanol oxidation (Fig. 19). The band at about 1840 cm^{-1} is associated with CO adsorbed on the palladium catalyst. This signal arises from decarbonylation reactions of the aldehyde. The bands at 1402 and 1555 cm^{-1} indicate acetic acid adsorbed on the Al_2O_3 catalyst support; the acid is formed by oxidation of the aldehyde. The various species exhibit considerably different kinetics that result when the reaction is started by switching from hydrogen- to oxygen-saturated ethanol.

This example illustrates another important issue of ATR spectroscopy carried out during heterogeneous catalytic reactions. Concentrations of products determined by ATR can be different from those observed by other techniques such as GC analysis (49,75). There are primarily two reasons for the differences:

- (a) ATR selectively probes the solid–liquid interface, where the products are formed. The products then diffuse through the stagnant layer into the bulk and are thus diluted. Because ATR measures the region near the interface, whereas other methods, such as GC, measure the bulk fluid, the absolute concentrations as determined by these methods can be significantly different. Such an effect was observed, for example, in the heterogeneous enantioselective hydrogenation of a pyrone (48). The conversion as observed by ATR in the catalyst film was significantly larger than the conversion determined by GC analysis of the flow-cell effluent.
- (b) Adsorption of products on the catalyst can also have a larger effect on the composition of the solid–liquid interface. Strongly adsorbed species are the ones observed predominantly in the ATR experiment. The effect is illustrated by oxidation of primary alcohols catalyzed by supported platinum-group metals. In the absence of water in organic solvents, the reaction stops at the aldehyde. Formation of the acid requires hydration of the aldehyde to the geminal diol, which is subsequently oxidized to the acid. The formation of the geminal diol is not possible in the absence of water. Still, in ATR experiments carried out with the catalyst in organic solvents, prominent signals indicative of carboxylic acids adsorbed on the catalyst support as carboxylates are visible, even though the acid is not detected (or hardly detected) by other methods. The small amount of acid formed has such a strong affinity for the catalyst surface relative to the other reactants that it accumulates on the surface (48,75), as is also evident from Fig. 20.

Another example also illustrates the point that the composition of the catalytic solid–liquid interface as observed by ATR can be significantly different from the composition of the bulk phase as probed by other methods. The hydrogenation of ethyl pyruvate in supercritical ethane at 310 K and 73.5 bar was investigated with the high-pressure ATR cell depicted in Fig. 17 (76). Although the transmission spectrum of the single supercritical phase changed significantly during reaction as a result of the transformation of reactants into products, the ATR spectrum of the catalyst hardly changed. The ATR spectrum was dominated by strongly adsorbed species and was therefore much less sensitive to the conversion than the spectrum of the fluid phase.

A strength of ATR spectroscopy in heterogeneous catalysis is the opportunity it affords for detection of adsorbed species while the catalyst is working. Detection is

the first step toward identification of adsorbed species, which is one of the most direct ways to unravel reaction mechanisms and to learn how a catalytic system works. The step from the detection of a species to its identification may be easy in some cases, but complicated in others. An example of an easy case, and an important one, is the detection of carbon monoxide, a catalyst poison, on the catalyst surface (26,38,46,47). Figure 21 shows ATR spectra recorded during the oxidation of cinnamyl alcohol in toluene in the presence of a Pd/Al₂O₃ catalyst (46). The spectra in the left panel (a) demonstrate the buildup of CO on the palladium surface in the presence of an argon-saturated solution, as indicated by bands at about 2000, 1900, and 1840 cm⁻¹. The latter two bands are associated with bridging CO and the former with linearly bound CO (82). CO was formed by decarbonylation of cinnamylaldehyde. When argon was replaced by air (panel (b)), the CO was efficiently removed from the palladium surface as a result of oxidation by oxygen. Concomitantly, the oxidation rate increased sharply. It was therefore inferred that an important role of oxygen for achieving high oxidation rates is the removal of carbon monoxide from the active sites.

Identification of an adsorbate may be facilitated by simple adsorption of a precursor that resembles it, or just the adsorbate itself, such as CO (e.g., panel (c), Fig. 21). Adsorbed reaction intermediates on Pd/Al₂O₃ for 2-propanol oxidation were identified by using time-resolved ATR spectroscopy and quantum chemical calculations (45), as described in detail below. Reaction intermediates are usually

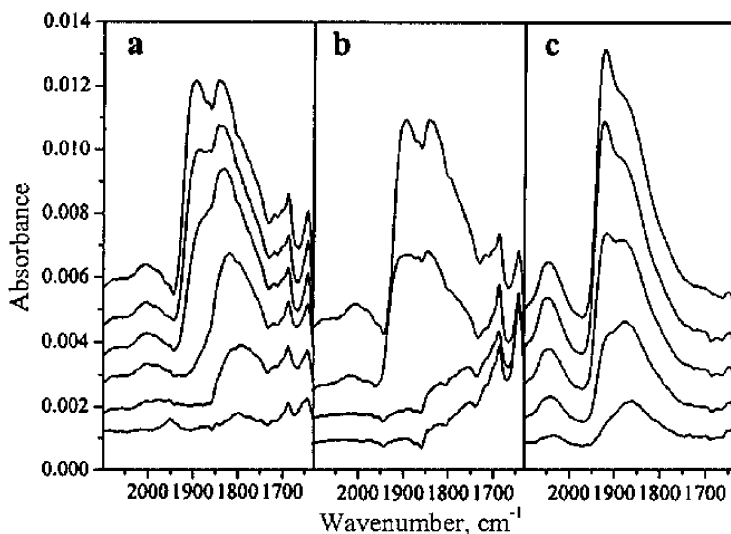


FIG. 21. ATR spectra (a) recorded during flow of a solution of 0.056 mol/L cinnamyl alcohol in argon-saturated toluene over a Pd/Al₂O₃ catalyst. The time between the first (bottom) and last (top) spectrum was 17 min. (b) Spectra recorded during subsequent flow of an identical solution—except that it was saturated with air—over the same sample. The time between the first (top) and last (bottom) spectrum was 2 min. (c) Spectra recorded during subsequent flow of dissolved CO (0.5% in argon) over the same catalyst. Time between first (bottom) and last (top) spectrum was 10 min. The background for the spectra shown in (a) and (b) was recorded before admitting the alcohol to the sample. For the spectra in (c), the background was recorded before admitting CO (46).

short-lived and present in low abundance on surfaces, and their identification is difficult, but in prospect one of the most significant applications of ATR spectroscopy. Their detection requires specialized techniques such as, for example, time-resolved spectroscopy, as discussed below for ethylene hydrogenation catalyzed by Pt/Al₂O₃ (83). A fundamental difficulty is the step from the observation of an intermediate to its identification. In favorable cases, identification of an adsorbed species can be accomplished by comparison with available spectra, such as those determined under ultra-high vacuum conditions. An increasingly important strategy, and in many cases the only viable one for the identification of reaction intermediates, is comparison with calculated spectra determined by high-quality *ab initio* and DFT quantum chemical calculations.

ATR is most powerful for the investigation of adsorbed species, but in some circumstances it provides useful information about the structure of the catalyst itself. For example, some vibrations of oxides fall within the spectral region typically accessible in ATR spectroscopy. Figure 22 shows ATR spectra of Ti–Si oxide aerogel catalysts used for epoxidation of olefins in the presence of a peroxide oxidant (50). The spectra were recorded during adsorption of TBHP on aerogels containing 0, 10, and 20 wt% TiO₂ (nominal). The sharp bands, notably at 1250, 1191, 844, and 749 cm⁻¹, are associated with adsorbed TBHP. However, bands attributed to the catalyst are also visible, at 980 (negative), 1020, and 944 cm⁻¹ (broad). The band at 980 cm⁻¹ is associated with silanol groups of the catalyst and indicates their interaction with TBHP. The latter two bands are assigned to catalyst framework vibrations, which are affected by adsorption of the peroxide. Comparison of the results for the various catalysts indicated some differences at approximately 930 cm⁻¹, where Ti–O–Si vibrations absorb. In contrast to the oxides of this investigation, many catalytic materials are characterized by vibrations that are very low in frequency and difficult to access by conventional ATR spectroscopy. Raman spectroscopy (84) is more suitable to probe these low-frequency modes.

ATR IR spectroscopy is also applicable to supported metal catalysts. Metals absorb IR and visible radiation strongly. Small changes of the optical constants of the metal can be measured with high sensitivity; such measurements in the visible spectral range are used in electroreflectance spectroscopy (85). Changes of the metal optical constants with changes in the electrochemical potential arise as a consequence of an increase or decrease of the concentration of free electrons (86,87) or changes in electronic transitions (88), possibly involving surface states (89). Similar effects can be observed in the IR region; ATR IR spectroscopy is therefore quite sensitive to changes in the state of a metal.

The reduction of palladium supported on TiO₂ can be followed easily by ATR spectroscopy. Figure 23 shows spectra of a Pd/TiO₂ powder catalyst deposited onto a ZnSe IRE in contact with toluene solvent. The catalyst was stored in air for several months, and the palladium was completely oxidized. The reference spectrum was recorded while argon-saturated toluene flowed over the sample (before exposure of the catalyst to hydrogen). When this stream was replaced by hydrogen-saturated toluene (Fig. 23), the absorbance increased rapidly and stabilized after about 3 min. The increase in absorbance at 1700 cm⁻¹ was about 25%. When the stream was replaced by oxygen-saturated solvent, the absorbance decreased, but

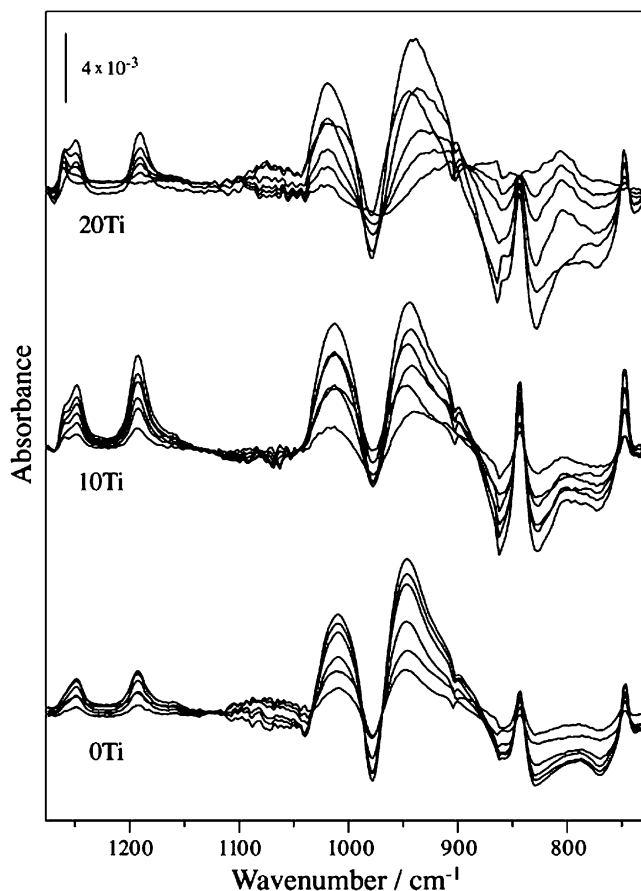


FIG. 22. Demodulated ATR spectra representing adsorption/desorption of TBHP at room temperature on Ti-Si aerogels with various Ti contents and Si reference sample (0Ti): 10Ti (10% TiO₂), 20Ti (20% TiO₂). The TBHP concentration in cyclohexane was modulated between 0 and 3 mmol/L (50).

only by 2.5%. Under these conditions, the dissolved oxygen cannot oxidize the palladium particles. The ATR signals shown in Fig. 23 arise as a result of the transformation of palladium oxide into metallic palladium upon admission of dissolved hydrogen. The markedly different optical constants of the oxide and the metal account for the observed signals.

Exposing palladium alternately to dissolved oxygen and hydrogen also leads to changes in the IR spectrum, which can be followed by ATR spectroscopy (49). The absorbance over the whole mid-IR region increased when the sample was in the presence of hydrogen and decreased when it was in the presence of oxygen. This effect was observed for supported Pd/Al₂O₃ and Pd/TiO₂ powder catalysts (Figs 19 and 20) as well as for palladium films evaporated onto Ge IREs.

The latter system was also modeled on the basis of the formalism outlined above (Eqs. (11)–(22)), which provided insight into the origin of the observed changes (49).

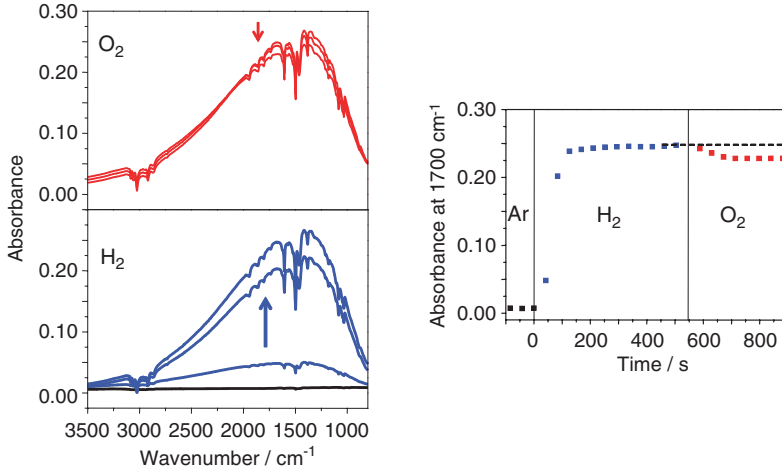


FIG. 23. ATR spectra (left) of a 5% Pd/TiO₂ catalyst. The powder catalyst was deposited on a ZnSe IRE. Toluene saturated with various gases then flowed over the sample. At the beginning the palladium was oxidized. First, toluene saturated with argon flowed over the catalyst (bottom left, bottom spectrum). Then the flow was switched to hydrogen-saturated toluene, which led to reduction of the palladium (bottom, left). Afterwards, the flow was switched to oxygen-saturated toluene (top, left). The right graph shows the absorbance at 1700 cm⁻¹ as a function of time during the treatments (49).

The optical constants of a metal are determined to a large degree by the free electrons. According to the Drude model, the contribution of the free electrons to the frequency-dependent dielectric function is expressed as follows (16):

$$\tilde{n}(\omega)^2 = [n(\omega) + ik(\omega)]^2 = \varepsilon(\omega) = 1 - \frac{\omega_p^2}{\omega^2 + (i\omega/\tau)}, \quad (24)$$

where ω_p is the plasma frequency given by

$$\omega_p^2 = \frac{4\pi N e^2}{m^*}. \quad (25)$$

Here e is the electron charge, m^* the effective electron mass, N the concentration of free electrons, and τ is the relaxation time of the electron. Thus, the Drude model predicts a change in the optical constants with a change in the concentration of the free electrons of the metal. The latter slightly increases (decreases) as a consequence of the adsorption of hydrogen (or oxygen). Modeling of the system Ge IRE/Al₂O₃/Pd/solvent according to Eqs. (11)–(22), using the optical constants for palladium predicted by the Drude model (Eqs. (24) and (25)), allows determination of the response of the overall system to adsorption of hydrogen and oxygen. The reflectivity calculations predict an increase of the absorbance upon adsorption of hydrogen (leading to an increased concentration of free electrons) and a decrease of the absorbance upon adsorption of oxygen (leading to a decreased concentration of free electrons), as observed in the experiment.

The advantages of sensing changes of a supported metal catalyst by ATR spectroscopy are obvious: Such changes can be correlated with information characterizing the adsorbate layer or reaction products measured simultaneously by ATR spectroscopy. The good time resolution of the method makes it possible to follow the response of a catalytic process to an external stimulation, as is demonstrated for the reaction of 2-propanol on a Pd/TiO₂ catalyst (Fig. 19). 2-Propanol can be oxidized to acetone by dehydrogenation on platinum-group metals in the presence of oxygen (90). The appearance of the reaction product acetone can be followed as the state of the palladium metal changes. If the experiment is started under reducing conditions, the acetone formation rate increases when oxygen is admitted. The rate increases and then decreases after a short time. The reaction rate is determined by a balance between adsorption of the reactant, dehydrogenation of the reactant, and adsorption of oxygen (81). The latter process influences the optical properties of the palladium particles and is thus observable in ATR experiments.

In our experience, the principal challenges in the application of ATR IR spectroscopy for investigations of functioning solid catalysts are associated with the sensitivity of the measurement and the complexity of the samples. The former is an issue common to most surface spectroscopies. The latter has to do with the simultaneous presence of many species at a catalytic solid-liquid interface; these species include dissolved reactants, adsorbed intermediates, spectators, and products. The spectra are a superposition of the spectra of the individual species. The question of whether a species is a spectator or instead involved in the catalytic cycle is not easily answered and represents a challenge for *in situ* spectroscopy in general. Thus, there is a need for specialized techniques to be used in combination with ATR spectroscopy to enhance sensitivity and introduce selectivity.

In the following, we describe such techniques, which are, besides time-resolved spectroscopy, modulation excitation spectroscopy (MES) (14,48,91) and single-beam signal reference (SBSR) spectroscopy (14).

VI. Specialized Techniques

A. MODULATION EXCITATION SPECTROSCOPY

If a system is disturbed by periodical variation of an external parameter such as temperature (92), pressure, concentration of a reactant (41,48,65), or the absolute configuration of a probe molecule (54,59), then all the species in the system that are affected by this parameter will also change periodically at the same frequency as the stimulation, or harmonics thereof (91). Figure 24 shows schematically the relationship between stimulation and response. A phase lag ϕ between stimulation and response occurs if the time constant of the process giving rise to some signal is of the order of the time constant $2\pi/\omega$ of the excitation. The shape of the response may be different from the one of the stimulation if the system response is non-linear. At the beginning of the modulation, the system relaxes to a new quasi-stationary state, about which it oscillates at frequency ω , as depicted in Fig. 24. In this quasi-stationary state, the absorbance variations $A(\tilde{\nu}, t)$ are followed by measuring spectra

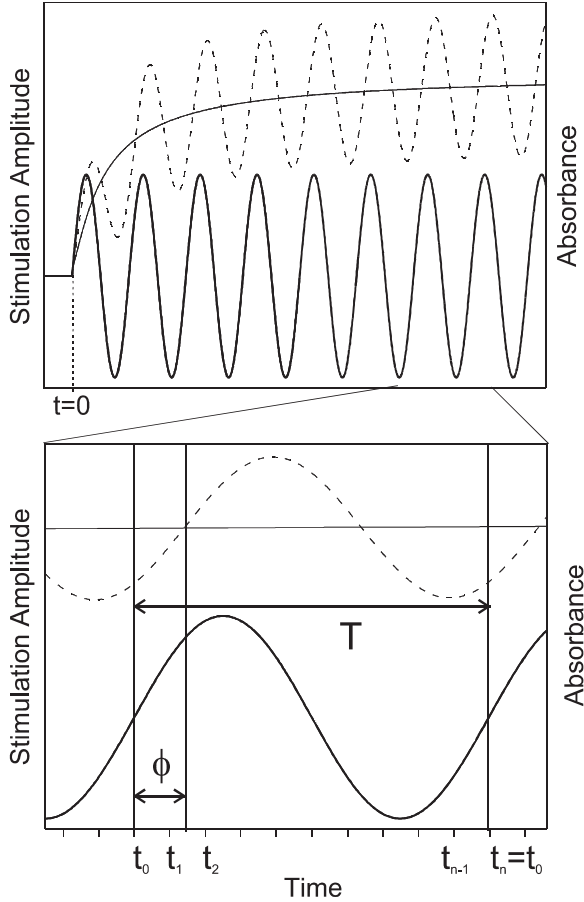


FIG. 24. Schematic behavior of the absorbance of a species with a concentration in the system affected by a periodic (in this case sinusoidal) change of an external parameter. Thick solid line: stimulation amplitude; dashed line: absorbance $A(\tilde{\nu}, t)$ of a species in the system at a particular wavelength; thin solid line: mean absorbance $A_0(\tilde{\nu})$. At time $t = 0$, one parameter in the system starts to be modulated with a particular stimulation amplitude around a mean value. The concentration of the species (which are affected by the external stimulation) and hence the absorbance associated with these species are changing periodically at the same frequency as the stimulation. After an initial period, a quasi-stationary state is reached, at which the mean absorbance is constant. Typically, modulation experiments are performed at this stationary state by recording n time-resolved spectra at t_0, t_1, \dots, t_n , within the modulation period T . Data acquisition is synchronized with the stimulation. The response (absorbance) can be retarded with respect to the stimulation (characterized by a phase lag ϕ) (48).

at times t_0, t_1, \dots, t_n within the modulation period T (Fig. 24). These spectra, the time-resolved absorbance spectra, are then converted into phase-resolved absorbance spectra according to:

$$A_k^{\phi_k^{\text{PSD}}}(\tilde{\nu}) = \frac{2}{T} \int_0^T A(\tilde{\nu}, t) \sin(k\omega t + \phi_k^{\text{PSD}}) dt, \quad k = 1, 2, \dots \quad (26)$$

Mathematically, a phase-sensitive detection (PSD) is carried out by multiplying $A(\tilde{\nu}, t)$ by a sine function of the same frequency as the stimulation or harmonics thereof, $\sin(k\omega t + \phi_k^{\text{PSD}})$, followed by a normalized integration of the product over the modulation period T . With one set of time-resolved spectra, Eq. (26) can be evaluated for various phase settings ϕ_k^{PSD} (demodulation phase angle) to determine different phase-resolved absorbance spectra. The parameter k determines the frequency at which the time-dependent signals are demodulated (i.e., the fundamental of the excitation frequency, the first harmonic, and so on). Note that this procedure is analogous to a digital lock-in amplification.

Concentration modulation experiments have been reported for applications to heterogeneous catalysis (48). The experimental implementation was accomplished by periodically flowing solutions with different (reactant) concentrations over the catalyst immobilized on the IRE. Fast concentration modulation in the liquid phase is limited by mass transport (diffusion and convection), and an appropriately designed cell is essential. The cell depicted in Fig. 12 has two tubes ending at the same inlet (65). This has the advantage that backmixing in the tubing upstream of the cell can be avoided. With this cell, concentration modulation periods of about 10 s were achieved (45,65).

Figure 25 demonstrates the power of the modulation technique. In this application of ATR and MES spectroscopies, the epoxidation of cyclohexene catalyzed by a Ti-Si mixed oxide aerogel with *t*-butylhydroperoxide (TBHP) as the oxidant was investigated. The catalyst was fixed on a ZnSe IRE, and the catalytic system was stimulated by modulating the concentration of cyclohexene by admitting periodically TBHP solutions and solutions of TBHP and cyclohexene. The only parameter that was changed was the concentration of the cyclohexene. The spectra shown in Fig. 25(a)–(c) represent the same data in different form obtained from one modulation experiment. The top spectra are time-resolved, recorded during the modulation. The reference spectrum was recorded with the sample in the presence of neat solvent before the start of the modulation (i.e., before the reactants were admitted). The spectra did not change much with time; most of the signal is static and originates from species strongly adsorbed on the catalyst. No doubt these spectra contain useful information, because they show what was present on the catalyst surface during the reaction.

In the modulation experiment, the reaction is turned on and off by periodically admitting one of the two reactants while the concentration of the other reactant is held constant. Therefore, species involved in the catalytic cycle are expected to change periodically with time. The corresponding signals, which are small, are more interesting than the very strong static signals. The changing signals can be shown by difference spectra determined from the spectra shown in Fig. 25(a); the resulting spectra are shown in Fig. 25(b). The changing signals were small and the spectra noisy.

Figure 25(c) shows demodulated spectra obtained in the same experiments from the data set represented in Fig. 25(a) by applying digital PSD according to Eq. (26). It is evident that the demodulated spectra are of much higher quality than the ordinary difference spectra. PSD is a narrow-band technique, and noise at frequencies different from the stimulation frequency is efficiently filtered out. By the PSD the periodically varying signals are enhanced, and the (huge) static signals are

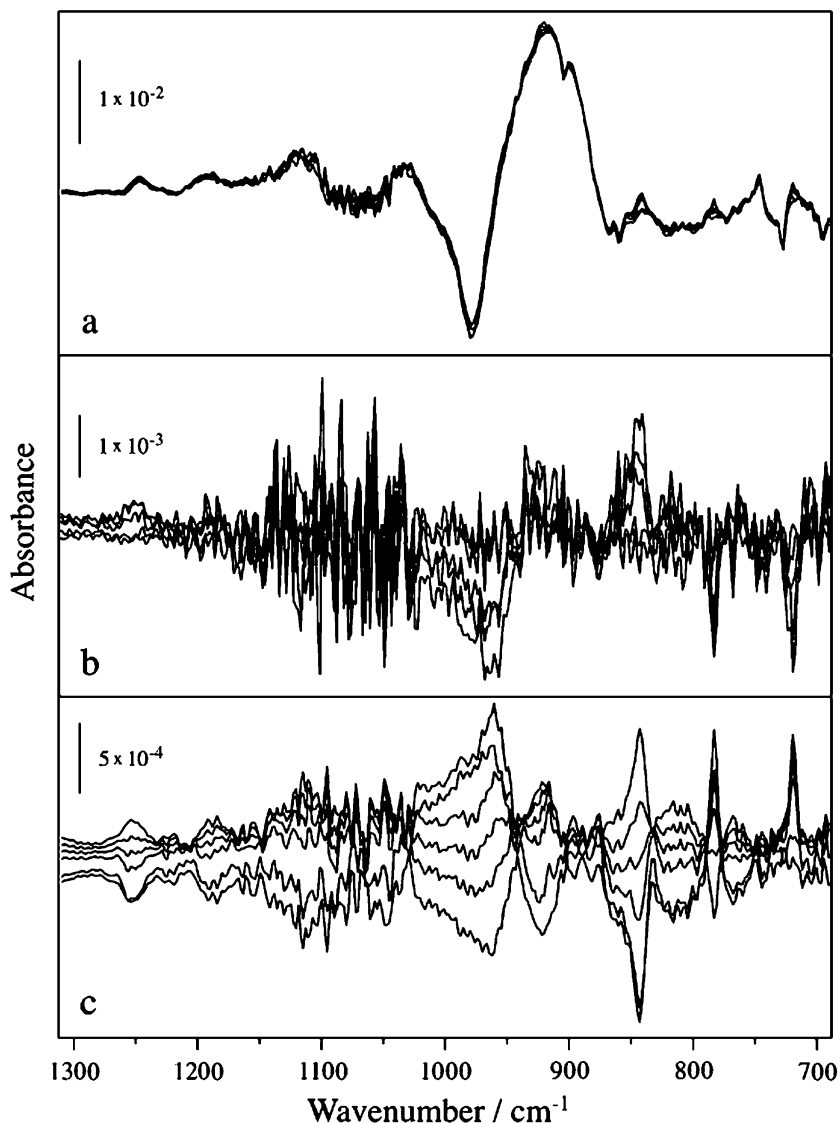


FIG. 25. ATR spectra recorded during epoxidation of cyclohexene catalyzed by a Ti-Si aerogel with TBHP as the oxidant under the influence of forced modulation of the cyclohexene concentration: (a) time-resolved spectra (reference recorded before modulation); (b) difference spectra obtained by subtracting one (arbitrarily chosen) spectrum; (c) phase-resolved (demodulated) spectra. The data set for the spectra in (a)–(c) is the same (50).

cancelled out. This procedure introduces selectivity into the resulting spectra, in the sense that the only species observed are those affected by the stimulation. Spectator species that are not affected by the stimulation do not give rise to the demodulated spectra (Fig. 25(c)), whereas the spectators give rise to signals in the spectra of the type shown in Fig. 25(a).

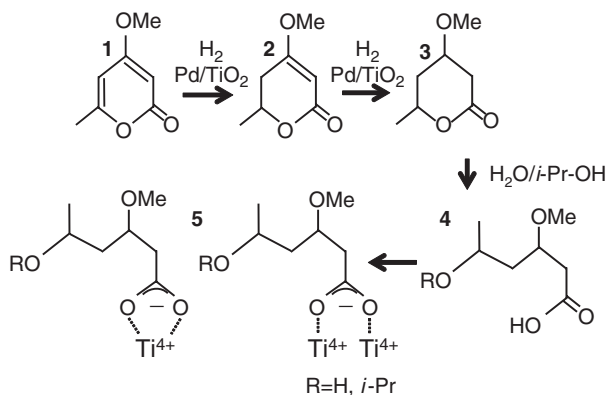


FIG. 26. Reactions observed during the enantioselective hydrogenation of pyrone **1** catalyzed by Pd/TiO₂ modified by CD. After the fast hydrogenation resulting in **2** (target reaction), a considerably slower second hydrogenation reaction follows. Once lactone **3** is formed, it can undergo ring opening to yield the corresponding acid **4**, which then adsorbs in various ways **5** on the catalyst support (48).

The MES technique has further advantages when the species in the system respond to the stimulation with different kinetics. This point is illustrated with the example of the heterogeneous enantioselective hydrogenation of a pyrone catalyzed by Pd/TiO₂ modified by CD (Fig. 26) (48). The target reaction is the hydrogenation of the C=C bond adjacent to the methyl group. After this first hydrogenation, a slower second hydrogenation follows. Once the lactone is formed, it can be hydrolyzed or alcoholized (in alcoholic solvent). The resulting acid adsorbs strongly on the support. When the pyrone reactant concentration is changed periodically (stimulation), the response of the species in Fig. 26 is different, as a consequence of the different kinetics. Thus, different phase lags result between stimulation and response for the several species. As a consequence, the demodulated spectra change with phase angle, as is shown in Fig. 27. Signals belonging to one and the same species change at the same rate and therefore vanish at the same demodulation phase angle ϕ_k^{PSD} . A comparison of spectra demodulated at different phase angles ϕ_k^{PSD} is therefore helpful for the disentanglement of crowded spectra arising from many species. The demodulation phase angle can be chosen such that the signal of a particular species completely vanishes.

The advantages of MES can be summarized as follows:

- (i) With respect to conventional difference spectra, at least one order of magnitude better signal-to-noise ratios can be obtained as a consequence of the narrow-band advantage. The signal-to-noise ratio can be further improved by averaging over several modulation periods, without losing time- (phase-) resolution. This point is important for investigations at catalytic solid-liquid interfaces, for which the signals from the adsorbed species are typically small.
- (ii) PSD allows the unambiguous separation of static (dc-term) and periodically varying (ac-term) signals (compare time- and phase-resolved spectra in Fig. 27).

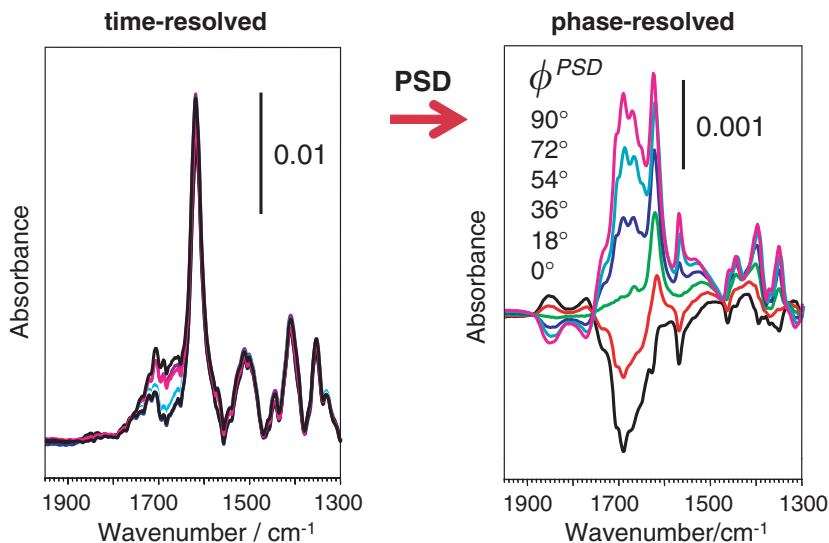


FIG. 27. Time-resolved (left) and phase-resolved (right) ATR spectra recorded during the enantioselective hydrogenation of pyrone **1** (Fig. 26) catalyzed by a 5% Pd/TiO₂ powder catalyst. The concentration of the reactant (pyrone **1**, Fig. 26) was modulated between 0 and 10 mM. The modulation period T was 420 s. Other parameters were as follows: concentration of CD, 2×10^{-5} M; room temperature. The reference spectrum for the time-resolved spectra was recorded before admitting the reactant for the first time. A large fraction of the signal is static. The demodulated spectra show only the signals that change periodically at the same frequency as the stimulation (48).

- (iii) Direct information characterizing kinetics can be gained. Species that show different characteristic time constants for the processes induced by the excitation will exhibit different phase lags. The phase lag and the modulation amplitude of a signal can be rigorously correlated to the underlying kinetics (although this has not been demonstrated here) (9,11). The phase lag between excitation and response and the modulation amplitude of a signal associated with a particular species depend on the modulation frequency. This dependence gives the operator an additional degree of freedom. However, we emphasize that rigorous analysis of the kinetics can become tedious for complicated kinetics. The quantitative analysis of the kinetics is simplified by application of a sinusoidal excitation function.
- (iv) Crowded spectra, which typically characterize catalytic solid–liquid interfaces, can be analyzed more easily if species exhibit different phase lags (Fig. 27), which allow the unambiguous subtraction of the bands associated with one species by choice of the appropriate phase setting. Furthermore, slowly responding species can be suppressed in the spectra by increasing the modulation frequency.
- (v) Phase resolution of overlapping bands can be achieved for bands with different phase lags. A limitation is the fact that only processes that are reversible, at least to a certain degree, can be investigated by MES.

B. TIME-RESOLVED SPECTROSCOPY

Time-resolved spectroscopy is conceptually similar to MES. An advantage of the former is the possibility it offers for investigation of irreversible processes. Following the response of a catalytic system to a change of a reaction parameter in the form of a pulse or step helps in the elucidation of the importance of observed species within a catalytic cycle and enables the “catching” of reaction intermediates. For example, an intermediate in the hydrogenation of ethylene catalyzed by Pt/Al₂O₃ was observed at the solid–gas interface by transmission IR spectroscopy after a short pulse of the reactant (83). This intermediate (identified as ethyl) had a lifetime of approximately 100 ms. The assignment of the ethyl as an intermediate was based on the time behavior of the species after the pulse.

A similar strategy was applied to “catch” intermediates in the oxidation of 2-propanol catalyzed by Pd/Al₂O₃. This reaction is well suited to the characterization of intermediates because it proceeds with high selectivity. Only the reactant 2-propanol and the product acetone are normally observed in the ATR. This situation is different from that encountered in the oxidation of primary alcohols such as ethanol, for which a variety of species can be observed simultaneously corresponding to the more complex reaction network. The oxidation of 2-propanol can be accelerated by switching the solvent flow between hydrogen and oxygen-saturated 2-propanol. In the short transient period after the switch, the state of the palladium catalyst is favorable for the oxidation reaction, and a large acetone signal can be observed. In contrast, in the presence of hydrogen, the surface is covered by hydrogen and no oxidation is observed. In the presence of oxygen at room temperature, the surface is covered by oxygen after a short time as a consequence of over-oxidation of the catalyst (80,81). The overall result is a pulsed production of acetone as a response toward the step-like alteration of the dissolved gas, as shown in Fig. 28(a). The observed acetone pulse has a full-width at half-maximum of about 2 s, which indicates the excellent time resolution that can be achieved, even with liquid-phase reactants. Besides 2-propanol and acetone, another species was observed in the time-resolved ATR experiments described above, characterized by a prominent band in the IR spectrum at 1065 cm⁻¹ (Fig. 28(b)). The time behavior of this species is compatible with its being an intermediate; with the help of density functional theory, the intermediate was identified as 2-propoxide, a result that shows that the initial step in the oxidation of the alcohol is its dissociative adsorption, which leads to adsorbed alkoxide and hydrogen. This step requires free surface sites. Not surprisingly, the rate of product formation is dependent on the abundance of the intermediate on the catalyst surface. The observation of the 2-propoxide intermediate furthermore shows that the abstraction of the second hydrogen (C–H bond breaking) is the rate-limiting step, thus providing insight into the reaction mechanism. Some of the most valuable information that can be obtained from ATR spectroscopy is insight into reaction mechanisms, and we emphasize that determination of such information is challenging, typically requiring specialized techniques such as time-resolved spectroscopy.

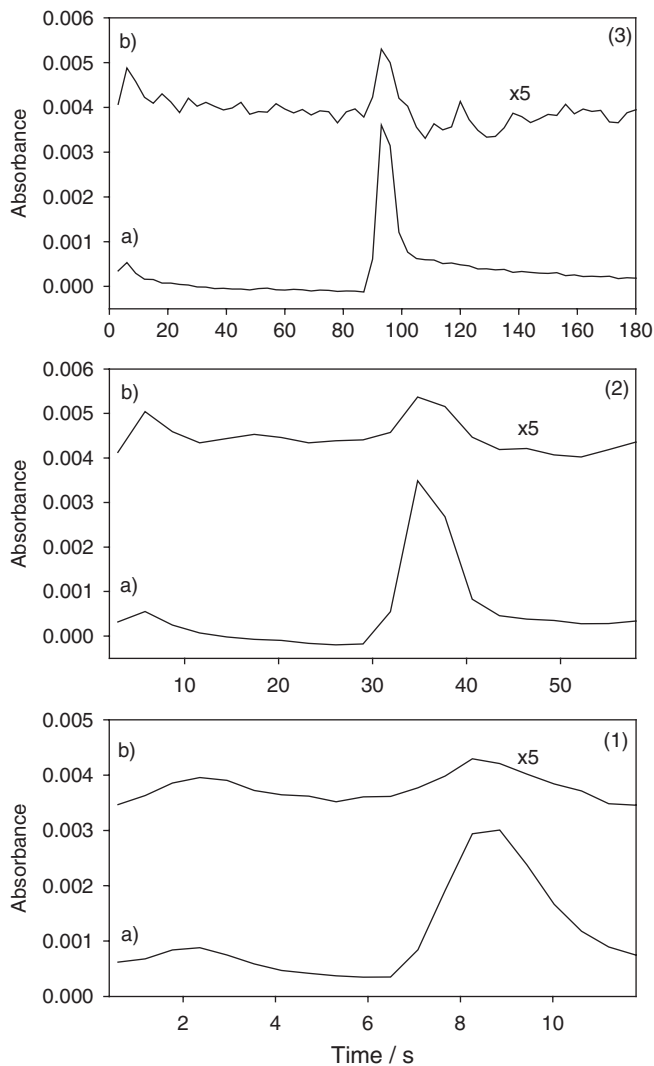


FIG. 28. Time dependence of ATR signals of (a) acetone (1711-cm^{-1} band) and (b) isopropoxide (1065-cm^{-1} band) for various modulation experiments (hydrogen-, oxygen-, and hydrogen-saturated 2-propanol). (1) Modulation period $T = 12$ s, flow rate, 2.7 mL/min . (2) $T = 58$ s; flow rate, 0.85 mL/min . (3) $T = 180$ s; flow rate, 0.85 mL/min (45).

C. SINGLE-BEAM SIGNAL REFERENCE

Time resolution is a strength of modern FTIR spectrometers that makes them powerful tools for investigations of fast processes. For the investigation of slow processes, the same single-beam FT spectrometers have a disadvantage; sensitive IR measurements require the acquisition of a reference spectrum, which is usually done

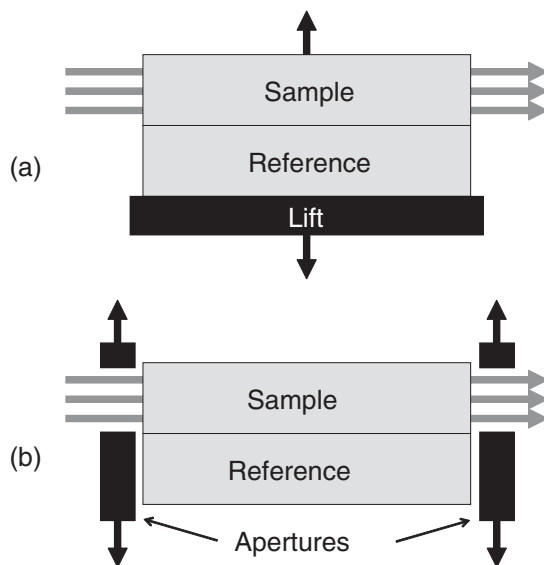


FIG. 29. Schematic representation of two variants of the SBSR method. In variant (a), the cell and IRE are translated by a lift, so that the sample and reference are alternately probed by the IR beam. In variant (b), the beam is alternately blocked on the sample and reference side.

before the start of an experiment. For investigations that last several hours, the reference may not be satisfactory because of instrument drift and changes in the sample, such as caused by a contamination. Drift will show up as spurious signals superimposed on the actual spectrum. The SBSR method (14,93) largely overcomes this problem by converting single-beam instruments into quasi-double-beam instruments. A reference is measured almost simultaneously with the sample. Figure 29 shows two variants of the SBSR method. In Fig. 29(a), the ATR cell is mounted on a lift and contains two compartments, one for the reference and one for the sample. The lift translates sample and reference alternately in and out of the measurement beam. Effects of instrument drift are cancelled out, as the sample and reference have the same history, for example, a temperature program. This method has proved to be useful, for example, for the investigation of membranes (9,14). The variant depicted in Fig. 29(b) does not require the translation of the whole cell. Instead, an aperture is translated and half of the beam is blocked. A disadvantage of this approach is that, besides losing half of the intensity, the beams that probe sample and reference are not identical, because the IR source (such as a glow bar) is not homogeneous. Besides the advantage of increased sensitivity of the measurement attributed to the elimination of long-term drift, a carefully designed SBSR experiment offers the advantage of providing more information than a conventional experiment. To understand this point, imagine the following situation: A catalyst is brought in contact with a reactant solution at elevated temperature. The changes in the spectra after some time could be caused by changes in the catalyst caused by the contact with the reactant or solvent or the transformation of the catalyst associated

with the elevated temperature or some long-term drift of the instrument. The discrimination between the various effects is barely possible in a conventional experiment. In contrast, in an SBSR experiment in which the sample and reference are the same, except that there is no reactant present in the reference, the effect of the reactant on the catalyst sample can be isolated from these other possible effects.

The SBSR technique has not yet been used extensively for catalysis applications. In one of the few examples of such applications, it was used to investigate epoxidation of cyclohexene catalyzed by Ti–Si mixed oxide aerogels with TBHP as the oxidant (50). A cyclohexane solution of TBHP or the reaction mixture was allowed to flow through the upper compartment of the ATR cell, while neat cyclohexane flowed through the lower part, used as a reference. On both the sample and reference sides of the IRE, a layer of catalyst was deposited. The whole cell was heated to reaction temperature, and the changes of the catalyst were investigated. The SBSR technique made it possible to distinguish effects of temperature and the contact of the catalyst with reactants. The results showed that the peroxide adsorbs both on Si–OH and Ti sites with adsorption on the latter being stronger. It was furthermore shown that only the peroxide adsorbed on the Ti sites is involved in the catalytic cycle.

An application using variant (b) of the SBSR method depicted in Fig. 29 and the high-pressure cell depicted in Fig. 17 involved characterization of CO₂ in mesoporous silica with mean pore diameters of 2, 10, and 15 nm (94). Supercritical CO₂ offers good prospects as a solvent in catalysis (95) associated with the tunability of its solvent properties, which can affect phase behavior and rates of mass transport; this solvent also offers environmental and safety benefits. The properties of the solvent within the small pores of a catalyst may be different from those of the bulk. In the experiment, only one side of an IRE was coated with the mesoporous silica, so that it was possible to measure the spectra of CO₂ inside and outside of the pores under identical conditions at various temperatures and pressures. Figure 30 shows ATR spectra of the ν_2 spectral region of CO₂ for the bulk phase (dashed lines) and the silica-supported phase (solid lines) at various subcritical pressures. At pressures below the saturation pressure, the absorbance was greater for the CO₂ in the pores, and a shifted signal was observed in addition to the gas-phase CO₂ signal. The shift indicates that CO₂ within the pores has a density slightly greater than that of liquid CO₂, even under supercritical conditions.

VII. Combination with Other Techniques

It is often fruitful to characterize functioning catalysts with more than one technique. ATR-IR and UV–vis spectroscopies were used in combination to investigate alcohol oxidation on a Pd/Al₂O₃ catalyst (96). The two methods provide complementary information; ATR spectroscopy was used to identify dissolved reaction products and species adsorbed on the catalyst and support, and UV–vis spectroscopy is sensitive to changes of the catalyst itself.

The equipment for the combination of spectroscopies is shown schematically in Fig. 31 (96). The ATR cell was equipped with a fused silica window for UV–vis

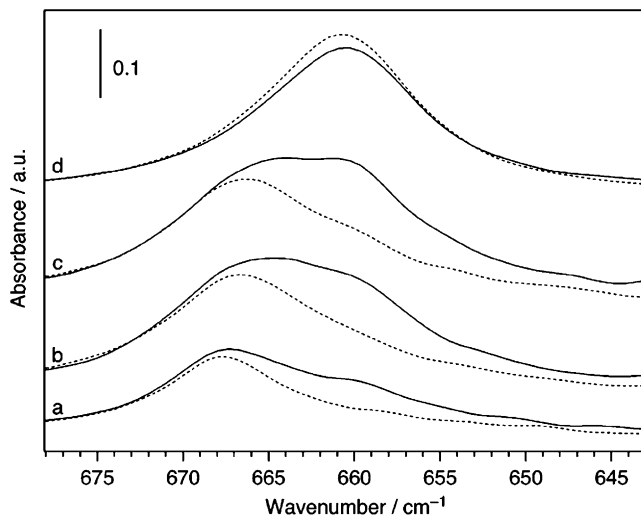


FIG. 30. ATR-IR spectra of CO_2 (bending mode) in the bulk (dashed lines) and within a layer of mesoporous silica (pore size 14.5 nm, solid lines) as a function of relative pressure. Conditions: 294 K, $P/P_{\text{sat}} =$ (a) 0.829, (b) 0.989, (c) 0.993, and (d) 1.00. Spectra are offset for clarity, and spectra (d) are scaled by a factor of 0.25. The reference spectra (both for the bulk and the silica phase) were recorded in the absence of CO_2 (94).

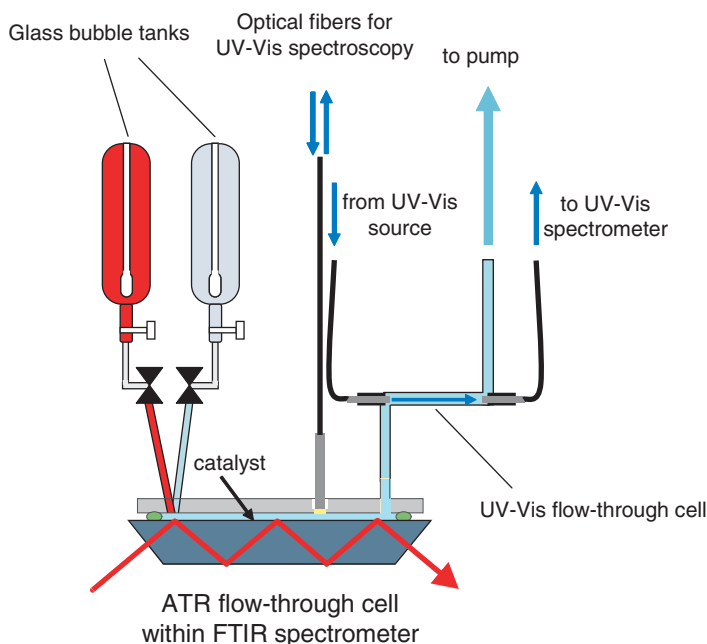


FIG. 31. Schematic representation of equipment for combined simultaneous ATR and UV-vis spectroscopy measurements during heterogeneous catalytic reactions (96).

measurements. A UV–vis probe was positioned in front of the window perpendicular to the IRE surface, so that the end of the probe was located approximately 4 mm above the catalyst layer. The probe consisted of six fibers that guide the light from a deuterium halogen source to the sample and one fiber that guides the reflected light to a UV–vis spectrometer equipped with a 2024-pixel CCD detector array. Such UV–vis spectrometers allow relatively fast measurements and are easily synchronized with the IR data acquisition.

The UV–vis spectrum of a 5% Pd/Al₂O₃ catalyst indicated some changes during ethanol oxidation catalysis. Figure 32 shows UV–vis spectra recorded during the flow over the catalyst of hydrogen-saturated ethanol for 30 min (the three bottom spectra) followed by a flow of oxygen-saturated ethanol (the three top spectra). When the catalyst was in the presence of hydrogen, the spectrum hardly changed. However, when it was present in oxygen, the spectrum changed significantly. The inset of Fig. 32 shows the absorbance at 330 nm as a function of time. It is clear that the slow changes of the UV–vis spectra were not reversible in hydrogen. During the experiment, acetaldehyde was observed by ATR spectroscopy. During 35 min of oxygen flow, the acetaldehyde signal decreased, but by only about 10% or less. Several processes could have led to spectral changes in the UV–vis spectra. It was argued (97) that the changes observed during oxidation are evidence of redispersion

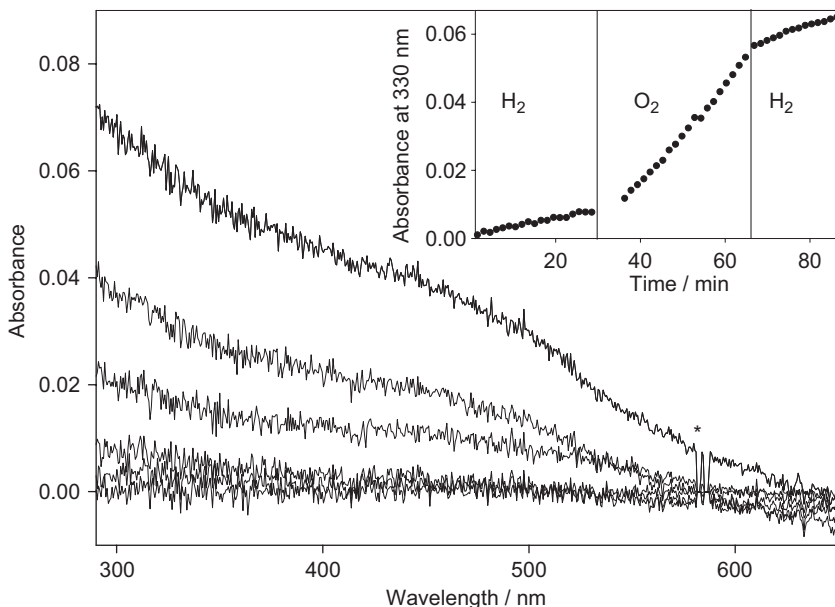


FIG. 32. UV–vis spectra of a 5% Pd/Al₂O₃ catalyst determined with the equipment depicted in Fig. 31. The reference was recorded at time $t = 0$ during the flow of hydrogen-saturated ethanol. The three bottom spectra were recorded during the flow of hydrogen-saturated ethanol at $t = 1, 15,$ and 30 min. The three top spectra were recorded during the flow of oxygen-saturated ethanol at $t = 40, 49,$ and 66 min. The inset shows the absorbance at 330 nm as a function of time. The spectra represent averages of 200 scans with 100 ms accumulation time each. The flow rate was 0.3 mL/min (96).

of the palladium catalyst particles, promoted by the presence of strongly chelating species (acetates, as evidenced by ATR spectroscopy) and adsorbed oxygen.

VIII. Selected Applications

In the following we discuss examples that further illustrate the range of possible applications of ATR-IR spectroscopy in catalysis research.

A. ELUCIDATION OF ADSORPTION MODE AND INTERACTION OF CO-ADSORBED SPECIES

The modification of platinum-group metals by adsorbed chiral organic modifiers has emerged as an efficient method to make catalytic metal surfaces chiral. The method is used to prepare highly efficient catalysts for enantioselective hydrogenation of reactants with activated C = O and C = C groups. The adsorption mode of the chiral modifier is crucial for proper chiral modification of the active metal surfaces. The most efficient chiral modifiers known today are cinchona alkaloids, particularly CD, which yields more than 90% enantiomeric excess in the hydrogenation of various reactants.

Some ultra-high vacuum techniques (XPS (98), LEED (98), and NEXAFS (99)) have provided important information concerning the adsorption mode of 10,11-dihydrocinchonidine on Pt(1 1 1), but investigations of the working catalysts are indispensable to provide information about the adsorption mode in the presence of solvent and hydrogen. ATR-IR spectroscopy has emerged as the most useful of these techniques (39,40,42,44). For example, CD adsorption was investigated with the catalyst in a flow-through cell (similar to that shown in Fig. 12) with the Ge IRE being coated by physical vapor deposition with a Pt/alumina or a Pd/alumina catalyst. ATR spectra of CD adsorbed from H₂-saturated CH₂Cl₂ solvent on Pt/alumina and on Pd/alumina are shown in Fig. 33. Prior to recording of the ATR spectra, hydrogen-saturated solvent flowed through the cell, and subsequently the background spectra were recorded. Upon addition of CD to the feed, positive and negative signals with respect to the reference spectrum were immediately observed in the ATR spectra. Positive signals arise from CD molecules added to the catalyst surface and negative signals from molecules removed from it (solvent and solvent decomposition products). The spectra demonstrate clearly that CD has to compete with solvent decomposition products for adsorption sites on the metals. The spectra recorded for CD adsorption on the two catalysts showed both time and concentration dependence; Fig. 33 (top) illustrates the concentration dependence of CD adsorption. The assignments of the bands arising from CD adsorption in the spectral region 1650–1450 cm⁻¹ were supported by results of an investigation of the adsorption of reference compounds such as pyridine, quinoline, 2-methylquinoline, and quinuclidine, in combination with calculations based on theory. The quinoline moiety was found to be responsible for the adsorptive anchoring of CD, in accord with results of investigations carried out under UHV conditions. The orientation of this quinoline moiety was estimated from the direction of the dynamic dipole moment of a selection of vibrations and by application of the metal surface selection rule (100).

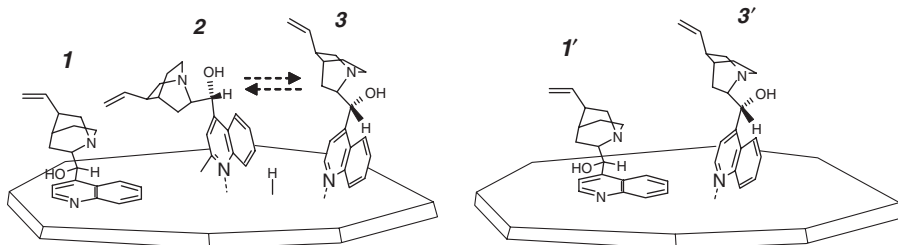
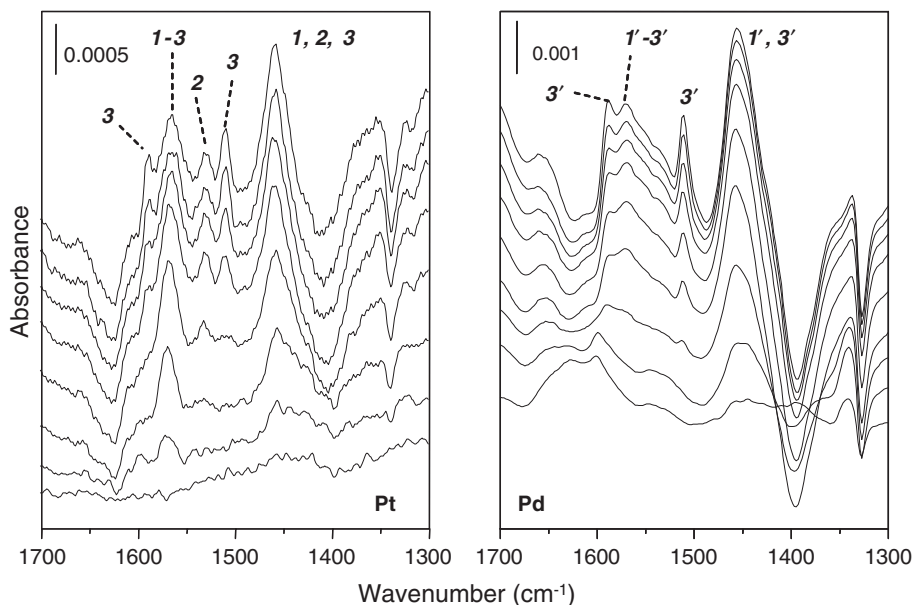


FIG. 33. CD adsorption on alumina-supported platinum (40) and palladium (42) characterized by ATR-IR spectroscopy during catalysis. Top: spectra taken at different CD concentrations in hydrogen-saturated CH_2Cl_2 . The CD concentration increases from bottom to top ($0\text{--}3 \times 10^{-5}$ M for platinum and $0\text{--}4.3 \times 10^{-5}$ M for palladium). Vibrational bands indicative of various adsorption modes of CD (bottom) are marked. Bands indicative of species 2 are absent from spectra observed for CD adsorption on palladium (40,42).

On the basis of the dependence of the spectra on time and concentration, at least three different sets of signals could be distinguished for the species on platinum, corresponding to three differently adsorbed CD species (Fig. 33). The abundance of these species was found to depend on the CD concentration (and thus surface coverage) and time. At low coverages, CD was adsorbed in a nearly flat orientation, via the π -aromatic system of the quinoline moiety (species 1). When the coverage was increased, tilted species appeared, bound via a Pt–C σ -bond (α -hydrogen abstraction, species 2), and nitrogen lone pair bonding (species 3), respectively. Species 3 were only weakly adsorbed and were in a fast dynamic equilibrium with dissolved CD species. In contrast, the α -H abstracted and π -bonded species were strongly

bound and remained adsorbed in the presence of neat solvent. Time-resolved spectra (not shown) indicated that the appearance of species **2** and **3** was anticorrelated, indicating a slow concentration-dependent transformation of **2** into **3**.

Adsorption of CD on palladium showed distinct differences from that on platinum, which is already apparent from the spectra compared in Fig. 33. The ATR spectra did not show any indication of the presence of a species covalently bound by Pt–C σ -bond (α -hydrogen abstraction, species **2** in the case of platinum). The strongly adsorbed π -bonded flat species (**1** and **1'**) were found to be more favored on platinum, whereas on palladium the tilted, nitrogen lone-pair-bound species (**3'**) were dominant. Furthermore, the comparative study showed that CD is more strongly adsorbed on platinum than on palladium, indicated by the more prominent shift of the vibrational modes with respect to the free molecule on platinum than on palladium.

Although these investigations of CD adsorption on platinum and on palladium uncovered important features contributing to a better understanding of the role of modifier adsorption for chirally modified metal catalysts, the ultimate goal was to gain some knowledge about the molecular interaction between the co-adsorbed chiral modifier and a specific reactant. Recently, we made an attempt to characterize this molecular interaction by using the CD–ketopantolactone (KPL) system as an example (41). KPL can be hydrogenated with high enantiomeric excess (>90%) on platinum chirally modified by CD. Model calculations had led to the proposition that hydrogen bonding between the quinuclidine nitrogen atom of CD and the oxygen atom at the α -carbonyl bond of KPL is crucial for the enantio-differentiation (101). This interaction is not possible for *N*-methyl cinchonidine, because the lone pair on the quinuclidine nitrogen atom is blocked.

For the experimental test of the theoretical proposition, we combined ATR and MES in a flow-through cell. The KPL reactant concentration was changed periodically, and the response of the catalytic interface was followed by ATR. KPL adsorption, both on platinum modified by CD and on platinum modified by *N*-methyl-cinchonidine chloride was investigated. As discussed above, the key advantages of MES over conventional IR spectroscopy for characterizing interactions at complex catalytic solid–liquid interfaces are associated with the higher sensitivity resulting from the PSD of periodically varying signals and the high selectivity for species that are affected by the stimulation. Figure 34 is a comparison of the demodulated ATR spectra of KPL modulation experiments. Spectrum (a) was recorded with the sample in the presence of CD, and spectrum (b) was recorded when *N*-methyl-CD was used instead of CD for chiral modification of the platinum surface. The data show that the 2580 and 1725-cm⁻¹ bands are missing when *N*-methyl-CD chloride was used as the modifier, a result that gives evidence of an interaction complex involving a N–H \cdots O hydrogen bond, as shown in Fig. 34 (complex (a)). The broad band at 2580 cm⁻¹ falls within the region where N⁺–H \cdots O hydrogen bonds are expected to absorb, whereas the band at 1725 cm⁻¹ was assigned to carbonyl stretching vibrations of KPL, shifted to lower frequencies as a consequence of hydrogen bonding. We emphasize that the observation of these bands would not have been possible without application of MES.

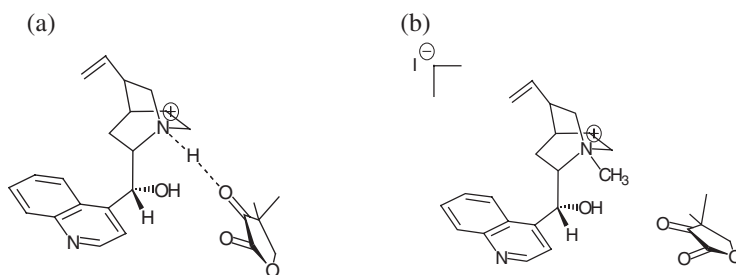
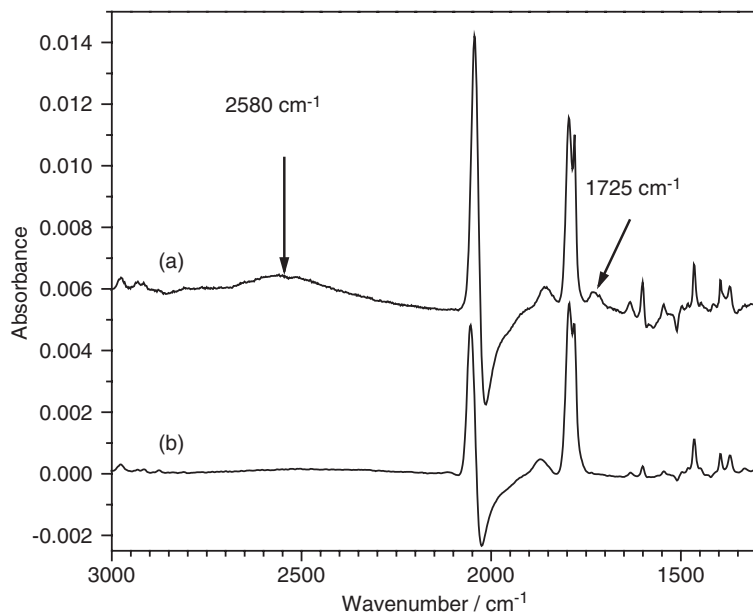


FIG. 34. Investigation of the molecular interaction between adsorbed chiral modifier and KPL by MES (41). The modifiers were the following: (a) CD and (b) *N*-methyl cinchonidine chloride. The KPL concentration was modulated (modulation period $T = 180$ s) between 0 and 5×10^{-2} mol/L in CH_2Cl_2 . The modifier concentration was 5×10^{-4} mol/L. The proposed model for the CD–KPL interaction is shown at the bottom (a). This hydrogen bonding interaction is prohibited when *N*-methyl-cinchonidine (b) is used as a chiral modifier instead of CD.

B. INVESTIGATION OF PHASE BEHAVIOR IN MULTIPHASE HETEROGENEOUS CATALYTIC REACTION

In many catalytic reactions, solid, liquid, and gas phases are involved, and the phase behavior often has a strong influence on mixing and mass transfer and consequently on the catalytic performance. Supercritical fluids, especially supercritical CO_2 , have gained considerable attention as environmentally benign solvents (e.g., (94)). The combined use of *in situ* transmission and ATR-IR spectroscopy together with video monitoring is a promising approach for elucidation of the behavior of a

multiphase reaction system, as was demonstrated recently for the palladium-catalyzed oxidation of benzyl alcohol with oxygen in the presence of supercritical CO₂ (102,103). For this purpose, the high-pressure reactor/cell combining transmission- and ATR-IR spectroscopy described above (Fig. 17) was applied. Transmission IR spectroscopy allowed the researchers to probe the reaction mixture at the top of the reactor, while ATR (located at the bottom) simultaneously provided information about the region of the catalytic solid–liquid interface. Visual observation of the reaction mixture by video monitoring provided complementary information about the phase behavior in the reactor. The commercial Pd/Al₂O₃ catalyst was deposited on the IRE (ZnSe) located on the bottom of the cell. Figure 35 shows how pressure affected the reaction rate, expressed as turnover frequency (TOF). A marked increase of TOF from 900 to 1800 h⁻¹ was observed when the pressure was raised from 140 to 150 bar. Video monitoring of the bulk fluid phase behavior (Fig. 35) and the simultaneous investigation by transmission and ATR-IR spectroscopies showed that the sharp increase in activity is correlated with a transition from a biphasic (region A) to a monophasic (region B) reaction mixture, which occurred at a pressure between 140 and 150 bar. In the single-phase region (B), both oxygen and benzyl alcohol were dissolved in the supercritical CO₂ phase, which led to a reduction of the interfacial mass transfer resistances. Analysis of the ν_2 bending mode of CO₂ gave information about the fluid composition inside and outside the catalyst pores. The two ATR spectra shown in Fig. 35 (middle) depict the changes caused by increasing the pressure from 145 to 150 bar. The bands assigned to the alcohol corresponding to the C–H out of plane deformation (736 cm⁻¹) and to the C = C deformation (697 cm⁻¹), visible in the spectra taken at 145 bar (biphasic region A), disappeared when the pressure was raised to 150 bar, indicating that the liquid phase containing the alcohol dissolved completely in the supercritical CO₂ (monophasic region B). This change of the phase behavior was further indicated by the shift of the ν_2 band of CO₂ from 657 to 663 cm⁻¹ and the visual images of the reaction mixture. The observed change in the phase behavior in the near-surface region of the catalyst was not reflected in the corresponding transmission spectra probing the bulk fluid properties, because the alcohol concentration in the homogeneous supercritical phase was too low.

C. INVESTIGATION OF COMPLEX REACTION NETWORK OCCURRING AT CATALYTIC SOLID–LIQUID INTERFACE

ATR provides opportunities to follow changes resulting from catalytic processes at solid–liquid interfaces without disturbing interference caused by the intense bands of the bulk fluid. This capability is particularly important when complex reaction networks are targeted. A recent example illustrating the potential value of the method involved palladium-catalyzed reactions of benzyl alcohol in the presence and absence of oxygen (75). The 5 wt% Pd/Al₂O₃ catalyst, containing palladium nanoparticles of 3.4 nm mean diameter, was fixed in an ATR-IR cell serving as a continuous flow reactor. The reaction conditions (cyclohexane solvent, 323 K, 1 bar) were set in the range commonly applied in the heterogeneous catalytic aerobic oxidation of alcohols. The *in situ* ATR-IR investigation of the solid–liquid

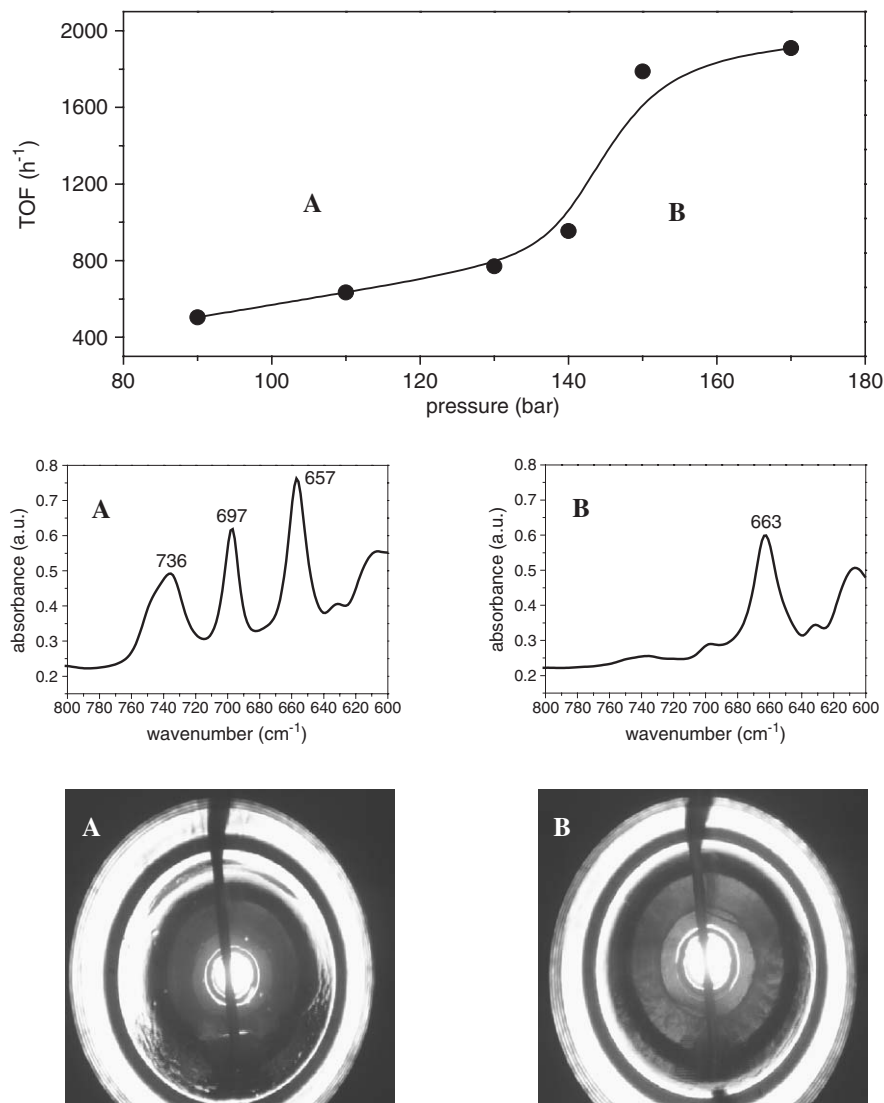


FIG. 35. Effect of phase behavior on palladium-catalyzed oxidation of benzyl alcohol to benzaldehyde in supercritical CO₂ characterized by transmission- and ATR-IR spectroscopy combined with video monitoring of the reaction mixture (102). The figure at the top shows the pressure dependence of the reaction rate. Note the strong increase of the oxidation rate between 140 and 150 bar. The *in situ* ATR spectra (middle) taken at 145 and 150 bar, respectively, indicate that a change from a biphasic (region A) to a monophasic (B) reaction mixture occurred in the catalyst surface region in this pressure range. This change in the phase behavior was corroborated by the simultaneous video monitoring, as shown at the bottom of the figure.

interface demonstrated a complex reaction network (Fig. 36), including dehydrogenation of benzyl alcohol to benzaldehyde, decarbonylation of benzaldehyde, oxidation of hydrogen and CO on the surface of the palladium nanoparticles, and formation of benzoic acid catalyzed by both palladium and Al_2O_3 . Continuous formation of CO and its oxidative removal by air resulted in significant steady-state CO coverage of palladium during oxidation of benzyl alcohol. Unexpectedly, benzoic acid formed even in the early stages of the reaction and adsorbed strongly (irreversibly) on the basic sites of Al_2O_3 , and thus it remained undetectable in the effluent. This observation raises a question of the reliability of product distributions determined conventionally from analysis of the liquid phase. The occurrence of the hydrogenolysis of the C–O bond of benzyl alcohol and formation of toluene on the palladium nanoparticles indicates that palladium was present in a reduced state (Pd^0) even in the presence of oxygen, in agreement with the dehydrogenation mechanism of alcohol oxidation.

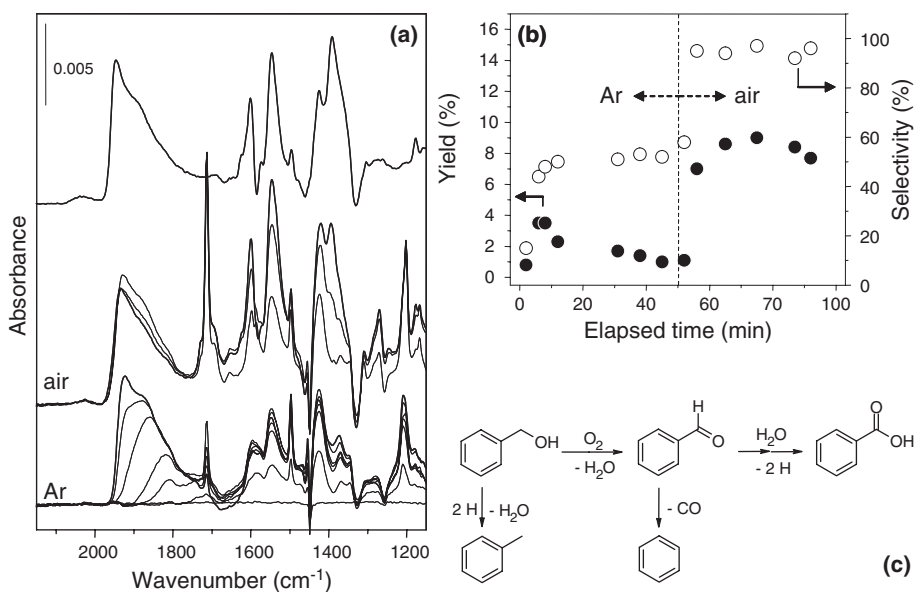


FIG. 36. Reactions of benzyl alcohol occurring on Pd/alumina in the absence and in the presence of oxygen in the liquid phase (75). (a) Shows *in situ* ATR spectra taken with the sample under inert gas (argon), in air, and during flushing with pure solvent (top spectrum). The ATR spectra display the characteristic signals of adsorbed CO (2000–1700 cm^{-1}), dissolved benzaldehyde (1713 cm^{-1}), unreacted alcohol (1495 cm^{-1}), and adsorbed benzoic acid (1600, 1546, 1425, and 1390 cm^{-1}). (b) Shows the GC analysis of the cell reactor effluent of the corresponding experiment, indicating a strong enhancement of the yield as a consequence of the increased reaction rate resulting from a change from the inert atmosphere to air. On the basis of the spectroscopic and chromatographic analysis, the reaction scheme (c) was proposed. Note the complementary information obtained by the two techniques: toluene and benzene were detected only by GC, whereas adsorbed benzoic acid and CO could be observed only by use of IR spectroscopy.

D. CATALYST DEACTIVATION

ATR-IR spectroscopy can also be rewarding in characterization of catalyst deactivation (104–106). Monitoring of the changes occurring in the bulk liquid phase by transmission IR spectroscopy is often insufficient for elucidation of deactivation phenomena occurring at the catalyst surface, and probing of the near-surface region by ATR becomes indispensable. An example illustrating the potential value of ATR-IR spectroscopy for investigation of catalyst deactivation has been reported in Reference (104). The deactivation of a Pd/alumina catalyst during the hydrogenation of citral to citronellal, 3,7-dimethyl-2-octenal, and dihydrocitronelal was investigated under reaction conditions at low pressure by use of the flow-through cell described above. The results show that citral as well as the 3,7-dimethyl-2-octenal intermediate are decarbonylated on the palladium surface, resulting in strongly adsorbed CO and C_xH_y -type hydrocarbon fragments. Reactivation of the catalyst with air was only partially successful, indicating that the decarbonylation alone cannot account for the irreversible deactivation observed. The irreversible deactivation was attributed to dimerization and oligomerization products of citral and its partially hydrogenated derivatives, which block the active palladium sites. The results clearly show the limitation of ATR spectroscopy in such investigations, because bands assigned to the dimerization and oligomerization products could not be properly identified. On the one hand, interpretation of spectra can become extremely demanding if various species are involved in the deactivation process, and on the other some species may not exhibit significant vibrational bands, which are necessary for proper assignments.

IX. Other Methods for IR Spectroscopy of Catalytic Solid–Liquid Interfaces

Electrochemists have used IR spectroscopy for many years to probe electrode–electrolyte interfaces (107). The most popular technique is IR reflection absorption spectroscopy (IRRAS) (108). A schematic comparison of the principle of ATR and IRRAS experiments is shown in Fig. 37. One advantage of the ATR over the IRRAS technique for catalytic applications concerns diffusion. In IRRAS experiments, the IR beam passes through a thin liquid film between a window and the sample. This

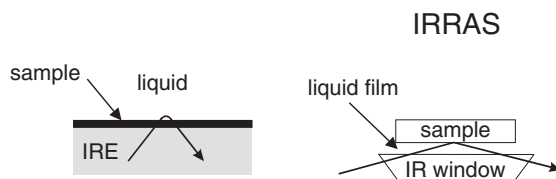


FIG. 37. Schematic comparison between ATR-IR and IR reflection absorption (IRRAS) spectroscopy. In IRRAS, the sample (e.g., an electrode) is typically metallic and reflects the incident IR radiation. The IR beam has to pass through a liquid film twice.

gap has to be kept thin enough that the IR radiation is not fully absorbed, which leads to severe mass transport limitations parallel to the IR window. This is not a problem in ATR spectroscopy, because the solution above the sample can be exchanged rapidly by use of a flow-through cell. IRRAS, on the other hand, has some advantages over ATR as concerns the sample. In ATR experiments, the sample has to be prepared directly on the IRE. In IRRAS experiments, the sample has to be reflecting, which enables the use of structurally well-defined single crystals.

A variant of IRRAS is polarization modulation IR reflection absorption spectroscopy (PM-IRRAS). In this method, the polarization of the IR beam incident on the sample is modulated between parallel and perpendicular polarization. When the sample is metallic, only the parallel-polarized light yields signals from adsorbed molecules, because the electric field amplitude of perpendicular-polarized light vanishes at the metal surface. This statement is the basis for the metal surface selection rule (100,109). When the medium above the sample (gas or liquid phase) is isotropic, both polarizations are equivalent. The PM-IRRAS method thus enables the measurement of signals from adsorbates on a metal surface in the presence of an absorbing gas or liquid phase.

The method has been applied, for example, in electrochemical investigations (110) and also for surface catalytic reactions in the presence of a gas phase (111). When PM-IRRAS is used with a thin-layer cell, as depicted in Fig. 37, the contribution from dissolved molecules in the liquid phase can be minimized. Still, the layer thickness has to be small to prevent complete absorption of the IR radiation by the solvent. The combination of polarization modulation and ATR for metal films was demonstrated recently and applied in an investigation of self-assembled octadecylmercaptan monolayers on thin gold films (112). This combination could emerge as a valuable technique for the investigation of model catalysts.

IR sum frequency generation (SFG), a non-linear optical method (113), has already been applied to characterize catalytic gas–solid interfaces (114,115), and the method also holds promise for solid–liquid interfaces (116). Two laser beams, one in the IR and one in the visible, meet at the sample, where, through the second-order susceptibility, a sum frequency beam is generated. No SFG signals are generated from isotropic media such as bulk gas or liquid phases, and so the method is surface sensitive. Disadvantages of the method are associated with the rather limited accessible spectral range (mostly the C–H and carbon monoxide stretching regions) defined by the tunable IR laser and the relatively long time required to measure a spectrum. Furthermore, the SFG method has been combined with internal reflection (117) for characterization of adsorbed molecules in the presence of water on thin gold films deposited on a sapphire prism.

X. Conclusions

Attenuated total reflection IR spectroscopy is an established tool in a variety of research fields. The theory is well documented, but the application of this method for investigations of catalysts under working conditions has been explored only

recently. The examples discussed above reflect the versatility of the technique for answering a wide range of questions related to heterogeneous catalysis.

ATR-IR spectroscopy can be used as a spy inside a reactor for on-line monitoring and control of a reaction. The emphasis in this kind of application of ATR spectroscopy is on the detection of reactants and products in the bulk fluid phase. Such applications benefit from the excellent time resolution of FTIR instruments compared to other analytical tools, such as chromatographs. The method can be used in investigations of kinetics of reactions in batch reactors; instrumentation has been developed and even commercialized that allows measurements at elevated temperatures and pressures.

An important advantage of ATR-IR spectroscopy, which is hardly rivaled by any other technique, is the possibility it offers to detect species adsorbed at the solid-liquid interface—while the catalyst is working. Several reports demonstrate how in this respect the method is complementary to other analytical methods. For example, products that are not formed in large quantity but adsorb strongly on the catalyst are the predominant species observed in the ATR spectra, but they may be undetectable by analytical tools probing the bulk phase. As a consequence of the strong absorption of IR radiation by metals, ATR spectroscopy is sensitive to changes of the state of metal catalysts, an effect that can be taken advantage of for diagnostic purposes.

The fact that ATR-IR spectroscopy uses an evanescent field and therefore probes only the volume very close to the IRE has important consequences for its application in heterogeneous catalysis, in investigations of films of powder catalysts. The catalyst particle size and packing affect the size of the detectable signals from the catalyst and bulk phase. Furthermore, if the catalyst layer is much thicker than the penetration depth of the evanescent field, diffusion of reactants and products may influence the observed signals. In fast reactions, gradients may exist within the catalyst layer, and ATR probes only the slice closest to the IRE.

Sensitivity and complexity represent challenges for ATR spectroscopy of catalytic solid-liquid interfaces. The spectra of the solid-liquid interface recorded by ATR can comprise signals from dissolved species, adsorbed species, reactants, reaction intermediates, products, and spectators. It is difficult to discriminate between the various species, and it is therefore often necessary to apply additional specialized techniques. If the system under investigation responds reversibly to a periodic stimulation such as a concentration modulation, then a PSD can be applied, which markedly enhances sensitivity. Furthermore, the method discriminates between species that are affected by the stimulation and those that are not, and it therefore introduces some selectivity. This capability is useful for discrimination between spectator species and those relevant to the catalysis. As with any vibrational spectroscopy, the task of identification of a species on the basis of its vibrational spectrum can be difficult, possibly requiring an assist from quantum chemical calculations.

Weighing the potential and limitations of the technique as elaborated in this article—and furthermore on the basis of the fact that the technique and instrumentation are easily accessible, we predict that ATR-IR spectroscopy will become a powerful and widely used tool for the investigation of heterogeneous catalytic reactions occurring in the presence of liquid-phase reactants.

Acknowledgments

The Swiss National Science Foundation and the Foundation Claude & Giuliana are acknowledged for funding.

References

1. Ryczkowski, J., *Catal. Today* **68**, 263 (2001).
2. Bockris, J.O.M., and Kahn, S.U.M., "Surface Electrochemistry: A Molecular Level Approach." Plenum, New York, 1993.
3. Newton, I., "Optics", 2nd Edition; Book III, 1717.
4. Harrick, N.J., *Phys. Rev. Lett.* **4**, 224 (1960).
5. Harrick, N.J., "Internal Reflection Spectroscopy." Interscience Publishers, New York, 1967.
6. Fahrenfort, J., *Spectrochim. Acta* **17**, 698 (1961).
7. Mirabella, F.M., and Harrick, N.J., "Internal Reflection Spectroscopy: Review and Supplement." Harrick Science Corporation, Ossining, NY, 1985.
8. Mirabella, F.M., "Internal Reflection Spectroscopy, Theory and Applications." Dekker, New York/Basel, 1993.
9. Fringeli, U.P., Baurecht, D., Siam, M., Reiter, G., Schwarzott, M., Bürgi, T., and Brüesch, P., in "Handbook of Thin Film Materials." (H.S. Nalwa, Ed.), Vol. 2, p. 191. Academic Press, New York, 2001.
10. Urban, M.W., "Attenuated Total Reflection Spectroscopy of Polymers." American Chemical Society, Washington, DC, 1996.
11. Fringeli, U.P., Baurecht, D., and Günthard, H.H., in "Infrared and Raman Spectroscopy of Biological Materials" (H.U. Gremlich, and B. Yan, Eds.), Dekker, New York/Basel, p. 143, 2000.
12. Fringeli, U.P., and Günthard, H.H. "Molecular Biology, Biochemistry and Biophysics." (E. Grell, Ed.), Springer, Heidelberg, 1981.
13. Born, M., and Wolf, E., "Principles of Optics." 3rd Edition, Pergamon, Oxford, UK, 1979.
14. Fringeli, U.P., in "Internal Reflection Spectroscopy, Theory and Applications" (F.M. Mirabella, Ed.), Dekker, New York, p. 255, 1992.
15. Abelès, F., *Ann. Phys. (Paris)* **11**, 307 (1950).
16. Hansen, W.N., *J. Opt. Soc. Am.* **58**, 380 (1968).
17. Dluhy, R.A., *J. Phys. Chem.* **90**, 1373 (1986).
18. Bürgi, T., *Phys. Chem. Chem. Phys.* **3**, 2124 (2001).
19. Yamamoto, K., and Ishida, H., *Appl. Spectrosc.* **48**, 775 (1994).
20. Hartsein, A., Kirtley, J.R., and Tsang, J.C., *Phys. Rev. Lett.* **45**, 201 (1980).
21. Nishikawa, Y., Fujiwara, K., Ataka, K., and Osawa, M., *Anal. Chem.* **65**, 556 (1993).
22. Osawa, M., and Ataka, K.-I., *Surf. Sci.* **262**, L118 (1992).
23. Osawa, M., and Ikeda, M., *J. Phys. Chem.* **95**, 9914 (1991).
24. Nishikawa, Y., Nagasawa, T., Fujiwara, K., and Osawa, M., *Vib. Spectrosc.* **6**, 43 (1993).
25. Nakao, Y., and Yamada, H., *Surf. Sci.* **176**, 578 (1986).
26. Ferri, D., Bürgi, T., and Baiker, A., *J. Phys. Chem. B* **105**, 3187 (2001).
27. Zhu, Y., Uchida, H., and Watanabe, M., *Langmuir* **15**, 8757 (1999).
28. Johnson, B.W., Bauhofer, J., Doblhofer, K., and Pettinger, B., *Electrochim. Acta* **37**, 2321 (1992).
29. Zippel, E., Kellner, R., Krebs, M., and Breiter, M.W., *J. Electroanal. Chem.* **330**, 521 (1992).
30. Osawa, M., *Bull. Chem. Soc. Jpn.* **70**, 2861 (1997).
31. Ataka, K.-I., Yotsuyanagi, T., and Osawa, M., *J. Phys. Chem.* **100**, 10664 (1996).
32. Osawa, M., and Yoshii, K., *Appl. Spectrosc.* **51**, 512 (1997).
33. Pham, M.-C., Aeiyaich, S., Moslih, J., Soubiran, P., and Lacaze, P.-C., *J. Electroanal. Chem.* **277**, 327 (1990).
34. Miki, A., Ye, S., Senzaki, T., and Osawa, M., *J. Electroanal. Chem.* **563**, 23 (2004).
35. Palik, E.D., "Handbook of Optical Constants of Solids." Academic Press, New York, 1985.
36. Zippel, E., Kellner, R., and Breiter, M.W., *J. Electroanal. Chem.* **289**, 297 (1990).

37. Ishida, K.P., and Griffiths, P.R., *Anal. Chem.* **66**, 522 (1994).
38. Ferri, D., Bürgi, T., and Baiker, A., *Phys. Chem. Chem. Phys.* **4**, 2667 (2002).
39. Ferri, D., Bürgi, T., and Baiker, A., *J. Chem. Soc. Chem. Commun.* 1172 (2001).
40. Ferri, D., and Bürgi, T., *J. Am. Chem. Soc.* **123**, 12074 (2001).
41. Bonalumi, N., Bürgi, T., and Baiker, A., *J. Am. Chem. Soc.* **125**, 13342 (2003).
42. Ferri, D., Bürgi, T., and Baiker, A., *J. Catal.* **210**, 160 (2002).
43. Ferri, D., Bürgi, T., and Baiker, A., *J. Phys. Chem. B* **108**, 14384 (2004).
44. Bonalumi, N., Vargas, A., Ferri, D., Bürgi, T., Mallat, T., and Baiker, A., *J. Am. Chem. Soc.* **127**, 8467 (2005).
45. Bürgi, T., and Bieri, M., *J. Phys. Chem. B* **108**, 13364 (2004).
46. Keresszegi, C., Bürgi, T., Mallat, T., and Baiker, A., *J. Catal.* **211**, 244 (2002).
47. Ortiz-Hernandez, I., and Williams, C., *Langmuir* **19**, 2956 (2003).
48. Bürgi, T., and Baiker, A., *J. Phys. Chem. B* **106**, 10649 (2002).
49. Bürgi, T., Wirz, R., and Baiker, A., *J. Phys. Chem. B* **107**, 6774 (2003).
50. Gisler, A., Bürgi, T., and Baiker, A., *Phys. Chem. Chem. Phys.* **5**, 3539 (2003).
51. Gisler, A., Bürgi, T., and Baiker, A., *J. Catal.* **222**, 461 (2004).
52. Ferri, D., Frauchiger, S., Bürgi, T., and Baiker, A., *J. Catal.* **219**, 425 (2003).
53. Murphy, E.F., Ferri, D., Baiker, A., Van Doorslaer, S., and Schweiger, A., *Inorg. Chem.* **42**, 2559 (2003).
54. Wirz, R., Bürgi, T., and Baiker, A., *Langmuir* **19**, 785 (2003).
55. Degenhardt, J., and McQuillan, A.J., *Chem. Phys. Lett.* **311**, 179 (1999).
56. Degenhardt, J., and McQuillan, A.J., *Langmuir* **15**, 4595 (1999).
57. Dobson, K.D., and McQuillan, A.J., *Spectrochim. Acta A* **55**, 1395 (1999).
58. Dobson, K.D., and McQuillan, A.J., *Spectrochim. Acta A* **56**, 557 (2000).
59. Wirz, R., Bürgi, T., Lindner, W., and Baiker, A., *Anal. Chem.* **76**, 5319 (2004).
60. Ninness, B.J., Bousfield, D.W., and Tripp, C.P., *Appl. Spectrosc.* **55**, 655 (2001).
61. Maxwell-Garnett, J.C., *Philos. Trans. Roy. Soc. A* **203**, 385 (1904).
62. Bruggemann, D.A., *Ann. Phys. (Leipzig)* **24**, 636 (1935).
63. Niklasson, G.A., and Granqvist, C.G., *Appl. Phys.* **55**, 3382 (1984).
64. Grunwaldt, J.D., Caravati, M., Hannemann, S., and Baiker, A., *Phys. Chem. Chem. Phys.* **6**, 3037 (2004).
65. Urakawa, A., Wirz, R., Bürgi, T., and Baiker, A., *J. Phys. Chem. B* **107**, 13061 (2003).
66. Rivera, D., and Harris, J.M., *Anal. Chem.* **73**, 411 (2001).
67. McCain, K.S., and Harris, J.M., *Anal. Chem.* **75**, 3616 (2003).
68. Suer, M.G., Dardas, Z., Lu, Y., Moser, W.R., and Ma, Y.H., *AICHE J.* **43**, 1717 (1998).
69. Moser, W.R., Marshik-Guerts, B.J., and Okrasinski, S.J., *J. Mol. Catal. A: Chem.* **143**, 57 (1999).
70. Moser, W.R., Cnossen, J.E., Wang, A.W., and Krouse, S.A., *J. Catal.* **95**, 21 (1985).
71. Dardas, Z., Stier, M.G., Ma, Y.H., and Moser, W.R., *J. Catal.* **159**, 204 (1996).
72. Wolf, U., Leiberich, R., and Seeba, J., *Catal. Today* **49**, 411 (1999).
73. Pintar, A., Malacea, R., Pinel, C., Fogassy, G., and Besson, M., *Appl. Catal. A General* **264**, 1 (2004).
74. Mul, G., Hamminga, G.M., and Moulijn, J.A., *Vib. Spectrosc.* **34**, 109 (2004).
75. Keresszegi, C., Ferri, D., Mallat, T., and Baiker, A., *J. Phys. Chem. B* **109**, 958 (2005).
76. Schneider, M.S., Grunwaldt, J.D., Bürgi, T., and Baiker, A., *Rev. Sci. Instrum.* **74**, 4121 (2003).
77. Fischer, A., Maciejewski, M., Bürgi, T., Mallat, T., and Baiker, A., *J. Catal.* **182**, 373 (1999).
78. Fischer, A., Mallat, T., and Baiker, A., *Angew. Chem. Int. Ed.* **38**, 351 (1999).
79. Schneider, M.S., Urakawa, A., Grunwaldt, J.D., Bürgi, T., and Baiker, A., *J. Chem. Soc. Chem. Commun.* 744 (2004).
80. Mallat, T., and Baiker, A., *Catal. Today* **19**, 247 (1994).
81. Besson, M., and Gallezot, P., *Catal. Today* **57**, 127 (2000).
82. Gelin, P., Siedle, A.R., and Yates, J.T., *J. Phys. Chem.* **88**, 2978 (1984).
83. Ko, M.K., and Frei, H., *J. Phys. Chem. B* **108**, 1805 (2004).
84. Wachs, I.E., *Top. Catal.* **8**, 57 (1999).
85. Feinleib, J., *Phys. Rev. Lett.* **16**, 1200 (1966).

86. Hansen, W.N., and Probst, A., *Phys. Rev.* **174**, 500 (1968).
87. McIntire, J.D.E., *Surf. Sci.* **37**, 658 (1973).
88. Brodsky, A.M., Daikhin, L.I., and Urbakh, M.I., *J. Electroanal. Chem.* **171**, 1 (1984).
89. Ho, K.M., Fu, C.L., Liu, S.H., Kolb, D.M., and Piazza, G., *J. Electroanal. Chem.* **150**, 235 (1983).
90. Cosimo, R.D., and Whitesides, G.M., *J. Phys. Chem.* **93**, 768 (1989).
91. Baurecht, D., and Fringeli, U.P., *Rev. Sci. Instrum.* **72**, 3782 (2001).
92. Muller, M., Buchet, R., and Fringeli, U.P., *J. Phys. Chem.* **100**, 10810 (1996).
93. Fringeli, U.P., Goette, J., Reiter, G., Siam, M., and Baurecht, D., in "Fourier Transform Spectroscopy: 11th International", (J.A. deHaseth, Ed.), American Institute of Physics, Vol. AIP Conference Proceedings 430, 1998.
94. Schneider, M.S., Grunwaldt, J.D., and Baiker, A., *Langmuir* **20**, 2890 (2004).
95. Baiker, A., *Chem. Rev.* **99**, 453 (1999).
96. Bürgi, T., *J. Catal.* **229**, 55 (2005).
97. Mallat, T., and Baiker, A., *Catal. Today* **24**, 143 (1995).
98. Simons, K.E., Meheux, P.A., Griffiths, S.P., Sutherland, I.M., Johnston, P., Wells, P.B., Carley, A.F., Rajumon, M.K., Roberts, M.W., and Ibbotson, A., *Recl. Trav. Chim. Pays-Bas* **113**, 465 (1994).
99. Evans, T., Woodhead, A.P., Gutierrez-Soza, A., Thornton, G., Hall, T.J., Davis, A.A., Young, N.A., Wells, P.B., Oldman, R.J., Plashkevych, O., Vahtras, O., Agren, H., and Carravetta, V., *Surf. Sci.* **436**, L691 (1999).
100. Greenler, R.G., *J. Chem. Phys.* **44**, 310 (1966).
101. Schuerch, M., Schwalm, O., Mallat, T., Weber, J., and Baiker, A., *J. Catal.* **169**, 275 (1997).
102. Caravati, M., Grunwaldt, J.D., and Baiker, A., *Phys. Chem. Chem. Phys.* **7**, 278 (2005).
103. Caravati, M., Grunwaldt, J.D., and Baiker, A., *Appl. Catal. A* **298**, 50 (2006).
104. Burger, M., Wirz, R., Mallat, T., and Baiker, A., *J. Catal.* **228**, 152 (2004).
105. Ferri, D., Diezi, S., Maciejewski, M., and Baiker, A., *Appl. Catal. A* **297**, 165 (2006).
106. Kereszegi, C., Ferri, D., Mallat, T., and Baiker, A., *J. Catal.* **234**, 65 (2005).
107. Beden, B., and Lamy, C., "Spectroelectrochemistry." Plenum, New York, 1989.
108. Greenler, R.G., *J. Phys. Chem.* **44**, 310 (1966).
109. Francis, S.A., and Ellison, A.H., *J. Opt. Soc. Am.* **49**, 131 (1959).
110. Saez, E.I., and Corn, R.M., *Electrochim. Acta* **38**, 1619 (1993).
111. Ozensoy, E., Hess, C., and Goodman, D.W., *J. Am. Chem. Soc.* **124**, 8524 (2002).
112. Hutter, E., Assiongon, K.A., Fendler, J.H., and Roy, D., *J. Phys. Chem. B* **107**, 7812 (2003).
113. Shen, Y.R., "The Principles of Nonlinear Optics." Wiley, New York, 2002.
114. Cremer, P.S., Su, X.C., Shen, Y.R., and Somorjai, G.A., *J. Phys. Chem.* **100**, 16302 (1996).
115. Rupprechter, G., Unterhalt, H., Morkel, M., Galletto, P., Dellwig, T., and Freund, H.J., *Vacuum* **71**, 83 (2003).
116. Chen, Z., Gracias, D.H., and Somorjai, G.A., *Appl. Phys. B—Lasers Opt.* **68**, 549 (1999).
117. Williams, C.T., Yang, Y., and Bain, C.D., *Langmuir* **16**, 2343 (2000).

Index

A

- Acetone, 253, 259, 265
- Acid-catalyzed reactions, transition states of
carbenium ions, 172–179
keto–enol isomerization, on acidic zeolite
HZSM-5, 180–182
- Acidic zeolite
aniline alkylation, 200–203
aromatic compounds alkylation, 196–205
hydrocarbon pool compounds formation on,
215–216
keto–enol isomerization, 180–182
methoxy species preparation on, 209–210
MTBE synthesis on, 194–196
MTHC conversion on, 205–216
surface methoxy species formation on, 207–209
- Adsorbed species, 254
identification, 255–256
- Adsorption mode elucidation, 271–274
- Alcohol oxidation, 241, 268
- Aldol condensation, 180, 181
- Alkylation
of toluene, 196–198
of aniline, 198–203
- ²⁷Al MAS NMR spectra, 182–183, 191, 192
- ²⁷Al spin-echo NMR spectroscopy, 188–189
- Ammonia synthesis catalyst
complex nanostructure of, 84–86
- Aniline alkylation, 198–203
on acidic zeolite HY, 200–203
on basic zeolite CsOH/Cs₂NaY, 199–200
- Aromatic compounds alkylation
on acidic and basic zeolites, 196–205
- Atomic force microscope (AFM)
of insulating materials, 141
- Atomic-scale imaging, of supported metal
nanocluster catalysts, 77
catalysts characterization, in reactive
atmospheres, 80–84
HRTEM, in reactive atmospheres, 84–91
transmission electron microscopy (TEM),
79–80
- Atom-resolved STM image, *see also* STM image
of atomic-hydrogen-pretreated MoS₂ cluster,
128
of CoMoS nanocluster, 133
of triangular single-layer MoS₂ nanocluster,
119, 126
of ultrathin RuO₂(1 1 0) film, 140
- Attenuated total reflection (ATR) IR
spectroscopy
adsorption mode elucidation, 271–274
catalyst deactivation, 278
cell design, 242–251
complex reaction network, at catalytic
solid–liquid interface, 275–277
fundamentals, 229–234
for *in situ* investigations, in catalysis, 234–242
phase behavior investigation, in catalytic
reaction, 274–275
potential and limitations, 251–259
of solid catalysts, with liquid-phase reactants,
227
specialized techniques, 259–268
and UV–vis spectroscopy, 268–271
- Au(1 1 1), 117–119, 125, 133
MoS₂ nanoclusters on, 116–117

B

- B₅-type sites, 85
- Barium-promoted ruthenium nanocrystals, 85
- Basic zeolites
aniline alkylation, 199–200
aromatic compounds alkylation, 196–205
- 4-bromobenzoic acid, 59
- Brunauer Emmett Teller (BET) isotherm, 34
- Bubble-train flow, *see* Taylor flow
- Bulk rare medium
electric field components, 230–232
- t*-Butyl hydroperoxide (TBHP), 256, 261

C

- Capacitance tomography, 54
- Carbenium ions
existence, by trapping experiments, 175–177
indirect experimental evidence of, 172–179
in zeolites characterized by NMR spectroscopy,
179
- Carbon nanofiber growth
in steam reforming catalysts, 89–91

- Catalyst deactivation, 278
- Catalyst pellets
 catalyst preparation, 34–35
 coke deposition, 37–38
 liquid redistribution during reaction, 35–37
 microimaging studies of, 2–3
 structure–transport relationships, 32–34
- Catalyst samples preparation
 for MAS NMR investigation, under batch
 reaction conditions, 162
 in MAS NMR rotor, 163
 under shallow-bed conditions, 163
- Catalysts and catalytic processes, MRI of, 1
 catalyst pellets imaging, 32–38
in situ reactions imaging, 59–70
 MRI techniques, 5–32
 reactors, hydrodynamics in, 38–59
- Catalysts characterization, in reactive
 atmospheres
 differentially pumped TEM instruments, 80–83
 thin-window cells, 84
- Catalytic solid–liquid interface, 228, 254, 259, 263,
 264, 273, 275, 280
 complex reaction network investigation,
 275–277
 IR reflection absorption spectroscopy
 (IRRAS), 278–279
 IR sum frequency generation (SFG), 279
- Catalytic transformation of methane into
 aromatics
 under non-oxidative conditions, 182–183
- ^{13}C CF MAS NMR spectrum, 198, 199, 208
- ^{13}C distortionless enhancement by polarization
 transfer (DEPT) spectroscopy, 65–70
- Cell design, for IRE/ATR
 flow-through cell, 245–248
 high-pressure view cell, 248–251
 on-line process control and reaction
 monitoring, 242–245
- Ceramic monoliths, 20
 two-phase flow, 52–57
- CF MAS NMR spectroscopy, 165, 197–198,
 213
- Chemical information obtaining
 by MRI technique, 19–22
- Chemical shift imaging (CSI), 19, 22
n-dimensional, 20–21
- Chiral modifier, 271–274
- Chlorine-containing organic compounds on
 titanium oxide
 photocatalytic conversion of, 186–187
- ^{13}C imaging, probing selectivity with, 65–68
- Cinchonidine (CD), 271–273
- ^{13}C magnetization, 66
- ^{13}C MAS NMR spectroscopy, 177, 178, 194,
 203–204, 205
- Cobalt-promoted catalyst
 atomic-scale structure, 133–134
- Coherent transport process, 15
- Coke deposition, 37–38
- Coking, 38, 106
- Co–Mo structures (CoMoS), 133–134
- Constant-current STM images, 102, 105
- Convection–diffusion model, 245–248
- Coordinatively unsaturated sites (CUS), 115
- Copper nanoclusters, 86
- Cross polarization (CP) experiment, 157, 171
- Crowded spectra, 263, 264
- Cryogenic adsorption vessel enabling rotor
 nestling (CAVERN), 161
- Cu/ZnO-containing methanol synthesis catalysts
 gas-induced shape changes in, 86–88
- Cyclohexane, 35
- D**
- DANTE method, 19
- Density functional theory (DFT), 85, 90–91, 105,
 107, 108, 110–111, 121, 122, 129
- 2-D flow images, 43
- Dichroic ratio, 231–232
- Differentially pumped TEM instruments, 80–83
- Differential pumping system, 81–82, 84, 92–93
- Diffusion layer model, 245, 247
- n*-dimensional CSI, 20–21
- Drude model, 258
- Dynamic liquid holdup, 48–49
- E**
- Echo planar imaging (EPI), 26–28
- Edge states, 122, 134
 metallic, 129–133, 135
- Effective medium theories, 239
- Effective thickness
 in hypothetical transmission experiment, 230
- Electric field components
 in bulk rare medium, 230–232
- Electron energy loss spectroscopy (EELS), 79, 85,
 87, 92
- Energetics and reaction pathways, 129–133
- Energy dispersive X-ray spectroscopy (EDS), 79
- Energy loss near edge structure (ELNES), 87
- Esterification reaction, 60–65
- Ethane hydrogenolysis, 112
- Evanescent field, 229, 230, 240, 243, 280
 wave, penetration depth, 229–230
- Ex situ* TEM, *see Quasi in situ* TEM

Extended X-ray absorption fine structure (EXAFS) spectroscopy, 87, 108, 113

F

Fast data acquisition, MRI technique, 25–32
 Fast low-angle shot (FLASH) imaging, 30
 Field emission gun (FEG), 81
¹⁹F imaging, 59
 Fixed-bed reactors
 high spatial resolution of fluid flow, 39–43
 single-phase flow, 39–45
 single-phase reactions, 60–68
 two-phase flow, 45–52, 68–70
 two-phase reaction, 68–70
 unsteady-state flow, 43–45
 FLASH MRI technique, 57–58
 Flow imaging, 5, 41
 and microimaging of reactors, 3–4
 Flow technique, MAS NMR spectroscopy, 171–172
 Flow-through cell, 245–248, 279
 Fluidized beds, 57–59
 Fourier transform IR (FTIR) spectrometers, 245, 266–267
 Free induction decay (FID), 6, 7
 Frequency-encoding gradient, 12
 Fresnel reflection coefficient, 233–234

G

Gas chromatography (GC) analysis, 254, 277
 Gas-fluidized-bed reactor, 57
 Gas-phase MRI, 24
 Gas reactor and solid sample hopper (GRASSHopper) device, 168–169
 Ge IRE, 235, 241
 GERVAIS, 27–28, 44
 Glass ampoules preparation
 equipment for, 161
 Gold/nickel surface alloy catalyst
 for steam reforming, 106–109
 Graphene sheet, 90

H

HDS model catalyst, with STM, 113, 115–119
 hydrotreating catalyst structure and reactivity, 113–115
 MoS₂ nanoclusters, atomic-scale structure of, 119–123
 MoS₂ nanoclusters, preparation, 117–119
 MoS₂ nanoclusters, support on Au(1 1 1), 116–117
 single-layer MoS₂ nanoclusters, 124–135

Herringbone reconstruction forms, 116
 Heterogeneous catalysis
 ATR spectroscopy strength, 254–255
 Hexachloroplatinate dianion, 35
 Hexamethylbenzenium ions, 216
 High-pressure view cell, 248–251
 High-resolution TEM (HRTEM), 77, 78, 80, 82, 84–91, 91–93
¹H MAS NMR spectroscopy, 178, 185
¹H microimaging, 35
¹H nucleus, 59
 Holdup efficiency, trickle flow, 45–49
 Homonuclear linewidth, 155
 Homonuclear magnetic dipole–dipole interaction, 155
 HRTEM characterization of catalysts, in reactive atmospheres
 ammonia synthesis catalyst, 84–86
 carbon nanofiber growth in steam reforming catalyst, 89–91
 Cu/ZnO-containing methanol synthesis catalyst, 86–88
 HRTEM image, 78, 80, 84, 85, 90, 92
 of barium-promoted ruthenium nanocrystals, 85
 of Cu/ZnO model catalyst, 87
 H-SAPO-34, 190–194
 H-SAPO-37, 190–194
 Hydrocarbon pool characterization, 213–215
 on acidic zeolites, 215–216
 Hydrodenitrogenation (HDN) process, 135
 Hydrodynamics, in reactors
 fluidized beds, 57–59
 single-phase flow, 39–45
 two-phase flow, in ceramic monoliths, 52–57
 two-phase flow, in fixed bed reactors, 45–52
 Hydrotreating catalyst, 113
 metallic brim states as active sites in, 135
 structure and reactivity, 113–115
 Hyperpolarization, 24

I

Imaging
 atomic-scale, 77, 84
 chemical shift imaging (CSI), 19, 20–21
 echo planar, 26–28
 FLASH/SNAPSHOT, 30
 HRTEM, 80, 84–85, 92
 individual catalyst pellets, 32–38
 low excitation angle, 30–32
 MRI technique, 3, 5–7
 of reactions *in situ*, 59–70
 spin-density, 33
 of surfaces with STM, 138–141

- TEM, 89, 92
 TOF, 18
 unsteady-state flows, in fixed-bed reactors, 43–45
 volume-selective, 21–22
 Incoherent transport process, 15
 Infrared (IR) spectroscopy, 228
 ATR, 228, 256, 259, 271, 278, 280
 of catalytic solid–liquid interfaces, 278–279
In situ ^{13}C MAS NMR spectroscopy, 177, 178, 187
In situ reactions imaging, 59–70
 single-phase reactions, in fixed beds, 60–68
 two-phase flow and reaction, in fixed beds, 68–70
 Internal reflection element (IRE), 229, 230, 234, 238, 241, 245, 247, 261, 268, 279, 280
 IR reflection absorption spectroscopy (IRRAS), 278
 PM-IRRAS, 279
 Isotope scrambling, 177–179
 Isotopic labeling, 177, 182
 Isotropic chemical shift, 153
- K**
- Keto–enol isomerization
 on acidic zeolite HZSM-5, 180–182
 Ketopantolactone (KPL), 273
 Koch reaction, 176
k-space raster, 10–13
- L**
- Larmor frequency, 5, 6, 19, *see also* Resonance frequency
 Laser heating technique, 165
 Lattice-Boltzmann code, 43
 Liquid holdup, 46–49
 Local density of states (LDOS), 102–104
 Local pulses, 51, 52
 Low excitation angle imaging, 30–32
 Lysozyme–urea separation, 29
- M**
- Macroscopic models, 50
 Magic-angle hopping (MAH) experiment, 168–169
 Mars-van Krevelen mechanism, 139
 MAS NMR rotor reactor, 166
 MAS NMR spectroscopy, of working catalyst, 160–172
 batch conditions, 161–165
 flow conditions, 165–170
 Medical imaging magnet technology, 3–4
 Methane into aromatics, catalytic transformation of, 182–183
 Methanol to hydrocarbons (MTHC) conversion on acidic zeolites, 189, 205–216
 Methanol to olefin (MTO) process, 205
 investigation, under steady-state conditions, 212–216
N-methylethaniline, 200
 Methyl *tert*-butyl ether (MTBE) synthesis on acidic zeolites, 194–196
 on boron-modified pentasil, under batch conditions, 194–195
 on zeolite H-beta, under CF conditions, 195–196
 Microimaging, 5
 and flow imaging of reactors, 3–4
 Microporous silicoaluminophosphates
 chemical behavior and local structure of, 190–194
 Microscopic models, 50
 Model catalyst, 234
 surface investigation, by STM, 97
 Modulation excitation spectroscopy (MES), 259–263
 advantages, 263–264
 Molybdenum, 114, 115, 117, 120, 121, 127, 134
 Moments of magnetic field gradient, 16
 MoS₂ nanoclusters
 atomic-scale structure, 119–123
 Au(1 1 1), supported on, 116–117
 fundamental characterization, 119–120
 hydrogen-activated, 125–127, 127–129
 morphology and edge structure, 120–123
 preparation, 117–119
 single-layer, 124–135
 thiophene on, 124–125, 127–129
 MRI techniques, 5–32
 contrast mechanisms, 19–24
 fast data acquisition, 25–32
 gas-phase MR, 24–25
 MR measurements principles, 5–13
 temperature, 24
 transport processes measurement, 13–19
 MTO process investigation
 under steady-state conditions, 212–216
 Multiphase heterogeneous catalytic reaction
 phase behavior investigation, 274–275
- N**
- Nafion, silica supported, 244
 Navier–Stokes equations, 50
 Nickel(1 1 1) surface, 107, 109, 111

Nickel catalysts, 108–109
 designing, by step blocking, 110–112
Nickel step edges, 90
Nuclear spin
 relaxation times, 7–10
 solid-state interactions of, 151–154

O

On-line process control and reaction monitoring
 for ATR spectroscopy, 242–245
Oxygenates on titanium oxide
 photocatalytic conversion of, 187–188

P

Palladium, 256–257, 263
Phase encoding gradient, 12–13
Phase-encoding methods, 13–18
Phase shift measurements of transport,
 see Phase-encoding methods
Phase-sensitive detection (PSD), 259–261
Photocatalytic conversion
 of chlorine-containing organic compounds on
 titanium oxide, 186–187
 of oxygenates on titanium oxide, 187–188
Photocatalytic reactions
 on solid catalysts, 185–188
Polarization modulation IRRAS (PM-IRRAS),
 279
Poppy seeds, granular bed of, 58
Powder catalysts, 238–242
Pressure gap, 138
Propagator measurement, 17–18
Propane activation and aromatization
 on solid acid catalysts, 183–185
2-Propanol oxidation, 253–254, 259, 265
Propionic-acid-butyl-ester, 63
2-Propoxide, 265
Pulsed field gradient (PFG), 2, 13–15
Pulsed gradient spin echo (PGSE) MR, 15

Q

Quadrupole coupling constant, 153–154
Quarternary ammonium ions in zeolites
 synthesis and immobilization, 203–205
Quasi in situ TEM, 79–80
Quinoline moiety, 271

R

Rapid acquisition with relaxation enhancement
 (RARE), 28–30
Rapid image acquisition, MRI, 19

Reaction intermediates, 132, 255–256
Reactive atmospheres
 catalysts characterization, 80–84
 HRTEM characterization of catalysts, 84–91
Reactors
 hydrodynamics in, 38–58
 microimaging and flow imaging of, 3–4
Read gradient, *see* Frequency-encoding gradient
Relaxation and transport contrast, 22–24
Relaxometry experiment, 9
Reproducibility, of metal films, 238
Resonance frequency, 5–6, 7, 24, *see also* Larmor
 frequency
Reynolds number (Re), 27, 40, 41
Rubidium, 158

S

Saturated hydrocarbons activation
 on solid catalysts, 182–185
Scanning-TEM (STEM), 78, 92
Scanning tunneling microscopy (STM), 97–106
 atomic force microscopy, of insulating
 materials, 141
 design considerations, 101–102
 gold/nickel surface alloy catalyst, for steam
 reforming, 106–109
 HDS model catalyst, investigations with,
 113–135
 model catalyst surfaces, 97
 nickel catalyst designing, by step blocking,
 110–112
 surfaces imaging, during reaction, 138–141
 Tersoff–Hamann theory, 103–105
 theory, 102–106
 time-resolved investigations, 135–138
SEMI-RARE, 55–56, 56, 57
SF MAS NMR spectroscopy, 200, 210
Shrinking-core model, 38
Signal enhancement techniques, 65, 156–159
Signal-to-noise ratio
 temperature effect, 158–159
Single-beam signal reference (SBSR),
 266–268
Single catalyst pellets, microimaging studies of,
 2–3
Single-pore models, *see* Microscopic models
Slice selection phase, 12
SNAPSHOT imaging, *see* Fast low-angle shot
 imaging
Solid catalyst characterization in functioning state
 by NMR spectroscopy, 149
Solid catalysts, 98
 ATR-IR spectroscopy, with liquid-phase
 reactants, 227

- photocatalytic reactions on, 185–188
 - saturated hydrocarbons activation, 182–185
 - Solid-state NMR spectroscopy, 149
 - discrimination, 156–158
 - at elevated temperatures, 158–160
 - limitations and advantages, for investigations of working catalyst, 170–172
 - MAS techniques, 154–156
 - principles, 151–160
 - Spin-density map, 32
 - Spin-echo phase encoded velocity, 43–44
 - Spin isochromat, 9
 - Spin-lattice relaxation process, 7–9, 32, 33
 - Spin-spin relaxation process, 7, 9–11
 - Spin tagging methods, *see* Time-of-flight methods
 - SPRITE, 38
 - Steam reforming catalysts
 - carbon nanofiber growth, 89–91
 - gold/nickel surface alloy catalyst, 106–109
 - STM image, 119, *see also* Atom-resolved STM image
 - of Au(1 1 1) surface, 116
 - of C₄H₇S molecules, 129, 130
 - constant-current, 100, 102
 - of hydrogen-saturated Pd(1 1 1) surface, 137
 - of molybdenum deposited on Au(1 1 1) surface, 117
 - of MoS₂ nanoclusters, 119–120, 124, 127–128, 132
 - of nickel(1 1 1) surface, 107, 110, 111–112
 - of nitrogen atom adsorbates on Fe(1 0 0) surface, 104
 - of oxygen pre-covered platinum(1 1 1) surface, 136
 - of platinum film electron beam, 236
 - simulation of, 105–106
 - of thiophene on triangular MoS₂ nanoclusters, 124
 - Stratified media, spectra simulation of, 232–234
 - Sulfonic acid resins, 194
 - Sum frequency generation (SFG), 279
 - Supercritical CO₂, 268, 274–275
 - SuperTwin objective lens, 81
 - Supported metal nanocluster catalysts, atomic-scale imaging of, 77
 - Surface alkoxy species, with carbenium-ion-like properties
 - formation, 173–175
 - Surface enhanced IR absorption (SEIRA), 235
 - Surface ethoxy species, 174–175
 - Surface methoxy species, 207–212
 - formation, during conversion of methanol to DME, 207–209
 - higher hydrocarbons formation by, 211–212
 - preparation, on acidic zeolites by SF technique, 209–210
 - role, in the formation of DME, 210
- T**
- Taylor flow, 55
 - TEM instruments, differentially pumped, 80–83
 - Temperature calibration
 - solid-state NMR spectroscopy, 159–160
 - Temperature-jump MAS NMR technique, 194
 - Tersoff–Hamann STM theory, 103–105
 - Thin metal films, 234–238
 - Thiophene, 132
 - on fully sulfided MoS₂ nanoclusters, 124–125
 - hydrogen-activated MoS₂ nanoclusters, reaction on, 127–129
 - Time-of-flight (TOF) methods, 18–19
 - Time-resolved spectroscopy, 265–266
 - Time-resolved STM, 135–138
 - Titanium oxide (TiO₂), 186–188
 - Toluene alkylation, 196–198
 - Transfer Hamiltonian approach, 103
 - Transfer of population in double resonance (TRAPDOR) experiment, 156
 - Transition states
 - of acid-catalyzed reactions, 172–182
 - Transmission electron microscopy (TEM), 78, 89, 99
 - limitations in catalysts characterization, 79–80
 - Transport processes measurement
 - phase-encoding methods, 13–18
 - rapid image acquisition, 19
 - time-of-flight (TOF) methods, 18–19
 - Trichloroethylene (TCE), 186–187
 - Trickle-bed reactors, 45, 50, 69
 - Trickle flow
 - holdup and wetting in, 45–49
 - to pulse flow transition, 50–52
 - N,N,N*-trimethylanilinium ions, 200–202
 - Tunneling, 100, 106
- U**
- UHV-compatible Aarhus STM instrument, 102
 - UV/Vis spectroscopy, 172
 - and ATR-IR spectroscopy, 268

V

Vespe[®], 167–168
Vibrational spectroscopy, 228
Volume-selective spectroscopy, 19, 21–22, 60

W

Wetting efficiency, trickle flow, 45–49
Wulff constructions, 88

Z

Zeolites
 chemical behavior and local structure,
 188–190
 persistent carbenium ions in,
 179
 quarternary ammonium ions in,
 203–205
ZnSe IRE, 238, 248, 250, 261

Contributors

Numbers in parentheses indicate the pages on which the author's contributions begin.

- ALFONS BAIKER, *Institute for Chemical and Bioengineering, Department of Chemistry and Applied Biosciences, ETH Zürich, Hönggerberg, HCI CH-8093 Zürich, Switzerland (227)*
- F. BESENBACHER, *Interdisciplinary Nanoscience Center (iNANO), Department of Physics and Astronomy, University of Aarhus, DK-8000 Aarhus C, Denmark (97)*
- THOMAS BÜRGI, *Institut de Microtechnique, Université de Neuchâtel, Rue Emile-Argand 11, 2009-Neuchâtel, Switzerland (227)*
- ABHAYA K. DATYE, *Department of Chemical and Nuclear Engineering, University of New Mexico, MSC 01-1120, Albuquerque, NM 87131-0001, USA (77)*
- LYNN F. GLADDEN, *Department of Chemical Engineering, University of Cambridge, Pembroke Street, Cambridge CB2 3RA, UK (1)*
- POUL L. HANSEN, *Haldor Topsøe A/S, Nymøllevvej 55, DK-2800 Kgs. Lyngby, Denmark (77)*
- STIG HELVEG, *Haldor Topsøe A/S, Nymøllevvej 55, DK-2800 Kgs. Lyngby, Denmark (77)*
- M. HUNGER, *Institute of Chemical Technology, University of Stuttgart, D-70550 Stuttgart, Germany (149)*
- J. V. LAURITSEN, *Interdisciplinary Nanoscience Center (iNANO), Department of Physics and Astronomy, University of Aarhus, DK-8000 Aarhus C, Denmark (97)*
- MICHAEL D. MANTLE, *Department of Chemical Engineering, University of Cambridge, Pembroke Street, Cambridge CB2 3RA, UK (1)*
- ANDREW J. SEDERMAN, *Department of Chemical Engineering, University of Cambridge, Pembroke Street, Cambridge CB2 3RA, UK (1)*
- W. WANG, *State Key Laboratory of Applied Organic Chemistry, Lanzhou University, 730000 Gansu, P.R. China (149)*

Preface

For more than five decades, the methods of surface physics and chemistry have provided some of the most incisive results advancing our understanding of the catalytic action of solids at the molecular scale. Characterizations by physical methods have demonstrated the dynamic nature of catalyst surfaces, showing that their structures, compositions, and reactivities may all be sensitive to temperature and the composition of the reactive environment. Thus, the most insightful catalyst characterizations are those of catalysts as they function. This volume of *Advances in Catalysis* is dedicated to the topic of physical characterization of solid catalysts in the functioning state. Because the literature of this topic has become so extensive, the representation will extend beyond the present volume to the subsequent two volumes of the *Advances*.

The literature of this subject has generated its share of jargon, which has been held to a minimum in the following contributions. The term *in-situ* is widely used to describe catalyst characterization experiments, but with inconsistent meanings. We suggest that it might be best to use this term to describe experiments with strict control of all parameters that might affect the surface properties of a catalyst, whether or not a catalytic reaction may be operative. We have preferred to minimize use of this term and to refer explicitly to functioning, working, or operating catalysts when appropriate. Alternatively, the term *operando* has been applied (e.g., B. M. Weckhuysen, *Phys. Chem. Chem. Phys.* **5**, 4351 (2003)) to the characterization of catalysts by spectroscopic methods with simultaneous measurements of catalytic activity (and/or selectivity and/or stability). Unfortunately, many authors have used this term more loosely, for example, without reporting any catalyst performance data, and it seems to be at risk of becoming as vague in usage as “in situ;” we largely avoid it in this set of volumes.

It is generally desirable to integrate measurements representing a working catalyst surface with measurements that characterize the activity, selectivity, and/or stability of the catalyst, such as can be determined by use of gas chromatography or mass spectrometry of products. It is important to keep in mind that when a reactor is designed to serve optimally as a cell for measurements of catalyst surface properties, it may not be the kind of ideal reactor that would provide activity, selectivity, or stability data that can be interpreted fundamentally in terms of kinetics and chemical reaction engineering.

The growing interest in physical characterization of solid catalysts as they function has stimulated a new series of congresses, the first held in Lunteren (The Netherlands) in 2003 and the second in Toledo in 2006. The subject has been documented in recent books (B. M. Weckhuysen, Ed., "In situ Spectroscopy of Catalysts," American Scientific Publishers, 2004, and J. F. Haw, Ed., "In situ Spectroscopy in Heterogeneous Catalysis," Wiley-VCH, 2002) and in topical issues of journals: *Top. Catal.* **15** (2001); *Phys. Chem. Chem. Phys.* **5**, issue 20 (2003); and *Catal. Today* **113** (2006). It is our intention that our set of volumes be more nearly comprehensive than these publications, as well as providing many newer results.

In the present volume, Gladden, Mantle, and Sederman summarize the application of magnetic resonance imaging techniques to represent both local flow fields in reactors containing solid catalyst particles and conversions within model reactors. The techniques provide a non-invasive, chemically specific measurement technique that leads to representation of a reactor over length scales ranging from Angstroms to centimeters.

Hansen, Helveg, and Datye report on atomic-scale imaging of supported metal nanocluster catalysts in the working state. High-resolution transmission electron microscopy allows atomic-resolution imaging of transition metal catalysts during exposure to reactive gases at elevated temperatures, providing insights into the structure, morphology, and dynamics of supported catalysts with various surfaces and interfaces as they function. Examples include evidence of the location of a barium promoter in a ruthenium catalyst for ammonia synthesis and environment-induced morphology changes in supported copper catalysts for methanol synthesis.

Lauritsen and Besenbacher summarize research on model catalyst surfaces investigated by scanning tunneling microscopy (STM). They show atomic-scale information obtained by STM elucidating the formation of surface alloys; wetting; blocking of reactive step edges; and identification of electronic states at the edges of nanoclusters. These results have helped to guide the preparation of new high-surface-area catalysts.

Hunger and Wang provide an account of advances in the characterization of solid catalysts in the functioning state by nuclear magnetic resonance spectroscopy. Examples include investigations of zeolite-catalyzed reactions with isotopic labels that allow characterization of transition states and reaction pathways as well as characterization of organic deposits, surface complexes, and reaction intermediates formed in catalyst pores.

Bürgi and Baiker summarize progress in the application of attenuated total reflection infrared spectroscopy for investigation of solid catalysts functioning in the presence of liquid-phase reactants. The technique allows the detection of liquid-phase products and the investigation of species adsorbed on catalysts during reaction, even in the presence of strongly adsorbing solvents. Under some conditions, changing catalyst structures can be investigated with this technique.

H. KNÖZINGER
B. C. GATES